



University of Naples Federico II

Department of Structures for Engineering and Architecture

# The effect of vegetation on slope stability of shallow pyroclastic soil covers

By

Ana Sofia Rodrigues Afonso Dias

Thesis to obtain the degree of *Doctor of Philosophy* in  
**Structural, Geotechnical and Seismic Engineering**

XXXI Cycle

Supervisor: Prof. Gianfranco Urciuoli

Co-supervisor: Dr. Alexia Stokes

February 2019

**THÈSE POUR OBTENIR LE GRADE DE DOCTEUR  
DE L'UNIVERSITÉ DE MONTPELLIER**

**En Ecologie Fonctionnelle et Sciences Agronomiques**

**École doctorale GAIA**

**Unité de recherche AMAP**

**En partenariat international avec University of Naples Federico II, Italy**

**THE EFFECT OF VEGETATION ON SLOPE  
STABILITY OF SHALLOW PYROCLASTIC  
SOIL COVERS**

**Présentée par Ana Sofia RODRIGUES AFONSO DIAS**

**Le 25 Janvier 2019**

**Sous la direction de Gianfranco URCIUOLI  
et Alexia STOKES**

**Devant le jury composé de**

**Domenico GALLIPOLI, Prof., UPPA**

**Enrique ROMERO MORALES, Prof., UPC**

**Jan Willem VAN DE KUILEN, Prof., TUM**

**Michele CALVELLO, Prof., UNISA**

**Roberto VASSALO, Prof., UNIBAS**

**Wolfgang GARD, Dr., TU Delft**

**Examineur**

**Examineur**

**Examineur**

**Examineur**

**Examineur**

**Examineur**



**UNIVERSITÉ  
DE MONTPELLIER**

# Abstract

The effect of the local vegetation, composed of cultivated *Castanea sativa*, on slope stability was investigated on a test site in Mount Faito (Campania, Southern Italy). In Campania, shallow pyroclastic soil covers are susceptible to landslides triggered by rainfall. Prolonged rainfall periods followed by heavy short-term rainfall events trigger fast moving and highly destructive landslides in road cuts and pyroclastic scarps on rocky cliffs in the areas surrounding the Vesuvius volcano.

Undisturbed pyroclastic soil samples containing roots of mature *C. sativa* were used for hydraulic characterization through an extensive set of laboratory experiments. Saturated permeability, evaporation and imbibition response, water content for high suction ranges, and the root dry biomass were determined.

The presence of roots increased the hydraulic permeability by one order of magnitude in the most surficial soil ( $10^{-7}$  to  $10^{-6}$  m s<sup>-1</sup>) and decreased the air-entry value of the water retention curves (6 to 4 kPa). The variability of soil permeability among soil layers was identified as conditioning of the groundwater flow with regard to the speed of the wetting front movement and generation of positive pore-water pressures within the soil profile. The calibration of hysteretic model to characterize natural pyroclastic soil provided a more approximate manner of modelling in situ hydraulic responses. A good agreement between the model and the field observations was obtained.

Field monitoring was performed with the intent of showing that the distribution of roots of *C. sativa* is associated to the groundwater regime. The spatial and vertical distribution of root density and traits were quantified for *C. sativa* roots collected from several boreholes performed in Mount Faito. Minimum suction, minimum water content and minimum gradient (indicative of downward water flow), were monitored throughout the year and related to root distribution and spatial distribution of trees. An increasing root density was found to be associated to lower values of suction and higher gradients of infiltration, which can potentially have a negative influence of the slope stability.

A modelling investigation on the mechanical reinforcement of soil by tree roots allowed us to understand the importance of hydraulic and mechanic components on the stability of a slope. Roots increase greatly the shear strength of soil (up to 25.8 kPa in Mount Faito) through mechanical reinforcement and consequently, the safety factor of the slope increased significantly. Considering the root reinforcement in the estimation of potential failure surfaces safety factor showed that the weakest failure surface was found at 2.2 m, where the root reinforcement was 1.3 kPa, instead of 0.9 m without the root reinforcement of 13.8 kPa. The weakest failure surface found was in agreement with the failure surfaces observed from previous landslides near the test site. The test site did not present the characteristics of a landslide triggering area. The slope angle of the landslide triggering areas (35° to 45°) can easily exceed the soil friction angle (36.5° to 38.5°) and the hydraulic effect (the contribution of suction to the shear strength) would not be enough to

guarantee the stability of the slope during the wet season (0 to 10 kPa). However, the root reinforcement was estimated to be able to sustain the slopes until an angle of 42°.

Therefore, the presence of tree roots was found to affect hydraulically and mechanically stability of pyroclastic soil covers. Such conclusions may be extended to the areas of Campania where *C. sativa* plantations are present. The hydraulic effect of vegetation was greatly compensated by the mechanical reinforcement of roots.

**Key-words:** Rainfall-induced landslides, unsaturated pyroclastic soils, roots distribution, slope stability, unsaturated soil characterization



# Sommario

È stato investigato l'effetto della vegetazione locale, composta da *Castanea sativa* coltivata, alla stabilità dei versanti mediante un ampio studio sperimentale condotto in un sito di prova sul Monte Faito (Campania, Italia meridionale). In Campania, le coperture piroclastiche superficiali sono soggette a frane innescate da precipitazioni. Lunghi periodi di piogge, seguiti da eventi piovosi intensi e di breve durata, innescano frane rapide altamente distruttive; l'innescò avviene in genere sui tagli stradali e sulle scarpate piroclastiche impostate sul margine di falesie rocciose nelle zone circostanti il Vesuvio.

La caratterizzazione idraulica dei terreni del sito sperimentale è stata una delle attività centrali della tesi; essa è consistita in una vasta serie di prove di laboratorio su campioni indisturbati di terreno piroclastico contenente radici di *C. sativa* matura. Sono stati determinati la permeabilità saturata, la risposta all'evaporazione e all'imbibizione, il contenuto d'acqua ad alti valori di suzione e la biomassa secca delle radici.

La presenza di radici incrementa la permeabilità idraulica di un ordine di grandezza, soprattutto nel terreno più superficiale (da  $10^{-7}$  a  $10^{-6}$  m s<sup>-1</sup>), e riduce il valore di ingresso dell'aria delle curve di ritenzione idrica (da 6 a 4 kPa). La variazione della permeabilità rilevata fra i vari strati di sottosuolo è responsabile della velocità di flusso delle acque sotterranee e quindi della propagazione del fronte umido da piano campagna verso gli strati più profondi, con possibile generazione di pressioni neutre positive lungo il profilo del terreno. La calibrazione del modello isteretico per caratterizzare il terreno piroclastico naturale fornisce uno strumento efficace per modellare la risposta idraulica in situ. In tal modo è possibile ottenere un buon accordo tra il modello e le osservazioni sul campo.

Il monitoraggio sul campo è stato effettuato con l'intento di investigare l'influenza della distribuzione delle radici di *C. sativa* sul regime delle acque sotterranee. La distribuzione spaziale e verticale della densità e dei caratteri delle radici è stata quantificata per le radici di *C. sativa* raccolte da diversi sondaggi eseguiti sul campo sperimentale del monte Faito. La suzione minima, il contenuto minimo d'acqua ed il gradiente (indicativo del flusso d'acqua verso il basso), sono stati monitorati durante tutto l'anno, in relazione alla distribuzione radicale e spaziale degli alberi. L'aumento della densità radicale è stato associato a valori più bassi di suzione e gradienti di infiltrazione più elevati, che possono avere un'influenza negativa sulla stabilità del pendio.

Un'analisi del rinforzo meccanico esercitato dalle radici degli alberi ha permesso di comprendere l'importanza del ruolo meccanico delle radici, oltre che idraulico, sulla stabilità del pendio. Le radici accrescono notevolmente la resistenza al taglio del terreno (fino a 25,8 kPa nel caso esaminato) attraverso il rinforzo meccanico; di conseguenza, il fattore di sicurezza del pendio aumenta significativamente. Considerando il rinforzo delle radici nella stima del fattore di sicurezza lungo le superfici di rottura

potenziale, la superficie critica si trova alla profondità di 2,2 m, dove il rinforzo delle radici è quantificabile in 1,3 kPa, invece che alla profondità di 0,9 m come accadrebbe in assenza del rinforzo, stimabile a quella profondità in 13,8 kPa. La superficie critica trovata è in accordo con le superfici di rottura osservate in frane precedenti a breve distanza dal sito di prova. Il sito di prova non presenta le caratteristiche di un'area suscettibile di frana. L'angolo di acclività delle aree di distacco (da 35° a 45°) può facilmente superare l'angolo di attrito del terreno (da 36,5° a 38,5°) e l'effetto idraulico (il contributo della suzione alla resistenza) non sarebbe sufficiente a garantire la stabilità del pendio durante la stagione umida (da 0 a 10 kPa). Tuttavia, il rinforzo delle radici è, secondo la stima eseguita in questa tesi, in grado di sostenere i pendii fino ad un angolo di 42°.

Pertanto, la presenza delle radici degli alberi è risultata incidere sensibilmente sulla stabilità delle coperture piroclastiche del terreno mediante i suoi effetti idraulico e meccanico. Tali conclusioni possono essere ritenute valide per tutte le aree della Campania dove sono presenti piantagioni di *C. sativa*. L'effetto idraulico della vegetazione, leggermente negativo, è ampiamente compensato dal rinforzo meccanico delle radici.

**Parole chiave:** Frane indotte dalle piogge, terreni piroclastici insaturi, distribuzione delle radici, stabilità dei versanti, caratterizzazione insatura del suolo.

# Résumé

L'effet de la végétation locale, composée de *Castanea sativa* cultivé, sur la stabilité des pentes a été étudié sur un site d'essai au Mont Faito (Campanie, Italie). En Campanie, les sols pyroclastiques peu profonds sont sensibles aux glissements de terrain provoqués par les précipitations. Des périodes de pluies prolongées suivies de précipitations extrêmes à court terme déclenchent des glissements de terrain rapides et destructeurs au niveau des coupes routières et des escarpements pyroclastiques sur les falaises rocheuses dans les régions autour du volcan Vésuve.

Des échantillons de sol pyroclastiques non perturbés contenant des racines de *C. sativa* matures ont été utilisés pour la caractérisation hydraulique par le biais d'un ensemble d'expériences en laboratoire. La perméabilité saturée, la réponse à l'évaporation et l'imbibition, la teneur en eau pour les fortes valeurs de succion et la biomasse sèche des racines ont été déterminées.

La présence de racines a augmenté la perméabilité d'un ordre de grandeur dans les sols les plus superficiels ( $10^{-7}$  à  $10^{-6}$  m s<sup>-1</sup>) et diminué la valeur d'entrée d'air des courbes de rétention (6 à 4 kPa). La variabilité de la perméabilité entre les couches de sol a été identifiée comme conditionnant l'écoulement de l'eau souterraine par rapport à la vitesse du mouvement du front de mouillage et à la génération de pressions positives de l'eau interstitielle dans le profil. L'étalonnage du modèle hystérétique pour caractériser les sols pyroclastiques naturels a fourni une méthode plus approximative de modélisation des réponses hydrauliques. Une bonne concordance entre le modèle et les observations a été obtenue.

L'étude sur le terrain a permis de montrer que la distribution des racines de *C. sativa* est associée au régime des eaux souterraines. Les distributions spatiales et verticales de la densité et des traits des racines ont été quantifiées pour les racines de *C. sativa* prélevées dans des forages réalisés au Mont Faito. La succion minimale, la teneur minimale en eau et la pente minimale (indiquant un débit d'eau descendant) ont été surveillées tout au long de l'année et confrontées avec la distribution des racines et à la distribution spatiale des arbres. Une densité racinaire croissante était associée à des valeurs de succion plus faibles et à des gradients d'infiltration plus élevés, ce qui peut avoir une influence négative sur la stabilité de la pente.

La modélisation du renforcement mécanique du sol par les racines des arbres a permis de comprendre l'importance des composantes hydrauliques et mécaniques sur la stabilité d'une pente. Les racines augmentent la résistance au cisaillement (jusqu'à 25,8 kPa) grâce à un renforcement mécanique et donc le facteur de sécurité de la pente augmente. L'examen du renforcement dû aux racines dans l'estimation du facteur de sécurité des surfaces de rupture potentielles a montré que la surface de rupture la plus faible a été trouvée à 2,2 m, où le renforcement dû aux racines était de 1,3 kPa, au lieu de 0,9 m sans le renforcement de 13,8 kPa. La surface de rupture la plus faible correspond aux surfaces de rupture

observées lors de glissements de terrain antérieurs. Le site d'essai ne présentait pas les caractéristiques d'une zone de déclenchement d'un glissement de terrain. L'angle de pente des zones de déclenchement des glissements de terrain ( $35^{\circ}$  à  $45^{\circ}$ ) peut dépasser l'angle de frottement du sol ( $36,5^{\circ}$  à  $38,5^{\circ}$ ) et l'effet hydraulique ne serait pas suffisant pour garantir la stabilité de la pente pendant la saison humide (0 à 10 kPa). On estime que le renforcement dû aux racines peut maintenir les pentes jusqu'à un angle de  $42^{\circ}$ .

On a donc constaté que la présence de racines d'arbres affectait la stabilité hydraulique et mécanique des couvertures de sol pyroclastiques. Ces conclusions peuvent être étendues aux autres zones de plantations de *C. sativa*. L'effet hydraulique de la végétation a été largement compensé par le renforcement mécanique dû aux racines.

**Mots-clés:** Glissements de terrain induits par les précipitations, sols pyroclastiques insaturés, répartition des racines, stabilité des pentes, caractérisation des sols insaturés.

# Acknowledgements

First and foremost, I would like to thank my supervisors Prof. Urciuoli and Alexia. In particular, I would like to thank Prof. Urciuoli for the discussions on the research and for sharing deep technical knowledge in the subject. I would like to thank Alexia for teaching me good research practices and opening up my mind to other research fields and approaches. The collaboration of both supervisors was essential for a balance in the work and for its success. I would express my appreciation to Marianna Pirone for the supervisor-like contribution to the studies. I am sincerely thankful for accompanying me throughout all the developed research showing understanding and patience in the discussion of the work.

I would like to thank for all the opportunities I have been given to learn and collaborate with other students and researchers in all the institutions in Italy and France: University of Naples Federico II, University of Montpellier, INRA, AMAP and CIRAD. Other researchers and professors had a contribution that was essential for the successful completion of the present thesis. I would like to thank Raffaele Papa for participating in the field instrumentation and for teaching me how to use the direct shear test apparatus in unsaturated conditions. I would like to thank Giovanni and Prof. Santo for sharing insight and expertise in the study of landslides in Campania from a geological engineering perspective. I am especially thankful for all the field trips that allowed me to have a direct look into the problems I am dealing with in my research. I would like to thank Mao for sharing his knowledge on spatial root distribution models. Finally, I would like to thank Prof. Nicotera for the constructive criticism of my work namely in the soil hydraulic characterization.

I am thankful to the bachelor and master students that accompanied me in the laboratory and field experimentation, in particular Luca, Natale, Vittorio, Sebastiano, Sara, Brenda, Carmine, Enrica, Nelly and Federico. All them made me improve the communication skills and acquire more in-depth and confidence in theoretical concepts. Indeed, the best way to learn is to teach. I would like to express my appreciation to the dedication of the laboratory technicians Alfredo and Antonio. Thanks to them equipment was repaired, sensors were calibrated, setups were installed and all the experiments were possible. Additionally, a special thank to students and technicians for forcing me to learn Italian.

I would like to thank Prof. Alessandro Tarantino for giving me the opportunity to be part of the TERRE project. It was an amazing opportunity to integrate a multidisciplinary team of experts and brilliant students. I would like to express my appreciation for the feedback coming from the professors and researchers, in particular Romero, David Toll, Thierry, Jan-Willem, Wolfgang, Domenico Gallipoli, Alessio Ferrari, Simon Wheeler, Giacomo Russo and again Alessandro Tarantino. I would like to thank all the early stage researchers that accompanied me throughout the project: Roberta, Elena, Riccardo, Lorenzo, Alessia, Raniero, Jacopo, Alessandro, Gianluca, Javier, Elodie, Pavlina, Sravan and Emmanuel. I would like to express a special appreciation to Abhi for the interesting discussions and for becoming my best friend throughout the three years of PhD. I am thankful to all them for making research fun and joyful.

I would like to thank to my family, in particular my mother, father, brother and grandparents, for the support and patience. I appreciate the fact that father asks my mother to call me and I thank my mother and grandmother for listening to me. I am sorry for all I put my parents through for being far from home.

I would like to thank my friends in Portugal, that I missed a lot, for being always positive and kind to me throughout the PhD. They are the Filipas 'a Figueiredo' and 'a Marques', Rute, Marta, Margarida, Bruno and Joao Nuno. I would like to thank the friends I made in Naples, in particular Akiko, Mariana, Bikash, Farhad, Mohammed and Sara, for standing my sarcasm and humour and for helping through the PhD.

# Index

Abstract .....	i
Sommario .....	iii
Résumé .....	v
Acknowledgements .....	vii
Index .....	ix
Index of figures .....	xv
Index of tables .....	xxvii
List of symbols .....	xxx
Chapter 1 Introduction and literature review .....	1
1.1 Introduction .....	1
1.1.1 Motivation .....	1
1.1.2 Organization of the document .....	2
1.2 Unsaturated soils .....	3
1.2.1 Water potential .....	3
1.2.2 Water retention curves .....	4
1.2.3 Hysteretic k-S-P models .....	6
1.2.3.1 Hysteretic water retention model .....	7
1.2.3.2 Hysteretic water conductivity model .....	9
1.2.4 Effective stress in unsaturated soil mechanics .....	10
1.3 Pyroclastic slopes in Campania .....	10
1.3.1 Landslides .....	10
1.3.2 Hydraulic behaviour .....	12
1.3.3 Unsaturated pyroclastic soils .....	16
1.4 Vegetation effect on slope stability .....	19
1.4.1 Root systems and root growth .....	21
1.4.2 Useful traits for reinforcing soil on slopes .....	22
1.4.3 Hydraulic effect of vegetation on slope stability .....	23

1.4.3.1	Effect of roots on the soil hydraulic properties .....	23
1.4.3.2	Rainfall partition.....	25
1.4.3.3	Effect of vegetation on the groundwater regime .....	26
1.4.4	Mechanical effect of vegetation on slope stability.....	27
1.4.4.1	Roots in a shallow landslide.....	27
1.4.4.2	Root failure modes .....	28
1.4.4.3	Root reinforcement.....	30
1.5	Objectives.....	33
Chapter 2	Test site overview.....	37
2.1	Introduction.....	37
2.2	Stratigraphy .....	38
2.3	Soil physical properties .....	41
2.4	Slope topography .....	43
2.5	Vegetation and ground cover .....	44
Chapter 3	Hydraulic characterization of natural unsaturated pyroclastic soils .....	49
3.1	Introduction.....	49
3.2	Methods and materials .....	51
3.2.1	Void ratio of root-permeated soil .....	51
3.2.2	Hydraulic characterization .....	55
3.2.2.1	Saturated permeability .....	56
3.2.2.2	Wetting and drying cycles .....	58
3.2.2.3	High suction range .....	60
3.2.3	Dry biomass .....	61
3.2.4	Experimental data processing and filtering .....	61
3.2.4.1	Saturated permeability .....	61
3.2.4.2	Ku-pf apparatus data filter .....	62
3.2.5	Inverse analysis.....	63
3.2.5.1	Objective function.....	63
3.2.5.2	Sensitivity analysis .....	63



3.2.5.3	Main drying curve fitting .....	64
3.2.5.4	Hysteretic model calibration .....	68
3.2.6	Water capacity.....	71
3.3	Results and discussion .....	72
3.3.1	Saturated permeability .....	72
3.3.2	Drying and wetting cycles .....	73
3.3.3	High suction range .....	75
3.3.4	Inverse analysis.....	76
3.3.4.1	Main drying curve fitting .....	76
3.3.4.2	Main wetting curve fitting.....	80
3.3.4.3	Sensitivity analysis of the hysteretic model.....	80
3.3.4.4	Assessment of the data sets size.....	81
3.3.4.5	Test replication and parameter dependency on porosity .....	83
3.3.5	Soil water capacity .....	89
3.3.6	Effect of roots on the soil hydraulic properties .....	90
3.4	Conclusions.....	93
Chapter 4	Groundwater regime interaction with atmosphere and vegetation .....	95
4.1	Introduction.....	95
4.2	Methods and materials .....	96
4.2.1	Test site characterization .....	96
4.2.2	Climate data .....	97
4.2.3	Meteorological data interpretation.....	99
4.2.3.1	Potential evapotranspiration.....	99
4.2.3.2	Evapotranspiration calculation parameters .....	102
4.2.3.3	Relative humidity estimation .....	103
4.2.4	Field instrumentation: TDR probes and tensiometers.....	103
4.2.5	Equipment calibration.....	107
4.2.5.1	Relation between dielectric constant and volumetric water content .....	107
4.2.5.2	Calibration of tensiometers .....	110

4.2.6	Root distribution .....	112
4.2.6.1	Roots sampling.....	112
4.2.6.2	Roots scanning and image analysis.....	113
4.2.6.3	Root vertical distribution model .....	114
4.2.6.4	Root spatial distribution model .....	115
4.2.7	Water flow in the soil .....	116
4.2.8	Hydraulic response of the soil related to spatial root distribution.....	117
4.3	Results and discussion .....	117
4.3.1	Meteorological monitoring .....	117
4.3.1.1	Previous rainfall records in Moiano and Pimonte.....	117
4.3.1.2	Meteorological monitoring of Mount Faito .....	119
4.3.2	Considerations on vegetation and ground cover .....	126
4.3.3	Root distribution .....	127
4.3.3.1	Measurements of root density .....	127
4.3.3.2	Fitting of the root vertical distribution model .....	132
4.3.3.3	Fitting of the root lateral distribution model .....	134
4.3.4	Equipment calibration.....	137
4.3.4.1	Relation between dielectric constant and volumetric water content .....	137
4.3.4.2	Tensiometers.....	143
4.3.5	Monitored suction and volumetric water content.....	146
4.3.6	Comparison of field data and laboratory water retention curves .....	151
4.3.7	Groundwater vertical flow.....	155
4.3.8	Spatial distribution of water content and suction associated to root density .....	159
4.3.8.1	Fitting of the spatial distribution model to soil hydraulic behaviour observations .....	159
4.3.8.2	Relate root density indicators and soil hydraulic properties indicators .....	161
4.3.8.3	Considerations on the relations between root distribution and hydraulic properties indicators	165
4.4	Conclusion.....	166
Chapter 5	The relative contribution of suction, soil and root shear resistance to slope stability .....	168

5.1	Introduction.....	168
5.2	Methods and materials .....	169
5.2.1	Soil strength considering the presence of roots .....	169
5.2.2	Soil hydro-mechanical characterization .....	169
5.2.2.1	Standard direct shear test .....	169
5.2.2.2	Direct shear test in unsaturated conditions .....	171
5.2.3	Quantification of the mechanical reinforcement of the soil by the roots .....	174
5.2.3.1	Root area ratio.....	175
5.2.3.2	Root tensile strength .....	175
5.2.3.3	Wu and Waldron model.....	176
5.2.3.4	Fibre bundle model.....	178
5.2.4	Slope stability analysis .....	181
5.3	Results and discussion .....	181
5.3.1	Soil hydro-mechanical properties.....	181
5.3.1.1	Saturated conditions direct shear test.....	181
5.3.1.2	Unsaturated direct shear test .....	186
5.3.2	Mechanical reinforcement of the soil by the roots.....	190
5.3.3	Slope stability .....	191
5.3.3.1	Adopted parameters.....	191
5.3.3.2	Safety factor .....	192
5.3.3.3	Relative contribution of roots, suction and soil shear strength to the stability .....	197
5.4	Conclusion.....	200
Chapter 6	Conclusion and future work.....	202
6.1	Conclusion.....	202
6.2	Future work .....	203
	References.....	206
	Annexes .....	216
	Annex A – List of boreholes for physical, hydraulic and mechanical characterization.....	a
	Annex B – Species identified in Mount Faito.....	c

Annex C – Data sampler for inverse analysis .....	f
Annex D – Saturated permeability.....	r
Annex E – Water content in the high suction range .....	t
Annex F – Fitting of the main drying from inverse analysis.....	u
Annex G – Fitting of the main wetting with inverse analysis .....	y
Annex H – Sensitivity analysis examples of the main wetting fitting parameters.....	bb
Annex I – Examples of simulations using fitting parameters of 1 and 2 cycles.....	dd
Annex J – Examples of simulations used for ku-pf apparatus test replication. ....	ff
Annex K – Root dry biomass in the ku-pf samples .....	ii
Annex L – WinRIZHO analysis procedure.....	jj
Annex M – Fitting of the vertical root distribution model procedure .....	ll
Annex N – Fitting of the spatial root distribution model procedure.....	nn
Annex O – Tree survey: DBH and tree-to-vertical distance .....	pp
Annex P – Root vertical distribution raw characterization .....	rr
Annex Q – Vertical root distribution model fitting .....	tt
Annex R – Root lateral distribution model fitting .....	vv
Annex S – Monitored volumetric water content in Mount Faito.....	kkk
Annex T – Monitored suction.....	ooo
Annex U – Field suction and water content in the water retention plan .....	sss
Annex V – Spatial distribution of hydraulic observations .....	uuu
Annex W – Spatial distribution of hydraulic (model fitting).....	vvv
Annex X – Fitting parameters of the spatial distribution model adapted to hydraulic observations .....	kkkk
Annex Y – Practical steps for the operation of the unsaturated direct shear testing equipment .....	llll
Annex Z – Calculation of root cohesion.....	pppp
Annex AA – Root cohesion calculated using different load distribution criteria in FBM.....	tttt

## Index of figures

Figure 1 – Number of victims in the Campania region caused by landslides from 1580 to 1998 (Cascini et al., 2008). .....	1
Figure 2 – Inventory map of the January 1997 landslides in the Sorrento Peninsula, (adapted from Calcaterra and Santo, 2004). .....	2
Figure 3 – Typical water retention curve (adapted from Vanapalli et al., 1999). .....	5
Figure 4 – Illustration of main and scanning water retention curves (adapted from Switala, 2016). .....	5
Figure 5 – Water retention curves of sandy, silty and clayey soils (Fredlund and Xing, 1994). .....	6
Figure 6 – Hysteretic loops in the water retention plan when saturation is (a) actual water saturation and (b) apparent water saturation. ....	8
Figure 7 – Scheme of the events and conditions that lead to landslides in pyroclastic soil covers.....	11
Figure 8 – Scheme of the main morphology associated to debris flow type of landslide (Di Crescenzo and Santo, 2005). .....	12
Figure 9 – Grain size distribution of the soils present at Monteforte Irpino test site (adapted from Pirone et al., 2015b). .....	13
Figure 10 – Evolution of the matric suction with time in different soil layers (Pirone et al., 2015a). .....	14
Figure 11 – Monitoring data of a test site in Cervinara (adapted from Urciuoli et al., 2016). .....	15
Figure 12 – Evolution of matric suction and degree of saturation with depth for different instants during the wet season in Monteforte Irpino (adapted from Urciuoli et al., 2016). .....	16
Figure 13 – Hourly measurements of total head during a rainfall even in the test site at Cervinara (adapted from Urciuoli et al., 2016). .....	16
Figure 14 – Main drying WRCs and HPFs (Nicotera et al., 2010). .....	17
Figure 15 – Comparison of the main drying WRC and the field measurements of Monteforte Irpino (Pirone et al., 2014). .....	18
Figure 16 – Results of the saturated triaxial tests (Papa et al., 2008), in which $f'$ represents the critical friction angle.....	18
Figure 17 – Vegetation-slope interactions (Wilkinson et al., 2002). .....	19
Figure 18 – Different types of root systems (adapted from Switala, 2016). .....	22
Figure 19 – Changes in infiltration rate under alfalfa culture with time (in Angers and Caron, 1998). .....	24
Figure 20 – Drying (a) and wetting (b) branch of the water retention loop of bare soil (B) and vegetated soil with increasing distance between seedlings (60, 120 and 180 mm) presented in Ng et al. (2016b). .....	25
Figure 21 – Weight of each component contributing to the slope stability of different vegetation covers and cultivations in comparison to fallow soil (red line) by Kim et al. (2017). .....	27
Figure 22 – Solicitation of the root reinforcement at different locations along the sliding surface of a shallow landslide: (a) tension, (b) shear and (c) compression (Dias et al., 2017). .....	28
Figure 23 – Required forces to originate each failure mechanism for different diameters (Pollen, 2007)..	29

Figure 24 – Measured critical load compared with the theoretical solutions (adapted from Wu et al., 1988).	30
Figure 25 – Scheme of the stresses in the root during shear (Dias et al., 2017a).	32
Figure 26 – Comparison of the root-permeated soil reinforcement as a function of displacement of FBM and W&W models (Schwarz et al., 2010).	32
Figure 27 – Measured and simulated force-displacement behaviour of a bundle of roots (adapted from Schwarz et al., 2013).	33
Figure 28 – Soil aggregates and pumices hanging from roots in a cultivated area near Sarno (Campania, Italy).	34
Figure 29 – Macropores created by roots (Ghestem et al., 2011).	35
Figure 30 – Roots that failed by pull out in a previous landslide in the region of Campania.	36
Figure 31 – Test site location on satellite images (source: Google Earth).	37
Figure 32 – Areas of pyroclastic deposition of several eruptions of Vesuvius volcano (adapted from Di Crescenzo and Santo, 2005). Approximate location of Mount Faito test site.	38
Figure 33 – Boreholes performed in Mount Faito test site and their spatial distribution.	40
Figure 34 – Mean soil stratigraphic profile present at Mount Faito and soil classification according to the USCS.	41
Figure 35 – Grain size distribution of Mount Faito soils.	42
Figure 36 – Projected longitudinal profile of cell 1 and 2.	44
Figure 37 – Photograph of the site on February 17 <sup>th</sup> , 2017.	44
Figure 38 – Dominant species in Mount Faito test site: (a) <i>Castanea sativa</i> , and (b) <i>Pteridium aquilinum</i> .	45
Figure 39 – Photos of cell 1 from March to October 2017.	46
Figure 40 – Photos of cell 1 from November 2018 to April 2018.	47
Figure 41 – Soil erosion exposing roots.	48
Figure 42 – Formation of a frozen soil layer.	48
Figure 43 – Comparison of laboratory main drying curves and field measurements (adapted from Papa et al., 2013).	50
Figure 44 – Variation of the roots of <i>Castanea sativa</i> specific gravity with depth in Mount Faito: individual measurements and mean and respective standard deviation.	52
Figure 45 – Specific gravity of the <i>Castanea sativa</i> roots for different diameter classes.	53
Figure 46 – Scheme of the test sequence and summarized description.	55
Figure 47 – Soil sample extrusion from the borehole.	55
Figure 48 – Soil sample after extrusion.	55
Figure 49 – Setup used to determine the saturated permeability at constant head.	56
Figure 50 – Scheme of the setup to determine the saturated permeability and indication of basic operation instructions.	56

Figure 51 – Permeameter: soil mould and upper and bottom supports. ....	57
Figure 52 – ku-pf apparatus used in the experimentation. ....	58
Figure 53 – Sample support on the scale of the ku-pf apparatus. ....	58
Figure 54 – Scheme of the sample support (adapted from Nicotera et al., 2010). ....	58
Figure 55 – Tensiometer (do not hold the tensiometer in this manner during the saturation). ....	59
Figure 56 – Setup of the saturation of tensiometers. ....	59
Figure 57 – Setup for the calibration of the tensiometers. ....	59
Figure 58 – ku-pf software on the calibration of tensiometers. ....	59
Figure 59 – Support with guides to make holes in the sample to insert the tensiometers. ....	60
Figure 60 – Equipment used to make the holes for the tensiometers. ....	60
Figure 61 – Full pressure plate system. ....	61
Figure 62 – Position of the samples inside the pressure plate chamber. ....	61
Figure 63 – Measurements of a single test presented as an example of the water flow through the sample with time, where the slope of the linear regression is equal to the saturated permeability of the soil. ....	62
Figure 64 – Soil profile and identified observation points. ....	67
Figure 65 – Interface for the definition of the initial conditions in terms of suction head of HYDRUS-1D. ....	67
Figure 66 – Comparison of the water capacity resultant from two different water retention curves with different AEV (Fredlund & Rahardjo, 2012). ....	72
Figure 67 – Comparison of mean saturated permeability and mean porosity of different soil layers with depth. ....	73
Figure 68 – Monitored suction at bottom and top tensiometers and wet soil weight of the sample 1.4.1 (soil A2) by the ku-pf apparatus. ....	74
Figure 69 – Suction at the bottom and top tensiometer, vertical gradient and wet soil weight of a single wetting step monitored at the ku-pf apparatus of sample 1.7.2 (soil A1). ....	75
Figure 70 – Experimental drying-wetting loops obtained for sample 1.7.2 (soil A1), in terms of volumetric water content (vwc). ....	75
Figure 71 – Main drying WRC of sample 1.7.2 (soil A1) with the objective function data sets. ....	76
Figure 72 – HPF of the main drying of sample 1.7.2 (soil A1) with the measured saturated permeability. ....	76
Figure 73 – Mean main drying WRC obtained from inverse analysis. ....	77
Figure 74 – Mean main drying HPF obtained from inverse analysis. ....	77
Figure 75 – Representation of the mean and standard deviation of the fitting parameters of the main drying curve for each soil type. ....	78
Figure 76 – Sensitivity analysis of the fitting parameters of the main drying performed on sample 1.7.2 (soil A1). ....	79
Figure 77 – Main loop of the WRC with the experimental measurements of sample 1.7.2 (soil A1). ....	80
Figure 78 – Sensitivity analysis of the fitting parameters of the main wetting performed on sample 1.7.2 (soil A1). ....	81

Figure 79 – Simulation of the full test using the fitting parameters from 1 cycle (left side) and 2 cycles (right side) and comparison with the experimental data.....	82
Figure 80 – Comparison of the fitted parameters of the main wetting curve using 1 or 2 cycles. ....	83
Figure 81 – Main wetting branch fitting parameters comparison with soil porosity per soil type. ....	84
Figure 82 – Relationship between the parameters $\alpha d$ and $\alpha i$ per soil type and respective standard deviation. ....	85
Figure 83 – Relationship between $\theta_{sd}$ and $\theta_{si}$ and soil porosity of the tested samples. ....	85
Figure 84 – Simulation of drying-wetting cycles of sample 1.7.2 with the fitting parameters of sample 1.9.2 (soil A1). ....	87
Figure 85 – Differences between suction estimations of the best fitting (case 4) and the fitting cases 1, 2 and 3. ....	88
Figure 86 – Water capacity and hydraulic permeability function of each soil type computed with the mean fitting parameters of the main (a) drying and (b) wetting branch. ....	89
Figure 87 – Mean and standard deviation of the maximum water capacity ( $C_{max}$ ) of each soil type. ....	90
Figure 88 – Saturated permeability, soil porosity and root dry biomass in each soil layer with depth per soil layer.....	91
Figure 89 – Main water retention loop of soil (a) A1 and (b) A1sup. ....	92
Figure 90 – Water capacity ( $C$ ) of the main wetting curves of soil A1 and A1sup. ....	92
Figure 91 – Location of the meteorological stations (Google Earth image).....	97
Figure 92 – Meteorological station at Mount Faito test site. ....	98
Figure 93 – Extra-terrestrial radiation along the year for Mount Faito. ....	103
Figure 94 – Instrumented area: trees location (red numbered circles) relative to the profiles' location (identified by letters) grouped in cell 1 and cell 2.....	104
Figure 95 – Location of the instrumentation in each profile. ....	105
Figure 96 – The soil is being removed from the tube and identified with the help of a geologist. ....	106
Figure 97 – The tube is being pushed into the soil using a hammer. ....	106
Figure 98 – Interior and exterior cooper tubes to install tensiometers.....	106
Figure 99 – Tube and extension used to open a borehole for the installation of TDR probes. ....	106
Figure 100 – Vacuum dial gauge and digital measurement adaptor installed on a Jet Fill tensiometer sided with a tradition SDEC France tensiometer.....	107
Figure 101 – TDR probe dimensions. ....	109
Figure 102 – Plexiglas base glued to the mould. ....	110
Figure 103 – Cap, weight and latex disc.....	110
Figure 104 – Pressure regulator and vacuum dial gauge.....	110
Figure 105 – Vacuum converter.....	110
Figure 106 – Equipment used to read the dielectric constant (computer, battery, TDR100 and cables). ....	110
Figure 107 – SDEC France tensiometers with different initial air columns.....	111



Figure 108 – Borehole extrusion (a), sectioning (b) and root washing (c).	112
Figure 109 – Bag storing roots in alcohol 15%.	112
Figure 110 – Procedure to scan roots: (a) root washing in a sieve, (b) spreading of roots on the glass board with a film of water, and (c) roots drying with absorbent paper.	113
Figure 111 – Example of a scanned roots image.	113
Figure 112 – Shadows created by the water meniscus.	114
Figure 113 – Root before (a) and after (b) erasing the mycorrhizas.	114
Figure 114 – Total rainfall cumulated along each year in Pimonte and Moiano meteorological stations.	118
Figure 115 – Maximum daily rainfall recorded in each year in Pimonte and Moiano meteorological stations.	118
Figure 116 – Mean and standard error of the monthly rainfall in Pimonte and Moiano meteorological stations.	118
Figure 117 – Daily rainfall registered by the meteorological stations at Moiano, Pimonte and Mount Faito.	119
Figure 118 – Comparison of the daily rainfall recorded in Moiano and Pimonte with Mount Faito.	119
Figure 119 – Daily rainfall at Mount Faito from January 2017 to September 2018.	120
Figure 120 – Mean and standard error of the monthly rainfall of Moiano and Pimonte meteorological stations and the monthly rainfall recorded in Mount Faito.	120
Figure 121 – Small landslide on the side of the road that leads to the study site.	121
Figure 122 – Maximum, mean and minimum temperature recorded in Moiano and Mount Faito along the year.	122
Figure 123 – Comparison of the Maximum, mean and minimum temperature recorded in Moiano and Mount Faito.	122
Figure 124 – Maximum, mean and minimum temperature at Mount Faito from January 2017 to September 2018.	123
Figure 125 – Comparison of the measured and calculated relative humidity (RH).	123
Figure 126 – Relative humidity (RH) in Mount Faito from September 2017 to September 2018.	124
Figure 127 – Recorded maximum, mean and minimum daily relative humidity at Mount Faito.	124
Figure 128 – Recorded mean wind velocity at Mount Faito.	125
Figure 129 – Recorded mean soil temperature at the depths of 0. 2m and 0.5 m at Mount Faito.	125
Figure 130 – Recorded net radiation at Mount Faito.	125
Figure 131 – Reference evapotranspiration (ET <sub>0</sub> ) calculated with the meteorological data of Mount Faito.	126
Figure 132 – Comparison of two methods of calculating reference evapotranspiration (ET <sub>0</sub> ).	126
Figure 133 – Location of the soil profiles (identified with letters) in the polygons and trees (identified with numbers).	127

Figure 134 – Increase in cumulative root dry biomass relative to the total root biomass with depth for all soil cores.....	128
Figure 135 – Dry roots biomass measured in profiles NT and T per unit volume of soil. ....	128
Figure 136 – Example of grouped root characteristics in four diameter classes for a typical soil core (1S). .....	129
Figure 137 – Mean and standard error of the root length per unit soil volume for four diameter classes with depth. ....	130
Figure 138 – Mean and standard error of the root volume per unit soil volume for four diameter classes with depth. ....	130
Figure 139 – Mean and standard error of the number of root tips per unit soil volume for four diameter classes with depth. ....	130
Figure 140 – Mean and standard error of the root dry biomass per unit soil volume with depth.....	130
Figure 141 – Relation between root dry biomass and the mean (a) root length, (b) number of root tips, and (c) root volume per unit volume of soil, and (d) the relation between root length and number of root tips. .....	131
Figure 142 – Cumulative relative (a) root length, (b) root volume, (c) number of root tips, and (d) root biomass with depth given by the fitted $\beta$ -model. ....	133
Figure 143 – Spatial root distribution fitting to the root density in terms of biomass ( $0.25 < z < 0.5$ m). ....	135
Figure 144 – Determination coefficient ( $R^2$ ) of the root lateral distribution for different root density indicators. .....	136
Figure 145 – Comparison of the grain size distribution of the soil of Mount Faito (A1, A2, C1) and Monteforte (1, 2, 6) (adapted from Dias et al., 2018). ....	138
Figure 146 – Soil dielectric constant and respective volumetric water content (vwc) along the wetting and drying phases of each tested soil. ....	139
Figure 147 – Comparison of the dielectric constants and volumetric water content (vwc) of all tested soils to the universal equations (Topp and Ledie). ....	140
Figure 148 – Comparison of the models fitted to Mount Faito data and Monteforte to the experimental data. .....	142
Figure 149 – Comparison between the experimental data of soil B and the soil studied by Papa and Nicotera (2012). ....	143
Figure 150 – Scheme of the setup and reference water pressures. ....	144
Figure 151 – Relation between digital measurement and the real pressure. ....	144
Figure 152 – Evolution of the suction (s) along time for different initial air columns. ....	145
Figure 153 – Evolution of the air column along time for different initial air columns. ....	145
Figure 154 – Daily rainfall (a) and mean and standard deviation of the volumetric water content (vwc) measured in cells 1 and 2 in soil A1 and A2 (b), soil B (c) and soil C1 and C2 (d). ....	147

Figure 155 – Volumetric water content (vwc) in the profiles NT and T comparison with the mean values in soil A1 and A2. ....	148
Figure 156 – Average and standard deviation of the suction (s) in cells 1 and 2 in comparison with the rainfall. ....	149
Figure 157 – Monitored suction (s) in profiles T and NT in comparison with the mean suction in soil A1 and A2. ....	150
Figure 158 – Comparison of the mean water content (vwc) and suction (s) measured in situ and the envelope of the main loop obtained in the laboratory. ....	152
Figure 159 – Mean field measurements of suction (s) and volumetric water content (vwc) of soils A and C. ....	153
Figure 160 – Measurements in profiles NT and T of suction (s) and volumetric water content (vwc). ....	154
Figure 161 – Comparison between field measurements of suction (s) and volumetric water content (vwc) in profiles T and NT and WRC envelops. ....	154
Figure 162 – Mean hydraulic head (h) for cells 1 and 2 per soil layer. ....	156
Figure 163 – Mean vertical gradient in couples of measurements in comparison with rainfall and reference evapotranspiration (ET <sub>0</sub> ). ....	157
Figure 164 – Mean suction (s) and volumetric water content (vwc) along the soil profile before and after the rainfall events of September 2017. ....	158
Figure 165 – Vertical gradient in profiles T and NT in comparison to rainfall and reference evapotranspiration (ET <sub>0</sub> ). ....	159
Figure 166 – Coefficient of determination ( $R^2$ ) of different hydraulic observations in soil A1 and A2 to fit the spatial distribution model for a maximum tree-to-profile distance of (a) 10 m, (b) 8 m, and (c) considering only the nearest tree to the profile. ....	160
Figure 167 – Competition index for each profile fitted for the data of (a) root biomass, and (b) vertical distribution of the number of root tips. ....	162
Figure 168 – Coefficient of determination ( $R^2$ ) for each hydraulic properties' indicator fixing the competition index of the root density in terms of biomass. ....	163
Figure 169 – Minimum volumetric water content (min vwc), minimum vertical gradient and root biomass for the same competition indexes considering all the trees in a range of up to 10 m from the soil profiles. .	163
Figure 170 – Coefficient of determination ( $R^2$ ) for each hydraulic properties' indicator fixing the competition index of the vertical root distribution parameter ( $\beta$ -value) in terms of root tips. ....	164
Figure 171 – Minimum suction and $\beta$ -values (number of root tips) for the same competition indexes considering all the trees in a range of up to 8 m from the profiles. ....	164
Figure 172 – Insert soil sample in the shear box. ....	170
Figure 173 – Traditional direct shear test equipment (Esposito, 2017). ....	170
Figure 174 – Shear box (adapted from Evangelista et al., 2004). ....	171

Figure 175 – Unsaturated conditions direct shear testing equipment (adapted from Evangelista et al., 2004): A represents the top view and B the transversal view. ....	172
Figure 176 - Scheme of pressure regulation circuits and transducers used in the suction-controlled direct shear test (adapted from Papa and Nicotera, 2011). ....	173
Figure 177 – Assemblage of the unsaturated direct shear test in unsaturated: (a) lower the water level and moist the porous stone; (b) place the lower ring with screws and position the metallic strips; (c) position the upper part and connect it to the loading cell; (d) push the soil sample into the box using an extruder; and (e) position the upper porous stone and the sphere. ....	174
Figure 178 – Tensile strength relation with diameter of different species (Bischetti et al., 2009). ....	176
Figure 179 – Scheme of the response of the roots with different orientations with the shear zone. ....	178
Figure 180 – Flowchart for the FBM computation. ....	179
Figure 181 – Vertical displacements ( $\delta v$ ) during the consolidation phase in samples of soil A1. ....	183
Figure 182 – Vertical displacements ( $dv$ ) during the saturation phase in samples of soil A1. ....	183
Figure 183 – Ratio between shear and confining stress ( $\tau/\sigma'$ ), and vertical displacement ( $dv$ ) measured during the shear phase with horizontal displacement ( $dh$ ) in samples of soil A1. ....	184
Figure 184 – Ratio between shear and confining stress ( $\tau/\sigma'$ ), and vertical displacement ( $dv$ ) measured with horizontal displacement ( $dh$ ) during the shear phase of NC and OC samples of soil C1. ....	185
Figure 185 – Limit shear strength and Mohr-Coulomb failure envelope of soil (a) A1 and (b) C1: confining stress ( $\sigma'_v$ ) and correspondent shear strength ( $\tau$ ). ....	185
Figure 186 – Measurement of suction ( $s$ ) after applying the chamber air pressure. ....	186
Figure 187 – Initial (a) void ratio ( $e$ ) and (b) volumetric water content ( $vwc$ ) for each measured suction ( $s$ ) (the mean WRCs from Chapter 3 and an additional point correspondent to saturation). ....	187
Figure 188 – Vertical settlement ( $dv$ ) during consolidation. ....	187
Figure 189 – Shear stress ( $\tau$ ) and vertical displacement ( $dv$ ) with horizontal displacement ( $dh$ ) during the shear phase. ....	188
Figure 190 – Ratio between shear and Bishop stress ( $t/s'$ ), and vertical displacement ( $dv$ ) measured with horizontal displacement ( $dh$ ) during the shear phase. ....	189
Figure 191 – Limit shear strength ( $\tau$ ) and Mohr-Coulomb failure envelopes of soil C1 obtained from direct shear tests in saturated (sat) and unsaturated (unsat) conditions. ....	189
Figure 192 – Mean root cohesion obtained from W&W model when $k''=1$ (W&W0) and when $k''=0.56$ (W&W) after Bischetti et al. (2009) and FBM with load distribution according with the number of roots, the roots diameter and the roots area class (referred as number, diameter, and area, respectively) with depth. ...	190
Figure 193 – Safety factor (SF) along the monitoring period (a) assuming failure surfaces at different depths and (b) a close up in the most critical depths (2.2 m, 2.5 m and 2.7 m). ....	192
Figure 194 – Variation of the safety factor (SF) with increasing depth of the failure surface in soil A1 and A2. ....	193

Figure 195 – Sliding surfaces and geological profiles in the sliding zone of previous landslides (adapted from Di Crescenzo and Santo, 1999).....	194
Figure 196 – Safety factor (SF) ignoring the root contribution assuming failure surfaces at different depths (a) and a zoom of the lower range of SF (b). ....	195
Figure 197 – Safety factor over time assuming a failure surface in different soil layers in the profile of Monteforte Irpino (adapted from Pirone et al., 2015b). ....	196
Figure 198 – Minimum estimated safety factor (SF) for different slope angles considering and not the presence of roots. ....	197
Figure 199 – Contribution of the soil, roots and suction to the safety factor (SF) in soil (a) A1(z=0.2 m) and (b) A2 (z=0.5 m), and (c) A2 (z=0.9 m) .....	198
Figure 200 – Contribution of the soil, roots and suction to the safety factor (SF) in soil C1 and C2. ....	199
Figure 201 – Excel worksheet SSA to with ku-pf monitoring data to be used as source. ....	f
Figure 202 – Output worksheet HYDRUS# containing the sampled boundary conditions (INPUT 1), the data sets (INPUT 2), data set size and time information on the top right corner, initial estimation of the input parameters right bellow, and the initial conditions at the bottom right. ....	g
Figure 203 – Output worksheet ‘hysteresis’ containing the sampled boundary conditions (columns A to D), the data sets (columns F to P), data set size and time information on the top right corner, initial estimation of the input parameters right bellow, the initial conditions, and the fitted parameters of the main drying curve. ....	h
Figure 204 – Probability density function of the saturated permeability of soil A1sup, A1, A2 and C1. ....	s
Figure 205 – Main drying WRC of each soil type (a-e) and comparison among their mean (f) obtained from inverse analysis.....	w
Figure 206 – Main drying HPF of each soil type (a-e) and comparison among their mean (f) obtained from inverse analysis.....	x
Figure 207 – Examples of main drying-wetting loops of different soil types.....	z
Figure 208 – Sensitivity analysis of the fitting parameters of the main wetting performed on sample N1 (soil A1sup). ....	bb
Figure 209 – Sensitivity analysis of the fitting parameters of the main wetting performed on sample 1.4.1 (soil A2). ....	bb
Figure 210 – Sensitivity analysis of the fitting parameters of the main wetting performed on sample 2.12.2 (soil C1). ....	cc
Figure 211 – Simulation of the full test using the fitting parameters from 1 cycle (left side) and 2 cycles (right side) and comparison with the experimental data of sample 1.7.2 (soil A1). ....	dd
Figure 212 – Simulation of the full test using the fitting parameters from 1 cycle (left side) and 2 cycles (right side) and comparison with the experimental data of sample 1.4.1 (soil A2). ....	dd
Figure 213 – Simulation of the full test using the fitting parameters from 1 cycle (left side) and 2 cycles (right side) and comparison with the experimental data of sample 2.12.2 (soil C1). ....	ee

Figure 214 – Simulation of the full test using the fitting parameters from 1 cycle (left side) and 2 cycles (right side) and comparison with the experimental data of sample 1.1 (soil C2). .....	ee
Figure 215 – Simulation of the drying and wetting cycles of sample N2 with the fitting parameters of sample N1 (soil A1sup). .....	ff
Figure 216 – Simulation of the drying and wetting cycles of sample 1.4.1 with the fitting parameters of sample 1.2.1 (soil A2). .....	gg
Figure 217 – Simulation of the drying and wetting cycles of sample 2.13.1 with the fitting parameters of sample 2.12.2 (soil C1). .....	hh
Figure 218 – Sequence of steps followed in the image analysis. ....	kk
Figure 219 – Root density in terms of root dry biomass per unit volume of soil with depth. ....	rr
Figure 220 – Cumulative root density in terms of root dry biomass per unit volume of soil with depth. ....	rr
Figure 221 – Total root length per unit soil volume with depth in cell 1 (a) and cell 2 (b). ....	rr
Figure 222 – Total root volume per unit soil volume with depth in cell 1 (a) and cell 2 (b). ....	ss
Figure 223 – Total number of root tips per unit soil volume with depth in cell 1 (a) and cell 2 (b). ....	ss
Figure 224 – Estimation of root length for verticals with different competition indexes ( $d_{\max} = 10$ m). ....	ww
Figure 225 – Estimation of root length for verticals with different competition indexes ( $d_{\max} = 8$ m). ....	xx
Figure 226 – Estimation of root length for verticals with different competition indexes ( $d_{\min}$ ). ....	yy
Figure 227 – Estimation of number of root tips for verticals with different competition indexes ( $d_{\max} = 10$ m). ....	zz
Figure 228 – Estimation of number of root tips for verticals with different competition indexes ( $d_{\max} = 8$ m). ....	aaa
Figure 229 – Estimation of number of root tips for verticals with different competition indexes ( $d_{\min}$ ). ....	bbb
Figure 230 – Estimation of beta-values for verticals with different competition indexes ( $d = 10$ m, all trees) ....	ccc
Figure 231 – Estimation of beta-values for verticals with different competition indexes ( $d = 10$ m, uphill) ....	ddd
Figure 232 – Estimation of beta-values for verticals with different competition indexes ( $d = 10$ m, downhill) ....	eee
Figure 233 – Estimation of beta-values for verticals with different competition indexes ( $d = 8$ m, all trees). ....	fff
Figure 234 – Estimation of beta-values for verticals with different competition indexes ( $d = 8$ m, uphill). ....	ggg
Figure 235 – Estimation of beta-values for verticals with different competition indexes ( $d = 8$ m, downhill). ....	hhh
Figure 236 – Estimation of beta-values for verticals with different competition indexes ( $d = d_{\min}$ ). ....	iii
Figure 237 – Monitored volumetric water content (vwc) in cell 1 in soil A1 and A2 at Mount Faito. ....	kkk
Figure 238 – Monitored volumetric water content (vwc) in cell 1 in soil B, C1 and C2 at Mount Faito. ....	lll
Figure 239 – Monitored volumetric water content (vwc) in cell 2 in soil A1 and A2 at Mount Faito. ....	mmm

Figure 240 – Monitored volumetric water content (vwc) in cell 2 in soil B, C1 and C2 at Mount Faito.....	nnn
Figure 241 – Monitored suction (s) in cell 1 in soil A1 and A2.....	ooo
Figure 242 – Monitored suction (s) in cell 1 in soil C1 and C2. ....	ppp
Figure 243 – Monitored suction (s) in cell 2 in soil A1 and A2.....	qqq
Figure 244 – Monitored suction (s) in cell 2 in soil C1 and C2. ....	rrr
Figure 245 – Field measurements in cell 1 of volumetric water content (vwc) and suction (s). ....	sss
Figure 246 – Field measurements in cell 2 of volumetric water content (vwc) and suction (s). ....	ttt
Figure 247 – Spatial distribution of the hydraulic gradient considering the effect of all the trees in a range of 8 m from the verticals.....	vvv
Figure 248 – Spatial distribution of suction in soil A1 considering the effect of all the trees in a range of 8 m from the verticals.....	www
Figure 249 – Spatial distribution of suction in soil A2 considering the effect of all the trees in a range of 8 m from the verticals.....	xxx
Figure 250 – Spatial distribution of the volumetric water content in soil A1 considering the effect of all the trees in a range of 8 m from the verticals.....	yyy
Figure 251 – Spatial distribution of the volumetric water content in soil A2 considering the effect of all the trees in a range of 8 m from the verticals.....	zzz
Figure 252 – Spatial distribution of the hydraulic gradient considering the effect of all the trees in a range of 10 m from the verticals.....	aaaa
Figure 253 – Spatial distribution of suction in soil A1 considering the effect of all the trees in a range of 10 m from the verticals.....	bbbb
Figure 254 – Spatial distribution of suction in soil A2 considering the effect of all the trees in a range of 10 m from the verticals.....	cccc
Figure 255 – Spatial distribution of the volumetric water content in soil A1 considering the effect of all the trees in a range of 10 m from the verticals.....	dddd
Figure 256 – Spatial distribution of the volumetric water content in soil A2 considering the effect of all the trees in a range of 10 m from the verticals.....	eeee
Figure 257 – Spatial distribution of the hydraulic gradient considering the effect of the closest tree from the vertical.....	ffff
Figure 258 – Spatial distribution of suction in soil A1 considering the effect of the closest tree from the vertical.....	gggg
Figure 259 – Spatial distribution of suction in soil A2 considering the effect of the closest tree from the vertical.....	hhhh
Figure 260 – Spatial distribution of the volumetric water content in soil A1 considering the effect of the closest tree from the vertical.....	iiii
Figure 261 – Spatial distribution of the volumetric water content in soil A2 considering the effect of the closest tree from the vertical.....	jjjj

Figure 262 – Root cohesion per vertical with depth FBM (load distributed according to the root cross-section area). .....	tttt
Figure 263 – Root cohesion per vertical with depth FBM (load distributed according to the root diameter). .....	tttt
Figure 264 – Root cohesion per vertical with depth FBM (equally distributed load by all roots). .....	uuuu



## Index of tables

Table 1 – Common classification of landslides occurring in shallow pyroclastic soil covers according to the updated Varnes classification proposed by Hungr et al. (2014). .....	12
Table 2 – Beneficial and negative effects of vegetation on slope stability (Gray and Sotir, 1996). .....	20
Table 3 – Rooting depth of different types of plants and soil layer thicknesses (Stokes et al., 2009). .....	21
Table 4 – Lateral root growth in terms of radius for different plants (Stokes et al., 2009). .....	21
Table 5 – Summarized desirable root traits to be considered in the slope stability analysis (Stokes et al., 2009). .....	23
Table 6 – Detailed description of the geological profile at Mount Faito. ....	39
Table 7 – Thickness of each soil layer found in the boreholes represented in Figure 33. ....	40
Table 8 – Liquid limit, plastic limit, and plasticity index of soil C1 and C2 collected at Mount Faito performed by Mastantuono (personal communication). ....	43
Table 9 – Mean and standard deviation of soil physical properties: specific gravity ( $G_s$ ), dry density ( $\gamma_d$ ) and soil porosity. ....	43
Table 10 – Summary of the specific gravity (dimensionless) of the root wood to be adopted in the calculation of root volume for each experiment and respective soil and root conditions. ....	54
Table 11 – Scheme of the input table of the initial estimation of the fitting parameters of the main drying curve in HYDRUS-1D (an example). ....	66
Table 12 – Scheme of the input table of the boundary conditions for the main drying curve fitting in HYDRUS-1D. ....	66
Table 13 – Scheme of the input table of the data sets for the main drying curve fitting in HYDRUS-1D. ....	67
Table 14 – Scheme of the input table of the initial estimation of the fitting parameters of the main wetting curve in HYDRUS-1D (an example). ....	70
Table 15 – Scheme of the input table of the boundary conditions for the main wetting curve fitting in HYDRUS-1D. ....	70
Table 16 – Scheme of the input table of the data sets for the main drying curve fitting in HYDRUS-1D. ....	70
Table 17 – Mean and standard deviation of $\log(K_{sat})$ of each soil type. ....	72
Table 18 – Coefficient of determination of the logarithm of suction along time in the fitting of 1 or 2 cycles (drying-wetting loops). ....	83
Table 19 – Fitted parameters adopted from the sample 'Fit' and 'Simulate' for each of the cases (1 to 4). ....	86
Table 20 – Location of the meteorological stations. ....	98
Table 21 – Time resolution of data recording and working period in each meteorological station. ....	99
Table 22 – Constants necessary for the calculation of the psychrometric constant. ....	100
Table 23 – List of constants used in the calculation of the reference evapotranspiration. ....	102
Table 24 – Instrumentation depths of TDR probes and tensiometers in profiles. ....	105

Table 25 – Input parameters to PC-TDR. ....	109
Table 26 – Objectives of the calibration tests of the tensiometers. ....	111
Table 27 – Root density indicators (D is root diameter).....	115
Table 28 – Selected hydraulic property indicators for the fitting of the spatial distribution model. ....	117
Table 29 – Parameter $\beta$ obtained per soil profile.....	132
Table 30 – Recommended spatial root distribution models. ....	137
Table 31 – Mean soil physical properties of Mount Faito (A1, A2 and C1) and of Monteforte (1, 2 and 6 in Pirone et al., 2015a) (adapted from Dias et al.,2018). ....	137
Table 32 – Properties of the tested samples (adapted from Dias et al.,2018). ....	138
Table 33 – Calibration parameters of the polynomial model. ....	140
Table 34 – Calibration parameters of the logarithmic model. ....	141
Table 35 – Calibration parameters of the Roth model. ....	141
Table 36 – Initial air column of the tests. ....	145
Table 37 – Vertical settlements (dv) and void ratio (e) change along the tests on soil A1. ....	182
Table 38 – Vertical settlements (dv) and void ratio (e) change along the tests on soil C1 in saturated conditions. ....	182
Table 39 – Settlements (dv) and void ratio (e) change along the tests on soil C1 in unsaturated conditions. ....	186
Table 40 – Adopted soil properties in the calculation of slope stability. ....	191
Table 41 – Date, trench, soil type and depth of each borehole collected at Mount Faito for physical and hydraulic characterization. ....	a
Table 42 – List of samples collected in Mount Faito for mechanical characterization.....	b
Table 43 – List of identified species in July and September 2017 at Mount Faito test site (Annalisa Santangelo and Sandro Strumia, personal communication). ....	c
Table 44 – Saturated permeability of individual tests and average value per sample.....	r
Table 45 – Saturated permeability of several samples performed by Mastantuono (personal communication). ....	s
Table 46 – Measured and adopted values of volumetric water content (vwc) and suction for the objective function (inverse analysis) in the high suction range. ....	t
Table 47 – Fitted parameters of the main drying WRC and HPF of each sample and respective R <sup>2</sup> -index of the fitting.....	u
Table 48 – Mean fitted parameters of the main drying WRC and HPF of each soil type. ....	u
Table 49 – Standard deviation of the fitted parameters of the main drying WRC and HPF of each soil type. ....	v
Table 50 – Fitted parameters of the main wetting WRC and HPF of each sample and respective R <sup>2</sup> -index of the fitting using data from 1 cycle, as well as the saturated hydraulic conductivity adopted in the model. ....	y

Table 51 – Mean fitted parameters of the main wetting WRC and HPF of each soil type. ....	aa
Table 52 – Standard deviation of the fitted parameters of the main wetting WRC and HPF of each soil type. .....	aa
Table 53 – Roots dry biomass collected in the samples tested in the permeameter and/or the ku-pf apparatus. ....	ii
Table 54 – Diameter at breast height (DBH) and tree to profile distance. ....	pp
Table 55 – Tree position relatively to a profile (1 – uphill, 2 – downhill). ....	qq
Table 56 – $\beta$ -value from the calibration of the exponential model (D stands for root diameter in mm). ....	tt
Table 57 – $R^2$ -index relative to the fitting of the $\beta$ -value (D stands for root diameter in mm). ....	uu
Table 58 – Observed root density indicators (D stands for root diameter in mm). ....	vv
Table 59 – Fitting parameters of the spatial root distribution model for each root density indicator and each tree position and distance tree-to-vertical range. ....	jjj
Table 60 – Observed parameters for the fitting of the spatial distribution model. ....	uuu
Table 61 – Constants added to the hydraulic observations of gradient. ....	uuu
Table 62 – Fitting parameters of the spatial distribution model adapted to hydraulic observations. ....	kkkk
Table 63 – Mean root cohesion with depth using different models in MPa. ....	uuuu
Table 64 – Standard deviation of the root cohesion with depth using different models in MPa. ....	vvvv
Table 65 – Coefficient $k''$ variation with depth for each load distribution criteria of FBM. ....	vvvv

# List of symbols

## Greek letters

$\alpha$	Calibration constant, fitting parameter
$\alpha$	Slope angle
$\alpha$	Fitting parameter of the Roth model
$\alpha$	Van Genuchten equation fitting parameter
$\alpha^d$	Van Genuchten fitting parameter of the main drying branch
$\alpha^i$	Van Genuchten fitting parameter of the main wetting branch
$\alpha^w$	Van Genuchten equation fitting parameter of the main wetting curve
$\beta$	Calibration constant, fitting parameter
$\beta$	Fitting parameter vector
$\gamma$	Soil unit weight
$\gamma$	Psychometric constant
$\gamma_d$	Soil dry density
$\gamma_w$	Water density
$\Delta$	Slope of the vapour pressure curve
$\Delta t$	Time interval
$\Delta V$	Volume of water that flew through the sample in the time interval $\Delta t$
$\Delta z$	Effective soil depth
$\varepsilon$	Ratio of the molecular weight of water vapour/dry air
$\varepsilon_a$	Dielectric constant of the air
$\varepsilon_c$	Dielectric constant of the soil
$\varepsilon_s$	Dielectric constant of the solid particles
$\varepsilon_w$	Dielectric constant of the water
$\eta_w$	Water absolute viscosity
$\theta$	Shear distortion
$\theta$	Volumetric water content
$\theta_{FC}$	Water content at field capacity
$\theta_r$	Residual volumetric water content
$\theta_s$	Saturated volumetric water content
$\theta_s^w$	Saturated volumetric water content of the main wetting curve
$\theta_{WP}$	Water content at wilting point
$\lambda$	Latent heat of vaporization
$\rho_s$	Specific gravity of the soil

$\sigma$	Total normal stress
$\sigma'$	Effective stress
$\sigma_{aw}$	Air-water interface tension
$\sigma_r$	Normal stress in a root
$\sigma_{\varepsilon h}$	Standard deviation of the suction measurement error estimated from the tensiometers calibration
$\tau$	Soil shear stress
$\tau$	Root-soil frictional resistance
$\tau_f$	Soil shear stress at failure
$\tau_r$	Shear stress in a root
$v_j$	Weighting coefficient for the squared residuals of the data set $j$
$\phi'$	Effective friction angle
$\Phi(\beta)$	Objective function
$\chi$	Effective stress parameter
$\Psi$	Water potential
$\Psi_g$	Gravitational water potential
$\Psi_s$	Matric water potential
$\Psi_\pi$	Osmotic water potential
$\Psi_p$	Pressure water potential

#### Latin letters

$A$	Area of reference
$A$	Cross-section area of the sample
$a, b, c, d$	Calibration constants of the models for the relation between dielectric constant and volumetric water content
$A_r$	Area of the roots cross-section
Alpha	Van Genuchten equation fitting parameter
AlphaW	Van Genuchten equation fitting parameter of the main wetting branch
$C$	Water capacity; water storage modulus
$c'$	Effective cohesion
$c_p$	Specific heat at constant pressure
$c_r$	Root cohesion
$c_s$	Soil heat capacity
$CDR_z$	Cumulative value of the root density from the surface to the depth $z$ dimensionless by the total root density of a give soil profile

$CV_{\beta_i}$	Coefficient of variation of the parameter $\beta_i$
$d$	Root diameter at the section of breakage
$D_{e,i-1}$	Cumulative depth of evaporation from the soil surface layer at the end of the previous day
$d_i$	Distance on the horizontal plane between tree $i$ and the soil profile
$d_{max}$	Maximum distance from the profile to the tree to be considered
$d_n$	Root diameter of the class $n$
$D_r$	Root zone depletion
$DBH_i$	Diameter at breast height of tree $i$
$dh$	Horizontal displacement
$dy$	Vertical displacement
$e$	Soil void ratio
$e^0$	Saturation vapour pressure
$e_0$	Void ratio before root permeation
$e_a$	Actual vapour pressure
$e_s$	Saturation vapour pressure
$ET_c$	Crop evapotranspiration under non-standard conditions
$ET_o$	Reference crop evapotranspiration or reference evapotranspiration
$F_B$	Root tensile resistance
$f_c$	Effective fraction of soil surface covered by vegetation
$f_{ew}$	Exposed and wetted soil fraction
$F_p$	Force necessary to break the root-soil bond or pull out resistance
$f_w$	Fraction of soil surface wetted by irrigation or precipitation
FBM	Fibre bundle model
$G$	Soil heat flux density
$G_b$	Specific gravity for oven-dry and green volume
$G_{b_d}$	Specific gravity for oven-dry and green volume in the diameter class $d$
$G_m$	Specific gravity at a given moisture content $m$
$G_s$	Solid particles specific gravity
GLS	Global load sharing
$GR$	Gross rainfall
$h$	Mean plant height during the mid or late season stage
$h$	Capillary head
$h_{in}$	Elevation of the bottom of the sample
$h_{out}$	Elevation of the top of the sample
HPF	Hydraulic permeability function
$i$	Number of root diameter classes

$i$	Hydraulic gradient
$I$	Interception
$j$	Weakest root removed at each simulation step
$k'$	Parameter that depend on the soil friction angle and on the root distortion angle ( $k' = \sin \theta + \cos \theta \tan \phi'$ )
$k''$	Correction coefficient of the W&W model based on the FBM estimations
$K(h)$	Unsaturated hydraulic conductivity
$K_{c,max}$	Maximum $K_c$ immediately following wetting
$K_{c,min}$	Minimum $K_c$ for dry bare soil with no ground cover
$K_0$	Saturated hydraulic conductivity
$K_{cb}$	Basal crop coefficient
$K_e$	Soil water evaporation coefficient
$K_r$	Soil evaporation reduction coefficient
$k_{rw}$	Relative permeability of water
$K_s$	Saturated permeability
$K_s$	Water stress coefficient
$K_{sat}$	Saturated permeability
$K_{sat}^w$	Saturated permeability of the main wetting curve
$K_{SW}$	Saturated permeability of the main wetting branch
$l$	Mualem equation fitting parameter
$L$	Root length
LLS	Local load sharing
$m$	Fitting parameter
$m$	Wood moisture content (gravimetric)
$m$	Number of measurement sets
$M$	Wood moisture content (gravimetric) in %
$M_{dry}$	Total dry biomass
$N$	Total number of trees
$N$	Number of roots
$N$	Number of root classes
$n$	Root number ordered from strongest to weakest
$n$	Porosity
$n$	Fitting parameter
$n$	Van Genuchten equation fitting parameter
$N_c$	Capillary number
$n_i$	Number of roots of the class diameter $i$

$n_j$	Number of measurements of the set $j$
$NR$	Net rainfall
$P$	Atmospheric pressure
$p$	Average fraction of $TAW$ that can be depleted from the root zone before suffering water stress
$p$	Competition index
$p$	Index indicative of the WRC branch
$p_{in}$	Water pressure flowing inward the soil sample
$p_{out}$	Water pressure flowing outward of the soil sample
$\hat{q}_{j,i}(\beta)$	Estimated value of $q_{j,i}$ based on the parameter vector $\beta$
$\hat{q}_i$	Estimated value of $q_i$
$q_{j,i}$	A specific measurement of the set $j$
$q_w$	Darcian water flux
$Q_m$	Lenhard hysteretic model fitting parameter
$Q_r$	Residual volumetric water content
$Q_s$	Volumetric water content at saturation
$Q_{sW}$	Volumetric water content at saturation of the main wetting branch
$R$	Rainfall
$R^2$	Coefficient of determination
$r^2$	Parameter to determine the goodness of a fit
$R_a$	Extra-terrestrial radiation
$R_n$	Net radiation at the crop surface
$R_v$	Root volume ratio
$RAR$	Root area ratio
$RAR_n$	Root area ratio of the entire root diameter class
$RBM$	Root bundle model
$RBMw$	Root bundle model with a Weibull survival function
$RD$	Root density indicator
$\widehat{RD}$	Estimated root density indicator
$REW$	Cumulative depth of evaporation at the end of stage 1
$RH_{max}$	Maximum relative humidity
$RH_{min}$	Minimum relative humidity
$RLD$	Root length density
$s$	Suction
$\bar{S}_a$	Effective air saturation
$\bar{S}_{ar}$	Residual saturation of the scanning curve starting from $\bar{S}_w^A$



$\bar{S}_{ar}^i$	Residual air saturation of the main wetting branch
$\bar{S}_{at}$	Effective entrapped air saturation
$\bar{S}_w$	Effective water saturation
$\bar{\bar{S}}_w$	Apparent water saturation
$\bar{S}_w^\Delta$	Saturation at the reversal point on the main drying branch
$S_{h,\beta_l}(z, t)$	Dimensionless scaled sensitivity of the matric suction head to the generic parameter $\beta_l$
$S_a$	Actual air saturations
$s_f$	Shear stress at failure
$S_m$	Irreducible water saturation
$S_r$	Degree of saturation
$s_r$	Shear strength component due to the root system
$s_s$	Effective shear strength of the soil matrix
$S_w$	Actual water saturation
$s_\psi$	Shear strength component due to matric suction
$SF$	Stemflow
SRL	Specific root length
$T$	Mean daily air temperature at 2 m height from the surface
$t$	Time
$T_{r,j}$	Strength of the weakest remaining root
$T_{r,n}$	Average tensile strength of the root class
$T_i$	Air temperature at time $i$
$T_{max}$	Maximum temperature
$T_{min}$	Minimum temperature
$t_r$	Mobilized tensile stress of root fibre per unit area of soil
$T_r$	Root tensile strength
TAW	Soil total available water
TDR	Time-domain reflectometry
TEW	Maximum cumulative depth of evaporation from the soil surface layer when $K_r = 0$
TF	Throughfall
$u_2$	Wind speed at 2 m above ground surface
$u_a$	Air pressure
$u_w$	Pore-water pressure
$u_z$	Measured wind speed at $z$ m above ground surface
$V_d$	Root volume in the diameter class $d$
$V_m$	Wood volume at a given moisture content $m$
W&W	Wu and Waldron model

$w_{j,i}$	Weighting factor of the experimental value $q_{j,i}$
$W_{oven-dry}$	Oven-dry weight of the wood
$w_i$	Weights associated to a given experimental measurement $q_i$
WCF	Water capacity function
WRC	Water retention curve
$z$	Thickness of the soil layer above the adopted failure surface
$z$	Elevation above sea level
$z$	Depth
$z$	Position in the soil column where suction head was measured
$Z_r$	Rooting depth

# Chapter 1 Introduction and literature review

## 1.1 Introduction

### 1.1.1 Motivation

The region of Campania, in the South of Italy, is characterized by mountainous areas composed of fractured limestone, usually covered by several layers of pyroclastic deposits originated from explosive type eruptions of the nearby Vesuvius volcano. Landslides frequently occur in these areas leading to human and economic losses (Figure 1), as the events of Sarno in 1998 and Nocera in 2004. The landslides in this area are triggered by prolonged and intense rainfall events, originating flow of pyroclastic material characterized by its great velocity and fluidity.

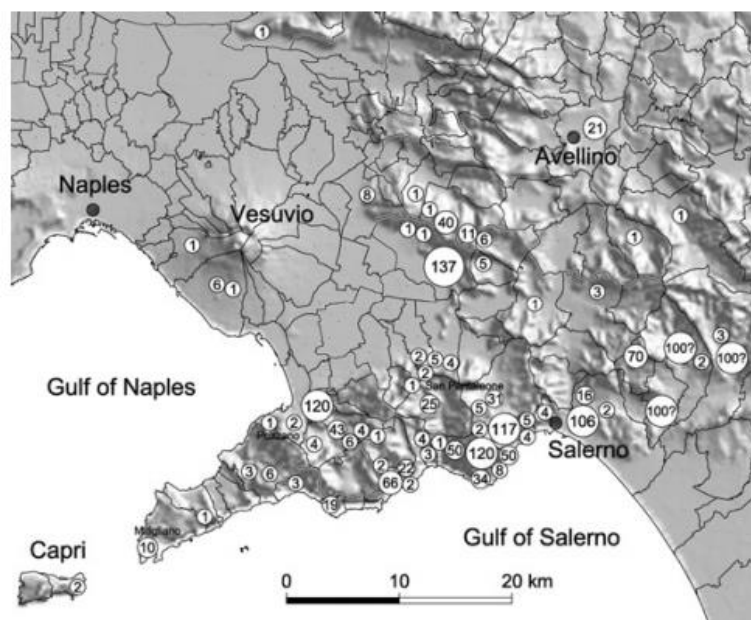


Figure 1 – Number of victims in the Campania region caused by landslides from 1580 to 1998 (Cascini et al., 2008).

Employed mitigation measures involve the use of early warning systems. Construction of basins to prevent the landslide deposits to reach localities have also been made in the region of Salerno after the incident of Sarno in 2004. However, the pyroclastic soil deposits cover a vast area that might require a diffuse mitigation solution. One single rainfall event usually leads to many landslides, of different types and spread through an immense area. Take the example of the inventory of landslides of January 1997 presented in Figure 2.

Environmentally friendly approaches are becoming more popular in the latest years as a landslide mitigation measure due to their low relative cost and for decreasing the carbon emissions. The use of vegetation in slope stability and erosion problems is common among ecologists but less work has been done in the perspective of the geotechnical engineering.

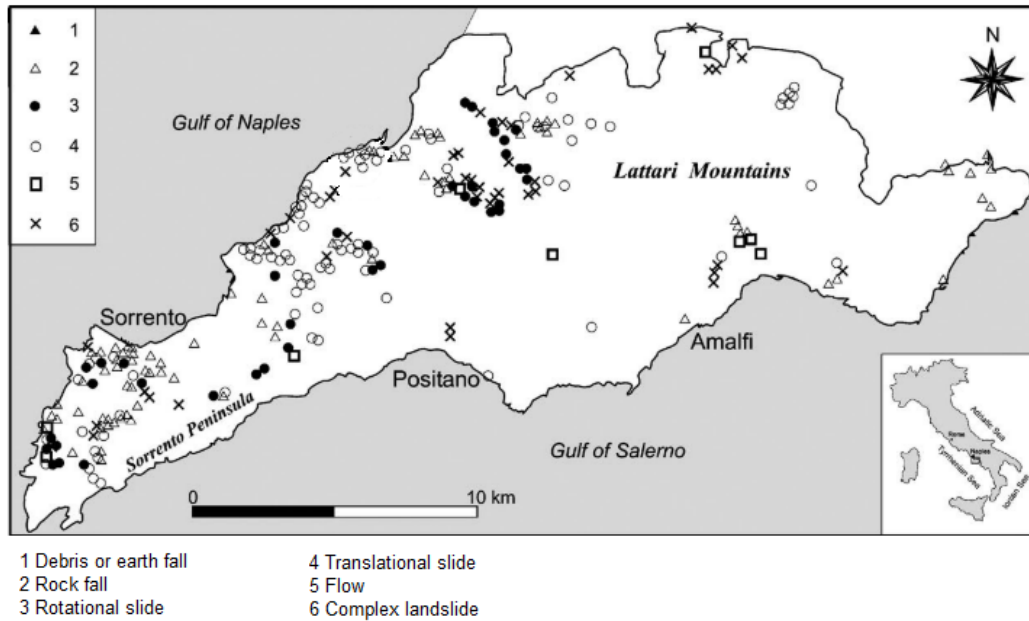


Figure 2 – Inventory map of the January 1997 landslides in the Sorrento Peninsula, (adapted from Calcaterra and Santo, 2004).

Vegetation is known for changing the soil hydraulic and mechanical properties but its quantification has been poorly investigated in pyroclastic soils in the region of Campania (Comegna *et al.*, 2013). The vegetation presents some potential positive and negative effects on the stability of slopes that require detailed investigation. As shown in previous works, the landslides are deeply controlled by the water flow within the pyroclastic soil cover (Urciuoli *et al.*, 2016; Pirone *et al.*, 2015a).

### 1.1.2 Organization of the document

The present thesis is divided into six chapters which overview is made in this section.

In Chapter 1 “Introduction and Literature Review”, the base concepts necessary for the development of this thesis research work are presented, as well as the research objectives. The literature review presented in this chapter includes concepts of unsaturated soil, the research that has been done on pyroclastic soil in the region of Campania, and previous landslides and groundwater regimes in the soil covers of the investigated area. Some research on the use of vegetation in civil engineering was also explored. At last, the objectives, research questions and hypothesis are presented.

In Chapter 2 “Mount Faito test site overview” was included in this thesis because the research work was made with focus on a test site which was representative of the general characteristics of slopes where landslides occur in Campania (Italy). This test site was located in Mount Faito, which is part of the Lattari mountains and is in the surroundings of the Vesuvius volcano. Different features of this test site were

presented in what regards the topography, stratigraphy (geological profile), vegetation, and soil physical properties necessary for the elaboration of the geotechnical model. All these elements were necessary for the studies processed in Chapters 3 to 5.

In Chapter 3 “Hydraulic characterization of natural unsaturated pyroclastic soils”, an extensive hydraulic characterization of pyroclastic soil collected in Mount Faito was presented. Focus was given to the fact that it was natural soil so that the soil structure, porosity and presence of roots was accounted in the studies. The experimental data was used to calibrate and validate a model that considers the hysteresis of hydraulic properties of unsaturated soils.

The monitoring of the groundwater and meteorological conditions of Mount Faito test site are presented in Chapter 4 “Groundwater regime interaction with atmosphere and vegetation”. The root distribution was investigated and models of root vertical and spatial distribution were fitted. The response of the soil to the seasons and to the single rainfall events were studied through the monitored data. The spatial distribution of several hydraulic soil responses was related to the spatial distribution of trees and roots.

Chapter 5 “The relative contribution of suction, soil and root shear resistance to slope stability” is devoted to understand if the overall presence of trees in Mount Faito test site was positive or negative for the stability of the slope. The soil mechanical properties and root mechanical reinforcement were assessed. Slope stability analysis was performed in order to quantify the weight of each of the shear resistance components: soil, suction and roots.

Lastly, the main contributions of the developed research were summarized in Chapter 6 “Conclusion and future work”. The future work section explores possible improvements to the thesis and ways of complementing the developed work. Suggestions on topics that constitute knowledge gaps detected during the thesis developed are presented as well.

## 1.2 Unsaturated soils

### 1.2.1 Water potential

The water potential is the potential energy per unit volume of water in the soil relative to pure water at atmospheric pressure and at a predefined elevation (Hillel, 2004). The total water potential is a sum of four components: gravitational potential ( $\Psi_g$ ), matric potential ( $\Psi_s$ ), osmotic potential ( $\Psi_\pi$ ), and pressure potential ( $\Psi_p$ ) as represented in Equation 1.

$$\Psi = \Psi_g + \Psi_s + \Psi_\pi + \Psi_p \quad 1$$

The matric suction is the component of water potential that is associated to the adsorptive forces binding water to the soil matrix. The osmotic potential results from different concentrations of ions in the water.

Gravitational potential reflects elevation differences between the observation point and the reference level. The pressure potential depends on the hydrostatic or pneumatic pressure on the water.

In the geotechnical engineering field, matric suction refers to the matric potential component of the water potential (Boldrin, 2018). Matric suction is commonly used in the field because it is closely related to the stress state of the soil (Alonso *et al.*, 1990). The concept of total suction, which is the sum of matric and osmotic potential, is also a commonly used concept specially in the study of clayey soils (Romero, 2001). Osmotic suction values range in values close to the matric suction in fine grained soils (in the order of MPa), so that saline solutions osmotic potential influence the total suction in the soil, commonly known as vapour equilibrium technique (Dias, 2015). The hydraulic head, also a geotechnical engineering concept, that refers to the sum of the matric, pressure and gravitational water potential, is used to study the direction of the water flow within a soil, as explained in detail in Fredlund and Rahardjo (2012).

The water movement in the soil-plant-atmosphere continuum, which is driven by the evaporation of water from the leaves, occurs as long as the water potential in the plant is lower than in the soil. This difference in water potential is what generates the plant water uptake. When soil-plant-atmosphere interactions through evapotranspiration are studied, water potential gradients are investigated, as by Boldrin (2018).

### **1.2.2 Water retention curves**

The water retention curve (WRC), also referred as soil water characteristic curve, relates suction and water content. The water content can be represented in terms of volume as volumetric water content, in terms of mass as gravimetric water content or in terms of degree of saturation. Throughout the thesis, the preferred manner of representing the water content is in terms of volume. Suction is the difference between air and water pressure resultant from the formation of water meniscus in soil pores.

A typical shape of the WRC can be found in Figure 3, which is divided into three zones: (i) boundary effect zone, (ii) transient zone, and (iii) residual zone of saturation. In the first zone, suction increases and almost no variation of water content is observed. The air enters to soil voids once suction reaches the air-entry value (AEV). In the transient zone, suction gradually increases with decrease of water content keeping both fluid phases continuous. The residual zone of unsaturation starts and the water phase losses continuity after the residual water content is reached. The suction increases greatly for a small decrease of water content in this zone. The maximum value of suction of 1000 MPa is common to all types of soils (Fredlund and Xing, 1994; Vanapalli *et al.*, 1999).

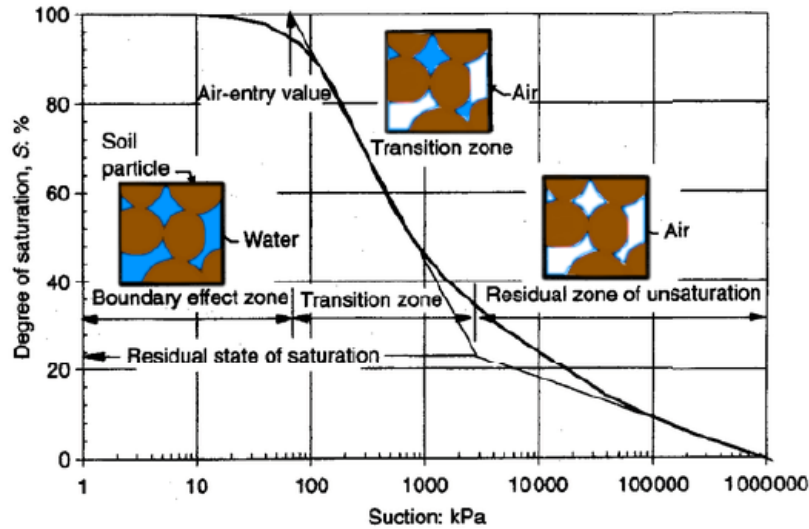


Figure 3 – Typical water retention curve (adapted from Vanapalli et al., 1999).

The soil does not respond in the same manner during wetting and drying in the water retention plan. The suction is lower for the same water content if the soil is going through wetting than if it is being dried. Therefore, there are two main branches of the water retention curve, as observed in Figure 4, usually referred as the main hysteretic loop. This loop does not usually close because entrapped air remains in the pores of the soil as a result of the wetting process. If the wetting or drying process is inverted at any instance, the followed path corresponds to a scanning curve. Any path is only possible in the range delimited by the main hysteretic loop (main drying and wetting curves).

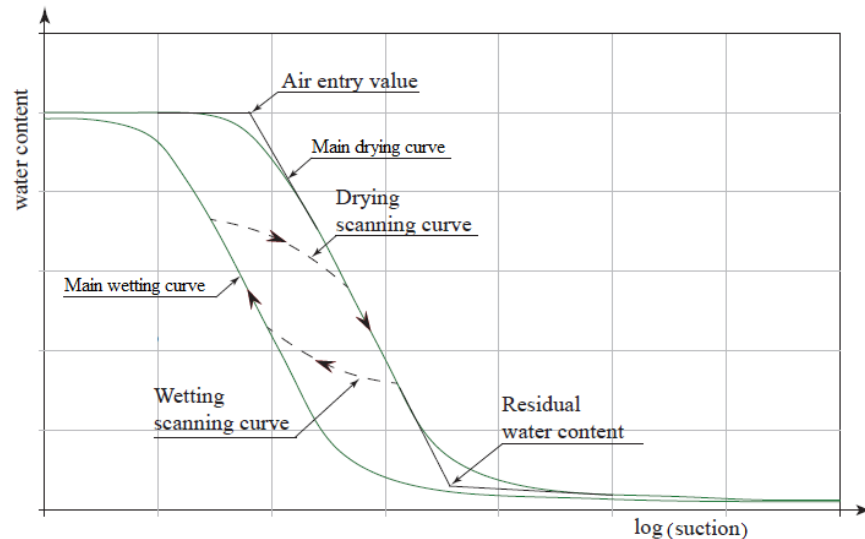


Figure 4 – Illustration of main and scanning water retention curves (adapted from Switala, 2016).

Many equations are available in the literature to describe the WRC, among the most popular are van Genuchten (1980) and Fredlund and Xing (1994), which are empirical equations.

The typical shapes of the WRC of different types of soils are presented in Figure 5. Finer soils have higher AEV than course-grain soils. The techniques adopted for the characterization of each type of soils need to be adequate for the expected range of suction values.

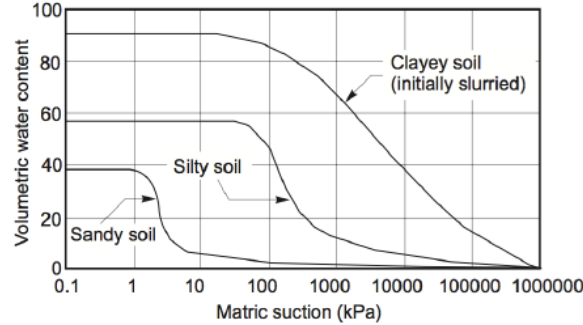


Figure 5 – Water retention curves of sandy, silty and clayey soils (Fredlund and Xing, 1994).

### 1.2.3 Hysteretic k-S-P models

Hysteresis in K-S-P (permeability-saturation-pressure) relations are observed when there is a reversal of the wetting or drying process. The hysteresis has been attributed to the changes in the water contact angle, irregular pore geometry, and air entrapment effects.

In the work of Lenhard *et al.* (1991), each of the causes that lead to hysteresis has been individually considered in the study. Hysteresis results from air entrapment because, during wetting, air remains in the soil when water enters into large pores and, during drying, entrapped air is released when water enters into smaller pores. The entrapped air also causes hysteresis in the K-S relation because it obstructs the water movement, increasing its resistance to flow. However, the entrapped air forces the water to flow through the larger cavities. Overall, higher water conductivity in wetting paths than in drying paths is the observed effect for the same saturation (Lenhard *et al.*, 1991).

The entrapped air can move out from soil by dissolution or due to water movement but it is unlikely because the water is air-saturated at the atmospheric pressure. Additionally, dissolution of air is a phenomenon that takes weeks to months to occur. On the other hand, the water velocity necessary to displace entrapped air bubbles requires a capillary number ( $N_c$ ) greater than  $10^{-5}$ . The capillary number is given by Equation 2, where  $q_w$  is the Darcian water flux,  $\eta_w$  is the water absolute viscosity, and  $\sigma_{aw}$  is the air-water interface tension. It was concluded that the Darcian water velocity would have to exceed  $2.6 \text{ m h}^{-1}$  to displace entrapped air, which is a high velocity (Lenhard *et al.*, 1991).

$$N_c = \frac{q_w \eta_w}{\sigma_{aw}} \quad 2$$



### 1.2.3.1 Hysteretic water retention model

Models have been proposed to describe the hysteresis. Kool and Parker (1987) model was simple but the hysteretic loops were not closed which led to the so called pumping effect. The pumping effect is obtained when the water retention path moves outside the main hysteretic loop, taking impossible values, after several inversions are accumulated. Lenhard and Parker (1987) proposed a model with close loops avoiding the pumping effect in the simulations. This model was simplified by Lenhard *et al.* (1991) to consider only two fluids as described in this section.

Lenhard *et al.* (1991) introduced the concept of apparent saturation ( $\bar{\bar{S}}_w$ ) in order to consider the effect of entrapped air in the WRC. During a wetting phase, the water that enters in larger pores entraps air that becomes discontinuous. Water is considered to be always a continuous media in this model. The apparent saturation ( $\bar{\bar{S}}_w$ ) refers to the water containing entrapped air as in Equation 3, which is the sum of the effective water saturation ( $\bar{S}_w$ ) and the effective entrapped air saturation ( $\bar{S}_{at}$ ).

$$\bar{\bar{S}}_w = \bar{S}_w + \bar{S}_{at} \quad 3$$

The effective water saturation ( $\bar{S}_w$ ) and the effective air saturation ( $\bar{S}_a$ ) are given by Equations 4 and 5 where  $S_w$  and  $S_a$  are actual water and air saturations, respectively, and  $S_m$  is an irreducible water saturation.

$$\bar{S}_w = \frac{S_w - S_m}{1 - S_m} \quad 4$$

$$\bar{S}_a = \frac{S_a}{1 - S_m} \quad 5$$

The amount of air that is entrapped when there is a wetting starting from any point of the main drying curve ( $\bar{S}_{ar}$ ) is calculated with the algorithm proposed by Land (1968) given by Equations 6 and 7. The value  $\bar{S}_{ar}$  corresponds to the amount of entrapped air after the re-saturation of the soil, i.e. when the water pressure returns to zero, the parameter  $\bar{S}_w^\Delta$  is that saturation at the reversal point on the main drying branch,  $\bar{S}_{ar}$  is referred as the residual saturation of the scanning curve starting from  $\bar{S}_w^\Delta$ , and  $\bar{S}_{ar}^i$  is the residual air saturation of the main wetting branch. These parameters can easily be visualized in Figure 6(a) in terms of actual saturation.

$$\bar{S}_{ar} = \frac{1 - \bar{S}_w^\Delta}{1 + R_{aw}(1 - \bar{S}_w^\Delta)} \quad 6$$

$$R_{aw} = \frac{1}{\bar{S}_{ar}^i} - 1 \quad 7$$

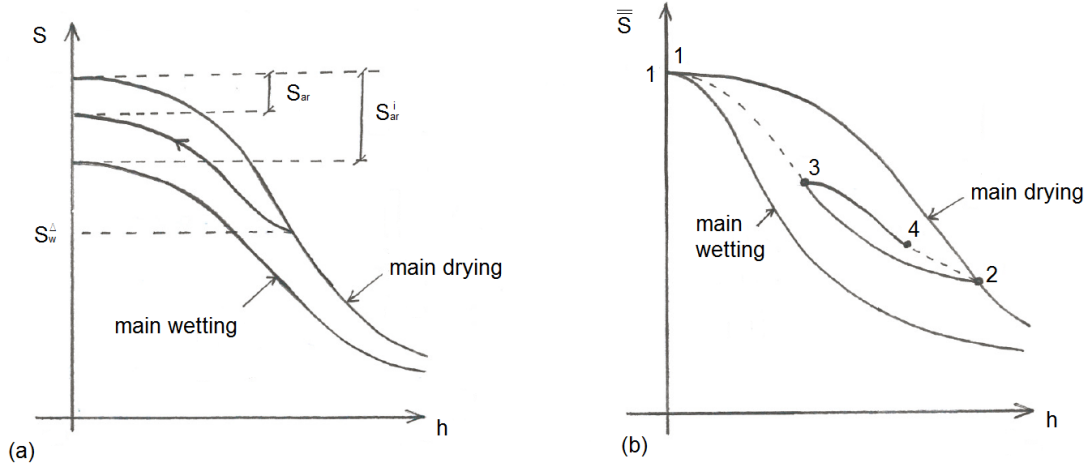


Figure 6 – Hysteretic loops in the water retention plan when saturation is (a) actual water saturation and (b) apparent water saturation.

The effective entrapped air ( $\bar{S}_{at}$ ) was assumed to vary linearly between zero, as starting condition of the main drying curve, and the residual saturation of the main wetting curve ( $\bar{S}_{ar}$ ), as in Equation 8. In the main drying curve, when the apparent water saturation is equal to the saturation at the reversal point, then there is no entrapped air ( $\bar{S}_w = \bar{S}_w^\Delta \rightarrow \bar{S}_{at} = 0$ ), and in the main wetting curve, when the apparent water saturation is maximum, then the entrapped air saturation is maximum and equal to the residual air saturation ( $\bar{S}_w = 1 \rightarrow \bar{S}_{at} = \bar{S}_{ar}$ ). Consequently, air is entrapped as the water enters larger pores in the same amount it is released when  $\bar{S}_w$  decreases in drying phase according to this formulation. In this model, the main drying curve is followed when  $\bar{S}_w$  is less than the historic  $\bar{S}_w^\Delta$  and  $\bar{S}_w^\Delta$  set equal to  $\bar{S}_w$ .

$$\bar{S}_{at} = \bar{S}_{ar} \left( \frac{\bar{S}_w - \bar{S}_w^\Delta}{1 - \bar{S}_w^\Delta} \right), \bar{S}_w \geq \bar{S}_w^\Delta \quad 8$$

The main drying and wetting curves are assumed to have the same shape by adopting the van Genuchten (1980) equation for both cases (Figure 6,b) and each of the main branches has its own set of parameters. The fitting parameter  $n$  is considered equal in both equations ( $n = n^d = n^w$ ). The effect of the changes in contact angle of water and irregular pore geometry in the hysteretic loop are taken into account by Lenhard *et al.* (1991) in the fitting parameters  $\alpha^d$  and  $\alpha^i$  of the main drying and wetting curves, respectively, as suggested in Kool and Parker (1987). Equation 9 refers to the main drying branch as indicated by the index  $d$  in  $\bar{S}_w^d(h)$ , which is the apparent saturation at a capillary head  $h$ , the same is applicable for Equation 10 that refers to the main wetting branch.

$$\bar{S}_w^d(h) = [1 + (\alpha^d h)^n]^{\frac{1}{n}-1} \quad 9$$

$$\bar{S}_w^i(h) = [1 + (\alpha^i h)^n]^{\frac{1}{n}-1} \quad 10$$

The scanning curves were scaled from the main curves using the method described in Parker and Lenhard (1987) in which the scanning curves pass through reversal points so that hysteretic loops close and no pumping effect is obtained. The method can be written in the form of Equation 11, where the coordinates  $(\bar{S}_l^\Delta, h_l^\Delta)$  are the apparent saturation and hydraulic head of the reversal point, and the coordinates  $(\bar{S}_{l-1}^\Delta, h_{l-1}^\Delta)$  are the apparent saturation and hydraulic head of the reversal point before  $(\bar{S}_l^\Delta, h_l^\Delta)$ . The index  $p$  refers to the branch that is intended to be described, i.e. if the curve corresponds to a drying branch, then  $p = d$ , otherwise  $p = i$  and it refers to a wetting branch. This method requires the storage of the previous reversal points.

$$\bar{S} = \frac{[\bar{S}^p(h) - \bar{S}^p(h_{l-1}^\Delta)](\bar{S}_l^\Delta - \bar{S}_{l-1}^\Delta)}{\bar{S}^p(h_l^\Delta) - \bar{S}^p(h_{l-1}^\Delta)} + \bar{S}_{l-1}^\Delta \quad 11$$

As an example, if the path between the points 2 and 3 of Figure 6(b) is intended to be described, then the coordinates  $(\bar{S}_l^\Delta, h_l^\Delta)$  are of point 2, the coordinates  $(\bar{S}_{l-1}^\Delta, h_{l-1}^\Delta)$  are of the point 1 and  $p = i$  because it is a wetting scanning curve. On the other hand, to describe the path from point 3 to 4, the coordinates  $(\bar{S}_l^\Delta, h_l^\Delta)$  are of point 3, the coordinates  $(\bar{S}_{l-1}^\Delta, h_{l-1}^\Delta)$  are of the point 2 and  $p = d$ .

Note that the water retention loop in terms of apparent saturation is closed at null capillary head (Figure 6,b) and the air saturation at null water pressure of the main wetting curve ( $\bar{S}_{ar}^i$ ) is required in order to observe the air entrapment in the water retention plan.

### 1.2.3.2 Hysteretic water conductivity model

The entrapped air can produce hysteresis in the K-S relations. The entrapped air is an obstacle for water movement increasing the resistance to flow. The entrapped air also makes water move into larger pores, which facilitates the water flow. According to Lenhard *et al.* (1991), the balance is that water conductivity tends to be higher in wetting branches than in drying branches for the same actual water saturation. Nonetheless, hysteresis of hydraulic conductivity is little and only increases important for high saturation values (Kool and Parker, 1987). A modification of the Mualem (1976) model was implemented by Lenhard and Parker (1987) and Equation 12 was obtained, where  $k_{rw}$  is the relative permeability of water and  $m = 1 - 1/n$ .

$$k_{rw} = \bar{S}_w^{1/2} \left[ 1 - \left( 1 - \frac{\bar{S}_{ar}}{1 - \bar{S}_w^\Delta} \right) \left( 1 - \bar{S}_w^{\frac{1}{m}} \right)^m - \left( \frac{\bar{S}_{ar}}{1 - \bar{S}_w^\Delta} \right) \left( 1 - \bar{S}_w^{\frac{1}{m}} \right)^m \right]^2 \quad 12$$

The relative hydraulic conductivity ( $k_{rw}(h)$ ) is the ratio between the unsaturated ( $K(h)$ ) and saturated ( $K_0$ ) hydraulic conductivity as in Equation 13.

$$K(h) = K_0 \cdot k_{rw}(h) \quad 13$$

### 1.2.4 Effective stress in unsaturated soil mechanics

The stress acting on the soil particles is referred as effective stress, which affects the soil mechanical behaviour, i.e. shear strength and volume changes. In saturated soils, the Terzaghi's definition of effective stress is represented by Equation 14, where the effective stress ( $\sigma'$ ) is the difference between the total stress ( $\sigma$ ) and the pore water pressure ( $u_w$ ).

$$\sigma' = \sigma - u_w \quad 14$$

However, in unsaturated soils, effective stresses are more complex to quantify because the soil in those conditions present three phases (solid particles, air and water) instead of two as in the saturated soil. The effective stress depends on the pore air pressure and on suction. In the formulation of Bishop (1954), the effective stress in unsaturated conditions represented by Equation 15, where  $\chi$  is the effective stress parameter, and the term  $(u_a - u_w)$  refers to matric suction. The parameter  $\chi$  varies between 0 and 1, in which 1 corresponds to the soil saturation and 0 to the dry soil. The parameter  $\chi$  can be considered equal to the degree of saturation.

$$\sigma' = (\sigma - u_a) + \chi(u_a - u_w) \quad 15$$

## 1.3 Pyroclastic slopes in Campania

### 1.3.1 Landslides

Urciuoli *et al.* (2016) investigated two different sites in areas prone to rainfall induced landslides in Campania, southern Italy. Both sites presented a slope angle between 30° and 40°, composed of a pyroclastic soil cover of alternating volcanic ashes and pumices layers with a total thickness varying from 2.4 to 4 m. These sites were located in Cervinara and Monteforte Irpino.

Slopes of such type in this area of Campania are characterized for steepness that can be up to 40-45°. The friction angle of the soil that composes the pyroclastic cover varies between 35° and 38°. The slope stability is usually attributed to the apparent cohesion resultant from the unsaturated conditions in which these materials are found. Field monitoring showed that the rainfall events, occurring from September to December, reduce the suction in the soil to values close to the AEV (Papa *et al.*, 2013; Pirone *et al.*, 2015a; Urciuoli *et al.*, 2016). Then, during a long period of time, suction is maintained low, so the predisposing conditions for the occurrence of landslides are present. An extreme rainfall event can be the trigger of the landslide (Urciuoli *et al.*, 2016). The sequence of events that lead to the landslide are schematized in Figure 7. The predisposing conditions depend on the hydraulic behaviour of pyroclastic soil covers and its importance was specially highlighted by Calcaterra and Santo (2004). More details on the hydraulic behaviour of pyroclastic soil covers are presented in the next section.

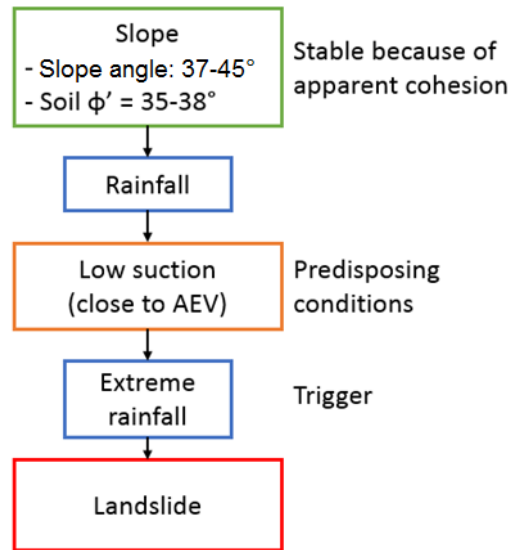


Figure 7 – Scheme of the events and conditions that lead to landslides in pyroclastic soil covers.

The common type of landslides identified in Urciuoli *et al.* (2016) are classified according to the system proposed by Hungr *et al.* (2014) as sand/silt/debris flowslides, debris flows and debris avalanches. All these three types of landslides fall into the category of flow-like landslides and are characterized by fast flow of coarse grain material as summarized in Table 1.

Di Crescenzo and Santo (2005) identified three stages in the development of these type of landslides: (i) the triggering, (ii) the translational sliding, and (iii) the channelized flow and accumulation, as identified in Figure 8. The characteristics that are associated to the each phase of the landslide development were investigated in Di Crescenzo and Santo (2005) landslide inventory of debris flow landslides. Landslides were triggered in small areas due to brief and intense meteorological events after long a period of rainfall. The trigger occurred mostly in the presence of man-made cuts (Del Prete *et al.*, 1998; Di Crescenzo and Santo, 1999; Calcaterra and Santo, 2004). Indeed, 86% of the landslides identified in Di Crescenzo and Santo (2005) developed above or below roads and rocky cliffs, the steepness of most triggering zones fell between 35° and 45°, and the landslide frequency was higher in shrublands rather than in coppiced chestnuts areas.

The presence of the layer of pumices in the slopes was identified as critical in the sliding phase. Di Crescenzo and Santo (2005) recognized that if the pumice layer was present in the underlying portion of the slope, less steep and planar sliding of greater dimensions occurred. The sliding surface, in this case, was frequently at the base or in a pumice level because the layer was confined by less permeable soil layers, containing large quantities of water that once released can increase the fluidity of the landslide mass related to its greater velocity and travel distance.

Table 1 – Common classification of landslides occurring in shallow pyroclastic soil covers according to the updated Varnes classification proposed by Hungr et al. (2014).

Type of landslide	Description
Sand/silt/debris flowslide	“Very rapid to extremely rapid flow of sorted or unsorted saturated granular material on moderate slopes, involving excess pore-pressure or liquefaction of material originating from the landslide source. The material may range from loose sand to loose debris (fill or mine waste), loess and silt. Usually originates as a multiple retrogressive failure. May occur sub-aerially, or under water.”
Debris flow	“Very rapid to extremely rapid surging flow of saturated debris in a steep channel. Strong entrainment of material and water from the flow path.”
Debris avalanche	“Very rapid to extremely rapid shallow flow of partially or fully saturated debris on a steep slope, without confinement in an established channel. Occurs at all scales.”

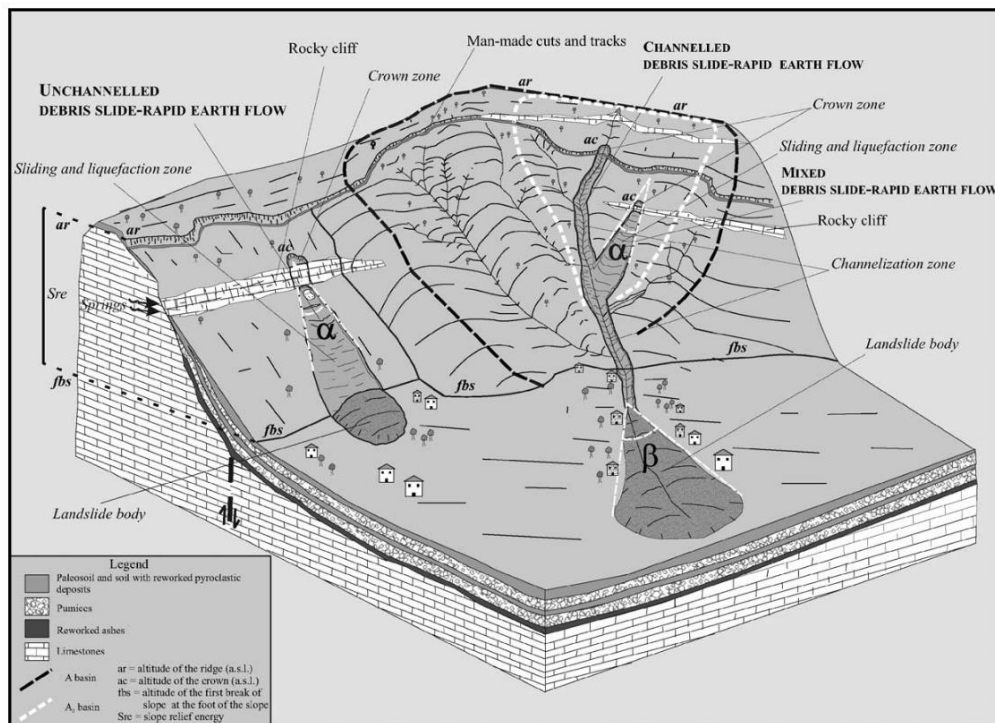


Figure 8 – Scheme of the main morphology associated to debris flow type of landslide (Di Crescenzo and Santo, 2005).

### 1.3.2 Hydraulic behaviour

The rainfall-induced landslides that occur in pyroclastic shallow covers in the region of Campania require the predisposing conditions to be verified and a triggering rainfall event. The landslide of Pozzano in 1997 was triggered by a rainfall event with a return period of 13 years but the mean annual precipitation had a

much greater return period of 80 years. Calcaterra and Santo (2004) concluded that events like the Pozzano landslide can be triggered by “ordinary extreme” short-term rainfall events but are controlled by “extraordinary extreme” long-term antecedent rainfall. Additionally, the driving forces that led to this landslide resulted from groundwater circulation prevented from rainfall and bedrock ephemeral springs. The importance of studying the predisposing hydraulic conditions was recognized.

Pirone *et al.* (2015b) highlighted the importance of a correct definition and understanding of the boundary conditions in the study of the hydraulic slope behaviour. Factors that may influence the hydraulic boundary conditions are topographic irregularities, cracks on the soil surface and vegetation, among others.

The slope studied in Pirone *et al.* (2015b) was at Monteforte Irpino (Campania, Italy). This slope presented a mean angle of 25° to 30°, with local slope angles that could go up to 35° to 40°. The stratigraphic profile consisted of a sequence of unsaturated pyroclastic soils with a total thickness that varied between 3 and 5.5 m over a weathered limestone bedrock. The sequence was composed of six layers of volcanic ashes intercalated by two layers of pumices, which grain size distributions are presented in Figure 9.

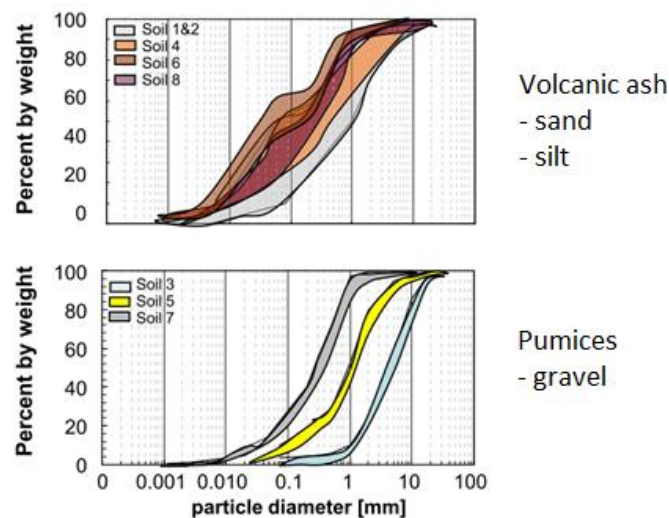


Figure 9 – Grain size distribution of the soils present at Monteforte Irpino test site (adapted from Pirone *et al.*, 2015b).

Pirone *et al.* (2015b) analysed the soil water balance in the slope in order to investigate the soil-atmosphere interaction and the pyroclastic soil interaction with the bedrock, i.e. the upper and the lower hydraulic boundaries, respectively. The upper boundary, controlled by the rainfall and evapotranspiration, presented variations along the seasons (Figure 10). In winter, from October to April, the evapotranspiration was singularly controlled by meteorological conditions because there was no shortage of water in the soil for the evaporation to occur. In spring, evapotranspiration reached 3 to 4 mm day<sup>-1</sup> due to the peak in vegetation growth. In summer, from July to September, the evapotranspiration ranged between 1.5 and 2 mm day<sup>-1</sup>, being limited by the available water in the soil.

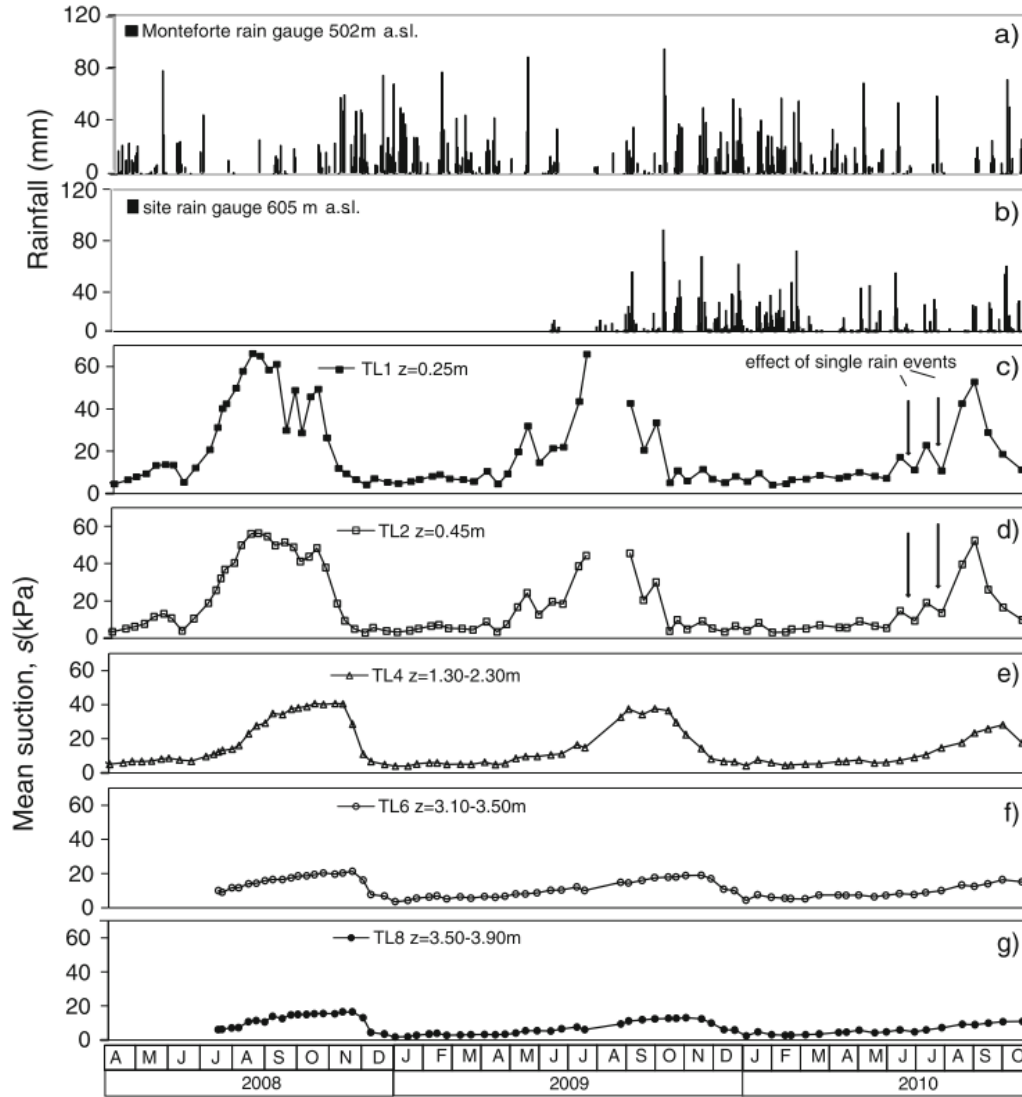


Figure 10 – Evolution of the matric suction with time in different soil layers (Pirone et al., 2015a).

Periods of different groundwater regime were influenced by the boundary conditions and by the soil hydraulic properties. In the winter, from the end of September to April, the mean direction of the water flow was almost vertical and directed downward in all the soils as a consequence of the rainwater infiltration (2 to 6 mm day<sup>-1</sup> in the superficial layers and 0 to 2 mm day<sup>-1</sup> in deeper layers). This infiltration contributed to the increase of the stored water in the fall (transient period). In the early summer, during May and June, the flow became parallel to the slope in the deeper layers and upwards in the more superficial layers due to the increase of evapotranspiration.

Pirone et al. (2015b) observed that all the ashy soil layers presented variations caused by the seasonal meteorological conditions, proving that perturbations of the upper boundary propagate through the profile



(Figure 10). Consequently, the capillary barrier due to contrasting hydraulic properties of the pumices layers (coarse grained soil) and the pyroclastic layers (silt to sand) is broken (Mancarella and Simeone, 2012).

Pirone *et al.* (2015b) suggested that the drainage in the lower boundary was explained as an evaporation flux controlled by the relative humidity of the air in the limestone fractures (20 to 80%). According to the hypothesis proposed by Pirone *et al.* (2015b), a downward heat flux due to conduction and convection mechanisms causes the water to condensate on the fractures surface. The water would move downwards due to gravity, reducing the humidity in the air of the fractures. The evaporation at the lower boundary in the summer was reduced because relative humidity was not enough to remove water from the soil, which presented suction values of approximately 15 kPa.

Same observations were made by Papa *et al.* (2013), Pirone *et al.* (2015a) and Urciuoli *et al.* (2016) regarding the monitored groundwater regime of test sites in Monteforte Irpino (Figure 10) and Cervinara (Figure 11). Three main stages were identified along a hydrological year: (i) a transient stage from September to November when suction decreases, (ii) a transient period from June to August when suction increases, and (iii) a long period of a steady regime from December to May when suction is maintained low. These seasonal fluctuations were observed presented delay and a decrease in amplitude in soil layers of increasing depth.

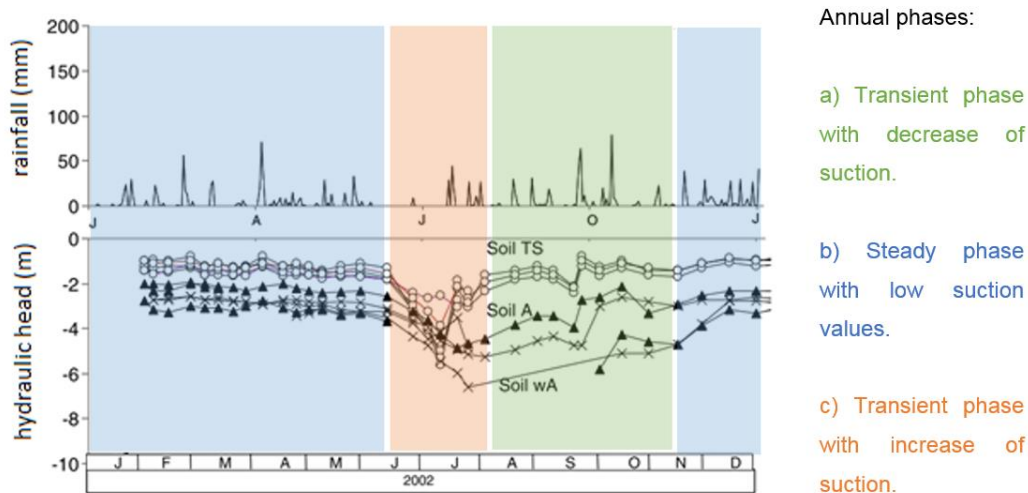


Figure 11 – Monitoring data of a test site in Cervinara (adapted from Urciuoli *et al.*, 2016).

The steady phase, which is established during the wet season, corresponds to the critical period for the occurrence of landslides. During this period, extreme rainfall can lead to failure because the soil shear strength is low (Urciuoli *et al.*, 2016). The constant profile of matric suction in Figure 12 corresponds to an inflow equal to the soil permeability. Additionally, the registered values of matric suction varied between 2 and 12 kPa, which is close to the AEV of all the examined soils (Pirone *et al.*, 2015a).

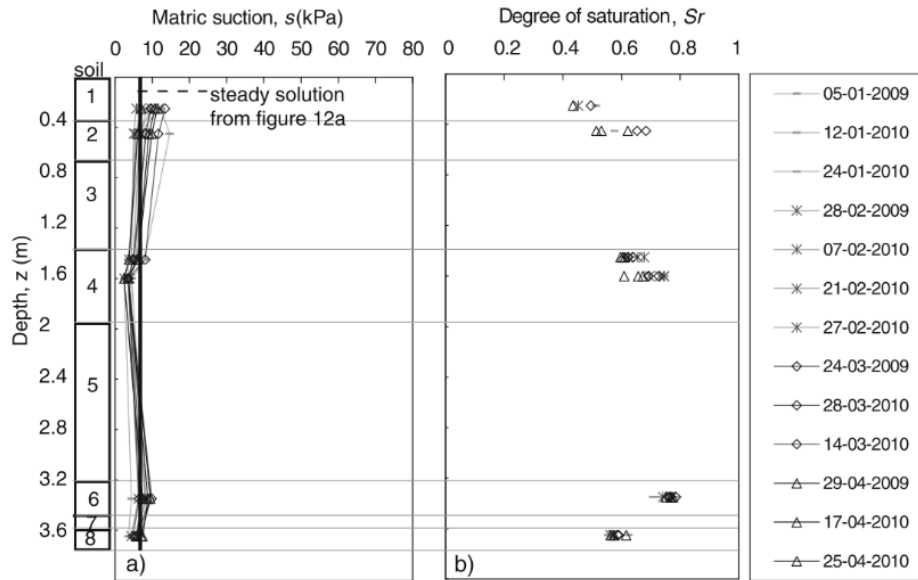


Figure 12 – Evolution of matric suction and degree of saturation with depth for different instants during the wet season in Monteforte Irpino (adapted from Urciuoli *et al.*, 2016).

Only the two upper layers in Figure 10 were affected by single rainfall events for which drops in suction were observed, especially during the transient phases (Pirone *et al.*, 2015a). Figure 13 shows the variation of total head as a response to a heavy rainfall event. The total head profile before the rainfall event was almost vertical. Urciuoli *et al.* (2016) observed that the water tended to flow parallel to the slope, still presenting a downward component affecting the first metre of soil.

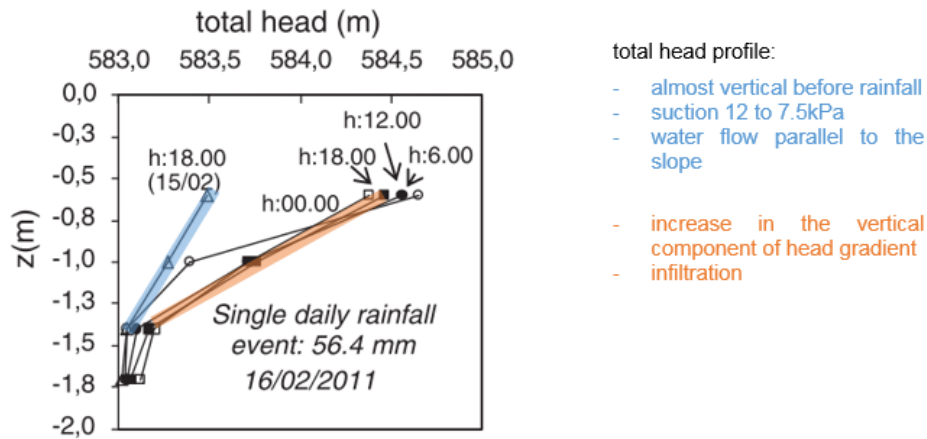


Figure 13 – Hourly measurements of total head during a rainfall event in the test site at Cervinara (adapted from Urciuoli *et al.*, 2016).

### 1.3.3 Unsaturated pyroclastic soils

The pyroclastic soils in Campania have been characterized hydro-mechanically by several authors (Nicotera *et al.*, 2010, 2015; Pirone *et al.*, 2014). A detailed hydraulic characterization of the pyroclastic

soils in Monteforte Irpino (Campania, Italy) was performed by Nicotera *et al.* (2010), which results are present in Figure 14. The main drying branch of the WRC and HPF was obtained for the soil found at different depths at that test site. The shallowest soils (1 and 2) presented saturated hydraulic permeability ranging from  $10^{-6}$  to  $10^{-5}$  m s<sup>-1</sup>, then soil 4 presented a lower permeability by one order of magnitude, and the deepest and finer soils (6 and 8) presented permeability ranging from  $10^{-7}$  to  $10^{-6}$  m s<sup>-1</sup>. The AEV of soils 1, 2 and 4 varied between 3 and 6 kPa, which is characteristic of sandy soils. The deepest soils found in the profile presented slightly higher AEV.

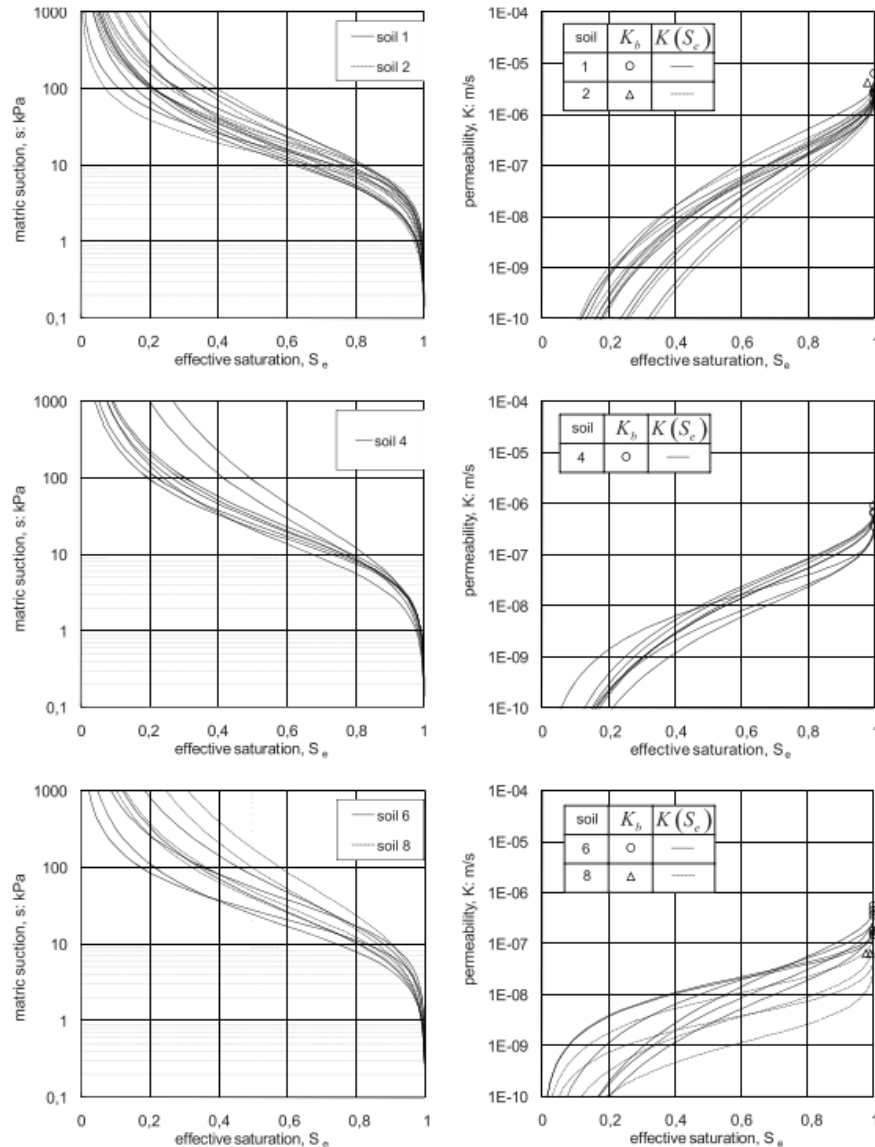


Figure 14 – Main drying WRCs and HPFs (Nicotera *et al.*, 2010).

When the hydraulic properties obtained with the procedure proposed by Nicotera *et al.* (2010), where compared with measurements obtained in situ, a discrepancy was found. The suction values measured in

situ were much lower than the main drying curve obtained in the laboratory (Figure 15). Pirone *et al.* (2014) emphasized the importance of the representativeness of the soil samples for the determination of the soil hydraulic properties. Nonetheless, the difference would be expected because the measurements obtained in the test site correspond to greater sampling volumes with no controlled boundary conditions. The soil at the test site is subjected to cycles of drying and wetting following scanning paths.

This same soil was characterized hydro-mechanically in Papa *et al.* (2008) based on triaxial tests in saturated and unsaturated conditions. The critical friction angle of each soil is presented in Figure 16. The results varied from 36.2° for soil 2 and 40.3° for soil 7. Papa *et al.* (2008) also concluded that representing the data in terms of Bishop's stress allowed a satisfactory interpretation of the results. Other pyroclastic soils in Campania have also been investigated in unsaturated triaxial tests (Nicotera *et al.*, 2015) and direct shear tests (Evangelista *et al.*, 2004).

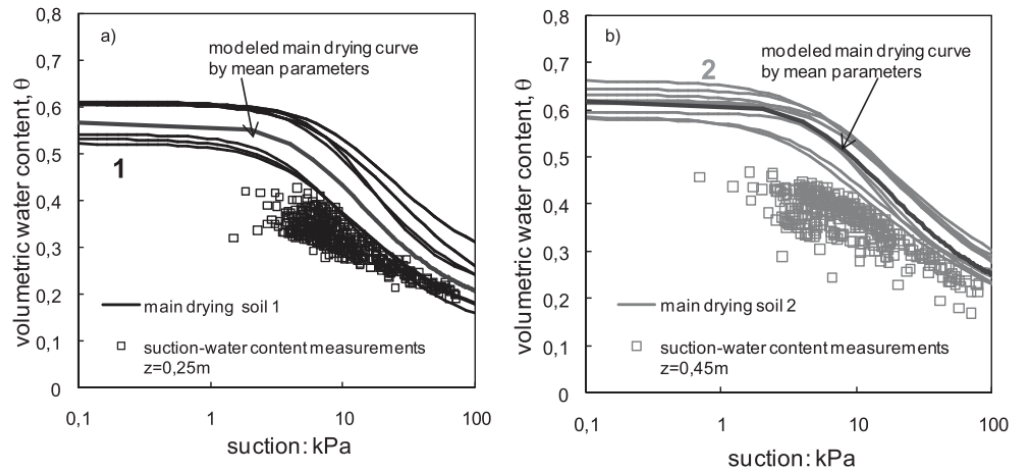


Figure 15 – Comparison of the main drying WRC and the field measurements of Monteforte Irpino (Pirone *et al.*, 2014).

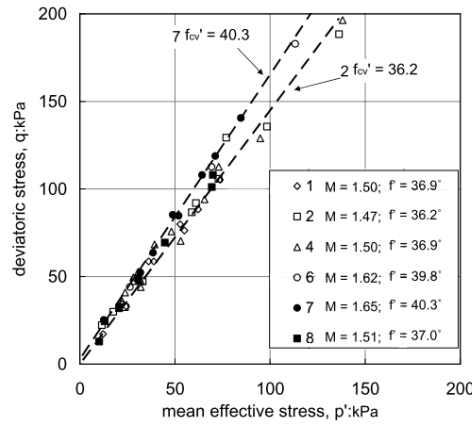


Figure 16 – Results of the saturated triaxial tests (Papa *et al.*, 2008), in which  $f$  represents the critical friction angle.

## 1.4 Vegetation effect on slope stability

The soil-plant-atmosphere interactions that might affect the slope stability are complex and interconnected. Figure 17 presents a summarized scheme of these interactions. The effect of vegetation can be divided into two main groups: hydraulic and mechanic, which are not independent. The hydraulic effect includes the rainfall partition, evapotranspiration, and changes in the soil hydraulic properties. The mechanic effect includes the mechanical root reinforcement and anchoring. Nonetheless, the vegetation effect can be negative or positive as summarized in Table 2 (Gray and Sotir, 1996).

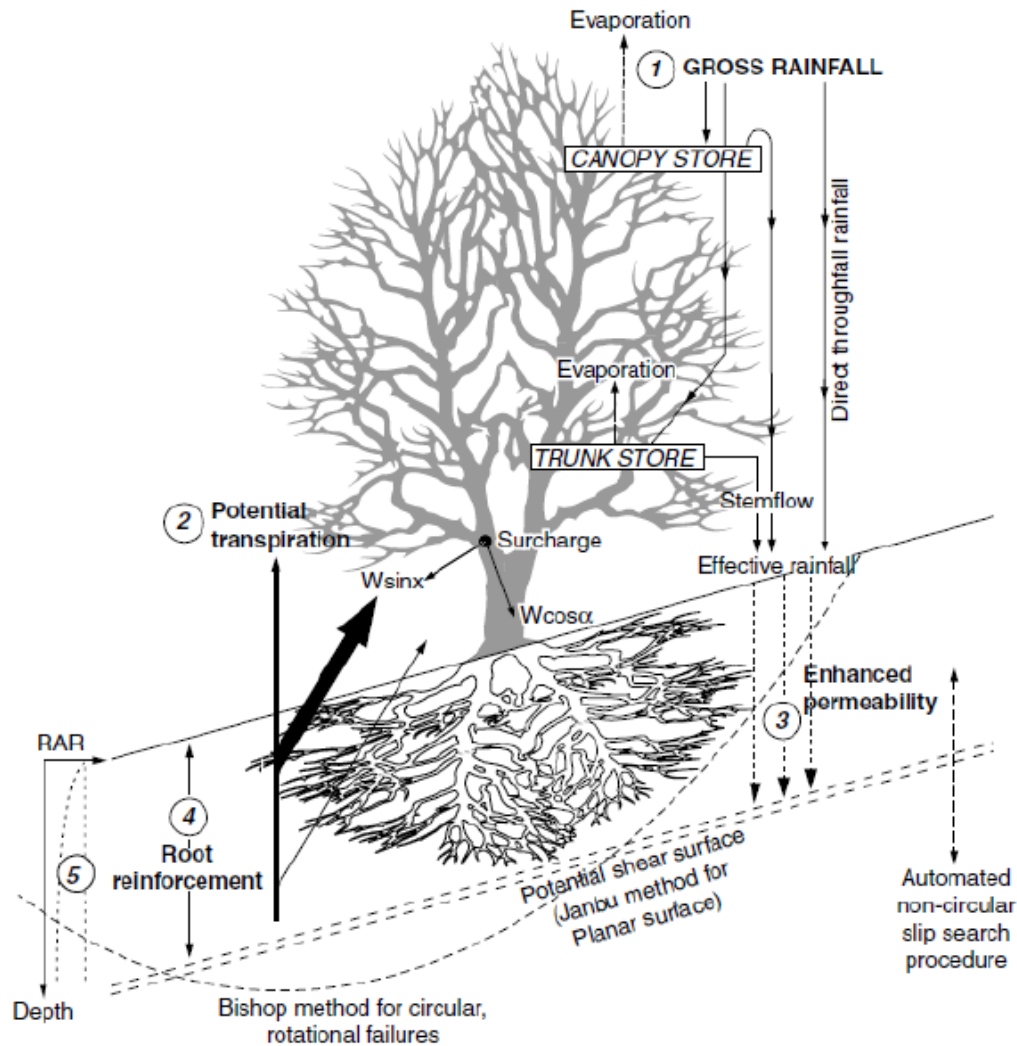


Figure 17 – Vegetation-slope interactions (Wilkinson et al., 2002).

The woody plants, such as shrubs and trees, with deep vertical root systems and high root/shoot ratio are the type of vegetation with the most prominent effect on slope stability (Gray and Sotir, 1996). Stokes *et al.* (2009) highlighted that woody vegetation, particularly trees, can help prevent shallow landslides (soil

movements of 1-2m depth) by modifying the soil moisture regime via evapotranspiration and by providing root reinforcement within the soil.

*Table 2 – Beneficial and negative effects of vegetation on slope stability (Gray and Sotir, 1996).*

Beneficial Effects	Negative Effects
<ul style="list-style-type: none"> <li>• Root reinforcement – Roots mechanically reinforce the soil by increasing its shear strength.</li> <li>• Soil moisture depletion – Evapotranspiration results in soil water content decrease and suction increase.</li> <li>• Buttrressing and arching – Anchored and embedded stems can act as buttress piles and counteract downslope shear forces.</li> <li>• Surcharge – The weight of vegetation can, in certain instances, increase stability (e.g. at the base of a slope).</li> </ul>	<ul style="list-style-type: none"> <li>• Water infiltration – Roots and stems increase the roughness of the ground surface and permeability of soil, leading to increased infiltration capacity.</li> <li>• Soil cracking – Depletion of soil moisture may accentuate desiccation cracking in the soil, resulting in higher infiltration capacity.</li> <li>• Surcharge – The weight of trees surcharges the slope increasing destabilizing force components.</li> <li>• Dynamic loading – Vegetation exposed to wind transmits dynamic forces into the slope.</li> </ul>

The hydraulic influence of plants on soil is not very relevant for the prevention of shallow landslides and debris flows that occur during an extended rainy season because in most temperate regions, soils are nearly saturated and evapotranspiration is low during autumn and winter rainstorms, which is when shallow slope failures typically occur. Evapotranspiration may reduce the potential of shallow landslides occurrence only if large and high intensity storms occur during drier periods or near the beginning or end of the rainy season (Stokes *et al.*, 2009). Therefore, in the assessment of the hydraulic effect, the minimum induced suction in absence of transpiration is required and the most preponderant effect of roots is actually on the WRC (Leung *et al.*, 2015).

On the other hand, Stokes *et al.* (2009) considered that the additional soil strength or cohesion consequence of the presence of roots is a much more significant contribution of vegetation to the stability of shallow soils, as shown by Pollen (2007) and Kim *et al.* (2017). This is because dense lateral root systems in upper soil horizons form a membrane that stabilizes the soil and large tree roots can provide reinforcement across planes of weakness along the flanks of potential slope failures. However, in case of deep failure surfaces are formed, roots provide no contribution to the basal resistance because root density decreases dramatically with depth.

### 1.4.1 Root systems and root growth

Plants present a mat of roots at surface which main function is to uptake water and minerals. Deeper roots intend to anchor the plant to the ground and uptake water, while large tap roots are generally used for storage. However, the plants root growth depends on the species and on environment constrains. For example, roots in well-drained soils need to explore a much greater soil volume than roots in soil with easily available water (Coppin and Richards, 2007).

Based on previous works, Stokes *et al.* (2009) mentioned the following typical values for the rooting depth presented in Table 3. The degree to which roots are able to penetrate underlying bedrock depends on the nature and on the extent of discontinuities (fractures) in the bedrock. Trees growing in shallow, coarse-textured soils can develop sinker and taproots that penetrate into fissures of the bedrock. If the overlying soil is coarse and permeable (incapable of holding moisture), roots seek out water in the fractures and fissures of the bedrock, which leads the roots to anchor to the slope restraining the soil movement by a combination of buttressing and arching actions (Gray and Leiser, 1982).

*Table 3 – Rooting depth of different types of plants and soil layer thicknesses (Stokes et al., 2009).*

Plant	Rooting depth (m)
Perennial herbs and forbs	0.75
Annuals herbs and forbs	< 0.5
Shrubs and trees on deep soils	2.2
Shrubs and trees growing on shallow soils over bedrock	7.9

On the other hand, roots of woody plants on shallow soils that tend to grow along fractures deep into the bedrock and sometimes enlarge the cracks, thus destabilising the rock and causing it to fracture, leading in turn to slope failure. Some species that are not able to penetrate the bedrock grow along the discontinuity between soil and bedrock, which can also generate instability. The rooting depth is also conditioned by the water infiltration depth (Stokes *et al.*, 2009).

In terms of lateral growth, Stokes *et al.* (2009) collected the information reported in Table 4. The rule of thumb presented by Gray and Sotir (1996) is that the roots of trees spread out a distance of at least 1.5 times the radius of the crown and the influence in the ground water regime is detected at a distance of at least the height of the tree.

*Table 4 – Lateral root growth in terms of radius for different plants (Stokes et al., 2009).*

Plant	Lateral growth (m)
Shrubs and trees	2 to 16
Herbaceous	0.1 to 0.6

The root system of herbaceous plants is composed of thin roots presenting tensile strengths similar to roots of woody species but with greater RAR. The roots of herbaceous plants tend to form shallow mats that can easily tear away from the subsoil in humid conditions providing almost no resistance against shallow and deep landslides. On the other hand, it may provide protection against surface erosion (Stokes *et al.*, 2009).

In general, tree root systems can be classed into three types, depending on their overall shape: plate, heart and tap (Figure 18). The plate root systems have large lateral roots and vertical sinker roots, heart systems possess many horizontal, oblique and vertical roots and tap systems present one large central root and smaller lateral roots. However, many species have a mixture of root system types and they are also influenced by the changing environmental constrains (Coppin and Richards, 2007). The identification of the type of root system shape of species used for slope protection is important because it has different responses to shearing and uprooting (Stokes *et al.*, 2009).




Class of the root system	Real morphology
Heart root system	
Tap root system	
Plate root system	

Figure 18 – Different types of root systems (adapted from Switala, 2016).

#### 1.4.2 Useful traits for reinforcing soil on slopes

A trait is defined as a distinct, quantitative property of organisms, usually measured at the individual level and used comparatively across species (Stokes *et al.*, 2009). In the case of plants, functional traits can be the plant height, architecture, root depth, wood density, leaf size and leaf nitrogen concentration, among others. The traits of interest for the present work are related to the influence of the plants on slope stability. Some of the traits presented by Stokes *et al.* (2009) that are useful when adopting vegetation as a method to stabilize slopes and prevent shallow landslides are reported in Table 5.



Table 5 – Summarized desirable root traits to be considered in the slope stability analysis (Stokes *et al.*, 2009).

Trait	Explanation
Root area ratio (RAR)	The soil shear strength increases with increasing RAR.
Tensile strength ( $T_r$ )	Therefore, for a constant RAR, many small roots are more desirable than a few thick roots, provided that roots do not slip out, because the tensile strength per unit area ( $T_r$ ) is greater.
Rooting depth	It is preferable if roots cross the shear surface and if they are anchored to the bedrock.
Root length density (RLD)	Higher RLD results in an increase of pull-out resistance up to the critical length correspondent to the breakage of the root. Additionally, the water uptake rate from a given horizon increases with RLD.
Specific root length (SRL)	For the same dry mass, many thin roots result in high values of SRL, and few thicker roots results in low SRL values. Therefore, a relation between the resistance and the prevalent typology of roots can be established. The usefulness of this trait is in the fact that more long and fine roots are preferable.
Topology	Root topology can significantly change the distribution of stresses and plastic strains within the soil medium, thus modifying root resistance to pull-out.
Root clustering	If roots are clumped within cracks and bio-pores in the soil, the water has to flow a great distance to be removed. Root clustering may also create preferential water paths. Therefore, a homogenous distribution of roots within the soil is more desirable.
Root decay rate	Roots which decay slowly fix soil for a longer period but also may create preferential flow pathways in soil.

### 1.4.3 Hydraulic effect of vegetation on slope stability

#### 1.4.3.1 Effect of roots on the soil hydraulic properties

The presence of roots in the soil changes the soil hydraulic properties, namely the water retention curve and the hydraulic permeability. The changes have been attributed to the volume occupancy of the pores by the roots (Ng *et al.*, 2016b), changes in soil structure (Angers and Caron, 1998) and water uptake by the plants (Leung *et al.*, 2015). As roots influence soil structure by subjecting the soil surrounding the root (rhizosphere) to wetting-drying cycles and by being a source of carbon, via root turnover and exudation (Stokes *et al.*, 2009). Therefore, so the pore size distribution changes, which closely related to the soil water retention properties (Romero *et al.*, 1999; Wijaya and Leong, 2017).

The hydraulic conductivity in steady state was higher in presence of roots than in bare soil (Leung *et al.*, 2015) said to be caused by the clogging of soil pores when plant roots are present, therefore the reduction in suction upon rainfall was smaller in vegetated soil. Similar observations were made by Ng *et al.* (2016b) when the plantation density was low. However, the presence of decaying roots was associated to a quick loss in suction and high infiltration rates in comparison to bare soil. Already in Angers and Caron (1998), differences in infiltration rates were associated to the activity of the roots. If the roots are active and growing, the infiltration rate decreases in comparison to bare soil, but if the roots decay, then infiltration rates increase. Evidences were also reported in Angers and Caron (1998) as shown in Figure 19, the infiltration rate increases with increasing number of years of *Medicago sativa* cultivation. The hydraulic permeability was also found to increase with increasing growth time attributed to the development of macro pores by Vergani and Graf (2016). The increase was only observed up to a threshold value of root density of 0.1 cm of root length per cm<sup>3</sup> of soil.

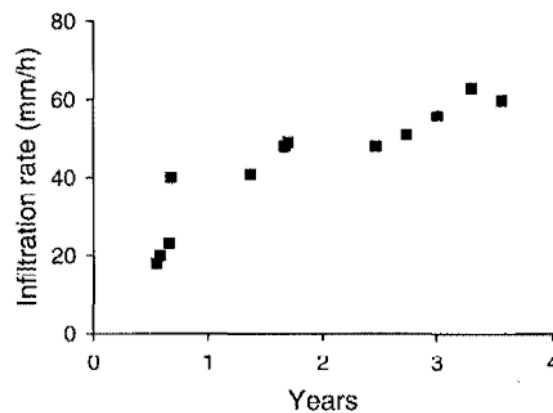


Figure 19 – Changes in infiltration rate under alfalfa culture with time (in Angers and Caron, 1998).

In the experiments of Leung *et al.* (2015), the vegetated soil was able to preserve higher suction values than bare soil upon rainfall. The effect of roots presence on the soil water retention capacity was separated from the suction induced by the roots water uptake. Leung *et al.* (2015) concluding that the roots induced substantial change of the WRC. The roots were responsible for an increase of the AEV from 1 to 4 kPa as well as an increase in the hysteresis of the water retention loop. Same observations were made by Ng *et al.* (2016b) for low seedlings density as observed in Figure 20.

However, the increase of seedlings density was associated to an increase of competition between individuals which caused a water content decrease and suction increase in the experiments of Ng *et al.* (2016b). The root growth was affected by the individuals competition leading to a reduction of the total root volume and more root decaying. Consequently, the soil water retention ability reduced, i.e. the AEV reduced in comparison to bare soil. The presence of decaying roots was also associated to an increase of the hysteresis in the WRC (Figure 20).

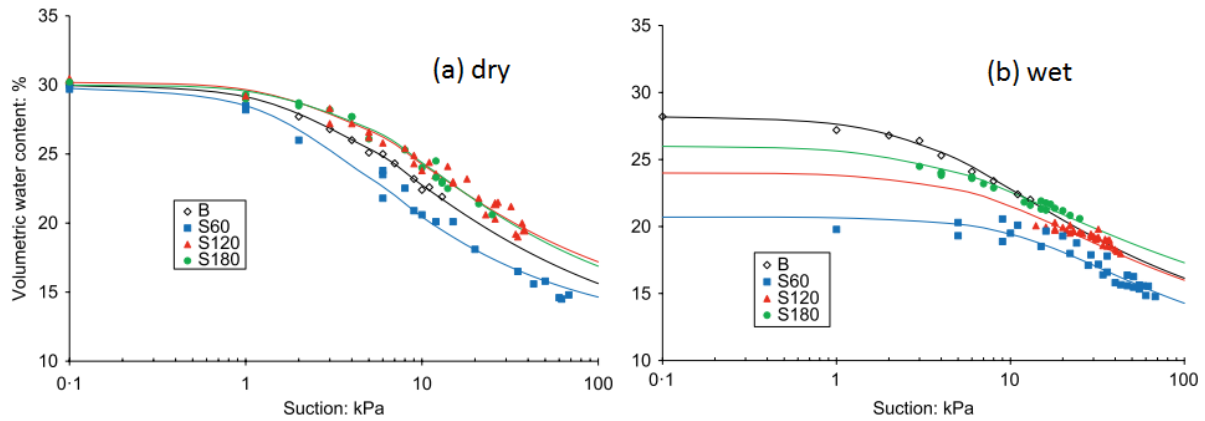


Figure 20 – Drying (a) and wetting (b) branch of the water retention loop of bare soil (B) and vegetated soil with increasing distance between seedlings (60, 120 and 180 mm) presented in Ng et al. (2016b).

#### 1.4.3.2 Rainfall partition

The rainfall partition performed by vegetation canopies modifies evaporation and redistribution of incident rainfall (Llorens and Domingo, 2007). This phenomenon has the ability of modifying the vegetation cover with significant effect on the hydrology and on the water balances. Part of the rainfall ( $R$ ) is throughfall ( $TF$ ), stemflow ( $SF$ ) and interception ( $I$ ) as presented in Equation 16.

$$R = TF + SF + I \quad 16$$

The throughfall is the portion of water that reaches the floor by falling over the uncovered part of the surface (direct throughfall) or by dripping from the plant canopy. The portion that flows through the branches and the trunk eventually reaching the ground is the stemflow ( $SF$ ). The drainage of the plant is the sum of the water that drips from the leafs and the stemflow ( $SF$ ). The plant drainage initiates when the water storage in the plant reaches the retention capacity of the plant, before which only direct throughfall is registered (Serrato and Diaz, 1998). The partition the gross rainfall ( $GR$ ) can be divided simply into net rainfall ( $NR$ ) and interception loss ( $I$ ), as represented in Equation 17 (Llorens and Domingo, 2007). The net rainfall represents the sum of the portion of rainfall that effectively reaches the ground, i.e. throughfall ( $TF$ ) and stemflow ( $SF$ ), as in Equation 18.

$$GR = NR + I \quad 17$$

$$NR = TF + SF \quad 18$$

This division is particularly important because the  $TF$  and the  $SF$  influence the soil moisture gradients and soil erosion processes, as well as the location of understory herbs (Ahmadi et al., 2009). The  $TF$  affects

the superficial layers of the soil and the *SF* can reach deeper layers of the soil to be used by the roots (Llorens and Domingo, 2007).

Each of the fractions considered in the rainfall partition have considerable participation (Serrato and Diaz, 1998). The weight of each of the fractions depends on (i) the incident rainfall characteristics (amount, intensity, duration and temporal distribution of rainfall events), (ii) meteorological conditions (air temperature, relative humidity, wind speed and wind direction), (iii) forest structure (canopy morphology and architecture, species composition, stand age and stand density), and (iv) the interaction between these factors (Staelens *et al.*, 2008; Ahmadi *et al.*, 2009).

Nevertheless, not only the vegetation is responsible for the interception of the rainfall stopping the water to reach the soil, the forest litter also prevents water from reaching the soil (Putuhena and Cordery, 1996). The forest floor components can be divided into several groups. The highest contribution for the forest floor storage capacity is provided by leaves (47% to 45%).

#### **1.4.3.3 Effect of vegetation on the groundwater regime**

At the slope scale, in the monitoring work performed by Leung and Ng (2013), the evapotranspiration was responsible for a substantial decrease in the soil pore-water pressure and volumetric water content in soil up to the double of the root depth. The evapotranspiration during the dry period was not limited by water stress but it was controlled by the atmospheric conditions, as the relative humidity. Gonzalez-Ollauri and Mickovski (2017) also detected a desaturation of the soil that was greater in the presence of vegetation in comparison to bare soil.

Kim *et al.* (2017) assessed the temporal variability of how vegetation affects slope stability including the surcharge, hydraulic effect and mechanical reinforcement. The monitoring data of sites with and without trees were compared showing that slopes with woody vegetation were more stable and less sensitive to climate and soil factors, such as climatic humidity and soil hydraulic conductivity, than slopes with herbaceous vegetation. The consequent effect of the evapotranspiration in presence of vegetation was discernible in terms of *SF* of potential failure surfaces in different locations as reported in Figure 21. Indeed, the hydric contribution to the stability was almost null in the wet season, even though its contribution was much higher in the dry season. The impact of evapotranspiration was also influenced by the cultivation practices.

The effect of vegetation on the groundwater regime of pyroclastic soil covers is not known and cannot be extrapolated from previous studies due to the unique particularities of these sites. Pyroclastic soil covers are very shallow and the soil is very porous and composed of sequence of soil layers with different water retention characteristics (Nicotera *et al.*, 2010). These factors condition the growth of vegetation, as well as the management practices and meteorological conditions (Coppin and Richards, 2007). Mao *et al.* (2014) and Switala (2016), among others, accounted for the spatial distribution of the root mechanical

reinforcement in the study of slope stability but did not investigate in depth the spatial hydraulic effect of vegetation that can be in terms of water uptake or changes in the soil hydraulic properties as seen by Leung *et al.* (2015).

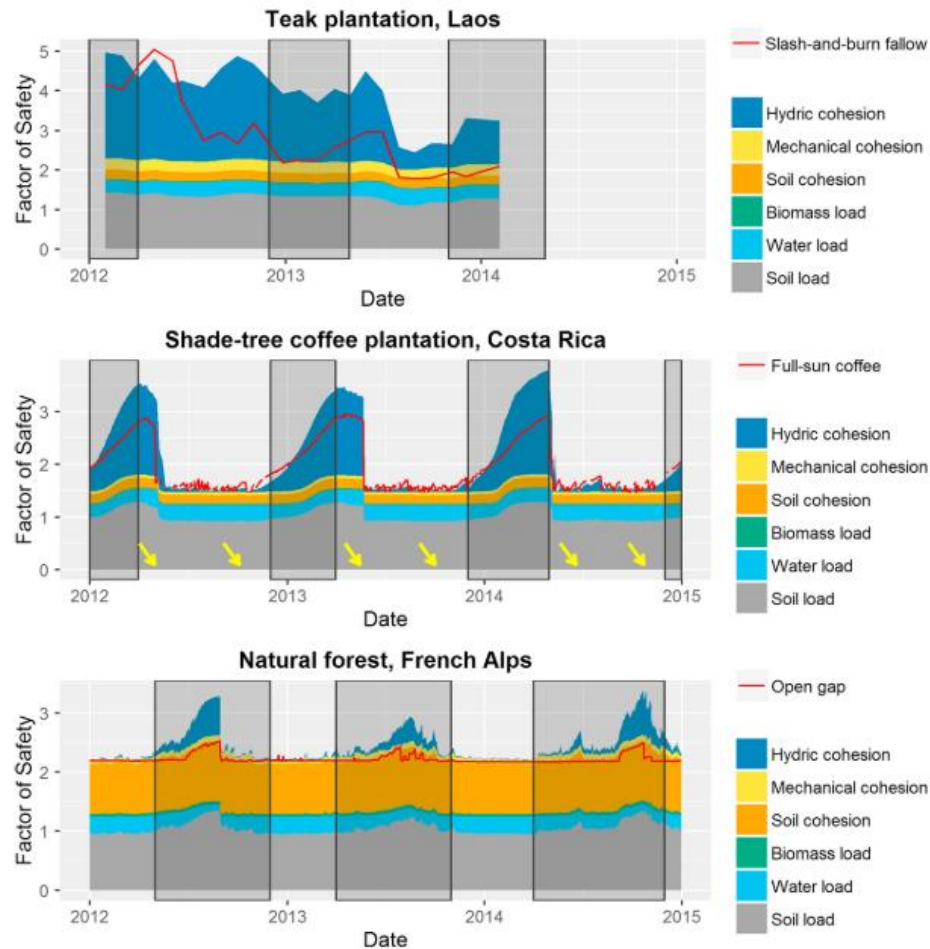


Figure 21 – Weight of each component contributing to the slope stability of different vegetation covers and cultivations in comparison to fallow soil (red line) by Kim *et al.* (2017).

## 1.4.4 Mechanical effect of vegetation on slope stability

### 1.4.4.1 Roots in a shallow landslide

Failure surfaces of shallow landslides reach depths of 1 to 2 m presenting a high probability of crossing roots when the slope is vegetated because roots can easily reach those depths depending on the soil conditions and on the species. Roots, which are fibrous elements, introduce changes on the global mechanical behaviour of the soil which becomes a composite material (root-permeated soil). Consequently, the safety of a slope changes due to the modified mechanical properties of the soil as shown by Danjon *et*

*al.* (2008), Genet *et al.* (2008, 2010), Sonnenberg *et al.* (2010), Mao *et al.* (2014) and Liang *et al.* (2015), among others.

The mechanical response of the roots depends on the applied actions, which vary along the failure surface, as observe in Figure 22. Roots may be acted by pull out (a), shear (b) or compression (c) forces (Schwarz *et al.*, 2015). In general, the root in the situations (a) and (b) may slip out or break depending on the soil type, moisture and root-soil friction (Ennos, 1990; Mickovski *et al.*, 2007; Pollen, 2007). In situation (c), Wu *et al.* (1988) and Schwarz *et al.* (2015) showed that the most common failure mechanism is the occurrence of buckling, even though root bending or root tensioning may be observed at large shear displacements. The mechanisms previously appointed are complex and depend on the root interaction with the surrounding soil, as well as on root traits. The quantification of the increase of soil strength provided by roots was developed by several authors, such as Wu (1976), Pollen & Simon (2005) and Schwarz *et al.* (2010, 2013).

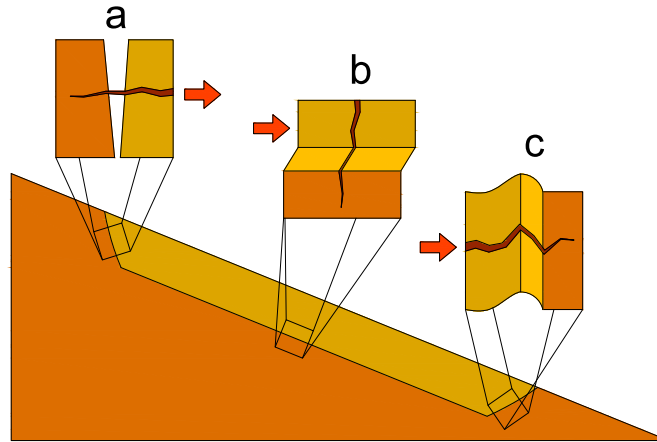


Figure 22 – Solicitation of the root reinforcement at different locations along the sliding surface of a shallow landslide: (a) tension, (b) shear and (c) compression (Dias *et al.*, 2017).

#### 1.4.4.2 Root failure modes

A root breaks when a pull-out force is applied at the failure surface and it exceeds the tensile strength of the root provided that it is well anchored in the soil to mobilize reaction forces. Experimental works on root tensile strength proposed a simple relation with the form of a power-law as represented by Equation 19, where  $T_r$  is the root tensile strength (force distributed in the area of the cross section of the root) [MPa],  $d$  is the root diameter at the section of breakage [mm], and the parameters  $\alpha$  and  $\beta$  are calibration constants. This relation has been calibrated by many researchers and extensive inventories can be found in Gray and Sotir (1996), Comino *et al.* (2010) and Burylo *et al.* (2011). Conversely, the root tensile resistance ( $F_B$ ) is given by Equation 20.

$$T_r = \alpha d^\beta$$

19

$$F_B = \frac{\pi d^2 T_r}{4} \quad 20$$

Nonetheless, when a root is being tensioned, it can also slip out. The force necessary to break the root-soil bond or pull out resistance is symbolized by  $F_p$  in Equation 21, where  $L$  is the root length and  $\tau$  is the root-soil frictional resistance (Cazzuffi *et al.*, 2014).

$$F_p = 2\pi R\tau L \quad 21$$

The root model used to estimate the root tensile and slip-out resistance estimated from Equations 20 and 21, respectively, requires the following simplifications to be made: (i) ignoring the variation of overburden stresses depending on the depth where the roots are found, (ii) considering roots of constant diameter, (iii) ignoring the root tortuosity and branching, and (iv) ignoring root bundle interactions. These simplifications were investigated in the work of Dupuy *et al.* (2005), Mickovski *et al.* (2007), Schwarz *et al.* (2010), and Giadrossich *et al.* (2013).

Pollen (2007) observed a threshold value of root diameter that separates the occurrence of breakage from slippage of the roots for a given load. This threshold value depends on the strength of frictional between the roots and soil, and on the tensile strength of the roots of that specie. Slippage occurred in small root diameters and in larger diameters breaking forces were lower than pull out forces. This means that above this threshold value friction exceeds the tensile strength of the root (Figure 23).

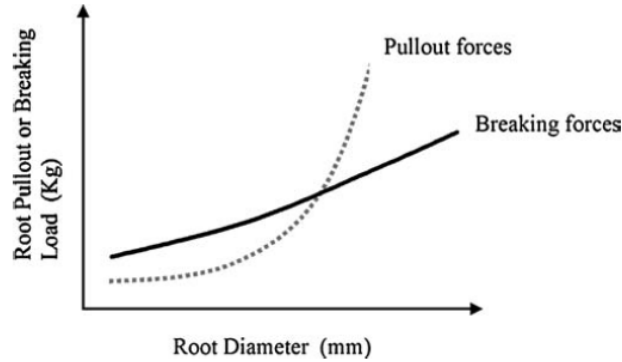


Figure 23 – Required forces to originate each failure mechanism for different diameters (Pollen, 2007).

The first models proposed in the literature, roots were assumed to be fibrous elements without shear and bending strength, presenting only tensile resistance, as in Wu (1976) and Gray and Ohashi (1983). It is generally accepted that roots present an elastic behaviour, as Comino *et al.* (2010), Burylo *et al.* (2011) and Vergani *et al.* (2014), among others, did. However, roots of greater diameters may present bending resistance, and consequently shear resistance, which is of undeniable importance of the quantification of the root reinforcement when the root is acted by a lateral load, i.e. when a root is intersected by a shear surface. In this regard, pile solutions and beam on elastic foundation solutions have been adapted to describe the response of roots and then the reinforcement provided by them (Wu *et al.*, 1988; Nghiem *et al.*, 2003; Wu, 2013; Mao *et al.*, 2014a; Liang *et al.*, 2015).

Schwarz *et al.* (2015) investigated the influence of the roots on soil resistance under compression focusing on failure due to passive earth pressures in the toe of a landslide. When root orientation was the opposite of the movement of the unstable layer, compression may occur (Gray and Ohashi, 1983; Wu *et al.*, 1988). In fact, Wu *et al.* (1988) observed that all compressed roots failed by buckling because of the low confining pressure.

The reinforcement provided by roots under compression has been neglected based on the assumption that the compressive strength of roots is low in comparison to that of soil (Cazzuffi *et al.*, 2014). Instead, it was found that the resistance of some roots in compression was of the same order of the tension. In fact, roots of diameters of 4 and 8mm, failing at tensile forces of approximately 200 and 400N could stand compression loads of 50 and 150N, respectively, before buckling occurs (Wu *et al.*, 1988). The range of the measured values can be found in Figure 24. The measured values of the critical load were compared with the theoretical solutions by Euler (solution 2) and Toakley (solution 1).

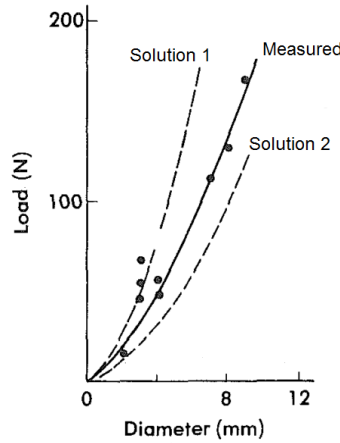


Figure 24 – Measured critical load compared with the theoretical solutions (adapted from Wu *et al.*, 1988).

#### 1.4.4.3 Root reinforcement

The root reinforcement can be evaluated by either a macro model or a soil-root interaction model (Wu, 2013; Cazzuffi *et al.*, 2014). The first is preferable in case the soil is permeated by roots with small dimensions and spacing. The rooted soil is represented by a homogeneous material with given resistant properties obtained from shear tests on root-permeated soil. The second is more convenient when roots are large and disperse, so that they are investigated as soil-embedded elements allowing the estimation of the stresses in the fibre (Cazzuffi *et al.*, 2014).

Independently of the model used for the quantification of root-permeated soil resistance, the roots presence is considered to provide an additional shear resistance to the soil as suggested by Wu (1976). This way, the shear stress at failure  $s_f$  is a sum of three terms as in Equation 22, where  $s_s$  is the effective



shear strength of the soil matrix,  $s_{\psi}$  is the shear strength component due to matric suction and  $s_r$  is the shear strength component due to the root system, according to the formulation of Veylon *et al.* (2015).

$$s_f = s_s + s_{\psi} + s_r \quad 22$$

Nevertheless, Schwarz *et al.* (2010) pointed out that the maximum root reinforcement operates in a range of large displacements, depending on the root distribution, while cementation and suction act at much smaller displacements. Consequently, root reinforcement is activated at different time scales and has effects of different magnitudes compared to suction and cementation.

In the majority of the literature, roots are considered to provide increase of cohesion to the soil. The works stating that roots influence the composite material's friction angle are very scarce (Graf *et al.*, 2009; Zhang *et al.*, 2010).

The root reinforcement provided by macro models requires the performance of direct shear tests or triaxial tests on root-permeated soil. Care is usually taken in the size of the tested samples that should be representative of the variability of a root system and allow the anchorage of roots to the soil. Low stress states are also selected in order to simulate the natural conditions on growth of roots.

In the case of the soil-root interaction models, two approaches can be followed: (i) the estimation of the maximum reinforcement by bundle of roots as a sum of the resistance provided each individual (Wu, 1976; Pollen and Simon, 2005; Schwarz *et al.*, 2010, 2013), or (ii) to use numerical models, which consider the stresses on soil and roots (Mao *et al.*, 2014a; Liang *et al.*, 2015). Among the most popular soil-root interaction models are W&W by Wu (1976) and Waldron (1977), fibre bundle model (FBM) by Pollen and Simon (2005), root bundle model (RBM) by Schwarz *et al.* (2010), and root bundle model introducing a Weibull survival function (RBMw) by Schwarz *et al.* (2013).

The shearing of the soil causes an elongation and a distortion of the roots that cross the failure surface (Figure 25). The roots, that are assumed to behave like cables resisting simply to tensile stresses, provide an increase of shear resistance in the form of cohesion. Assuming that the root out of the shear zone stays perpendicular to it and that the root is properly anchored, tension can be divided into two components, normal and shear stress as represented by Equation 23, (Wu, 1976). In this equation,  $\sigma_r$  and  $\tau_r$  are the normal and shear stresses in the root, respectively, and  $\theta$  is the shear distortion.

$$\begin{cases} \sigma_r = t_r \cos \theta \\ \tau_r = t_r \sin \theta \end{cases} \quad 23$$

The tangential component resists shear and the normal component increases the confining stress on the shear zone, as presented in Figure 25. Therefore, the increase of shear strength provided by the root ( $s_r$ ) may be translated by Equation 24.

$$s_r = \sigma_r \tan \phi' + \tau_r = t_r (\sin \theta + \cos \theta \tan \phi') \quad 24$$

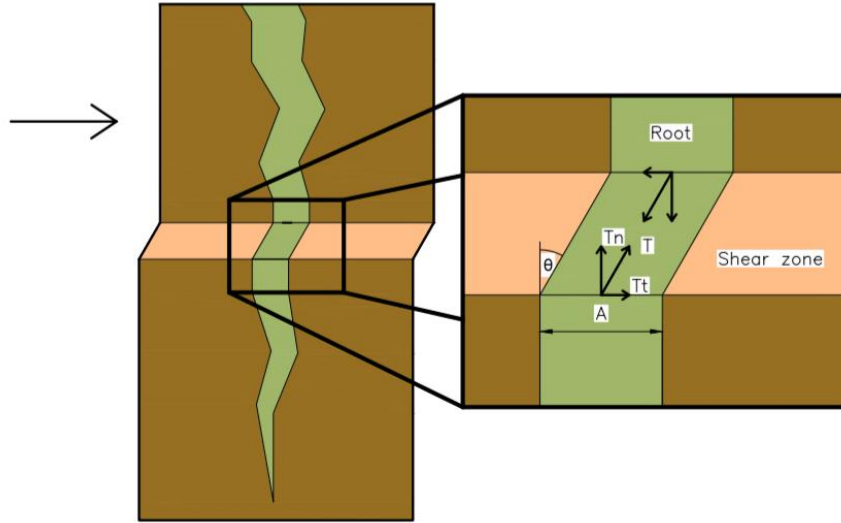


Figure 25 – Scheme of the stresses in the root during shear (Dias *et al.*, 2017a).

In the W&W model, roots are assumed to break simultaneously, which usually leads to an overestimation of the root cohesion, as the root cohesion results from the sum of the tensile strength of all roots that cross the shear plane. The FBM assumes that the roots break at different instances using an algorithm that distributes the load through root diameter classes according to different criteria. This model verifies what is the maximum load withstood by the root bundle through the identification of the order by which roots fail.

The RBM comes in the sequence of the FBM in the sense that increments of displacements are used to compute the distribution of load taken by the roots. This model requires the assessment of the roots Young's modulus, apart from the root tensile strength. The W&W model overestimation can reach trice the value estimated based on RBM, as reported by Schwarz *et al.* (2010) in Figure 26.

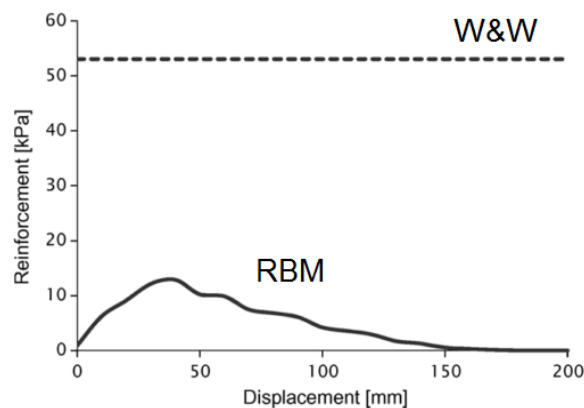


Figure 26 – Comparison of the root-permeated soil reinforcement as a function of displacement of FBM and W&W models (Schwarz *et al.*, 2010).

The RBMw uses a Weibull survival function to compute a more realistic failure sequence accounting for the variability in the roots strength properties. In Figure 27, the measured pull out resistance as function of displacement is presented. The use of the RBMw provides a more realistic simulation of the resistance provided by the root bundle than the traditions RBM (represented as RBMw with  $w=100$ ).

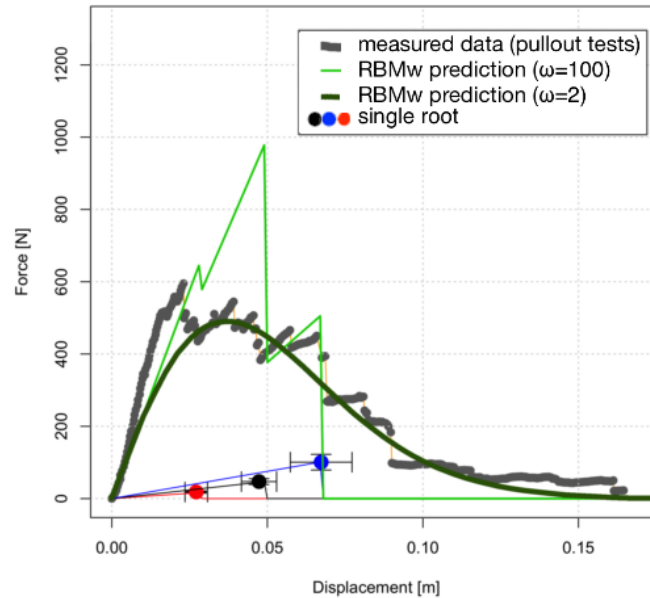


Figure 27 – Measured and simulated force-displacement behaviour of a bundle of roots (adapted from Schwarz *et al.*, 2013).

Numerical models also have been proposed to estimate the root reinforcement provided by roots, such as Nghiem *et al.* (2003), Mickovski *et al.* (2011), Tiwari *et al.* (2012), Mao *et al.* (2014a) and Liang *et al.* (2015). In these models, roots are considered embedded elements in the soil, usually compared to beams. However, some limitations regarding the root orientation assumptions, distinction of root classes, consideration of stiffness and root-soil surface interaction, as well as root branching pattern have been identified as reported by Stokes *et al.* (2009).

## 1.5 Objectives

In this section, three research questions are presented as well as considerations on the hypothesis. Each of the research questions is investigated in Chapters 3 to 5 of this thesis. The posed questions intend to provide tools for a better hydraulic characterization of soil in presence of roots, insight of the effect of vegetation on the groundwater regime and how it is related to the root distribution in situ and quantify the mechanical contribution of vegetation to slope stability.

1. How are the hydraulic properties of the soil in Mount Faito affected by the presence of roots?

The soil hydraulic properties of interest for the study of water flow through soil are the WRC and the HPF. Factors affecting these properties are the soil structure, soil porosity, pores tortuosity, organic matter, soil grain size distribution, among others (Fredlund and Xing, 1994; Romero *et al.*, 1999).

The microbial activity, chemicals interactions between soil and plants, and varying climatic conditions, such as cycles of wetting-drying and freezing-thawing, lead to the formation of aggregates that change the soil structure, or the pore size distribution (Angers and Caron, 1998). The consequence of this change might be visible on the shape of the water retention curve. In Figure 28, soil aggregates and pumices are observed in a cultivated area near Sarno (Campania, Italy).



Figure 28 – Soil aggregates and pumices hanging from roots in a cultivated area near Sarno (Campania, Italy).

The presence of roots in the soil also changes its porosity. In some cases, roots clogged the pores in the soil, leading to a decrease of the permeability (Ng *et al.*, 2013; Leung *et al.*, 2015). In other studies, the presence of roots led to an increase of the soil porosity by loosening up the soil or by creating preferential flow channels. The flow through these channels operates on the surface of roots and through decaying roots (Ghestem *et al.*, 2011). In Figure 29, the pores formed by roots are shown. Indeed, if tillage is not made and the plants present cycles of growing and dying, then an increase of the pores size in the soil with increasing amount of roots in Mount Faito would be expected. The consequence of the formation of preferential flow channels should also be understood from changes in the hydraulic conductivity of the soil.

In order to isolate the effect of vegetation on the soil hydraulic properties, transpiration has to be isolated as in Leung *et al.* (2015). The water uptake by the roots stops if the plant does not transpire, which occurs when there is no sunlight or when the plant is dormant, which are the conditions verified during winter, when predisposing conditions for the occurrence of landslides are verified.

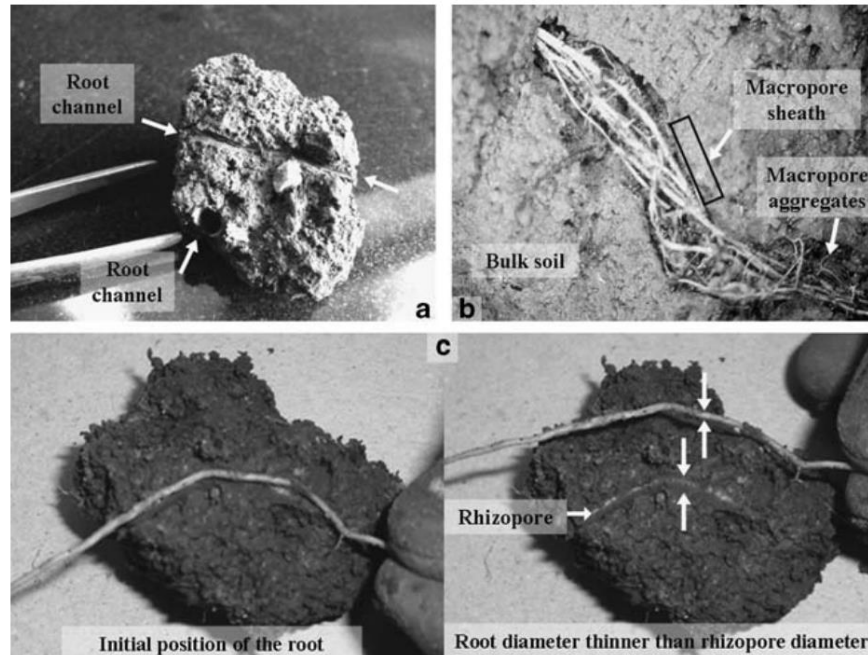


Figure 29 – Macropores created by roots (Ghestem *et al.*, 2011).

## 2. How is the effect of vegetation on the hydraulic response of the soil at slope scale?

Two main periods might be identified in the study of the hydraulic effect of vegetation. During summer, the water is up taken by the roots and transpired in greater quantity than in winter. The suction that was generated during summer, is accompanied by a decrease in the hydraulic permeability that might protect the slope upon rainfall. The plants might also be able to maintain higher values of suction if leaves are green. Nonetheless, previous studies have shown that the hydraulic effect of vegetation is irrelevant for slope stability because no transpiration occurs during winter and suction is lost. In this regard, the effect of vegetation on the soil hydraulic properties might play a more important role (Leung *et al.*, 2015). As plants create preferential flow channels and change the porosity of the soil, the infiltration might be facilitated. Therefore, a fast moving wetting front and a quick loss of suction might be detected.

The effect of vegetation is not limited to the rooting area but certain root traits might be associated to particular hydraulic soil responses. As seen by Stokes *et al.* (2009), greater root length is related to preferential water flow, as this occurs along the root surface, and greater number of root tips in woody species are associated to water uptake, generating suction. The water uptake by woody species is made in the area right before the root tip where root hairs are present. A spatial root distribution investigation might provide a relation between the hydraulic behaviour of the soil and the root systems.

As the root distribution is not uniform in space, it decreases with increasing depth and distance from the trees stem, the effect of vegetation might decrease. Competition among individuals might change the

hydraulic properties, and so a spatial variation of suction and water content in the soil is expected with different root traits.

3. Is the mechanical reinforcement by roots relevant for slope stability of pyroclastic soil covers?

As mentioned by Stokes *et al.* (2009), the contribution of vegetation to slope stability is mostly mechanical because suction usually decreases when rainfall occurs. Winter is usually the rainy season and plants are dormant during this period, not up taking water.

Root mechanical reinforcement has been considered in previous works, but not in pyroclastic soil covers in the areas surrounding the Mount Vesuvius. The root distribution in these soils is also not known. As mentioned before, the root growth is conditioned by the surrounding conditions, as competition with other individuals, water holding capacity of the soil, thickness of the soil cover, and management techniques. The root mechanical reinforcement depends on the root spatial distribution. The fact that most of the root systems are developed in the upper soil layers might not change greatly the safety factor associated to the weakest failure surface. However, if roots tend to grow deeper, then the weakest potential failure surface might be found deeper in the soil cover and with a greater associated safety factor.

In the work of Di Crescenzo and Santo (2005), a smaller number of landslides were identified when trees was present in the sliding zone, but landslides were triggered in both chestnut plantations and shrublands. Roots were reported to be found hanging on a landslide scar (Di Crescenzo and Santo, 1999), which shows that the roots failed by pull out, just like in Figure 30.



Figure 30 – Roots that failed by pull out in a previous landslide in the region of Campania.



## Chapter 2 Test site overview

### 2.1 Introduction

The work developed in the present thesis was based on the study of a test site located in Mount Faito, part of the Lattari mountains. Mount Faito belongs to the municipality of Vico Equense and Castellammare di Stabia in the region of Campania in the South of Italy (Figure 31). The test site, in particular, is located at latitude  $40^{\circ}40'32.29''\text{N}$  and longitude  $14^{\circ}28'23.35''\text{E}$  on a slope facing North at approximately 850 m of altitude.

Further description of the site is made in this chapter starting from the stratigraphy, followed by the physical characterization the soil layers. Then, the topography of the site is presented, as well as the development of the soil layers thickness along the slope. Finally, the characterization of local vegetation and its management are presented alongside with considerations on the groundcover.

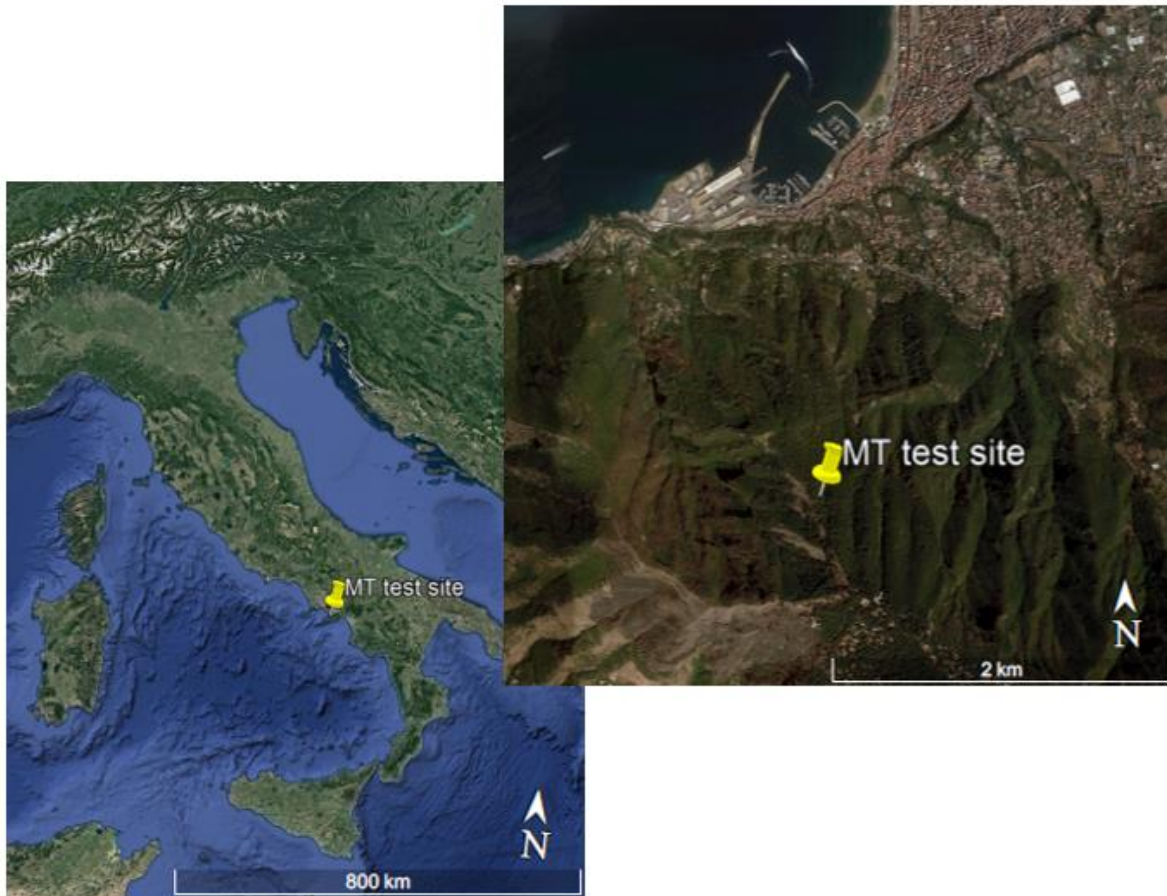
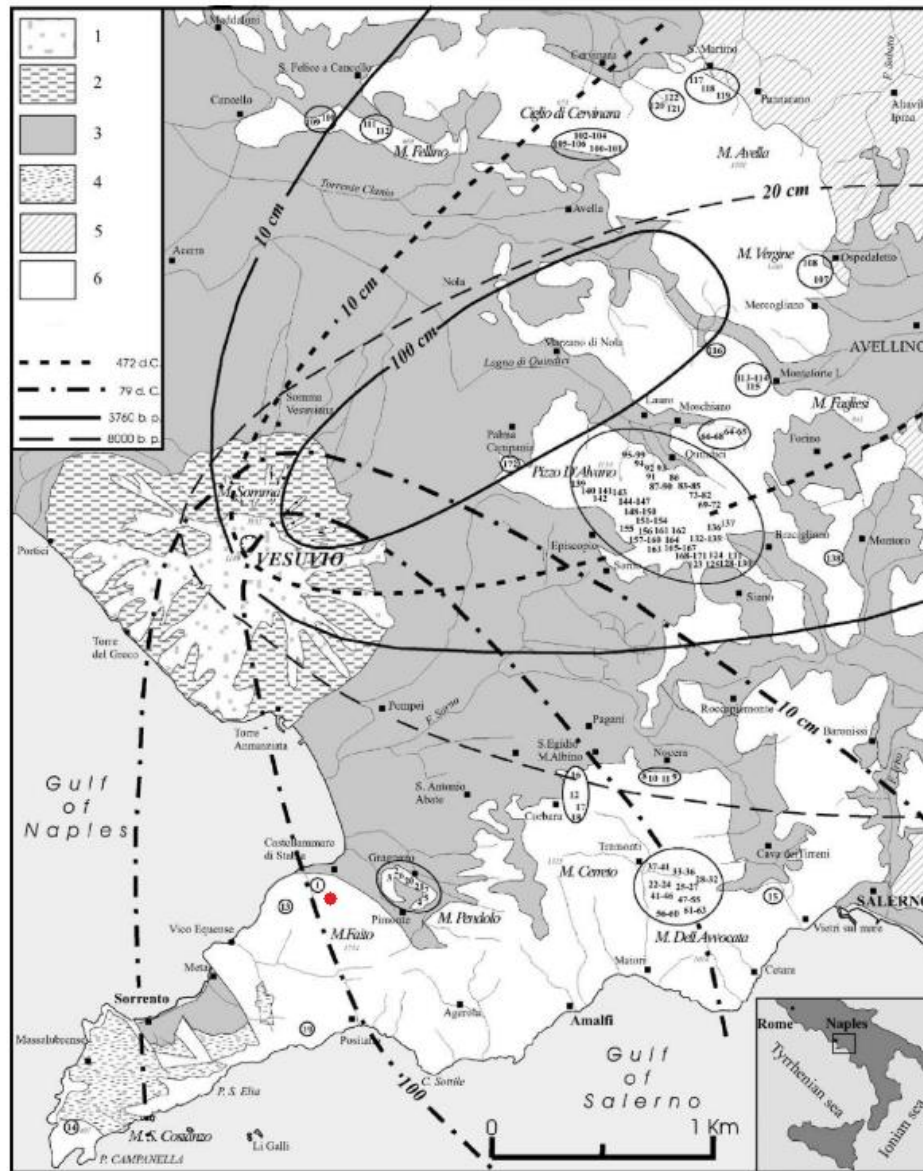


Figure 31 – Test site location on satellite images (source: Google Earth).

## 2.2 Stratigraphy

The stratigraphic profile in the areas surrounding Mount Vesuvius is composed of pyroclastic deposits resultant from explosive eruptions of the volcano. Mount Faito test site is located in the area of deposition of the eruption of 79 AD and over a limestone bedrock (Figure 32).



(1) Lavas; (2) Pyroclastic flow; (3) Pyroclastic fall and detrital-alluvial deposits; (4) Mio-Pliocene terrigenous deposits; (5) Miocene terrigenous deposits; (6) Mesozoic limestones

● Mount Faito test site

Figure 32 – Areas of pyroclastic deposition of several eruptions of Vesuvius volcano (adapted from Di Crescenzo and Santo, 2005). Approximate location of Mount Faito test site.



The identification of the geological profile was performed by Santo, Forte and De Falco (personal communication) at Mount Faito test site. The detailed description can be found in Table 6. The soil profile is composed of three main groups of soil layers, which are A, B and C, resting on a fractured limestone bedrock (R).

*Table 6 – Detailed description of the geological profile at Mount Faito.*

Lithotype	Description
A1	Soil and organic soil. Sandy reddish brown sandy cinerite with abundant pumices and the presence of root systems.
A2	Deposit for the eruption of 79 AD. Cinerite and angular pumices in size from a few millimetres to a few centimetres.
B	Pumices of the eruption of 79 AD. Angular pumices of whitish grey colour and of dimensions up to 3-4 cm. Clasts of lava slag and sporadic pyroxenes are frequently found. The pumices are not well graded and has a scarce presence of matrix.
C1a	Deposit of an ancient eruption before 79 AD. Sandy cinerite, slightly silty, of grey colour with few millimetric pumices.
C1b	Deposit of an ancient eruption before 79 AD. Brownish yellow silty cinerite. Rare yellowish pumices of dimensions from millimetres to centimetres are present.
C2	Deposit of an ancient eruption before 79 AD. Silty sandy clayey cinerite of reddish brown colour with few small altered pumices. The degree of argilification gradually increases with depth.
C3	Deposit of an ancient eruption before 79 AD. Sub-rounded slag of dimensions of 1-2 cm in a sand matrix with pyroxenes.
R	Fractured and karsified limestone.

The thickness of each soil layer identified in Table 6 vary spatially in the test site as observed in the boreholes presented in Figure 33. The thickness of soil layer A1 varies between 0.1 and 0.6 m, soil A2 varies between 0.3 and 1.0 m, and soil layer B varies between 0.7 and 1.4 m (Table 7). The thickness of the soil layers C1 and C2 were not possible to be assessed based on these boreholes, nor the position of the bedrock. However, the bedrock is expected to be found at depths between 2.7 to 3 m. In fact, the borehole 1N revealed that the bedrock was at 2.6 m from the surface.

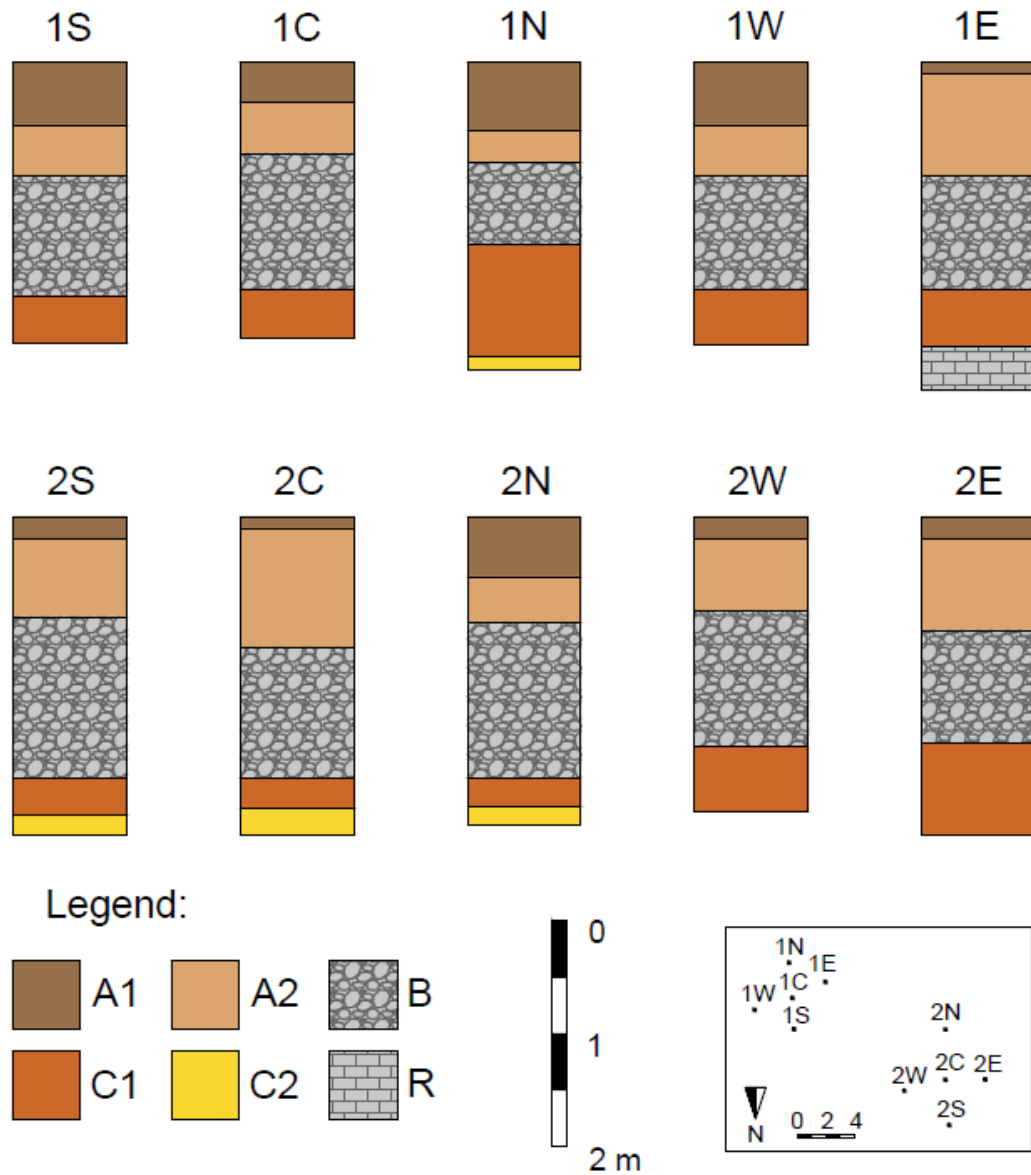


Figure 33 – Boreholes performed in Mount Faito test site and their spatial distribution.

Table 7 – Thickness of each soil layer found in the boreholes represented in Figure 33.

soil	profile									
	1C	1E	1N	1S	1W	2C	2E	2N	2S	2W
A1	0.4	0.1	0.6	0.6	0.6	0.1	0.2	0.5	0.2	0.2
A2	0.5	0.9	0.3	0.4	0.5	1.1	0.8	0.4	0.7	0.6
B	1.2	1.0	0.7	1.1	1.0	1.2	1.0	1.4	1.4	1.2
C1	0.4	0.5	0.9	0.4	0.5	0.3	0.8	0.3	0.3	0.6
C2	?	-	>0.2	?	?	>0.2	?	>0.2	>0.2	?

## 2.3 Soil physical properties

The physical characterization of the soil was composed of three main properties: grain size distribution, Atterberg limits and specific gravity of the soil particles. Horizontal boreholes were performed to collect undisturbed soil samples of different soil types at different depths. The list of collected boreholes is presented in Annex A.

The grain size distribution was performed according to the recommendations provided by the AGI (Italian Geotechnical Association). The Atterberg limits were determined following the ASTM D4318 - 00 norm, however some of the tested soil did not contain plastic fines for which the liquid and plastic limits were not possible to be determined. The specific gravity of the soil particles was determined using the ASTM D854-14 norm.

The soil was classified according to the Unified Soils Classification System (USCS) described in the norm ASTM D2487-17 is presented in Figure 34 based on the grain size distributions in Figure 35. The first soil layer A1 is a silty sand with gravel, and right bellow soil A2 is a silty gravel with sand. Soil layer B, which is a well graded gravel with sand, is clearly distinguishable from the remaining due to its course texture. The gravel present in all the soil layers is pumices (porous rock material resultant from explosive volcanic eruptions). At the bottom of the pyroclastic soil cover, two soil layers can be found classified as sandy silt. The Atterberg limits presented in Table 8 show that soil C1 and C2 vary from medium and high compressibility silt.

The profile presented in Figure 34 with the mean physical characteristics presented in Table 9 was built based on the geological profile identification of Table 6, on the boreholes of Figure 33 and on the soil classification according to the grain size distributions presented in Figure 35. This profile constitutes the bases for the development of the geotechnical model, which requires complementary information regarding the hydraulic (Chapter 3) and mechanical (Chapter 5) properties of each soil layer.

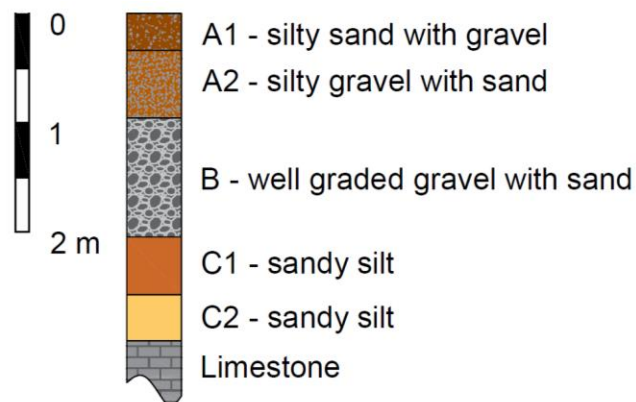


Figure 34 – Mean soil stratigraphic profile present at Mount Faito and soil classification according to the USCS.

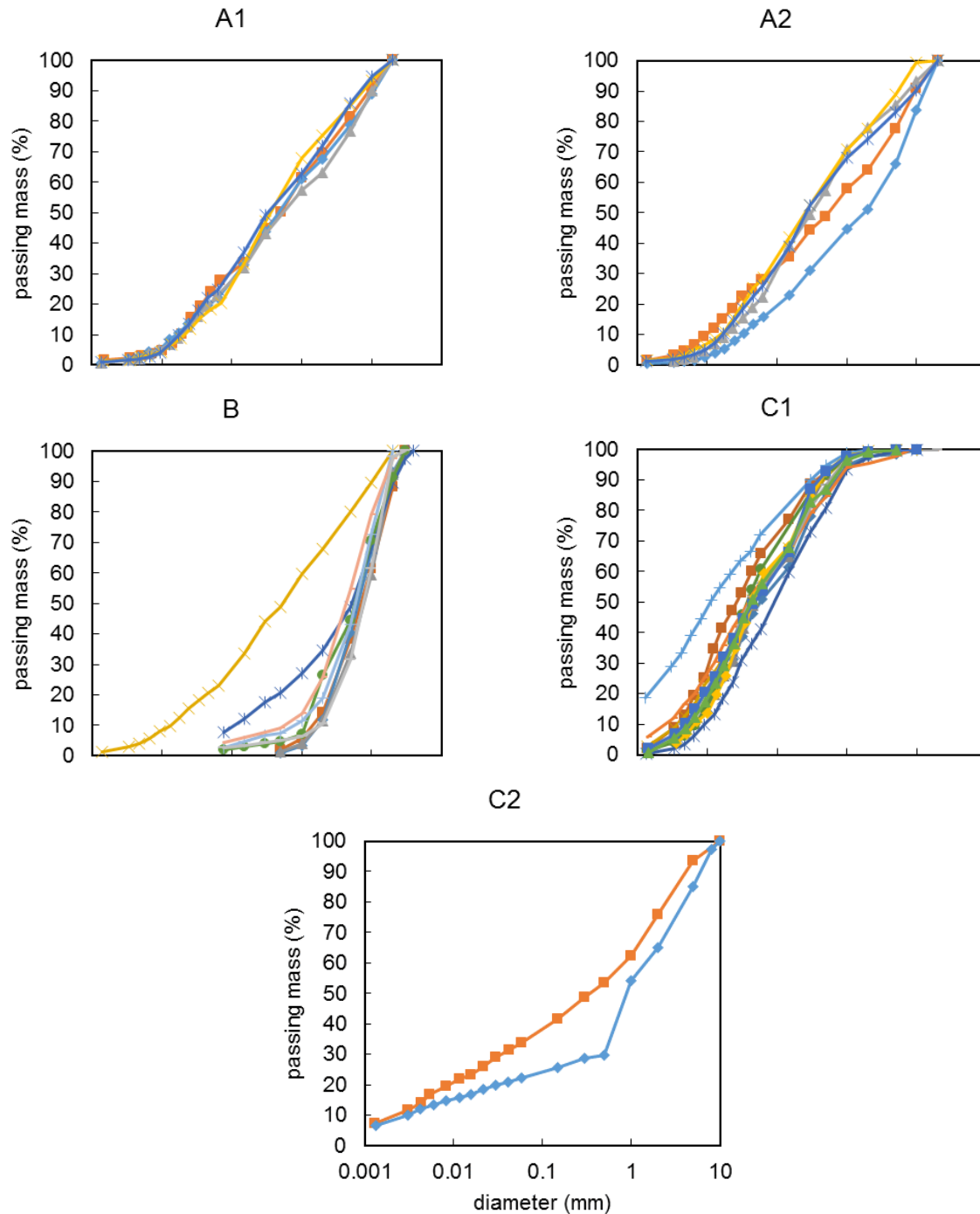


Figure 35 – Grain size distribution of Mount Faito soils.

Due to the great differences of porosity and root dry biomass, a sublayer of soil A1 was defined referred as A1sup. The soil layer A1sup corresponds to the first 0.1 m of soil and is largely intersected by plant roots containing litter and other live organisms. The average specific gravity ( $G_s$ ), dry density ( $\gamma_d$ ) and soil porosity are presented in Table 9.

Table 8 – Liquid limit, plastic limit, and plasticity index of soil C1 and C2 collected at Mount Faito performed by Mastantuono (personal communication).

soil	depth (m)	liquid limit (%)	plasticity limit (%)	plasticity index (%)
C1	88	58	50	8
C1+C2	100	36	23	13
C2	126	46	29	17
C1+C2	130	63	60	3

Table 9 – Mean and standard deviation of soil physical properties: specific gravity ( $G_s$ ), dry density ( $\gamma_d$ ) and soil porosity.

Soil	Specific gravity, $G_s$ (-)	Dry density, $\gamma_d$ (g cm <sup>-3</sup> )	Porosity, n
A1	2.606 ± 0.042	0.918	0.643 ± 0.168
A1sup	2.580 ± 0.041	0.776	0.682 ± 0.171
A2	2.688	0.819	0.694 ± 0.159
C1	2.656 ± 0.017	0.735	0.722 ± 0.267
C2	2.528	0.831	0.666 ± 0.282

## 2.4 Slope topography

The topography and stratigraphy of the sequence of boreholes 1N-1C-1S and 2N-2C-2S were projected along a single longitudinal profile, as in Figure 36. The topography was merged laterally along the direction of maximum angle of the slope. The thickness of the soil layers A1 and C1 decreases in the downslope direction and in opposition, the thickness of the soil layers B and A2 increases.

The mean angle of the slope is 26.5°. The surface of the ground presents undulations, as observed in Figure 37, that may have resulted from abandoned terraces made for cultivation. Terraces are in fact common in the region (Mazzoleni *et al.*, 2005) and they might have been abandoned in this location to be replaced by the sweet chestnut trees plantation. Consequently, local minimum and maximum angles of 13.2° and 44.3° were observed, respectively.

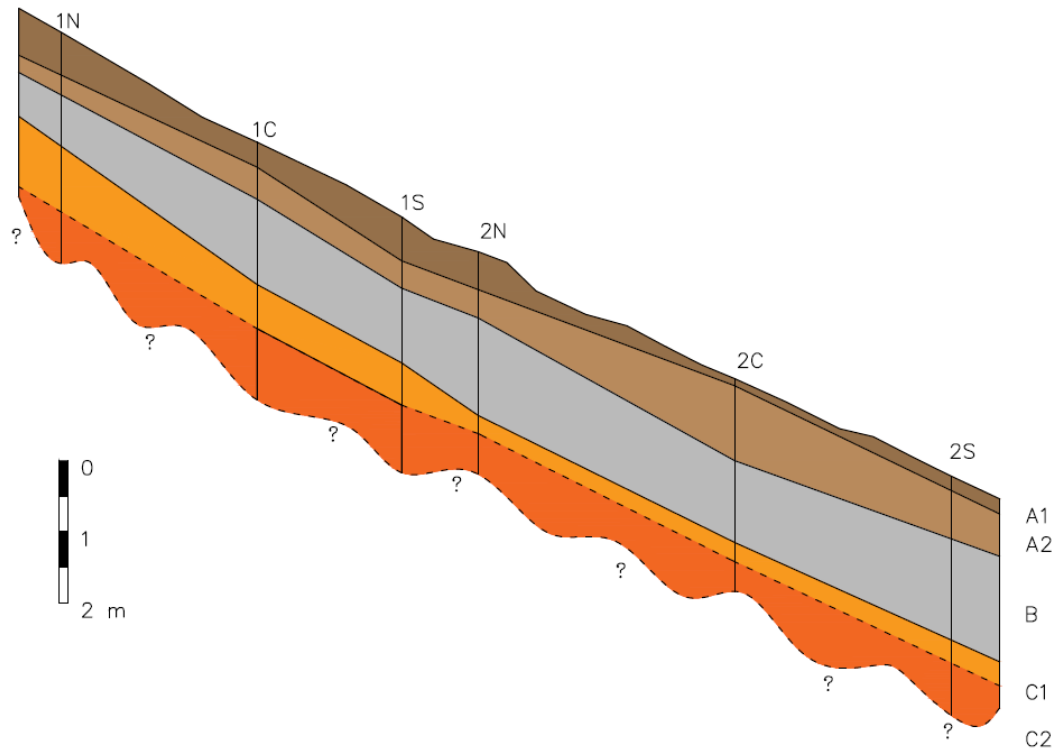


Figure 36 – Projected longitudinal profile of cell 1 and 2.



Figure 37 – Photograph of the site on February 17<sup>th</sup>, 2017.

## 2.5 Vegetation and ground cover

The vegetation presented at the test site is composed of mature *Castanea sativa*, commonly known as sweet chestnut trees (Figure 38,a). The understory was dominated by *Pteridium aquilinum*, which are ferns



(Figure 38,b). The list of species identified in Mount Faito test site by Annalisa Santangelo and Sandro Strumia (personal communication) are present in Annex B.

In the region, two types of chestnut cultivation are present: (i) coppiced chestnut trees for wood production and (ii) fruit production trees. The chestnut trees at the test site are cultivated for fruit production. The vegetation in this site is managed and the understory is reduced and affected by the human activity, which controls its growth.



(a) *Castanea sativa*



(b) *Pteridium aquilinum*

Figure 38 – Dominant species in Mount Faito test site: (a) *Castanea sativa*, and (b) *Pteridium aquilinum*.

The species identified at the test site do not dry, but rather become dormant during the winter. In the spring, the plants use the water stored in the soil because they do not present organs to store water. Nonetheless, the growth of plants in the spring is not initiated all the same instant. The species that require sunlight are the first ones to appear. The species that prefer shadow appear after the growth of leaves in the chestnuts.

The vegetation growth in the instrumented area cell 1 (described in detail in Chapter 4) was recorded every week during the monitoring period in order to register the state of growth and ground cover, as presented in Figure 39 and Figure 40. The monitoring started in a stage when soil is bare (10 March 2017) and the ground is simply covered by the chestnuts litter. The leaves on shrubs and trees start to grow in the middle of April (21 April 2017). This growth is quite fast through May (22 May 2017) until July, when the peak is reached for which the mid-season was then defined to start in May 15th and finish in September 1st, corresponding to a period of high transpiration. There is a decline in the ground cover in September (26 September 2017) because some leaves start to dry and in October (26 October 2017) the understory is



removed. The shrubs and ferns are removed by the local farmers as a consequence of the cultivation of chestnuts in this area. A reduction in the transpiration might occur during this period but evaporation might increase because a greater fraction of the soil is exposed.



10 March 2017



21 April 2017



22 May 2017



19 July 2017



26 September 2017



26 October 2017

*Figure 39 – Photos of cell 1 from March to October 2017.*





2 November 2017



15 November 2017



6 December 2017



16 February 2018



12 April 2018



24 April 2018

*Figure 40 – Photos of cell 1 from November 2018 to April 2018.*

In November the leaves of the chestnuts turn yellow and drop (2 November 2017 – 15 November 2017). From this moment, the soil is bare but some ground cover is present due to the presence of some shrubs, herbs and grasses that did not dry. Therefore, most of the water being removed from the soil is through evaporation. The soil remains bare throughout the winter (6 December 2017), sporadically occurring snowfalls (16 February 2018) until the plant growth restarts in April (12 April 2018 – 24 April 2018).



The ground cover is taken into account in the calculation of evapotranspiration, as observed in the previous section. However, other factors should be taken into account in the study of the effect of vegetation in the soil-atmosphere interaction. It is important to notice the occurrence of runoff, i.e. not all the rainfall infiltrates into the ground (Figure 41). Also, the rainfall partition by the trees canopy prevents some of the water to reach the ground and its distribution in space (Putuhena and Cordery, 1996; Llorens and Domingo, 2007). Another interesting observation was the formation of a frozen soil layer (Figure 42), which means that the water of a rainfall event only infiltrates upon the ice melting.



*Figure 41 – Soil erosion exposing roots.*



*Figure 42 – Formation of a frozen soil layer.*

## Chapter 3      Hydraulic characterization of natural unsaturated pyroclastic soils

### 3.1 Introduction

Landslides involving the pyroclastic soil cover in Campania (Italy) are usually triggered by extreme rainfall events during the wet season. The wetting reduces soil suction that provides an apparent cohesion which constitutes a major contribution to maintain the slope stable (Urciuoli *et al.*, 2016). The groundwater regime is controlled by the boundary conditions of the shallow pyroclastic soil cover, i.e. the atmospheric conditions, the groundcover and the hydraulic properties of the bedrock. Nonetheless, the manner by which the water infiltrates and evaporates from this soil cover is also dependent on the soil hydraulic properties, such as the water retention curve (WRC) and the hydraulic permeability function (HPF).

The common procedure to investigate soil hydraulic properties in the laboratory is by determining the soil main drying WRC, even if the soil hydraulic properties are known to be hysteretic, i.e. the soil response is different if it is being dried or wetted. However, water infiltration upon rainfall is a wetting process that follows wetting main or scanning WRCs. The speed of the wetting front can be inferred from the water storage capacity of the soil (Fredlund and Rahardjo, 2012). In the study of infiltration processes, as the ones responsible for the triggering of rainfall-induced landslides, a correct estimation of the speed of the wetting front upon rainfall may allow the development of more accurate early warning systems.

In previous studies, the hydraulic properties of pyroclastic soils were inferred from drying WRCs obtained from laboratory experimentation (Nicotera *et al.*, 2010). When the main drying branch was compared with field measurements, the curve was observed to be an upper boundary to the field data (Figure 43). Differences between field and laboratory were attributed to the fact that in the field, air is not allowed to escape at surface which leads to an increase of entrapped air in the soil pores (Pirone *et al.*, 2014). An attempt to investigate the wetting branch of the WRC was also made from which was concluded that the hysteresis is small. Nonetheless, the need for the soil characterization considering hysteresis in the hydraulic properties was identified in order to improve the simulation of wetting processes.

On another perspective, soil is considered to be a 3-phase medium containing solid particles, water and air, by geotechnical and geological engineers. The biological component, which is known by ecologists and agronomists to be relevant to in the study of water flow, is being ignored in the study of the pyroclastic soil covers. Thus, considering the soil as a 4-phase medium, i.e. solid particle, water, air and roots, can lead to an improvement in the hydraulic characterization of natural soils and a better understanding of the infiltration processes.

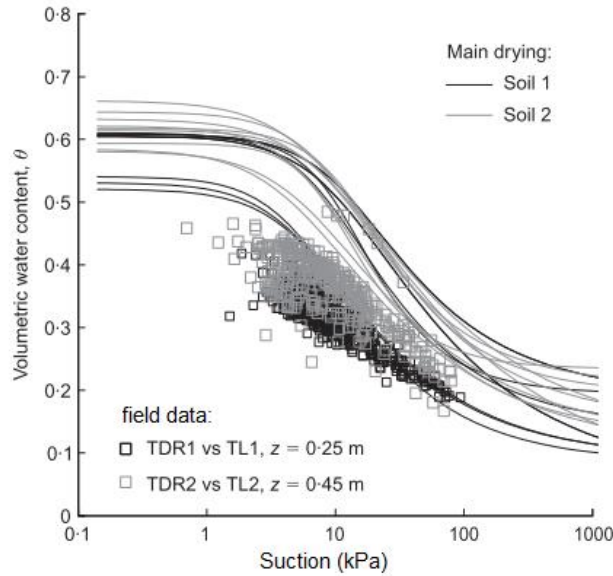


Figure 43 – Comparison of laboratory main drying curves and field measurements (adapted from Papa *et al.*, 2013).

Ng *et al.* (2016b) observed that the volume of soil pores occupied by the roots was related to the changes in the WRC. Leung *et al.* (2015) compared the relative importance of changes in the soil hydraulic properties affected by the presence of vegetation and the suction resultant from water uptake. The difference between bare and root-permeated soil is detected in terms of suction that can result from the plant water uptake or from the soil changes caused by the plants. The most preponderant effect was on the changes on the soil hydraulic properties. Indeed, the pore size distribution, and so the soil structure, is closely related to the soil hydraulic properties (Romero *et al.*, 1999).

Roots increase soil porosity, increase the pores size, and create preferential flow paths (Angers and Caron, 1998; Ghestem *et al.*, 2011; Zhang *et al.*, 2016). The preferential flow occurs on the root surface and in channels created by decaying roots. However, not all studies reported an increase of soil permeability (Ng *et al.*, 2016b).

The microbial and chemical interactions lead to the formation of soil aggregates which change the micro and macro structure of the soil. The macro-aggregates are formed first and are related to root growth and mycorrhizal fungal hyphae (branching filamentous structure of a fungus collectively refereed as mycelium). The organic matter in the macro-aggregates contributes to the aggregate stabilization by promoting the growth of fungal hyphae and microbes that result in the deposition of polysaccharides (sugar). The accumulation of carbon and the formation of very stable micro-aggregates (association of carbon to the mineral fraction) results from certain favourable moisture and temperature conditions and adequate amounts of clay minerals and polyvalent cations (Jastrow, 1996). The same observations were detected in volcanic soil by Lynch and Elliott (1983).

The research question that was intended to be investigated in the present chapter is “How are the hydraulic properties of the soil in Mount Faito affected by the presence of roots?”. Indeed, previous studies showed that the presence of vegetation changes the soil hydraulic properties. Improvements can also be made in the hydraulic characterization of soil to study infiltration processes in the pyroclastic soil covers in Campania (Italy).

## 3.2 Methods and materials

### 3.2.1 Void ratio of root-permeated soil

The fact that the soil voids are occupied by roots makes the soil overall less porous resulting in changes in the soil mechanic and hydraulic behaviour. The volume of roots is hard to quantify but the weight of roots is not. In this work, the volume of roots was calculated based the root wood density, which is dependent on the species, on the oven-dry weight of roots, and on the moisture content. This section intends to elaborate on the determination of root wood specific gravity and on its use to determine root volume in different experimental scenarios and their implication on the soil porosity.

The work of Ng *et al.* (2016a) proposed an approach to take into account the volume occupied by the roots for the calculation of porosity of root-permeated soil. Equation 25 was used in the present work to calculate the soil void ratio ( $e$ ) based on the root volume ratio ( $R_v$ ), which is defined as the total volume of roots per unit volume of soil, and on the void ratio before root permeation ( $e_0$ ) values.

$$e = \frac{e_0 - R_v(1 + e_0)}{1 + R_v(1 + e_0)} \quad 25$$

The relation between soil porosity and void ratio is given by Equation 26. Porosity and void ratio are equivalent parameters that quantify how porous is a soil. In the present work, porosity was the adopted parameter.

$$n = \frac{e}{1 + e} \quad 26$$

The specific gravity at a given moisture content  $m$  ( $G_m$ ) is given by Equation 27, where  $W_{oven-dry}$  is the oven-dry weight of the wood and  $V_m$  is the wood volume at a given moisture content  $m$ . Note that the water content referred in this part of the work is gravimetric, i.e. in terms of weight. The specific gravity is dimensionless because it is defined as the ratio between the wood density (or soil) and the water density ( $\rho_{water} = 0.9982 \text{ g cm}^{-3}$  at 20 °C).

$$G_m = \frac{W_{oven-dry}}{V_m} \cdot \frac{1}{\rho_{water}} \quad 27$$

The relation between the specific gravity for oven-dry and green volume ( $G_b$ ) and the specific gravity  $G_m$  is given by Equation 28 for moisture contents ( $M$ , in %) lower than 30% (Simpson, 1993).

$$G_m = \frac{G_b}{1 - 0.265 \frac{30 - M}{30} G_b} \quad 28$$

The dominant species found in the study site in Mount Faito was the sweet chestnut (*Castanea sativa*) whose roots were found in the boreholes for soil characterization. A survey was performed at the site in order to determine the root distribution, vertical and horizontal, that is described in detail in the Chapter on field monitoring. The collected roots were scanned and their volume was determined using an image analysis software (WinRHIZO by Regent Instruments Inc.). Note that the volume obtained is that of the green wood because the scanned roots were preserved in alcohol after being collected to prevent the root volume change. The correspondent oven-dry weight was measured as well. A more detailed description of the root distribution quantification is presented in Chapter 4 of this thesis.

The mean value of the wood specific gravity  $G_b$  of the root wood of *Castanea sativa* at Mount Faito was determined as well as the standard deviation for each scanned image (Figure 44). The most surficial roots seem to have a lower specific gravity  $G_b$  and roots collected between 1.5 and 2.5 m present higher variability. The average value of the specific gravity for all the depths is 0.387 with a standard deviation of 0.184.

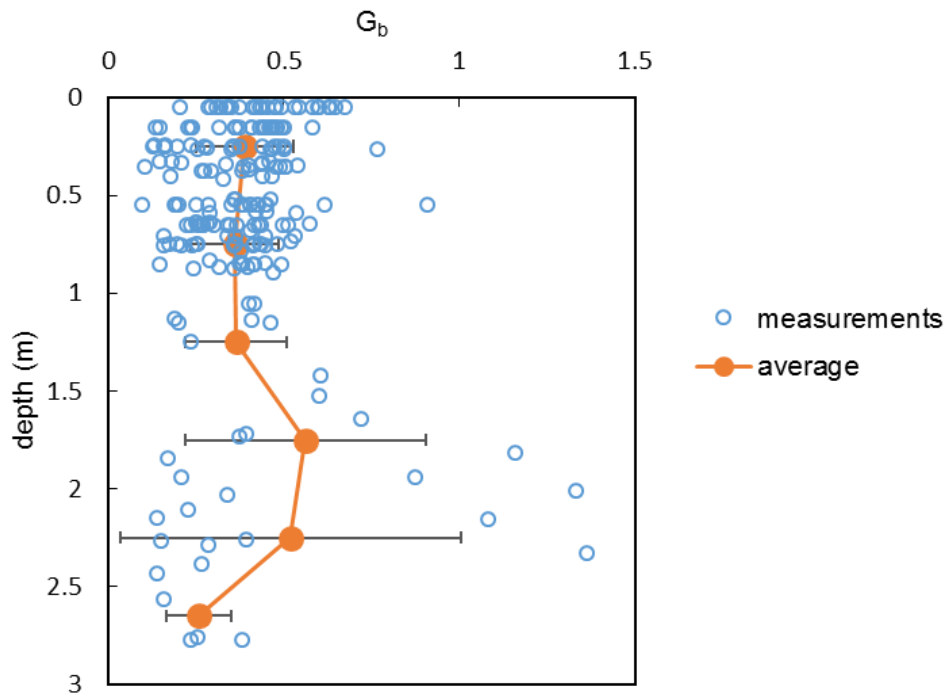


Figure 44 – Variation of the roots of *Castanea sativa* specific gravity with depth in Mount Faito: individual measurements and mean and respective standard deviation.

According to the Wagner meters database (<https://www.wagnermeters.com/specific-gravity/>), sweet chestnut (*Castanea sativa*) wood has a specific gravity of 0.51 for a volume with water content of 12%. Therefore, the specific gravity  $G_b$  of sweet chestnut is 0.472. This value is higher than the one obtained

from the root wood of chestnuts of Mount Faito ( $G_b = 0.387$ ). The values of specific gravity of timber and root wood will be assumed as equal because, as referred in the work of Donaldson (1985), the density of the branch and root wood is very similar.

The following study intends to show the variation of specific gravity with root diameter. The root volume given by the image analysis was grouped into four diameter classes ( $V_d$ ) and the total dry biomass in each image ( $M_{dry}$ ) is equal to the sum of the product of the volume of roots by the specific gravity ( $G_{b_d}$ ) of each diameter class  $d$ , as expressed in Equation 29.

$$M_{dry} = \sum_{d=1}^4 V_d \cdot G_{b_d} \quad 29$$

The values of  $G_{b_d}$  were allowed to vary in order to minimize the difference between the estimated and the measured dry biomass. The final values are presented in Figure 45 corresponding to an  $R^2$ -value in the estimation of dry biomass of 0.835. No major differences in the specific gravity were observed. Indeed, there was simply a slight decrease towards the roots of greater diameter, which can be explained by the decrease of the overall fraction of lignin with increasing diameter of the root, found in Thomas *et al.* (2014).

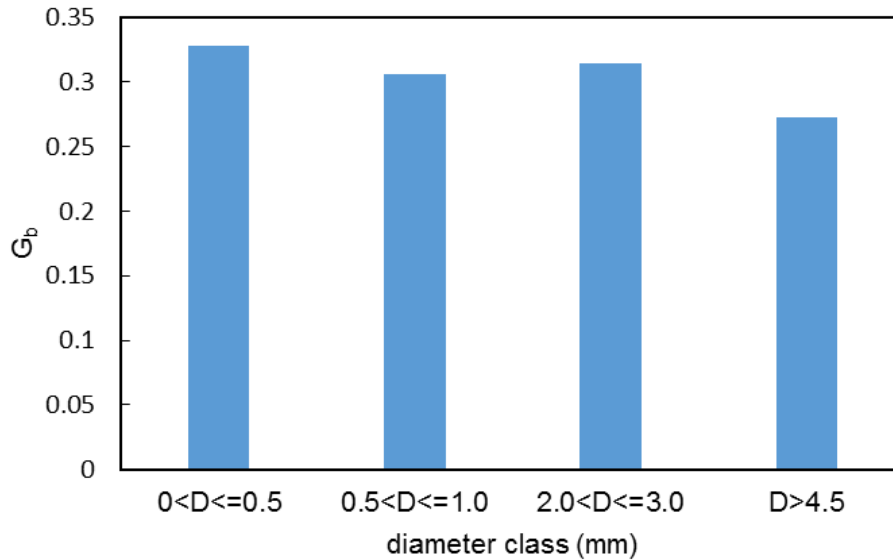


Figure 45 – Specific gravity of the *Castanea sativa* roots for different diameter classes.

The physical characterization of the soil from the study site in Mount Faito was made using the samples used for the hydraulic characterization. The conditions in which the soil is being studied along this thesis vary and so the root volume as a consequence of variations of moisture. The relative humidity of the surroundings of roots during several laboratory and field experiments results in variations of volume that should be considered. As seen before, the wood volume changes with relative humidity water contents lower than 30% (Simpson and TenWolde, 1999), as in Equation 27.

Three situations were identified in which the root volume may be taken into account:

1. Soil during the wetting and drying cycles in the ku-pf apparatus → where the roots are dead and their volume depends on the relative humidity of the surroundings;
2. Soil in standard direct shear tests → where the roots are dead and the volume is the one correspondent to submersion, i.e. green wood volume;
3. Soil in situ → where roots are alive and the volume taken by the roots corresponds to the green wood volume.

In the first identified situation, during the drying and wetting cycles in the ku-pf apparatus, suction varies between 0 and 100 kPa. The relative humidity correspondent to a suction of 100 kPa at 20°C is 99.9% according to the psychrometric law, for which the moisture content of the wood is approximately 23% using to the tables presented in Simpson and TenWolde (1999). Therefore, the relative humidity is always approximately 100% for which no volume variations in the wood are expected during the test.

The specific gravity of the wood at a moisture content of 23% is 0.564 applying Equation 27. This value is useful for the determination of the volume occupied by the roots during the testing in the ku-pf apparatus. On the other hand, if the specific gravity of the roots of Mount Faito is used, the specific gravity of the wood at a moisture content of 23% is 0.399 (Table 10). However, this estimation assumes that the roots do not absorb or release water into the soil.

In the second and third situations, the roots occupy the maximum volume possible. In the second case because the roots are submersed and in the third because the wood is green. For the calculation of the volume taken by the roots in situ, the density of 0.472 g cm<sup>-3</sup> (according to database of Wager meters) or 0.387g cm<sup>-3</sup> (according to the laboratory data) should be used (Table 10). The volume occupied by roots in the ku-pf is approximately 84% of the volume at the site when alive (green wood).

*Table 10 – Summary of the specific gravity (dimensionless) of the root wood to be adopted in the calculation of root volume for each experiment and respective soil and root conditions.*

Experiment	Specific gravity during experiment		Conditions	
	Wager meters database	Image analysis	Soil	Roots
Ku-pf wetting and drying cycles	0.564	0.399	0 to 100 kPa (or 100 to 99.9 % relative humidity)	Dead and dry
Direct shear test	0.472	0.387	Saturated	Dead and saturated
In situ	0.472	0.387	0 to >100 kPa	Green



### 3.2.2 Hydraulic characterization

The hydraulic characterization was composed of three tests performed in a fixed sequence (Figure 46). In some cases, only one or two of these tests were performed but always in the presented order. The first test was performed with the objective of obtaining the saturated permeability. Then, the samples were subjected to a series of evaporation and imbibition phases monitored by the ku-pf apparatus in order to record the drying and wetting paths in the water retention plan. Finally, the residual water content was obtained using a pressure plate.

Small samples (diameter = 72 mm; height = 60 mm) were made by extrusion (Figure 47) from the horizontal boreholes listed in Annex A. The soil samples were therefore undisturbed in order to preserve the original soil structure and porosity found at the site (Figure 48).

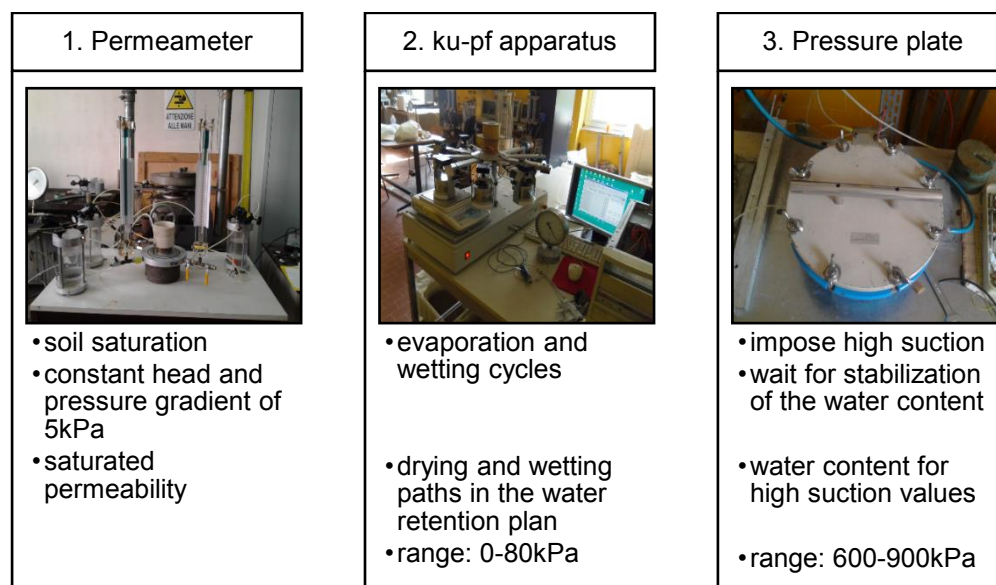


Figure 46 – Scheme of the test sequence and summarized description.



Figure 47 – Soil sample extrusion from the borehole.



Figure 48 – Soil sample after extrusion.

### 3.2.2.1 Saturated permeability

The saturated permeability test was performed at constant head on saturated soil samples using the setup presented in Figure 49. The setup is composed of one permeameter, two burettes, three water reservoirs, three air pressure regulators and one pressure transducer. A closer look into the scheme of the setup represented in Figure 50 allows a better understanding of its operation, where basic instructions for its operation are summarized.

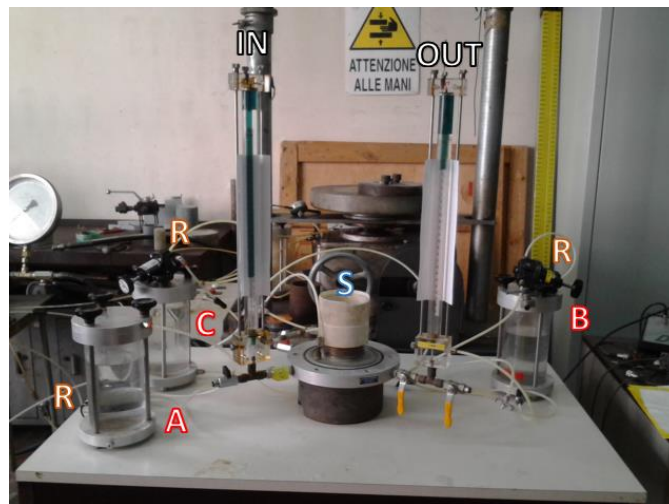


Figure 49 – Setup used to determine the saturated permeability at constant head.

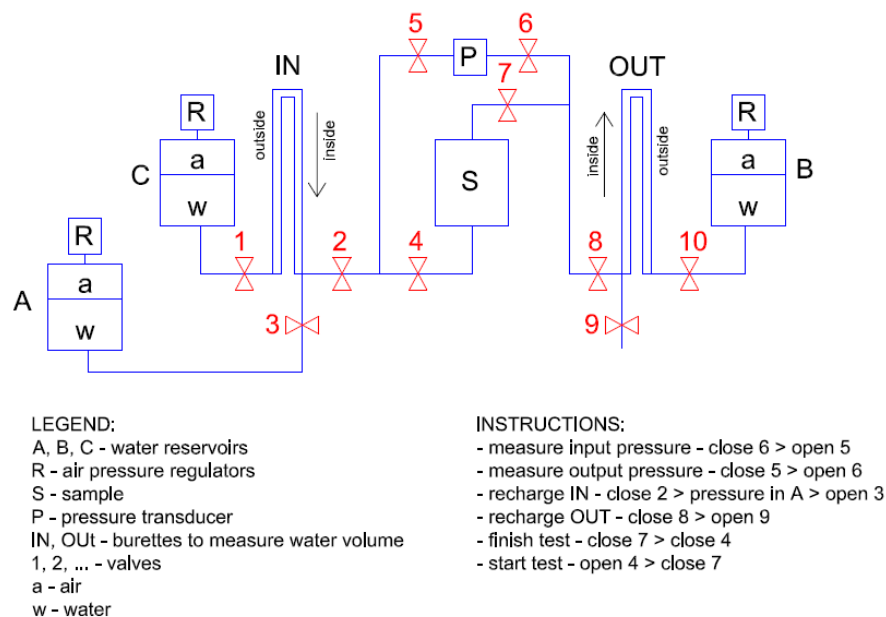


Figure 50 – Scheme of the setup to determine the saturated permeability and indication of basic operation instructions.

Filter paper was placed on the supports of the permeameter and humidified with distilled water to prevent the dragging of material when water flows through the sample. The O-rings in the interior of the support were covered with silicone grease to help inserting the samples to the support. The samples were closed at both ends using the permeameter supports as shown in Figure 51.



*Figure 51 – Permeameter: soil mould and upper and bottom supports.*

The samples were saturated by connecting it to the system upstream. A pressure of 5 kPa was used to force the water to flow through the sample. Then, a pressure of 10 kPa was applied in the system upstream from the sample and 5 kPa were applied to the downstream. If the water that was moving inward (measured in IN, Figure 50) was equal to the volume of water that got out (measured in OUT, Figure 50), then the soil sample was considered saturated.

The permeability tests were made following two procedures, here referred as type 'a' and 'b'. The test type 'a' fixes the time intervals at which the volume of flowing water variations are registered. In the test type 'b', the water volume variation is fixed and the time is registered instead. The test type 'a' was more adequate when the permeability of the sample is low, allowing an adequate number of readings. The test type 'b' was preferable when the permeability of the sample is high. At least one of the tests (type 'a' or 'b') was repeated 3 times.

After the permeability test was completed, the sample was carefully removed from the setup, closed and weighted. If necessary storage, the samples were sealed using paraffin and sealing plastic bags to prevent water evaporation. In some cases, no other test was performed and so the samples are oven dried at 105°C for 24 hours in order to determine the saturated water content and porosity. The samples weight was recorded using a precision scale with a resolution of 0.01g.

### 3.2.2.2 Wetting and drying cycles

The behaviour of the soil in the water retention plan was investigated by subjecting soil samples to wetting and drying cycles. This allows the determination of main and scanning water retention curves depending on the initial state of the soil.

A ku-pf MP10 by UGT, referred shortly as ku-pf apparatus or ku-pf, was used to record the water content and suction along time. This equipment (Figure 52) is composed of a scale and ten rotating arms, each holding a basket. Each basket can hold a soil sample in which suction is monitored at 15 mm and 55 mm from the bottom using mini-tensiometers (Figure 53). The scheme of the basket is presented in Figure 54. More details regarding this equipment can be found in Punzel and Berding (2010).



Figure 52 – ku-pf apparatus used in the experimentation.



Figure 53 – Sample support on the scale of the ku-pf apparatus.

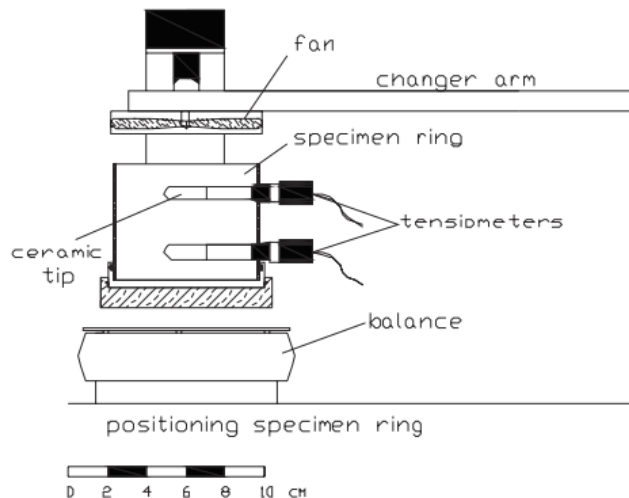


Figure 54 – Scheme of the sample support (adapted from Nicotera et al., 2010).



The preparation of the ku-pf apparatus involves the mini-tensiometers saturation (Figure 55). Each tensiometer of the basket is connected to a reservoir, which is connected to a vacuum pump (Figure 56). The tensiometers were inserted in distilled water and water was forced to flow through the porous stone by applying vacuum with the pump. The tensiometers of the basket were then calibrated using the procedure suggested by the ku-pf apparatus software in which both tensiometers were connected to a vacuum dial gauge, which is then connected to a vacuum pump (Figure 57). The negative pressures of 0kPa and 50kPa were applied and set as calibration points by the software (Figure 58).



Figure 55 – Tensiometer (do not hold the tensiometer in this manner during the saturation).



Figure 56 – Setup of the saturation of tensiometers.



Figure 57 – Setup for the calibration of the tensiometers.

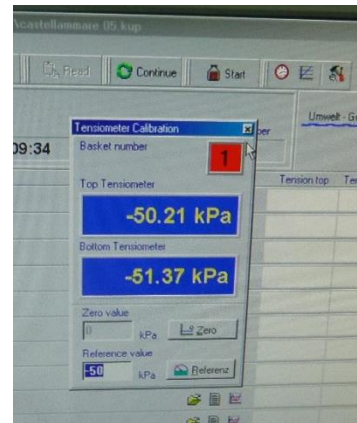


Figure 58 – ku-pf software on the calibration of tensiometers.

The extruded soil samples were added to the ku-pf apparatus either starting from the natural water content at the time of field collection or starting from saturation after the saturated permeability test. The bottom of the sample was sealed by covering it with cling film and with the plastic base that contains an O-ring. Two holes were made using the support with guides (Figure 59) and a drilling equipment (Figure 60). The removed soil was collected in order to determine the dry soil that was removed from the sample so that the water content of the sample could be better determined. The tensiometers were inserted in the holes in a

way that the good contact between the porous stones and the soil was guaranteed. Soil sample was always covered with cling film and a metallic cap.



Figure 59 – Support with guides to make holes in the sample to insert the tensiometers.



Figure 60 – Equipment used to make the holes for the tensiometers.

The drying phase was initiated by removing the cling film and the metallic cap at the top allowing the water to evaporate from the sample. The sample started from hydrostatic conditions. The drying phase should not exceed the maximum suction measured by the mini-tensiometers (80 kPa).

The wetting phase took place in steps, i.e. in each step, a small quantity of water was added to the top of the sample using a syringe and a new hydrostatic condition would have to be reached before a new step could be initiated. If the suction values were above 15 kPa, 5 g of distilled water were added, otherwise, 3 g were added. The hydrostatic condition corresponds to a steady state of water flow and that was reached when the difference in suction values was approximately 0.3 kPa, in which the higher absolute value should be observed in the top tensiometer.

### 3.2.2.3 High suction range

Some of the samples tested in the ku-pf apparatus or in the permeameter were used to determine a complementary value of water content in the high suction range in the pressure plate (Figure 61). The objective of this step was to extend the range of suction and water content in order to improve the fitting of the water retention model as suggested by Nicotera *et al.* (2010).

The samples were placed inside the pressure plate on the porous stone (Figure 62) guaranteeing a good contact. The porous stone was connected to the exterior of the pressure plate and the air pressure in the chamber was increased to 650-1000 kPa. The samples exchanged water with the porous stone until the pore pressure in the soil samples became equal to the porous stone (atmospheric pressure). This process took usually two weeks during which the weight of the samples is controlled using a precision scale with a resolution of 0.01g. The test finished when the variation of samples weight was despicable. The water content was then determined using the gravimetric method.



Figure 61 – Full pressure plate system.



Figure 62 – Position of the samples inside the pressure plate chamber.

### 3.2.3 Dry biomass

The dry biomass of the samples used for the hydraulic characterization was determined after all the tests were performed. The dry samples were destroyed after 24 hours in the oven at 105 °C and the roots were collected using scissors. The weight of the roots was measured using a scale with a resolution of 0.001 g.

### 3.2.4 Experimental data processing and filtering

#### 3.2.4.1 Saturated permeability

The saturated permeability was calculated based on the Darcy's law that is described by Equation 30, where  $K_{sat}$  is the saturated permeability,  $A$  is the cross-section area of the sample,  $\Delta V$  is the volume of water that flowed through the sample in the time interval  $\Delta t$ , and  $i$  is the hydraulic gradient.

$$\frac{\Delta V}{i \cdot A} = K_{sat} \cdot \Delta t \quad 30$$

The volume of water flowing through the sample ( $\Delta V$ ) is the average of the volume of water flowing inside ( $\Delta V_{in}$ ) and outside ( $\Delta V_{out}$ ) of the sample for each interval of time (Equation 31). If the variation of water volume going in and out of the sample was constant, the considered time interval was the average of measured time to inflow and outflow that fixed volume of water.

$$\Delta V = \frac{\Delta V_{in} + \Delta V_{out}}{2} \quad 31$$

The hydraulic gradient  $i$  is given by Equation 32, where  $p_{in}$  and  $p_{out}$  are the water pressure flowing inward and outward of the soil sample, respectively,  $\gamma_w$  is the water density,  $h_{in}$  and  $h_{out}$  is the elevation of the bottom and top of the sample, respectively.

$$i = \frac{\left(\frac{p_{in}}{\gamma_w} + h_{in}\right) - \left(\frac{p_{out}}{\gamma_w} + h_{out}\right)}{h_{out} - h_{in}} \quad 32$$

The experimental results are plotted as shown in Figure 63, from which the saturated permeability is obtained. The saturated permeability is the slope of the linear regression presented in Figure 63. At least four tests were performed per sample. The saturated permeability adopted for each sample was the average of the determined values. The mean and standard deviation of the soil saturated permeability were calculated assuming a log-normal distribution per soil type.

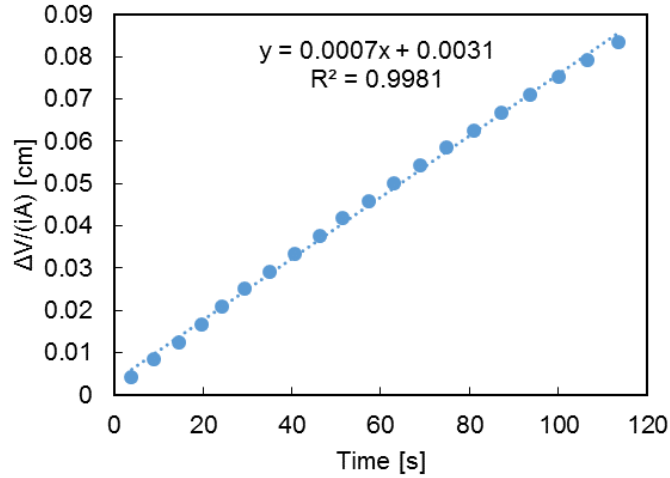


Figure 63 – Measurements of a single test presented as an example of the water flow through the sample with time, where the slope of the linear regression is equal to the saturated permeability of the soil.

### 3.2.4.2 Ku-pf apparatus data filter

The tests records are continuous over time but often contain measurements during the period of time that the tensiometers cavitated (invalid measurements), outliers in the sample weight records, and oscillations on the tensiometers measurements caused by non-dynamic equilibrium phenomena (Diamantopoulos and Durner, 2012), temperature oscillations in the laboratory, electric current oscillations, etc. These errors filtered for the interpretation of the results.

The first step was to identify manually each individual phase (drying or wetting), number the steps and identify the period during which there was a malfunction of the tensiometers. The suction measurements correspondent to the tensiometers cavitation was deleted and all the data organized using a method developed in VBA. Then, a filter developed to remove outliers in the weight measurements developed in MATLAB was used.



### 3.2.5 Inverse analysis

#### 3.2.5.1 Objective function

Inverse modelling was adopted in the present work to fit a hysteretic k-S-P model to experimental recordings. Numerical inversion is an optimization problem in which the deviations between the measured response of a real system and the numerical simulation is minimized, as defined in Nicotera *et al.* (2010).

An objective function measures the agreement between the measured data ( $q$ ) and the model estimations ( $\hat{q}$ ) associated to a fitting parameter vector  $\beta = (\beta_1, \beta_2, \dots, \beta_l, \dots)$ . Equation 33 represents the objective function ( $\Phi(\beta)$ ) used in HYDRUS-1D to estimate the parameter set  $\beta$  (Šimůnek *et al.*, 2013), where  $m$  is the number of measurement sets,  $n_j$  is the number of measurements of the set  $j$ ,  $q_{j,i}$  is a specific measurement of the set  $j$ ,  $\hat{q}_{j,i}(\beta)$  is the estimated value for  $q_{j,i}$  based on the parameter vector  $\beta$ ,  $v_j$  is the weighting coefficient for the squared residuals of the data set  $j$ , and  $w_{j,i}$  is the weighting factor of the experimental value  $q_{j,i}$ . The adopted objective function is minimized using the Levenberg-Marquardt nonlinear minimization method (Marquardt, 1963) in the implementation of HYDRUS-1D (Šimůnek *et al.*, 2013).

$$\Phi(\beta) = \sum_{j=1}^m v_j \left( \sum_{i=1}^{n_j} w_{j,i} [\hat{q}_{j,i}(\beta) - q_{j,i}]^2 \right) \quad 33$$

The goodness of the fit was obtained through Equation 34, where  $w_i$  is the weights associated to a given experimental measurement  $q_i$ , and  $\hat{q}_i$  is the estimated value of  $q_i$ . The best fitting is obtained when the value  $r^2$  is close to 1.

$$r^2 = \frac{\left( \sum w_i \hat{q}_i q_i - \frac{\sum \hat{q}_i \sum q_i}{\sum w_i} \right)^2}{\left( \sum w_i \hat{q}_i^2 - \frac{(\sum \hat{q}_i)^2}{\sum w_i} \right) \left( \sum q_i^2 - \frac{(\sum q_i)^2}{\sum w_i} \right)} \quad 34$$

This software provides a correlation matrix of the parameters  $\beta$  which helps assessing the fitting in the way that parameters that are strongly correlated should not be fitted together.

#### 3.2.5.2 Sensitivity analysis

The sensitivity analysis suggested in Nicotera *et al.* (2010) has the objective of verifying if variations in the model inputs lead to great differences in the estimations. An individual disturbance of each of the parameters of the fitted vector  $\beta$  was used to evaluate differences in the suction head predictions. This is a local sensitivity analysis to estimate model sensitivity close to optimal parameter values.

The quantification of the sensitivity is made by the parameter  $S_{h,\beta_l}(z, t)$ , which is the dimensionless scaled sensitivity of the matrix suction head to the generic parameter  $\beta_l$ , obtained from Equation 35, where  $CV_{\beta_l}$  is the coefficient of variation of the parameter  $\beta_l$ ,  $\sigma_{\varepsilon h}$  is the standard deviation of the suction measurement

error estimated from the tensiometers calibration,  $z$  is the position in the soil column where suction head was measured,  $t$  refers to time.

$$S_{h,\beta_l}(z, t) \cong 100 \cdot CV_{\beta_l} \cdot \left| \frac{\Delta h_m(z, t, \beta)}{\sigma_{\varepsilon h}} \right| \quad 35$$

The dimensionless scaled sensitivities can be used to compare the importance of different observations to the estimation of a single parameter  $\beta_l$ . Observations with large  $S_{h,\beta_l}$  are likely to provide more information about parameter  $\beta_l$  compared to observations associated with small  $S_{h,\beta_l}$ . Also, observations with large  $S_{h,\beta_l}$  can be considered more important for the estimation of parameter  $\beta_l$ .

### 3.2.5.3 Main drying curve fitting

The procedure adopted by Nicotera *et al.* (2010) consists of a sequence of three tests: (i) saturated permeability test at constant head, (ii) evaporation test monitored in the ku-pf apparatus, and continued in the (iii) pressure plate for higher suctions. The monitoring of the evaporation test in the ku-pf apparatus provides the measurement of a soil sample mean water content and the suction head measurements at two different elevations within the soil. The samples continue the evaporation test on the pressure plate in order to be able to obtain values of water content correspondent to imposed suction values higher than the ones allowed in the ku-pf apparatus. Note that the monitored data from ku-pf is in dynamic conditions because water is continuously evaporating from the soil sample, and the data obtained from the pressure plate is static because the water content in the soil is required to stabilize.

In the case of Nicotera *et al.* (2010), Equation 33 was used to estimate the parameter vector  $(\theta_s, \theta_r, \alpha, n, l)$  used for the definition of the WRC and HPF of the van Genuchten-Mualem model (van Genuchten, 1980; Mualem, 1976). The parameter  $K_0$ , saturated permeability, was not fitted because it was detected that it presents low sensitivity to the fitting, requiring it to be experimentally measured.

Several sets of experimental data  $(q_{j,i})$  were tested in order to verify which lead to a better agreement between model and experimental observations optimizing the number of data sets and its size. Nicotera *et al.* (2010) concluded that the most efficient combination was the measurements of suction head at two different positions within the soil sample along time ( $w_i = 1$ ), the water content at the start of the evaporation test and respective suction corresponding to the soil saturation ( $w_i = 5$ ), and the suction of 1 MPa and respective volumetric water content measured in the pressure plate ( $w_i = 5$ ).

In the present work, the calibration of the hysteresis model was divided into two phases because the main drying and wetting curves were calibrated individually. The calibration of the main drying curve was performed as suggested in Nicotera *et al.* (2010), described above, apart some modifications. The differences were in the objective function that contains the following data sets:

- Suction head measurements along time for each tensiometer. This data set was sampled from the original experimental measurements. The sample of points was optimized in order to collect between 300 and 600 pairs of measurements;
- Suction and water content correspondent to the air-entry value identified on the experimental data. The suction was adopted to be the average of the measured value in both tensiometers;
- Suction and water content measured in the pressure plate. The suction applied in the pressure plate varied between 600 and 900 kPa.

The last two data sets were given a weight ( $w_i$ ) equal to 5 in the objective function, and the suction measurements with time had a weight equal to 1 as found in Nicotera *et al.* (2010) to provide good fittings. The units selected for length was centimetres and time was hours.

The fitting was performed using HYDRUS-1D with the following input parameters:

1. Main processes
  - a. Simulate: water flow
  - b. Inverse solution
2. Inverse solution
  - a. Estimate: soil hydraulic parameters
  - b. Weighting of inversion data: weighting by standard deviation
  - c. Max number of iterations: 500
  - d. Number of data points in objective function: (depends on the test)
3. Geometry information
  - a. Number of soil layers: 1
  - b. Number of layers for mass balances: 1
  - c. Decline from vertical axes: vertical
  - d. Depth of the soil profile: 6cm
4. Time information
  - a. Time discretization
    - i. Initial time: 0 h
    - ii. Final time: (depends on the test)
    - iii. Initial time step: 0.01 h
    - iv. Minimum time step: 0.001 h
    - v. Maximum time step: 0.1 h
  - b. Time-variable boundary conditions
    - i. Number of time-variable boundary records: (depends on the test)
5. Iteration criteria
  - a. Iteration criteria
    - i. Maximum number of iterations: 20

- ii. Water content tolerance: 0.0001
    - iii. Pressure head tolerance: 0.1 cm
  - b. Time step control
    - i. Lower optimal iteration range: 3
    - ii. Upper optimal iteration range: 7
    - iii. Lower time step multiplication factor: 1.3
    - iv. Upper time step multiplication factor: 0.7
  - c. Internal interpolation tables
    - i. Lower limit of the tension interval: 1e-6 cm
    - ii. Upper limit of the tension interval: 10000
- 6. Hydraulic model
  - a. Single porosity models: van Genuchten – Mualem
  - b. Hysteresis: no hysteresis
- 7. Constraints on hysteresis model
  - a. Saturated water content:  $\Theta_{SW} = \Theta_{MW}$ ,  $\Theta_{SD} = \Theta_{MD}$
- 8. Water flow parameters – inverse solution – material 1

*Table 11 – Scheme of the input table of the initial estimation of the fitting parameters of the main drying curve in HYDRUS-1D (an example).*

	Qr	Qs	Alpha	n	Ks	I
Initial estimate	0.1644	0.5141	0.007933	1.6935	0.15652	0.5
Min. Value	0	0	0	0		-10
Max. Value	1	1	10	10		10
Fitted?	✓	✓	✓	✓		✓

- 9. Water flow boundary conditions
  - a. Upper boundary condition: atmospheric BC with Surface layer
  - b. Lower boundary condition: constant flux
  - c. Initial condition: in pressure heads
  - d. Max h at soil surface: 0
- 10. Constant boundary fluxes
  - a. Lower boundary flux: 0
- 11. Time variable boundary conditions

*Table 12 – Scheme of the input table of the boundary conditions for the main drying curve fitting in HYDRUS-1D.*

Time (hour)	Precip. (cm/hour)	Evap. (cm/hour)	hCritA (cm)
0.01	0	0	100000
...	...	...	...

## 12. Data for inverse solution

Table 13 – Scheme of the input table of the data sets for the main drying curve fitting in HYDRUS-1D.

x	y	type	position	weight
0.01	(suction head)	1	1	1
...	...	...	...	...
0.01	(suction head)	1	2	1
...	...	...	...	...
(suction head)	(Theta_s)	5	1	5
(-6000 to -9000)	(Theta)	5	1	5

## 13. Soil profile – graphical editor

- Observation points (Figure 64)
- Initial conditions (Figure 65)

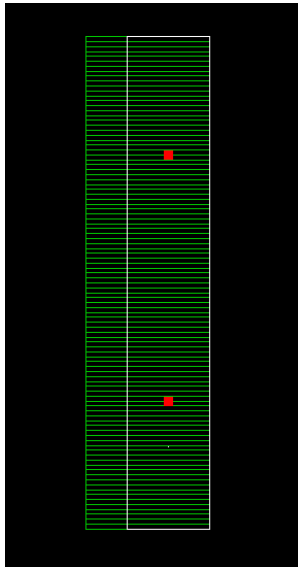


Figure 64 – Soil profile and identified observation points.

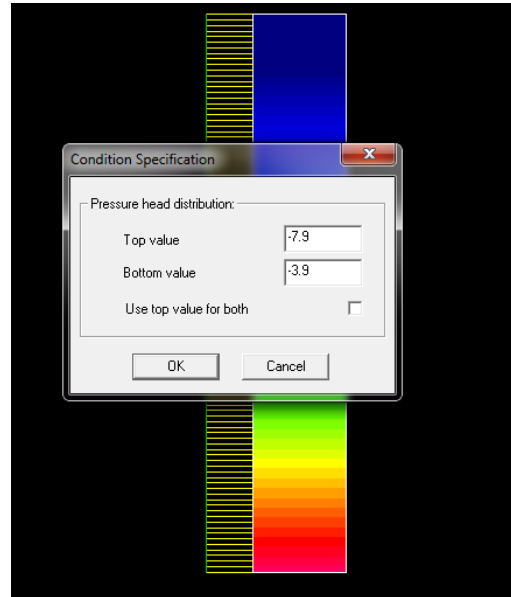


Figure 65 – Interface for the definition of the initial conditions in terms of suction head of HYDRUS-1D.

The parameters to input in point 8 of the previous list were estimated by fitting the van Genuchten equation using a routine implemented in Excel to minimize the difference between the estimated suction and the mean measured suction at each instant. The value of saturated permeability that was measured is used here. The maximum and minimum values allowed to each parameter are allowed to vary in the range of possible values. The parameters to input in point 11 were estimated from the ku-pf apparatus records of the sample weight. During the drying phase, evaporation flow was calculated from the sample weight variation divided by the time interval between records and by the surface area of the sample. The parameters to input in point 12 were the data sets of the objective function already described before.

The location of both tensiometers was identified in the soil profile graphic editor in the grid as shown in Figure 64. The “top value” and “bottom value” referred in Figure 65 were estimated based on the initial value of suction head measured in the tensiometers through a linear interpolation because the initial distribution of suction in the sample was assumed to be hydrostatic.

A sensitivity analysis was performed adopting the method presented in Nicotera *et al.* (2010) by varying each of the parameters of a standard deviation up and down of the fitted parameter. The standard deviation was calculated from the fitted parameters of all the samples of the same soil type. One sample was tested per soil type.

#### **3.2.5.4 Hysteretic model calibration**

The used hysteresis model is described in Lenhard and Parker (1987), Parker and Lenhard (1987) and Lenhard *et al.* (1991). The model has already been implemented in the software HYDRUS-1D that was used for the calibration of the parameters using inverse analysis. Several trials were necessary to identify an efficient way of calibrating the model. This study required the following sequence of steps:

1. Use one hysteretic loop (main drying and scanning wetting) to fit the parameter vector  $(\theta_s^w, \alpha^w, K_{sat}^w)$ ;
2. Sensitivity analysis of each parameter;
3. Use one hysteretic loop (main drying and scanning wetting) to fit the parameter vector  $(\theta_s^w, \alpha^w)$  setting  $K_{sat}^w = K(\theta_s^w)$ ;
4. Use two hysteretic loops (main drying, 2 scanning wettings and 1 scanning drying) to fit the parameter vector  $(\theta_s^w, \alpha^w)$  setting  $K_{sat}^w = K(\theta_s^w)$ ;
5. Simulation of the whole test (main drying and several scanning loops) using the parameter vector  $(\theta_s^w, \alpha^w)$  fitted with 1 and 2 cycles;
6. Simulation of the whole test (main drying and several scanning loops) using the parameters fitted for another sample. The simulations were repeated 4 times by adopting an increasing number of parameters from the original samples.

The model inputs used in HYDRUS-1D were very similar to the required for the fitting of the main drying curve. Nonetheless, the parameters are discriminated in the following points:

1. Main processes
  - a. Simulate: water flow
  - b. Inverse solution
2. Inverse solution
  - a. Estimate: soil hydraulic parameters
  - b. Weighting of inversion data: weighting by standard deviation
  - c. Max number of iterations: 500

- d. Number of data points in objective function: (depends on the test)
- 3. Geometry information
  - a. Number of soil layers: 1
  - b. Number of layers for mass balances: 1
  - c. Decline from vertical axes: vertical
  - d. Depth of the soil profile: 6cm
- 4. Time information
  - a. Time discretization
    - i. Initial time: 0 h
    - ii. Final time: (depends on the test)
    - iii. Initial time step: 0.01 h
    - iv. Minimum time step: 0.001 h
    - v. Maximum time step: 0.1 h
  - b. Time-variable boundary conditions
    - i. Number of time-variable boundary records: (depends on the test)
- 5. Iteration criteria
  - a. Iteration criteria
    - i. Maximum number of iterations: 20
    - ii. Water content tolerance: 0.0001
    - iii. Pressure head tolerance: 0.1 cm
  - b. Time step control
    - i. Lower optimal iteration range: 3
    - ii. Upper optimal iteration range: 7
    - iii. Lower time step multiplication factor: 1.3
    - iv. Upper time step multiplication factor: 0.7
  - c. Internal interpolation tables
    - i. Lower limit of the tension interval: 1e-6 cm
    - ii. Upper limit of the tension interval: 10000
- 6. Hydraulic model
  - a. Single porosity models: van Genuchten – Mualem
  - b. Hysteresis: hysteresis in retention curve (no pumping, Bob Lenhard), initially drying curve
- 7. Constraints on hysteresis model
  - a. Saturated water content:  $\Theta_{SW} = \Theta_{MW}$ ,  $\Theta_{SD} = \Theta_{MD}$
- 8. Water flow parameters – invers solution – material 1

Table 14 – Scheme of the input table of the initial estimation of the fitting parameters of the main wetting curve in HYDRUS-1D (an example).

	Qr	Qs	Alpha	n	Ks	l	Qm	QsW	AlphaW	KsW
Initial estimate	0.088	0.605	0.008	1.424	0.216	1.451	0.605	0.5	0.0174	0.004
Min. Value								0	0	0.001
Max. Value								0.605	10	0.216
Fitted?								✓	✓	

9. Water flow boundary conditions

- Upper boundary condition: atmospheric BC with Surface layer
- Lower boundary condition: constant flux
- Initial condition: in pressure heads
- Max h at soil surface: 0

10. Constant boundary fluxes

- Lower boundary flux: 0

11. Time variable boundary conditions

Table 15 – Scheme of the input table of the boundary conditions for the main wetting curve fitting in HYDRUS-1D.

Time (hour)	Precip. (cm/hour)	Evap. (cm/hour)	hCritA (cm)
0.01	0	0	100000
...	...	...	...

12. Data for inverse solution

Table 16 – Scheme of the input table of the data sets for the main drying curve fitting in HYDRUS-1D.

x	y	type	position	weight
0.01	(suction head)	1	1	1
...	...	...	...	...
0.01	(suction head)	1	2	1
...	...	...	...	...

13. Soil profile – graphical editor

- Observation points
- Initial conditions

The initial estimation and ranges of the parameters of the hysteretic model are in Table 14. The parameter “QsW” was defined as the final measured water content of the scanning wetting curve and allowed to vary between 0 and  $\theta_s$  or up to the maximum measured water content of the scanning wetting curve after visual inspection of the fitting. The parameter “AlphaW” was defined as  $\alpha^w = 2 \cdot \alpha$ , which is suggested by Lenhard *et al.* (1991) to be adopted in absence of data. The “KsW” was set as  $K_{sat}^w = K(\theta_s^w)$  assuming that the



hysteresis of the hydraulic conductivity, relatively to water content, is despicable, as it has been assumed observed (Lenhard and Parker, 1987).

The values of the Table 15 and Table 16 were sampled from the measured data using a code implemented in VBA (Annex C). The drying phase of the test is composed by a continuous evaporation, so the boundary conditions are calculated just like for the fitting of the main drying curve. On the other hand, the wetting phase is composed of a sequence of wetting steps that start with adding of water and end when the suction head measured in both tensiometers stabilize. In order to reproduce this boundary condition, the added water was inserted in the column "Precip. (cm/hour)" by calculating the variation of sample weight between the measurement right before and right after the water was added assuming that the imbibition was made at continuous rate during that time interval. A small decrease in the sample weight was detected while suction heads were allowed to stabilize. This process was defined as a continuous evaporation of very low intensity.

The data for the boundary conditions and objective function are sampled every time there is a weight variation greater than 0.5 g, or every four measurements (approximately every 40 minutes) if suction is not known, during the drying phase. The data sampling during the wetting phase is made right before and after the imbibition for the objective function and for the boundary conditions. The boundary conditions data is collected every four measurements (approximately every 40 minutes) and the objective function data set points are collected every six measurements (approximately every hour) during the equalization period.

### 3.2.6 Water capacity

Fredlund and Rahardjo (2012) suggested that the HPF and the water storage function, also referred as water capacity function (WCF), should be taken into consideration in the analysis of water infiltration into an unsaturated soil. Differences in the WCFs explain the different rates of the wetting front movement. The soils with lower AEV present higher values of water capacity than a soil with higher AEV (Figure 66), which is associated to a slower movement of the wetting front. A variation of suction in a soil with low AEV is smaller in the desaturation part of the WRC, which corresponds to a portion of the wetting curve in which there is a quick variation of suction for a small variation of water content close to the saturation.

The water capacity is given by the derivative of the water content  $\theta$  in relation to suction  $s$  as in Equation 36.

$$C = \frac{d\theta}{ds} \quad 36$$

Nonetheless, the soil suction is maintained unless the water flux is close to the saturated permeability of that soil. When the water capacity of two soils is equal, the infiltration rate is much higher in the soil with higher hydraulic permeability.

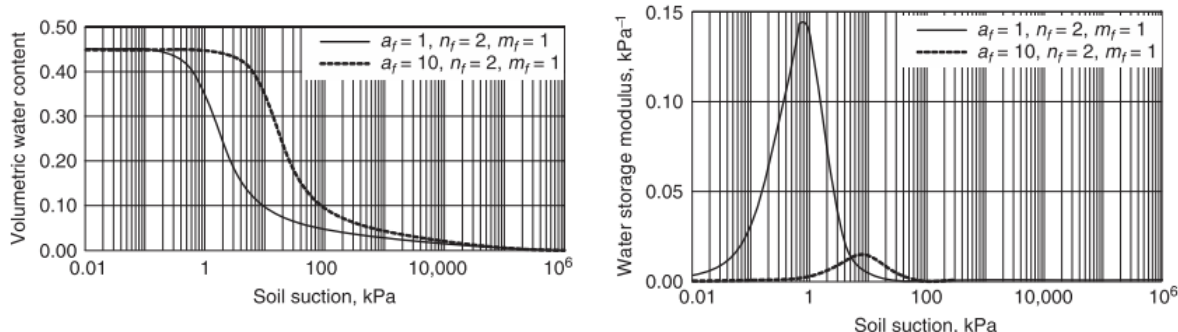


Figure 66 – Comparison of the water capacity resultant from two different water retention curves with different AEV (Fredlund & Rahardjo, 2012).

### 3.3 Results and discussion

#### 3.3.1 Saturated permeability

The results of all the performed tests are reported in Annex D, from which the average value was estimated per sample. In order to increase the number of replicates and to be able to do a statistical analysis with significance, 13 tests were added (from Mastantuono, personal communication), also reported in Annex D. The mean and standard deviation were calculated for each soil type, as reported in Table 17, knowing that the saturated permeability follows a log-normal distribution. The density function of the saturated permeability of each soil type is presented in Annex D, except for soil C2 because only 2 samples were tested.

Table 17 – Mean and standard deviation of  $\log(K_{sat})$  of each soil type.

Soil	Mean depth [m]	$K_{sat}$ [ $m\ s^{-1}$ ]	$\log(K_{sat}\ [m\ s^{-1}])$	
			Mean	Standard deviation
A1sup	0.06	2.82E-06	-5.550	0.508
A1	0.35	4.35E-07	-6.362	0.242
A2	0.75	1.43E-06	-5.844	0.573
C1	0.96	8.66E-07	-6.063	0.737
C2	1.96	7.10E-08	-7.149	0.983

The changes of porosity and saturated permeability are presented in Figure 67 with respective mean depth, where the soil layer B is missing because the soil samples were collected in the road cut without that layer. The difference in permeability between A1 and A1sup was attributed to different porosities. The saturated permeability of soil A2 appeared higher than A1 because of the greater quantity of pumices, as observed in the grain size distribution (Figure 67) even if the porosity was similar. Soils C presented lower permeability

compared to the soils A even if the first presented higher porosity because of the greater fraction of silt. Soil C2 presented the lowest permeability among all being also the one presenting the finest texture and lowest porosity, decreasing its permeability by 1 order of magnitude in comparison with soil C1.

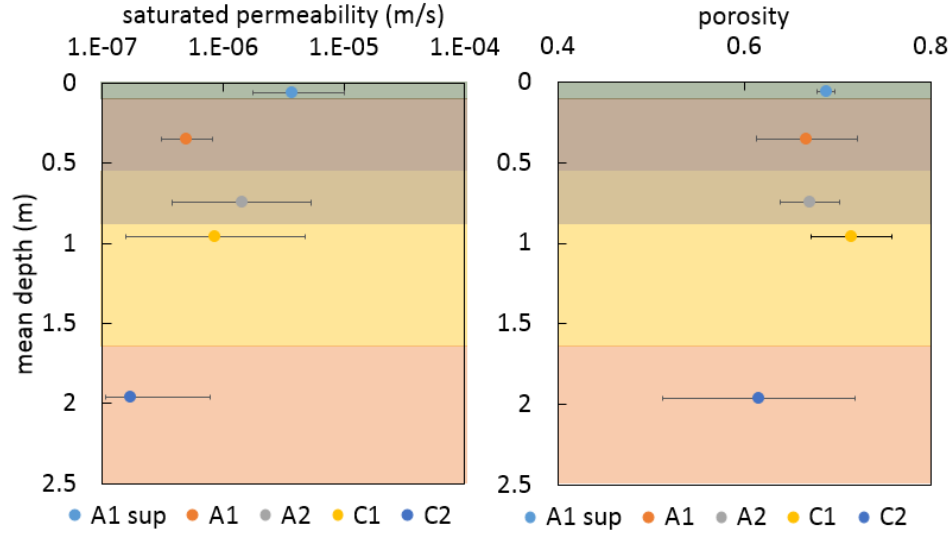


Figure 67 – Comparison of mean saturated permeability and mean porosity of different soil layers with depth.

The obtained values of saturated permeability are comparable to the reported values in Nicotera *et al.* (2010) for pyroclastic soils with high porosity present in Monteforte Irpino (Campania, Italy). The volcanic eruptions that originated the soils in Monteforte and in Mount Faito are different but the soils present in both sites are similar in terms of porosity and grain size distribution (Calcaterra and Santo, 2004; Dias *et al.*, 2018). A correspondence can be found between the soil of both sites Mount Faito – Monteforte Irpino: soil A1 – soil 1, soil A2 – soil 2, soil C1 – soil 6, and soil C2 – soil 8.

Pyroclastic soil with the same grain size distribution and porosity presented the same saturated permeability even if originated from different volcanic eruptions. This hydraulic characterization can be adopted in future studies in which the saturated hydraulic conductivity of pyroclastic soils in Campania (Italy) is required.

### 3.3.2 Drying and wetting cycles

The data monitored by the ku-pf apparatus along time is reported as in Figure 68. Suction is seen to increase in both tensiometer accompanied by a decrease in the wet soil weight during the wetting phase. On the other hand, the wetting phase, that is divided in wetting steps, corresponds to an overall decrease of suction and an increase of the wet soil weight. Nonetheless, the data reported in Figure 68 excludes already the outliers in the weight measurements and the tensiometer cavitation (discontinuities in the suction measurement).

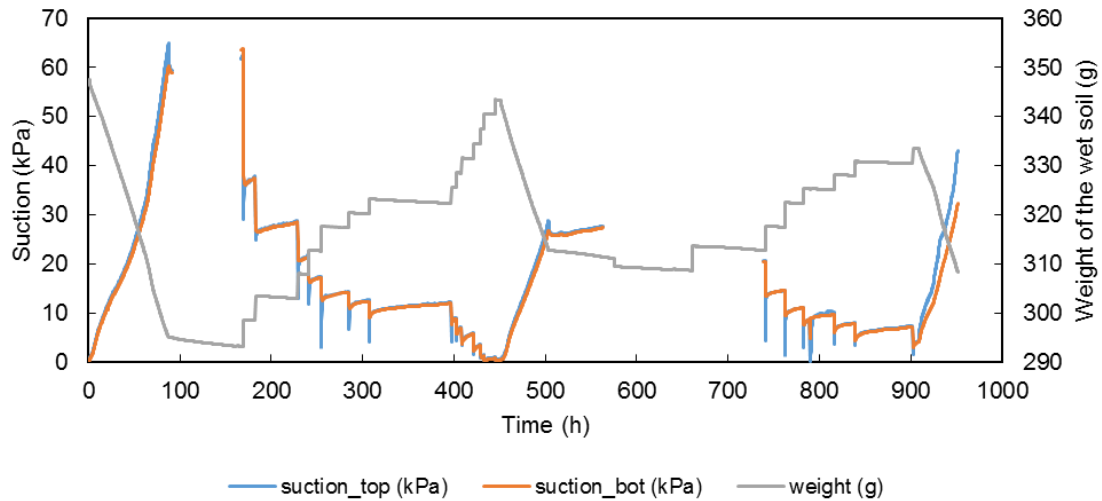


Figure 68 – Monitored suction at bottom and top tensiometers and wet soil weight of the sample 1.4.1 (soil A2) by the ku-pf apparatus.

The experimental WRC was built by considering the weight of the sample to calculate the water content of the sample and the suction is assumed to be the average of the measured value of both tensiometers. These measurements correspond to a WRC obtained in a transient state.

Due to the discontinuous nature of the wetting phase, the identification of the mean values of suction between the two tensiometers that corresponded to the measured water content required the identification of a steady condition. The vertical hydraulic gradient was calculated for each wetting step as presented in Figure 69. The gradient takes negative values at the beginning which indicate that the water flow is downward. The value then starts to increase gradually and it stabilizes at a low positive gradient value showing that the system is not actually completely sealed but there is a low rate continuous evaporation from the top of the sample. The mean suction and water content are collected at the instant at which the gradient becomes null because that is the moment at which there is a steady condition and hydrostatic distribution of pressures, as indicated in Figure 69. One point is collected per wetting step.

The water retention loops of samples 1.7.2 (soil A1) are represented in Figure 70, as an example. The drying phase is a continuous measurement and the wetting phase a sequence of spaced points. These curves are then compared with the simulations after the model calibration to validate its adequacy.

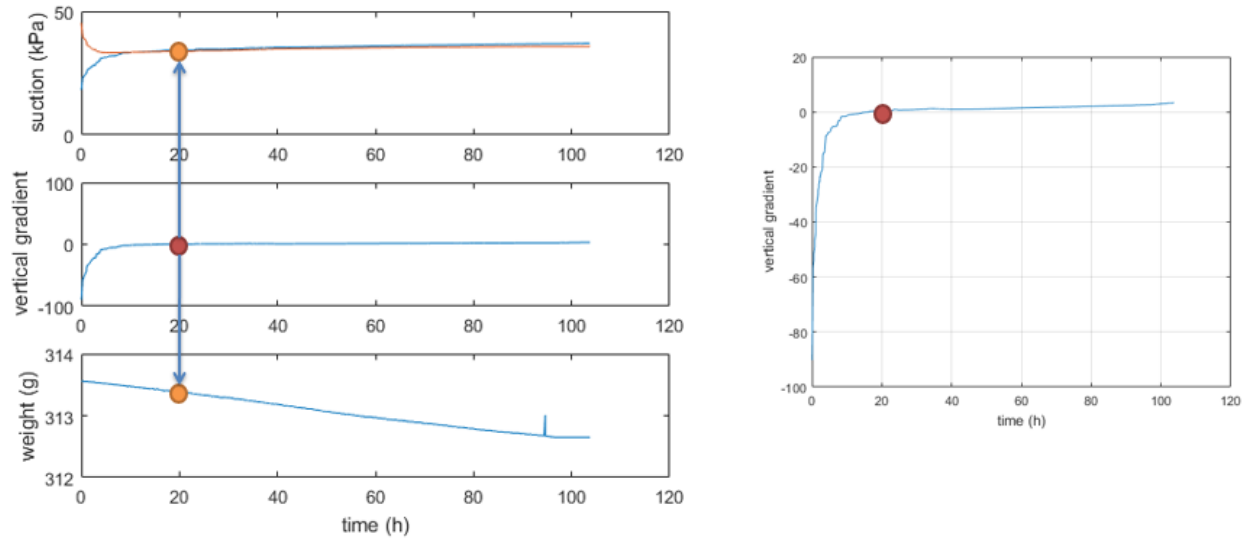


Figure 69 – Suction at the bottom and top tensiometer, vertical gradient and wet soil weight of a single wetting step monitored at the ku-pf apparatus of sample 1.7.2 (soil A1).

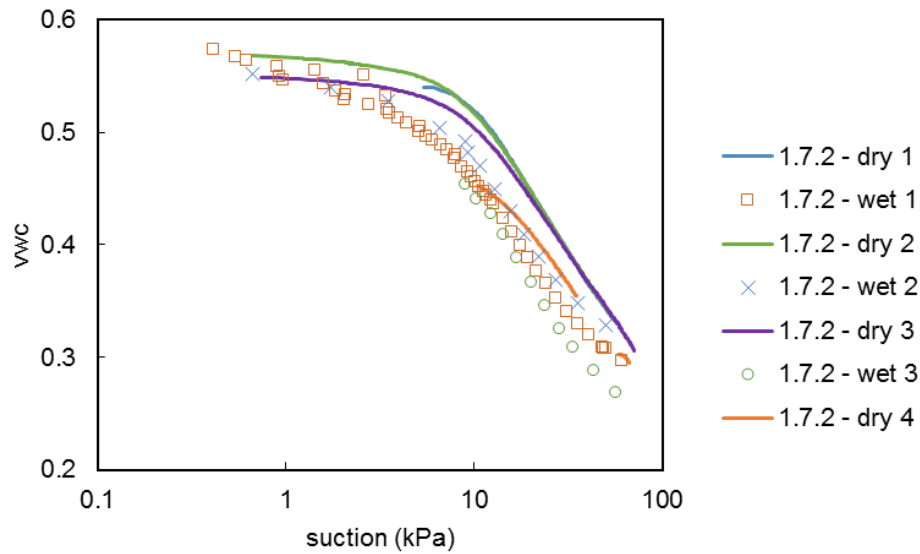


Figure 70 – Experimental drying-wetting loops obtained for sample 1.7.2 (soil A1), in terms of volumetric water content (vwc).

### 3.3.3 High suction range

In Annex E, the values of adopted and measured water content for suctions of 650 or 800 kPa are reported. Note that not all the tested samples were used to determine water content in the high suction range but this information is necessary for a good estimation of the fitting parameters obtained using inverse analysis as (Nicotera *et al.*, 2010).

### 3.3.4 Inverse analysis

#### 3.3.4.1 Main drying curve fitting

A good fitting between the mean suction measured in ku-pf apparatus and the main drying branch fitted with HYDRUS-1D was obtained as observed in the example of Figure 71 and Figure 71. The values of water content and suction correspondent to the AEV and the values measured in the pressure plate (PP) in the high suction range helped fitting the curve in critical parts.

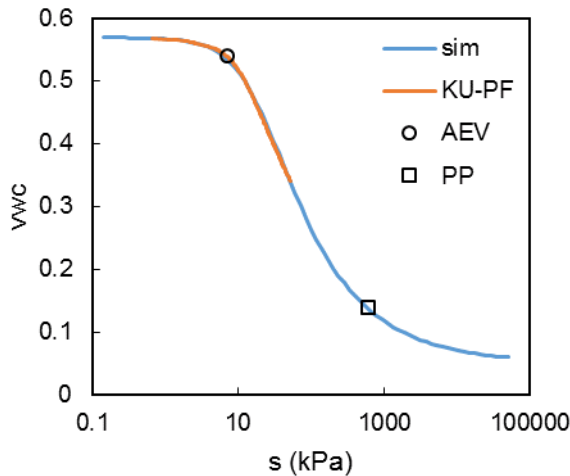


Figure 71 – Main drying WRC of sample 1.7.2 (soil A1) with the objective function data sets.

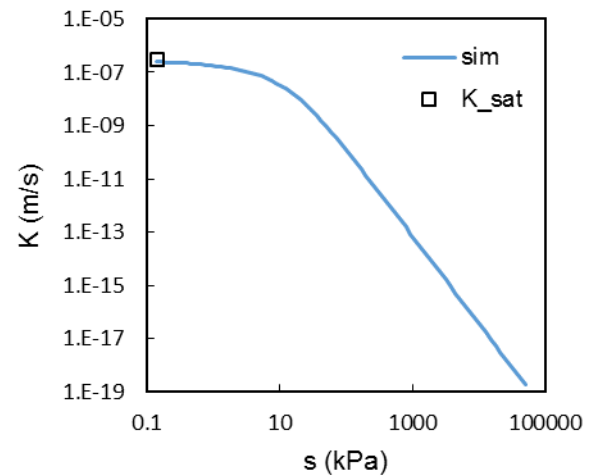


Figure 72 – HPF of the main drying of sample 1.7.2 (soil A1) with the measured saturated permeability.

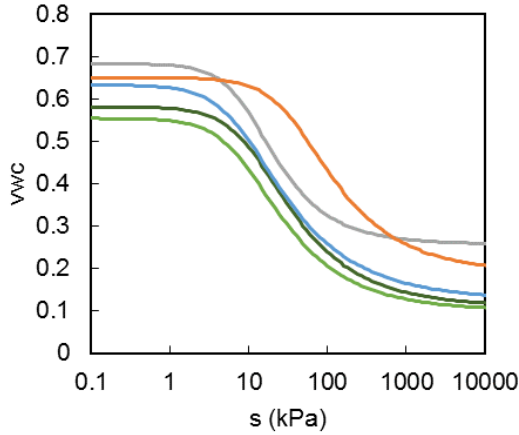
Note that the values obtained in the ku-pf apparatus were measured during a transient state, i.e. there was a continuous evaporation. On the other hand, the value measured in the pressure plate corresponds to a steady state. The values of suction given by the ku-pf apparatus might underestimate the real suction. However, a model calibrated with data obtained during transient conditions might lead to better results in the agreement between laboratory and field models because the values obtained in situ were also measured during transient conditions. Tough, this does not mean that the model represents better the field reality.

Figure 72 is an example of a fitted HPF. The saturated permeability obtained from the permeability test at constant head was assumed to be equal to the hydraulic conductivity at null suction. The only fitted parameter of the HPF is  $l$ . However, Nicotera *et al.* (2010) showed that suction presents low sensitivity to this parameter. This observation was also made in the present work as reported in the next section.

The mean main drying branches of each soil type are reported in Figure 73. The greatest differences among soil type affect  $\theta$  at saturation are caused by the variability of porosity. The tested samples of soils A1sup, A2 and C1 have the same residual water content because all the curves tend to the same value as suction increases. Soil C2 presents the highest AEV, which is consequence of the finer texture of this soil in

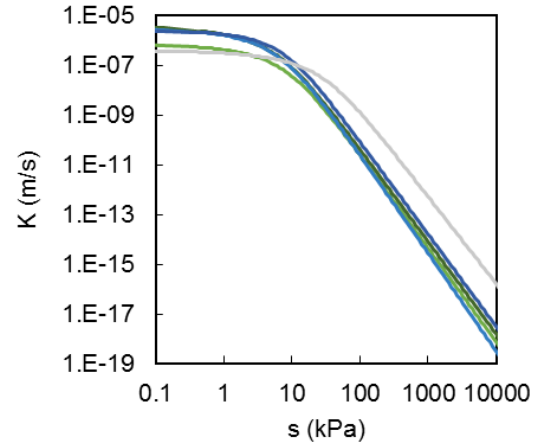
comparison with the remaining. The slope of the curve after the AEV as suction increases is lower than in the remaining soils, which is a consequence of the finer texture of this soil.

The mean main drying branches of the HPF are more homogeneous among soil type (Figure 74). Soil A1 presents lower values of hydraulic conductivity for suctions lower than its AEV, as a consequence of its lower saturated permeability. Soil C2 presents an HPF translated towards the higher values of suction, which is a consequence of the finer texture of this soil in comparison with the remaining.



— A1 dry mean      — A1 sup dry mean  
— A2 dry mean      — C1 dry mean  
— C2 dry mean

Figure 73 – Mean main drying WRC obtained from inverse analysis.



— A1 dry mean      — A1 sup dry mean  
— A2 dry mean      — C1 dry mean  
— C2 dry mean

Figure 74 – Mean main drying HPF obtained from inverse analysis.

The fitting parameters of each tested sample are reported in Annex F. The  $R^2$ -index obtained in this fitting was always greater than 0.99, which shows a good agreement between the model and the experimental data. The mean fitting parameters of the main drying curve (WRC and HPF) are represented accompanied by the standard deviation per soil type in Figure 75, whose values are reported in Annex F. The parameter  $\theta_s^d$  varies between 0.55 and 0.70 depending on the soil porosity. The parameter  $\theta_r$  is approximately 0.1 in the groups of soil A and in the soils C is twice as higher. The parameter  $\alpha^d$  presents a great variability. However, soil C2, which is finer, presented the lowest value of  $\alpha^d$  as a consequence of its high AEV. The parameter  $n$  varied between 1.5 and 1.6 except for soil C1. The curves of soil C1 have a much less inclined slope which might be a consequence of having a smaller gradient between  $\theta_s^d$  and  $\theta_r$ . The parameter that presents the greatest variability is  $l$  which refers to the HPF.

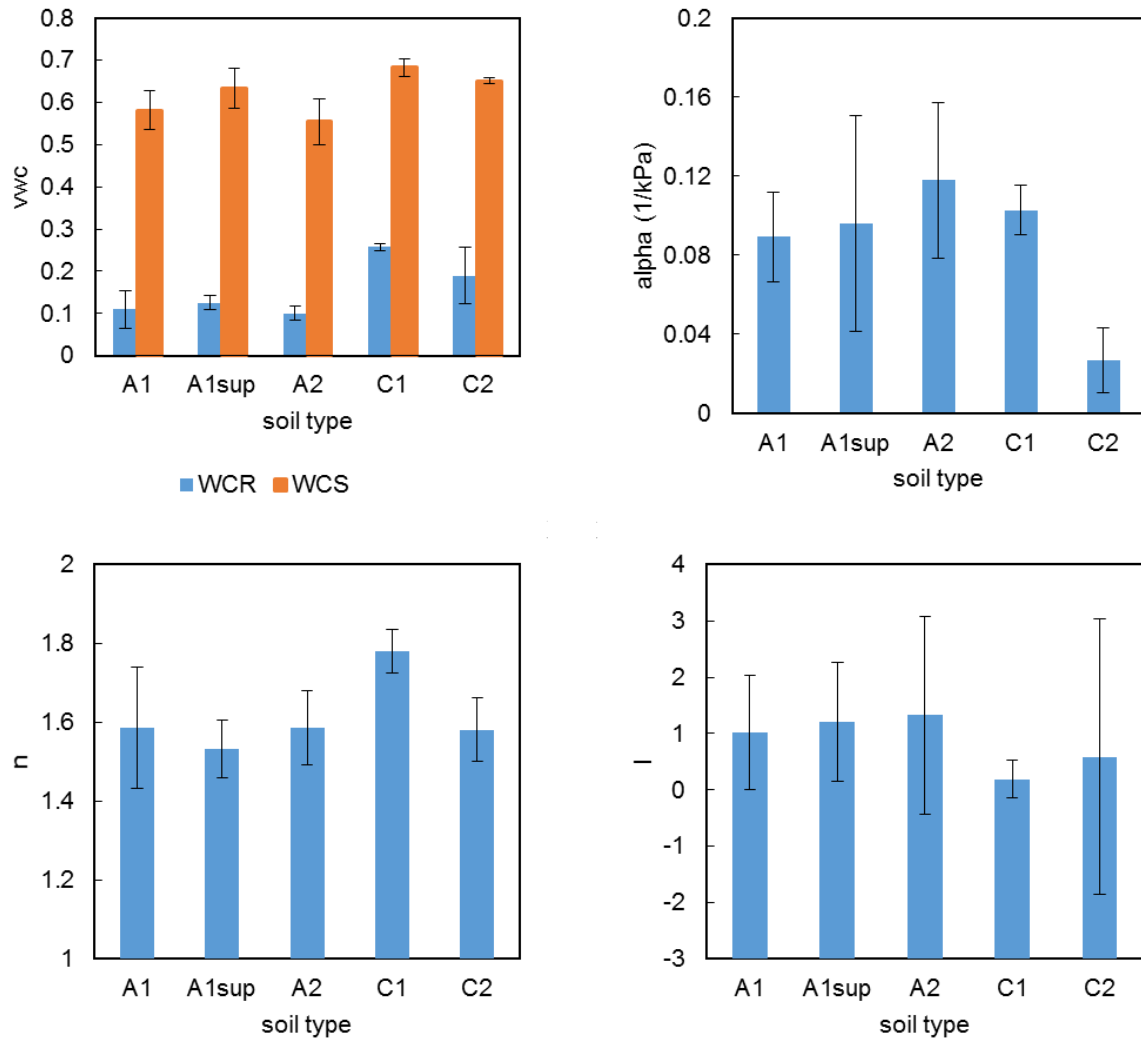


Figure 75 – Representation of the mean and standard deviation of the fitting parameters of the main drying curve for each soil type.

In Figure 76 the sensitivity analysis performed on sample 1.7.2 of soil A1 is shown as an example to verify the validity of the model calibration showing absolute values similar to those reported by Nicotera *et al.* (2010) and similar trends as well. This way, the suction values are proven to be sensitive to all the fitted parameters.



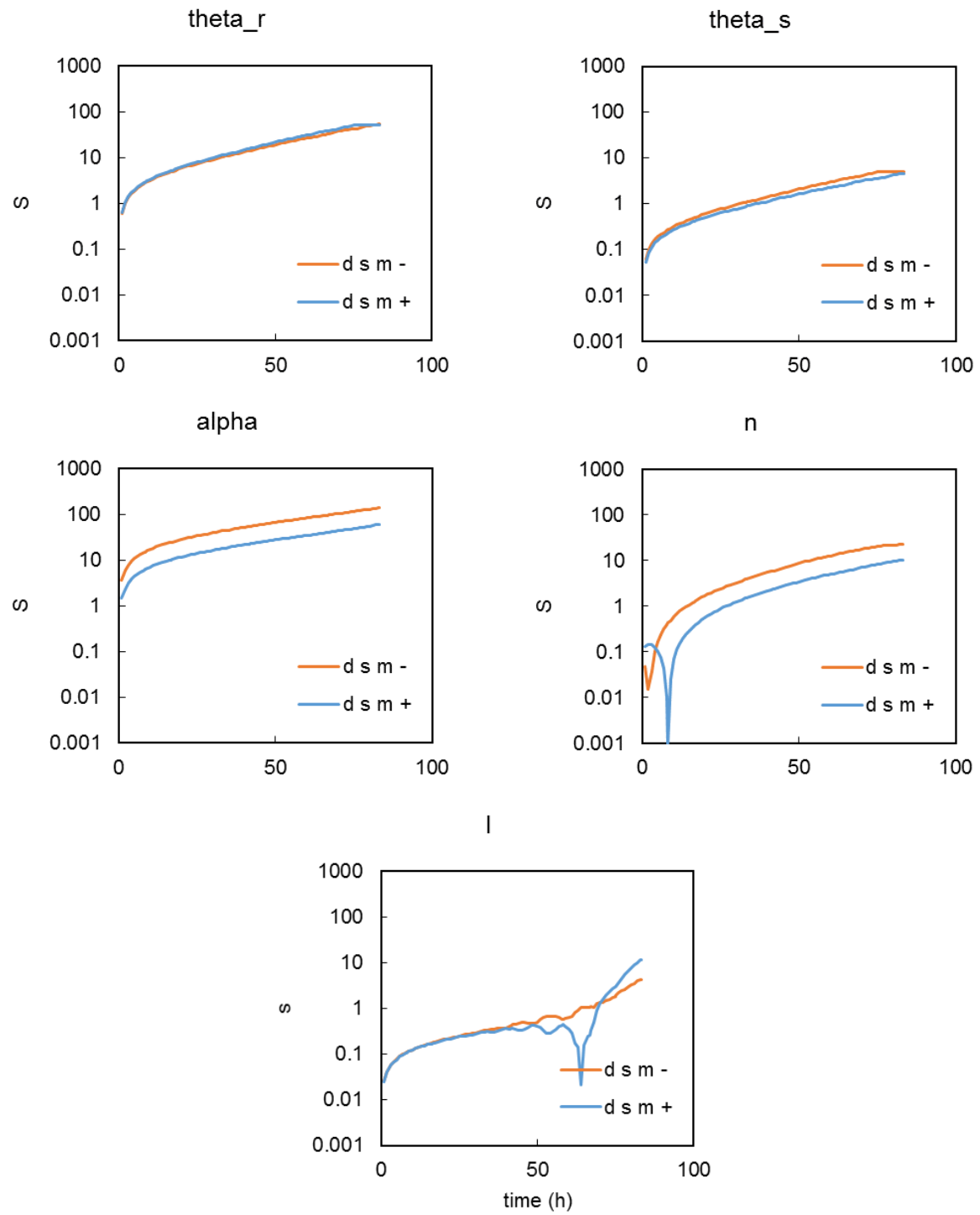


Figure 76 – Sensitivity analysis of the fitting parameters of the main drying performed on sample 1.7.2 (soil A1).

### 3.3.4.2 Main wetting curve fitting

The main drying curve of the model is in agreement with the experimental drying curves as observed in the example of Figure 77. The main drying branch of the WRC model and experimental data overlap. The wetting branch experimental values are above the fitted main wetting curve. Both curves appear to be parallel as well as the respective scanning curves. The scanning wetting experimental data which inversion point occurs at increasing suction values tend to be closer to the fitted main wetting curve.

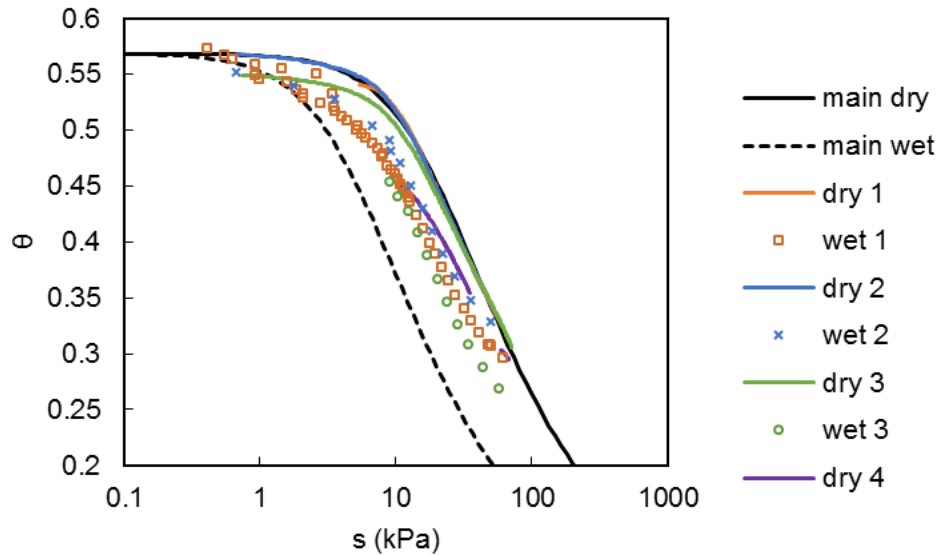


Figure 77 – Main loop of the WRC with the experimental measurements of sample 1.7.2 (soil A1).

The fitting parameters of the main wetting curve are reported in Annex G for each sample grouped by soil type. Not all the samples that were used in the fitting of the main drying curve allowed the fitting of the main wetting curve because at least a scanning wetting curve is necessary after the main drying curve. The  $R^2$ -index obtained in the fitting of the main wetting was lower than the value in the main drying, however values varied between 0.85 and 0.99, which still represents a good agreement between the model and experimental data.

The initial estimation of  $K_s^i$  was not altered after the inverse analysis was performed which shows that suction is not sensitive to variations of this parameter, fact that was confirmed in the sensitivity analysis presented in the next section. The values of  $K_s^i$  were recalculated after the fitting of  $\theta_s^i$  and  $\alpha^i$  as  $K_s^i = K^d(\theta_s^i)$ , i.e. the parameter  $K_s^i$  was not fitted but updated, which updated values are presented in Annex G.

### 3.3.4.3 Sensitivity analysis of the hysteretic model

A sensitivity analysis of suction to the fitting parameters of the main wetting curve was performed using the simulation of a full loop, i.e. the main drying and a scanning wetting branch. The mean and standard deviations of the fitting parameters are reported in Annex H. The sensitivity values are presented in Figure

78 and are used here as an example of the obtained results. Other sensitivity analysis examples for other soil types are shown in Annex H.

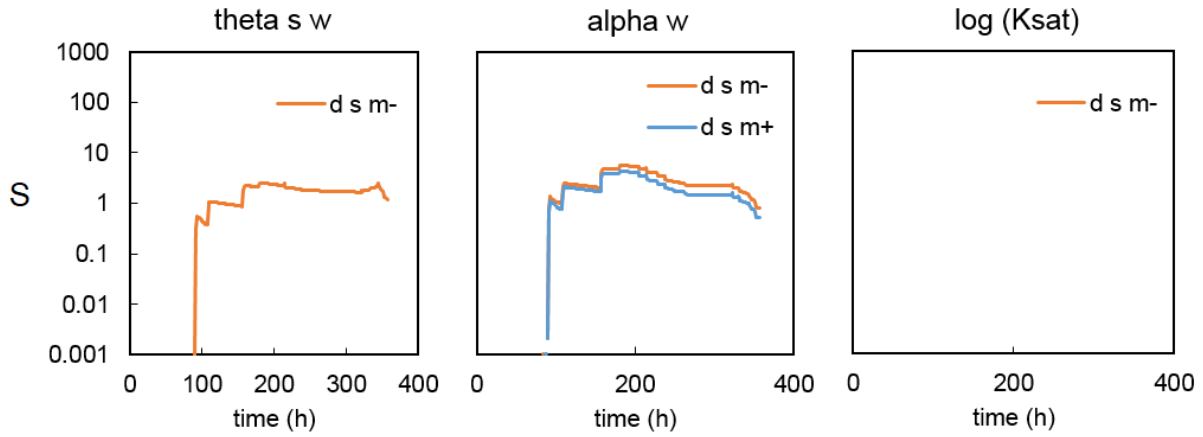


Figure 78 – Sensitivity analysis of the fitting parameters of the main wetting performed on sample 1.7.2 (soil A1).

In the first portion of plots, i.e. before approximately 100 hours have passed, the sensitivity of suction to the wetting parameters is null, as expected. The sensitivity of suction to parameter  $\theta_s^i$  and  $\alpha^i$  is lower in absolute values comparing to the same parameters of the drying curve. Suction is sensitive to  $\theta_s^i$  and to  $\alpha^i$  having both these parameters similar importance.

In some cases, suction was completely insensitive to the variation of  $K_s^i$  even if this variation was as high as one order of magnitude. Consequently, the parameter  $K_s^i$  should not be fitted using inverse analysis in this model as the results were independent of its value. In order to overcome this limitation, no hysteresis of the hydraulic conductivity as function of water content was adopted then on. The hysteresis was ignored by considering  $K_s^i = K^d(\theta_s^i)$ . The value  $\theta_s^i$  was fitted in the model but  $K_s^i$  was calculated with the initial estimation of  $\theta_s^i$ . Then,  $K_s^i$  was simply updated after the fitting of  $\theta_s^i$  and  $\alpha^i$  because the model results and fittings were insensitive to variations of  $K_s^i$ .

#### 3.3.4.4 Assessment of the data sets size

The necessary data sets size to be used in the objective function in order to obtain a good model fitting was investigated by considering different number of drying-wetting cycles. One soil sample of each soil type was tested, except for soil A1sup because no more than one cycle long test was available.

One and two cycles were used to fit the wetting curve. The simulation of the test using the fitted parameters for the two data sets are presented in Figure 79 (other examples in Annex I). No great differences in the fitted models with one and two cycles were observed for soils A. The fitting of the model to two cycles of data in case of soils C made the hysteresis more evident, which improves the agreement between the model and the experimental data in the low suction range.

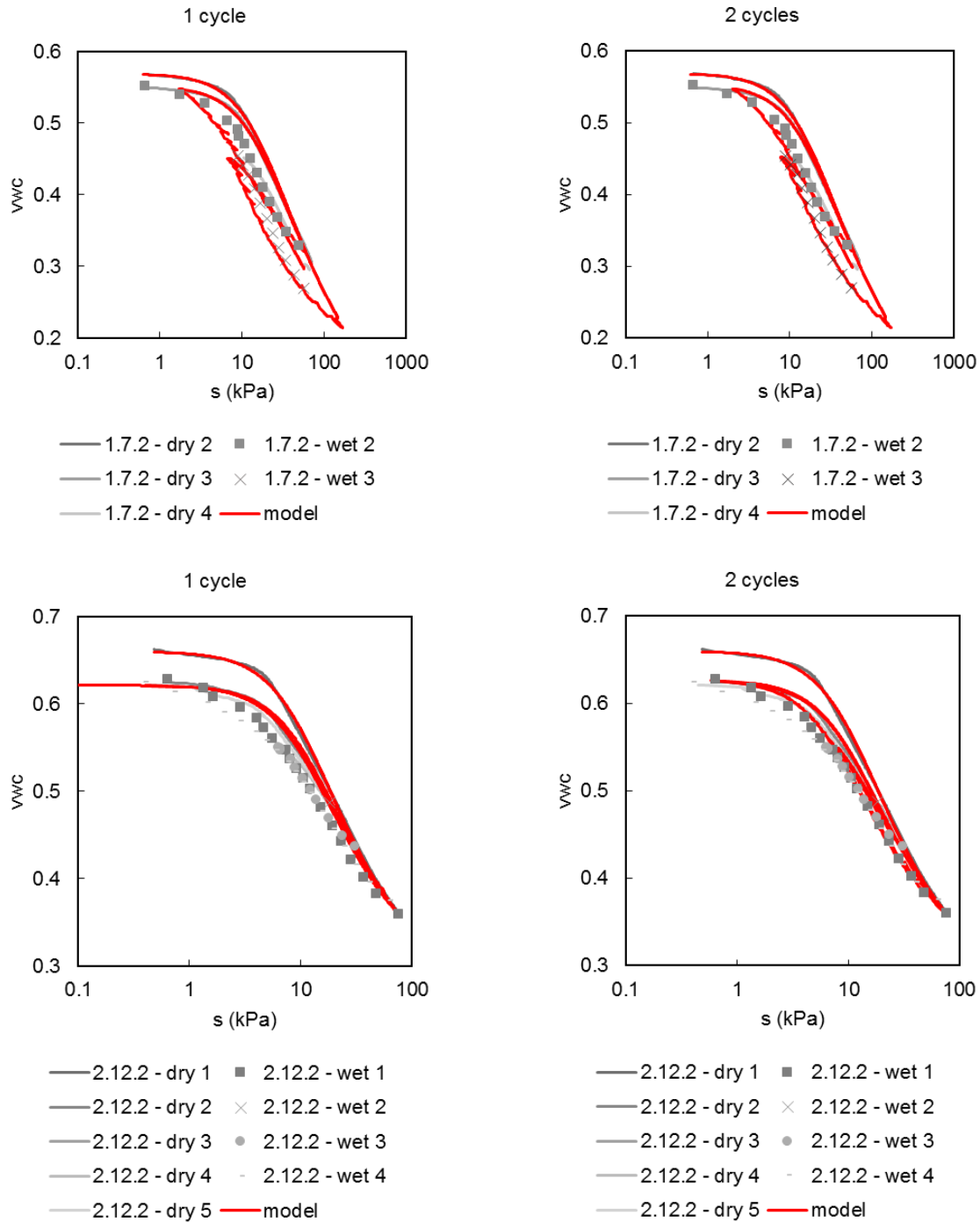


Figure 79 – Simulation of the full test using the fitting parameters from 1 cycle (left side) and 2 cycles (right side) and comparison with the experimental data.

Despicable variations of  $\theta_s^i$  in the fitting obtain from both data sets were found (Figure 80). The parameter  $\alpha^i$  presents greater changes depending on the data set. Note that the parameter  $\alpha^i$  increases in soil C when 2 cycles are adopted, which means that the AEV decreased and so a more open loop is obtained, as observed previously in Figure 79.

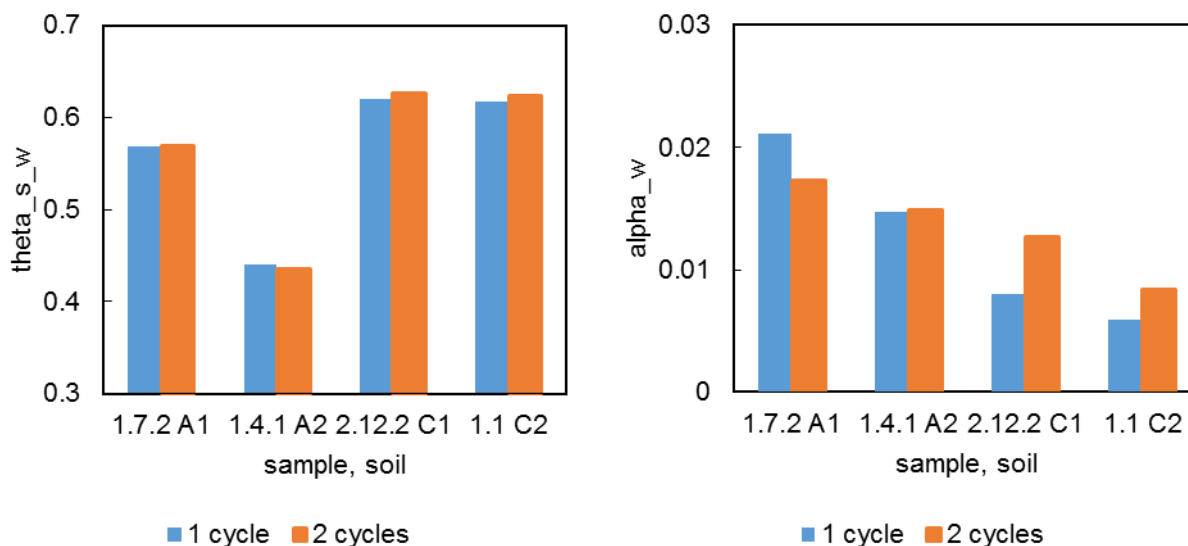


Figure 80 – Comparison of the fitted parameters of the main wetting curve using 1 or 2 cycles.

The coefficient of determination ( $R^2$ ) was calculated to access the differences between the experimental data and the simulations of the entire test (Table 18). Indeed,  $R^2$  increases in all tested cases which shows an improvement in the fitting with increasing data set size. However, this increase varies between 0.01 and 0.03, which translates in a small improvement in comparison with the necessary effort to produce one more drying-wetting loop in the laboratory and the additional time running the simulation data.

Table 18 – Coefficient of determination of the logarithm of suction along time in the fitting of 1 or 2 cycles (drying-wetting loops).

Soil	Sample	$R^2$ (log s)	
		1 cycle	2 cycles
A1	1.7.2	0.8656	0.8727
A2	1.4.1	0.9170	0.9271
C1	2.12.2	0.8932	0.9291
C2	1.1	0.8771	0.8920

### 3.3.4.5 Test replication and parameter dependency on porosity

All the model fitting effort would be useless if each fitting can only reproduce the behaviour of its soil sample of origin. The model should be able to replicate the behaviour of a group of soil samples of the same lithotype which would present similar hydraulic characteristics as a consequence of having the same physical properties.

The main wetting fitting parameters  $\theta_s^i$  and  $\alpha^i$  were compared with porosity, as well as  $K_s^i$ , per soil type, as presented in Figure 81. The correspondent parameters to  $\theta_s^i$  and  $\alpha^i$  in the main drying curve were compared in Figure 82 and Figure 83.

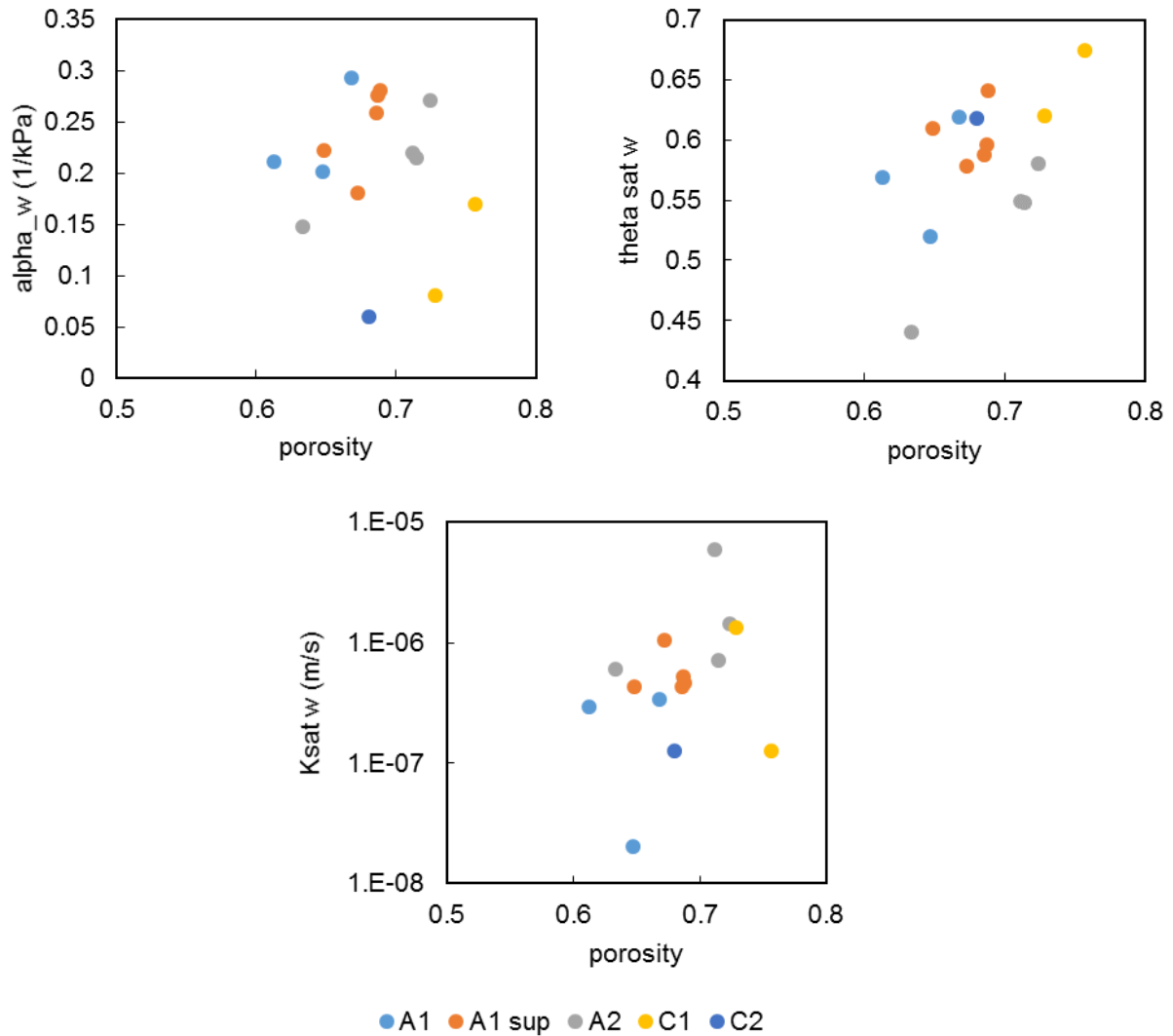


Figure 81 – Main wetting branch fitting parameters comparison with soil porosity per soil type.

The parameter  $\alpha^i$  is not dependent on porosity and a great dispersion of values are observed. The value  $\alpha^i$  is 1 to 3 times higher on average than  $\alpha^d$  as observed in Figure 82, which is in accordance with the suggestions in (Kool and Parker, 1987; Lenhard *et al.*, 1991). Note also that the values of  $\alpha^d$  and  $\alpha^i$  are similar in soils C, which is evident in the observed small hysteresis.

The parameter  $\theta_s^i$  increases with porosity, as  $\theta_s^d$ , even though air entrapment occurs differently among samples. The volumetric water content  $\theta_s^i$  never exceeds  $\theta_s^d$  but 5 tests (Figure 83) revealed equal values,

i.e. no air entrapment. The ratio between these two parameters also appears to depend on the porosity. More air entrapment is observed in soil samples with lower porosities.

The parameter  $K_s^i$  increases with porosity, as a consequence of its dependency on the parameter  $\theta_s^i$  and on the main drying HPF.

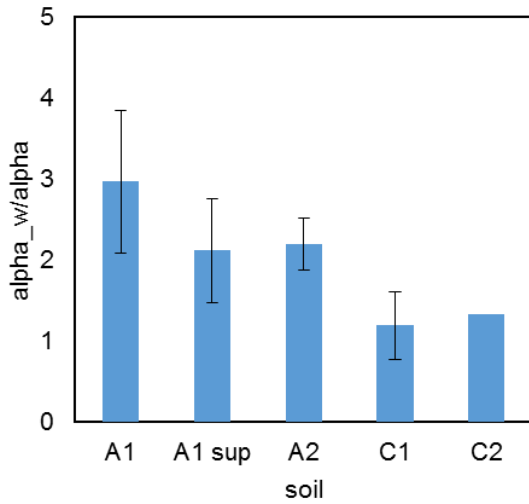


Figure 82 – Relationship between the parameters  $\alpha^d$  and  $\alpha^i$  per soil type and respective standard deviation.

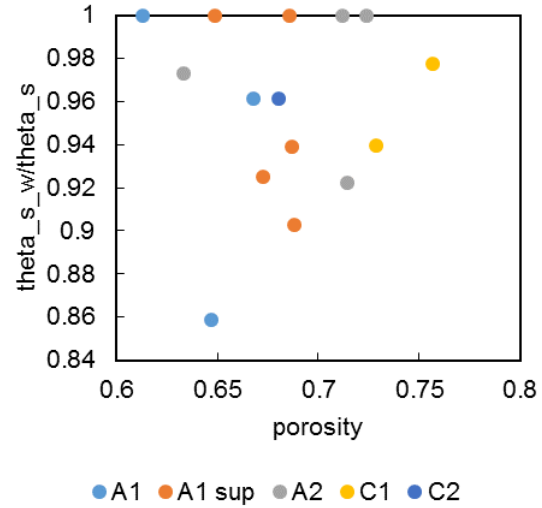


Figure 83 – Relationship between  $\theta_s^d$  and  $\theta_s^i$  and soil porosity of the tested samples.

In order to know how well a test can reproduce the remaining samples behaviour, the drying-wetting cycles monitored in the ku-pf apparatus on a sample were simulated by using the fitted parameters of another sample of the same lithotype. In this work, 'Fit' refers to the sample which parameters were adopted and 'Simulated' refers to the sample whose drying-wetting loops were simulated. The number of adopted parameters from the 'Fit' sample was modified according to four different cases summarized in Table 19, which are:

1. Adopted all the fitting parameters of the 'Fit' sample referent to the main drying and wetting curve;
2. Adopted the fitting parameters of the main drying curve of the 'Simulate' sample and the remaining parameters of the 'Fit' sample;
3. Adopted the fitting parameters of the main drying curve and the water content at saturation of the main wetting curve ( $\theta_s^i$ ) of the 'Simulate' sample and the remaining parameters of the 'Fit' sample;
4. All the adopted parameters belong to the 'Simulate' sample, i.e. main drying and wetting fitting parameters.

Table 19 – Fitted parameters adopted from the sample ‘Fit’ and ‘Simulate’ for each of the cases (1 to 4).

Case	1	2	3	4
‘Fit’ sample	$\theta_s^d, \theta_r, n, \alpha^d, l, K_s^d$ $\theta_s^i, \alpha^i, K_s^i$	$\theta_s^i, \alpha^i, K_s^i$	$\alpha^i, K_s^i$	
‘Simulate’ sample		$\theta_s^d, \theta_r, n, \alpha^d, l, K_s^d$	$\theta_s^d, \theta_r, n, \alpha^d, l, K_s^d$ $\theta_s^i$	$\theta_s^d, \theta_r, n, \alpha^d, l, K_s^d$ $\theta_s^i, \alpha^i, K_s^i$

In some samples, one or more cases could not be simulated because the parameters of sample ‘Fit’ and sample ‘Simulate’ were not compatible. For example, the  $K_s^i$  of the sample ‘Fit’ exceeded the value of  $K_s^d$  of the sample ‘Simulate’ in Case 2.

The initial suction distribution in the sample and initial volumetric water content were assumed to be known and were taken from the sample ‘Simulate’. The applied boundary conditions were also set equal to recorded during the evaporation and imbibition cycles in the ‘Simulate’ sample.

Figure 84 reports the results obtained for sample 1.7.2 of soil A1 as an example (other examples in Annex J). The comparison of the experimental data of ‘Simulate’ sample comparison with the model estimations revealed that:

- Case 1 provides a correct overall shape of the water retention path but deviations in the suction estimation;
- Case 2 results in a great improvement of the overall estimation;
- Case 3 improves considerably the estimation of the scanning loops that become much closer to the experimental measurements;
- Case 4 does not show great improvements in comparison with the previous case.

The sequence of improvements resultant from each case shows that the parameter  $\theta_s^i$ , which is related to the soil porosity, is the essential parameter to be obtained from main wetting branch in order to properly reproduce scanning hysteretic loops. Suction is not sensitive to  $K_s^i$  being simply dependent on  $\theta_s^i$ . So, the remaining parameter necessary to describe a wetting curve is  $\alpha^i$ , which is independent of porosity. This way, the differences between simulated tests among the same soil type are simply related to variations in porosity resulting from the variability of the soil in the same lithotype.



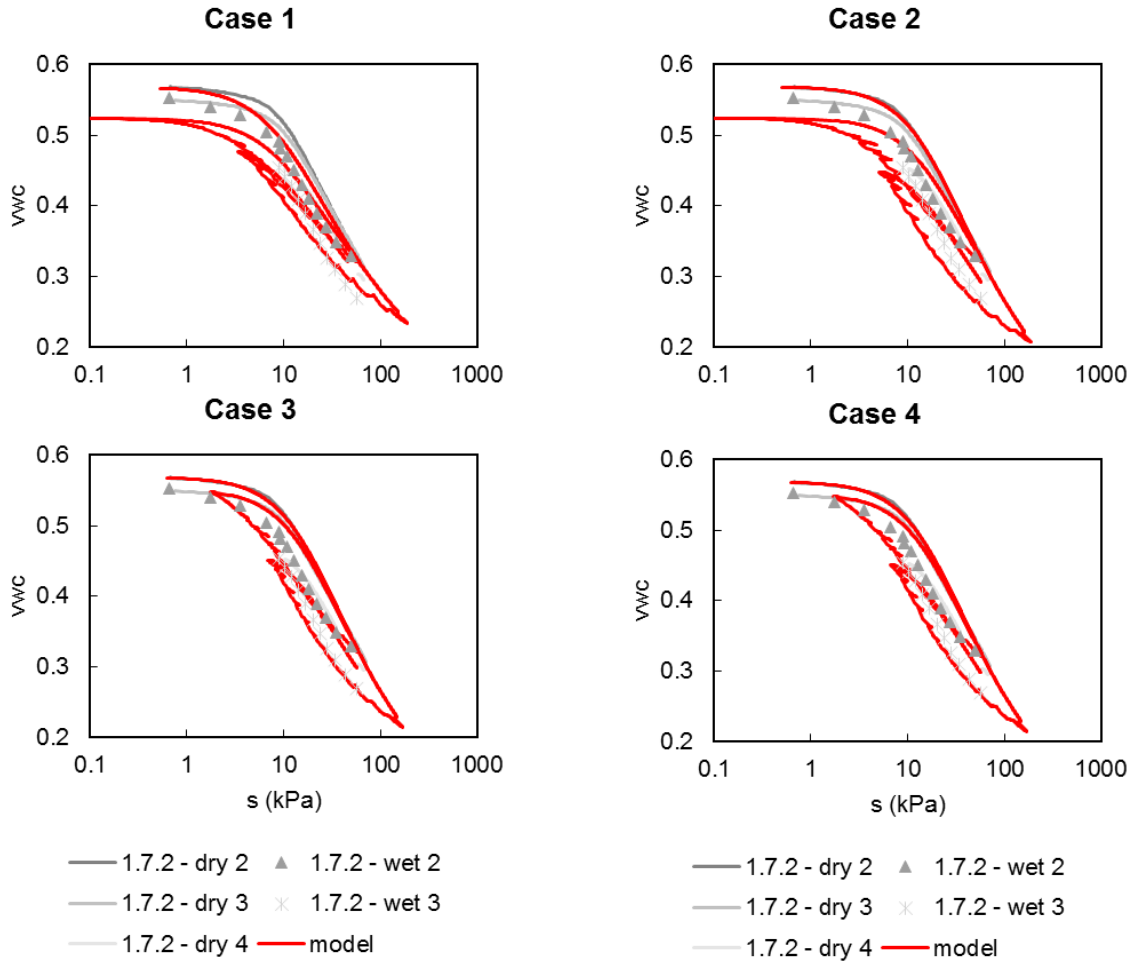


Figure 84 – Simulation of drying-wetting cycles of sample 1.7.2 with the fitting parameters of sample 1.9.2 (soil A1).

The best fit of the model to the experimental data, which corresponds to Case 4, was compared with the simulations of case 1 to 3 in Figure 85. The greatest suction deviations are correspondent to high suction values that have less important implications on the use of the model for practical purposes because a proper representation of the suction in the lower range is more relevant when handling propagation of wetting from problems. The maximum suction deviations are approximately 15 to 20 kPa in soils A1, A1sup and A2. A greater maximum suction deviation of approximately 80 kPa is reached in soil C1 because the soil is finer and all the WRC is shifted towards the higher suction values. Nonetheless, maximum suction deviations are dependent on the inversion point of the scanning curve because the higher is the water content of the inversion point, least errors are committed in the suction estimation.

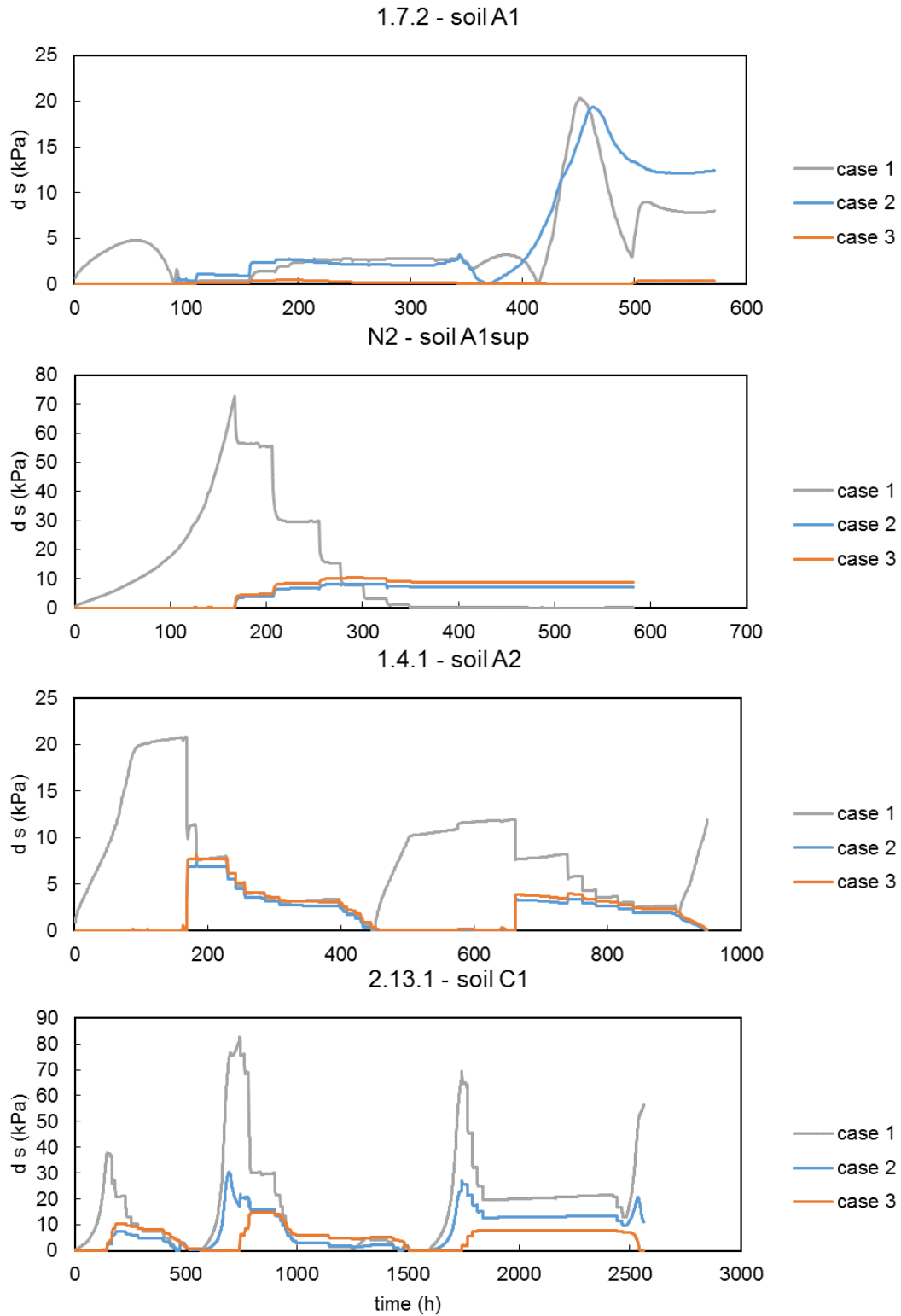


Figure 85 – Differences between suction estimations of the best fitting (case 4) and the fitting cases 1, 2 and 3.

### 3.3.5 Soil water capacity

The study of the water capacity functions intended to investigate how water infiltration is processed in an unsaturated soil because differences in WCF and HPF explain the different rates of the wetting front movement. An increase of the parameter  $\alpha$  of the van Genuchten equation represents a decrease of AEV and a consequent increase of the water capacity, or water storage modulus. This effect was particularly easy to observe in Figure 86.b, where the peak was translated towards the lower suction values accompanied of an intensity increase. Such observation was already reported in Fredlund and Rahardjo (2012).

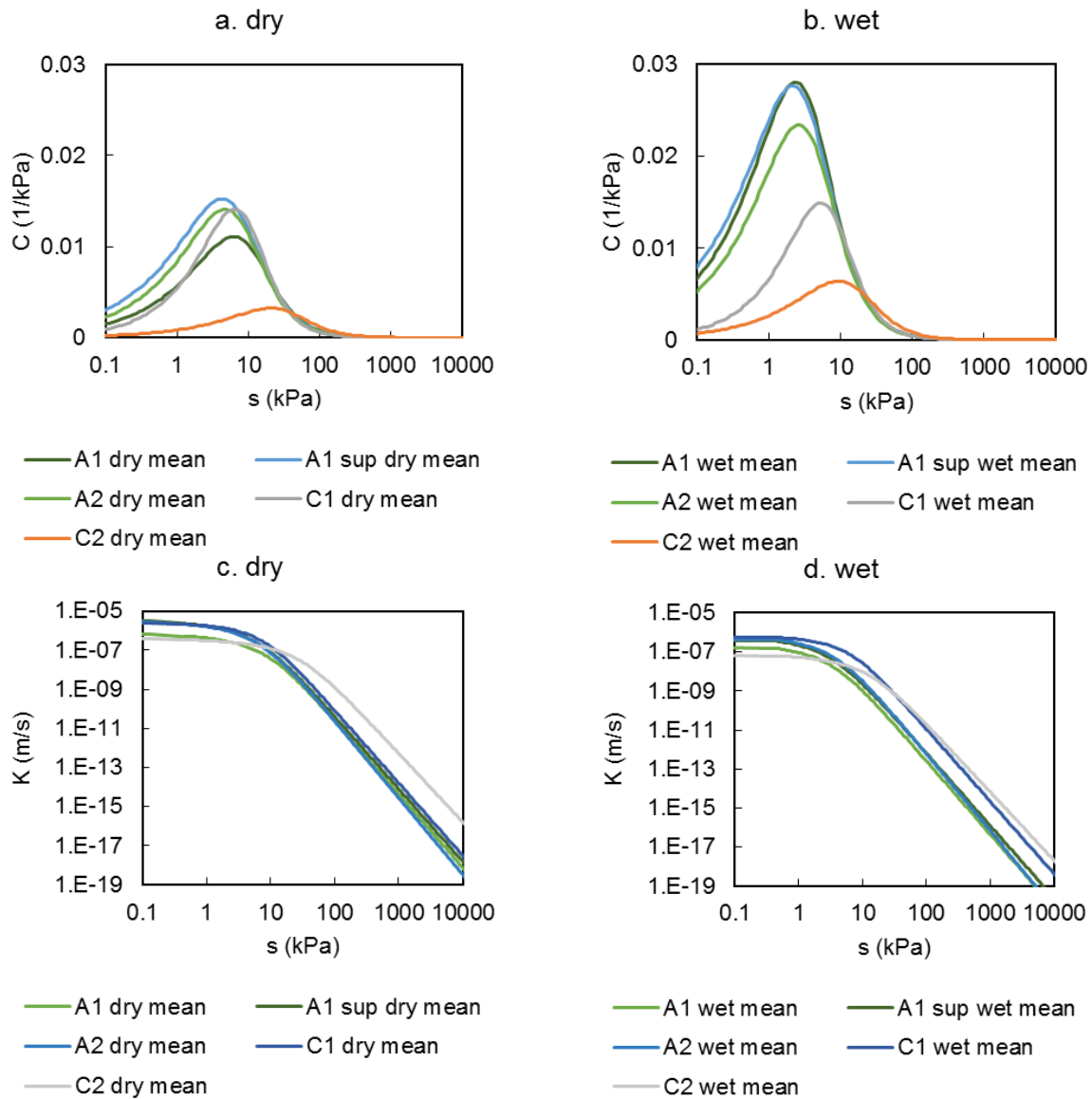


Figure 86 – Water capacity and hydraulic permeability function of each soil type computed with the mean fitting parameters of the main (a) drying and (b) wetting branch.

Soil C2 presents the lowest water capacity values because of its high AEV (low  $\alpha$  parameter), evident in Figure 86.a and .b. The water capacity of the main drying curve among the soils A presents the highest values and are similar among them. The water capacity values of the drying branch are closer among each soil type varying between  $0.003 \text{ kPa}^{-1}$  and  $0.015 \text{ kPa}^{-1}$  (Figure 87).

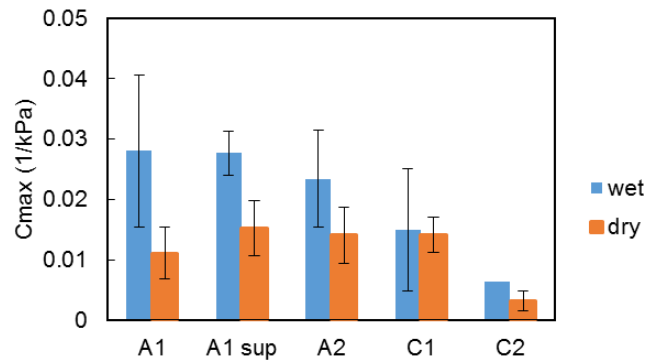


Figure 87 – Mean and standard deviation of the maximum water capacity ( $C_{max}$ ) of each soil type.

The values of water capacity are always higher in the wetting branch than in the drying branch (Figure 87). This results from the fact that the parameter  $\alpha^i$  is higher than  $\alpha^d$  in the fitted curves (Fredlund and Rahardjo, 2012).

Slower advance of the wetting front is expected when the hysteresis of the suction-water content relation is considered, i.e. when the development of the wetting front is characterized by a wetting curve (either main or scanning). Indeed, if a non-hysteretic model was adopted using the main drying curve as reference, the advancing of the wetting front would be much faster because the water capacity is lower.

Soil A1 and A1sup presented the same water capacity associated to the main wetting curve, however the hydraulic conductivity of soil A1sup was higher. In this case, the hydraulic conductivity would dictate the speed of wetting front movement. The soil with the greatest amount of roots, soil A1sup, would allow a faster infiltration of water. Note as well that soil A1sup and A2 present very similar hydraulic conductivity but soil A2 presented lower water capacity and so a faster propagation of the wetting front is expected in soil A2. Nonetheless, the propagation of the wetting front in a slope in soil A2 is limited by the saturated hydraulic conductivity of the layer A1. The depth and speed of the wetting front depends as well on the intensity and duration of rainfall events (Terlien, 1996).

### 3.3.6 Effect of roots on the soil hydraulic properties

The effect of vegetation on the soil hydraulic properties was investigated by separating the study of soil A1 from A1sup. Both soils presented the same grain size distribution and same specific gravity. The soil was characterized additionally by its root dry biomass in the other soil types. All the values are reported in Annex K. The presence and activity of roots results in changes in soil structure, like the formation of aggregates

or preferential flow channels (Angers and Caron, 1998; Ng *et al.*, 2016b). Pores of greater size are created that alter the manner by which water flows through the soil and the retention capacity of the soil (Ghestem *et al.*, 2011).

The average saturated permeability, porosity and dry biomass values per soil layer are presented in Figure 88. The saturated permeability was one order of magnitude higher in soil A1sup than in soil A1, which was a consequence of the greater porosity of soil A1sup. The greater amount of roots in soil A1sup was an indicator of the occurrence of preferential flow that translated in an increase of saturated permeability. An increase in permeability of soil was observed in previous studies with increasing root density and presence of decaying roots (Angers and Caron, 1998; Ng *et al.*, 2016b; Vergani and Graf, 2016), attributed to the change of soil structure and preferential flow channels.

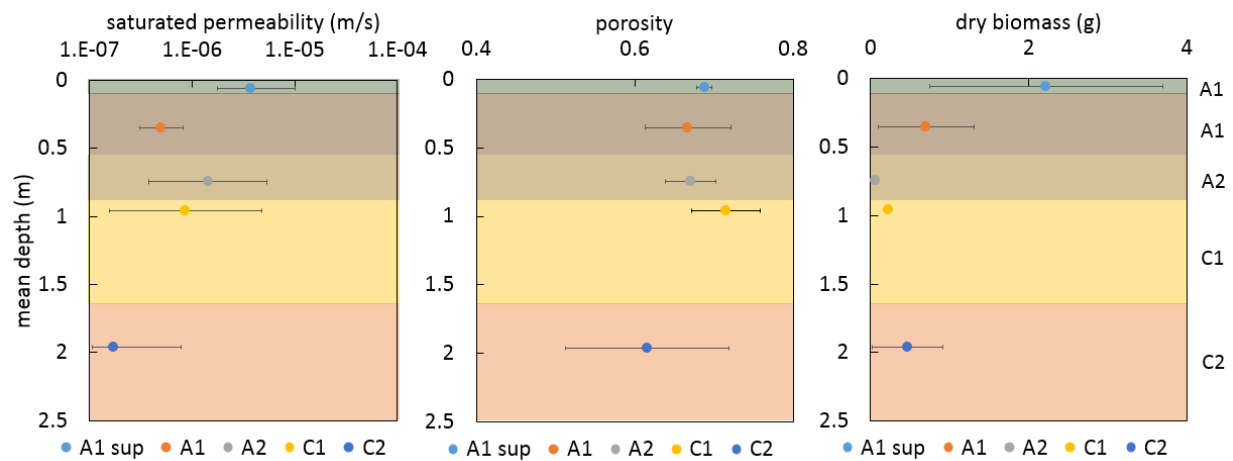


Figure 88 – Saturated permeability, soil porosity and root dry biomass in each soil layer with depth per soil layer.

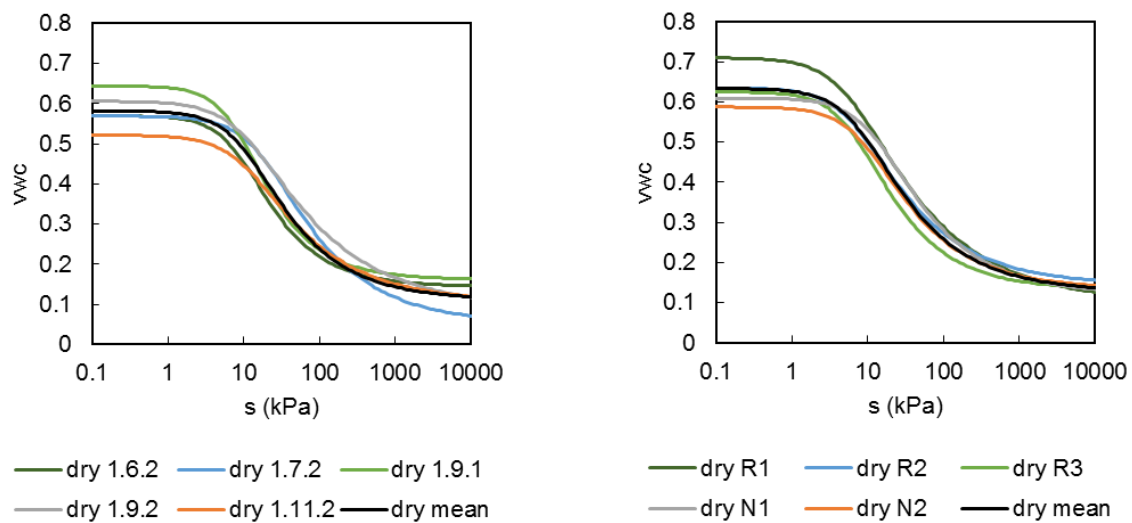
Soil A1 and A2 differed mostly in the grain size distribution. Soil A2 contained more pumices, which is the gravel fraction, than soil A1. The porosity of both samples was similar, apart from the soil A2 low variability. The permeability of A2 was higher than A1 and this observation was attributed to the higher amount of gravel of soil A2.

The finer soils in the profile, soil C1 and C2, differed greatly in terms of soil porosity and permeability. Soil C2 was much finer, its porosity much lower and it contained higher root dry biomass than soil C1. However, the presence of roots did not compensate the fact that soil C2 contained more silt and presented very low porosity. The low porosity and consequent low permeability of soil layer C2 may lead to an accumulation of water in soil layer C1 (as it was observed in the field measurements, reported in Chapter 4) generating positive water pressures which may be critical for the occurrence of landslides, investigated in Chapter 5.

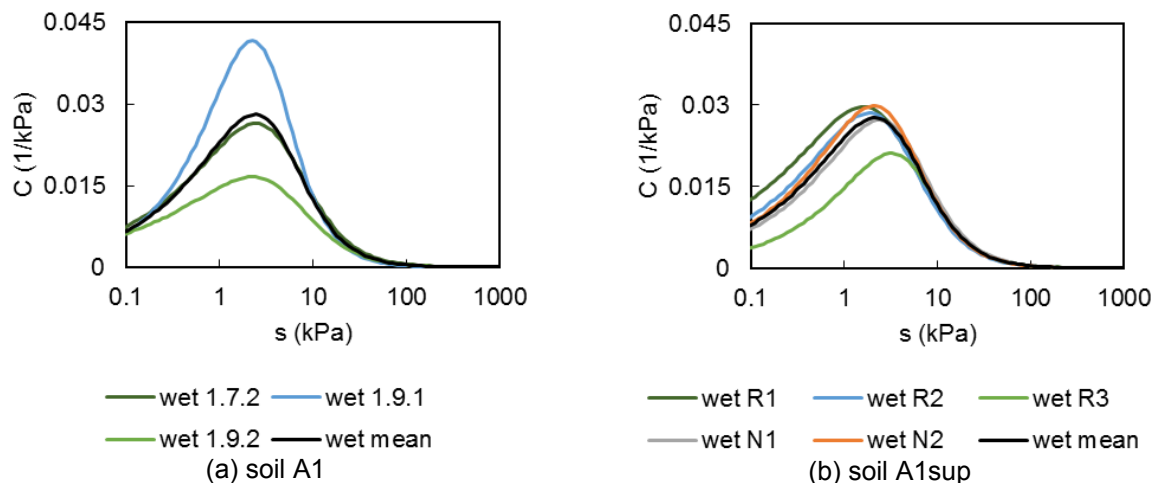
The presence of roots in the soil also changed the water retention properties of the soil (Figure 89). The soil with higher amount of roots, and so higher porosity, presented higher volumetric water content at saturation. The AEV of soil A1 varied between 4 and 10 kPa, while in soil A1sup the AEV varied between

2 and 6 kPa. The reduction of the AEV of the main drying branch of the WRC with increase root biomass is an evidence that roots change the soil structure. The same observation was made by Ng *et al.* (2016) when root decaying occurred.

The maximum values of water capacity associated to the main wetting curve in soil A1sup varied between 0.02 and 0.03 kPa<sup>-1</sup> (Figure 90, b). Soil A1 showed much higher variability in terms of water capacity peak, between 0.015 and 0.042 kPa<sup>-1</sup> (Figure 90, a). Nonetheless, both soils presented similar water capacity on wetting. As mentioned in the previous section and reported by Fredlund and Rahardjo (2012), the velocity of the wetting front of two soils with the same water capacity is controlled by the hydraulic conductivity function. On this base, the higher hydraulic conductivity of soil A1sup will lead to a faster propagation of the wetting front, which leads to higher risk of occurrence of landslides (Terlien, 1996).



(a) soil A1 (b) soil A1sup  
Figure 89 – Main water retention loop of soil (a) A1 and (b) A1sup.



(a) soil A1 (b) soil A1sup  
Figure 90 – Water capacity (C) of the main wetting curves of soil A1 and A1sup.

### 3.4 Conclusions

The improvement in the means of characterization of natural unsaturated soils considering the presence of roots for infiltration problems was developed showing that assuming a hysteretic k-S-P model provides results that show a slower advance of the wetting front. Considering the presence of roots showed however that the saturated permeability is the key factor to investigate the infiltration of water.

A sequence of tests was performed in the laboratory in order to characterize the soil hydraulic properties in a vast range of water contents. The saturated permeability was determined in a permeameter at constant head. The samples were subjected to cycles of evaporation and imbibition monitored by a ku-pf apparatus to determine a correspondence between water content and suction. At the end, samples were placed in a pressure plate to determine water contents in the high suction range for the type of soil tested.

The Lenhard *et al.* (1991) hysteretic k-S-P model was fitted to the experimental data in two stages. Firstly, the main drying curve was fitted following a procedure available in the literature described in Nicotera *et al.* (2010). Then, the main wetting curve parameters were determined using the experimental data correspondent to a main drying and a scanning wetting path.

The sensitivity analysis showed that the saturated permeability parameter of the main wetting curve should not be fitted and so hysteresis in HPF was ignored. This is a common assumption as usually hysteresis in the k-S relation is more evident in study of the flow of the gaseous phase in the soil (Parker and Lenhard, 1987). The fitting of the model was tested using two different experimental data set sizes. The results showed that a single drying and wetting loop was enough even if the use of two cycles provided better results.

The necessary parameters to obtain a good agreement between the model and the experimental were the fitting parameters dependent on porosity. The differences between simulated tests among the same soil type were simply related to variations of porosity resulting from the variability of the soil in the same lithotype. The difference between the best fitted model and the model assuming parameters of other test was observed in the high suction values that have less important implications on the use of the model for practical purposes. This way, an improvement in the manner by which soil hydraulic properties is represented was found.

The difference between the main drying and wetting showed that the main wetting presents a lower AEV that results in a higher water storage capacity. Consequently, a slower advance of the wetting front is expected if a hysteretic WRC model is considered.

The influence of root presence in the SHP was found mainly in the permeability of soil A1sup that was one order of magnitude higher than in soil A1, which was a soil with the same grain size distribution but lower porosity and less permeated by roots than soil A1sup. Evidences of the increase of the size of soil pores by roots were found through the decrease in the AEV of the main drying curve. On the other hand, these

two soils presented similar wetting water retention properties, so the higher hydraulic conductivity of soil A1sup commands the behaviour of the soil and would be the responsible for leading to a faster propagation of the wetting front.

In deeper soil layers, a greater amount of roots was not able to compensate a lower porosity in soil C2 in comparison with soil C1, which means that the deepest soil layer C2 still presented a lower permeability than soil C1. This might lead to an accumulation of water and generation of positive water pressures in soil C1 potentially being a negative factor for the slope stability.



## Chapter 4      Groundwater regime interaction with atmosphere and vegetation

### 4.1 Introduction

The groundwater regime is affected by the presence of vegetation in a complex manner. Firstly, the vegetation changes the manner by which the water reaches the ground through rainfall partition. The gross rainfall is divided into throughfall, stemflow and interception. The interception fraction never reaches the soil and evaporates directly from the plants canopy and ground litter. The stemflow reaches deeper soil layers as it infiltrates through the surface of the roots (Llorens and Domingo, 2007).

Plants also uptake water from the ground through transpiration. The decrease in the water content in the soil leads to an increase in the suction which is beneficial to slope stability. However, transpiration occurs mainly during the dry season when trees are in leaf (Leung and Ng, 2013). During the wet season, the critical period for the occurrence of landslides, trees affect only those soil hydraulic properties that are modified by the physical presence of roots.

In the previous chapter, the effect of plant roots on the soil hydraulic properties was investigated. A fast moving wetting front is expected in the upper soil layer due to the increase of soil porosity caused by the roots presence. The presence of roots in the soil and their microbial and fungal interactions with soil lead to the formation of soil aggregates, which change the soil structure, i.e. the arrangement of the soil particles and the pore size distribution. The soil structure is related to the soil hydraulic properties (Romero *et al.*, 1999). Additionally, roots create preferential flow channels that facilitate water infiltration. When roots decay, which increases with increasing cultivation time and with increasing competition among individuals, soil water permeability increases (Angers and Caron, 1998; Vergani and Graf, 2016). The amount of roots in the soil leads to different soil hydraulic properties (Ng *et al.*, 2013; Vergani and Graf, 2016).

Considerable differences among the soil layers found in Mount Faito test site (Campania, Italy) in terms of saturated permeability, which might condition water infiltration. The geological profile of the shallow pyroclastic soil cover present at the test site in Mount Faito investigated in the present thesis is composed of three soil layers with distinct grain size distribution and porosity, which are the main cause of different hydraulic properties. The shallowest soil layer (A, silty sand) presents a saturated permeability of the order of  $10^{-6} \text{ m s}^{-1}$  that can decrease to  $10^{-5} \text{ m s}^{-1}$  when strongly permeated by roots. The intermediate soil layer is composed of coarse pumices (B, well-graded gravel). The deepest soil layer (C, sandy silt) presents the lowest permeability in the whole profile being as low as  $10^{-7} \text{ m s}^{-1}$ .

However, previous works have shown poor agreement between laboratory and field measurements. Field measurements tend to be more representative of the conditions verified in situ but field experimentation is time-consuming and requires more resources than laboratory experiments. The field measurements collected at a test site in Monteforte Irpino (Campania, Italy) in a shallow pyroclastic soil cover were

compared with the laboratory hydraulic characterization of the same soil performed by (Nicotera *et al.*, 2010). The main drying branch of the water retention curve (WRC) constitutes an upper boundary to the field measurements and the hysteretic loop determined in the laboratory was not able to capture the field behaviour either because a small hysteresis was obtained. The differences were attributed to the higher air entrapment resultant from the wetting process in situ (Pirone *et al.*, 2014). The scale effect was observed by (Pirone *et al.*, 2016).

The groundwater regime monitored in pyroclastic soil covers in two different test sites in the region of Campania was reported by Damiano *et al.* (2012) and Pirone *et al.* (2015a). The seasonal trend was divided into three phases: (i) a transient period during which the suction in the soil increases (June to August), (ii) a transient period during which suction decreases (September to November), and (iii) a steady regime when suction is maintained low (December to May). The wet season, during which suction is maintained low, was identified to the critical period for the occurrence of landslides. The landslides triggered by rainfall require the suction to be close to the air-entry value (AEV) of the soil as a consequence of a prolonged period of rainfall. Once the predisposing conditions are verified, extreme rainfall events can trigger a landslide (Urcioli *et al.*, 2016).

The research question “How is the effect of vegetation on the hydraulic response of the soil at slope scale?” is being investigated in the present chapter. The effect of vegetation, even though considered more relevant in the changes induced in the soil hydraulic properties, constitutes a hydraulic upper boundary condition able to remove water from the soil and to change the manner by which rainfall reaches the soil (Llorens and Domingo, 2007; Leung *et al.*, 2015; Pirone *et al.*, 2015b). Previous studies have also observed that the seasonal groundwater regime relates to the predisposing conditions to the initiation of landslides (Damiano *et al.*, 2012; Pirone *et al.*, 2015a).

## **4.2 Methods and materials**

### **4.2.1 Test site characterization**

A test site located in Mount Faito (40°40'32.29"N, 14°28'23.35"E) in Campania, Southern Italy, was monitored during more than a hydrological year. The test site is located at 850 m of altitude in a slope with a mean slope angle of 26.5° facing North. The slope has a shallow pyroclastic soil cover with a thickness of approximately 3 m resting on a fractured limestone bedrock. The pyroclastic cover is composed of three main layers of approximately 1 m of thickness each. The shallowest is referred as soil A (divided into A1 and A2) which varies between silty sand and sandy silt with gravel according with the classification system USCS. At 1 m of depth, a layer of pumices is found (soil B), classified as a well-graded gravel. The deepest layer is soil C (divided into soil C1 and C2) being classified as sandy silt. All the soil identified in the profile presents high porosity (greater than 0.6) except for soil C2 which can present porosities as low as 0.4.

The vegetation growing at the test site is dominated by *C. sativa* and by ferns (*Pteridium aquilinum*). However, the ground cover changes considerably along the year as the ferns are removed by the local farmers in October and the leaf drop of trees occurs in November. Almost no soil cover is present during the wet season. The vegetation starts to grow in April and reaches its peak in July.

A more detailed description of the test site is presented in Chapter 2 and the soil hydraulic characterization is described in Chapter 3.

## 4.2.2 Climate data

The climatic data used in this work was obtained from three meteorological stations. The use of different sources was important for correction of data and filling any missing measurements. The meteorological stations were: (i) meteorological station of the test site of Mount Faito, (ii) meteorological station of Moiano managed by the Italian Civil Protection, and (ii) meteorological station of Pimonte managed by the Italian Civil Protection.

The location of these meteorological stations is presented in the Figure 91. The meteorological stations of Moiano and Pimonte are at approximately 2.5 km from the test site and at an altitude 400 m below the test site as presented in Table 20.



Figure 91 – Location of the meteorological stations (Google Earth image).

*Table 20 – Location of the meteorological stations.*

Meteorological stations	Moiano	Pimonte	Mount Faito
Distance to the test site (km)	2.57	2.58	-
Altitude (m)	485	438	850
Latitude	40°39'12.60"N	40°40'24.20"N	40°40'32.29"N
Longitude	14°27'50.00"E	14°30'14.30"E	14°28'23.35"E

The meteorological station of the test site allowed the measurement of rainfall every 10 minutes and the measurement of the air temperature, relative humidity, soil temperature (at depths of 0.20 m and 0.5 m), wind speed, wind direction and radiation every 4 hours. The sensors were installed at 2 m above ground (Figure 92) as by the standard. The meteorological stations at Pimonte and Moiano provide daily rainfall data. There was also available mean, minimum and maximum daily temperature from the station at Moiano. The summary of the collected data of all the meteorological stations is presented in Table 21 as well as the periods during which the data was recorded.



*Figure 92 – Meteorological station at Mount Faito test site.*

Table 21 – Time resolution of data recording and working period in each meteorological station.

Station	Record time	Recorded data						
		Rainfall	Air temperature	Relative humidity	Soil temperature	Wind speed	Wind direction	Radiation
Mount Faito	19/9/2017 to 08/9/2018	10 min	4 h	4 h	4 h	4 h	4 h	4 h
Moiano	1/1/2008 to present	1 day	Max, mean, min					
Pimonte	1/1/2001 to present	1 day						

## 4.2.3 Meteorological data interpretation

### 4.2.3.1 Potential evapotranspiration

The reference crop evapotranspiration or reference evapotranspiration ( $ET_0$ ), in some cases referred to as potential evapotranspiration, is the evapotranspiration rate from a reference surface, without a water deficit. This standardized vegetated surface is a hypothetical grass reference crop with specific characteristics. The only factors affecting  $ET_0$  are climatic parameters, which makes it possible to compute based on the meteorological data collected at Mount Faito test site. The most commonly used method is the Penman-Monteith method (Monteith, 1965; Penman, 1948), which is based on energy balance and mass transfer.

The Penman-Monteith method to estimate the reference evapotranspiration ( $ET_0$ ) is obtained from Equation 37, where  $R_n$  is the net radiation at the crop surface [ $\text{MJ m}^{-2} \text{day}^{-1}$ ],  $G$  is the soil heat flux density [ $\text{MJ m}^{-2} \text{day}^{-1}$ ],  $T$  is the mean daily air temperature at 2 m height [ $^{\circ}\text{C}$ ],  $e_s$  is the saturation vapour pressure [kPa],  $e_a$  is the actual vapour pressure [kPa],  $\Delta$  is the slope of the vapour pressure curve [ $\text{kPa } ^{\circ}\text{C}^{-1}$ ], and  $\gamma$  is the psychrometric constant [ $\text{kPa } ^{\circ}\text{C}^{-1}$ ]. The determination of the input parameters of Equation 37 are described in the following points based on Allen *et al.* (1998).

$$ET_0 = \frac{0.408\Delta(R_n - G) + \gamma \frac{900}{T + 273} u_2 (e_s - e_a)}{\Delta + \gamma(1 + 0.34u_2)} \quad 37$$

The reference evapotranspiration depends singularly on climate conditions, evident from the input parameters of Equation 37.

- Psychrometric constant

The psychrometric constant ( $\gamma$ ) in [ $\text{kPa } ^{\circ}\text{C}^{-1}$ ] is constant for each location and it is given by Equation 38, where  $c_p$  is the specific heat at constant pressure [ $\text{MJ kg}^{-1} ^{\circ}\text{C}^{-1}$ ],  $P$  is the atmospheric pressure [kPa],  $\varepsilon$  is the ratio molecular weight of water vapour/dry air [-], and  $\lambda$  is the latent heat of vaporization [ $\text{MJ kg}^{-1}$ ]. The

values of  $c_p$ ,  $\varepsilon$  and  $\lambda$  are known and represented in Table 22. Simplifications were made by assuming an air temperature of 20°C

$$\gamma = \frac{c_p \cdot P}{\varepsilon \cdot \lambda} \quad 38$$

Table 22 – Constants necessary for the calculation of the psychrometric constant.

$c_p$	1.013x10 <sup>-3</sup> MJ kg <sup>-1</sup> °C <sup>-1</sup>
$\varepsilon$	0.622
$\lambda$	2.45 MJ kg <sup>-1</sup>

The atmospheric pressure ( $P$ ) is estimated by Equation 39, where  $z$  is the elevation above sea level [m].

$$P = 101.3 \left( \frac{293 - 0.0065z}{293} \right)^{5.28} \quad 39$$

- Mean saturation vapour pressure

The mean saturation vapour pressure is given by Equation 40, where  $T_{max}$  and  $T_{min}$  are the maximum and minimum temperature [°C], respectively, and  $e^0$  is the saturation vapour pressure [kPa] that depends on the temperature ( $T$ ) in °C (Equation 41).

$$e_s = \frac{e^0(T_{max}) + e^0(T_{min})}{2} \quad 40$$

$$e^0(T) = 0.6108 \exp \left( \frac{17.27T}{T + 237.3} \right) \quad 41$$

- Slope of saturation vapour pressure curve

The slope of the relationship between saturation vapour pressure and temperature ( $\Delta$ ) in [kPa °C<sup>-1</sup>] is given by Equation 42, where  $T$  is the air temperature [°C]

$$\Delta = \frac{4098 \left[ 0.6108 \exp \left( \frac{17.27T}{T + 237.3} \right) \right]}{(T + 237.3)^2} \quad 42$$

- Actual vapour pressure

The actual vapour pressure ( $e_a$ ) can be calculated based on the relative humidity data, but also on the psychrometric data and on the dewpoint temperature. In this work, Equation 43 is used to determine  $e_a$  in kPa, where  $RH_{max}$  and  $RH_{min}$  are the maximum and minimum relative humidity [%], respectively.

$$e_a = \frac{e^0(T_{min}) \frac{RH_{max}}{100} + e^0(T_{max}) \frac{RH_{min}}{100}}{2} \quad 43$$

- Net radiation

The net radiation ( $R_n$ ) is given by Equation 44, where  $R_{ns}$  is the incoming net shortwave radiation and  $R_{nl}$  is the outgoing net longwave radiation.

$$R_n = R_{ns} - R_{nl} \quad 44$$

- Soil heat flux

Allen *et al.* (1998) suggests the use of Equation 45 calculate the soil heat flux ( $G$ ) in a simplified manner assuming that the soil temperature follows air temperature. Therefore, in the following equation,  $T_i$  is the air temperature at time  $i$  [ $^{\circ}\text{C}$ ] and  $T_{i-1}$  air temperature at time  $i - 1$  [ $^{\circ}\text{C}$ ],  $\Delta t$  is the length of time interval [day], and  $\Delta z$  is the effective soil depth [m]. The  $G$  is given in  $\text{MJ m}^{-2} \text{ day}^{-1}$ , once that  $c_s$  is the soil heat capacity and is given in  $\text{MJ m}^{-3} \text{ }^{\circ}\text{C}^{-1}$ .

$$G = c_s \frac{T_i + T_{i-1}}{\Delta t} \Delta z \quad 45$$

However, this value is commonly neglected, as in Pirone (2009), because the soil heat flux is small compared to  $R_n$ , especially when the surface is covered by vegetation.

Alternatively, the heat flow in soil can be calculated using the Fourier's Law as in Equation 46, where  $\lambda$  is the thermal conductivity of the soil [ $\text{W m}^{-1} \text{ K}^{-1}$ ] and  $\frac{\partial T}{\partial z}$  is the vertical temperature gradient [ $\text{K m}^{-1}$ ] of the soil layer (Sauer and Horton, 2005).

$$G = -\lambda \frac{\partial T}{\partial z} \quad 46$$

- Wind profile relationship

The wind speed decreases with the proximity to the ground surface because of the surface friction. Therefore, to estimate the wind speed at the required height of 2 m, Equation 47 is used, where  $u_2$  is the wind speed at 2 m above ground surface [ $\text{m s}^{-1}$ ] and  $u_z$  is the measured wind speed at  $z$  m above ground surface [ $\text{m s}^{-1}$ ].

$$u_2 = u_z \frac{4.87}{\ln(67.8z - 5.42)} \quad 47$$

Meteorological data is sometimes limited or of poor quality. However, the need to estimate reference evapotranspiration is still present. The following studies have related a small number of climatological parameters to the reference evapotranspiration. These relations can also be used to verify the quality of the measurements and to complete missing data in the records.

Allen *et al.* (1998) suggested Equation 48 for when there is missing data for the direct calculation of the reference evapotranspiration ( $ET_0$ ), where  $R_a$  is the extraterrestrial radiation, which variation along the year depends on the latitude of the site of interest.

$$ET_0 = 0.0023(T_{max} + 17.8)(T_{max} - T_{min})^{0.5}R_a \quad 48$$

#### 4.2.3.2 Evapotranspiration calculation parameters

The calculation of the evapotranspiration, both reference and crop, follow the procedure previously described. In here it is intended to summarize and give some enlightenment on the chosen parameters.

The constants used in the calculation of the reference evapotranspiration are summarized in Table 23. Additionally, the soil heat flux ( $G$ ) was assumed null as already previously done in Pirone (2009). This assumption is considered reasonable according to Allen *et al.* (1998).

Table 23 – List of constants used in the calculation of the reference evapotranspiration.

specific heat at constant pressure	$c_p$	1.01E-03	MJ kg <sup>-1</sup> °C <sup>-1</sup>
ratio molecular weight of water vapour/dry air	$\varepsilon$	0.622	
latent heat of vaporization	$\lambda$	2.45	MJ kg <sup>-1</sup>
atmospheric pressure	$P$	91.61295	kPa
psychometric constant	$\gamma$	6.09E-02	kPa °C <sup>-1</sup>

The extra-terrestrial radiation for the calculation of the reference evapotranspiration when only temperature readings are available depends singularly on the latitude of the studied location and on the day of the year. These values were collected for several days as presented in Figure 93. A polynomial regression of 4<sup>th</sup> degree was used to fit the data in order to be able to estimate the extra-terrestrial radiation along all year.



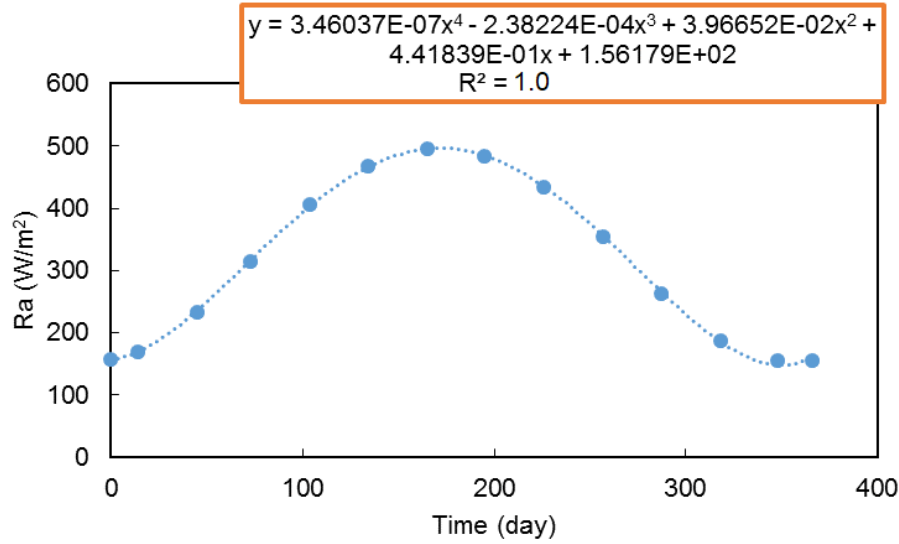


Figure 93 – Extra-terrestrial radiation along the year for Mount Faito.

#### 4.2.3.3 Relative humidity estimation

The calculation of the relative humidity in case of missing meteorological data or to validate the reasonability of the measured values based on temperature records is recommended in Allen *et al.* (1998). In this case, relative humidity ( $RH$ ) is given by Equation 49, where  $e_a$  is saturation vapour pressure and  $e^0(T)$  is the vapour pressure at the temperature  $T$ . For the calculation of these last two values, Equations 50 to 52 can be used in which  $T_{dew}$  is the dewpoint temperature,  $T_{nim}$  is the minimum temperature and  $k_0$  is correction parameter that is equal to 0 °C when the climate is humid or sub-humid or equal to 2 °C when the climate is arid or semiarid.

$$RH = 100 \frac{e_a}{e^0(T)} \quad 49$$

$$e^0(T) = 0.6108 \exp\left(\frac{17.27T}{T + 237.3}\right) \quad 50$$

$$e_a = e^0(T_{dew}) \quad 51$$

$$T_{dew} = T_{nim} - k_0 \quad 52$$

#### 4.2.4 Field instrumentation: TDR probes and tensiometers

Tensiometers, used to measure soil suction, and time domain reflectometry (TDR) sensors, used to measure volumetric water content, were installed in areas surrounded by *C. sativa* trees in the field. These instruments were coupled, i.e. installed at the same depth, along several vertical soil profiles. A profile

presents several coupled instruments installed at different depths. However, tensiometers were not installed in soil layer B due to the coarse texture of this soil.

Two groups of five profiles each, referred as cells, were installed in areas surrounded by trees. The area delimited by the trees is referred as a tree polygon (Figure 94). The maximum slope angle was identified, because Papa *et al.* (2013) and Pirone *et al.* (2015a, 2015b) observed that rainwater flow is along the direction of the steepest slope angle. Each of the cells has three profiles aligned along the direction of the maximum slope angle (N, C, S) and two others perpendicular to it (E, W), as in Figure 94. Two other profiles were instrumented near to a tree (profile T) and in the middle of a year in which trees were very far apart (profile NT). All the instrumented profiles and their relative location to trees is presented in Figure 94. The depth of installation of the equipment in each profile is indicated in Figure 95 and Table 24. This arrangement would therefore allow an estimation of the effect of slope angle and distance from trees on suction and volumetric water content.

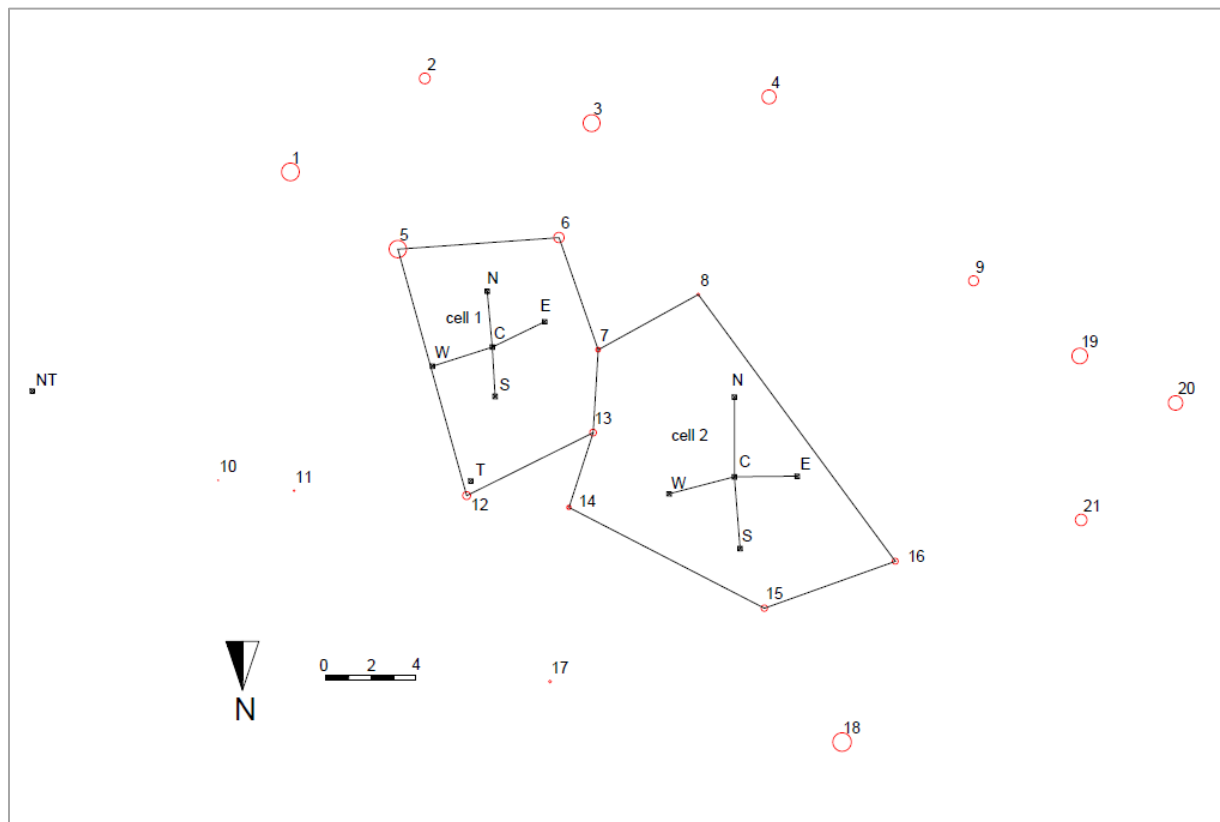


Figure 94 – Instrumented area: trees location (red numbered circles) relative to the profiles' location (identified by letters) grouped in cell 1 and cell 2.

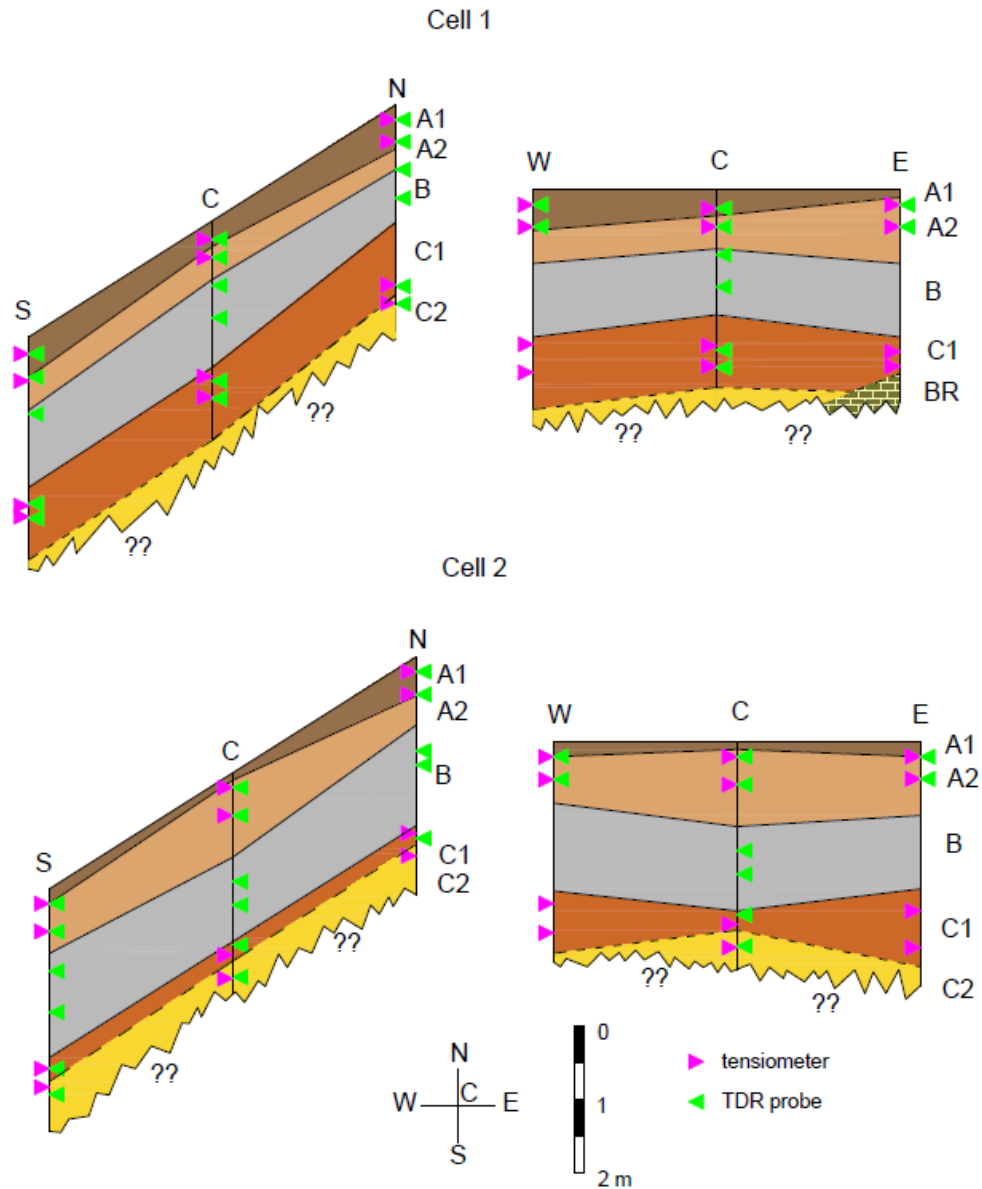


Figure 95 – Location of the instrumentation in each profile.

Table 24 – Instrumentation depths of TDR probes and tensiometers in profiles.

soil	profiles											
	1N	1C	1S	1E	1W	2N	2C	2S	2E	2W	T	NT
A1	0.2	0.3	0.2	0.2	0.2	0.2	0.2	0.2	0.2	0.2	0.3	0.3
A2	0.5	0.5	0.6	0.5	0.6	0.5	0.6	0.6	0.5	0.6	0.5	0.6
B	0.9	0.9	1.1			1.3	1.5	1.1				
B	1.3	1.3	1.1			1.5	1.8	1.7				
C1/C2	2.5	2.2	2.3	2.2	2.1	2.5	2.4	2.5	2.3	2.2		
C1/C2	2.7	2.4	2.5	2.4	2.5		2.8	2.8	2.8	2.6		

The tensiometers and the TDR probes in soil A were installed using tubes, such as the ones shown in Figure 96 and Figure 97, respectively. The boreholes to install the tensiometers had the same diameter of the tensiometer. The rods of the TDR probes are pushed into the soil at the bottom of the borehole after which the soil column was reconstructed.



*Figure 96 – The soil is being removed from the tube and identified with the help of a geologist.*



*Figure 97 – The tube is being pushed into the soil using a hammer.*

The installation in the soil layers B and C required the use of a tube to sustain the pumices because these do not present cohesion. An external tube, of larger diameter, was inserted into the soil after which its interior was cleaned using a smaller diameter tube as shown in Figure 98. The same procedure was followed for the installation of the TDR probes by adding an extension to the smaller diameter tube (Figure 99), that also helps the pushing of the rods of the TDR probes into the soil in the bottom of the borehole. The external tubes were removed after the equipment was inserted.



*Figure 98 – Interior and exterior cooper tubes to install tensiometers.*



*Figure 99 – Tube and extension used to open a borehole for the installation of TDR probes.*

The suction and dielectric constant measurements were collected weekly using the SMS 2500S tensiometer and the TDR100 connected to a computer and to a portable battery of 12V.

All the installed tensiometers have the working principle of the SDEC France even though Jet Fill tensiometers were used. The measurement with the SMS 2500S is allowed due to an adaptor used on the top of the tensiometer (Figure 100). In some of these Jet Fill tensiometers, a vacuum dial gauge was installed to provide an analogical reading for comparison.



*Figure 100 – Vacuum dial gauge and digital measurement adaptor installed on a Jet Fill tensiometer sided with a tradition SDEC France tensiometer.*

## **4.2.5 Equipment calibration**

### **4.2.5.1 Relation between dielectric constant and volumetric water content**

Time-domain reflectometry (TDR) was the method adopted for the determination of water content in situ. This technique provides the dielectric constant value of the medium in which a TDR probe is inserted. The soil dielectric constant is related to the soil water content and depends on other soil properties, such as soil-water salinity, soil texture, bulk density, mineralogy, and organic matter content (Hendrickx *et al.*, 2003).

The determination of the dielectric constant value is based on the interpretation of a signal that was reflected by the TDR probe and is detected by an oscilloscope. More details on the working principle can be found in the TDR User Guide (2000) and Reder *et al.* (2014).

Topp *et al.* (1980) and Ledieu *et al.* (1986) proposed a “universal” relation between the soil water content ( $\theta$ ) and the dielectric constant ( $\epsilon_c$ ), represented by Equations 53 and 54, respectively. However, these relations are not actually suited for organic and volcanic soils (Papa and Nicotera, 2012). The particular dielectric behaviour of volcanic materials is caused by the high dielectric constant and low bulk density. The dielectric constant of the solid particles was reported to be close to 15, while most mineral soils vary between 3 and 10, as mentioned by Comegna *et al.* (2013).

$$\theta = -5.3 \cdot 10^{-2} + 2.92 \cdot 10^{-2} \varepsilon_c - 5.5 \cdot 10^{-4} \varepsilon_c^2 + 4.3 \cdot 10^{-6} \varepsilon_c^3 \quad 53$$

$$\theta = 0.1138 \sqrt{\varepsilon_c} - 0.1758 \quad 54$$

There are some empirical models, such as the polynomial model represented by Equation 55 and the logarithmic model represented by Equation 56, where  $a$ ,  $b$ ,  $c$  and  $d$  are calibration constants.

$$\theta = a \cdot \varepsilon_c^3 + b \cdot \varepsilon_c^2 + c \cdot \varepsilon_c + d \quad 55$$

$$\theta = a + b \cdot \ln \varepsilon_c \quad 56$$

Semi-empirical models are available as well, such as the three-phase model by Roth *et al.* (1990) represented by Equation 57, where  $\varepsilon_w$ ,  $\varepsilon_s$  and  $\varepsilon_a$  are the water, solid particles and air dielectric constants, respectively,  $n$  is the soil porosity and  $\alpha$  is a fitting parameter which ranges between -1 and 1. The dielectric constant of the solid particles can be estimated through Equation 58 as in Papa and Nicotera (2012), where  $\rho_s$  is the specific gravity of the soil in g cm<sup>-3</sup> (Dobson *et al.*, 1985). The dielectric constants of water and air are respectively 80 at 20 °C and 1.

$$\theta = \frac{1}{\varepsilon_w^\alpha - \varepsilon_a^\alpha} [\varepsilon_c^\alpha - (1 - n) \varepsilon_s^\alpha + n \cdot \varepsilon_a^\alpha] \quad 57$$

$$\varepsilon_s = (1.01 + 0.44 \rho_s)^2 - 0.062 \quad 58$$

The calibration of the three previously presented models, polynomial, logarithmic and 3-phase models, were performed based on experimental data. The TDR100, produced by Campbell Scientific, Inc., is a time-domain reflectometer. The software that allows the interpretation of the signal recorded by the TDR100 to obtain the dielectric constant and electrical conductivity is the PC-TDR (used version 3.0).

The TDR probes were manufactured with the dimensions presented in Figure 101. The TDR probes were composed of 3 rods connected to a 3 or 5 m long coaxial cable through the head piece. These TDR probes were different from the standard probes produced by Campbell for which the software is prepared. In order to overcome this particularity, a calibration of the measure parameters for the probes was performed according to the procedure suggested by the software. The calibration provided the values of cable length, window length, probe length, probe offset, and parameters associated with measuring electrical conductivity (EC), such as the probe cell constant (Kp). These parameters were necessary in the software input to collect the dielectric constant and electrical conductivity.

The calibration was repeated for all the TDR probes used at the site assuming that they were of the type CS630 by Campbell because those are the most similar to the used manufactured probes in terms of geometry. The mean values of the parameters were used when collecting measurements at the site. The list of input parameters required by PC-TDR is presented in Table 25.

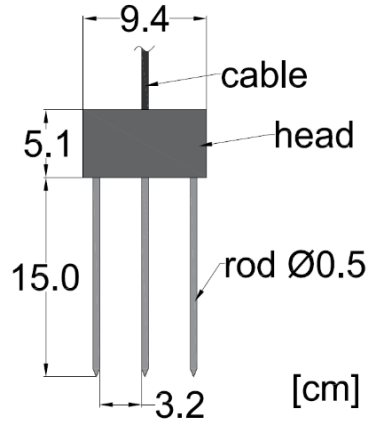


Figure 101 – TDR probe dimensions.

Table 25 – Input parameters to PC-TDR.

Vp	1
Averages	4
points	251
probe length	0.1534
probe offset	0.0611
probe Kp	4.01

The relation between the measured dielectric constant and the volumetric water content depends on the type of soil, even though there are fairly universal relations such as the ones presented by Topp *et al.* (1980) and Ledieu *et al.* (1986). Studies have shown that those relations are not appropriate to describe certain types of soils, such as organic and volcanic soils (Papa and Nicotera, 2012; Comegna *et al.*, 2013). The solid particles of volcanic soils present high dielectric constant values (closer to 15, while most vary between 3 and 10), and low bulk density (Comegna *et al.*, 2013).

Undisturbed soil samples of the layers A1, A2 and C1 were collected in Mount Faito by horizontally inserting the PVC moulds into the soil in excavated trenches for this purpose. The samples were sealed with paraffin and brought to the laboratory. A Plexiglas base was glued to the mould as in Figure 102. Then, the samples were saturated by adding water. To guarantee that all the pores were filled with water, the samples were closed using the cap and the latex disc shown in Figure 103 and a negative pressure of approximately 10 kPa was applied using the regulator and a vacuum converter (Figure 104 and Figure 105) connected to the compressed air system of the laboratory. Finally, TDR probes of known weight were inserted in the soil. The setup is presented in Figure 106.

The water was allowed to evaporate. The weight of the samples and the dielectric constant were recorded once or twice a day (drying phase). The procedure was also reversed by repeating the measurements



during several wetting steps (wetting phase). Water was added in such way that 6 steps of adding water would be necessary to reach saturation. The measurements were only performed after 24 hours to allow a redistribution of the water in the soil.

At the end, the soil was removed from the moulds and dried in the oven for 62 hours at 105°C. The weight of the moulds was registered in order to determine the porosity and volumetric water content during the test using a scale with a precision of 0.1g.



*Figure 102 – Plexiglas base glued to the mould.*



*Figure 103 – Cap, weight and latex disc.*



*Figure 104 – Pressure regulator and vacuum dial gauge.*



*Figure 105 – Vacuum converter.*



*Figure 106 – Equipment used to read the dielectric constant (computer, battery, TDR100 and cables).*

#### **4.2.5.2 Calibration of tensiometers**

The objective of this calibration was to obtain a curve for the correction of the values given by the tensiometer SMS 2500S, referred in this work as “digital” measurement and to demonstrate the good operation of the



tensiometers used in the field monitoring. Two tests were performed at the laboratory under controlled conditions as summarized in Table 26 and described as follows.

*Table 26 – Objectives of the calibration tests of the tensiometers.*

Test #	Name	Objective
1	Calibration of digital readings	Obtain a correction to the digital measurements provided by the SMS 2500S.
2	Influence of the initial air column in SDEC tensiometers on the readings and response time determination	Understand how the initial length of the air column in the SDEC France tensiometers interfere in the accuracy of the suction measurements. Show that the SDEC France tensiometers require less time to reach a stable measurement than the period between field measurements.

- TEST 1 – Calibration of digital readings

A Jet Fill tensiometer was connected to a 5 m long transparent pipe in which water was added. A vacuum dial gauge was installed as well as an adaptor for digital measurements. Enough air was left on the top of the tensiometer tube to allow the use of the SMS 2500S tensiometer. The water level inside the pipe varied and the correspondent values given by the tensiometer and the vacuum dial gauge were registered.

- TEST 2 – Influence of the initial air column in SDEC tensiometers on the readings and response time determination

A soil sample of a mixture of soil A1 and A2 was compacted and three tensiometers (SDEC France) were installed. A small tip tensiometer was installed as well to be used as reference (Figure 107). The water added in order to obtain three different initial water columns in each tensiometer. The suction and water level were recorded until the stabilization of the measurements was reached.



*Figure 107 – SDEC France tensiometers with different initial air columns.*

## 4.2.6 Root distribution

### 4.2.6.1 Roots sampling

Soil samples were collected from the study site in Mount Faito. Boreholes were made in order to collect soil in layers A1 and A2. Soil samples in soil B and C1 were collected in bags during the installation of the TDR probes. Each borehole was located where TDR probes were positioned (Figure 94).

The borehole moulds, 0.5 m long and with a diameter of 75 mm, were pushed into the soil with a hammer. The process was repeated two to three times per borehole until soil layer B was reached. The moulds were closed using tape on both ends and brought to the laboratory where they were stored in a wet room.

The soil in each mould was extruded into a container with the shape of a half cylinder as in Figure 108(a) and divided into sections of approximately 0.1 m as in Figure 108(b). The sections were crushed and sieved with a sieve with an opening of 2 mm. The roots of *C. sativa* trees were collected from the sieve and washed with water (Figure 108.c). The same procedure was followed to collect roots from the samples of soil B and C. The roots were preserved in sealed bags in a solution of 15% alcohol (Figure 109) stored in a fridge to prevent root decomposition.

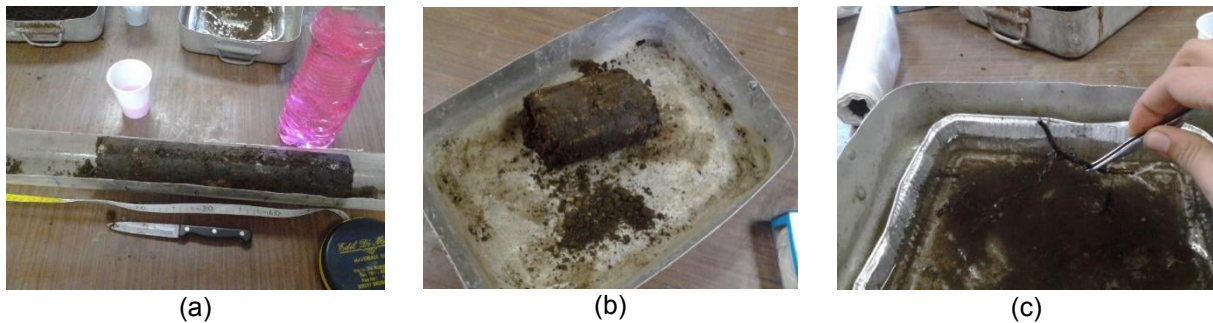


Figure 108 – Borehole extrusion (a), sectioning (b) and root washing (c).



Figure 109 – Bag storing roots in alcohol 15%.

#### 4.2.6.2 Roots scanning and image analysis

The roots were removed from the bags and were washed with water using a 5 mm sieve (Figure 110,a). Then, the roots were spread on a glass board containing a film of water using tweezers, as in Figure 110 (b). The image of roots was collected using the scanner EPSON Perfection V700 Photo, after which the roots were removed from the board, dried with absorbent paper (Figure 110,c) and weighed on a scale with a precision of three decimal places. The process was repeated if the roots contained in the bag did not fit in a single board to the maximum of three times. The remaining roots were dried and weighted without being scanned. The roots were maintained in an oven for 3 days at 40 °C and then weighed again. An example of the scanned roots image is presented in Figure 111.

When the roots are very tortuous or present a large diameter or when the water film is too thin, shadows appear in the scan image, as in Figure 112. These shadows, created by water meniscus, were removed using the image editing software Paint.net.

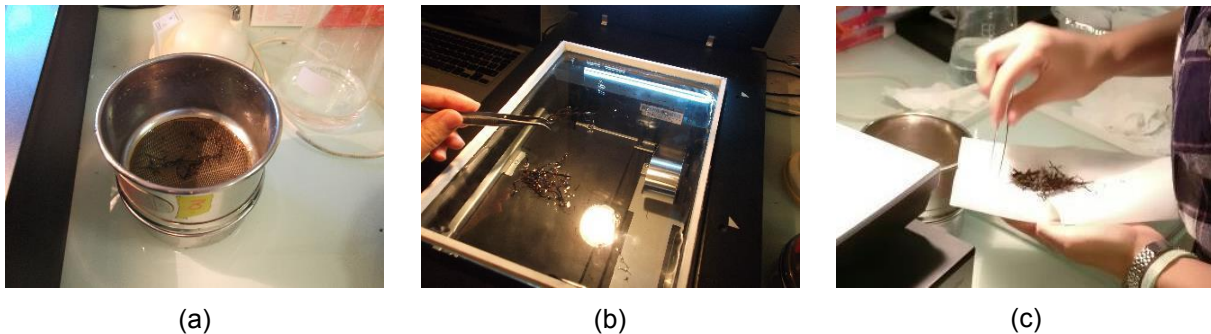


Figure 110 – Procedure to scan roots: (a) root washing in a sieve, (b) spreading of roots on the glass board with a film of water, and (c) roots drying with absorbent paper.

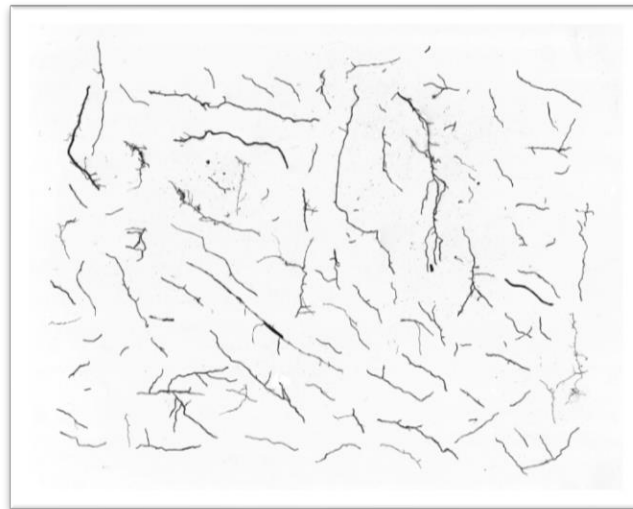


Figure 111 – Example of a scanned roots image.

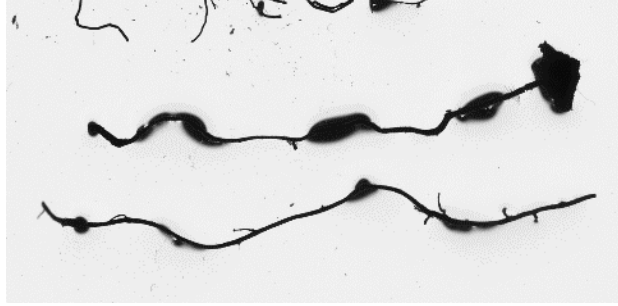


Figure 112 – Shadows created by the water meniscus.

A second set of images was created in which ectomycorrhizas were deleted. The difference can be observed between Figure 113(a), where mycorrhizas are present, and Figure 113(b), where only the root is shown.

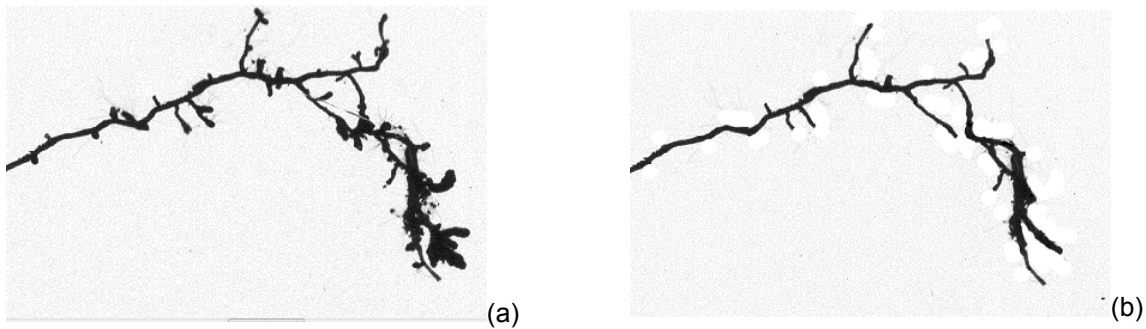


Figure 113 – Root before (a) and after (b) erasing the mycorrhizas.

The image analysis was made using the software WinRHIZO (by Regent Instruments Inc.). This analysis provided information regarding the root length, diameter, surface, area, volume and number of tips. Details on the steps followed in this analysis and how to operate the software can be found in Annex L.

#### 4.2.6.3 Root vertical distribution model

The exponential model (Gale and Grigal, 1987) defined by Equation 59 was adopted to describe the vertical distribution of the roots density with depth, where  $CDR_z$  is the cumulative value of the root density from the surface to the depth  $z$  dimensionless by the total root density of a given vertical, and  $\beta$  is the fitting parameter that varies between 0 and 1. The closer  $\beta$  approaches 1, the more roots tend to be less concentrated at the soil surface (Mao *et al.*, 2015).

$$CDR_z = 1 - \beta^z \quad 59$$

The fitting of parameter  $\beta$  was made through the least-square method using a MATLAB routine presented in Annex M. The data regarding the root density was considered only up to 1 m deep because the amount of roots beyond this depth are despicable and there is not information regarding the root density at such depth for all verticals.

#### 4.2.6.4 Root spatial distribution model

The competition index  $p$  of a given vertical is calculated using Equation 60, where  $DBH_i$  is the diameter at breast height of tree  $i$ ,  $d_i$  is the distance on the horizontal plane between tree  $i$  and the vertical,  $N$  is the total number of trees,  $\alpha$  is a fitting parameter, and  $d_{max}$  is a maximum distance from the vertical to the tree to be considered. The parameter  $d_{max}$  is a threshold that was made vary in order to understand the area of influence of the trees.

$$p = \sum_{i=1}^N \left( \frac{DBH_i}{d_i} \right)^\alpha, \text{ if } d_i \leq d_{max} \quad 60$$

The estimated root density indicator ( $\widehat{RD}$ ) was calculated according to Equation 61, where  $m$  and  $n$  are fitting parameters. The fitting parameters  $\alpha$ ,  $m$  and  $n$  of Equations 60 and 61 were obtained through least-square method using the solver function in Excel. A script and functions were also written in MATLAB. These codes can be found in Annex N.

$$\widehat{RD} = mp^n \quad 61$$

This analysis was based on the work of Mao *et al.* (2015) but simplified because no obstacles were considered and only one species of trees was present at the site. To account for the relative position of the tree in relation to the vertical, the fitting of Equation 60 was performed using (i) all the trees, (ii) only the trees uphill from the vertical, and (iii) only the trees downhill from the vertical, within the range defined by the threshold  $d_{max}$ . Three maximum tree-to-vertical distances ( $d_{max}$ ) were considered in the calculation of the competition index: (i) 10 m, (ii) 8m, and (iii) the closest tree only.

The selected root density indicator used in the fitting of Equation 61 were associated to the important root traits associated to preferential water flow, changes in soil structure and water uptake by plants (discussed in Chapter 1). Table 27 summarizes the list of root density indicators, on which root trait they are based and the range of depths considered.

Table 27 – Root density indicators ( $D$  is root diameter).

Parameter	Root trait	Range
$\beta$ -value	Biomass	-
	Root length	-
	Root volume	-
	No. root tips ( $D < 0.5\text{mm}$ )	-
Average density	No. root tips ( $D < 0.5\text{mm}$ )	$0.15 < z < 0.3 \text{ m}$
	No. root tips ( $D < 0.5\text{mm}$ )	$0.45 < z < 0.65 \text{ m}$
	Root length	$z < 0.3 \text{ m}$
	Root length	$z < 0.65 \text{ m}$
	Biomass	$0.25 < z < 0.5 \text{ m}$

#### 4.2.7 Water flow in the soil

The hydraulic head gradient was identified in Fredlund and Rahardjo (2012) as the fundamental driving potential for water flow. Conversely, the hydraulic head is the fundamental driving potential for flow in soils. The hydraulic head ( $h_w$ ) is a sum of three different terms: the gravitational head ( $y$ ), the pressure head ( $u_w/\gamma_w$ ), and the velocity head ( $v_w^2/2g$ ), as presented in Equation 62, where  $y$  is the elevation,  $u_w$  is the pore-water pressure,  $\gamma_w$  is the water unit weight,  $v_w$  is the water velocity, and  $g$  is the gravitational acceleration. Nonetheless, as the velocity head term in the soils is negligible comparing to the other two, Equation 62 is simplified into Equation 63.

$$h_w = y + \frac{u_w}{\gamma_w} + \frac{v_w^2}{2g} \quad 62$$

$$h_w = y + \frac{u_w}{\gamma_w} \quad 63$$

In the present work, the vertical water flow is being investigated, so the hydraulic head gradient is the difference of hydraulic head between two points, as presented in Equation 64, where the index  $T$  refers to the point at greater elevation (top) and  $B$  at lower elevation (bottom). The gradient is a measure of the available energy to cause water flow in the soil (Fredlund and Rahardjo, 2012).

$$i = \frac{h_T - h_B}{y_T - y_B} \quad 64$$

In the calculations performed in this work, the reference for determining  $y$  was fixed at the soil surface so that the position of the instruments correspond to a negative elevation (equivalent to depth) and suction is a negative pore-water pressure. So, the water flow occurs from the point with higher values of hydraulic head towards the points with lower values of hydraulic head. The gradient is positive when the flow is upwards, negative when the flow is downwards and null when there is no water flow.

The water flow in saturated soils is described by Darcy's law (Darcy, 1956), represented by Equation 65, where  $k_w$  is the coefficient of permeability. Nonetheless, this same equation is valid to describe flow of water in an unsaturated media because the rate of water flow through an unsaturated soil is linearly proportional to the hydraulic head gradient (Fredlund and Rahardjo, 2012). In unsaturated soils, the coefficient of permeability depends on the soil suction and it decreases greatly beyond the AEV, as seen in Chapter 3 and reported in Fredlund and Rahardjo (2012) and Nicotera *et al.* (2015). Indeed, a decrease of water phase in the soil is equivalent to a decrease of cross-section area available for the water flow accompanied by an increase of tortuosity in the path.

$$v_w = -k_w i \quad 65$$

#### 4.2.8 Hydraulic response of the soil related to spatial root distribution

The effect of root presence on the soil hydraulic behaviour was investigated by fitting a spatial distribution model, the same of the root density spatial distribution to particular observations. As the soil hydraulic properties are changed by the presence of roots in the soil, so the hydraulic response of the soil to the same rainfall and evapotranspiration will reflect that.

The spatial root distribution model, described previously, was adopted to relate trees in a given area to water content and suction in the soil. An observation point (i.e. a profile with coupled sensors), is characterized by a value of competition index, which depends on the size of the trees in a given area that will influence soil water content. The term root density indicator was replaced by hydraulic property indicator. The selected hydraulic property indicators are presented in Table 28. The data used for the fitting only referred to soil A1 and A2.

Equation 61, that relates the competition index to the root density indicator, is a power-law model, that is adequate for root distribution characterization because the values are always positive and monotonic. The selected hydraulic properties indicators are not always either positive or negative, for example the hydraulic vertical gradient. In that case there was the need of creating an artificial constant to be added to the observations in order to allow a good fitting.

*Table 28 – Selected hydraulic property indicators for the fitting of the spatial distribution model.*

Suction	Water content	Vertical gradient
<ul style="list-style-type: none"><li>• Maximum</li><li>• Minimum</li><li>• Mean during summer (transient phases from June to September)</li><li>• Mean during winter (steady phase from October to May)</li><li>• Maximum variation in time</li><li>• Minimum variation in time</li></ul>	<ul style="list-style-type: none"><li>• Maximum</li><li>• Minimum</li><li>• Mean during summer (transient phases from June to September)</li><li>• Mean during winter (steady phase from October to May)</li></ul>	<ul style="list-style-type: none"><li>• Maximum</li><li>• Minimum</li><li>• Mean during summer (transient phases from June to September)</li><li>• Mean during winter (steady phase from October to May)</li></ul>

### 4.3 Results and discussion

#### 4.3.1 Meteorological monitoring

##### 4.3.1.1 Previous rainfall records in Moiano and Pimonte

Rainfall and temperature data were collected from the meteorological stations of Pimonte (for the previous 17 years) and Moiano (for the previous 10 years). The cumulative rainfall along a year recorded in Pimonte was on average higher than in Moiano for the same time period (Figure 114). In Pimonte the average yearly rainfall from 2008 to 2017 was 1575 mm and in Moiano was 1378 mm for the same period.

The extreme events were identified through the maximum daily rainfall in each year (Figure 115). The rainfall measured in both meteorological stations was considerably different. The maximum daily rainfall recorded in Pimonte was of 187 mm in the past 16 years and in Moiano was 115 mm in the past 9 years. The wet period is from October to March and the dry season is from April to September (Figure 116).

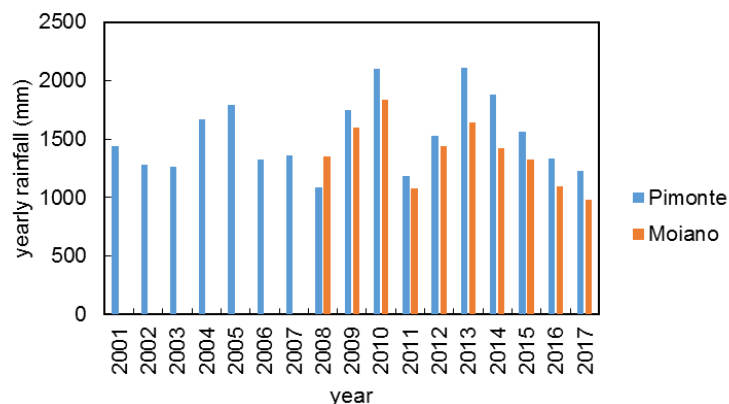


Figure 114 – Total rainfall cumulated along each year in Pimonte and Moiano meteorological stations.

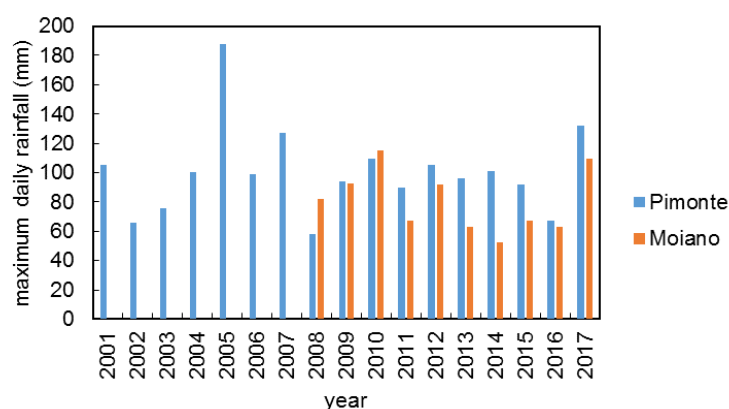


Figure 115 – Maximum daily rainfall recorded in each year in Pimonte and Moiano meteorological stations.

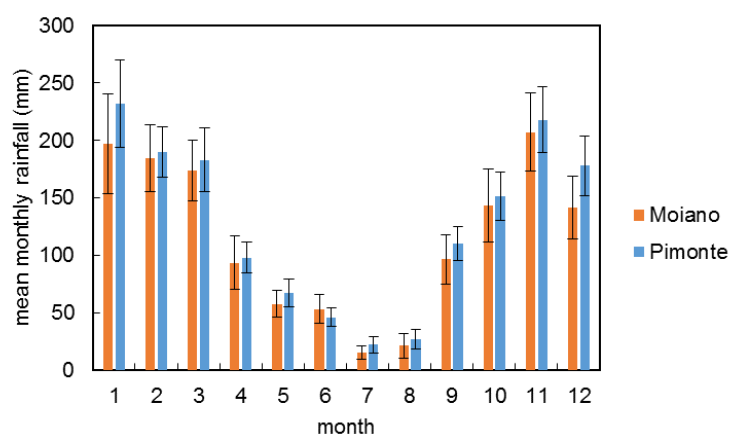


Figure 116 – Mean and standard error of the monthly rainfall in Pimonte and Moiano meteorological stations.



#### 4.3.1.2 Meteorological monitoring of Mount Faito

The meteorological records started in September 2017 but the groundwater monitoring started in February of the same year. Additionally, the temperature and relative humidity records were not available in the meteorological station of Mount Faito from December 2017 to April 2018. The gaps in the data were filled with the data available from Moiano and Pimonte meteorological stations. Note that the meteorological stations were just 2.5 km apart but the difference of altitude is of approximately 400 m.

##### • Rainfall

The rainfall registered in all the meteorological stations is presented in Figure 117. However, the meteorological monitoring of the test site started in September 2017, seven months after the monitoring of the groundwater regime. The daily rainfall recorded in Moiano and Pimonte was compared with Mount Faito, as in Figure 118, and linear interpolations were obtained that allowed the estimation the rainfall at Mount Faito when direct measurements were not available.

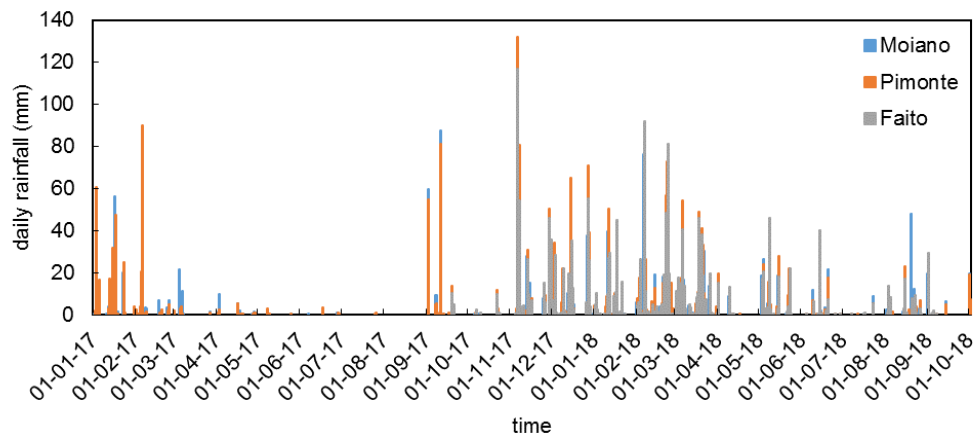


Figure 117 – Daily rainfall registered by the meteorological stations at Moiano, Pimonte and Mount Mount Faito.

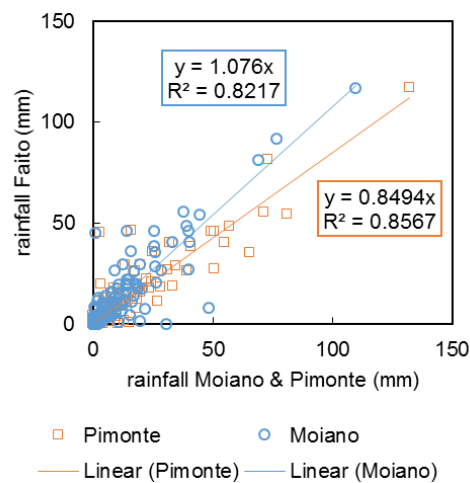


Figure 118 – Comparison of the daily rainfall recorded in Moiano and Pimonte with Mount Faito.

The linear interpolation that relates the daily rainfall of Pimonte and Mount Faito presents a higher determination coefficient. The equation was used to estimate the rainfall during all the period of monitoring of Mount Faito test site, as presented in Figure 119. The cumulative rainfall from September to August was estimated for the years of 2016/2017 and 2017/2018, which allows the rainfall of a wet season to be grouped in a single hydrological year. The cumulative rainfall of the wet season of 2016/2017 was much lower than in the wet season of 2017/2018, for which different groundwater regimes are expected. Additionally, almost no rainfall was recorded in the dry season (June to August) of 2017 in comparison to the dry season of 2018.

The monthly rainfall of the entire year of monitoring (September 2017 to September 2018) is presented in Figure 120 and compared with the average monthly rainfall recorded in the past 17 and 7 years in Pimonte and Moiano meteorological stations, respectively. Note that there are no records from Mount Faito in the month of September. The rainfall was greater in the recorded period than the average of the previous years in 7 months out of the 11 recorded months.

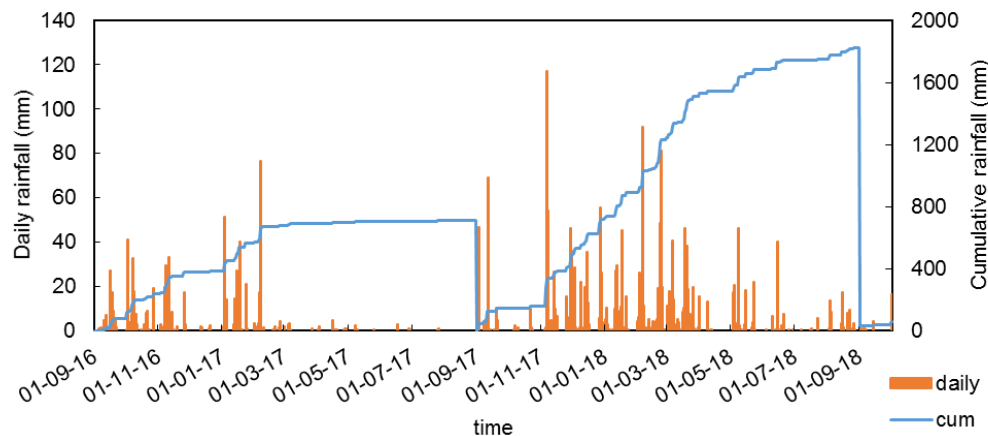


Figure 119 – Daily rainfall at Mount Faito from January 2017 to September 2018.

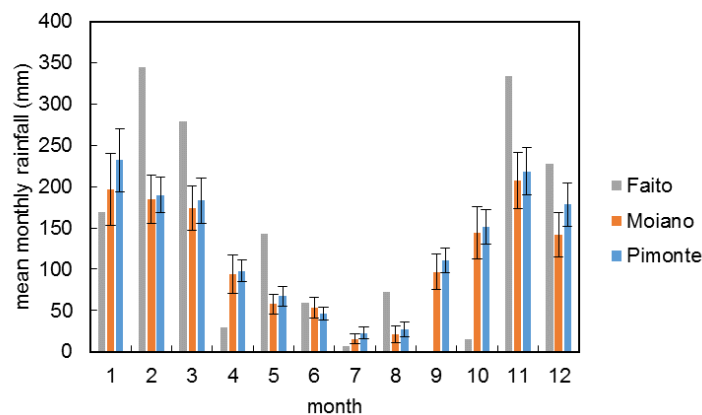


Figure 120 – Mean and standard error of the monthly rainfall of Moiano and Pimonte meteorological stations and the monthly rainfall recorded in Mount Faito.

The year of 2017 was a particular dry year and no major rainfall events were recorded from February 2017 until the end of August 2017. In September 2017, two major rainfall events were recorded with precipitations above 50 mm according to the measurements collected in Moiano and Pimonte.

On November 6<sup>th</sup> 2017, a major rainfall event occurred in which the rainfall was of 109 mm, 132 mm and 117 mm in Moiano, Pimonte and Mount Faito meteorological stations, respectively. This particular event was responsible for the landslides at Vico Equense in the South face of Mount Faito. Debris flows occurred blocking roads. On the Northern face of the mountain, several small landslides were observed along the closed road that leads to the test site. The landslide of very small dimensions can be observed in Figure 121. This landslide may have been caused by the fall of a tree that was on the wedge of a calcareous cut.

Later in 2018, two major rainfall events occurred with a rainfall of 92.0 mm on February 6<sup>th</sup> and 81.4 mm on February 23<sup>rd</sup>.



*Figure 121 – Small landslide on the side of the road that leads to the study site.*

- **Temperature**

The maximum temperatures were reached in August and the minimum in January. There is a large gap of data in terms of temperature from Mount Faito test site (Figure 122) caused by the malfunction of the air temperature and relative humidity sensor. Linear relations between the maximum, mean and minimum temperatures recorded in Mount Faito and Moiano meteorological stations were established, similarly to the manner described in the rainfall studies described in the previous section. Lower temperatures are recorded in Mount Faito when compared to Moiano (Figure 123), which is an expected observation due to the difference of altitudes.

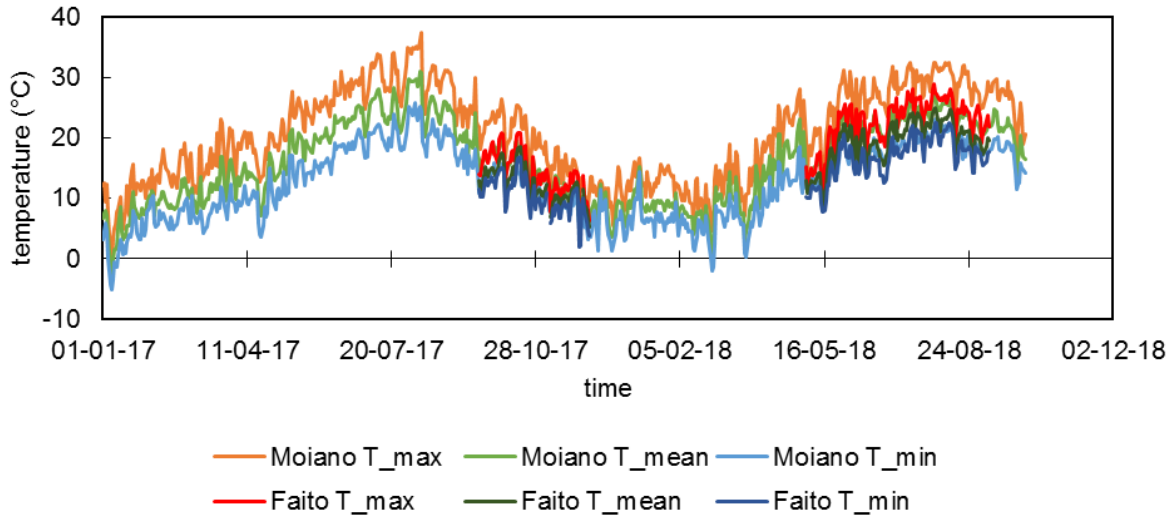


Figure 122 – Maximum, mean and minimum temperature recorded in Moiano and Mount Faito along the year.

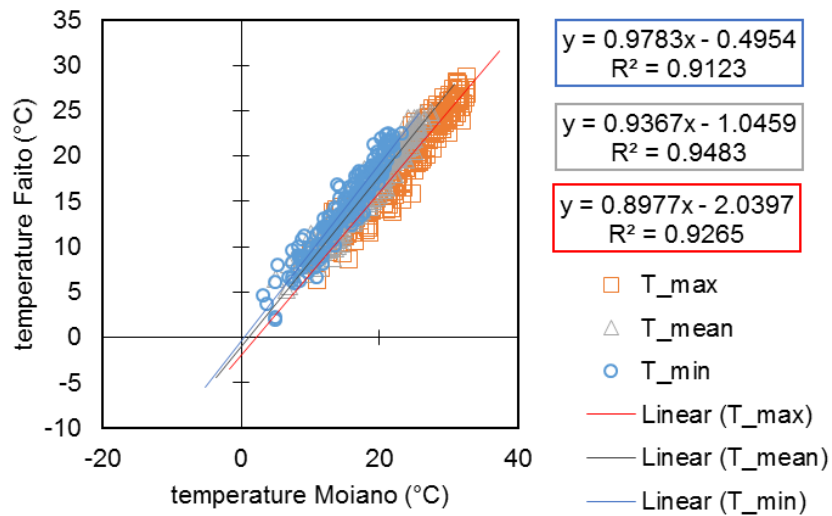


Figure 123 – Comparison of the Maximum, mean and minimum temperature recorded in Moiano and Mount Faito.

The linear relationships presented in Figure 123 were used to estimate Mount Faito temperature based on the records of Moiano. The estimated temperature at Mount Faito test site based on the measurements of Moiano (Figure 124) was used to complete the gap presented in Figure 122. The data, reported in Figure 124, is used ahead in the present chapter to estimate the potential evapotranspiration at Mount Faito.

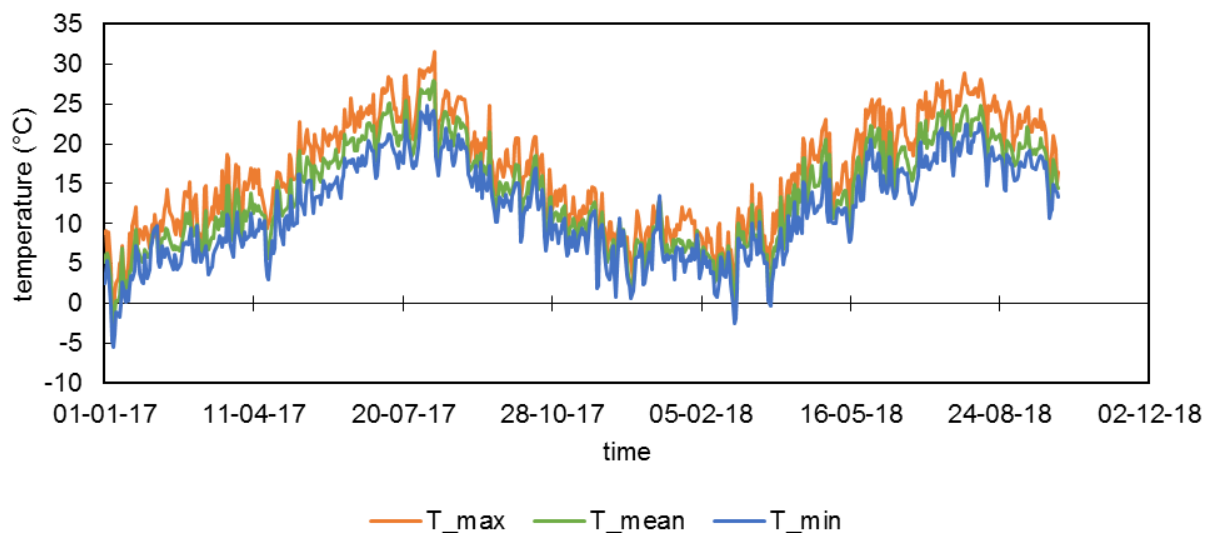


Figure 124 – Maximum, mean and minimum temperature at Mount Faito from January 2017 to September 2018.

- **Relative humidity estimation**

The values of calculated relative humidity were compared to the measured ones in order to verify the quality of the estimation method based on the temperature. The mean RH was estimated based on the mean temperature, the maximum RH based on the minimum temperature, and the minimum RH based on the maximum temperature. The estimation of the maximum RH is very poor and the best estimation was obtained for the minimum RH (Figure 125).

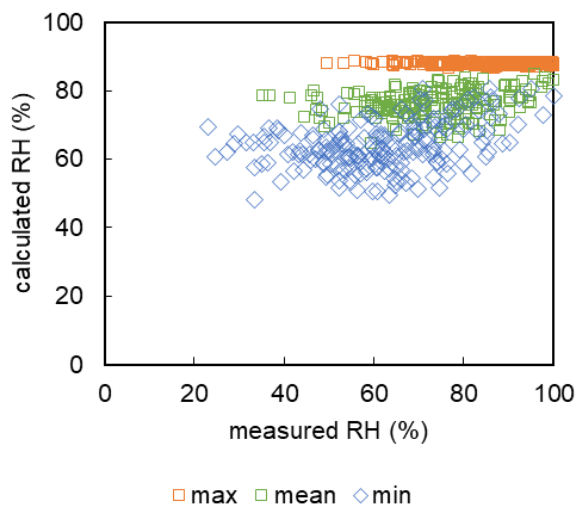


Figure 125 – Comparison of the measured and calculated relative humidity (RH).

The values presented in Figure 126 include the measured and estimated relative humidity for when direct measurements were not available. The estimated values tend to be lower than the measured, which led to an underestimation of the relative humidity.

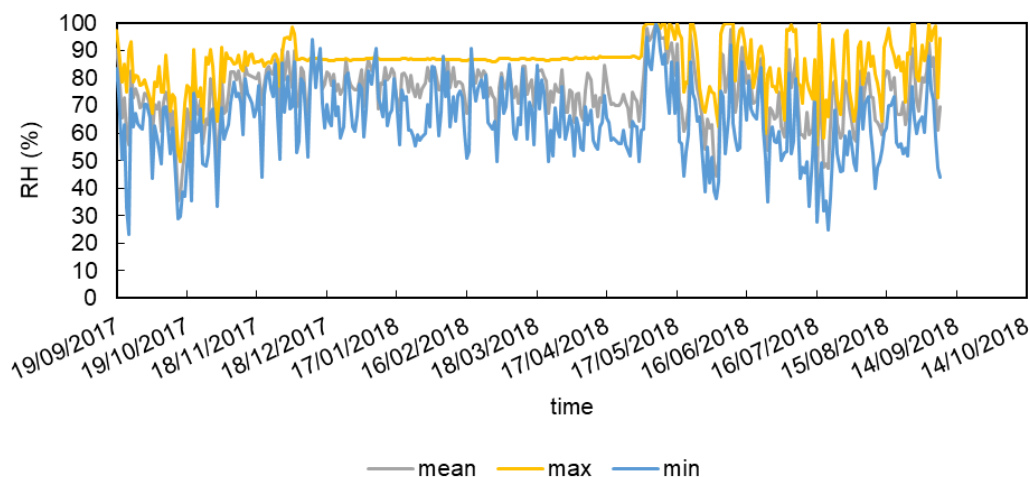


Figure 126 – Relative humidity (RH) in Mount Faito from September 2017 to September 2018.

- **Other meteorological data**

The meteorological data regarding relative humidity (Figure 127), wind speed (Figure 128), soil temperature (Figure 129) and net radiation (Figure 130) are presented in this section. The relative humidity in Mount Faito is relatively high, especially in months of winter (wet season), and even during the dry season the relative humidity does not go below 40% on average. The wind speed is usually between 0 and 6 m s<sup>-1</sup>. The soil temperature at surface presents greater variations along the year, i.e. the temperature is higher in the summer and lower in the winter than at 0.5 m. The net radiation is greater in the summer months because of the longer periods of time with sun light.

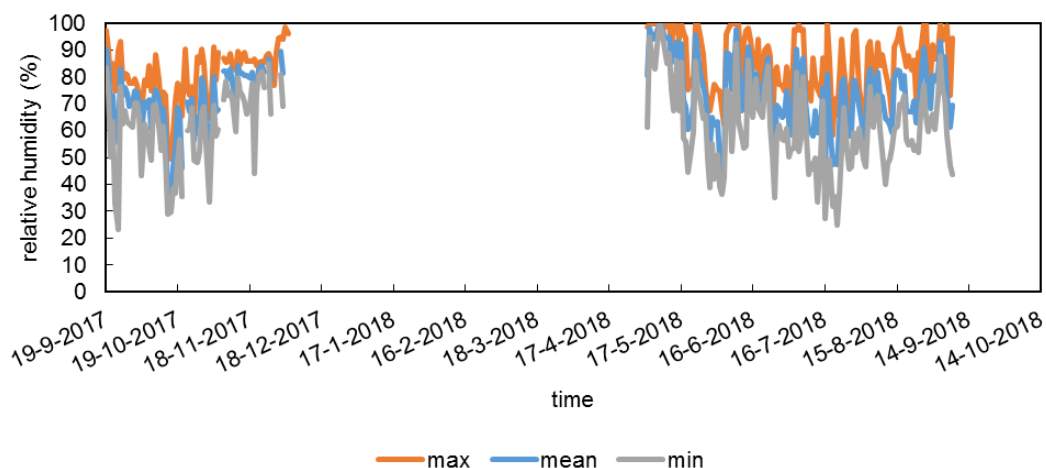


Figure 127 – Recorded maximum, mean and minimum daily relative humidity at Mount Faito.

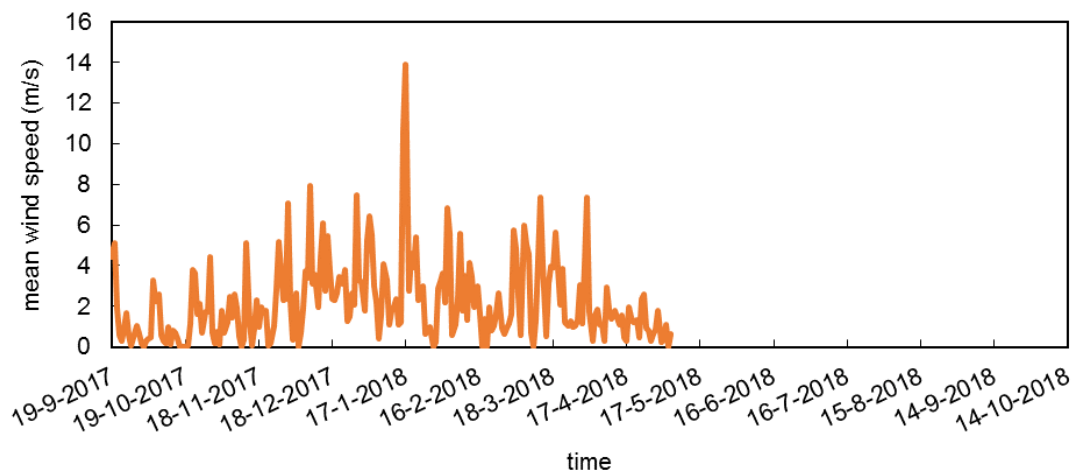


Figure 128 – Recorded mean wind velocity at Mount Faito.

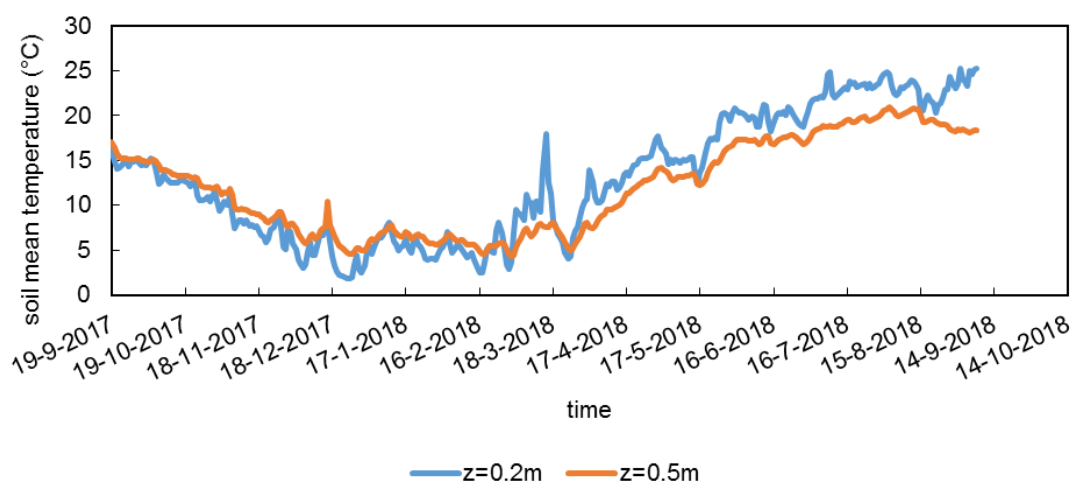


Figure 129 – Recorded mean soil temperature at the depths of 0. 2m and 0.5 m at Mount Faito.

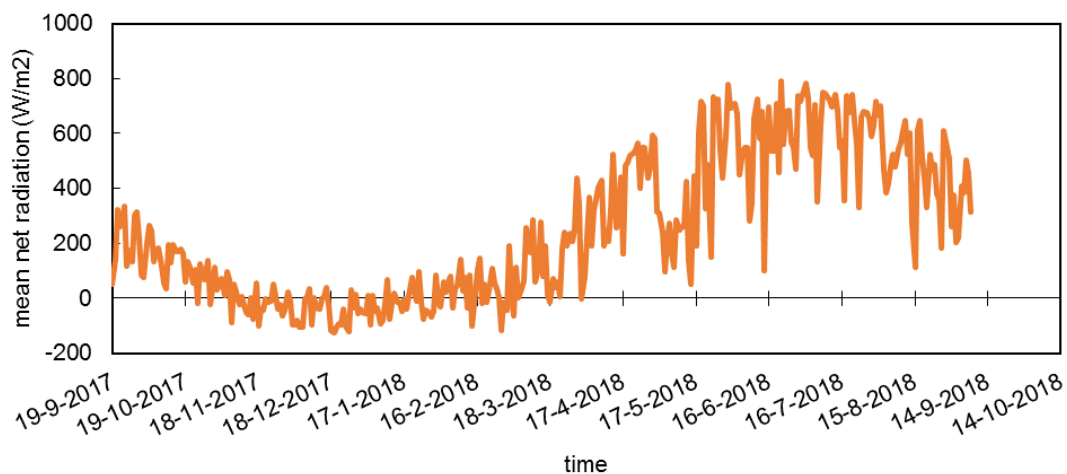


Figure 130 – Recorded net radiation at Mount Faito.

- **Evapotranspiration**

The reference evapotranspiration was calculated using the data of the meteorological station at Mount Faito using the procedure described in the previous sections (Figure 131). The “ET0 short” was calculated based on the temperature records and extra-terrestrial radiation, which provides higher values of reference evapotranspiration (Figure 132). The comparison of those two methods allows the determination of a correction to be used when there are missing meteorological data.

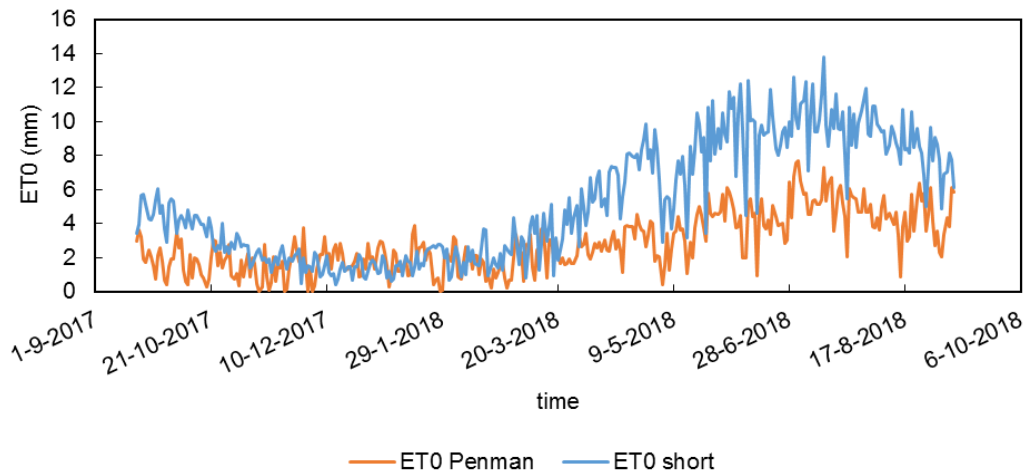


Figure 131 – Reference evapotranspiration (ET0) calculated with the meteorological data of Mount Faito.

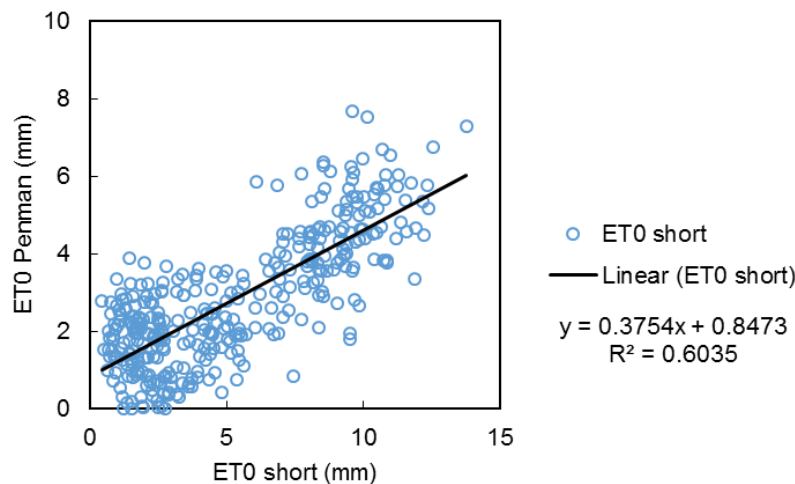


Figure 132 – Comparison of two methods of calculating reference evapotranspiration (ET0).

### 4.3.2 Considerations on vegetation and ground cover

The instrumented profiles are presented in Figure 133. Along these profiles, TDR probes and tensiometers for were installed at different depths to record water content and suction. For each profile, a borehole was



made in which the root density was quantified. The profile T is very close to a tree, uphill from it, and the profile NT is located in a very open tree polygon. The profiles of both cells are located inside similar three polygons. A tree polygon is defined at an area limited by trees inside which all the profiles of a given cell are located. A cell is composed of five profiles (N, S, C, W and E).

A detailed description of the groundcover of the site along the year was already reported in Chapter 2. The monitored area in terms of groundcover and plant growth corresponded to cell 1. A survey of the location of the trees in relation to the installed profiles is presented in Annex O, with respective diameter at breast height of the trees.

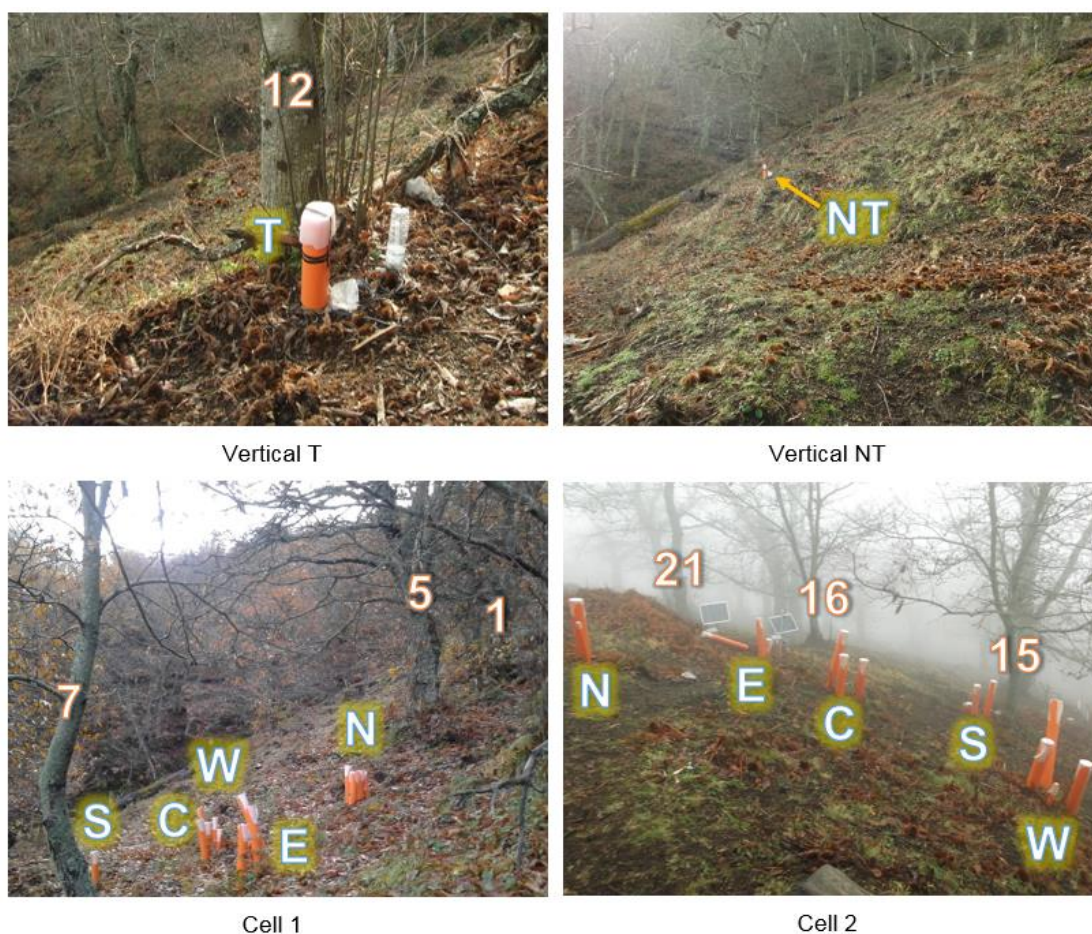


Figure 133 – Location of the soil profiles (identified with letters) in the polygons and trees (identified with numbers).

### 4.3.3 Root distribution

#### 4.3.3.1 Measurements of root density

The root distribution was determined using data from all soil cores extracted. The values of root biomass, number of root tips, root volume and root length per unit volume of soil are presented in Annex P.

The cumulative root biomass with depth relative to the total root biomass found in that borehole shows how the root distribution was along depth in each profile (Figure 134). Cumulative root biomass was related to the thickness of soil layers A1 and A2. The borehole with the highest relative fraction of root biomass was 1C that had a very thin layer A. Most of the roots in this soil core were in the upper 0.2 m of soil. The soil core with the smallest shallow increase in cumulative root biomass was 1S where a major increase in root density was observed at a depth of 0.5 m. This core also had a relatively thick layer A1. Soil core 2C had the most homogeneous distribution of roots throughout the soil profile, with a significant increase of root density below 1 m of depth. In this soil core 2C, the total soil layer A was very thick.

The root distribution in profiles T and NT in terms of dry root biomass is presented separately in Figure 135. The root density in soil A1 is equal independently of the profile but the soil core collected close to a tree (T) presented higher biomass in soil A2.

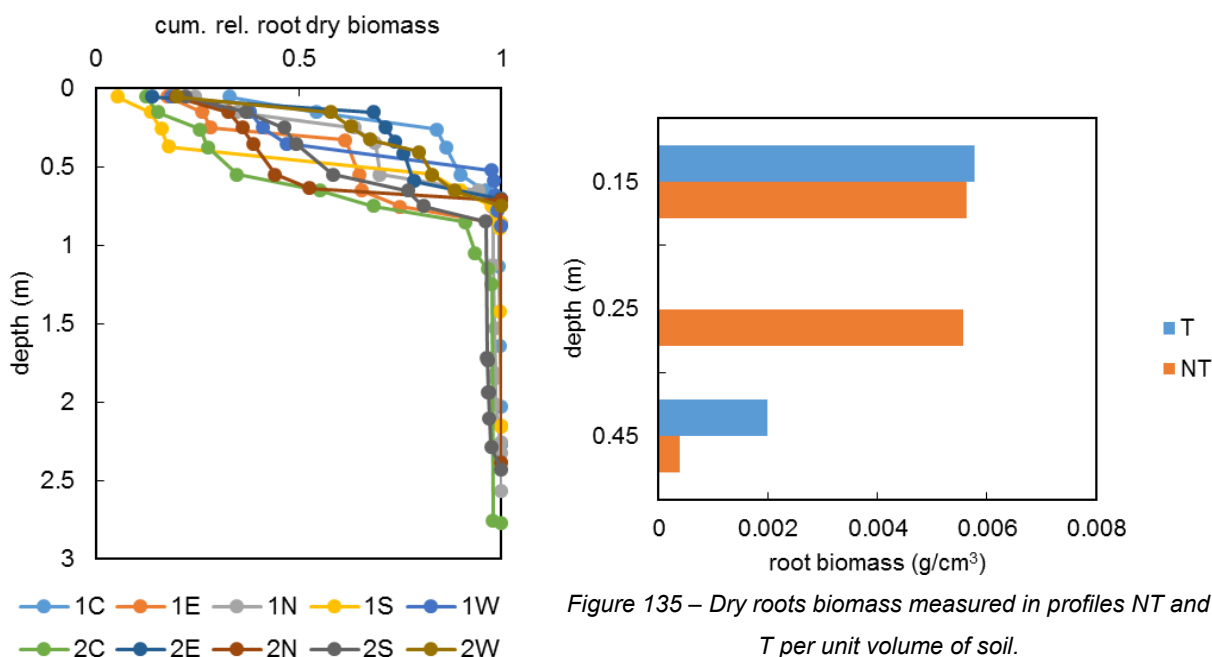


Figure 134 – Increase in cumulative root dry biomass relative to the total root biomass with depth for all soil cores.

Figure 135 – Dry roots biomass measured in profiles NT and T per unit volume of soil.

A typical example of the root trait data from one soil core is presented in Figure 136, with some variability in the data. When processing the mean values of the root traits with depth, a continuous decrease of in values was found (Figure 137 to Figure 140). Root density was negligible at depths between 1.5 and 2 m, corresponding to the soil layer B (Figure 134 and Figure 140). Again, some roots were identified in layer C at depths greater than 2 m. Root length for the diameter class “0<D<0.5” was substantially higher than the root length of the remaining diameter classes. The diameter class with the highest value of number of root tips was again the class “0<D<0.5”.

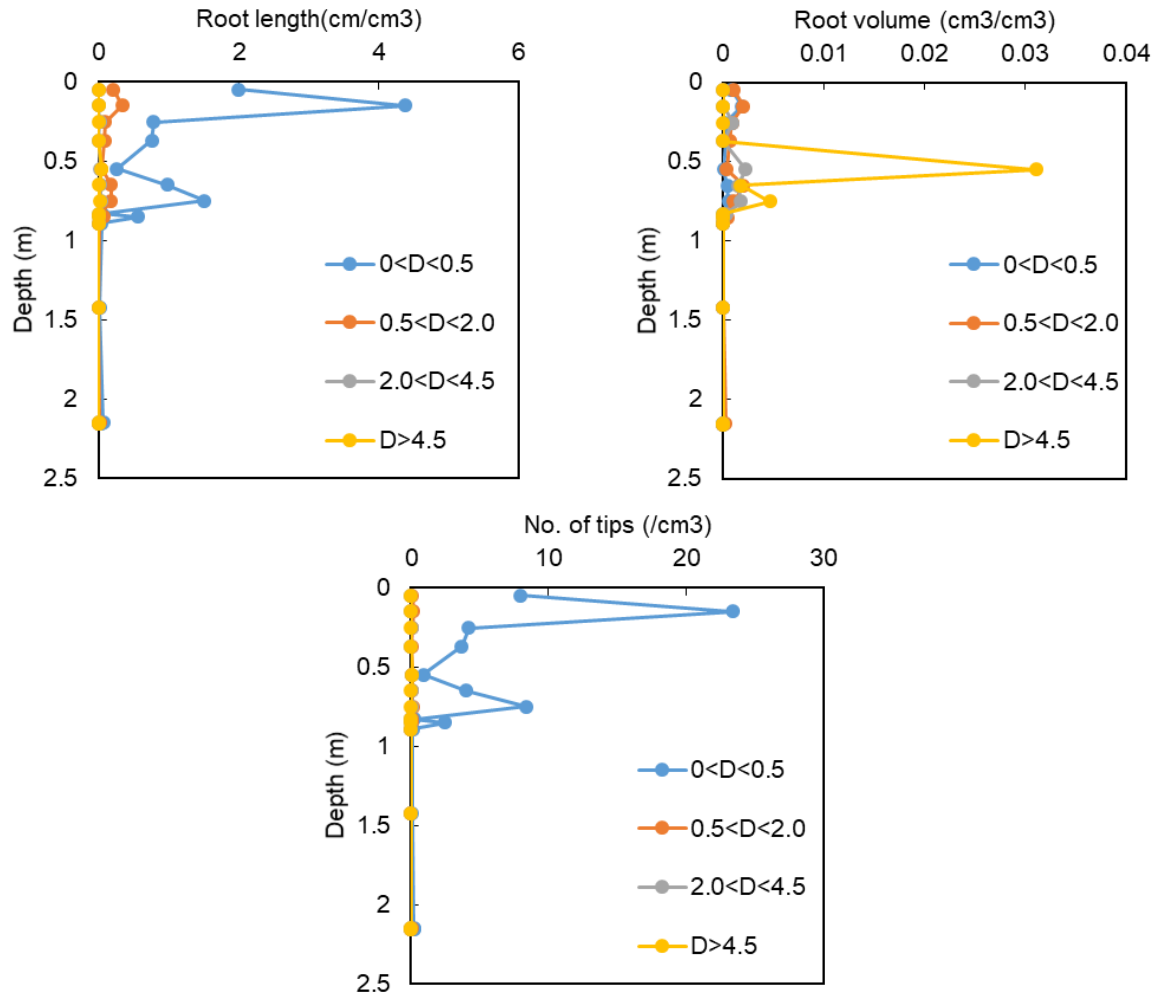


Figure 136 – Example of grouped root characteristics in four diameter classes for a typical soil core (1S).

The number of root tips obtained from the image analysis seems high given the fact the control soil volume is 1 cm<sup>3</sup>. For example, in Figure 139, there were 15 root tips per unit volume of soil at a depth of 0.05 m, probably because WinRHIZO cannot distinguish the root tips that are real root tips from those created by breaking a root. A topological analysis should be performed in order to distinguish real root tips from tips resultant from roots that were broken during the soil coring and washing.

The values of root volume among diameter classes were very similar. However, when a large diameter root was identified (diameter greater than 4.5 mm), the root volume in that section is high (e.g. Figure 138). Therefore, the collection of roots of larger diameter introduces variability into the results because they occur less frequently.

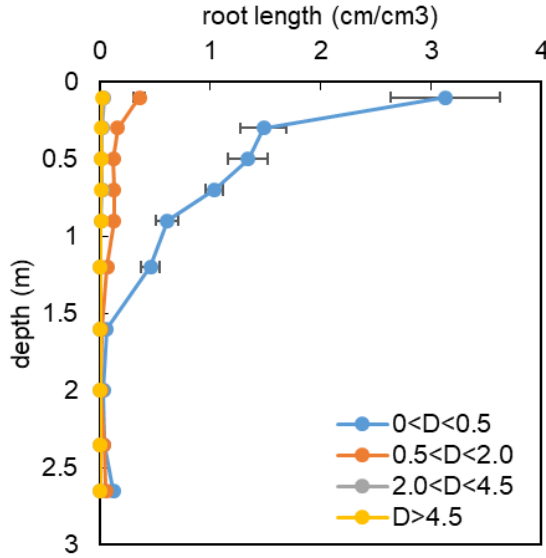


Figure 137 – Mean and standard error of the root length per unit soil volume for four diameter classes with depth.

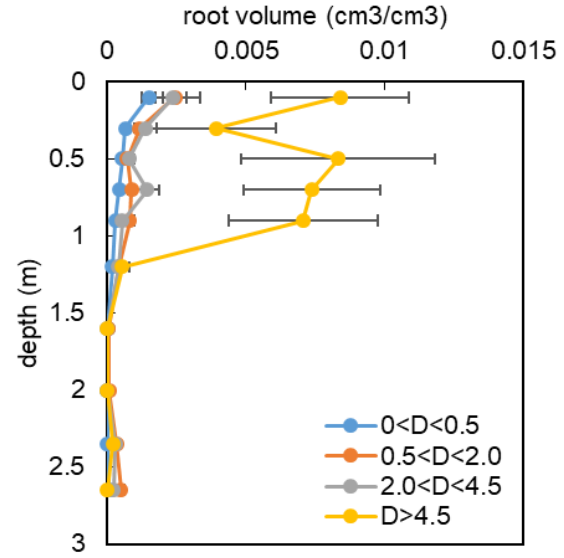


Figure 138 – Mean and standard error of the root volume per unit soil volume for four diameter classes with depth.

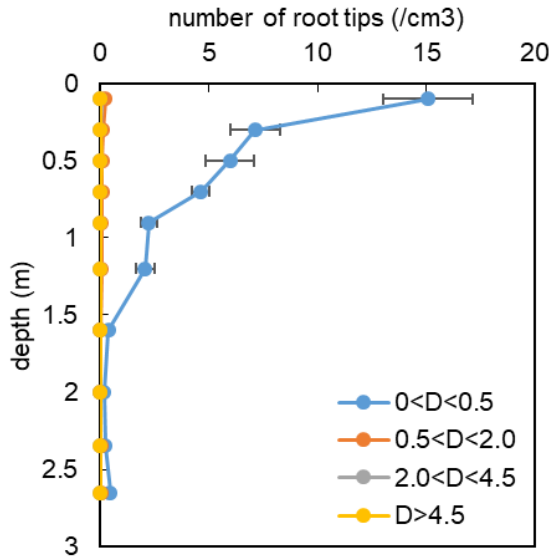


Figure 139 – Mean and standard error of the number of root tips per unit soil volume for four diameter classes with depth.

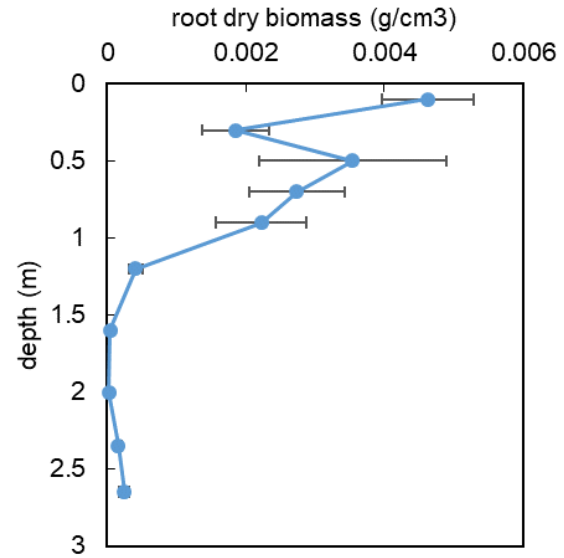


Figure 140 – Mean and standard error of the root dry biomass per unit soil volume with depth.

The models that are based on the study of root traits can be simplified if two or more of the root traits are related among them. Therefore, relationships were tested among mean values of the studied traits (Figure 141).

The coefficient of determination ( $R^2$ ) of the linear interpolations represented in Figure 141(a), relating the roots length to the dry biomass, and in Figure 141(c), relating the number of root tips to the roots dry

biomass, is low. Therefore, the number of root tips and the roots length seem not to be related to the root biomass.

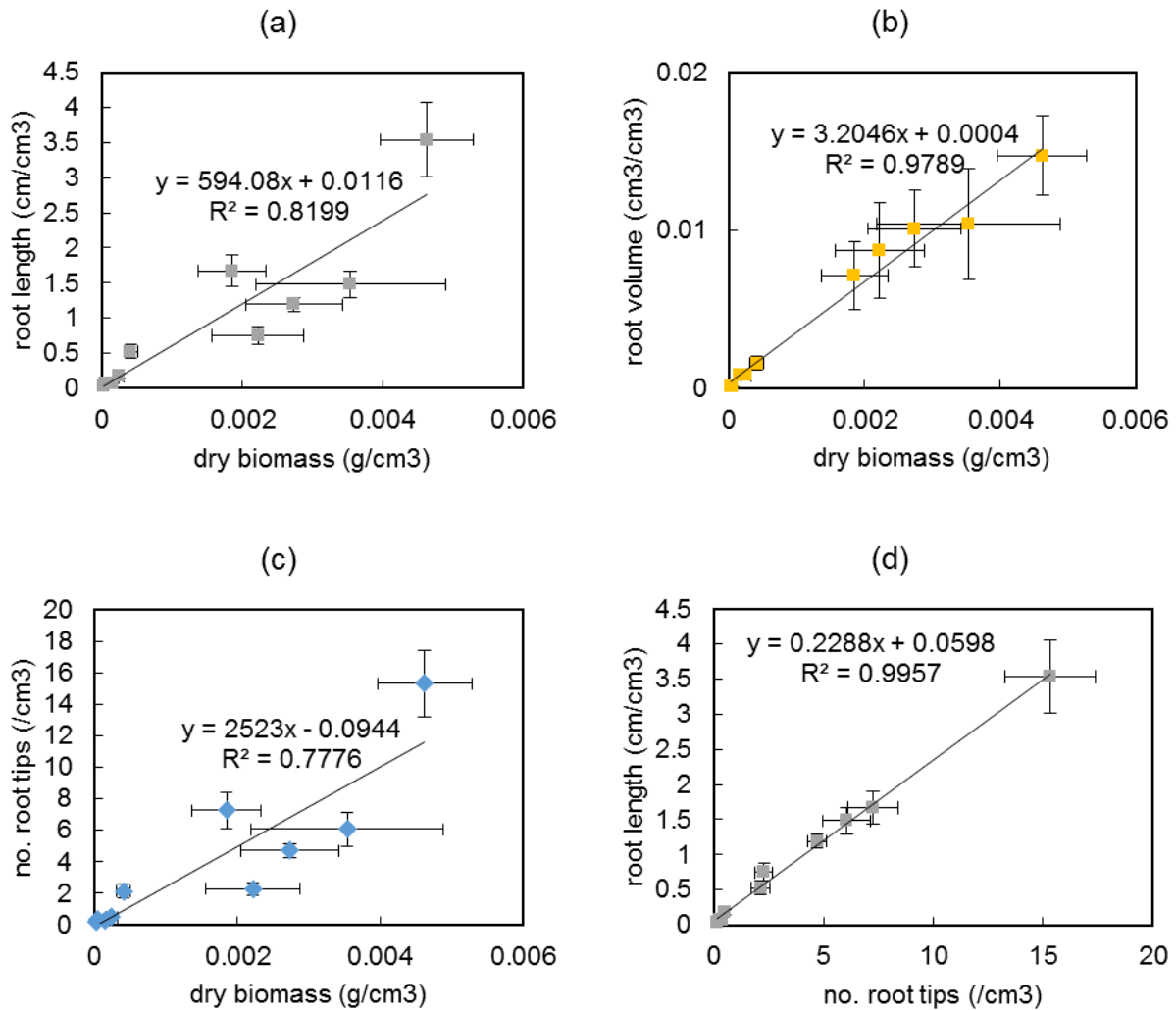


Figure 141 – Relation between root dry biomass and the mean (a) root length, (b) number of root tips, and (c) root volume per unit volume of soil, and (d) the relation between root length and number of root tips.

The root density in terms of biomass is closely related to the root volume as observed in the comparison of Figure 138 and Figure 140. A good fitting of the linear interpolation between root biomass and root volume was found with a  $R^2$ -index of 0.9789, as observed in Figure 141(b). Indeed, root volume and dry root biomass are related through the root wood density, which is a constant.

Unexpectedly, the number of root tips seems related to the root length (Figure 141,d). These two parameters are not related physically in any manner. Nevertheless, if longer roots are highly branched, they will possess a greater number of root tips.

The root characterization for the study of the effect of vegetation on the groundwater regime and on the slope stability cannot be simplified to a single parameter. However, the root volume is closely related to the dry biomass and so one of those parameters can be ignored.

#### **4.3.3.2 Fitting of the root vertical distribution model**

The fitting of the exponential model (Gale and Grigal, 1987) for each profile provided the parameter  $\beta$  presented in Table 29 for root densities in terms of root length, volume, number of tips and biomass. The fitted parameter  $\beta$  using other root densities is presented in Annex Q, as well as the  $R^2$ -index of the fittings. The graphic representation of the model is made in Figure 142.

Note that in Figure 142, the profiles with the highest  $\beta$ -value present root densities more homogeneously distributed along depth.

*Table 29 – Parameter  $\beta$  obtained per soil profile.*

Soil profile	Biomass	Root length	Root volume	Number of tips
1C	0.94	0.98	0.98	0.98
1E	0.98	0.98	0.98	0.98
1N	0.96	0.98	0.97	0.97
1S	0.98	0.99	0.99	0.98
1W	0.97	0.98	0.98	0.98
2C	0.99	0.98	0.98	0.98
2E	0.96	0.98	0.98	0.97
2N	0.98	0.97	0.98	0.97
2S	0.98	0.97	0.98	0.97
2W	0.96	0.99	0.98	0.98

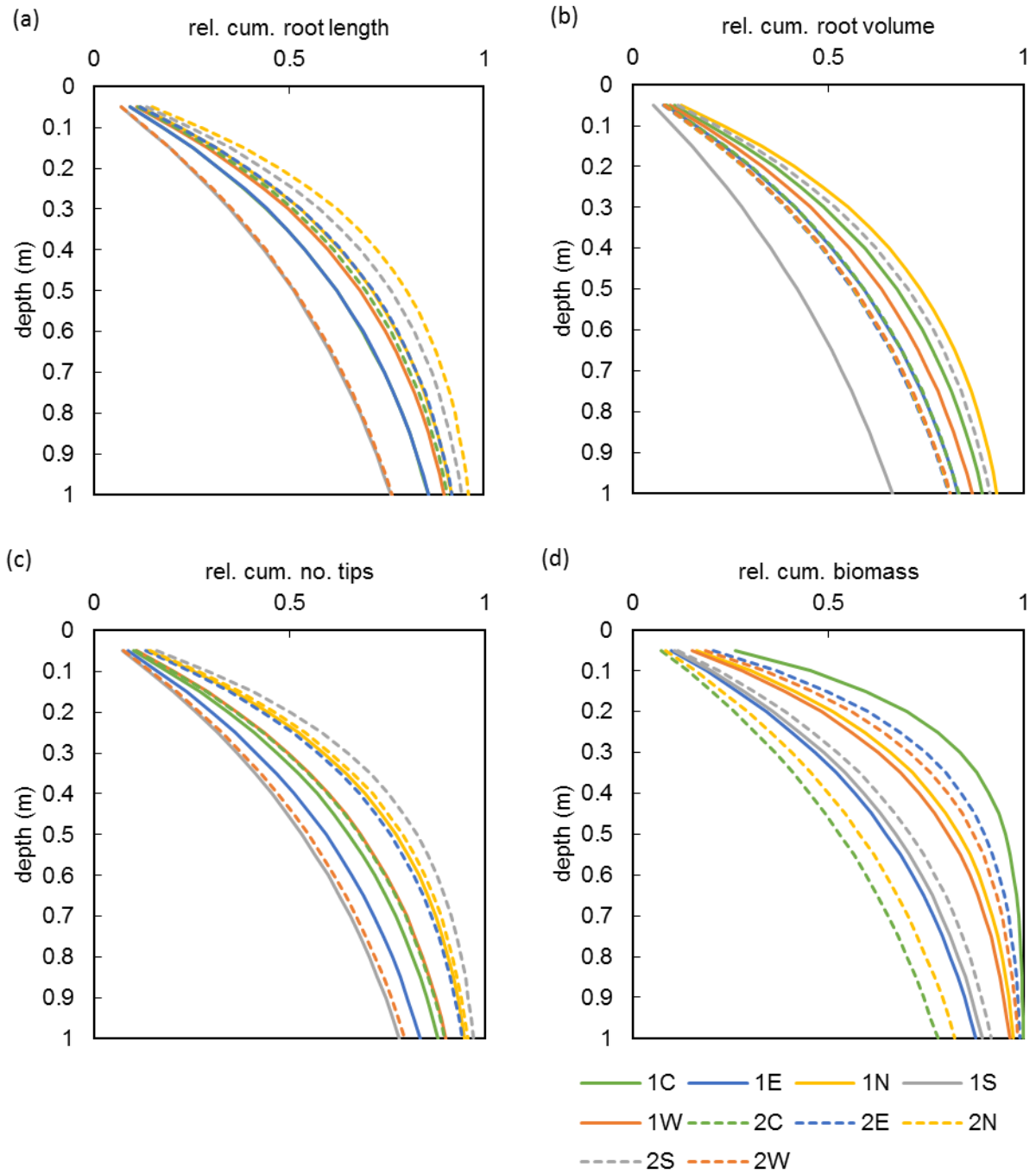


Figure 142 – Cumulative relative (a) root length, (b) root volume, (c) number of root tips, and (d) root biomass with depth given by the fitted  $\beta$ -model.



#### **4.3.3.3 Fitting of the root lateral distribution model**

The root lateral distribution was assessed through the calculation of a competition index for each soil core and related to a root density indicator. Several root density indicators were tested as well as range of influence of trees and relative position in the slope (uphill or downhill).

The fitting of the model to the experimental data is presented in Annex R. An example is presented in Figure 143 in which the root density indicator was the mean root dry biomass present from 0.25 m to 0.5 m. In this example, the best fitting was obtained when all the trees were considered within a range of 10 m from the position of collection of the soil core. The quality of the fitting decreased progressively with the decrease of the trees considered influence area and for when only the trees downhill from the profiles were considered.

The adequacy of the root density indicator was assessed through the coefficient of determination  $R^2$  presented in Figure 144. This study also allowed to determine what is the spatial range of influence of trees and if that influence is equal uphill and downhill. A good fitting is considered when the coefficient of determination is close or above 0.4 (Mao *et al.*, 2015). The case in which was considered all trees presented better fittings than when only uphill or only downhill trees were considered. The  $R^2$ -index was never above 0.4 when only the nearest tree was considered. The range of tree-to-profile distance of 10 m presented the greatest number of good fits (6, versus 4, when the distance was 8 m).

The most adequate root density indicators to investigate each effect of roots is presented in Table 30. The recommended root density indicator to investigate root cohesion distribution in space is the root biomass considering all the trees in a range of 10 m from the profile. The best root density indicator to study the effect of vegetation on water infiltration is the  $\beta$ -value in terms of root length and the root biomass root for all the trees in the range of 10 m from the profile.

The number of root tips did not perform well as a root density indicator. This might be because of the great variability associated to the parameter or its homogeneous distribution in space. Therefore, a good root density indicator to study the relation between the roots and water uptake was not found. Nonetheless, the number of root tips from 0.15 m to 0.3 m of depth can be considered if all the trees in a range of 10 m from the profile are used for the calculation of the competition index.



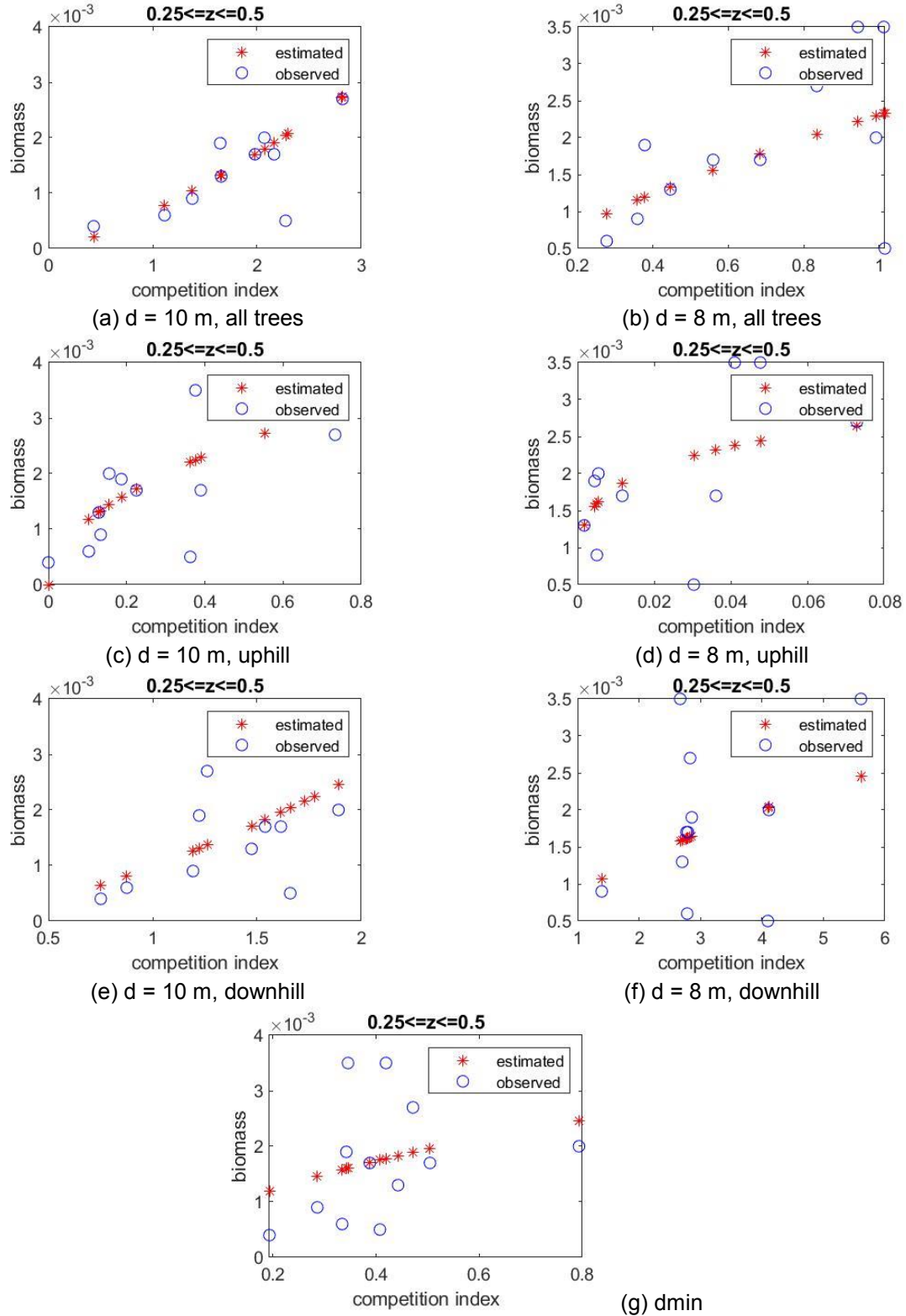


Figure 143 – Spatial root distribution fitting to the root density in terms of biomass ( $0.25 < z < 0.5$  m).

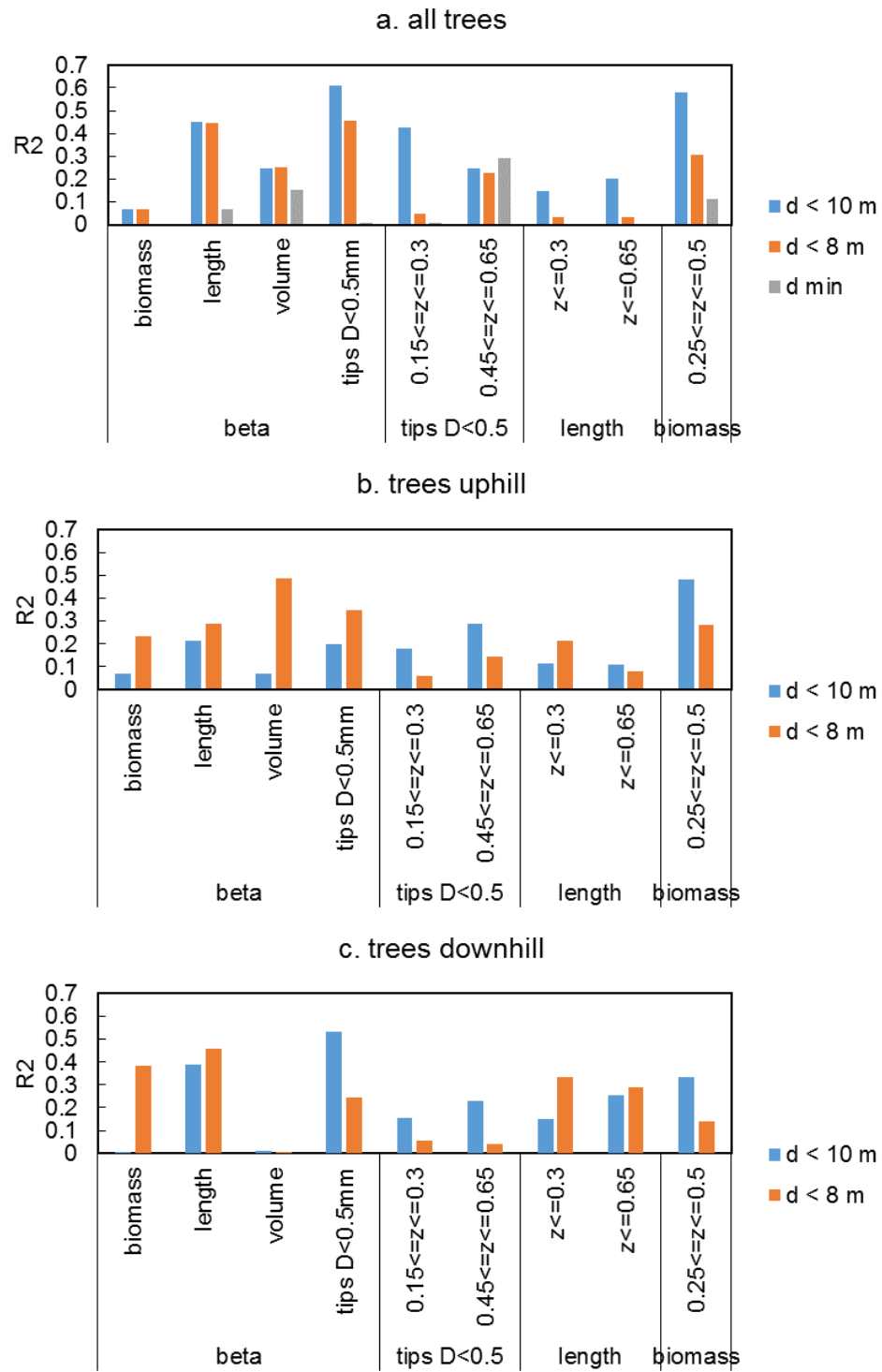


Figure 144 – Determination coefficient ( $R^2$ ) of the root lateral distribution for different root density indicators.

Table 30 – Recommended spatial root distribution models.

Focus/Study object	Root density indicator	Tree distance	Tree relative position
Root cohesion	Biomass	10	All
Infiltration	$\beta$ -value (length)	10	All
	Biomass	10	All
Water uptake	Tips $D < 0.5$ ( $0.15 \leq z \leq 0.3$ )	10	All
	-	-	-

#### 4.3.4 Equipment calibration

##### 4.3.4.1 Relation between dielectric constant and volumetric water content

The calibration results of the relation between volumetric water content and dielectric constants based on TDR are presented in Dias *et al.* (2018). The results of this calibration were compared to those of Papa and Nicotera (2012) for pyroclastic soils sampled at the Monteforte Irpino test site (40°54'13.11"N, 14°40'24.21"E; Avellino, Southern Italy). The experimental data in the present work was expanded in order to take into account the full range of dielectric constants measured in situ.

Firstly, the soil in Mount Faito was compared to the one of Monteforte in terms of physical properties (dry density and specific gravity), as presented in Table 31, and in terms of grain size distribution, as shown in Figure 145. The grain size distribution of the soils of Mount Faito and Monteforte fall in the same range. The physical properties of both soils are similar as well. Therefore, it was considered adequate their comparison in terms of dielectric constant and correspondent volumetric water content.

Cylindrical soil samples were used to determine the relationship between volumetric water content and dielectric constant. Five samples were tested out of which three were undisturbed and two were compacted at the laboratory (signed with “r” in Table 32). The porosity and sample size are summarized in Table 32.

Table 31 – Mean soil physical properties of Mount Faito (A1, A2 and C1) and of Monteforte (1, 2 and 6 in Pirone *et al.*, 2015a) (adapted from Dias *et al.*, 2018).

Soil	A1	1	A2	2	C1	6
Specific gravity	2.580	2.65	2.688	2.66	2.666	2.57
Dry density (g cm <sup>-3</sup> )	0.857	0.821	0.804	0.792	0.648	0.727
Porosity	0.668	0.69	0.701	0.70	0.757	0.72

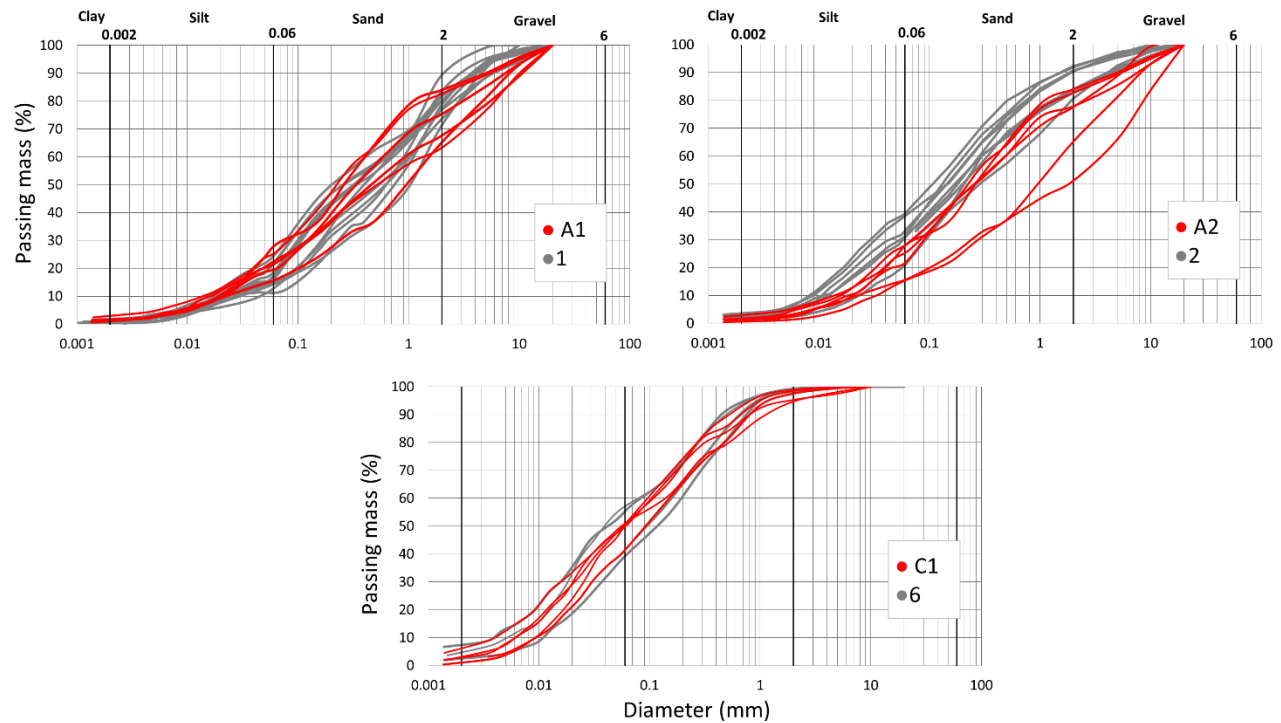


Figure 145 – Comparison of the grain size distribution of the soil of Mount Faito (A1, A2, C1) and Monteforte (1, 2, 6) (adapted from Dias et al., 2018).

Table 32 – Properties of the tested samples (adapted from Dias et al., 2018).

Soil	A1	A2	A2 r	B r	C1
Sample height (cm)	22.2	15.7	18.0	16.5	20.8
Dry density (g cm <sup>-3</sup> )	0.746	0.780	0.785	0.672	0.612
Porosity	0.711	0.710	0.709	0.737	0.758

Several wetting and drying phases were performed but little to no deviation was observed and the measured values follow the same trend (Figure 146). These small deviations maybe have been caused by small settlements occurring upon wetting. Therefore, the calibration curves fitting was made merging data of the wetting and drying paths. For soil A2, when two different samples were used to do the calibration, a deviation is observed in which the compacted sample (r) presents higher volumetric water content for the same dielectric constant value. The differences are more evident for values of dielectric constant higher than 25 even though both samples present the same porosity.

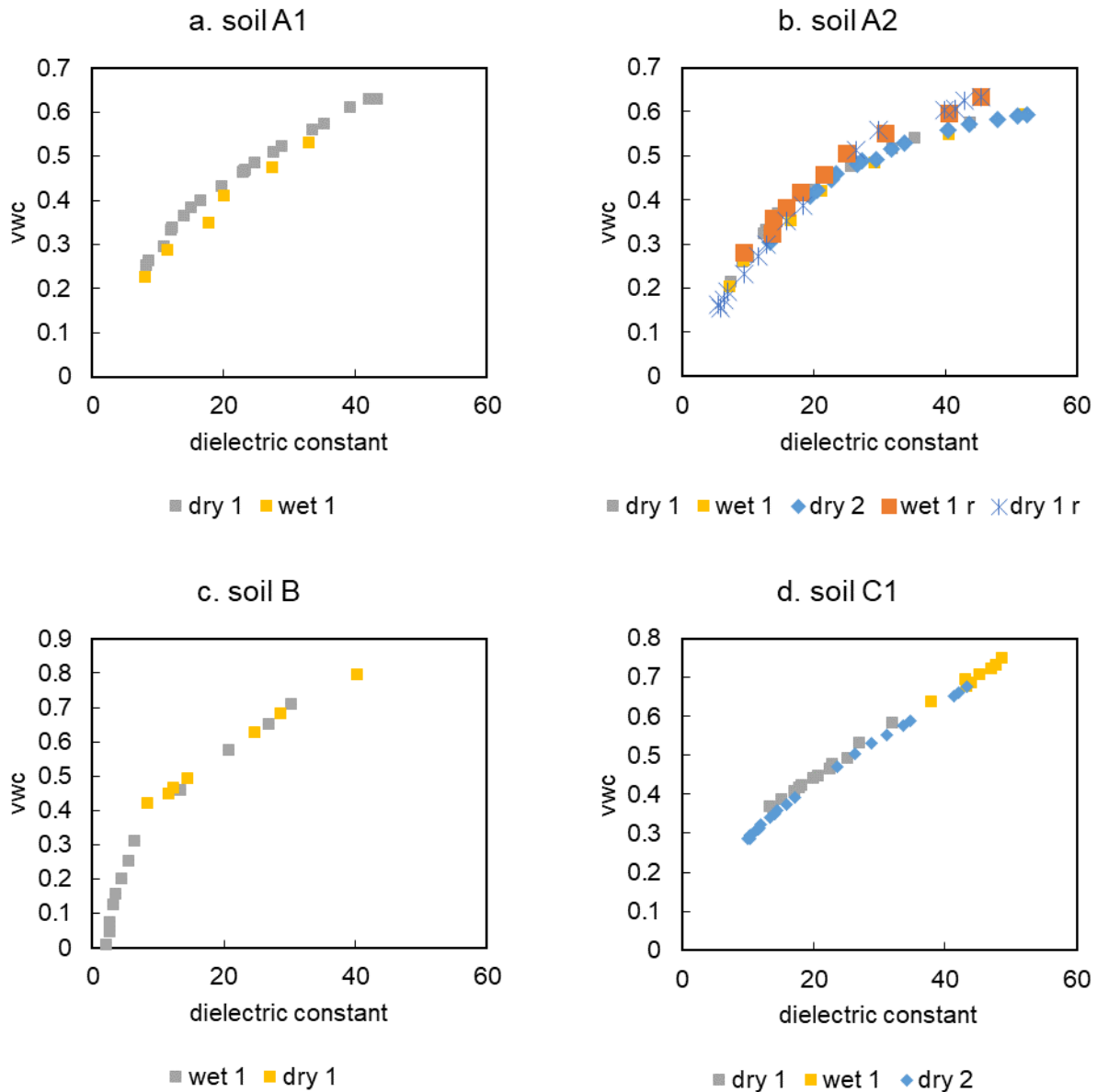


Figure 146 – Soil dielectric constant and respective volumetric water content (vwc) along the wetting and drying phases of each tested soil.

The need for the calibration of models that relate the dielectric constant to the volumetric water content of pyroclastic soil is evident in Figure 147. Indeed, the commonly used equations, such as Topp and Ledieu (Topp *et al.*, 1984; Ledieu *et al.*, 1986), underestimate the soil volumetric water content of the tested soil for the whole range of measured dielectric constant values.

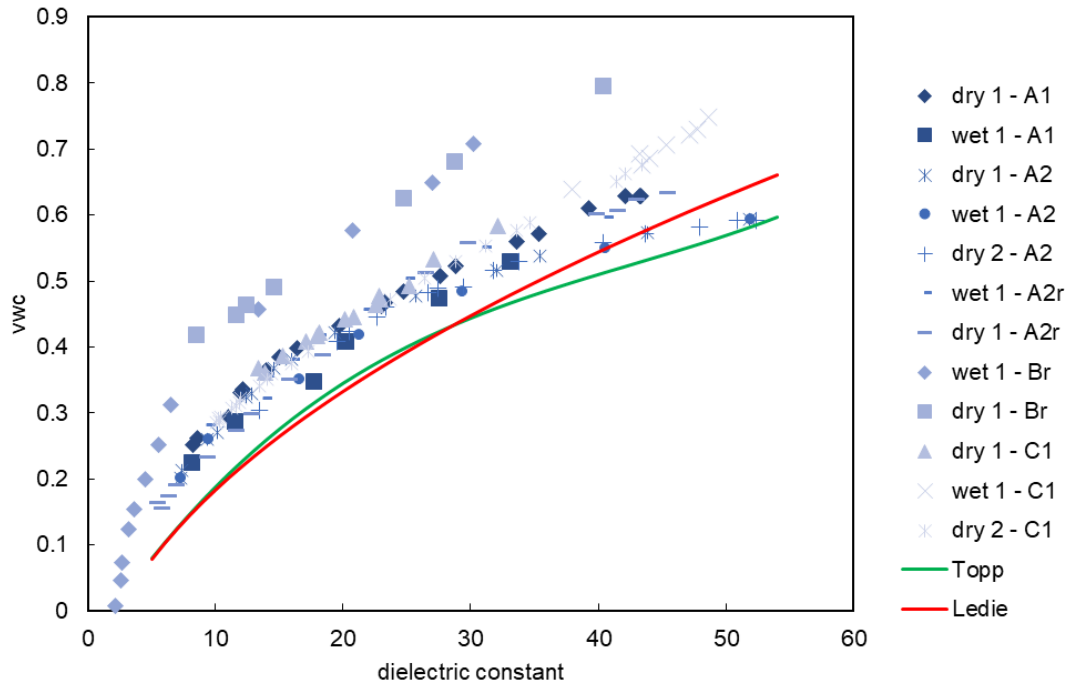


Figure 147 – Comparison of the dielectric constants and volumetric water content (vwc) of all tested soils to the universal equations (Topp and Ledie).

A fitting of the polynomial, logarithmic and Roth models to the experimental data was performed and the constants are presented in Table 33 to Table 35 as well as the  $R^2$ -index. The polynomial and the logarithmic model provided the best overall fitting to the experimental data. The Roth model was the one with the poorest fitting which may be due to: (1) the incorrect estimation of the solid particles dielectric constant ( $\epsilon_s$ ) because volcanic soil presents higher  $\epsilon_s$  values than other soils; or (2) lack of distinction of the dielectric constants of absorbed and free water (Dias *et al.*, 2018).

Table 33 – Calibration parameters of the polynomial model.

Soil	$a \cdot 10^{-6}$	$-b \cdot 10^{-4}$	$c \cdot 10^{-2}$	$d \cdot 10^{-2}$	$R^2$
A1	6.450	6.424	2.935	4.541	0.9817
A2	4.132	5.748	2.986	1.500	0.9889
A2r	1.891	4.207	2.871	1.153	0.9926
Br	30.066	2.413	7.063	-8.960	0.9864
C1	5.415	5.431	2.773	5.812	0.9971

Table 34 – Calibration parameters of the logarithmic model.

Soil	a	b	R <sup>2</sup>
A1	-0.2547	0.2304	0.9756
A2	-0.1859	0.2003	0.9910
A2r	-0.2716	0.2362	0.9857
Br	-0.1838	0.2574	0.9944
C1	-0.3787	0.2781	0.9821

Table 35 – Calibration parameters of the Roth model.

Soil	$\epsilon_s$	$\alpha$	R <sup>2</sup>
A1	4.54	0.425	0.9813
A2	4.75	0.428	0.9550
A2r	4.77	0.408	0.9839
Br	4.50	0.073	0.9938
C1	4.44	0.451	0.8749

In Figure 148, the experimental data of Mount Faito and respective calibrated models are compared with the curves provided by Papa and Nicotera (2012) referred by “P&N” and correspondent number of the soil. Three different models are presented: the polynomial (referred as “Poly”), the logarithmic (referred as “Log”), and Roth model (referred as “Roth”).

The curves provided by Papa and Nicotera (2012) fit the experimental data of Mount Faito reasonably well. The curves of Monteforte were calibrated for volumetric water contents lower than 0.50, which leads to a bad estimation of the water content in the soil of Mount Faito when used outside the range of calibration. This is very obvious in soil A2. In soil A1, the curves of Papa and Nicotera (2012) underestimate the water content, except for the Roth model. The logarithmic model fitted satisfactorily the data over the complete range of values and the polynomial model performs well when the dielectric constant is lower than 30 (Dias *et al.*, 2018).

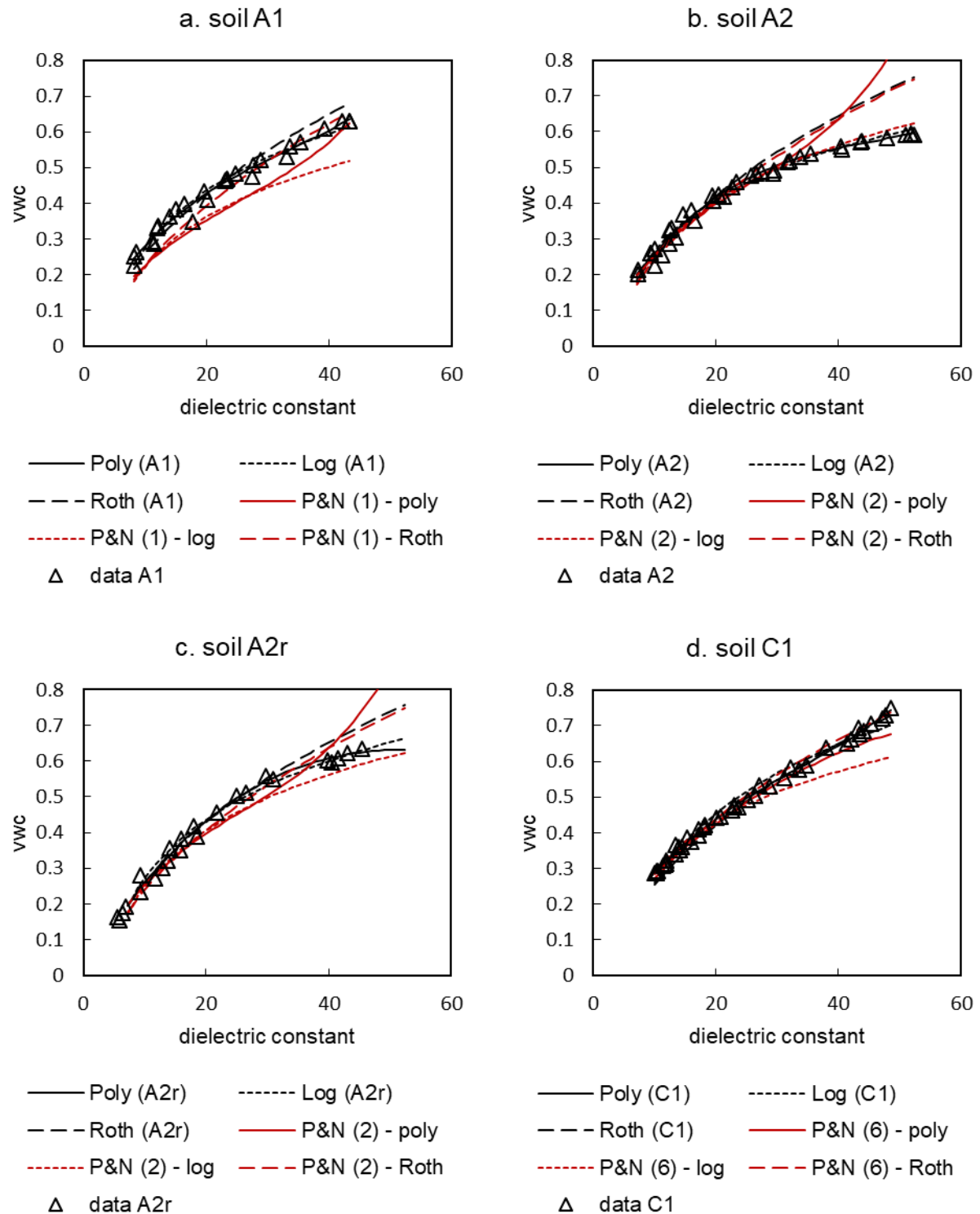


Figure 148 – Comparison of the models fitted to Mount Faito data and Monteforte to the experimental data.

The model that best fitted the experimental data of soil B was the logarithmic, with the lowest  $R^2$  value. The Roth model presented a good fit but seems to underestimate the volumetric water content for values of



dielectric constant higher than 30 (Figure 149). The polynomial model presents the worst fit. The dielectric constant of the soil tested by Papa and Nicotera (2012) is significantly higher than the one of Mount Faito, that might be caused by the higher mean porosity of 0.799 present in Mountforte pumices. A higher porosity implies that for the same volumetric water content there is more water which increases the value of the dielectric constant of the soil.

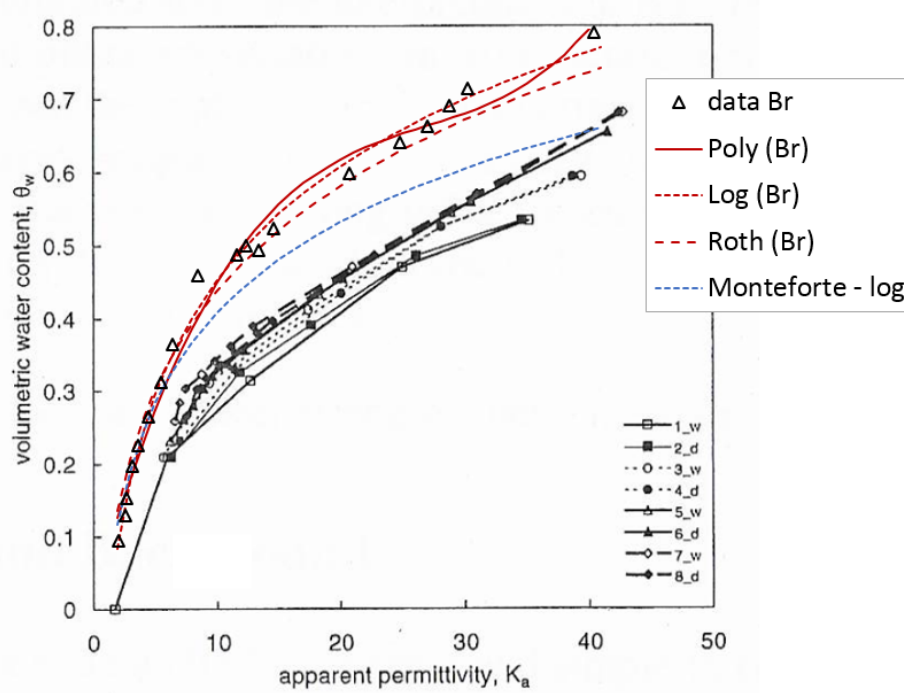


Figure 149 – Comparison between the experimental data of soil B and the soil studied by Papa and Nicotera (2012).

The polynomial model was adopted for soil A1 and A2. In case of soil A2, the parameters adopted corresponded to the reconstituted sample. The model adopted for soil B was the logarithmic using the calibration parameters developed in this work. The calibration of the relation between volumetric water content and soil dielectric constant was not performed for soil C2. Papa (personal communication) performed the experiment on soil 8 of Monteforte Irpino (Papa and Nicotera, 2012) taking the form of Equation 66.

$$\theta = 3.7 \cdot 10^{-7} K_a^3 - 2.811 \cdot 10^{-4} K_a^2 + 1.74867 \cdot 10^{-2} K_a + 7.62248 \cdot 10^{-2} \quad 66$$

#### 4.3.4.2 Tensiometers

The results of the tests performed for the calibration of the suction measurements and validation of the field measurements using SDEC France tensiometers are described in the points that follow.

- TEST 1 – Calibration of digital measurements

The scheme of the setup used for the experiment is represented in Figure 150, where the pressure at the level of the free water in the tube is null. The pressure at the position of the vacuum dial gauge (analogical) and at the top of the water column in the tensiometer (digital) was estimated based on the vertical distance between the level of the free water and the reference positions.

The test was repeated 3 times and the summary of the results is represented in Figure 151, where the underestimation of the digital measurement is evident with a deviation of 31.85% from the estimated value. A calibration curve was made in order to correct the digital measurements by defining a linear regression. The expression that allows the correction takes the form of Equation 67, where  $s_{real}$  refers to the corrected value of suction and  $s_{digital}$  is the digital measurement given by SMS2500S.

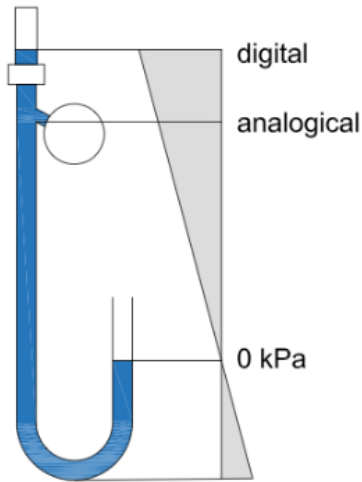


Figure 150 – Scheme of the setup and reference water pressures.

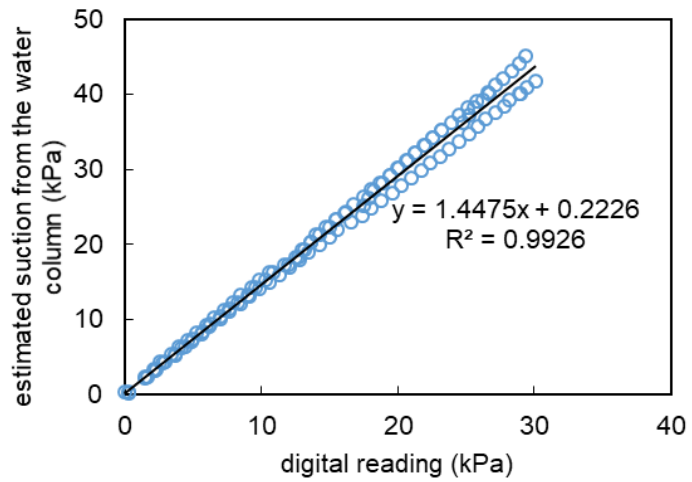


Figure 151 – Relation between digital measurement and the real pressure.

$$s_{real} = 1.4475s_{digital} + 0.2226$$

67

- TEST 2 – Influence of the initial air column in SDEC tensiometers on the measurements and response time determination

The test was performed in traditional SDEC France tensiometers with the same length. However, the initial air column after refill was different, as presented in Table 36. The measured values of suction and air column are represented in Figure 152 and Figure 153, respectively. All the curves of Figure 152 present the same trend independently of the initial air column, stabilizing after 7h. However, the same does not happen with the air column as both test A showed a malfunction of the tensiometer. Nevertheless, tests B and C present a stabilization of the length of the air column simultaneous to the suction measurement

stabilization. These two tests correspond to higher initial air column for which it is concluded that the initial air column does not play a role in the quality of the measurements and that the field monitoring period is adequate for the collection of measurements for this type of tensiometers.

Table 36 – Initial air column of the tests.

Test	Initial air column (cm)
A	22
A	21.4
B	42.5
C	54

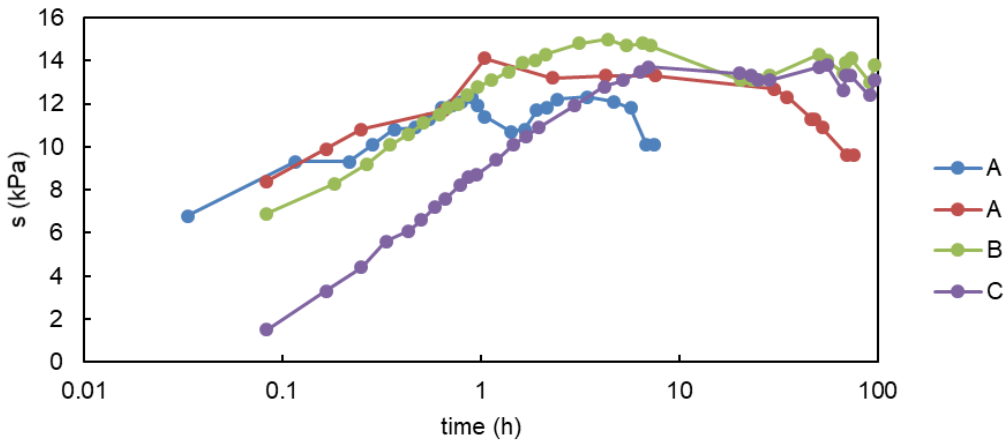


Figure 152 – Evolution of the suction (*s*) along time for different initial air columns.

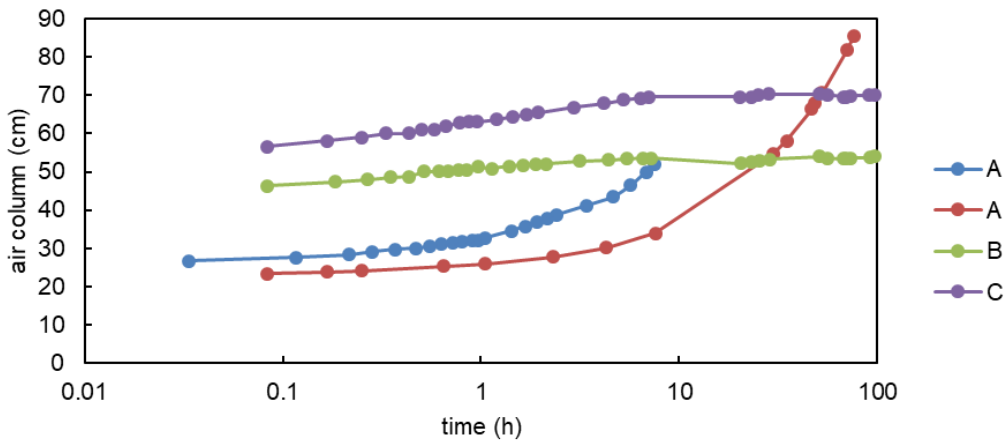


Figure 153 – Evolution of the air column along time for different initial air columns.

Other mechanisms may be present that lead to an underestimation of the measurement. Even though they are not controllable, the operators should be aware of them.

Due the normal working principle of the SDEC France tensiometers, once the tensiometer is installed or refilled, the air pressure in the air column is the same as the atmospheric. Then, the tensiometer loses water because of the negative pore pressure in the soil, which leads to the decrease the pressure in the air column in order to be able to sustain the water column inside the tensiometer. As water was taken by the soil, suction decreased.

Other mechanism that leads to the underestimation of the suction is the air diffusion into the water inside the tensiometer. Due to a difference of pressure between the air in the soil, considered to be atmospheric, and the air inside the tensiometer, which is smaller, the air diffuses into the water in the tensiometers and accumulates on the upper part of the tensiometer. This way, the air column increases and there is a relaxation of the pressure that sustains the water column which leads to a release of water by the tensiometer decreasing the measured suction (Nicotera and Tarantino, 2005).

#### **4.3.5 Monitored suction and volumetric water content**

The monitored volumetric water content and suction along the year is presented in this section complemented by the rainfall data. The individual measurements in all the profiles of water content are reported in Annex S and suction reported in Annex T. The mean volumetric water content measurements are presented in Figure 154, as well as the standard deviation, grouped in layers A, B and C.

Soil A1 and A2 behaved similarly except from August to the end of October, presenting the same trend, but the water content in soil A1 was higher it is shallower and is the first soil layer to be affected by the rainfall events. The rainfall events of September 2<sup>nd</sup> and 11<sup>th</sup> 2017, the first rainfall events with intensities higher than 40 mm after the dry season, caused an increase of water content in soil A1 and A2, which was much greater in the shallowest layer. No major rainfall events occurred in October, which made the water content decreased again. Note that the water content was brought to the level of the winter steady conditions. The rainfall of November 6<sup>th</sup> occurred after the leaf drop and water content did not decrease after that.

The soil B at different presented similar trends. The water content increased with depth during the wet period (December to June). The behaviour was inverted in the summer, from August to October, in which the water content decreased with depth. This behaviour was a consequence of the fact that soil B is coarse and has low water retaining capacity. Soil B showed an increase of water content as a response to the rainfall events in September 2017 but with lower intensity than in soil A1.

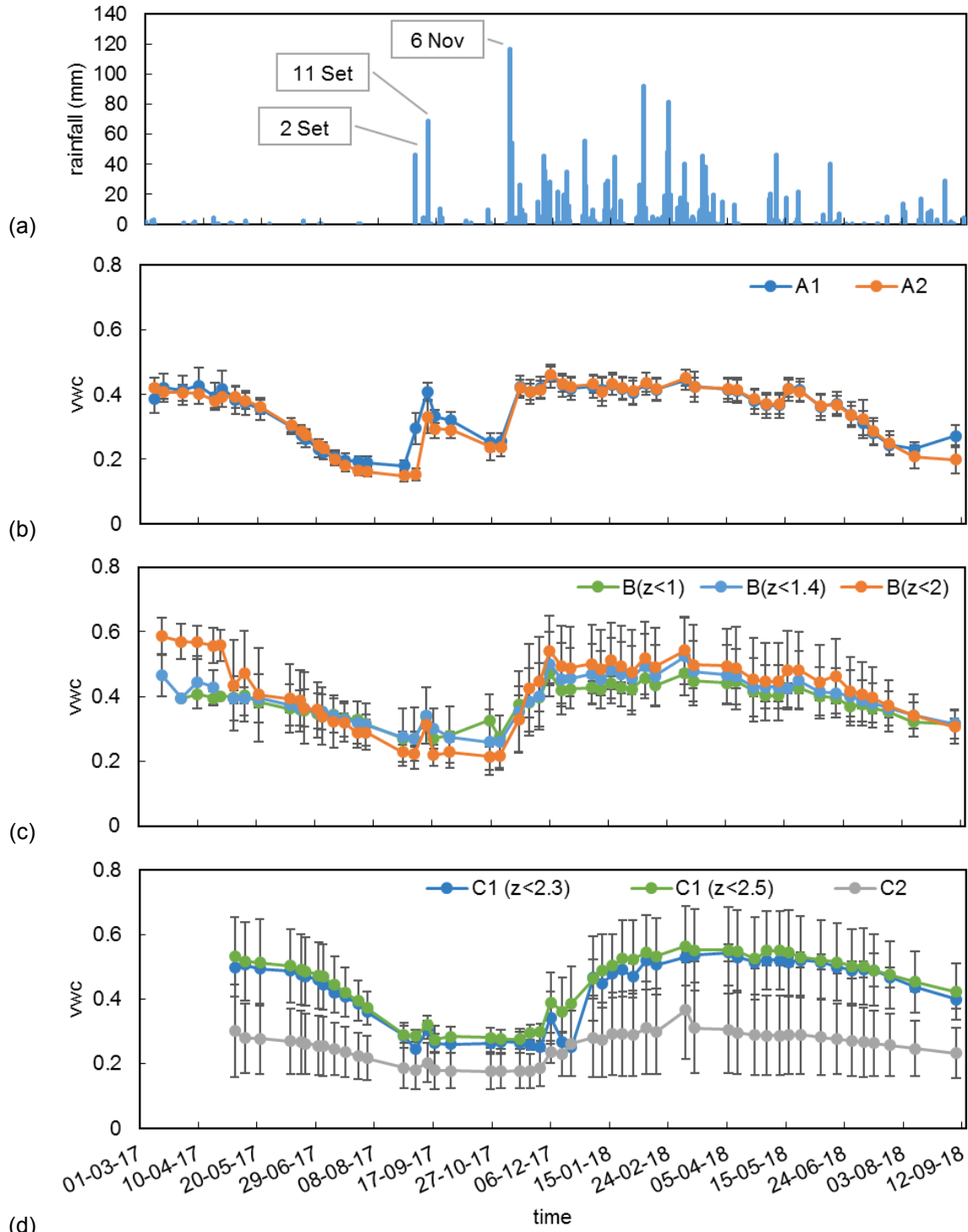


Figure 154 – Daily rainfall (a) and mean and standard deviation of the volumetric water content (vwc) measured in cells 1 and 2 in soil A1 and A2 (b), soil B (c) and soil C1 and C2 (d).

Soil C1 presented lag in the response to rainfall and evapotranspiration in comparison with the upper layers. Note that the lowest value of water content was reached in the end of the dry season (end of September). This soil presented similarly high water content in all depths from April to August, and the water content increased with increasing depth from August to November.

Finally, soil C2 presented a very distinct behaviour from the remaining layers due to its low porosity. The volumetric water content remained almost constant along the year.

The monitored water content in profiles NT (far from the trees) and T (close to the tree) are presented in Figure 155 in comparison to the mean values from the cells monitoring. The water content in the profile T is lower during the entire monitored period in soil A1 and A2. The water content of the profile NT is much more similar to the average values in the cells.

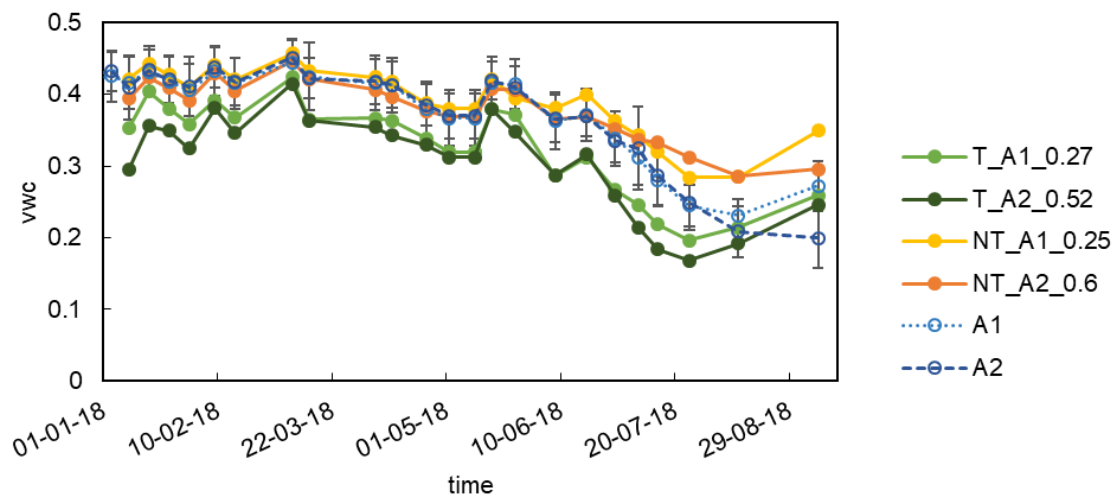


Figure 155 – Volumetric water content (vwc) in the profiles NT and T comparison with the mean values in soil A1 and A2.

The mean and standard deviation of suction is presented in Figure 156. Three phases can be identified as in Pirone *et al.*, (2012, 2015a, 2015b) and Urciuoli *et al.* (2016): (i) a transient phase in which suction increases, followed by (ii) a transient phase during which suction decreases, and (iii) a steady phase with constant low suction. The period corresponding to each of these phases depends on the soil layer because all these phases are delayed with the increase of depth.

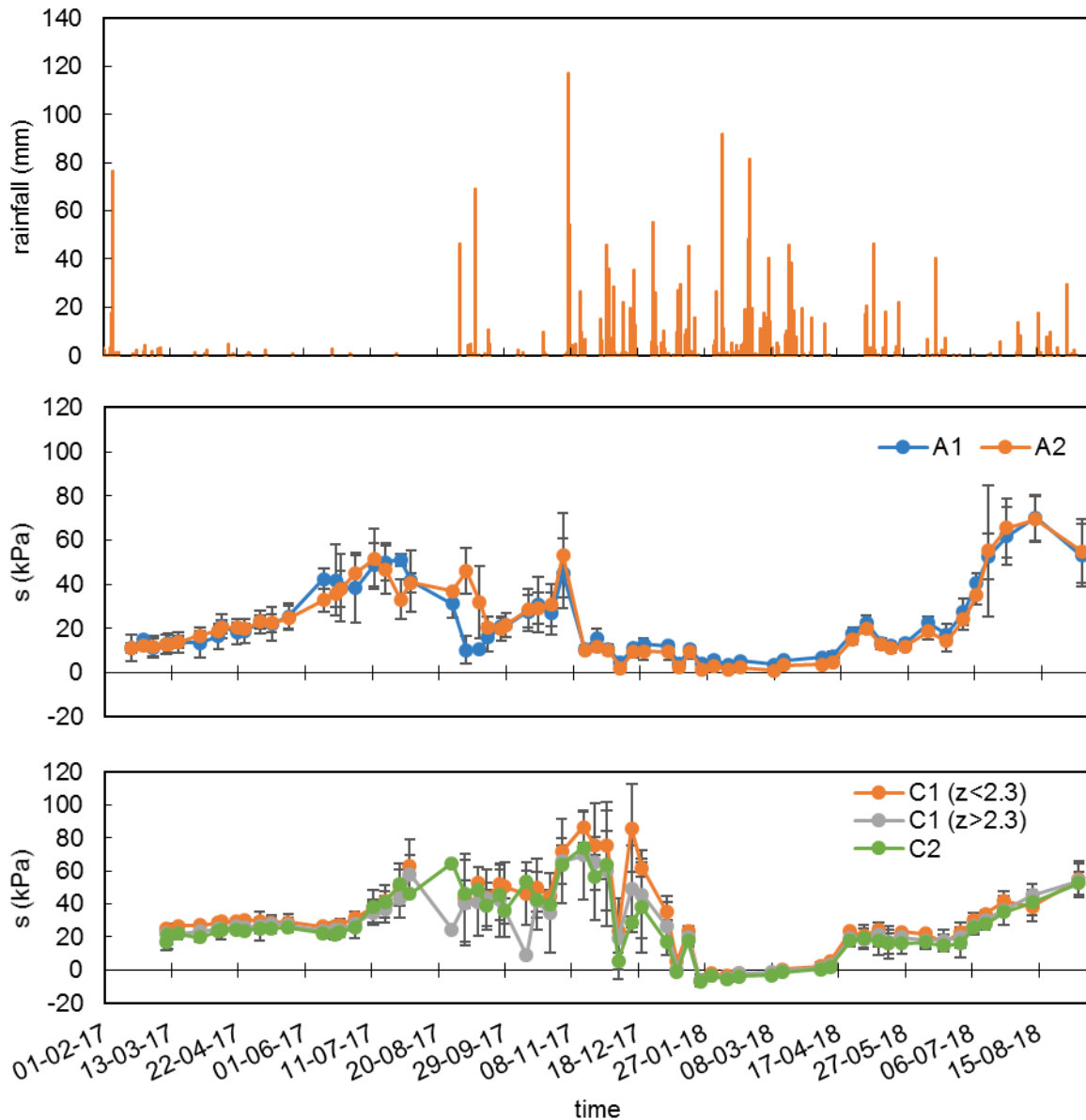


Figure 156 – Average and standard deviation of the suction ( $s$ ) in cells 1 and 2 in comparison with the rainfall.

The steady phase in soil A1 and A2 occurs from November to April but in soil C1 and C2 occurs from January to June in 2017 and until April in 2018. Note that in 2018 the suction appears constant below 10 kPa from January to April 2018 but it increases to 10-20 kPa in May and June. Indeed, the cumulative rainfall during the steady phases were very different. In Moiano meteorological station was recorded a total of 790 mm of rain from September 2016 to April 2017, and 1303 mm from September 2017 to April 2018. In Pimonte meteorological station was recorded a total of 825 mm of rain from September 2016 to April 2017, and 1554 mm from September 2017 to April 2018. Therefore, suction during the first steady state was much higher than in the following year.

The increase of suction started in April in both years in soils A1 and A2. The increase of suction in soil C1 started in June 2016 and in July of the next year. During summer suction can easily exceed measurement range of the tensiometers and some malfunction can be observed in the oscillations detected during August.

The suction presented a quick drop after the rainfall events in September. The rainfall of September 2<sup>nd</sup> led to a decrease of suction of 20 kPa in soil A1. Then, the rainfall of September 11<sup>th</sup> did not change the suction in the soil as it reached values close to its AEV. The first rainfall did not change suction in soil A2 on average but the second rainfall caused a drop of 13 kPa. Soil layers C1 and C2 were not affected by the rainfall as its suction continued to increase. The same can be observed in September of 2018, where suction values in soil A1 and A2 decrease and in soil C1 and C2 continue to increase.

The month of October was dry and suction easily increased to the values usually observed in the summer as evapotranspiration is still high during this period. The rainfall of November 6<sup>th</sup> resulted in a decrease in suction in all soil layers. The suction dropped 34 kPa and 43 kPa in soil A1 and A2, respectively. Suction in soil C1 continued to increase and a decrease of suction ranging from 11 to 2 kPa was measured in the time interval of November 15<sup>th</sup> to 22<sup>nd</sup>, which shows that soil C1 has a response lag of approximately 2 weeks.

The suction measurements in profiles NT and T are compared in Figure 157 with the mean values of each soil layer in the cells. All profiles present the same behaviour from the start of the monitoring until the end of May. The suction in the profile close to the tree increased much faster in June and July than the remaining profiles. The suction in soil A1 in profile NT reached the same values as in profile T but with a delay. The soil A2 in profile NT maintained the suction lower during the summer in comparison with the mean values observed in the cells.

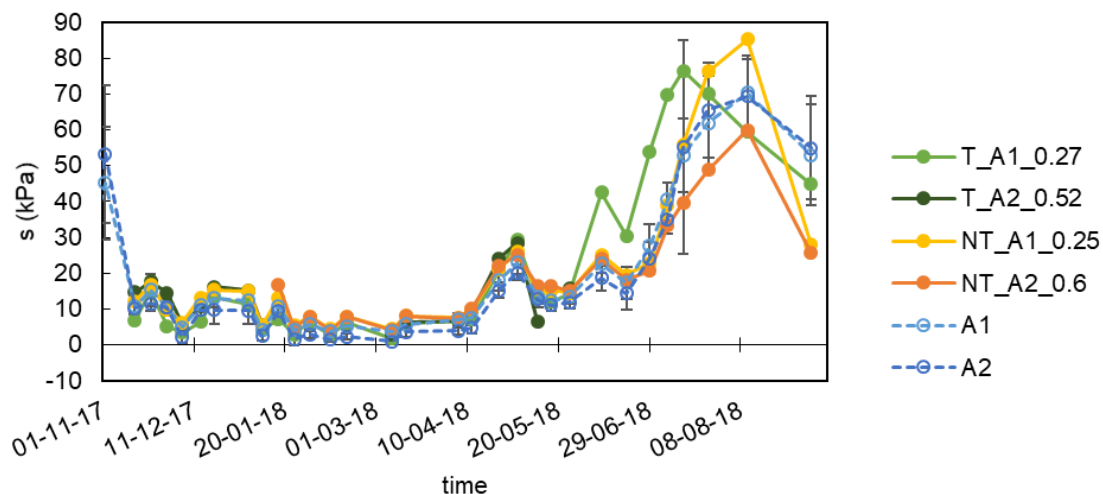


Figure 157 – Monitored suction ( $s$ ) in profiles T and NT in comparison with the mean suction in soil A1 and A2.



#### **4.3.6 Comparison of field data and laboratory water retention curves**

The coupled measurements of water content and suction were represented in the water retention plan (suction versus water content) to be compared with the laboratory tests. A good agreement between field and laboratory measurements is necessary to validate the usefulness of the laboratory hydraulic characterization of the soil.

Laboratory tests are preferable because they are less costly, the boundary conditions are easily controlled and there is more accuracy in the measurements. The field tests are more time consuming, there is more variability and the conditions are harder to control and measure but field measurements allow a closer look into the real behaviour of the system. A perfect agreement between laboratory and site measurements is not possible because of the different boundary conditions, different equipment and methods, and the scale effect.

All the field monitored data is represented in the water retention plan in Annex U. The average values of suction and water content presented in the previous section were compared with the maximum drying and minimum wetting curves obtained in Chapter 3 for the respective soil type (Figure 158). The maximum drying and minimum wetting curves represent the range of possible values because they were derived from the main drying curves.

The water content tends to values close to or below the water content at saturation of the main wetting curve envelope. This might mean that the porosity of the samples tested in the laboratory was higher than the field soil. The samples tested in the laboratory were in fact undisturbed but collected at shallower depths. The differences are especially evident in soil C1. The samples of soil C1 were collected at an average depth of 2 m but the instruments installed in situ ranged from 2.1 to 2.8 m.

The hysteretic model approximates the field behaviour to the laboratory characterization. Indeed, the paths followed in the field correspond to scanning curves that are considered scaled main drying curves to account for the air entrapment.

The hydraulic characterization of soil C2 in the laboratory and the measured results in the field are completely different. The high AEV and presented in laboratory and field results show that the soil is actually fine but the porosity of the samples and field conditions result in a huge overestimation of the water content at saturation. The hydraulic characterization of soil C2 performed in the laboratory should be disregarded, as it will not be able to reproduce the hydraulic behaviour of the suction in the site.

If soil samples are to be collected for laboratory hydraulic characterization, soil consolidation can be performed to reduce soil porosity in order to obtain a better agreement between field and laboratory measurements.

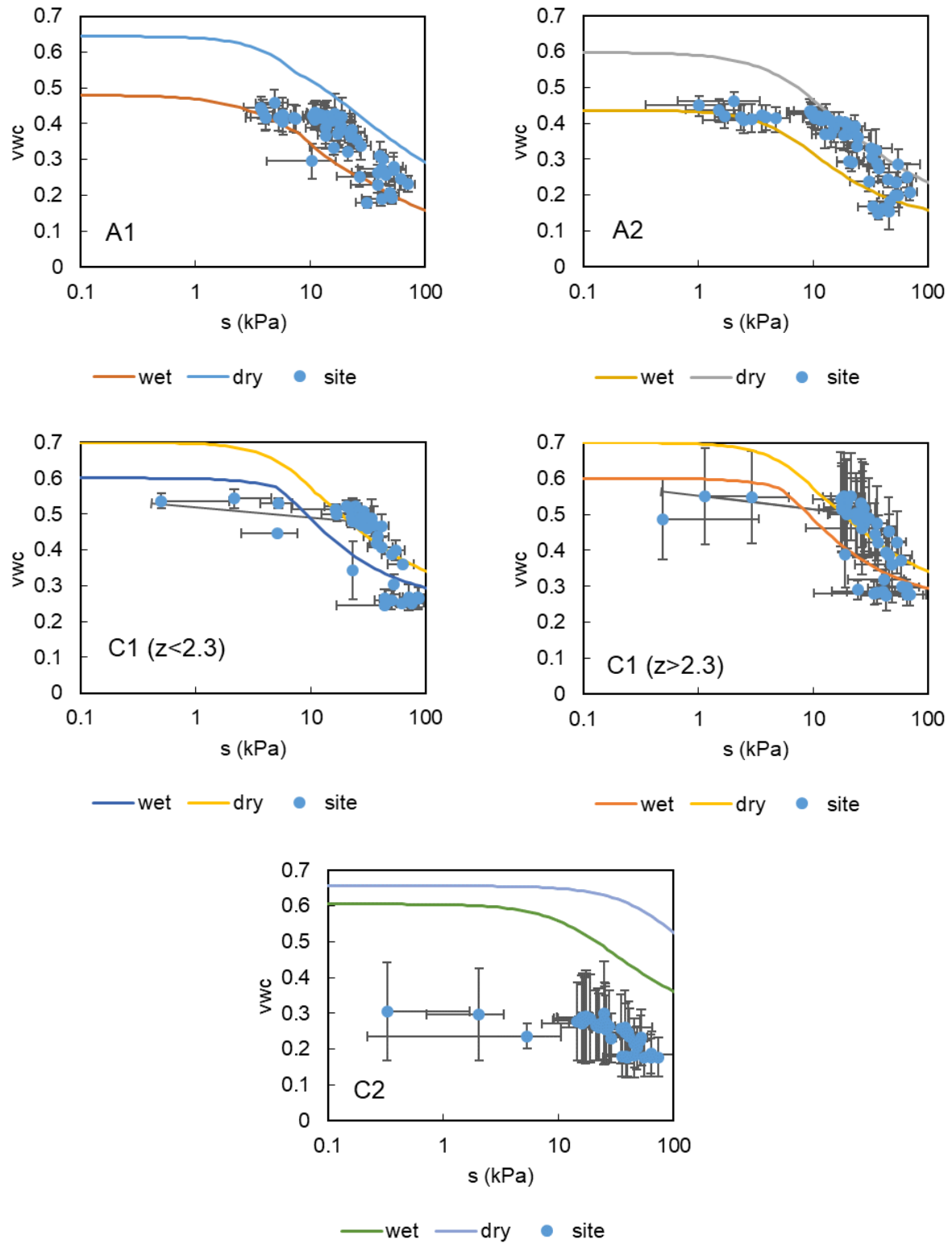


Figure 158 – Comparison of the mean water content ( $vwc$ ) and suction ( $s$ ) measured in situ and the envelope of the main loop obtained in the laboratory.

The three different soil types are easily distinguishable in Figure 159. The behaviour of soil A1 was very similar to A2 tending to the same water content at saturation and having the same AEV and the slope of the suctions higher than 10 kPa follow the same trend. The soil C1 in different depth ranges presented the same behaviour for the same reasons presented for soil A1 and A2. Soil C1 presented the same translation of the curve as in the laboratory tests as a consequence of being a finer material.

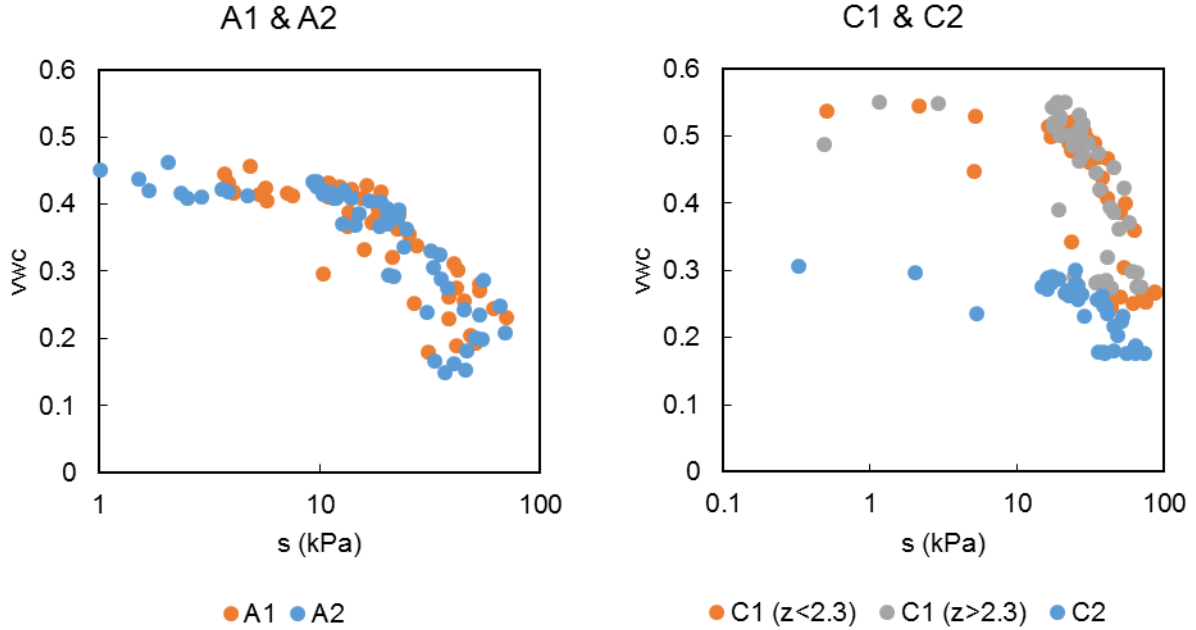


Figure 159 – Mean field measurements of suction ( $s$ ) and volumetric water content ( $vwc$ ) of soils A and C.

Soil C1 is the most porous soil, followed by soil A1 and A2 and finally soil C2, which is the least porous. The values of porosity of the samples tested in the ku-pf apparatus (Chapter 3) seem to be higher because the volumetric water content at saturation is higher than the field measurements tending values.

The AEV of soil C1 ranges between 15 and 20 kPa. The EAV of soil A1 and A2 is between 10 and 15 kPa. In both cases the estimation obtained from the laboratory was lower, which means that the laboratory results overestimate the water storage capacity and underestimate the velocity of wetting front propagation upon a rainfall event occurs.

Soil C2 presents a very different behaviour from soil C1. The water content at saturation tends to approximately 0.3 and the AEV is approximately 20 to 40 kPa, as observed before.

The data from profiles T and NT was investigated separately from the data from the cells (Figure 160). In soil A1, where is root density is equal in both profiles, suction is higher in profile NT for the same water content and the AEV also appears to be higher ( $\sim 10.5$  kPa) than in profile T ( $\sim 7$  kPa). The same is observed when compared both profiles in soil A2 (“T\_A2\_0.52” and “NT\_A2\_0.6”). The suction is higher in profile NT than in profile T for the same water content but the root biomass is lower.

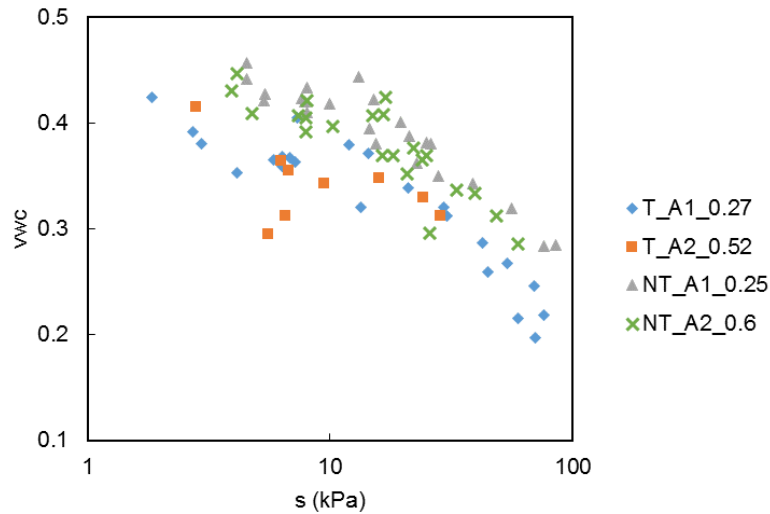


Figure 160 – Measurements in profiles NT and T of suction ( $s$ ) and volumetric water content ( $vwc$ ).

The AEV in profile NT is higher independently of the soil, which was associated to low water storage capacity in Chapter 3. Consequently, a faster movement of the wetting front is expected in that region when a rainfall event occurs. In order to confirm this hypothesis, field infiltration tests could be performed.

The comparison between field and laboratory data is presented in Figure 161. The shallowest monitored data was compared to soil A1, and not A1sup, because of the depth of installation was greater than 0.1 m.

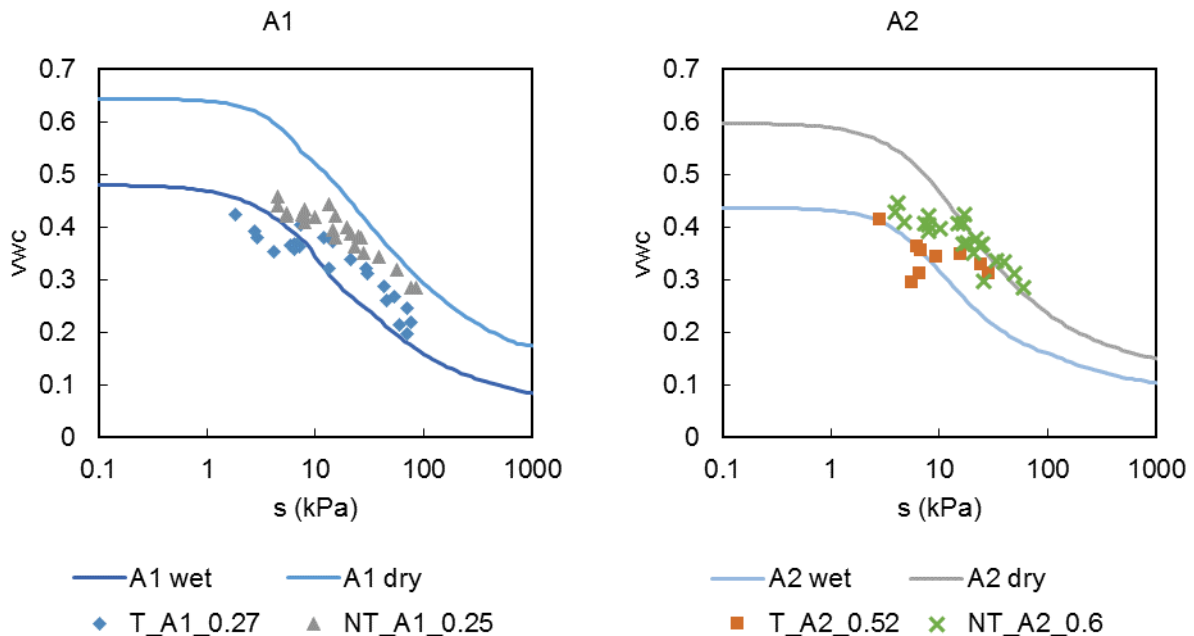


Figure 161 – Comparison between field measurements of suction ( $s$ ) and volumetric water content ( $vwc$ ) in profiles T and NT and WRC envelopes.

The fitting of the field data from these two profiles was similar to the observed in the cells, i.e. the values tended to the volumetric water content at saturation of the main wetting envelop as water content increase, showing that there is air entrapment in the wetting process or/and that the porosity of the laboratory tested samples is higher. The AEV value observed in the laboratory was also higher than what is indicated in the field measurements, even though this might be as well caused by the fact that scanning paths (field) are being compared to main curves (laboratory).

In the field monitoring along time it was seen that there was a long period during which the water content was maintained high and suction low. Those measurements correspond to the cluster of points obtained below 20 kPa. The soil then dried and suction increased forming the sequence of points parallel to the main drying envelop.

#### **4.3.7 Groundwater vertical flow**

The vertical hydraulic gradient is calculated based on the differences of hydraulic head between two points. The water movement occurs towards the point at which the hydraulic head is lower as a consequence of the convention assumed in the 'Method and materials' section. The hydraulic head is directly related to the suction (negative pore-water pressure), so the hydraulic head decreases with the increase of suction (Figure 162). The hydraulic head in soil A2 was slightly lower than in soil A1 (Figure 162), which indicated a downward water flux. Indeed, the vertical gradient was negative until June 2017 (Figure 163). The hydraulic head in soil C1 and C2 presented significant oscillations from August to December 2017. The hydraulic head reached maximum values from January to April 2018, during which positive water pressures were observed.

The water flux was downwards during the wet season of 2017 and 2018 but presenting a lower gradient in 2018 in the soil layers A1 and A2 (Figure 163). The highest values were observed in June, July and August of 2017. The gradient was observed to be negative after the rainfall of September 2<sup>nd</sup> 2017, which indicates that the water flow was downwards. The negative gradient was observed in the start of the wet season in both years (September and October). The lower values of gradient correspond may indicate that the flow was horizontal and further studies can be conducted for its assessment. The groundwater movement in soil C1 showed an upward flow during 2017. In January 2018, the gradient decreased significantly, after which it became negative, indicating the occurrence of water infiltration.

The mean suction and water content were represented along depth in Figure 164 before and after the first rainfall events after the dry season of 2017. Soil suction before the rainfall events was 31 kPa and 37 kPa in soil A1 ( $z = 0.2$  m) and A2 ( $z = 0.5$  m), respectively, and the water content was 0.18 and 0.15. In soil C1 there is only available data at 2.7 m of depth correspondent to suction of 60 kPa.

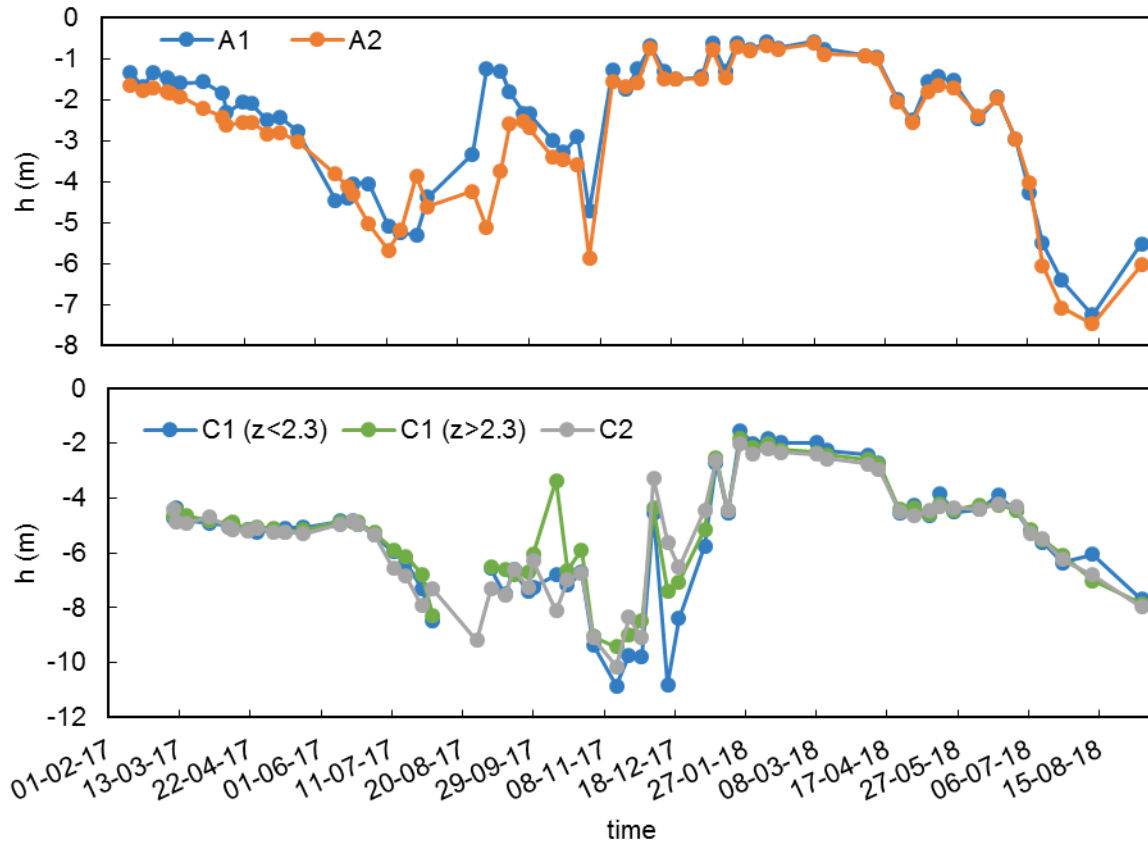


Figure 162 – Mean hydraulic head ( $h$ ) for cells 1 and 2 per soil layer.

After the first rainfall event (September 2<sup>nd</sup>), suction decreased to 10 kPa, and water content increased to 0.30, in soil A1. In opposition, suction increased by 8 kPa and the water content was kept constant in soil A2. The second rainfall (September 11<sup>th</sup>) caused an increase in water content in soil layers up to 2 m of depth. The suction decreased in soil A2 by 13 kPa but in soil A1 remained constant as it reached the AEV. The water content and suction in soil C1 did not change greatly. A decreased in suction was observed at 2.2 m in the measurements of September 18<sup>th</sup>. The decrease at 2.5 m was observed on 26<sup>th</sup> and at 2.7 m on 18<sup>th</sup> and 29<sup>th</sup>.

The time resolution of the field measurements was too sparse to allow observation of the movement of the wetting front. However, an increase of water content from 0.18 to 0.30 in soil A1 caused by a rainfall of 46.5 mm (September 2<sup>nd</sup>) would have to be homogeneously distributed through a depth of 0.38 m.

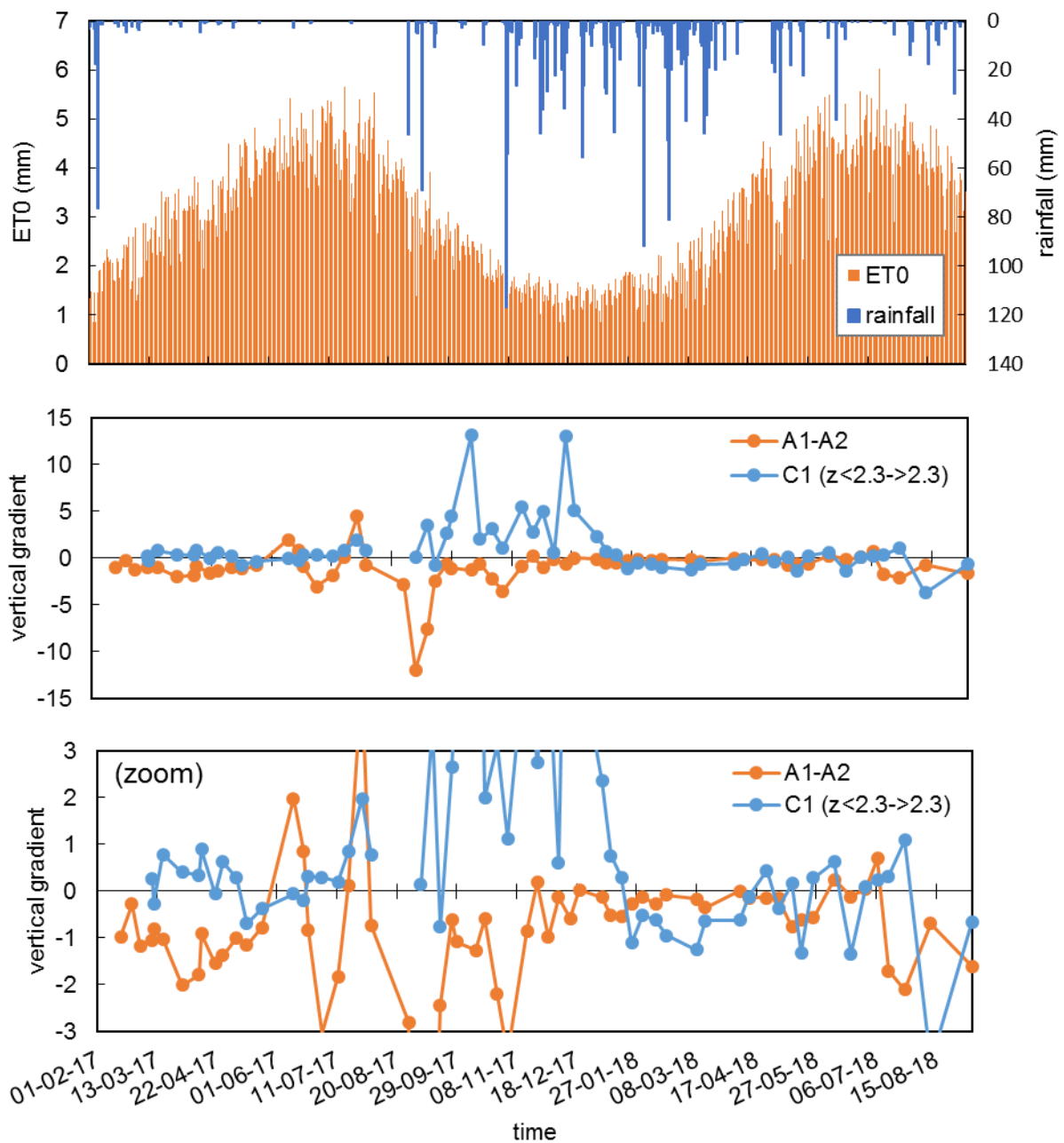


Figure 163 – Mean vertical gradient in couples of measurements in comparison with rainfall and reference evapotranspiration (ET0).

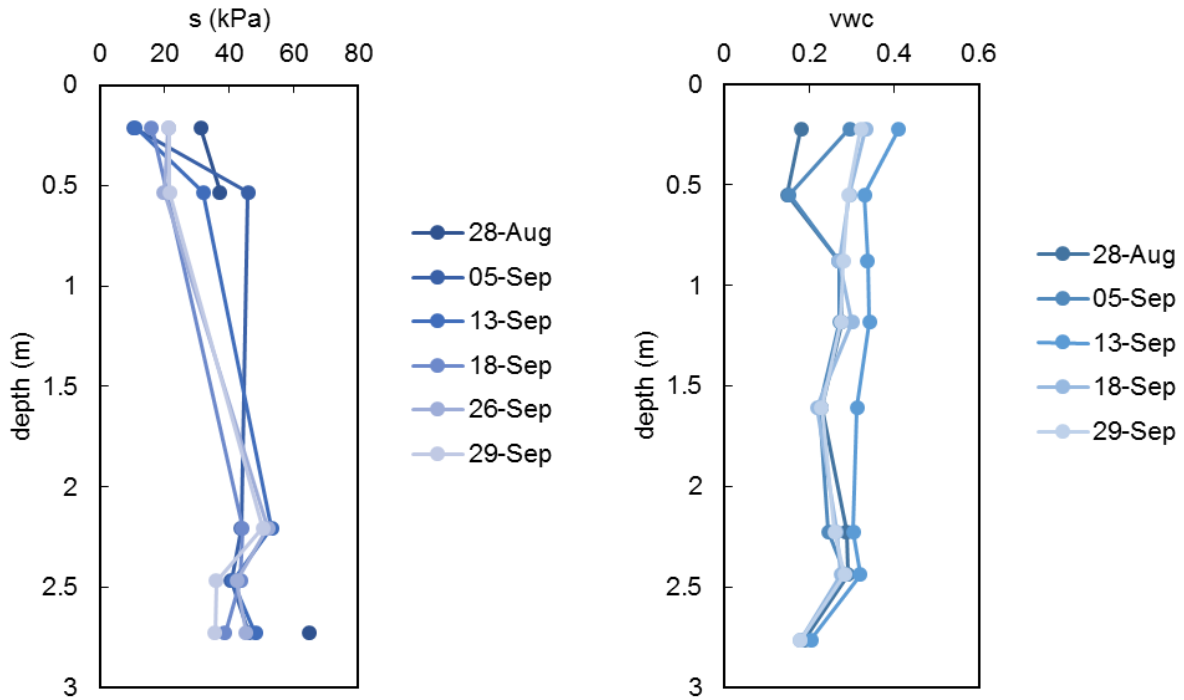


Figure 164 – Mean suction ( $s$ ) and volumetric water content (vwc) along the soil profile before and after the rainfall events of September 2017.

The profiles NT and T were investigated separately as presented in Figure 165, however there were not enough information to make a comparison between both profiles. The rainfall events in November and December 2017 caused an oscillation in the gradient showing the occurrence of water infiltration. The remaining period of the year before July showed the same constant downward water flow that was observed in the cells. A slight increase in the gradient in profile T was observed during the dry period in April. The increase of water evaporation was detected in July and August but reduced again after the rainfall events in the end of the monitoring period in profile NT.



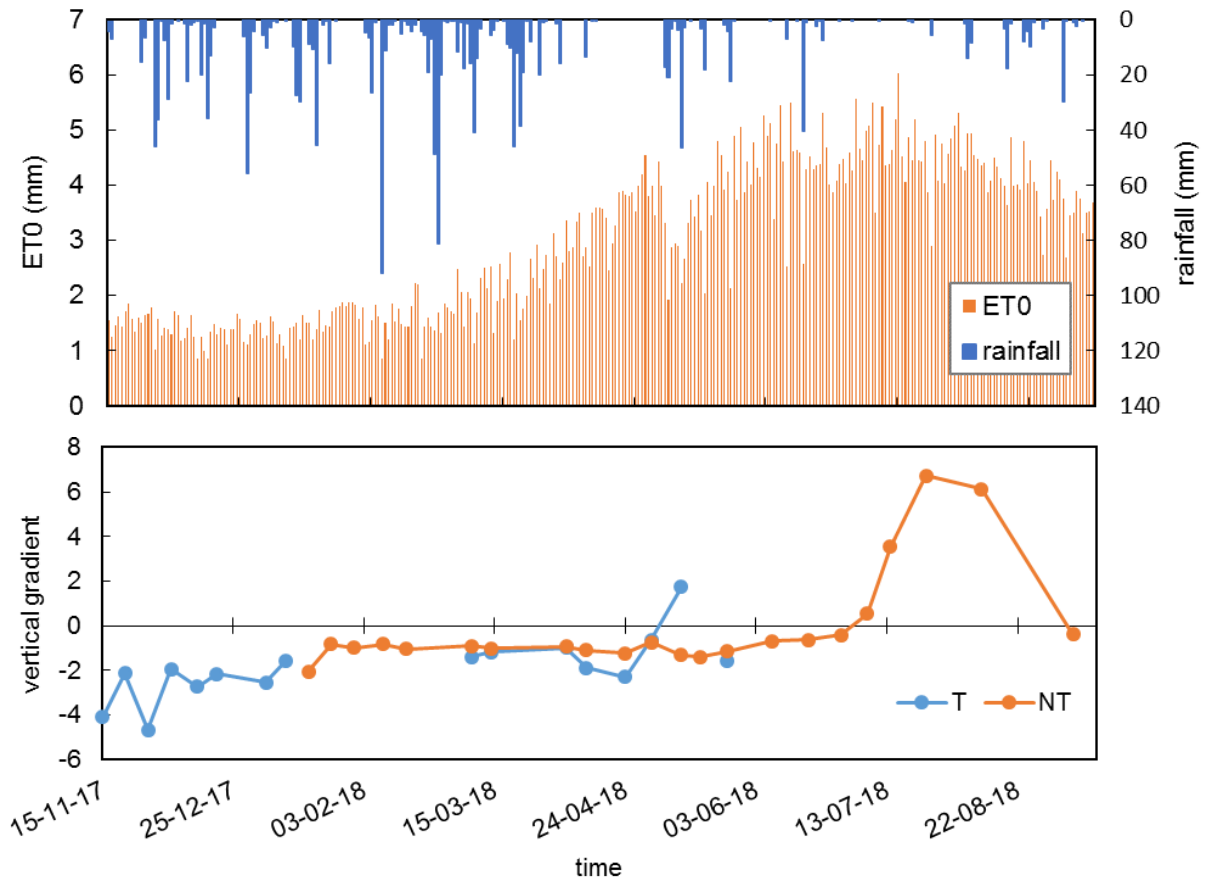


Figure 165 – Vertical gradient in profiles T and NT in comparison to rainfall and reference evapotranspiration (ET0).

### 4.3.8 Spatial distribution of water content and suction associated to root density

#### 4.3.8.1 Fitting of the spatial distribution model to soil hydraulic behaviour observations

The hypothesis that the presence of roots affects the soil hydraulic properties as well as the ground water regime was posed. In order to test this hypothesis, the model used for the spatial distribution of roots was fitted using observations from the groundwater monitoring data. The monitored water content and suction varies along time but particular observations of these values can provide information about the hydraulic properties of the soil and the root activity, i.e. the water uptake in a given point. Several indicators of soil hydraulic properties were tested.

The coefficient of determination ( $R^2$ ) of the fitting of the hydraulic properties' indicators to the spatial distribution model is presented in Figure 166. Different areas of influence of trees were taken into in the form of maximum distance tree-to-profile assumed ( $d_{max}$ ). The same criteria to identify good fittings of the root spatial distribution model was used ( $R^2 > 0.4$ ). The fitting parameters and respective coefficient of determination are presented in Annex V. The fitted data comparison with the observations are reported in Annex W.

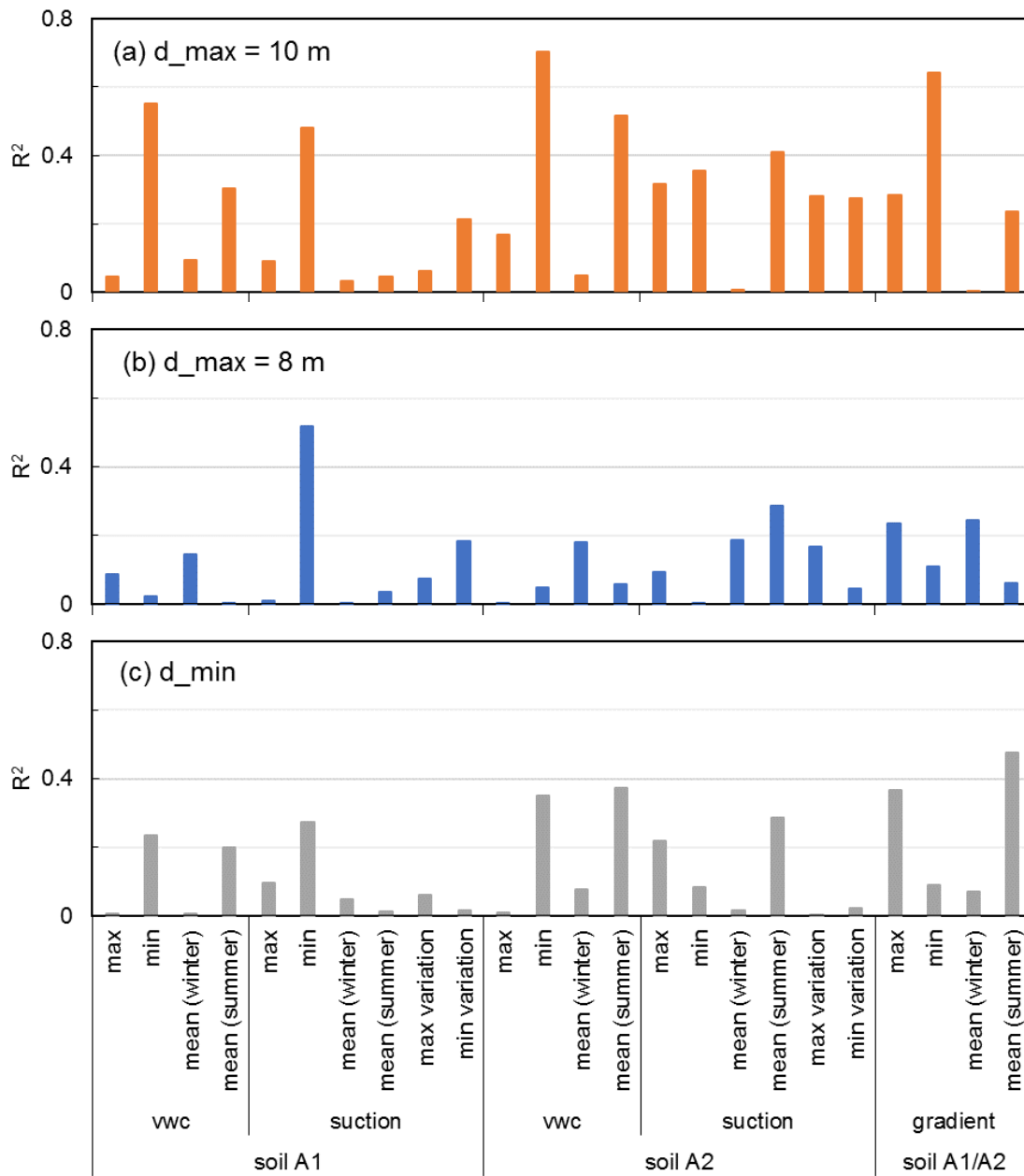


Figure 166 – Coefficient of determination ( $R^2$ ) of different hydraulic observations in soil A1 and A2 to fit the spatial distribution model for a maximum tree-to-profile distance of (a) 10 m, (b) 8 m, and (c) considering only the nearest tree to the profile.

The range of tree-to-profile distance that resulted in best fittings was 10 m, as in the root distribution model, presented in Figure 166(a).

The best fittings were obtained for the minimum measurements of water content (vwc) for soil A1 and A2. The minimum water content occurs during summer and can be associated to the water uptake by plants, as the evaporation fraction was reduced during this period. Increasing values of suction would be observed for decreasing water content but suction was not possible to be measured consistently during the dry period.

The minimum suction observed in soil A1 also resulted in an acceptable fitting. A good understanding of the effect of trees on the minimum value of suction along the year allows low values of suction during the winter to be identified as they are predisposing factor for the occurrence of landslides (Papa *et al.*, 2013; Urciuoli *et al.*, 2016). If the potential to reach low values of suction was influenced, negatively or positively, by the presence of trees, then the location of sensitive areas can be identified. Nonetheless, potential landslides slip surfaces are expected to be found in this layer because it is too shallow (Di Crescenzo and Santo, 1999, 2005; Calcaterra and Santo, 2004).

Roering *et al.* (2003) observed that the spatial distribution of trees, which was related to the spatial root distribution and to the mechanical reinforcement of the soil by the roots, was associated to the occurrence of shallow landslides in Oregon Coast Range (USA). The hydraulic effect of vegetation was not considered but the root distribution was observed to condition the location of the scarps of landslides. Therefore, the effect of vegetation on slope stability is closely related to the size, species, and spacing between trees found in the slope.

A good fitting was obtained in terms of minimum gradient. Note that the minimum gradient is a negative value that indicates the occurrence of water infiltration, which was observed during the wet season. When the gradient is low, the greatest is the different between the upper and bottom layer, i.e. when the suction in soil A1 is low but in A2 is high. Suction was measured at the same instant in all profiles, so a lower value of gradient showed a delay in the water infiltration. Regions that presented lower gradients were more 'protected' from water infiltration. If all soils presented the same water retention characteristics (same WRC), low gradients would result from low permeability.

The mean gradient during summer if only the nearest tree is considered (Figure 166,c) presented a good fitting. The mean gradient during summer represents positive gradients, i.e. evaporation, that were observed in profiles that had a fast growth of suction in the upper soil layer in comparison to soil A2. In the example of the comparison of profiles NT and T was observed a faster increase in suction in the profile closer to the tree.

#### **4.3.8.2 Relate root density indicators and soil hydraulic properties indicators**

The hydraulic properties indicators can only be related to the root density indicators if the competition index of each profile is the same. Once identified the indicators with best fit, a relationship can be investigated between root density and soil hydraulic behaviour.

The root biomass was selected as root density indicator for this study to provide the parameter  $\alpha$  for the calculation of the competition index distribution in space. The competition index of each profile fitted for the root biomass considering all the trees in the range of 10 m from the profiles is presented in Figure 167(a). In this case, the competition index is not related to the relative position of the profiles within the cells but cell 2 presents lower values than cell 1. There is also a significant different between T and NT profiles.

Figure 167(b) presents the values of competition index based on the  $\beta$ -value of the vertical distribution of the number of root tips for all the trees in a range of influence of 8 m. The selection of this root indicator is justified ahead in this section. The values of competition index are very similar among cell 1. Data on profiles T and NT was not available for the fitting of the  $\beta$ -value, so they were excluded also here.

The fitting parameter  $\alpha$  of the relation between competition index and trees DBH and tree-to-profile distance is 0.371 for the root biomass and -0.268 for the  $\beta$ -value (root tips).

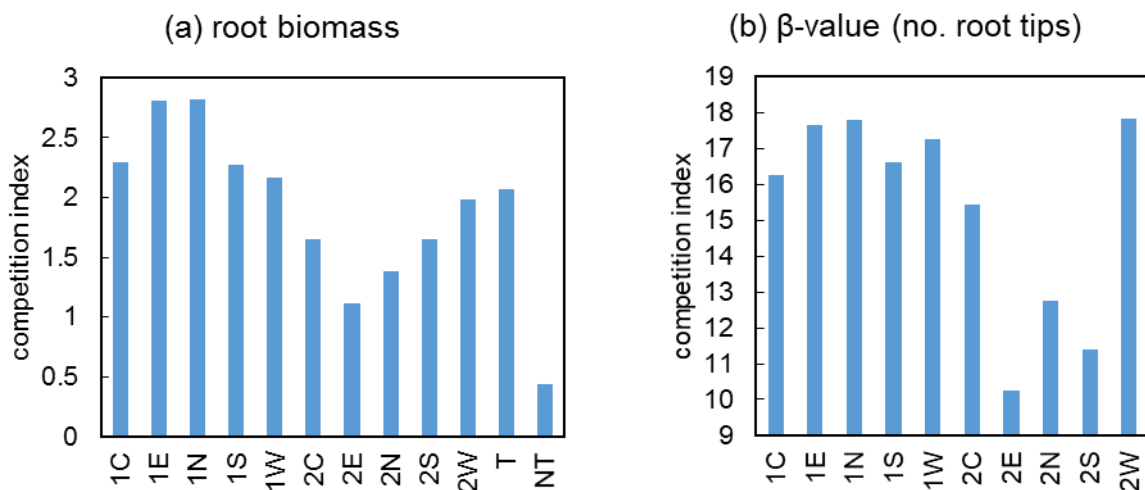


Figure 167 – Competition index for each profile fitted for the data of (a) root biomass, and (b) vertical distribution of the number of root tips.

The coefficients of determination after fitting the logarithmic model using the competition index of the roots biomass are presented in Figure 168. The  $R^2$  value of the minimum water content in soil A1 and A2 remains above the threshold, as well as the minimum gradient. The minimum suction in soil A1 presented a reduction in the quality of the fitting. So, the range of influence of the trees was reduced because a good relation was possible for a tree-to-profile range of 8 m, as well. The mean gradient during summer obtained when only the closest tree is considered was not related to the root distribution because no good fitting was obtained for the root distribution for that tree-to-profile distance. All the fitting parameter and coefficient of determination are presented for the new fittings of this section in Annex X.

The root biomass density was presented in Figure 169 for each competition index, as well as the minimum water content in soil A1 and A2, both observed values and fitted model. The minimum water content in both soils decreased with increasing competition index, in contrast to what happened to the biomass. So, a profile with a higher biomass, i.e. with greater root density, can be related to lower values of minimum water content, i.e. drier soil. On the plot of the right in Figure 169, lower vertical gradients were obtained in profiles with higher competition index and so higher biomass.

The coefficient of determination of the logarithmic model using the competition index fitting of the root distribution in terms of  $\beta$ -value from the number of root tips is presented in Figure 170. The  $R^2$ -index of the

minimum suction in A1 was still above 0.4, so the fitting is still considered acceptable. On the other hand, a general decrease of the  $R^2$  coefficient was obtained because the parameter  $\alpha$  was positive in most cases.

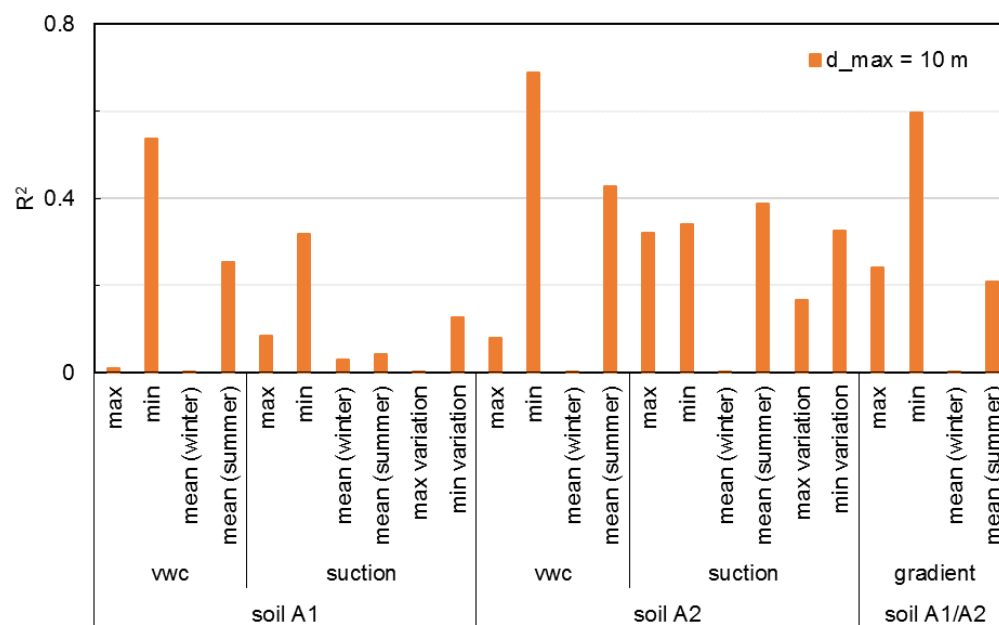


Figure 168 – Coefficient of determination ( $R^2$ ) for each hydraulic properties' indicator fixing the competition index of the root density in terms of biomass.

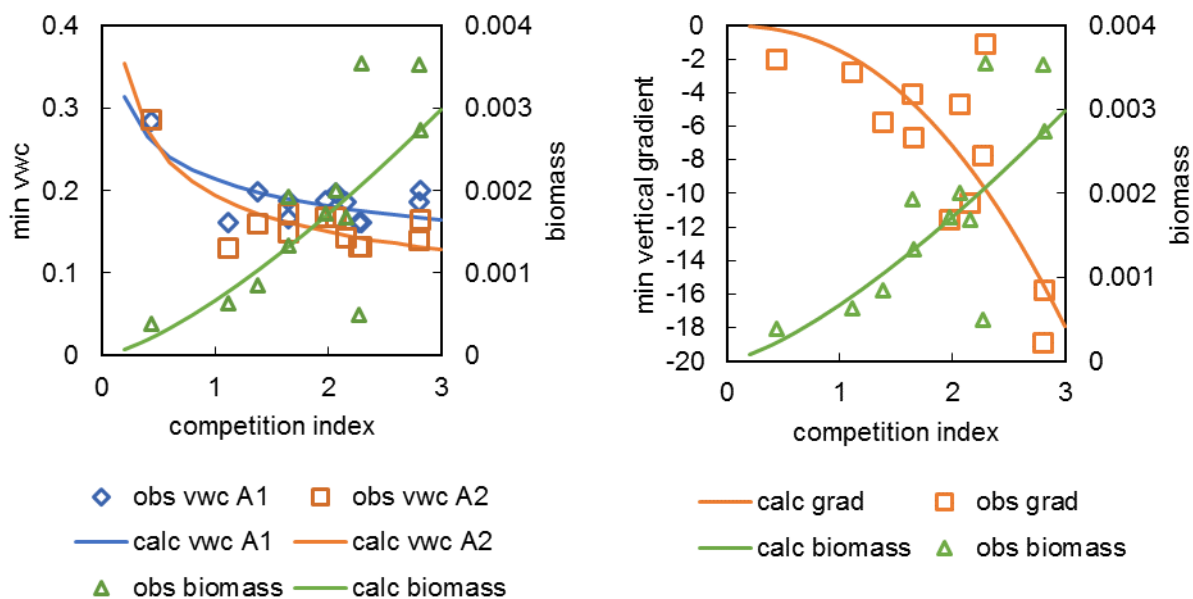


Figure 169 – Minimum volumetric water content (min vwc), minimum vertical gradient and root biomass for the same competition indexes considering all the trees in a range of up to 10 m from the soil profiles.

The observed values of the indicators are presented for the respective competition index in Figure 171. The minimum suction observed along the year was related to the vertical distribution of the number of tips. The

vertical distribution of the number of tips was characterized by the parameter  $\beta$ . Higher  $\beta$ -values result from having root tips less concentrated at the soil surface. So, when root tips were more evenly distributed with depth, the minimum suction value observed along the year tended to be lower. In the same way, when root tips were more concentrated at surface, suction tended to remain at higher values in that soil profile.

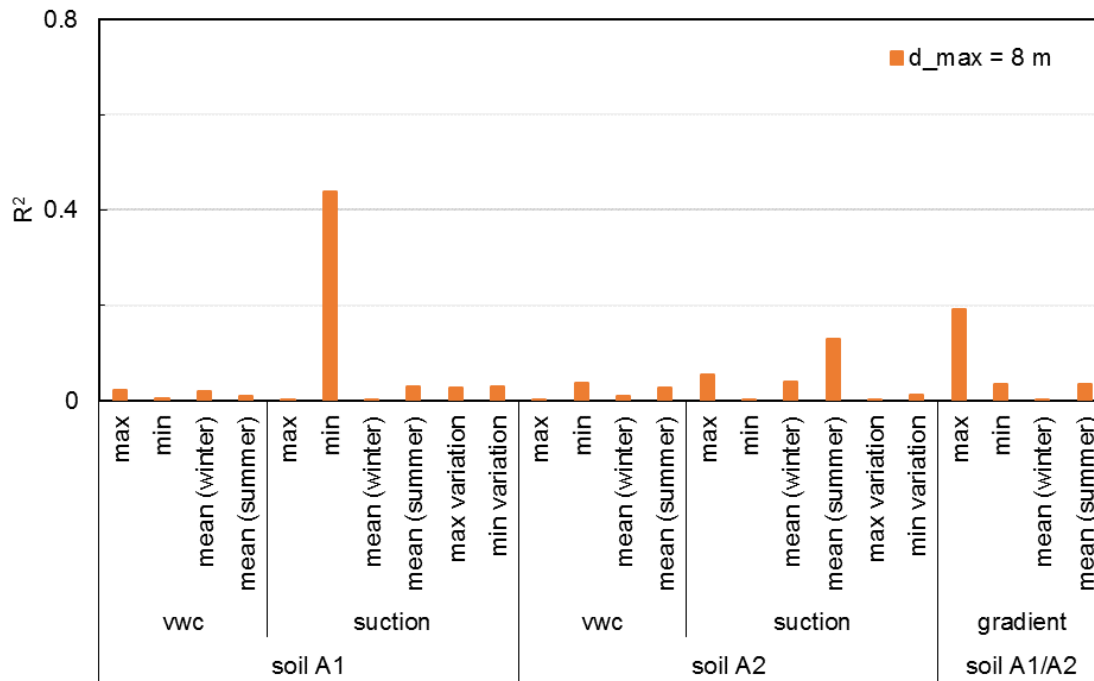


Figure 170 – Coefficient of determination ( $R^2$ ) for each hydraulic properties' indicator fixing the competition index of the vertical root distribution parameter ( $\beta$ -value) in terms of root tips.

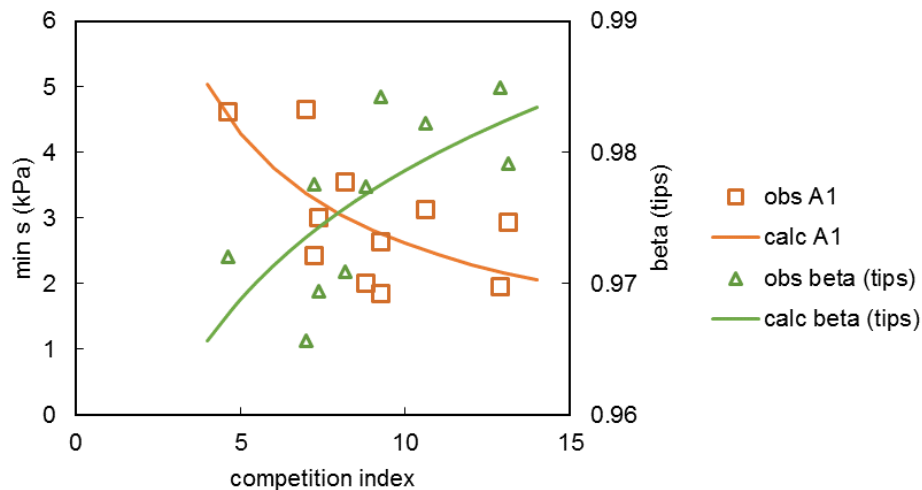


Figure 171 – Minimum suction and  $\beta$ -values (number of root tips) for the same competition indexes considering all the trees in a range of up to 8 m from the profiles.

Ni *et al.* (2018) proposed a model in which the decrease of hydraulic conductivity occurs with the growth of roots. Changes induced by the vegetation on the WRC are taken into account as proposed by Ng *et al.* (2016) in which the soil pores are occupied by roots. This way, the hydraulic effect of vegetation on soil hydraulic properties were contrary of the hydraulic characterization of Chapter 3. Indeed, if the presence of roots enhances the soil hydraulic properties by reducing its hydraulic conductivity and increasing the AEV, then the hydraulic effect of vegetation on slope stability is positive. Most of the studies report an increase of suction in the soil because of water uptake by the plants as being the major effect of plants on the soil groundwater regime. Nonetheless, in the wet season, the generated suction during the summer is irrelevant (Simon and Collison, 2002; Pollen, 2007; Kim *et al.*, 2017).

#### **4.3.8.3 Considerations on the relations between root distribution and hydraulic properties indicators**

Each soil layer presented a reasonably uniform variation of suction and water content along the year. The soil behaved similarly in all the instrumented area and using an average characterization of the soil would be acceptable. The root distribution was also uniform among different profiles. Variability among profiles can also be attributed to the size of the sampling borehole.

Soil A1 and A2 were the soil layers with the greatest portion of roots, which corresponded to the first meter of soil. Soil layers B and C presented a small portion of roots and a groundwater regime that was seasonal and not much affected by single events, which response was only observed 1 to 2 weeks after the rainfall event. Nonetheless, the lack of research on those layers did not mean that the potential failure surface crossing these layers were disregarded. In fact, in the wet season of 2018, a transient water table was observed in soil layers C1 and C2. However, the focus of the work was on the effect of vegetation.

Nonetheless, some potential in the use of spatial root distribution models to predict soil hydraulic responses were identified. Four different hydraulic properties indicators were successfully related to the competition index and to a root density indicator.

First, the minimum water content reached along the year in soil A1 and A2 was successfully related to the competition index and to the root density distribution. As mentioned before, greater amounts of roots are responsible for a greater uptake of water as higher biomass was observed to be related to greater number of root tips.

Soil cracking was not identified to be problem in Mount Faito because the pyroclastic soil in the test site do not present considerable changes of volume with variations of water content. However, knowing the spatial distribution of soil that has the potential to become drier may be of interest in other slopes with different soil types. The formation of cracks in the soil is actually a negative consequence of very dry periods because cracks allow the preferential infiltration of water in rainy seasons (Novák *et al.*, 2000).

The minimum vertical gradient was successfully related to the competition index and to the root density distribution. The vertical gradient, when negative, indicates water infiltration. Low values of vertical hydraulic head gradients were observed when the hydraulic head of the upper observation point (installed tensiometer) was higher than the bottom point.

Lastly, the minimum suction in soil A1 along the year was related to the number of root tips vertical distribution. An increase of competition index was associated to more evenly distributed number of root tips with depth and the increase of the potential of the surficial soil to reach lower values of suction during winter.

Low values of suction in the soil are guarantee the predisposing conditions for the initiation of a rainfall induced landslide (Pirone *et al.*, 2015a, 2015b; Urciuoli *et al.*, 2016). A relationship between the competition index and the minimum suction presents two potential uses: (i) the identification of areas that reach critically low suction values, and (ii) the adjustment of plantation densities minimizes the spreading of those areas.

## 4.4 Conclusion

The groundwater and meteorological monitoring of the test site in Mount Faito was presented, as well as a vertical and lateral root distribution characterization.

The vertical root distribution model showed that the greatest fraction of roots was present in soil layers A1 and A2. A homogeneous distribution of the roots was observed when these two layers were thicker. On the contrary, the roots were more concentrated at the surface when the soil layer A1 was shallower.

The root lateral distribution was observed to be related to the diameter at breast height of the trees and the distance from the trees. The best results were obtained if all the trees in a range of 10 m from the profiles are considered. Some suitable root density indicators were identified for each hydraulic property or behaviour to be investigated. The root density indicator to investigate the relation between roots and water infiltration was the  $\beta$ -value in terms of root length and the root biomass root. The trait that was expected to be related to the water uptake, and so increase of suction in the soil, would have been the number of root tips but no root density indicator produced a good model fit relative to the number of tips. However, different root traits are related among them and root biomass occurs simultaneously to the increase of number of root tips.

The monitoring of the groundwater, in terms of suction and volumetric water content, allowed the observation and understand of the differences among soil layers in terms of seasonal and single-event behaviour of the soil along the year. Three phases were identified:

- (i) A transient phase during which suction increases and water content decreases, that lasts from May to September, and corresponds to the dry season;



- (ii) The start of the wetting season, approximately from September to December, when the suction decreases and water content increases. It is a transient phase during which the water flow is mainly downwards characterized by low vertical hydraulic head gradients;
- (iii) A steady state during most of the year, from December to May, when the hydraulic head was null, the suction was maintained below 10 kPa and water content was constant along time. This period is considered critical for the occurrence of landslides because the predisposing conditions are verified.

Different soil layers behaved differently during each of the identified phases. Soil A1 and A2 presented a quick response to single rainfall events and were the fastest to respond to the increase of evapotranspiration in the dry season. The coarse layer B and finer layer C1 responded later to the seasonal and to the single rainfall events in comparison to the upper layers. Soil C2 was not sensitive to single rainfall events and almost insensitive to the seasons.

The monitored data validated the quality of the models obtained based on the inverse analysis of evaporation and imbibition tests performed in laboratory (Chapter 3). The hysteretic model considered in the fitting improved the agreement between field and laboratory WRCs in comparison to previous works.

The root spatial distribution was related to particular hydraulic observations that were referred as hydraulic properties indicators. Even though each soil layer presented similar behaviours among the instrumented profiles, four different hydraulic properties indicators were successfully related to the competition index and to a root density indicator. The minimum water content in soils A1 and A2 along the year, and the minimum vertical gradient were inversely related to the increase of biomass in the profiles.

## Chapter 5      The relative contribution of suction, soil and root shear resistance to slope stability

### 5.1 Introduction

Rainfall-induced landslides usually occur in the slopes in the region of Campania (Italy), such as the one of the test site in Mount Faito. The slopes are stable due to the reinforcement resultant from the unsaturated conditions in which the soil is found. In the wet season, a prolonged period in which soil suction is maintained low, close the air-entry value (AEV) of the respective (WRC), creates the predisposing conditions to the occurrence of landslides, which are triggered by extreme rainfall events of short duration (Urciuoli *et al.*, 2016).

The groundwater regime, investigated in Chapter 4, revealed the same behaviour observed in other shallow pyroclastic soil covers in Campania (Damiano *et al.*, 2012; Pirone *et al.*, 2015a). Moreover, the positive hydraulic effect of vegetation for the slope stability was irrelevant in the critical period during which most landslides occur. High values of suction in the soil resulting from high evapotranspiration rates during summer were not maintained throughout the wet season as the trees were not in leaf and the understory was removed. Similar observations have also been made in other parts of the world (Simon and Collison, 2002; Pollen, 2007; Kim *et al.*, 2017) in which the hydraulic effects contribution to slope stability are less relevant than the mechanical reinforcement of the soil by the roots of the plants.

Landslide inventories in Campania (Italy) revealed that less landslides occur in vegetated areas (Amato *et al.*, 2000; Di Crescenzo and Santo, 2005) but in Chapters 3 and 4 of the present work, vegetation was found to potentially have a negative effect on the slope stability. Indeed, faster propagation of the wetting fronts were expected in the upper soil layers because roots increased the soil permeability. The minimum suction measured along the year was also related to the root distribution. The increase of root biomass in the soil was related to an increase the potential of that given area to reach lower values of suction during winter. In deeper soils (soil C2), the presence of roots was not able to increase the permeability of these soils. Such low permeability would prevent water from infiltrating into the bedrock and an accumulation of water at the lower part of the pyroclastic soil cover was observed in the field monitoring data.

Vegetation does not only interact with the slope through hydraulic processes. The presence of roots in the soil acts as a mechanical reinforcement providing the root-permeated soil an increase of shear strength (Schmidt *et al.*, 2001; Schwarz *et al.*, 2010a; 2010b). In fact, Stokes *et al.* (2009) stated that vegetation contributes to slope stability mostly by mechanically increasing the shear strength of the soil and that trees are the preferable type of vegetation to stabilize slopes.

The mechanical reinforcement of the soil by the roots, which is commonly referred as root cohesion, has been estimated and used to assess slope stability showing its contribution in increase the safety factor associated to potential failure surfaces (Simon and Collison, 2002; Pollen, 2007; Kim *et al.*, 2017). Root

cohesion can be estimated from macro models, in which root-permeated soil is considered as a homogeneous material which resistance is obtained experimentally. The mechanical reinforcement can also be estimated based on the tensile strength of the roots and on their distribution along a failure surface. The tensile strength of the roots is directly related to the roots diameter. The reinforcement is greater when an increasing fraction of the failure surface is occupied by roots, which is quantified in terms of area as root area ratio (RAR). The estimated root cohesion is added to the soil shear strength.

The research question investigated in the present chapter intends to investigate the relative importance of the shear strength of root-permeated unsaturated soil stated in the form of “Is the mechanical reinforcement by roots relevant for slope stability of pyroclastic soil covers?”.

## 5.2 Methods and materials

### 5.2.1 Soil strength considering the presence of roots

Independently of the model used for the quantification of strength of root permeated soil, roots are considered to provide an additional shear strength or cohesion to the soil as suggested by Wu (1976) and Gray and Ohashi (1983). The shear stress at failure  $s_f$  of an unsaturated root-permeated soil is the sum of three terms as in Equation 68, where  $s_s$  is the effective shear strength of the soil matrix,  $s_{\psi}$  is the shear strength component due to matric suction and  $s_r$  is the shear strength component due to the root system, according to the formulation of Veylon *et al.* (2015).

$$s_f = s_s + s_{\psi} + s_r \quad 68$$

The shear stress at failure is given by Mohr-Coulomb criterion as presented in Equation 69, where  $c'$  is the effective cohesion,  $\sigma$  is the normal stress and the  $\phi'$  is the effective friction angle.

$$s_s = c' + \sigma \tan \phi' \quad 69$$

The mechanical reinforcement of soil by roots is generally considered in terms of additional cohesion. The reinforcement resulting from water capillarity (suction) is accounted for by adopting the Bishop formulation of effective stresses. In the present work, the root and soil shear strength are quantified separately. The adopted methods are described in the following two sections.

### 5.2.2 Soil hydro-mechanical characterization

#### 5.2.2.1 Standard direct shear test

The standard direct shear tests were performed on saturated undisturbed samples of soils A1 and C1. The samples were extruded from horizontal boreholes collected from trenches at Mount Faito test site just like the boreholes used for the soil hydraulic characterization. Soil samples with the dimensions of the shear

box (60x60x20 mm) were cut from the borehole with a mould with a sharp wedge. The soil was placed on the shear box as in Figure 172.

The soil sample was placed on the shearing device base (Figure 173). The consolidation was processed at the natural water content of the soil. The consolidation load was applied and settlements were recorded with a linear variable differential transformer (lvdt) by Megaris s.r.l (Italy). Then, the sample was submerged by adding water to the shear box and settlements were again recorded. Some tested samples were partial unloaded after the saturation. The vertical displacements were also recorded during this phase. The three final different confining stresses were 25 kPa, 50 kPa and 75 kPa. These stresses were higher than the stresses in the soil in the monitored area but confining stresses lower than 25 kPa are not recommended to be tested in the shear box.



*Figure 172 – Insert soil sample in the shear box.*



*Figure 173 – Traditional direct shear test equipment (Esposito, 2017).*

The shear phase was performed at  $0.005 \text{ mm min}^{-1}$ , which is a speed low enough to allow the test to be performed in drained conditions. The maximum measured horizontal displacement was limited by the dimension of the shear box container. In some cases, the maximum allowed horizontal displacement was not enough to be able to reach a limit state in the soil (constant volume and constant shear strength), so the upper part of the shear box was carefully and slowly brought back to its initial position and a second shear phase was processed. More details on the performance of traditional direct shear tests can be found in the adopted norm ASTM D 3080-98.

In the end of the testing, the soil was removed from the shear box and the failure surface was inspected in order to identify possible presence of pumices and roots that would have disturbed the test. The soil was used to determine water content and porosity using the gravimetric method. The sample was weighed in a precision scale with a resolution of 0.01 g and dried in the oven for 24 h at  $105^{\circ}\text{C}$ . The biomass in the soil samples was quantified by collecting the roots from the oven-dried sample with scissors and weighing the roots in a precision scale with a resolution of 0.001g. However, roots were not considered to contribute to increase the measured shear strength because the soil sample was too small and so roots were not anchored.

### 5.2.2.2 Direct shear test in unsaturated conditions

Pyroclastic soils in Campania (Italy) shear strength was tested in unsaturated conditions because that is the natural state in which they are found since the water table is at sea level in this region (Evangelista *et al.*, 2004).

A direct shear test apparatus that allows the control of suction in the soil through axis translation technique is presented by Evangelista *et al.* (2004). This apparatus is composed of a chamber where the shear box is installed (Figure 175). The air pressure in the chamber and the water pressure in the porous stone in the bottom of the shear box (Figure 174) are controlled by a compressed air system (Figure 176). Details on the operation and of this equipment can be found in Evangelista *et al.* (2004), Papa (2007) and Papa and Nicotera (2011).

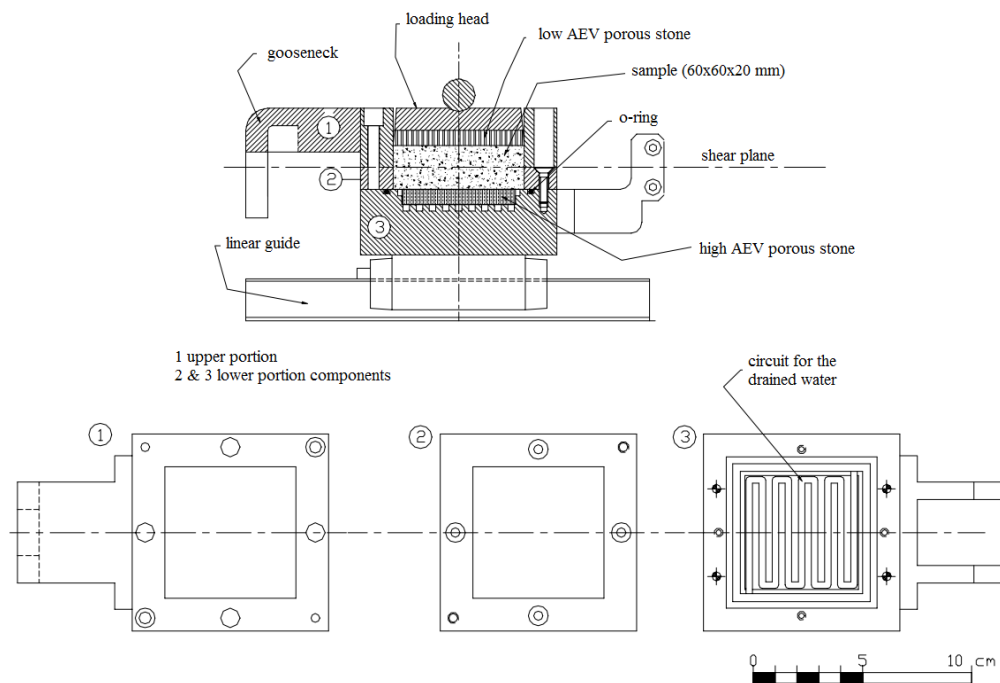


Figure 174 – Shear box (adapted from Evangelista *et al.*, 2004).

The tested soil was undisturbed and extruded from horizontal boreholes collected from the soil layer C1 from the test site at Mount Faito, like the samples tested in saturated conditions. The samples were placed in the shear box and the chamber was closed following the sequence of steps presented in Figure 177. A practical guide on the operation of the shear box can be found in Annex Y. The phases of the adopted testing procedure were the same of Papa (2007) and Esposito (2017) are described in the following points:

- Initial suction measurement: The air pressure in the chamber is applied to be 100 kPa by not allowing drainage. The increase of air pressure corresponds to an increase of the pore air pressure in the sample. The water content of the specimen remains constant and any change in the air

pressure corresponds to an equal variation in the pressure of the water (axis translation technique principle), i.e. the suction is maintained constant. Once passed enough time for the stabilization of the pore water pressure, the difference between the chamber pressure and the water pressure is equal to the initial suction of the soil sample.

- Suction application: A pressure equal to the water pressure measured in the previous phase is applied in the drainage system in order to force the suction to be maintained constant. The drainage system is opened afterwards.

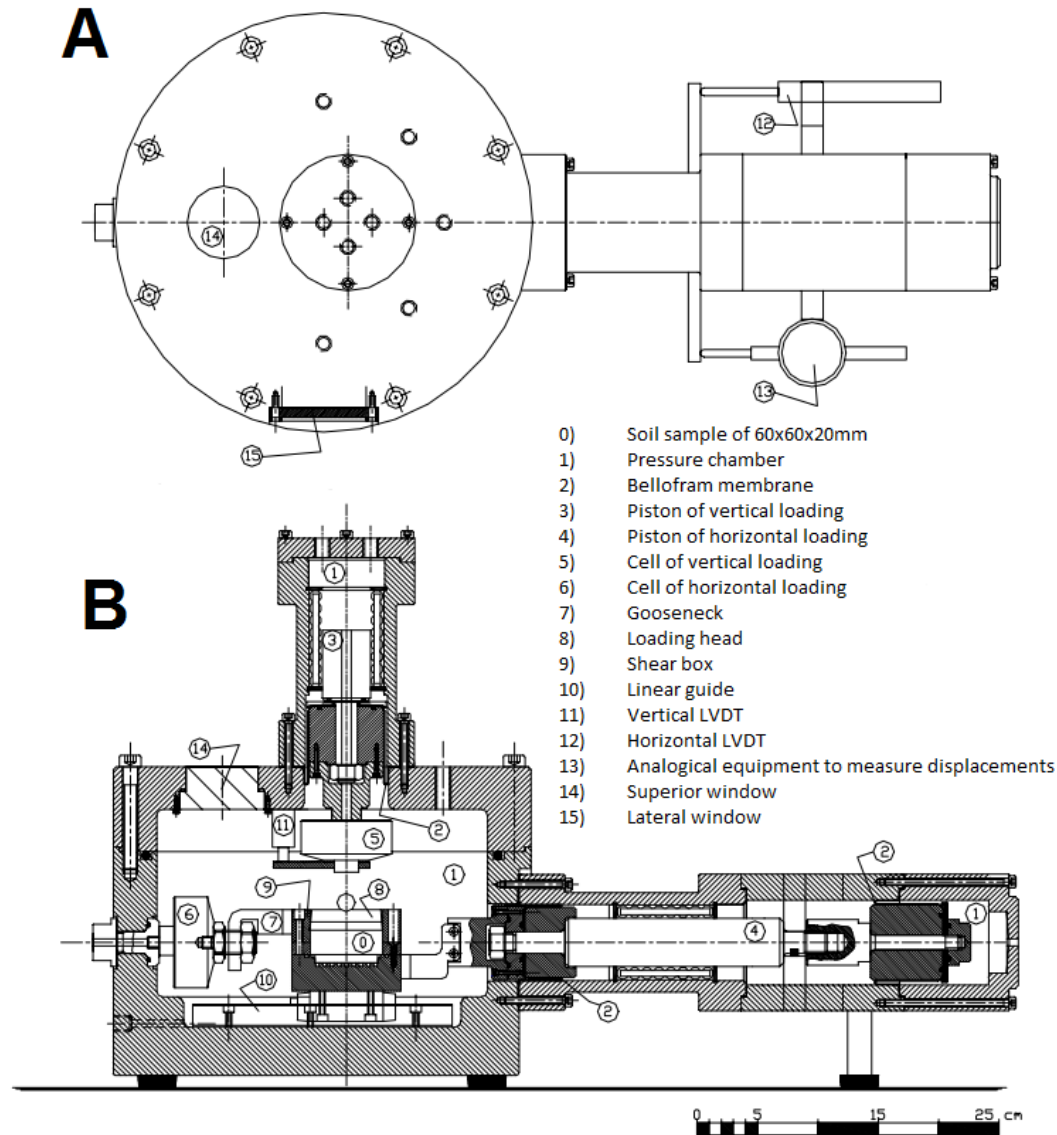


Figure 175 – Unsaturation conditions direct shear testing equipment (adapted from Evangelista et al., 2004): A represents the top view and B the transversal view.

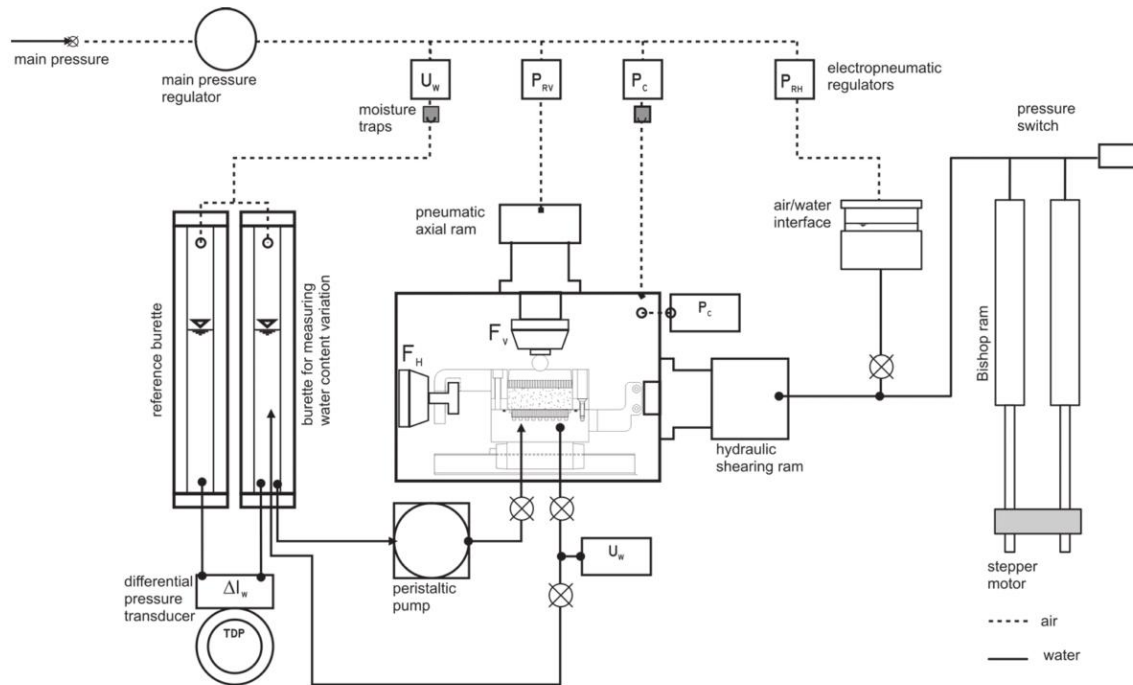
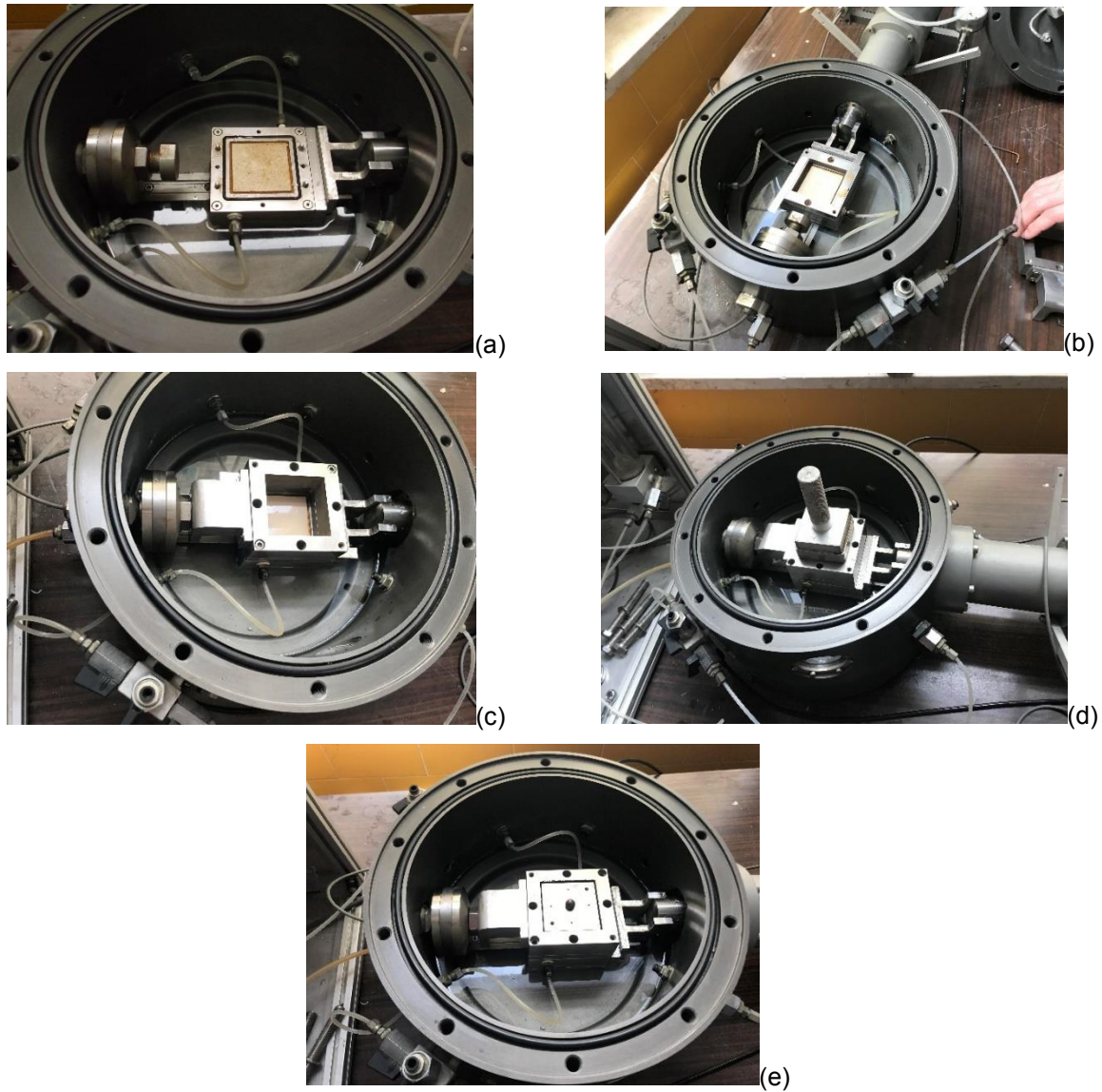


Figure 176 - Scheme of pressure regulation circuits and transducers used in the suction-controlled direct shear test (adapted from Papa and Nicotera, 2011).

- Consolidation: The vertical stress is applied on the sample by a piston which applied load is linearly increased. The vertical displacements are measured by a lvdt installed inside the chamber. The suction is maintained constant during this period because the variations of volume in the sample allowed a circulation of water through the drainage system. The consolidation phase lasts approximately 3 days. Samples are not unloaded after saturation. The variation of water content can be estimated from the variation of the water level in the burettes (Figure 176).
- Shear: The shear is processed at constant displacement rate of  $0.1 \text{ mm h}^{-1}$ . The load is applied by a piston controlled by the compressed air system and the displacements are measured by a lvdt installed outside the chamber.
- Disassembly of the specimen: At the end of the test, the drainage system is closed to prevent any variations of water content. The pistons are rewound and the air pressure is reduced to the atmospheric pressure. The chamber is open the sample is collected for porosity and water content determination using the gravimetric method just like in the standard direct shear test procedure.





*Figure 177 – Assemblage of the unsaturated direct shear test in unsaturated: (a) lower the water level and moist the porous stone; (b) place the lower ring with screws and position the metallic strips; (c) position the upper part and connect it to the loading cell; (d) push the soil sample into the box using an extruder; and (e) position the upper porous stone and the sphere.*

### **5.2.3 Quantification of the mechanical reinforcement of the soil by the roots**

The mechanical reinforcement of the soil by the roots, commonly referred as root cohesion, was calculated in the present work using the W&W model (Wu, 1976; Waldron, 1977) and the fibre bundle model FBM (Pollen and Simon, 2005). The models are presented in the next sections in detail, as well as their input parameters. MATLAB codes were written to implement the models and they are presented in Annex Z.



The root cohesion quantification requires information regarding the amount of roots crossing the failure surface, which is measured in terms of root area ratio (RAR), and the strength of the roots. Roots with a diameter <10 mm are elements that behave like cables, i.e. they only present resistance to tensile forces, so the root tensile strength is a necessary parameter to consider.

### 5.2.3.1 Root area ratio

The distribution of the roots in the ground provides a quantification of the amount of roots that might influence the root-permeated soil shear strength of a given area. The root area ratio (RAR) is defined as the ratio between the area of the roots cross-section ( $A_r$ ) and the area of reference ( $A$ ), as presented in Equation 70. As expected, more than one root will cross this area and probably of different diameters. The value of RAR depends on the number of roots  $N$  with a given diameter  $d_n$ .

$$RAR = \frac{A_r}{A} = \frac{\pi}{4A} \sum_{n=1}^N d_n^2 \quad 70$$

The RAR is a necessary parameter for the calculation of root cohesion in the adopted methods. The root distribution was quantified by collecting the roots from boreholes, as described in detail in the previous chapter, which made its representation forcefully in terms of volume. Therefore, the root area ratio was assumed to be equal to the root volume ratio, which is the volume of roots per unit volume of soil. This approximations was already made in Genet *et al.* (2008) based on the assumption that the root length is equal to the length of the respective section of the soil core.

### 5.2.3.2 Root tensile strength

The quantification of the root tensile strength is a necessary input parameter for the estimation of the reinforcement that a root can provide. In the adopted models, roots are considered to be fibrous elements which strength is mainly mobilized by tension (Wu, 1976).

Experimental works on root tensile strength proposed a simple empirical relation with the form of a power-law as represented by Equation 71, where  $T_r$  is the root tensile strength (force distributed in the area of the cross section of the root) [MPa],  $d$  is the root diameter at the section of breakage [mm] and the parameters  $\alpha$  and  $\beta$  are calibration constants. The experimental works showed that  $\beta$  takes values always lower than zero because the roots with larger diameters present lower tensile strengths.

$$T_r = \alpha d^\beta \quad 71$$

An example of these relations are presented in Figure 178, which were obtained by Bischetti *et al.* (2009). Some experimental values can be found in the works of Gray and Sotir (1996), Comino *et al.* (2010), Mao *et al.* (2012), and Burylo *et al.* (2011).

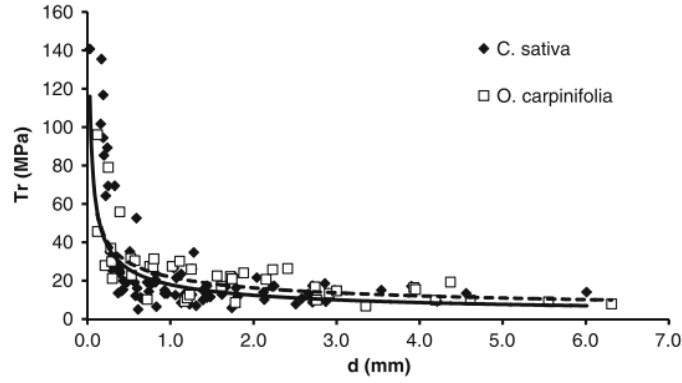


Figure 178 – Tensile strength relation with diameter of different species (Bischetti *et al.*, 2009).

Nonetheless, the quantification of such relations is very time consuming. In the present work, the relation obtained by Bischetti *et al.* (2009) for the roots of *Castanea sativa* was adopted, in which  $\alpha = 17.86$  MPa and  $\beta = 0.53$ . Genet *et al.* (2005) characterized the relation for this species. Both relations are available in the code in Annex Z. The relation proposed by Bischetti *et al.* (2009) was adopted because the estimated root cohesion would be more conservative because the tensile strength provided by this relation is lower. Moreover, the relation proposed by Bischetti *et al.* (2009) was obtained from *C. sativa* from the Italian Alps and a better approximation to the strength of the trees of Mount Faito is expected.

### 5.2.3.3 Wu and Waldron model

In the Wu's and Waldron's Model, also referred as W&W, by Wu (1976) and Waldron (1977), as soil shears, roots are elongated, resulting in mobilization of tensile strength, provided that there is sufficient interface friction and confining stress to lock the root in place and prevent it to slip (Figure 25, Chapter 1). Wu (1976) considered the case of Figure 25 in which the root is perpendicular to the shear zone.

The tensile stress in the root  $T_r$  is converted into the mobilized tensile stress of root fibre per unit area of soil  $t_r$  using Equation 72.

$$t_r = T_r \cdot \frac{A_r}{A} = T_r \cdot RAR \quad 72$$

According to scheme of Figure 25, and assuming that the root out of the shear zone does not deform, tension can be divided into two components, normal and shear stress as represented by Equation 73, where  $\sigma_r$  and  $\tau_r$  are the normal and shear stress, respectively, and  $\theta$  is the shear distortion.

$$\begin{cases} \sigma_r = t_r \cos \theta \\ \tau_r = t_r \sin \theta \end{cases} \quad 73$$

The tangential component resists shear and the normal component increases the confining stress in the shear zone. Therefore, the increase of shear strength provided by the root ( $s_r$ ) may be translated by Equation 74.

$$s_r = \sigma_r \tan \phi' + \tau_r = t_r (\sin \theta + \cos \theta \tan \phi') \quad 74$$

Wu (1976) noticed that the value of  $T_r$  is known and can be obtained from a power-law relation as presented in the section before. The value of  $t_r$  is obtained by knowing the root area. All roots break simultaneously and pull out does not occur was the assumption made in order to extend the previous relations to a root system. Therefore, expanding the tensile strength of root fibres per unit area of soil  $t_r$  is given by the sum of the maximum tensile force of each individual root of all the  $N$  roots that cross the area  $A$  as presented by Equation 75.

$$t_r = \frac{\sum_{n=1}^N T_{r,n} A_{r,n}}{A} = \sum_{n=1}^N T_{r,n} RAR_n \quad 75$$

For simplification, the roots are grouped in diameter classes so that the value of  $T_{r,n}$  is the average tensile strength of the root class,  $RAR_n$  is the root area ratio of the entire class,  $N$  is the number of classes, and the index  $n$  denotes the class. Thus, the predicted shear strength increase depends entirely on the mean tensile strength of the roots and the root area ratio.

The shear strength provided by roots also depend on the distortion angle in the shear zone (Equation 75). However, the value of the angle  $\theta$  is unknown, difficult to quantify and dependent on the thickness of the shear zone and root extension, which led to Wu (1976) to conduct an analysis on the variation of the term " $k' = (\sin \theta + \cos \theta \tan \phi')$ " with the angle  $\theta$ . Wu (1976) concluded that this term is insensitive to  $\theta$  in the range of likely values and it can be approximated to 1.2 simplifying Equation 74 into Equation 76, where  $k'$  is the approximated value. The approximation proposed by Wu (1976) is generally accepted because it was observed in laboratory and field investigations that  $k'$  ranges between 1.0 and 1.3.

$$s_r = k' \cdot t_r \quad 76$$

According to Comino *et al.* (2010), the value  $k'$  depends on the friction angle of the soil, the distortion angle of the sheared roots and on the initial root orientation relative to the failure plane. The W&W model assumed that the roots are perpendicular to the shear zone, which in natural conditions may not be realistic because roots are orientated in many different directions. Consequently, Gray and Ohashi (1983) showed that the perpendicular orientation is not the optimal orientation and that this model provides an average estimation of all possible orientations. This is because an acute angle ( $<90^\circ$ ) between the shear plane and the root as presented in Figure 179 results in the highest increase in shear strength. An oblique orientation ( $>90^\circ$ ) can cause a reduction in the shear strength because the fibres initially go into compression.

Gray and Ohashi (1983) concluded that the reinforcements (fibres, in this case roots) should be oriented in the direction of principal tensile strain in order to mobilize as much tensile strength in the reinforcement as possible. The root with an initial angle of  $60^\circ$  presented the greatest reinforcement, but roots with an angle of  $120^\circ$  had a negative effect.

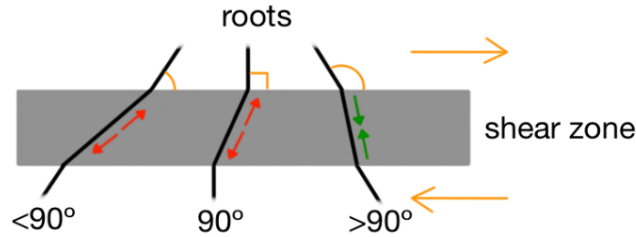


Figure 179 – Scheme of the response of the roots with different orientations with the shear zone.

Additionally, Gray and Ohashi (1983) showed that value  $k'$  does not vary significantly in magnitude for all reasonable and expected values of sand friction angle. In Comino *et al.* (2010) it is referred that  $k'$  takes the value of 1.15 in the work of Waldron (1977) and 1 in Waldron and Dakessian (1981). Thomas and Pollen-Bankhead (2010) recommended the use of a  $k'$  close to 1.0 since that the parameter  $k'$  also intends to take into account the initial angle between the root and the shear surface because the root is tensioned when it is inclined towards the movement direction. When the roots are inclined opposing the movement of the upper layer, the root is subjected to compression providing less strength.

Abe and Ziemer (1991) and Belfiore and Urciuoli (2004) also made some considerations on the simplification of the root deformation assumed by Wu (1976) because the angle  $\theta$  is the parameter that directly controls the tension in the roots, on which depends the root elongation in the shear zone.

Nonetheless, this model tends to overestimate the mechanical reinforcement of soil by roots because roots do not break simultaneously (Pollen and Simon, 2005; Thomas and Pollen-Bankhead, 2010). Better estimations are obtained for grass root systems because the root diameters are more homogeneous (Thomas and Pollen-Bankhead, 2010).

#### 5.2.3.4 Fibre bundle model

In order to respond to the limitations of the model W&W, Pollen and Simon (2005) introduced the Fibre Bundle Model (FBM) to simulate the soil reinforcement provided by the roots. The assumptions of this model are that all the fibres have the same elastic properties, the complexity of root tortuosity is not considered and all roots break rather than pull out of the soil. However, different ways of load distribution by the roots are taken into account so that each root breaks when the load applied to it reaches its maximum tensile strength. The consequence of such assumption is that roots break at different instants as loading increases. Therefore, the maximum load withstood by the bundle of fibres is less than the sum of each of their individual strengths. In other words, the maximum value of tensile strength provided by the bundle cannot be the same as if all the roots provided their maximum strength.

According to Pollen and Simon (2005), the redistribution of the load follows the flowchart presented in Figure 180. This way, the computation considers the following rules:

- The initial load is distributed by the roots;
- The load is increased gradually until it is sufficient to break a root;
- When a root breaks the load is redistributed by the remaining unbroken roots at each time step. It can follow two approaches:
  - Global load sharing (GLS), in which the load is evenly distributed by the remaining roots according to their diameters. This method is more appropriate in case of small failure planes;
  - Local load sharing (LLS), in which the load is redistributed by the neighbouring roots. This approach is more adequate in case a large shear plane is considered, as in slope failures;
- The redistribution of load may cause more roots to break with further redistribution of load (known as an avalanche effect) and so on until no more breakages occur.

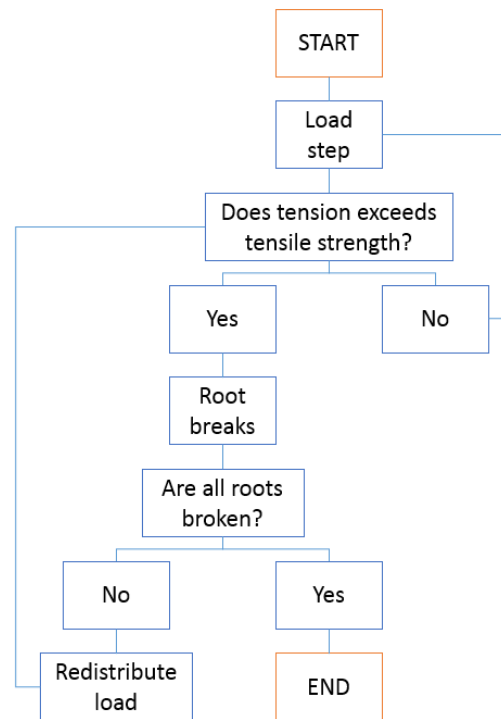


Figure 180 – Flowchart for the FBM computation.

The load can be distributed by the roots according to three different criteria as explained in Mao *et al.* (2012). If a root system with  $i$  different root diameters  $d_i$  with  $n_i$  roots each is considered, a tension force can be distributed by the roots according to the following criteria:

- Proportional to the root cross-section area;
- Proportional to the root diameter;
- Equally distributed by all the intact roots.

The additional cohesion provided by roots to the soil is calculated for a bundle of roots according with the conditions traduced by Equations 77 to 79, where  $n$  is root number ordered from strongest to weakest ( $n \in [1, N]$ ),  $j$  is the weakest root removed at each simulation step ( $j \in [1, N]$ ),  $RAR_n$  refers to the root  $n$  and  $T_{r,j}$  is the strength of the weakest remaining root.

a) Function of the cross-section area

$$s_r = k' \max \left( T_{r,j} \cdot \sum_{n=1}^j RAR_n \right) \quad 77$$

b) Function of the root diameter

$$s_r = k' \max \left( T_{r,j} \cdot RAR_j \cdot \frac{\sum_{n=1}^j d_n}{d_j} \right) \quad 78$$

c) Function of the root index  $i$

$$s_r = k' \max (T_{r,j} \cdot RAR_j \cdot j) \quad 79$$

As observed by several authors, such as Pollen and Simon (2005), Comino *et al.* (2010), Schwarz *et al.* (2010) and Mao *et al.* (2012), FBM provides better estimation of the mechanical reinforcement of soil by roots than W&W.

The ratio between the computed outcomes of the FBM and the W&W has been used to correct the estimated W&W cohesion by introducing this ratio as a coefficient  $k''$  in Equation 76, resulting into Equation 80. This way, the non-simultaneous root breakage predicted by FBM can be considered. Nevertheless, the coefficient  $k''$  is computed using the estimation of FBM according to the criteria that states that the tension is distributed in the bundle according to root area ratio (verify the three possible criteria previously presented).

$$s_R = k' k'' t_R \quad 80$$

In the work of Comino *et al.* (2010), this parameter presented values between 0.40 and 0.99 depending on the species. The range of values obtained by Loades *et al.* (2010) was between 0.48 and 0.82 and the range of Bischetti *et al.* (2010) was between 0.32 and 1.00, according to Comino *et al.* (2010). This coefficient is function of the number of roots (root distribution with depth), the heterogeneity of root diameters and the roots density (Comino *et al.*, 2010).

Thomas and Pollen-Bankhead (2010) investigated this model and recommended the use of GLS as a redistribution load criterion because the data required for a LLS model would be difficult to obtain, even though the real behaviour is somewhere between those two. The adopted load sharing approach in the present work was the GLS because no information was available on how the load is shared in a real case. The load distribution by roots made equally by all the roots independently of the roots diameter was showed to be the most conservative in the estimation of soil shear strength reinforcement.

### 5.2.4 Slope stability analysis

The slope stability study was made based on the calculation of the safety factor ( $SF$ ), which is the ratio between resisting forces and loads. Therefore, a slope is considered stable when the ratio is greater than 1, even though some margin should be left.

Limit equilibrium (LE) applied to an infinite slope model was the adopted method for the calculation of the SF. The infinite slope model was considered adequate because the slope is uniform, i.e. almost constant angle with soil layers of comparable thicknesses spread on a large area. Additionally, a previous study on slope stability of the same type of slope, pyroclastic soil covers in Monteforte Irpino, using the finite element method (FEM) revealed that the failure surface would be parallel to the ground surface (Pirone, 2009).

The safety factor was calculated as in Pirone *et al.* (2015a), in which the additional term related to the increase of shear strength by roots is now included. In Equation 81,  $\alpha$  is the slope angle,  $c_r$  is the root cohesion,  $S_r$  is the degree of saturation,  $s$  is the suction, and  $\varphi'$  is the soil friction angle.

$$SF = \frac{\tau_f}{\tau} = \frac{\tau_{soil} + \tau_{suction} + \tau_{roots}}{\tau} = \frac{\sigma \tan \varphi' + S_r s \tan \varphi' + c_r}{\tau} \quad 81$$

$$= \frac{z\gamma \cos^2 \alpha \tan \varphi' + S_r s \tan \varphi' + c_r}{z\gamma \sin \alpha \cos \alpha}$$

The term  $z\gamma$  is the product between the soil unit weight ( $\gamma$ ), given by Equation 82, and the thickness of the soil layer above the adopted failure surface ( $z$ ). As the soil profile is composed of soil layers of different thicknesses and with different soil unit weight resultant from the fact that water content varies along the year and each soil layer presents a particular porosity ( $n = e/(1 + e)$ ) and solid particles with particular specific gravity ( $G_s$ ).

$$\gamma = \gamma_d \left( 1 + \frac{S_r e}{G_s} \right) \quad 82$$

If a water table is detected during the monitoring period, the term  $z\gamma$  needs to be reduced by height of the water table above the adopted failure surface multiplied by the water unit weight ( $10 \text{ kN m}^{-3}$ ).

## 5.3 Results and discussion

### 5.3.1 Soil hydro-mechanical properties

#### 5.3.1.1 Saturated conditions direct shear test

The experimental results resultant from the direct shear tests performed on soil A1 and C1 in saturated conditions are here presented. Results also included in Esposito (2017).

The measured settlements during consolidation and saturation are presented for soil A1 as an example. In the shear phase of soil A1 and C1, the vertical displacement and the ratio between the confining stress and the shear stress are presented.

The estimation of the void ratio change was made based on the vertical settlements (Table 37 and Table 38). The initial void ratio varied between 1.6 and 3.9 for soil A1 (Table 37), which corresponds to porosities between 0.61 and 0.8. These porosity values are extremely high and in a greater range than the observed porosity observed in soil A1sup in the hydraulic characterization (Chapter 3). The samples that were partially unloaded are referred in the consolidation column with letter 'b' and the ones that were not unloaded are referred with letter 'a'.

*Table 37 – Vertical settlements (dv) and void ratio (e) change along the tests on soil A1.*

consolidation	initial load	final load	initial	consolidation		submersion		unload		final	
			e	dv (mm)	e	dv (mm)	e	dv (mm)	e	dv (mm)	e
a	25	25	1.616	0.492	1.552	0.524	1.483	-	-	0.223	1.454
a	50	50	1.812	1.933	1.540	0.925	1.410	-	-	-0.421	1.470
a	75	75	1.879	1.590	1.650	0.984	1.509	-	-	0.705	1.407
b1	75	25	3.966	3.839	3.013	1.297	2.691	-0.031	2.699	-0.241	2.759
b2	75	25	2.687	2.090	2.301	0.727	2.167	-0.109	2.187	-0.486	2.277
b	150	50	2.854	5.834	1.730	0.696	1.596	-0.133	1.621	-0.161	1.652
b	225	75	2.578	4.282	1.812	0.501	1.722	-0.111	1.742	-0.257	1.788

*Table 38 – Vertical settlements (dv) and void ratio (e) change along the tests on soil C1 in saturated conditions.*

consolidation	initial load	final load	initial	consolidation		submersion		unload		final	
			e	dy (mm)	e	dy (mm)	e	dy (mm)	e	dy (mm)	e
a1	50	50 (a)	2.206	0.149	2.182	0.044	2.175	-	-	0.106	2.158
a2	50	50 (b)	2.136	1.094	1.965	0.105	1.948	-	-	0.218	1.914
a	75	75	1.817	0.918	1.688	0.026	1.684	-	-	0.118	1.668
a	25	25	1.459	0.762	1.366	0.058	1.359	-	-	0.323	1.319
b	150	50	2.100	1.619	1.849	0.337	1.797	-0.171	1.824	-0.041	1.830
b	75	25	2.507	2.642	2.044	1.265	1.822	-0.323	1.879	-0.217	1.917
b	225	75	2.016	2.788	1.596	0.161	1.571	-0.120	1.589	-0.099	1.604



The void ratio decreased during the consolidation depending on the applied stress and on the initial void ratio (Figure 181). The saturation of the soil also produced a reduction of void ratio but smaller than the settlement resultant from the consolidation (Figure 182). The samples that were unloaded recovered some settlement with the swelling resultant from the unloading (Table 37).

The void ratio before shearing varied between 1.4 and 2.7, which corresponds to porosities of 0.58 to 0.73. The shear produced an increase in void ratio in the 'b' samples and a decrease of void ratio in two of the 'a' samples (Figure 183). The ratio  $\tau/\sigma'$  varied between 0.6 and 0.85. Almost all samples reached the limit state (constant shear stress and no variation of volume).

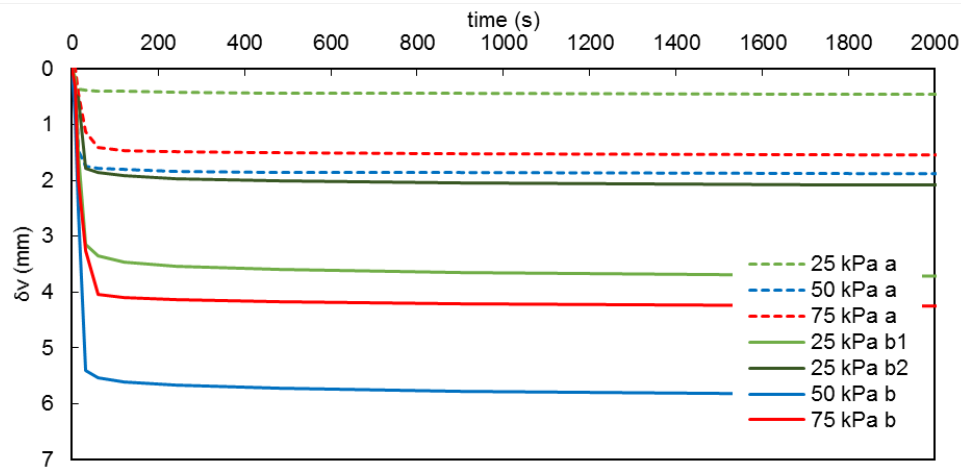


Figure 181 – Vertical displacements ( $\delta v$ ) during the consolidation phase in samples of soil A1.

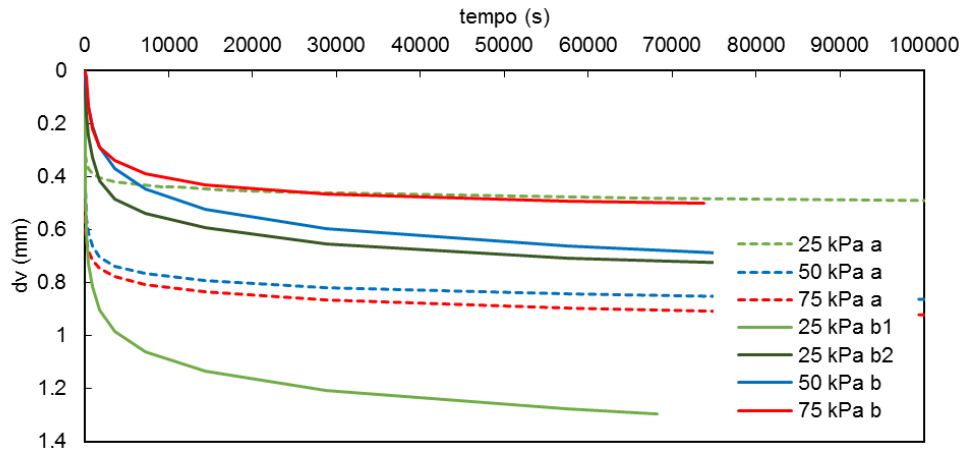


Figure 182 – Vertical displacements ( $dv$ ) during the saturation phase in samples of soil A1.

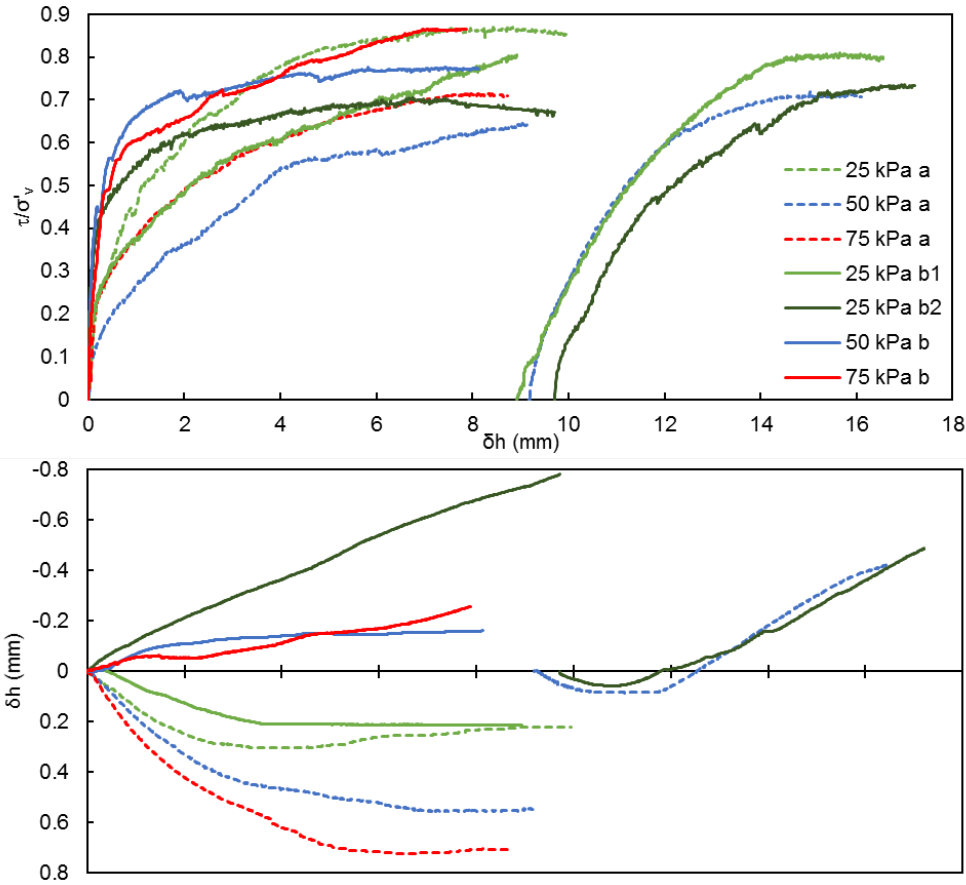


Figure 183 – Ratio between shear and confining stress ( $\tau/\sigma'$ ), and vertical displacement ( $dv$ ) measured during the shear phase with horizontal displacement ( $dh$ ) in samples of soil A1.

The initial void ratio varied between 1.4 and 2.5 in soil C1 (

Table 38), corresponding to porosities of 0.65 to 0.71. These values are similar the porosity observed in the hydraulic characterization of Chapter 3 but closer to the lower range. The porosity of the samples was even lower at the time of the shear phase reducing to 0.58 to 0.69.

The ratio  $\tau/\sigma'$  in soil C1 varied between 0.55 and 0.7 (Figure 184), which is lower than in soil A1, and so soil C1 presents a lower friction angle. The limit state was much easier to identify in soil C1 which presented very stable measurements.

In Figure 185 are represented the limit shear strength obtained from each shear test separated in type 'a' and 'b'. The envelope according to the Mohr-Coulomb criteria is also represented. The intrinsic soil friction angle obtained for soil A1 was  $36.5^\circ$  and  $32.1^\circ$  for soil C1. Soil A1 is comparable to soil 1 and soil C1 is comparable to soil 6 from Monteforte Irpino studied by Papa *et al.* (2008). The values of friction angle of soil 1 was  $36.9^\circ$ , which is similar to the obtained results in the present work. However, the friction angle of soil 6 ( $39.8^\circ$ ) is much higher than the value obtained in this work.

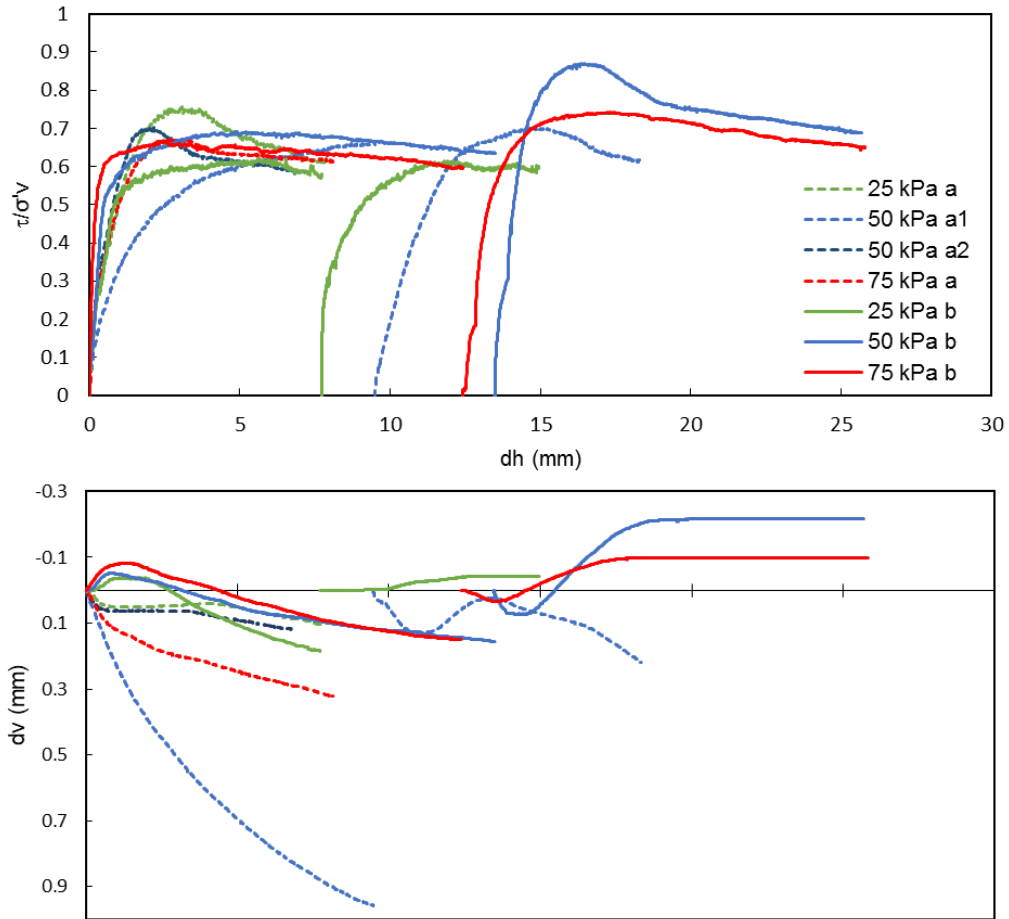


Figure 184 – Ratio between shear and confining stress ( $\tau/\sigma'_v$ ), and vertical displacement ( $dv$ ) measured with horizontal displacement ( $dh$ ) during the shear phase of NC and OC samples of soil C1.

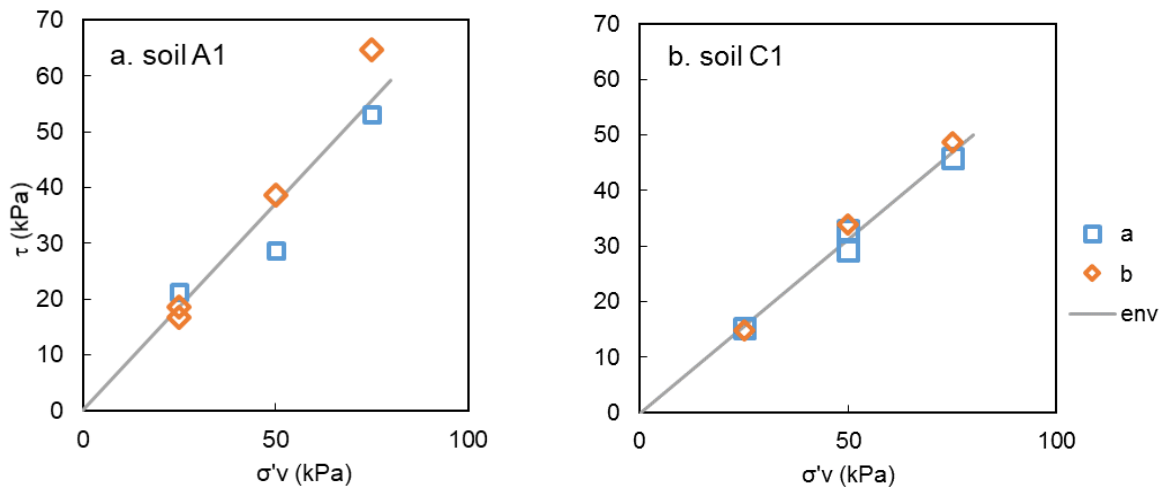


Figure 185 – Limit shear strength and Mohr-Coulomb failure envelope of soil (a) A1 and (b) C1: confining stress ( $\sigma'_v$ ) and correspondent shear strength ( $\tau$ ).

### 5.3.1.2 Unsaturated direct shear test

The list of tested samples is presented in Table 39 with the respective confining stress, suction, and evolution of the samples' void ratio ( $e$ ). The initial values of void ratio correspond to porosities of 0.50 to 0.68, similarly to the tested in the traditional direct shear test. The consolidation phase, processed at constant suction, led to smaller settlements than in the traditional direct shear tests in which the consolidation occurred at constant water content.

Table 39 – Settlements ( $dv$ ) and void ratio ( $e$ ) change along the tests on soil C1 in unsaturated conditions.

Tests #	Confining stress (kPa)	Suction (kPa)	Initial	Consolidation		Final	
			$e$	$dv$ (mm)	$e$	$dv$ (mm)	$e$
1	50	8	1.857	0.540	1.780	0.098	1.766
2	75	35	2.006	0.650	1.908	-0.053	1.916
3	25	7	2.148	0.401	2.085	0.426	2.018
4	50	30	1.580	1.158	1.431	0.903	1.314
5	50	35	1.100	0.610	1.036	0.323	1.002
6	25	30	1.012	0.200	0.992	-0.202	1.012

The suction in the samples was measured through the axis translation technique and it is calculated as the difference between the air pressure in the chamber and the water pressure measured in the porous stone located below the soil sample. An air pressure of 100 kPa was applied in the chamber as it was expected to exceed the suction value. Therefore, 100 kPa is the initial measured value of suction, that starts to decrease because initially water pressure is 0 kPa (Figure 186). Stable values of suction were obtained approximately 400 minutes after the air pressure was applied.

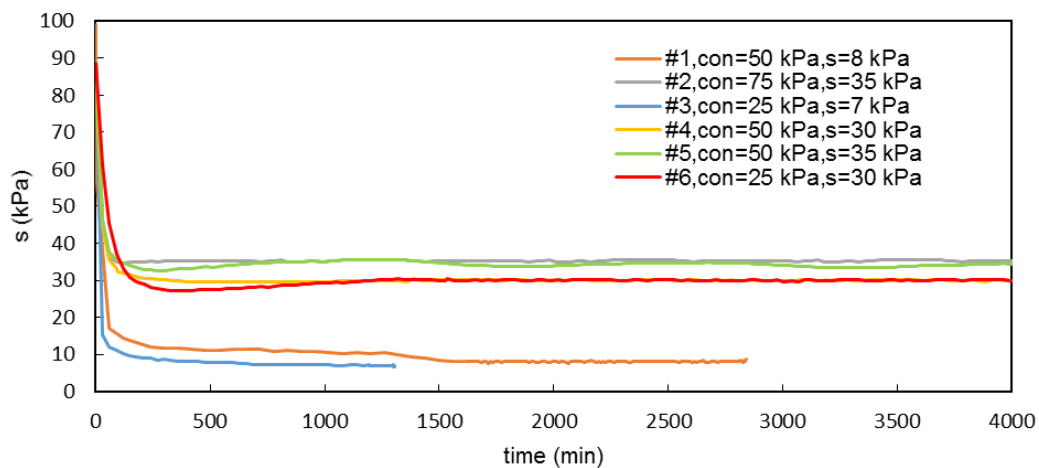


Figure 186 – Measurement of suction ( $s$ ) after applying the chamber air pressure.

The initial void ratio and volumetric water content are related to suction in Figure 187. The measured values present a considerable scatter but variability among soil samples should be accounted. The measured values are in agreement with the mean main WRCs obtained in Chapter 3 for soil C1 (Figure 187,b), except for the point correspondent to saturation (1 kPa) and the test #1 (8 kPa). The void ratio tends to decrease with increasing suction which is a consequence of the increasing stress to which the soil is subjected (Parent *et al.*, 2007; Cardoso *et al.*, 2011).

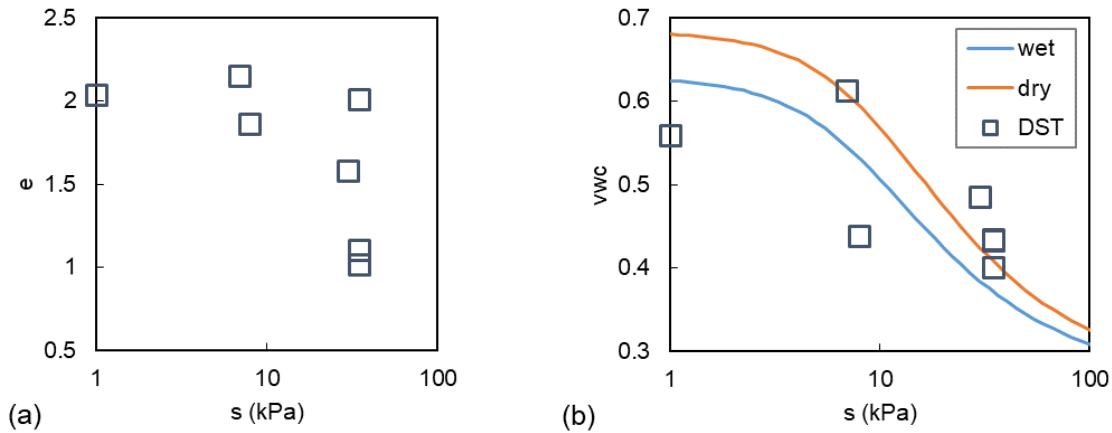


Figure 187 – Initial (a) void ratio ( $e$ ) and (b) volumetric water content ( $vwc$ ) for each measured suction ( $s$ ) (the mean WRCs from Chapter 3 and an additional point correspondent to saturation).

The vertical settlements during consolidation are presented in Figure 188. This phase was processed at constant suction for which water content was allowed to vary. The suction is maintained constant by applying a water pressure in the sample equal to the initial measured one. As the water and air pressures are maintained constant, the sample is forced to exchange water with the burette system during its change of volume.

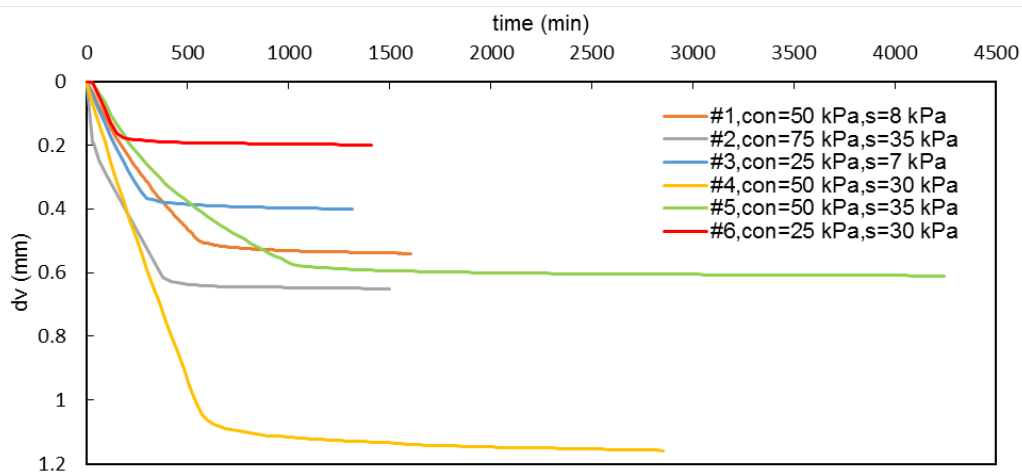


Figure 188 – Vertical settlement ( $dv$ ) during consolidation.

The shearing phase, represented in Figure 189, is also performed at constant suction. In most of the tested samples, the shear resulted in a decrease of void ratio (Table 39, Figure 189). The void ratio only increases in two tests with suctions of 30-35 kPa. The values of the ratio between the limit shear strength and the normal Bishop stress represented in Figure 190 varied between 0.6 and 1, higher than the ratio obtained in the traditional direct shear tests.

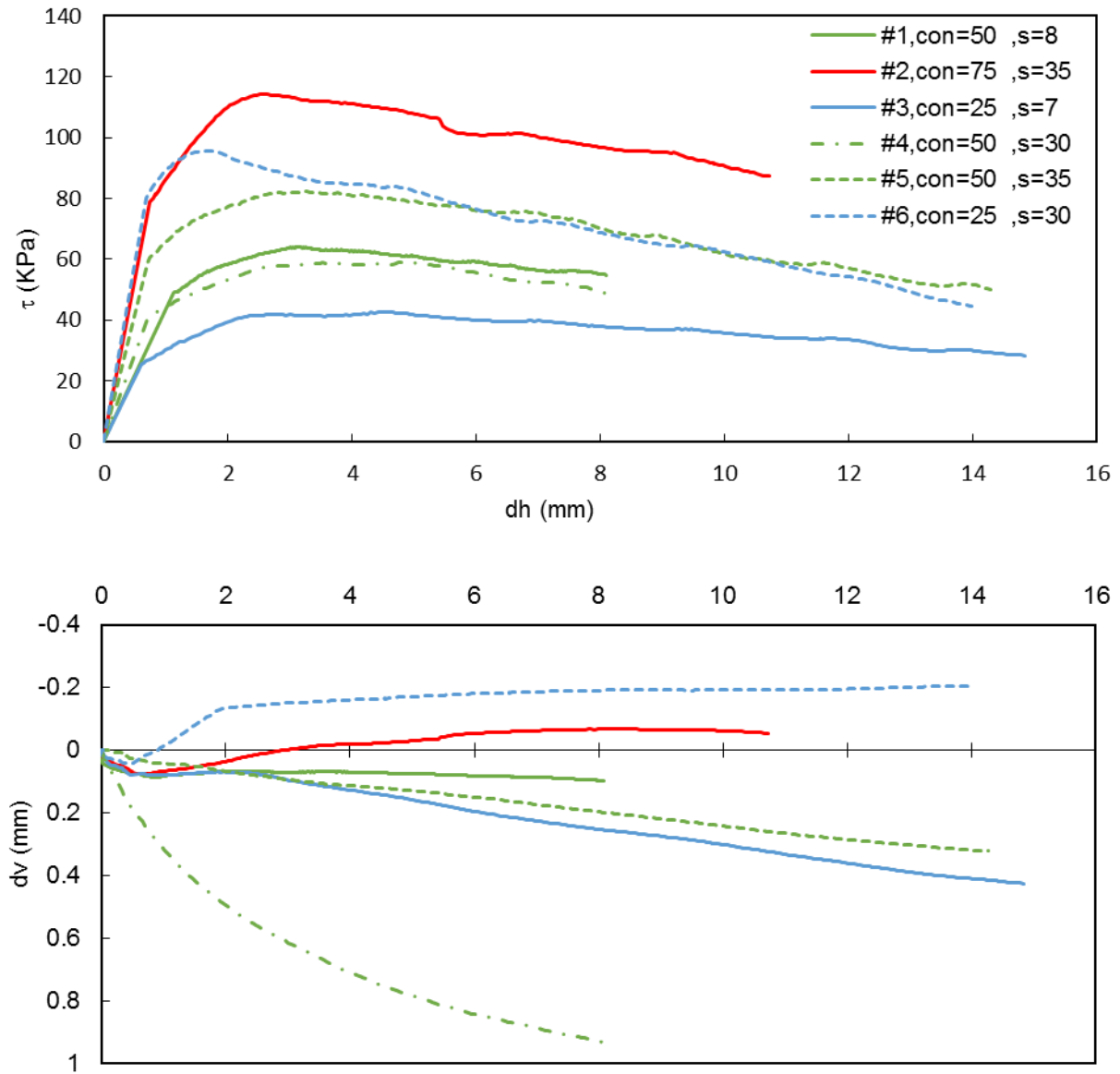


Figure 189 – Shear stress ( $\tau$ ) and vertical displacement ( $dv$ ) with horizontal displacement ( $dh$ ) during the shear phase.

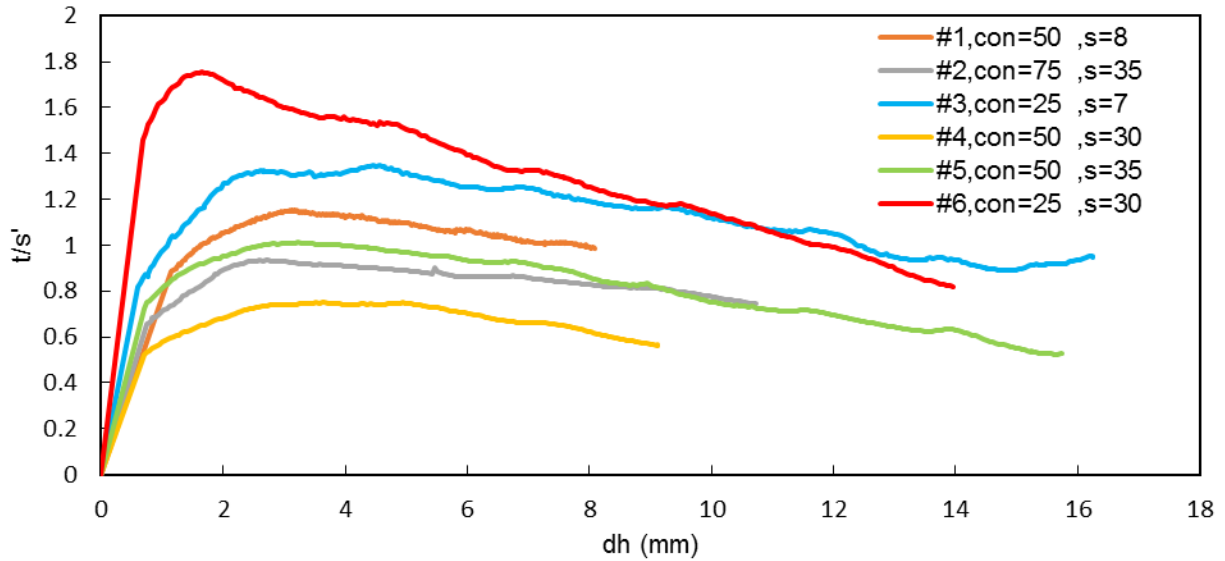


Figure 190 – Ratio between shear and Bishop stress ( $t/s'$ ), and vertical displacement ( $dv$ ) measured with horizontal displacement ( $dh$ ) during the shear phase.

The friction angle obtained from the direct shear tests performed at constant suction ( $38.5^\circ$ ) was higher than the values obtained in the traditional test ( $32.1^\circ$ ), as observed in Figure 191. The soil C1 is comparable to soil 6 of Monteforte Irpino (Papa *et al.*, 2008), as stated before, which presented a friction angle of  $39.8^\circ$  also obtained from unsaturated direct shears tests. In general, pyroclastic soils present high internal friction angles, varying between  $31^\circ$  and  $40^\circ$  in Urciuoli *et al.* (2016) and between  $30^\circ$  and  $41^\circ$  in Bilotta *et al.* (2005).

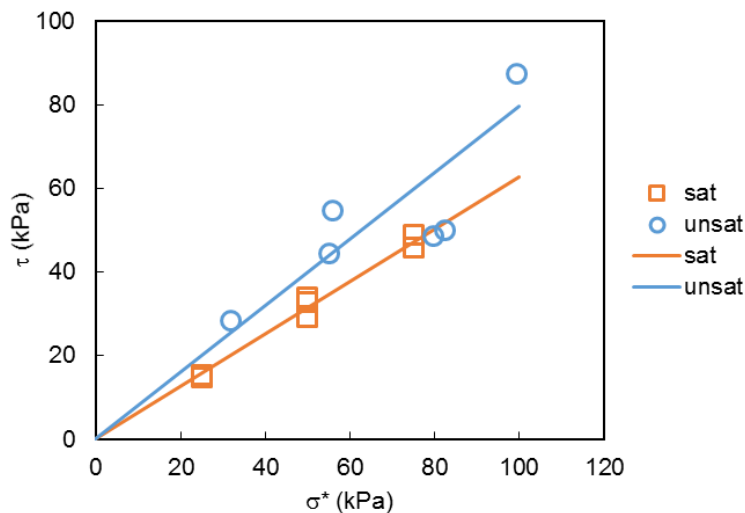


Figure 191 – Limit shear strength ( $\tau$ ) and Mohr-Coulomb failure envelopes of soil C1 obtained from direct shear tests in saturated (sat) and unsaturated (unsat) conditions.

### 5.3.2 Mechanical reinforcement of the soil by the roots

The mechanical reinforcement of the soil by the roots was observed to decrease with depth reaching its minimum between 1.5 and 2 m, which corresponds to the soil layer B. The reinforcement increases slightly again beyond 2 m of depth in the soil C1. All the results are reported in Annex AA, including the root cohesion along depth for each profile, the mean and standard deviation of the root cohesion for an average depth and the coefficient  $k''$ .

The highest mechanical reinforcement estimation was obtained using the W&W model with the coefficients  $k' = 1$  and  $k'' = 1$ , represented in Figure 192 with the label 'W&W0'. This method was already showed to overestimate the strength provided by roots by Thomas and Pollen-Bankhead (2010) and Schwarz *et al.* (2013), mainly because all roots are assumed to fail by breaking and that all roots fail simultaneously.

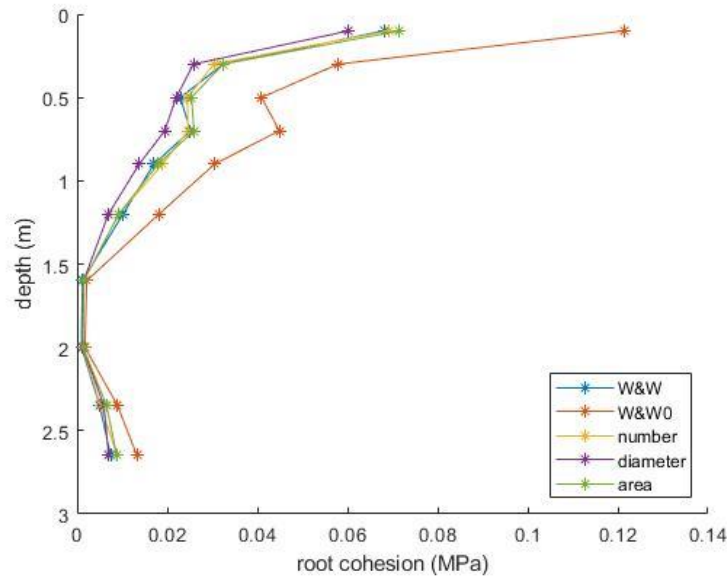


Figure 192 – Mean root cohesion obtained from W&W model when  $k''=1$  (W&W0) and when  $k''=0.56$  (W&W) after Bischetti *et al.* (2009) and FBM with load distribution according with the number of roots, the roots diameter and the roots area class (referred as number, diameter, and area, respectively) with depth.

Different load distribution criteria adopted in the estimation of mechanical reinforcement from the FBM were tested: (i) equally distributed by all the diameter classes, (ii) distributed in proportion to the mean root diameter of each class, and (iii) in proportion to the RAR of each class. The load distribution criteria i, ii, and iii are referred as 'number', 'diameter' and 'area' in Figure 192. All the alternatives presented similar results but still the option (ii), in proportion to the diameter, was the most approach. The root cohesion estimated with FBM was significantly lower than the values obtained with the W&W model. The  $k''$  coefficient presented values ranging from 0.77 to 0.38. Smaller differences between both models were obtained when to root cohesion is lower, i.e. in soil B (1.5 to 2 m). When the  $k''$  suggested in Bischetti *et al.*



(2009) was adopted ( $k'' = 0.56$ ), reported as 'W&W' in Figure 192, similar results were obtained to the FBM estimations.

The soil moisture was related to the mechanical reinforcement of the soil by the roots by Pollen (2007). Roots of greater diameter tended to break instead of pulling out. As the soil becomes drier, smaller diameter roots also tend to break because suction increases and so the soil-root shear strength. Consequently, the mechanical reinforcement of the soil by the roots is greater when the soil is drier. Pollen (2007) observed significant changes in the safety factor of the streambanks as a consequence of the effect of hydraulics in the mechanical reinforcement of the soil by roots. The mechanical reinforcement estimated in Mount Faito may still constitute an overestimation leading to potential failure surfaces with higher safety factors than in reality.

### 5.3.3 Slope stability

#### 5.3.3.1 Adopted parameters

The mean values of suction and water content presented in Chapter 4 were used for the calculation of the safety factor (SF) in the present chapter. The mean angle of the slope was adopted, corresponding to  $26.5^\circ$ . The root cohesion calculated using the FBM assuming load distribution among roots proportional to diameter of the roots of each class was adopted because it led to the lowest root cohesion values, and so, more conservative estimations.

The summary of the adopted properties for each soil layer is presented in Table 40. Some layers were subdivided and water content and/or suction were assumed constant and equal to the mean measured values in the equipment installed within that depth range.

*Table 40 – Adopted soil properties in the calculation of slope stability.*

Soil	Mean installation depth (m)	Porosity, $n$	Specific gravity, $G_s$	Mean layer thickness (m)	Friction angle, $\phi'$ ( $^\circ$ )	Root cohesion, $C_r$ (kPa)
A1	0.21	0.643	2.606	0.35	36.5	25.8
A2	0.54	0.694	2.688	0.60	36.5	22.0
B	1.11	0.800	2.550	0.56		
B	1.61	0.800	2.550	0.56		
C1	2.20	0.722	2.656	0.23	38.5	1.3
C1	2.47	0.722	2.656	0.23	38.5	5.9
C2	2.73	0.666	2.528	0.19	37.0	7.0

As the mean slope angle is smaller than the soil friction angle in any soil layer, the estimated SF of the slope is always greater than 1 even if suction and root cohesion are null. The stability of a slope can become

an issue when the slope angle is greater than the soil friction angle so that root cohesion and suction shear strength are necessary to maintain the SF above 1.

### 5.3.3.2 Safety factor

The safety factor associated to potential failure surfaces assumed at the depth of installation of the monitoring equipment (tensiometers and TDR probes) is presented in Figure 193(a). Soil A1 presented the highest SF but the failure surface is assumed at 0.2 m from the surface, which means that the confining stresses are very low. The SF decreased by one third when the failure surface was assumed in A2, 0.3 m below the soil surface. The lowest SF values were observed in soil layers C1 and C2 (Figure 193,b).

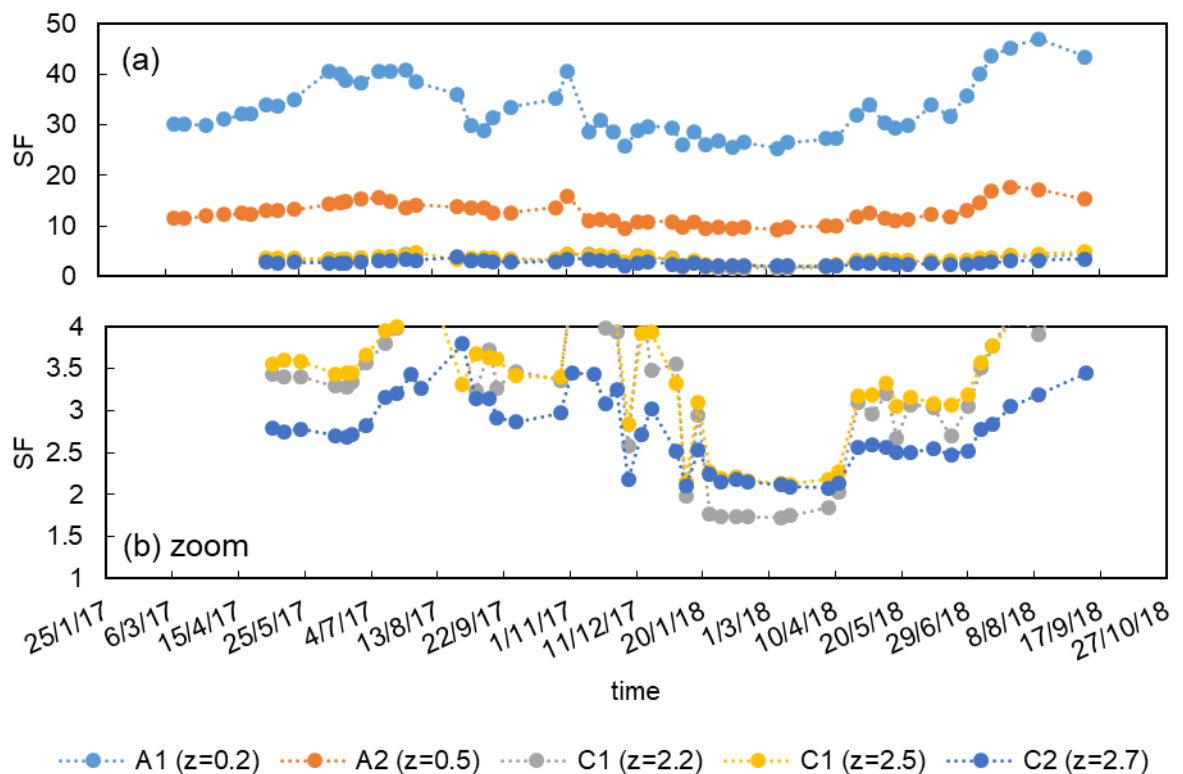


Figure 193 – Safety factor (SF) along the monitoring period (a) assuming failure surfaces at different depths and (b) a close up in the most critical depths (2.2 m, 2.5 m and 2.7 m).

The significant decrease in SF from a 0.2 to a 0.5 m deep failure surface observed in Figure 193 seemed alarming because the hydraulic head decreases with depth during the wet season. That means that suction decreases with increasing depth in soil A1 and A2, even if the same water content was measured in these two layers. Additionally, root cohesion also decreases with depth.

A simple test was made assuming that the failure surface was at the bottom of soil layer A2, at a depth of 0.9 m. The root cohesion at this depth is 13.8 kPa. Suction was calculated assuming a hydrostatic

distribution of pressure and the water content was assumed to be equal to the average measured in soil layers A1 and A2. The obtained SF along the year is presented in Figure 194 in comparison to the values obtained at 0.2 m (soil A1) and 0.5 m (soil A2). The SF considerably decreased and values closer to what was observed in soils C1 and C2. The lowest estimated SF of a failure surface at 0.9 m was 4.2 when the mechanical reinforcement of soil by roots was considered.

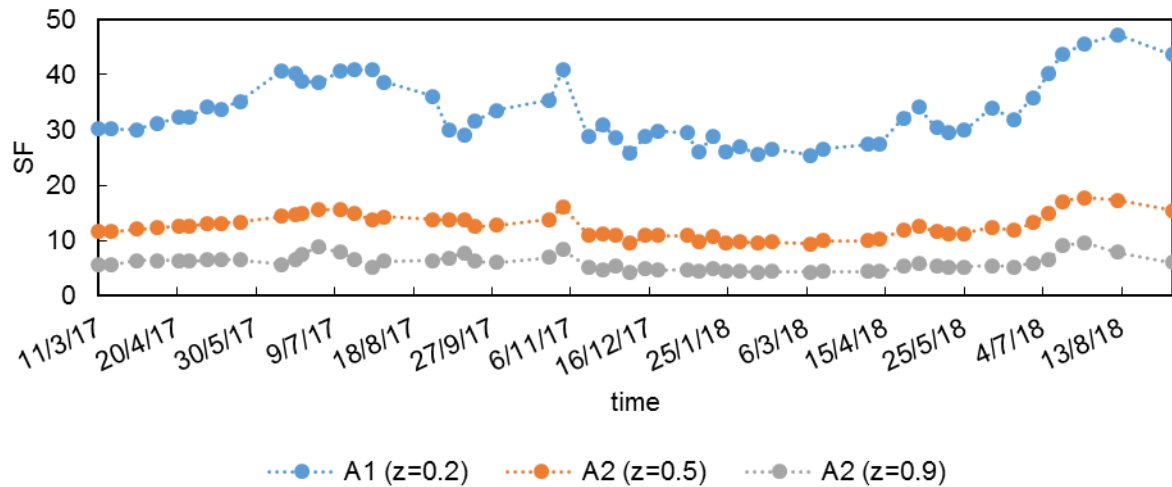


Figure 194 – Variation of the safety factor (SF) with increasing depth of the failure surface in soil A1 and A2.

The lowest SF observed along the year was of 1.7 in soil layer C1 for a failure surface at 2.2 m of depth, on March 8<sup>th</sup> 2018. No significant variations were observed from January 24<sup>th</sup> to March 14<sup>th</sup> in the SF, i.e. the SF was maintained at its lowest for approximately 1.5 months. This observation is in agreement with the failure surfaces, identified by Di Crescenzo and Santo (1999), of previous landslides that occurred in this region. The failure surface in the sliding zone of mud flows and debris flows type of landslides were identified in all the stratigraphic profiles containing the layer of pumices (gravel identified in Mount Faito by soil layer B) similarly to what might be expected from the result of the present work. The sliding surface was in the pumices layer or right below it (Figure 195). On the other hand, the landslides were usually triggered in areas of rocky cliffs and road cuts (Di Crescenzo and Santo, 2005). Indeed, landslides are not expected to be initiated at the test site in Mount Faito, especially because of the steepness of that site.

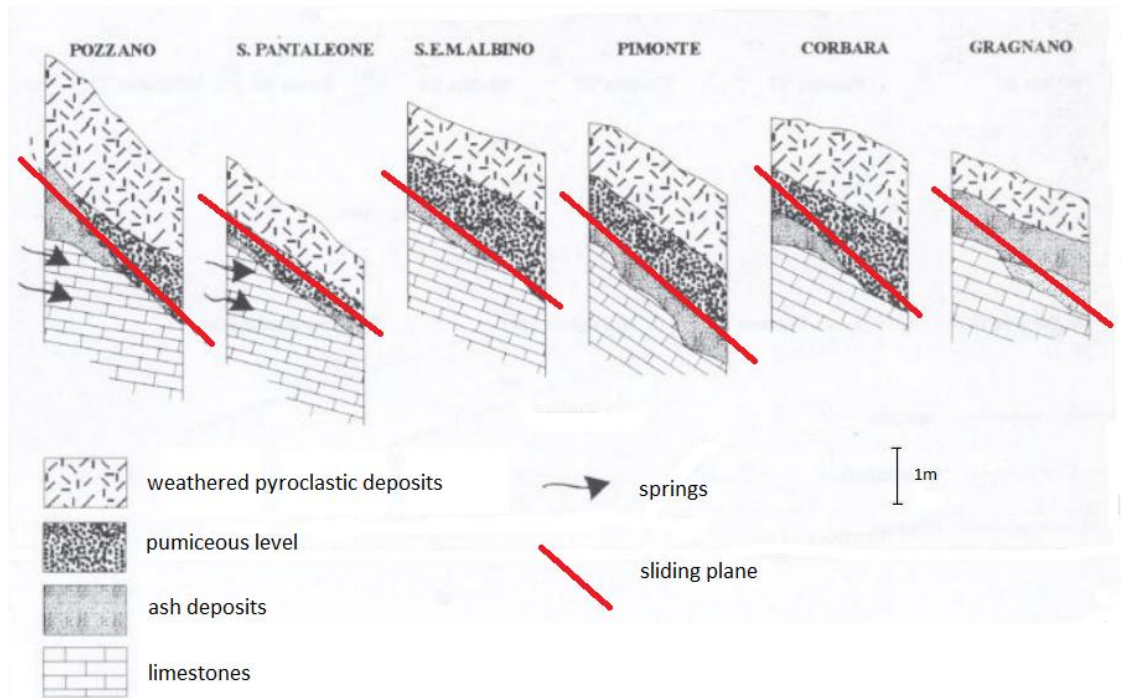


Figure 195 – Sliding surfaces and geological profiles in the sliding zone of previous landslides (adapted from Di Crescenzo and Santo, 1999).

The lowest SF values were observed in soil C2 over the rest of the year. The soil layers C1 and C2 were the most sensitive to seasonal trends of suction and water content and the effect of single extreme events were detected after approximately two weeks. Thus, the rainfall events that led to such low values of SF were not possible to be identified.

The stratigraphic profile of a test site in Monteforte Irpino, studied by Pirone *et al.* (2015b), and Cervinara (Italy, South Italy), studied by Damiano *et al.* (2012), present some resemblances to the profile of Mount Faito. The slope angle of Monteforte is of  $30^\circ$ , which is  $3.5^\circ$  higher than the angle of the slope at Mount Faito. The slope angle in Cervinara is of  $40^\circ$ , much higher than Mount Faito. At Monteforte test site, chestnuts were coppiced and bushes were the main present vegetation (Pirone *et al.*, 2015b), while chestnut trees “chestnut trees which are regularly cultivated” were present at Cervinara but have been purposely avoided in the installation of instruments. Damiano *et al.* (2012) and Pirone *et al.* (2015b) investigated the safety factor assuming a failure surface in each soil layer but ignoring the mechanical reinforcement provided by roots.

The mechanical contribution of roots was also ignored in the SF calculation at Mount Faito in Figure 196. The estimated SF of soil A1 and A2 of Mount Faito resemble the SF of soil layer 1 and 2 of Monteforte. The remaining soil layers in Monteforte are not comparable to any other of Mount Faito because soil layers 4 and 6 do not have a correspondent layer of the same grain size distribution at the same depth in the Mount

Faito profile. The soil profile of Monteforte Irpino and Cervinara test site are very similar and maybe directly compared as in Urciuoli *et al.* (2016).

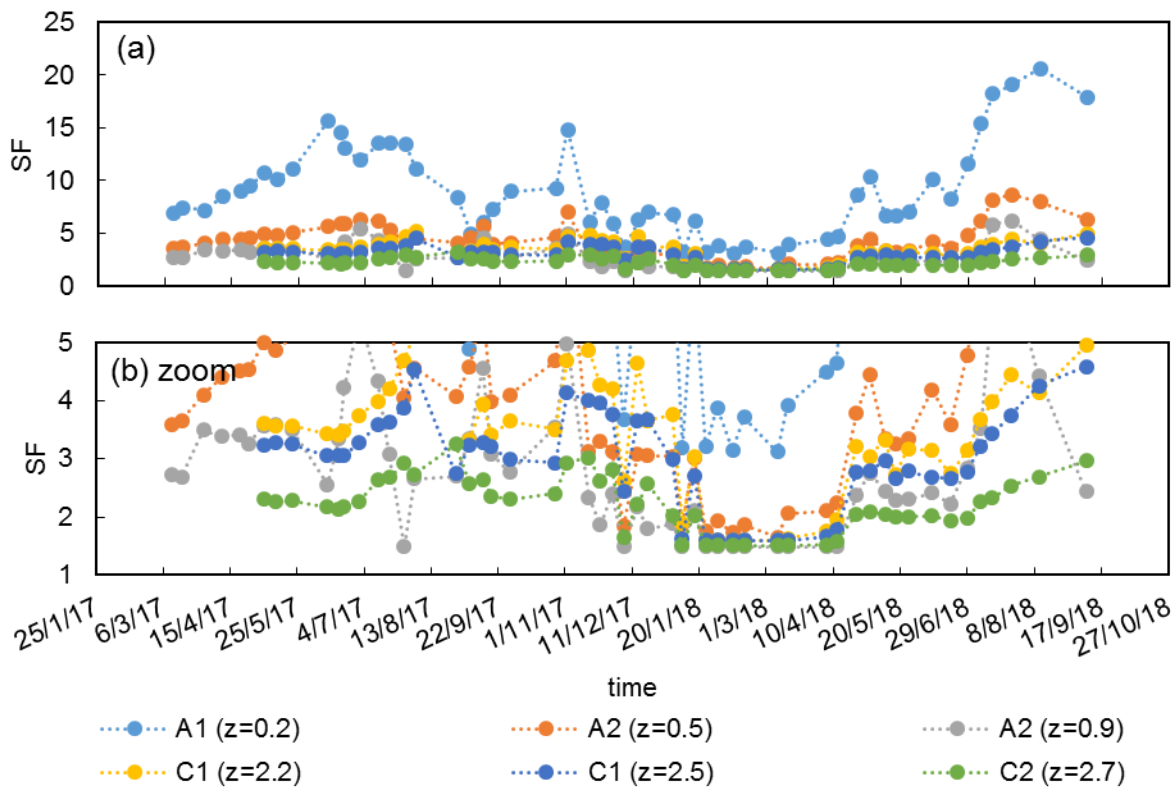


Figure 196 – Safety factor (SF) ignoring the root contribution assuming failure surfaces at different depths (a) and a zoom of the lower range of SF (b).

The minimum SF assessed in Monteforte was approximately 1.4 in soil layer 4 (Figure 197), while the lowest value at Mount Faito was 1.7 in soil C1 when the root shear strength was considered and 1.5 in soil A2 at 0.9 m and C2 at 2.7 m when the root contribution was not considered (Figure 196,b). In Cervinara, two extreme rainfall events have been identified as critical for leading to safety factors as low as 1.1 in two different potential failure surfaces. The potential failure surfaces were located at 0.6 m and 1.8 m in layers of volcanic ashes. The effect of the slope angle is evident in this comparison, as potential failure surfaces were identified at similar depths in all the test sites where volcanic ash deposits are found. The steepest test site (Cervinara) presented the lowest safety factor along the monitoring period, followed by Monteforte. Mount Faito, which was the test site with the lowest slope angle, presented the highest safety factor.

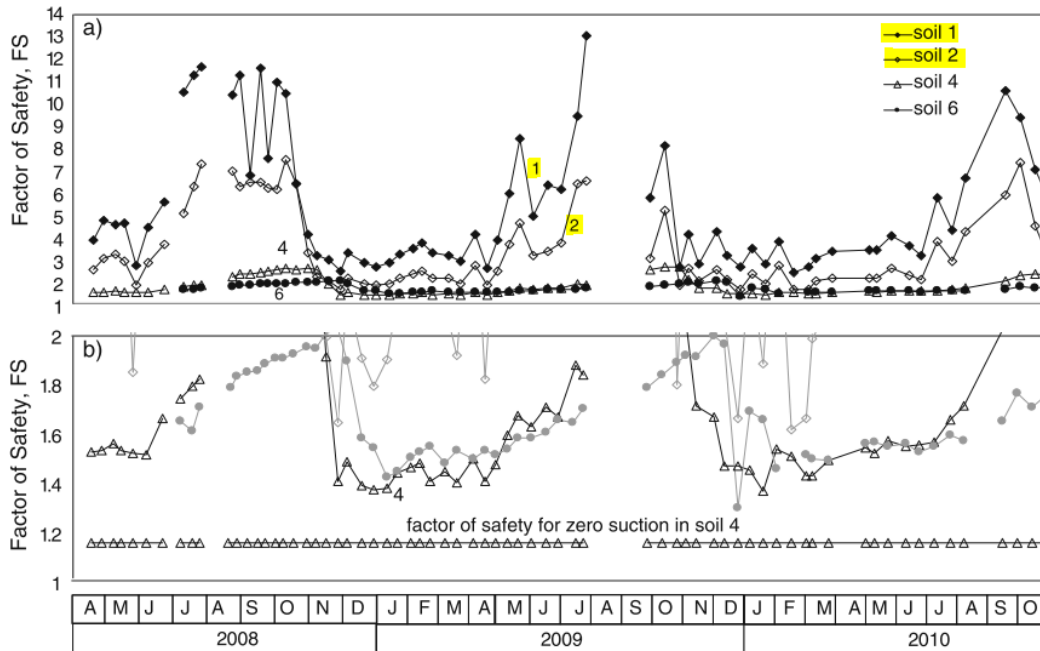


Figure 197 – Safety factor over time assuming a failure surface in different soil layers in the profile of Monteforte Irpino (adapted from Pirone et al., 2015b).

More than 74% of the landslides studied by Di Crescenzo and Santo (2005) in Campania occurred or were triggered in shrubland in comparison to less than 26% in *C. sativa* coppiced areas. This is an evidence that the hydro-mechanical effect of trees constitutes an important factor for the stability of the slopes composed of pyroclastic soil deposits and not considering the mechanical reinforcement of soil by roots may lead to an erroneous identification of the weakest failure surface.

The SF was estimated considering different slope angles if the mechanical reinforcement of soil by roots is considered and ignored, referred as 'with roots' and 'without roots' respectively in Figure 198. This calculation implies that the groundwater regime is assumed independent from the slope angle as well as the root distribution, which might be an excessive assumption. The values presented in Figure 198 are the minimum SF estimated at any time during the monitoring period among all the assumed failure surfaces. An increase of  $5.7^\circ$  in the angle of the slope is necessary to compensate the difference in the strength resultant from the presence of roots, i.e. from 'minimum  $\varphi$ ' to 'SF=1 with roots'. The local maximum angle detected in the monitored area results in the SF values lower than 1. The reason for the slope to be maintained stable is that the slope only presents this angle in a very restricted area.

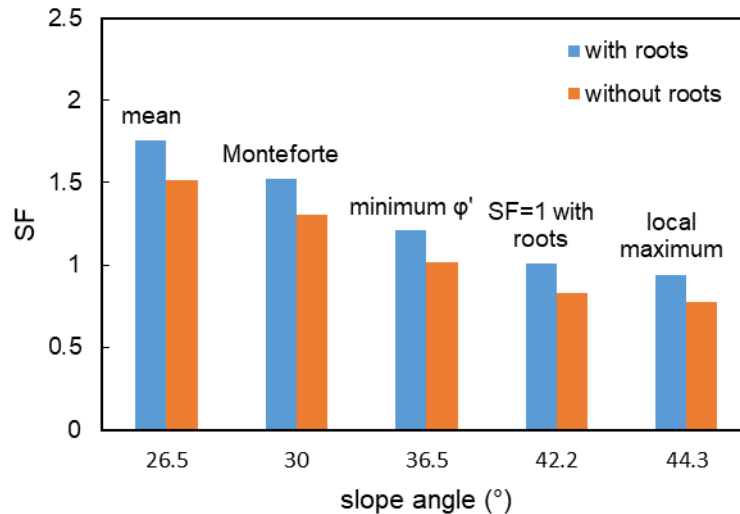


Figure 198 – Minimum estimated safety factor (SF) for different slope angles considering and not the presence of roots.

The mean slope angle of Mount Faito test site belongs in the range of critical steepness of the sliding zone identified by Di Crescenzo and Santo (2005), which is from 26° to 30°. The critical range of slope angles of the crown zones ranged between 35° to 45°, which corresponds to angle values where the mechanical reinforcement of the roots would no longer be enough to guarantee the slope stability in Mount Faito according to the estimations presented in Figure 198.

### 5.3.3.3 Relative contribution of roots, suction and soil shear strength to the stability

The additional strength provided by roots lead to an increase in the SF associated to all potential failure surfaces, especially in soil A1 and A2. The roots in soil A1 ( $z=0.2$  m) and A2 ( $z=0.5$  m) are responsible for an increase of 25.8 kPa and 22.0 kPa, respectively, in the soil shear strength through cohesion. This is a 74 % and 67 % increase in SF in both upper layers (Figure 199,a,b). The SF of the potential failure surfaces in soil A1 and A2 at less than 0.5 m of depth is very high mostly due to the mechanical reinforcement by roots (60 % to 90 %), nullifying any negative effect that the roots may have on the propagation of the wetting front within the upper soil layers or even in the possibility of occurrence of the soil saturation. The potential failure surface at 0.9 m in soil A2 shows that the root cohesion still presents a great contribution to the estimated safety factor and that suction contribution to the shear strength and soil shear strength present similar weight in the stability of the slope (Figure 199,c). Nonetheless, during of the wet period of January to March 2018, the contribution of suction was null.

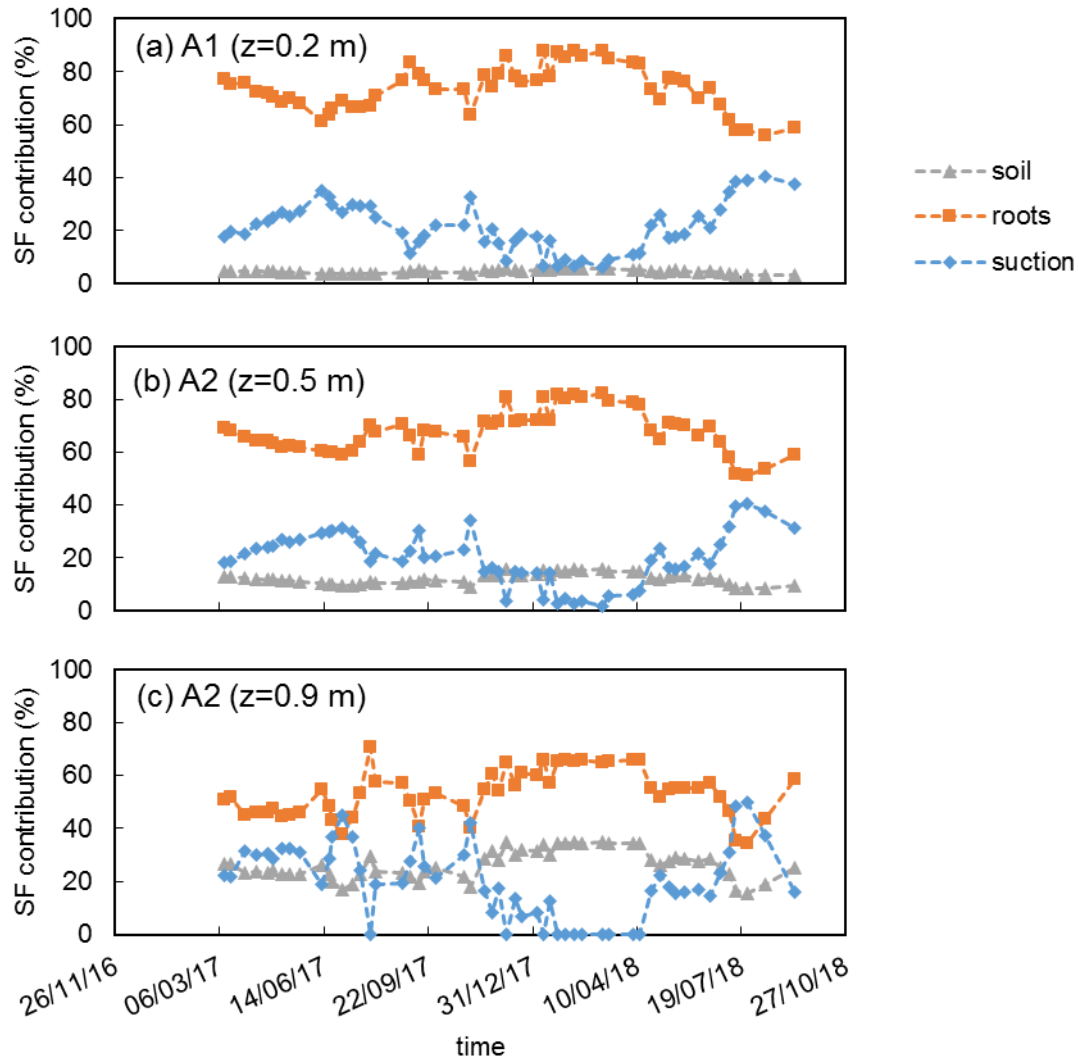


Figure 199 – Contribution of the soil, roots and suction to the safety factor (SF) in soil (a) A1( $z=0.2$  m) and (b) A2 ( $z=0.5$  m), and (c) A2 ( $z=0.9$  m)

The lowest SF observed during the monitoring period was identified in soil C1 at 2.2 m (Figure 193). At this depth, the contribution of roots was very small, providing a cohesion of 1.3 kPa (Figure 200). As depth increased, the contribution of roots cohesion to the SF also increased even if its weight was comparably smaller than the shear strength of the soil and the increase of strength resultant from suction. Nonetheless, root cohesion, unlike suction, was still present during the wet season, when its contribution became relevant for the stability by increasing the SF from 1.5 to 2.0 in soil C2 at 2.7 m. The increase of safety factor due to the contribution of roots for the weakest failure surface (soil C1 at 2.2 m of depth) is very small as it went from 1.6 without root cohesion to 1.7 with root cohesion. Nonetheless, the estimated SF at 0.9 m in the bottom of the soil layer A2 showed that the SF decreased to 1.5 if mechanical reinforcement of soil by roots was not considered, making it the weakest failure surface, as well as 2.7 m in soil C2.



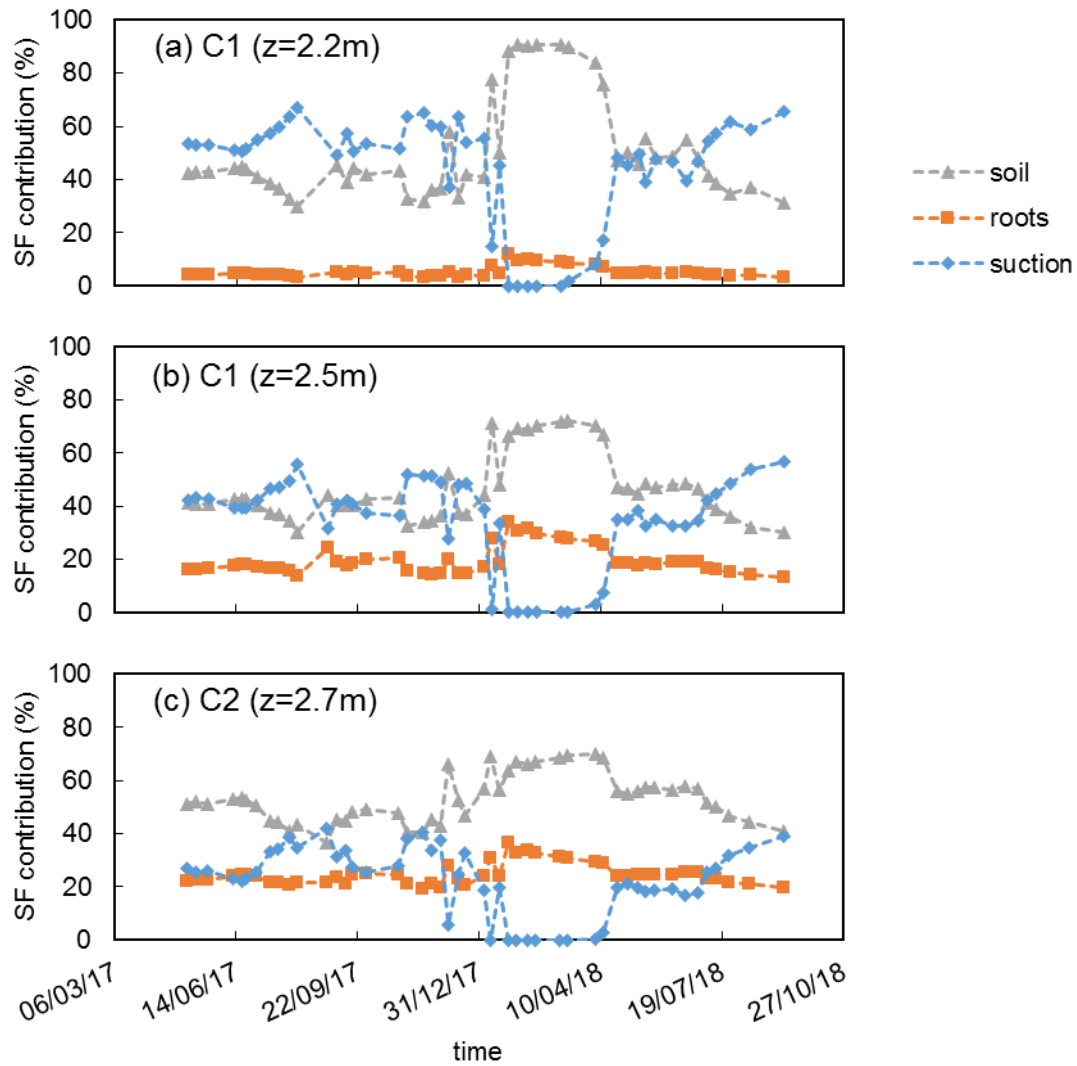


Figure 200 – Contribution of the soil, roots and suction to the safety factor (SF) in soil C1 and C2.

Simon and Collison (2002) and Kim *et al.* (2017) assessed separately the hydraulic and mechanic effects on slope stability. The hydraulic contribution to the slope stability is very high during the dry season or when plants are growing but it vanishes in both studies during the wet season. The wet season has been identified as the critical period of the occurrence of landslides, not only in Campania (Italy), but also in other sites around the world (Simon and Collison, 2002; Leung and Ng, 2013; Kim *et al.*, 2017). The mechanical soil reinforcement by roots represented a small increase of safety factor associated to the potential failure surfaces of the studied slopes but it became the most preponderant effect contributing for the slope stability during the wet season (Simon and Collison, 2002; Stokes *et al.*, 2009; Kim *et al.*, 2017). The positive effects resultant from the presence of vegetation overcompensated the negative due to the mechanical reinforcement of soil by roots.

In Kim *et al.* (2017), the failure surfaces were identified at the deepest monitored depths of 1.2 and 1.8 m. The mechanical reinforcement by roots also reduces greatly with depth leading to low root cohesion values. The hydraulic effects are more important at these depths. Indeed, the mechanical reinforcement is limited to the root growth depth but the presence of roots is responsible for an increase of the safety factor of a slope by changing the depth of the weakest potential failure surface. The difficulty in comparing the test site in Mount Faito with other investigated areas around the world seems to lay on the fact that a pumices layer of very particular hydraulic and mechanical characteristics is present at the depth of failure surfaces of other test sites where shallow landslides occur.

## 5.4 Conclusion

The soil mechanical properties were characterized using direct shear tests performed in saturated and unsaturated conditions. The unsaturated conditions tests had the objective of giving some insight on the behaviour of the soil present at the site in its natural state. The soil friction angle was found for soil A1 and C1 presenting comparable values to pyroclastic soils in other works.

The root cohesion was directly related to the volume of roots in the soil, so a decrease in root cohesion with depth in soil layers A1 and A2 was estimated. In soil layer B, root cohesion was close to null and in soil C1 root cohesion increased with depth but reaching lower values than in soil A2.

The most conservative method of quantifying root cohesion was adopted because all the tested models tend to overestimate root cohesion as roots are assumed to fail by breaking. The model FBM with load distribution proportional to the mean root diameter of a given class was the most conservative method for the quantification of the mechanical reinforcement of soil by roots for the root distribution present at Mount Faito test site.

The slope stability was investigated considering the contribution of the shear strength resultant from the soil, suction and roots. The slope stability was calculated assuming failure surfaces at different depths adopting the infinite slope model and the LE method.

The potential failure surfaces at 0.2 and 0.5 m presented the highest SF values. The contribution of roots was the highest and suction never became null in soil layers A1 and A2, where these failure surfaces were assumed. Nonetheless, a failure surface at 0.9 m of depth (at the bottom of the soil layer A2) presented an estimated SF closer to the values observed in soil layers C1 and C2 when a hydrostatic distribution of pressures was assumed. Additionally, this surface turned out to be the weakest when the root cohesion was not considered.

Root cohesion was much lower and it represented a much smaller contribution throughout the year to the slope stability in the deepest soil layers. Even though root cohesion was small in deeper soils, it presented a relevant weight in the SF during the wet season, when suction was null.

The safety factor associated to the failure surfaces in soil C1 and C2 were the lowest along the monitoring period. The weakest identified failure surface in Mount Faito was in soil C1 at 2.2 m of depth, which is coherent with the observed sliding surfaces identified by Di Crescenzo and Santo (1999) in historical landslides in the region. Nonetheless, the steepness of the test site is not included in the range of values of slope angles where triggering of landslides are more common (Di Crescenzo and Santo, 2005) but it is on the range of the values observed in the sliding zone.

## Chapter 6 Conclusion and future work

### 6.1 Conclusion

The work developed in this thesis focused on the hydraulic effect of vegetation on the stability of shallow pyroclastic soil covers found throughout Campania, Italy. The investigated test site was in Mount Faito, where the three layers that usually constitute these covers were found and where *Castanea sativa* Mill. is cultivated.

The hydraulic characterization of the soil layers present in Mount Faito was made by means of saturated permeability tests, monitoring of evaporation and imbibition processes and characterization of the soil water retention properties in the higher suction ranges using a pressure plate. The characterization was made on undisturbed soil samples in order to preserve the soil natural structure and porosity. Tree roots were found in these samples and its dry weight was quantified, referred as root dry biomass.

The presence of roots was found to be related to the soil physical and hydraulic properties. Indeed, soil with higher root dry biomass also presented higher porosity and higher saturated permeability. In terms of water retention properties, evidences were found that roots change the soil structure responsible for variations in the AEV of the soil. Finally, differences in the hydraulic conductivity of the soil layers was identified as the main factor potentially influencing the groundwater flow.

The investigation of the hysteretic behaviour of the soil hydraulic properties was considered imperative in the study of rainfall induced landslides. As rainfall water infiltration is the process by which the soil shear strength decreases, the need for a proper model to allow the simulation and understanding of the movement of the wetting front was evident. The results showed that using a hysteretic model would be less conservative because the wetting front would be expected to move faster if a single water retention curve was assumed (non-hysteretic model). However, more realistic representation of the real response of the soil can be obtained. Additionally, in Chapter 4, the comparison of the hysteretic models to the field measurements showed a better agreement in comparison to previous studies (Pirone *et al.*, 2015a, 2016) when hysteresis was not present.

A test site in Mount Faito as monitored in terms of spatial and vertical distribution of suction and water content in coupled measurements. The meteorological conditions were also monitored. The root distribution was quantified in each vertical profile in which the groundwater conditions were being monitored. The root distribution, quantified in terms of root traits, such as number of root tips, total root length and root biomass, was found to be associated to be spatial distribution and size of the chestnut trees. The vertical distribution of the roots was also found to vary laterally according to the position of trees in the area.

The root distribution was related to particular observations of hydraulic parameters. Points in which greater root biomass was found were also related to lower values of water content and to lower values of hydraulic head gradient (indicative of infiltration). The minimum suction detected along the year was related to the

roots vertical distribution. Lower values of suction are associated to roots less concentrated at the soil surface.

The seasonal trends identified in previous works, such as Pirone *et al.* (2015a) and Urciuoli *et al.* (2016), were also observed in Mount Faito test site. The response to single rainfall events was detected in the upper soil layers. The response of the soil to two hydrological years with significant differences in rainfall showed the generation of positive pore-water pressures in the deepest soil layer (C2). In fact, this result was expected because low hydraulic conductivities were measured in soil C2 (the deepest soil layer in the geological profile) in the soil hydraulic characterization presented in Chapter 3. The presence of roots in the upper soil layers (A1 and A2) increases the hydraulic conductivity of the soil and soil B also presents high hydraulic conductivity due to its grain size distribution (gravel), which facilitates the arrival of water to the bottom soil layers (C1 and C2). The hydraulic conductivity of soil C1 is very similar to the one of soil A2 due to its porosity, as the presence of roots is negligible. However, the hydraulic conductivity of soil C2 was very low, which prevented the water to percolate and reach the bedrock.

The mechanical reinforcement of the soil was assessed through the estimation of a root cohesion term calculated according to the FBM. The safety factor of the slope was estimated in several potential failure surfaces at different depths. The root cohesion increased substantially the safety factor of surficial soil. The contribution was minimal at 2.2 m, which was identified as the weakest in the entire profile. Indeed, the weakest identified potential failure surface was in agreement with the failure surfaces found by Di Crescenzo and Santo (1999) in the sliding zone of previous rainfall induced landslides. However, when mechanical reinforcement of soil by roots was not considered, the weakest failure surface was found at 0.9 m.

The Mount Faito slope was not found to be an area of triggering of landslides, as the soil friction angle was greater than the mean angle of the slope. The angle of the slope was in the range of angles correspondent to landslides sliding zones.

Overall, the vegetation effect on slope stability was found to be positive as the root mechanical reinforcement compensates negative effects of vegetation during the wet season. The presence of roots increases the soil permeability and so the velocity by which the wetting front moves downwards upon rainfall. A better hydraulic characterization of the soil was performed to allow a more precise assessment of the soil hydraulic behaviour.

## **6.2 Future work**

Some topics were left unexplored in the present thesis or which improvement is possible and recommended. Additionally, other topics of investigation were identified within this research field.

The hysteretic k-S-P calibrated model requires a final validation in order to guarantee that the performed hydraulic characterization is able to simulate the real behaviour of the slope. The hysteric model should be compared to the field measurements and it should be verified that the model is able to predict the groundwater regime at the test site in Mount Faito. Once the validation is complete, the model can be used to estimate rainfall patterns that lead to the triggering of a landslide. Prolonged rainfall events that decrease suction in the soil, so that the predisposing conditions for the occurrence of landslides are verified, followed by an intense rainfall event of short duration trigger landslides (Calcaterra and Santo, 2004). The study of such patterns allows the development of early warning systems based on rainfall forecasting (Pirone *et al.*, 2015b). The use of the hysteretic model is expected to be able to improve the accuracy of the early warning systems.

The preferential flow along root channels was not studied in depth in the present work as the soil was considered a homogenous medium in which the presence of roots would increase the hydraulic conductivity of the root-permeated soil. Due to the size of the tested samples at laboratory, the effect of large diameter roots and large diameter preferential flow channels were not investigated (greater than 20 mm). Performing infiltration tests in situ with dyed water would allow to understand the effect of the entire trees root system contributes the water infiltration. The root architecture at the slope scale, including interactions between individuals (Ghestem *et al.*, 2011).

The effect of vegetation constituted an upper boundary condition to the groundwater flow, which has already been considered in the present work and in Pirone *et al.* (2015b). In this thesis, plant roots changes in the soil hydraulic properties were identified, which also affect the groundwater regime of the pyroclastic soil covers. The lower boundary condition is the least investigated in terms of effects on the groundwater regime. Indeed, springs in the bedrock have been identified as a cause of previous landslides (Di Crescenzo and Santo, 2005), constituting a lower boundary problem. The interactions between the bedrock and the pyroclastic cover are a considerable gap in knowledge in the study of the landslides occurring in Campania.

The test site in Mount Faito, monitored in the present work, and the test sites in Monteforte Irpino and Cervinara (Urciuoli *et al.*, 2016), monitored in previous works, did not present slope angles of areas susceptible to landslide triggering (Di Crescenzo and Santo, 2005) because the mean slope angle of all the mentioned sites are below 40°. The study of slopes where the potential of landslide triggering is present, as in road cuts and rocky cliffs require investigation. As seen in the present work, the soil shear strength and suction would not be enough to guarantee the slope stability when slope angles exceed 36.5°.

The type of vegetation considered in the present study was limited to *C. sativa* for fruit production but in the area other types of cultivation are present. As seen by Amato *et al.* (2000) and Di Crescenzo and Santo (2005), the type of land use is related to different probability of being associated to landslide triggering. Nonetheless, the present work showed that the hydraulic response of the soil and the root distribution was similar among the monitored profiles, which allows the soil to be considered homogeneous in this type of cultivation. The mechanical reinforcement of the soil by the roots and the soil hydraulic properties are known

for cultivated areas of *C. sativa*. The spatial distribution study of the hydraulic effects of vegetation were associated to the position and size of trees, which is information possible to obtain from satellite images. Developments are also possible in the spatial distribution of mechanical reinforcement of the soil by trees. This would allow an upscaling and the prediction of a spatial distribution of the stability of a slope.

However, due to the particular characteristics of the soil profile found in Mount Faito and knowing that the root architecture depends on the local growth conditions, it would be hard to extend the present conclusions to other parts of the world in which other types of soil are present. Nonetheless, mechanical reinforcement of soil by the roots can be considered an essential component in future slope stability studies. The hydraulic effect can be considered secondary as suction during winter does not contribute to the stability of the slope.

The mechanical and hydraulic behaviour of root-permeated soil in artificial slopes require some investigation as not only ultimate limit states are necessary to be verified. The mechanical and hydraulic characteristics of the soil are engineered in artificial slopes in order to the embankment to fulfil the design requirements in terms of ultimate and serviceability limit states. This way, vegetation can be used to increase the permeability and the mechanical strength of the soil but less is known about the effects of vegetation on the serviceability of the slopes.

Finally, the studies performed to date are referent to rainfall events that do not account for the climate changes. Climate changes may be cause more extreme events of rainfall and an overall increase in the precipitation along the year (Favis-Mortlock and Guerra, 1999), factors that are relevant for the forecasting of landslides and early warning systems. Stabilization measures may become also necessity and accounting for the dispersion of areas at risk, the use of vegetation for soil mechanical reinforcement may be an attractive solution provided that a correct management is made.

## References

- Abe, K., & Ziemer, R. R. (1991). Effect of tree roots on a shear zone: modeling reinforced shear stress. *Canadian Journal of Forest Research*, 21(7), 1012–1019.
- Ahmadi, M. T., Attarod, P., Marvi Mohadjer, M. R., Rahmani, R., & Fathi, J. (2009). Partitioning rainfall into throughfall, stemflow, and interception loss in an oriental beech (*Fagus orientalis* Lipsky) forest during the growing season. *Turkish Journal of Agriculture and Forestry*, 33(6), 557–568.
- Allen, R. G., Pereira, L. S., Raes, D., & Smith, M. (1998). Crop evapotranspiration: Guidelines for computing crop requirements. *Irrigation and Drainage Paper No. 56, FAO*, (56), 300.
- Alonso, E. E., Gens, A., and Josa, A. (1990). A Constitutive Model for Partially Saturated Soils. *Géotechnique*, 40 (3), 405–30.
- Amato, M., Di Martino, P., Di Pasquale, G., Mazzoleni, S., Migliozi, A., & Strumia, S. (2000). Il ruolo della vegetazione nella frana di Quindici. *Quaderni Di Geologia Applicata*, 7(1), 97–108.
- American Society of Testing and Materials. (1998). *Standard Test Method for Direct Shear Test of Soils Under Consolidated Drained*. ASTM D 3080-98.
- American Society of Testing and Materials. (2010). *Standard Test Methods for Liquid Limit, Plastic Limit, and Plasticity Index of Soils*. ASTM D4318 - 00.
- American Society of Testing and Materials. (2010). *Standard Test Methods for Specific Gravity of Soil Solids by Water Pycnometer*. ASTM D854 - 10.
- American Society of Testing and Materials. (2017). *Standard Practice for Classification of Soils for Engineering Purposes (Unified Soil Classification System)*. ASTM D 2487 - 17.
- Angers, D. A., & Caron, J. (1998). Plant-induced changes in soil structure: Processes and feedbacks. *Biogeochemistry*.
- Belfiore, G., & Urciuoli, G. (2004). Analisi del contributo meccanico delle radici alla resistenza del terreno. In *Incontro Annuale dei Ricercatori di Geotecnica 2004 - IARG 2004*.
- Bilotta, E., Cascini, L., Foresta, V. & Sorbino, G. (2005). Geotechnical characterisation of pyroclastic soils involved in huge flowslides. *Geotechnical and Geological Engineering*. 23, 365–402.
- Bischetti, G. B., Chiaradia, E. A., Epis, T., & Morlotti, E. (2009). Root cohesion of forest species in the Italian Alps. *Plant and Soil*, 324(1), 71–89.
- Bishop, A. W. (1954). The Use of Pore-Pressure Coefficients in Practice. *Géotechnique*, 4(4), 148–152.
- Boldrin, D. (2018). Understanding Plant Water Relations and Root Biomechanics for Hydro-Mechanical Reinforcement of Slopes. University of Dundee.
- Burylo, M., Hudek, C., & Rey, F. (2011). Soil reinforcement by the roots of six dominant species on eroded mountainous marly slopes (Southern Alps, France). *Catena*, 84(1–2), 70–78.
- Calcaterra, D., & Santo, A. (2004). The January 10, 1997 Pozzano landslide, Sorrento Peninsula, Italy. *Engineering Geology*, 75(2), 181–200.



- Campbell Scientific. (2000). *User Guide TDR100 Time Domain Reflectometry Systems*.
- Cardoso, R., Vecchia, G., Jommi, C., & Romero, E. (2010). Water retention curve for evolving marl under suction cycles. In *Proceedings of the 5th International Conference on Unsaturated Soils* (pp. 6–8).
- Cascini, L., Cuomo, S., & Guida, D. (2008). Typical source areas of May 1998 flow-like mass movements in the Campania region, Southern Italy. *Engineering Geology*, 96(3–4), 107–125.
- Cazzuffi, D., Cardile, G., & Giofrè, D. (2014). Geosynthetic engineering and vegetation growth in soil reinforcement applications. *Transportation Infrastructure Geotechnology*, 1(3), 262–300.
- Comegna, A., Coppola, A., Dragonetti, G., Severino, G., Sommella, A., & Basile, A. (2013). Dielectric properties of a tilled sandy volcanic-vesuvian soil with moderate andic features. *Soil and Tillage Research*, 133, 93–100.
- Comegna, L., Damiano, E., Greco, R., Guida, A., Olivares, L., & Picarelli, L. (2013). Effects of the Vegetation on the Hydrological Behavior of a Loose Pyroclastic Deposit. *Procedia Environmental Sciences*, 19, 922–931.
- Comino, E., Marengo, P., & Rolli, V. (2010). Root reinforcement effect of different grass species: A comparison between experimental and models results. *Soil and Tillage Research*, 110(1), 60–68.
- Coppin, N. J., & Richards, I. G. (2007). *Use of vegetation in civil engineering*. London: Construction Industry Research and Information Association.
- Corniello, A. et al. (2018) 'Complex groundwater flow circulation in a carbonate aquifer: Mount Massico (Campania Region, Southern Italy). Synergistic hydrogeological understanding', *Journal of Geochemical Exploration*, 190, pp. 253–264.
- Damiano, E., Olivares, L., and Picarelli, L. (2012). Steep-Slope Monitoring in Unsaturated Pyroclastic Soils. *Engineering Geology*, 137–138 1–12.
- Danjon, F., Barker, D. H., Drexhage, M., & Stokes, A. (2008). Using three-dimensional plant root architecture in models of shallow-slope stability. *Annals of Botany*, 101(8), 1281–1293.
- Darcy, H. (1956). *Les Fontaines publiques de la ville de Dijon. Exposition et application des principes à suivre et des formules à employer dans les questions de distribution d'eau, etc.* (V. Dalmont, Ed.).
- Del Prete, M., Guadagno, F. M., & Hawkins, A. B. (1998). *Preliminary report on the landslides of 5 May 1998, Campania, southern Italy*. *Bull Eng Geol Env* (Vol. 57). Springer-Verlag 113.
- Di Crescenzo, G., & Santo, A. (1999). Analisi geomorfologica delle frane da scorrimento-colata rapida in depositi piroclastici della Penisola Sorrentina. *Geografia Fisica e Dinamica Quaternaria*, 22(14), 57–72.
- Di Crescenzo, G., & Santo, A. (2005). Debris slides-rapid earth flows in the carbonate massifs of the Campania region (Southern Italy): Morphological and morphometric data for evaluating triggering susceptibility. *Geomorphology*, 66, 255–276.
- Diamantopoulos, E., & Durner, W. (2012). Dynamic Nonequilibrium of Water Flow in Porous Media: A Review. *Vadose Zone Journal*, 11(3).

- Dias, A. S. (2015). Electrical Resistivity of Compacted Kaolin and Its Relation with Suction. University of Lisbon.
- Dias, A. S., Pirone, M., & Urciuoli, G. (2017). Review on the Methods for Evaluation of Root Reinforcement in Shallow Landslides. In *Advancing Culture of Living with Landslides. WLF 2017. Springer, Cham* (pp. 641–648).
- Dias, A. S., Pirone, M., & Urciuoli, G. (2017). Review on the Methods for Evaluation of Root Reinforcement in Shallow Landslides. In *Advancing Culture of Living with Landslides. WLF 2017. Springer, Cham* (pp. 641–648).
- Dias, A. S., Pirone, M., & Urciuoli, G. (2018). Calibration of TDR probes for water content measurements in partially saturated pyroclastic slope. *Proceeding UNSAT 2018*.
- Dobson, M. C., Ulaby, F. T., Hallikainen, M. T., & El-Rayes, M. A. (1985). Microwave Dielectric Behavior of Wet Soil-Part II: Dielectric Mixing Models. *IEEE Transactions on Geoscience and Remote Sensing, GE-23*(1), 35–46.
- Donaldson, L. a. (1985). Within and between-tree variation in lignin concentration in the tracheid cell wall of *Pinus radiata*. *New Zealand Journal of Forestry Science, 15*(3), 361–369.
- Dupuy, L., Fourcaud, T., & Stokes, A. (2005). A numerical investigation into factors affecting the anchorage of roots in tension. *European Journal of Soil Science, 56*(3), 319–327.
- Ennos, a. R. (1990). The Anchorage of Leek Seedlings: The Effect of Root Length and Soil Strength. *Annals of Botany, 65*(4), 409–416.
- Esposito, S. (2017). *Resistenza di terreni piroclastici in condizioni non sature*. University of Naples Federico II.
- Evangelista, A., Nicotera, M. V, & Aversa, S. (2004). Un'apparecchiatura di taglio a suzione controllata per lo studio delle condizioni di innesco dei fenomeni franosi nelle coltri piroclastiche. In *XXII Convegno Nazionale di Geotecnica, Palermo*.
- Favis-Mortlock, D.T., and Guerra, A.J.T. (1999). The Implications of General Circulation Model Estimates of Rainfall for Future Erosion: A Case Study from Brazil. *Catena, 37* (3–4), 329–54.
- Fredlund, D. G., & Rahardjo, H. (2012). *Unsaturated soil mechanics in engineering practice*.
- Fredlund, D. G., & Xing, A. (1994). Equations for the soil-water characteristic curve. *Canadian Geotechnical Journal, 31*(6), 1026–1026.
- Gale, M. R., & Grigal, D. F. (1987). Vertical root distributions of northern tree species in relation to successional status. *Canadian Journal of Forest Research, 17*(8), 829–834.
- Genet, M., Kokutse, N., Stokes, A., Fourcaud, T., Cai, X., Ji, J., & Mickovski, S. (2008). Root reinforcement in plantations of *Cryptomeria japonica* D. Don: effect of tree age and stand structure on slope stability. *Forest Ecology and Management, 256*(8), 1517–1526.
- Genet, M., Stokes, A., Fourcaud, T., & Norris, J. E. (2010). The influence of plant diversity on slope stability in a moist evergreen deciduous forest. *Ecological Engineering, 36*(3), 265–275.

- Genet, M., Stokes, A., Salin, F., Mickovski, S. B., Fourcaud, T., Dumail, J. F., & Van Beek, R. (2005). The influence of cellulose content on tensile strength in tree roots. In *Plant and Soil* (Vol. 278, pp. 1–9).
- Ghestem, M., Sidle, R. C., & Stokes, A. (2011). The Influence of Plant Root Systems on Subsurface Flow: Implications for Slope Stability. *BioScience*, 61(11), 869–879.
- Giadrossich, F., Schwarz, M., Cohen, D., Preti, F., & Or, D. (2013). Mechanical interactions between neighbouring roots during pullout tests. *Plant and Soil*, 367(1–2), 391–406.
- Gonzalez-Ollauri, A., & Mickovski, S. B. (2017). Hydrological effect of vegetation against rainfall-induced landslides. *Journal of Hydrology*, 549, 374–387.
- Graf, F., Frei, M., & Boll, A. (2009). Effects of vegetation on the angle of internal friction of a moraine. *Forest, Snow and Landscape Research*, 82(1), 61–77.
- Gray, D. H., & Leiser, A. T. (1982). *Biotechnical slope protection and erosion control*. Malabar, Florida: Krieger Publishing Company.
- Gray, D. H., & Ohashi, H. (1983). Mechanics of Fiber Reinforcement in Sand, 109(3), 335–353.
- Gray, D. H., & Sotir, R. B. (1996). *Biotechnical and soil bioengineering slope stabilization : a practical guide for erosion control*. John Wiley & Sons.
- Hendrickx, J. M. H., Dam, R. L. Van, Borchers, B., Curtis, J., Lensen, H. A., & Harmon, R. (2003). Worldwide distribution of soil dielectric and thermal properties. In *Proc. of SPIE*, 5089, 1158–1168.
- Hillel, D. (2004). Introduction to Environmental Soil Physics. *Elsevier Academic Press*.
- Hungr, O., Leroueil, S., & Picarelli, L. (2014). The Varnes classification of landslide types, an update. *Landslides*, 11(2), 167–194.
- Jastrow, J. D. (1996). Soil Aggregate Formation and the Accrual of Particulate and Mineral-Associated Organic Matter. *Soil Biol. Biochem*, 28 (4/5), 665–76.
- Kim, J. H., Fourcaud, T., Jourdan, C., Maeght, J. L., Mao, Z., Metayer, J., and Stokes, A. (2017). Vegetation as a driver of temporal variations in slope stability: The impact of hydrological processes. *Geophysical Research Letters*, 44(10), 4897–4907.
- Kool, J. B., & Parker, J. C. (1987). Development and evaluation of closed-form expressions for hysteretic soil hydraulic properties. *Water Resources Research*, 23(1), 105–114.
- Land, C. S. (1968). Calculation of imbibition relative permeability for two- and three-phase flow from rock properties. *Society of Petroleum Engineers Journal*, 8(2), 149–156.
- Ledieu, J., De Ridder, P., De Clerck, P., & Dautrebande, S. (1986). A method of measuring soil moisture by time-domain reflectometry. *Journal of Hydrology*, 88(3–4), 319–328.
- Lenhard, R. J., & Parker, J. C. (1987). A Model for Hysteretic Constitutive Relations Governing Multiphase Flow 2. Permeability-Saturation Relations. *Water Resources Research*, 23(12), 2187–2196.
- Lenhard, R. J., Parker, J. C., & Kaluarachchi, J. J. (1991). Comparing Simulated and Experimental Hysteretic Two-Phase Transient Fluid Phenomena. *Water Resources Research*, 27(8), 2113–2124.
- Leung, A. K., & Ng, C. W. W. (2013). Analyses of groundwater flow and plant evapotranspiration in a vegetated soil slope. *Canadian Geotechnical Journal*, 50(12), 1204–1218.

- Leung, A. K., Garg, A., & Ng, C. W. W. (2015). Effects of plant roots on soil-water retention and induced suction in vegetated soil. *Engineering Geology*, 193, 183–197.
- Liang, T., Knappett, J. A., & Duckett, N. (2015). Modelling the seismic performance of rooted slopes from individual root–soil interaction to global slope behaviour. *Géotechnique*, (12), 1–15.
- Llorens, P., & Domingo, F. (2007). Rainfall partitioning by vegetation under Mediterranean conditions. A review of studies in Europe. *Journal of Hydrology*, 335(1–2), 37–54.
- Loades, K. W., Bengough, A. G., Bransby, M. F., & Hallett, P. D. (2010). Planting density influence on fibrous root reinforcement of soils. *Ecological Engineering*, 36(3), 276–284.
- Mancarella, D., & Simeone, V. (2012). Capillary barrier effects in unsaturated layered soils, with special reference to the pyroclastic veneer of the Pizzo d'Alvano, Campania, Italy. *Bulletin of Engineering Geology and the Environment*, 71(4), 791–801.
- Mao, Z., Bourrier, F., Stokes, A., & Fourcaud, T. (2014). Three-dimensional modelling of slope stability in heterogeneous montane forest ecosystems. *Ecological Modelling*, 273, 11–22.
- Mao, Z., Saint-André, L., Bourrier, F., Stokes, A., & Cordonnier, T. (2015). Modelling and predicting the spatial distribution of tree root density in heterogeneous forest ecosystems. *Annals of Botany*, 116(2), 261–277.
- Mao, Z., Saint-andré, L., Genet, M., Jourdan, C., Rey, H., Courbaud, B., & Stokes, A. (2012). Engineering ecological protection against landslides in diverse mountain forests : Choosing cohesion models. *Ecological Engineering*, 45, 55–69.
- Mao, Z., Yang, M., Bourrier, F., & Fourcaud, T. (2014). Evaluation of root reinforcement models using numerical modelling approaches. *Plant and Soil*, 381(1–2), 249–270.
- Mazzoleni, S., Martino, P. Di, Strumia, S., Buonanno, M., & Bellelli, M. (2005). Recent Changes of Coastal and Sub-Mountain Vegetation Landscape in Campania and Molise Regions in Southern Italy. In *Recent Dynamics of the Mediterranean Vegetation and Landscape* (pp. 145–155).
- Mickovski, S. B., Bengough, A. G., Bransby, M. F., Davies, M. C. R., Hallett, P. D., & Sonnenberg, R. (2007). Material stiffness, branching pattern and soil matric potential affect the pullout resistance of model root systems. *European Journal of Soil Science*, 58(6), 1471–1481.
- Mickovski, S. B., Stokes, A., van Beek, R., Ghestem, M., & Fourcaud, T. (2011). Simulation of direct shear tests on rooted and non-rooted soil using finite element analysis. *Ecological Engineering*, 37(10), 1523–1532.
- Monteith, J. L. (1965). Evaporation and environment. In *Proceedings of the Society for Experimental Biology*, 19, pp. 205–234.
- Mualem, Y. (1976). A new model for predicting the hydraulic conductivity of unsaturated porous media. *Water Resources Research*, 12(3), 513–522.
- Ng, C. W. W., Leung, A. K., & Woon, K. X. (2013). Effects of soil density on grass-induced suction distributions in compacted soil subjected to rainfall. *Canadian Geotechnical Journal*, 51(3), 311–321.

- Ng, C. W. W., Ni, J. J., Leung, A. K., & Wang, Z. J. (2016a). A new and simple water retention model for root-permeated soils. *Géotechnique Letters*, 6, 1–6.
- Ng, C. W. W., Ni, J. J., Leung, A. K., Zhou, C., & Wang, Z. J. (2016b). Effects of planting density on tree growth and induced soil suction. *Géotechnique*, 66(9), 711–724.
- Nghiêm, Q. M., Nakamura, H., & Shiraki, K. (2003). Analysis of root reinforcement at slip surface. *Journal of the Japan Landslide Society*, 40(4), 302–310.
- Ni, J. J., Leung, A. K., Ng, C.W.W., and Shao., W. (2018). Modelling Hydro-Mechanical Reinforcements of Plants to Slope Stability. *Computers and Geotechnics*, 95, 99–109.
- Nicotera, M. V., & Tarantino, A. (2005). Laboratory measurements of matric suction in pyroclastic soil using vacuum and high-suction tensiometers. In *Unsaturated Soils: Experimental Studies* (pp. 193–205).
- Nicotera, M. V., Papa, R., & Urciuoli, G. (2010). An experimental technique for determining the hydraulic properties of unsaturated pyroclastic soils. *Geotechnical Testing Journal*, 33(4), 263–285.
- Nicotera, M. V., Papa, R., & Urciuoli, G. (2015). The hydro-mechanical behaviour of unsaturated pyroclastic soils: An experimental investigation. *Engineering Geology*, 195, 70–84.
- Novák, V., Simunek, J., & van Genuchten, M. T. (2000). Infiltration of water into soil with cracks. *Journal of Irrigation and Drainage Engineering*, 126(1), 41–47.
- Papa, R. (2007). *Indagine sperimentale sulla coltre piroclastica di un versante della Campania*. University of Naples Federico II.
- Papa, R., & Nicotera, M. V. (2011). Shear strength of a pyroclastic unsaturated soil from suction-controlled direct shear tests. *Unsaturated Soils - Proceedings of the 5th International Conference on Unsaturated Soils*, 1, 347–352.
- Papa, R., & Nicotera, M. V. (2012). Calibration of TDR probes to measure water content in pyroclastic soils. In *5th Asia-Pacific Conference on Unsaturated Soils 2012* (Vol. 1).
- Papa, R., & Nicotera, M. V. (2012). Use of TDR Probes to Measure Water Content in Pumiceous Soils. In *Unsaturated Soils: Research and Applications* (pp. 107–112). Berlin, Heidelberg: Springer Berlin Heidelberg.
- Papa, R., Evangelista, A., Nicotera, M. V., & Urciuoli, G. (2008). Mechanical properties of unsaturated pyroclastic soils affected by fast landslide phenomena. In *Proceedings of the 1st European Conference on Unsaturated Soils, E-UNSAT 2008* (pp. 917–924).
- Papa, R., Pirone, M., Nicotera, M., & Urciuoli, G. (2013). Seasonal groundwater regime in an unsaturated pyroclastic slope. *Geotechnique*, 63(5), 420–426.
- Parent, S.-É., Cabral, A., & Zornberg, J. G. (2007). Water retention curve and hydraulic conductivity function of highly compressible materials. *Canadian Geotechnical Journal*, 44(10), 1200–1214.
- Parker, J. C., & Lenhard, R. J. (1987). A model for hysteretic constitutive relations governing multiphase flow 1. Saturation pressure relations. *Water Resources Research*, 23(12), 2187–2196.
- Penman, H. L. (1948). Natural Evapotranspiration from Open Water, Bare Soil and Grass. In *Proceedings of the Royal Society of London. Series A, Mathematical and Physical Sciences*, 193:120–45.

- Pirone, M. (2009). Analysis of slope failure mechanism in unsaturated pyroclastic soils, based on testing site monitoring. University of Naples Federico II.
- Pirone, M., Damiano, E., Picarelli, L., Olivares, L., & Urciuoli, G. (2012). Groundwater-atmosphere interaction in unsaturated pyroclastic slopes at two sites in Italy.
- Pirone, M., Papa, R., Nicotera, M. V., & Urciuoli, G. (2014). Evaluation of the Hydraulic Hysteresis of Unsaturated Pyroclastic Soils by in Situ Measurements. *Procedia Earth and Planetary Science*, 9, 163–170.
- Pirone, M., Papa, R., Nicotera, M. V., & Urciuoli, G. (2015a). In situ monitoring of the groundwater field in an unsaturated pyroclastic slope for slope stability evaluation. *Landslides*, 12(2), 259–276.
- Pirone, M., Papa, R., Nicotera, M. V., & Urciuoli, G. (2015b). Soil water balance in an unsaturated pyroclastic slope for evaluation of soil hydraulic behaviour and boundary conditions. *Journal of Hydrology*, 528, 63–83.
- Pirone, M., Papa, R., Nicotera, M. V., & Urciuoli, G. (2016). Hydraulic Behaviour of Unsaturated Pyroclastic Soil Observed at Different Scales. *Procedia Engineering*, 158, 182–187.
- Pollen, N. (2007). Temporal and spatial variability in root reinforcement of streambanks: Accounting for soil shear strength and moisture. *Catena*, 69(3), 197–205.
- Pollen, N., & Simon, A. (2005). Estimating the mechanical effects of riparian vegetation on stream bank stability using a fiber bundle model. *Water Resources Research*, 41(7), 1–11.
- Punzel, J., & Berding, J. (2013). *Operating Instructions ku-pf Apparatus*. UGT.
- Putuhen, W. M., & Cordery, I. (1996). Estimation of interception capacity of the forest floor. *Journal of Hydrology*, 180(1–4), 283–299.
- Reder, A., Rianna, G., & Pagano, L. (2014). Calibration of TDRs and Heat Dissipation Probes in Pyroclastic Soils. *Procedia Earth and Planetary Science*, 9, 171–179.
- Reubens, B., Poesen, J., Danjon, F., Geudens, G., & Muys, B. (2007). The role of fine and coarse roots in shallow slope stability and soil erosion control with a focus on root system architecture: A review. *Trees*, 21(385–402).
- Roering, J. J., Schmidt, K. M., Stock, J. D., Dietrich, W. E., and Montgomery, D. R. (2003). Shallow Landsliding, Root Reinforcement, and the Spatial Distribution of Trees in the Oregon Coast Range. *Canadian Geotechnical Journal*, 40 (2), 237–53.
- Romero, E. (2001). Controlled Suction Techniques. In *4o Simpósio Brasileiro de Solos Não Saturados*, 535–42.
- Romero, E., Gens, A., & Lloret, A. (1999). Water permeability, water retention and microstructure of unsaturated compacted Boom clay. *Engineering Geology*, 54(1–2), 117–127.
- Roth, K., Schulin, R., Hler, H. F. L., & Attinger, W. (1990). Calibration of time domain reflectometry for water content measurement using a composite dielectric approach. *Water Resources*, 26(10), 2267–2273.
- Sauer, T. J., & Horton, R. (2005). Soil Heat Flux. In *Micrometeorology in Agricultural Systems* (Vol. 47, pp. 131–154). USDA-ARS/UNL Faculty.

- Schmidt, K. M., Roering, J. J., Stock, J. D., Dietrich, W. E., Montgomery, D. R., & Schaub, T. (2001). The variability of root cohesion as an influence on shallow landslide susceptibility in the Oregon Coast Range. *Canadian Geotechnical Journal*, 38(5), 995–1024.
- Schwarz, M., Cohen, D., & Or, D. (2010a). Root-soil mechanical interactions during pullout and failure of root bundles. *Journal of Geophysical Research: Earth Surface*, 115(4), 1–19.
- Schwarz, M., Giadrossich, F., & Cohen, D. (2013). Modeling root reinforcement using a root-failure Weibull survival function. *Hydrology and Earth System Sciences*, 17(11), 4367–4377.
- Schwarz, M., Lehmann, P., & Or, D. (2010b). Quantifying lateral root reinforcement in steep slopes - from a bundle of roots to tree stands. *Earth Surface Processes and Landforms*, 35(3), 354–367.
- Schwarz, M., Preti, F., Giadrossich, F., Lehmann, P., & Or, D. (2010c). Quantifying the role of vegetation in slope stability: A case study in Tuscany (Italy). *Ecological Engineering*, 36(3), 285–291.
- Schwarz, M., Rist, A., Cohen, D., Giadrossich, F., Egorov, P., Büttner, D., ... Thormann, J.-J. (2015). Root reinforcement of soils under compression. *Journal OfGeophysical Research: Earth Surface RESEARCH*, 120, 1–20.
- Serrato, F. B., & Diaz, a R. (1998). A simple technique for measuring rainfall interception by small shrub: “interception flow collection box.” *Hydrological Processes*, 12(December 1996), 471–481.
- Simon, A., and Collison, A. (2002). Quantifying the Mechanical and Hydrologic Effects of Riparian Vegetation on Streambank Stability.” *Earth Surface Processes and Landforms* 27: 527–46. <https://doi.org/10.1002/esp.325>.
- Simpson, W. T. (1993). *Specific Gravity , Moisture Content , and Density Relationship for Wood. General technical report FPL* (Vol. 76).
- Simpson, W., & TenWolde, A. (1999). *Physical properties and moisture relations of wood. Wood handbook : wood as an engineering material. Madison, WI : USDA Forest Service, Forest Products Laboratory, 1999. General technical report FPL ; GTR-113: Pages 3.1-3.24* (Vol. 113).
- Šimůnek, J., Šejna, M., Saito, H., Sakai, M., & Genuchten, M. T. van. (2013). *The HYDRUS-1D Software Package for Simulating the One-Dimensional Movement of Water, Heat, and Multiple Solutes in Variably-Saturated Media*.
- Sonnenberg, R., Bransby, M. F., Hallett, P. D., Bengough, A. G., Mickovski, S. B., & Davies, M. C. R. (2010). Centrifuge modelling of soil slopes reinforced with vegetation. *Canadian Geotechnical Journal*, 47(12), 1415–1430.
- Staelens, J., Schrijver, A. De, Verheyen, K., & Verhoest, N. E. C. (2008). Rainfall partitioning into throughfall, stemflow, and interception within a single beech (*Fagus sylvatica* L.) canopy: influence of foliation, rain event characteristics, and meteorology Jeroen. *Hydrological Processes*, 22, 33–45.
- Stokes, A., Atger, C., Bengough, A. G., Fourcaud, T., & Sidle, R. C. (2009). Desirable Plant root traits for protecting natural and engineered slopes against landslides. *Plant and Soil*, 324, 1–30.
- Switala, B. M. (2016). *Analysis of Slope Stabilization by Soil Bioengineering Methods Analysis of Slope Stabilisation by Soil Bioengineering Methods*. University of Natural Resources and Life Sciences.

- Terlien, M. T. J. (1996). Modelling spatial and temporal variations in rainfall-triggered landslides. International Inst. for Aerospace Survey and Earth Science (ITC).
- Thomas, F. M., Molitor, F., & Werner, W. (2014). Lignin and cellulose concentrations in roots of Douglas fir and European beech of different diameter classes and soil depths. *Trees*, 28, 309–315.
- Tiwari, R. C., Bhandary, N. P., Yatabe, R., & Bhat, D. R. (2013). New numerical scheme in the finite element method for evaluating the root-reinforcement effect on soil slope stability. *Géotechnique*, 63(2), 129–139.
- Topp, G. C., Davis, J. L., & Annan, A. P. (1980). Electromagnetic Determination of Soil Water Content: Measurements in Coaxial Transmission Lines. *Water Resources Research*, 16(3), 574–582.
- Topp, G. C., Davis, J. L., Bailey, W. G., & Zebchuk, W. D. (1984). The measurement of soil water content using a portable TDR hand probe. *Canadian Journal of Soil Science*, 64, 313–321.
- Urciuoli, G., Pirone, M., Comegna, L., & Picarelli, L. (2016). Long-term investigations on the pore pressure regime in saturated and unsaturated sloping soils. *Engineering Geology*, 212, 98–119.
- van Genuchten, M. T. (1980). A Closed-form Equation for Predicting the Hydraulic Conductivity of Unsaturated Soils. *Soil Science Society of America Journal*, 44(5), 892.
- Vanapalli, S. K., Fredlund, D. G., & Pufahl, D. E. (1999). The influence of soil structure and stress history on the soil-water characteristic of a compacted. *Geotechnique*, 49(9), 143–159.
- Vergani, C., & Graf, F. (2016). Soil permeability, aggregate stability and root growth: a pot experiment from a soil bioengineering perspective. *Ecohydrology*, 9(5), 830–842.
- Vergani, C., Schwarz, M., Cohen, D., Thormann, J. J., & Bischetti, G. B. (2014). Effects of root tensile force and diameter distribution variability on root reinforcement in the Swiss and Italian Alps. *Canadian Journal of Forest Research*, 44(11), 1426–1440.
- Veylon, G., Ghestem, M., Stokes, A., & Bernard, A. (2015). Quantification of mechanical and hydric components of soil reinforcement by plant roots. *Canadian Geotechnical Journal*, 52, 1839–1849.
- Waldron, L. J. (1977). The Shear Resistance of Root-Permeated Homogeneous and Stratified Soil1. *Soil Science Society of America Journal*, 41(5), 843.
- Waldron, L., & Dakessian, s. (1981). Soil reinforcement by roots: calculation of increased soil shear resistance from root properties. *Soil Science*, 132(6), 427–435.
- Wijaya, M., & Leong, E. C. (2017). Modelling the effect of density on the unimodal soil-water characteristic curve. *Geotechnique*, 67(7), 637–645.
- Wilkinson, P. L., Anderson, M. G., & Lloyd, D. M. (2002). An integrated hydrological model for rain-induced landslide prediction. *Earth Surface Processes and Landforms*, 27(12), 1285–1297.
- Wu, H. (1976). Investigation of Landslides on Prince of Wales Island , Alaska, (5).
- Wu, T. H. (2013). Root reinforcement of soil: review of analytical models, test results, and applications to design. *Canadian Geotechnical Journal*, 50(November 2012), 259–274.
- Wu, T. H., McOmber, R. M., Erb, R. T., & Beal, P. E. (1988). Study of soil-root interaction. *Journal of Geotechnical Engineering*, 114(12), 1351–1375.



- Zhang, C. B., Chen, L. H., Liu, Y. P., Ji, X. D., & Liu, X. P. (2010). Triaxial compression test of soil-root composites to evaluate influence of roots on soil shear strength. *Ecological Engineering*, 36(1), 19–26.
- Zhang, Y., Niu, J., Zhang, M., Xiao, Z., & Zhu, W. (2017). Interaction Between Plant Roots and Soil Water Flow in Response to Preferential Flow Paths in Northern China. *Land Degradation and Development*, 28(2), 648–663.

# **Annexes**

## Annex A – List of boreholes for physical, hydraulic and mechanical characterization

Table 41 – Date, trench, soil type and depth of each borehole collected at Mount Faito for physical and hydraulic characterization.

Sampling date	Trench number	Borehole number	Soil type	Borehole depth (m)
22/7/2016	1	1	B1	2
		2	B2	2
		3	B3	2
		1	A2	1.65
		2	A2	1.65
		3	A2	1.65
		4	A2	1.65
		5	A2	0.95
		6	A1/A2	0.8
		7	A1/A2	0.8
		8	A1/A2	0.8
	2	9	A1	0.5
		10	A1	0.5
		11	A1	0.5
		12	C1b	1.45
	4	13	C1b	1.3
		14	C1b	1.3
		15	C1b	1.3
3/10/2017	1	16	C1b	1.1
		17	C1b	1.81
		18	C2	2.2
	Vertical at ground level	1	C1	1.8
		2	C1	1.8
		3	C1	0.8
		1	A1	0.05
		2	A1	0.05
		3	A1	0.2
		4	A1	0
		5	A1	0

Table 42 – List of samples collected in Mount Faito for mechanical characterization.

#	soil	depth (m)
1	C2	0.8
2	C2	0.8
3	C1	0.7
4	A1	0.2
5	A1	0.3
6	C1	0.7
7	C2	0.8
8	A2	0.6
9	C1	0.7
10	A2	0.6
11	A1	0.2
12	A2	0.6
13	C1	0.9
14	A2	0.5
15	A1	0.2

## Annex B – Species identified in Mount Faito

Table 43 – List of identified species in July and September 2017 at Mount Faito test site (Annalisa Santangelo and Sandro Strumia, personal communication).

Taxonomic Group	Family name	Species /subsp. Names	Life forms	Chorology
Dycotiledones	Aceraceae	Acer opalus Mill. subsp. obtusatum (Waldst. & Kit. ex Willd.) Gams	P m	SE-Europ.
Dycotiledones	Betulaceae	Alnus cordata (Loisel.) Loisel.	P m	Subendem.
Dycotiledones	Brassicaceae (Cruciferae)	Barbarea bracteosa Guss.	H scap	S-Medit. (Steno-)
Monocotyledones	Poaceae (Graminaceae)	Brachypodium sylvaticum (Huds.) P. Beauv.	H caesp	Paleotemp.
Dycotiledones	Campanulaceae	Campanula rapunculus L.	H bien	Paleotemp.
Dycotiledones	Fagaceae	Castanea sativa Mill.	P m	SE-Europ.
Dycotiledones	Caryophyllaceae	Cerastium ligusticum Viv.	T er	W-Medit. (Steno)
Dycotiledones	Apiaceae (Umbelliferae)	Chaerophyllum temulum L.	T er	Eurasiat.
Dycotiledones	(Lamiaceae) Labiatae	Clinopodium vulgare L.	H scap	Circumbor.
Dycotiledones	Convolvulaceae	Convolvulus arvensis L.	G rhiz	Cosmop.
Dycotiledones	Compositae (Asteraceae)	Crepis leontodontoides All.	H scap	W-Medit.-Mont.
Monocotyledones	Poaceae (Graminaceae)	Cynosurus cristatus L.	H caesp	Europ.-Caucas.
Monocotyledones	Poaceae (Graminaceae)	Dactylis glomerata L.	H scap	Paleotemp.
Dycotiledones	Scrophulariaceae	Digitalis lutea L. subsp. australis (Ten.) Arcang.	H scap	Endem.
Dycotiledones	Onagraceae	Epilobium sp.		
Dycotiledones	Euphorbiaceae	Euphorbia amygdaloides L.	Ch suff	Europ.-Caucas.

Monocotyledone s	Poaceae (Graminaceae)	Festuca circummediterranea Patzke	H caesp	Euri-Medit.
Dycotiledones	Geraniaceae	Geranium robertianum L.	T er	Subcosmop.
Monocotyledone s	Poaceae (Graminaceae)	Holcus mollis L.	H caesp	Circumbor.
Dycotiledones	Guttiferae	Hypericum sp.		
Dycotiledones	Compositae (Asteraceae)	Lactuca muralis (L.) Gaertn.	H scap	Europ.-Caucas.
Dycotiledones	Compositae (Asteraceae)	Lapsana communis L. subsp. communis	T er	Paleotemp.
Dycotiledones	Boraginaceae	Myosotis sylvatica Hoffm.	H scap	Paleotemp.
Gymnosperm	Pinaceae	Pinus pinaster Aiton	P m	Avv. (Nordamer.)
Monocotyledone s	Poaceae (Graminaceae)	Poa sp.	H caesp	
Dycotiledones	(Lamiaceae) Labiatae	Prunella vulgaris L. subsp. vulgaris	H scap	Circumbor.
Ferns	Hypolepidacea e	Pteridium aquilinum (L.) Kuhn subsp. aquilinum	G rhiz	Cosmop.
Dycotiledones	Ranunculaceae	Ranunculus lanuginosus L.	H scap	Europ.-Caucas.
Dycotiledones	Rosaceae	Rubus ulmifolius Schott	P n	Euri-Medit.
Dycotiledones	(Lamiaceae) Labiatae	Salvia glutinosa L.	H scap	Paleotemp.
Dycotiledones	Apiaceae (Umbelliferae)	Sanicula europaea L.	H scap	Paleotemp.
Dycotiledones	Leguminosae	Trifolium campestre Schreb.	T er	Paleotemp.
Dycotiledones	Leguminosae	Trifolium pratense L.	H scap	Eurosib.
Dycotiledones	Compositae (Asteraceae)	Tussilago farfara L.	G rhiz	Paleotemp.
Dycotiledones	Urticaceae	Urtica dioica L. subsp. dioica	H scap	Subcosmop.
Dycotiledones	Scrophulariace ae	Verbascum thapsus L.	H bien	Europ.-Caucas.
Dycotiledones	Scrophulariace ae	Veronica chamaedrys L.	H scap	Eurosib.
Dycotiledones	Leguminosae	Vicia sp.		

Dycotiledones	Violaceae	Viola alba Besser subsp. dehnhardtii (Ten.) W. Becker	H rept	Euri-Medit.
Monocotyledone s	Poaceae (Graminaceae)	Vulpia ligustica (All.) Link	T caesp	W-Medit. (Steno)
Dycotiledones	Fagaceae	Castanea sativa Mill.	P m	SE-Europ.
	Lamiaceae	Clinopodium vulgare	H scap	
	Betulaceae	Corylus avellana	P caesp	
	Araliaceae	Hedera	P lian	
		Lamium sp.		
		Poa sp.		
Ferns	Hypolepidacea e	Pteridium aquilinum	G rhiz	Cosmop.
	Rosaceae	Rubus ulmifolius Schott	P caesp	
Dycotiledones	Leguminosae	Trifolium pratense	H scap	Eurosib.

## Annex C – Data sampler for inverse analysis

The sampling codes written to prepare the data for the fitting of the main drying and wetting require a source worksheet organized in the same manner. The outputs of the sampler are then introduced in output worksheets with specific format in the same excel file.

The source worksheet must be organized as in Figure 201 where the first column refers to the fact that the sample is during a wetting or drying phase, the second column is for the number of wetting steps or the number of the drying phase. The columns C and D are referent to time, in which the first is absolute time and the second is the lapsed time for each phase. Columns E and F refer to the suction at the top and bottom, respectively. Column G is the wet soil weight of the sample. Columns H and I are extra information regarding the weight variation since the beginning of each phase and the vertical gradient.

	A	B	C	D	E	F	G	H	I	J	K
1	phase	code	time (h)	time0 (h)	suction_top (kPa)	suction_bottom (kPa)	weight (g)	d_weight (g)	gradient		
2	1	0	0.0000	0.0000	34.11	33.69	274.86	0	0.4		
3	1	0	0.1667	0.1667	34.12	33.71	274.86	0	0.366667		
4	1	0	0.3333	0.3333	34.13	33.71	274.86	0	0.4		
5	1	0	0.5000	0.5000	34.13	33.71	274.86	0	0.4		
6	1	0	0.6667	0.6667	34.13	33.73	274.86	0	0.333333		
7	1	0	0.8333	0.8333	34.13	33.71	274.86	0	0.4		
8	1	0	1.0000	1.0000	34.14	33.74	274.86	0	0.333333		
9	1	0	1.1667	1.1667	34.14	33.74	274.86	0	0.333333		
10	1	0	1.3333	1.3333	34.14	33.73	274.86	0	0.366667		
11	1	0	1.5000	1.5000	34.15	33.73	274.86	0	0.4		
12	1	0	1.6667	1.6667	34.15	33.74	274.86	0	0.366667		
13	1	1	2.0003	0.0000	14.38	32.93	279.81	0	-62.8333		
14	1	1	2.1669	0.1667	16.58	32.56	279.8	-0.01	-54.2667		
15	1	1	2.3336	0.3333	17.8	32.25	279.8	-0.01	-49.1667		

Figure 201 – Excel worksheet SSA to with ku-pf monitoring data to be used as source.

The sampler code to collect the necessary information for the fitting of the main drying using inverse analysis in HYDRUS-1D is presented in Box 1 (VBA language). In order to run the code, a source worksheet named “SSA” must be organized as in Figure 201 and an output worksheet named “HYDRUS#” as in Figure 202, in which # should be replaced by the number of the drying phase correspondent to the main drying. For example, if the main drying was the second drying experienced by the sample, then the worksheet should be names “HYDRUS2”. Attention should be taken to the numbering of columns A and B represented in Figure 201. The code (Box 1) fills up the columns A to O and the cells Q3 and Q4. The values underlined in the Box 1 should be adapted in order to reach to a sample data set of approximately 500 values well distributed in terms of suction.



	A	B	C	D	E	F	G	H	I	J	K	L	M	N	O	P	Q	R	S	T	U	V	W
1	SAMPLE					INPUT 1					INPUT 2												
2	time0	top	bottom	weight		time0	precipitation	evaporation	H crit		x	y	type	position	weight		parameter						
3	(h)	suction	suction	(g)		(h)	(cm/h)	(cm/h)	(cm)								s						
4	0.16667	1.12	0.16	345.7		0.010	0	0.00000	100000		0.010	-10.0	1	1	1		420	number of data points in the objective function (INPUT 2)					
5	0.33333	1.2	0.23	345.6		0.177	0	0.01793	100000		0.177	-11.2	1	1	1		209	number of time-variable boundary records (INPUT 1)					
6	0.66667	1.29	0.35	345.39		0.343	0	0.01494	100000		0.343	-12.0	1	1	1		167.868	final time (h)					
7	1.00028	1.39	0.44	345.17		0.677	0	0.01569	100000		0.677	-12.9	1	1	1								
8	1.33361	1.49	0.55	344.97		1.010	0	0.01643	100000		1.010	-13.9	1	1	1								
9	1.66694	1.58	0.63	344.76		1.344	0	0.01494	100000		1.344	-14.9	1	1	1								
10	2.00028	1.66	0.72	344.56		1.677	0	0.01569	100000		1.677	-15.8	1	1	1		0.1644	Qr					
11	2.33361	1.74	0.8	344.36		2.010	0	0.01494	100000		2.010	-16.6	1	1	1		0.5691	Qs					
12	2.83389	1.85	0.91	344.08		2.344	0	0.01494	100000		2.344	-17.4	1	1	1		0.011044	alpha (1/cm)					
13	3.33389	1.94	1.02	343.8		2.844	0	0.01394	100000		2.844	-18.5	1	1	1		1.7678	n					
14	3.66722	2.02	1.09	343.61		3.344	0	0.01395	100000		3.344	-19.4	1	1	1		0.1565204	Ks (cm/h)					
15	4.16722	2.11	1.2	343.34		3.677	0	0.01420	100000		3.677	-20.2	1	1	1		0.5	I					
16	4.50139	2.19	1.27	343.15		4.177	0	0.01345	100000		4.177	-21.1	1	1	1		-45.60	suction AEV (cm)					
17	5.00111	2.29	1.37	342.88		4.511	0	0.01416	100000		4.511	-21.9	1	1	1		0.5263	wvc AEV					
18	5.50083	2.39	1.48	342.61		5.011	0	0.01346	100000		5.011	-22.9	1	1	1								
19	5.83417	2.47	1.55	342.43		5.511	0	0.01346	100000		5.511	-23.9	1	1	1								
20	6.33417	2.57	1.65	342.17		5.844	0	0.01345	100000		5.844	-24.7	1	1	1			initial conditions (geometry)					
21	6.83444	2.67	1.76	341.91		6.344	0	0.01295	100000		6.344	-25.7	1	1	1		depth (cm)	0	6				
22	7.16778	2.74	1.83	341.74		6.844	0	0.01294	100000		6.844	-26.7	1	1	1		pressure h <sub>v</sub>	-14.75	4.25				
23	7.50111	2.81	1.91	341.56		7.178	0	0.01270	100000		7.178	-27.4	1	1	1								
24	8.00111	2.9	2	341.31		7.511	0	0.01345	100000		7.511	-28.1	1	1	1								
25						8.011	0	0.01245	100000		8.011	-29.0	1	1	1								

Figure 202 – Output worksheet HYDRUS# containing the sampled boundary conditions (INPUT 1), the data sets (INPUT 2), data set size and time information on the top right corner, initial estimation of the input parameters right below, and the initial conditions at the bottom right.

Box 1 – VBA code to sample data the boundary conditions and data sets to be used in the inverse analysis of HYDRUS-1D to obtain the main drying parameters.

```

sampler
Sub sampler()

' to sample points to input in HYDRUS
' according to the criteria followed by Annie

Dim lread As Integer
Dim lwrite As Integer
lread = 3 ' line to read in SSA
lwrite = 3 ' line to write in HYDRUS
Dim medsuc As Double ' temporary variable to store the difference between suction
Dim phase As Integer ' phase to use for hydrus

' which dry phase to use for hydrus
phase = InputBox("which dry phase to use in HYDRUS?")

' find 1st line
Do While Worksheets("SSA").Range("A" & lread).Value <> "0" Or
Worksheets("SSA").Range("B" & lread).Value <> phase
    lread = lread + 1
Loop

' write 1st line
Worksheets("HYDRUS" & phase).Range("A3:D3").Value = Worksheets("SSA").Range("D" &
lread & ":G" & lread).Value

Do While Worksheets("SSA").Range("A" & lread).Value = "0"

    medsuc = (Worksheets("SSA").Range("E" & lread).Value + Worksheets("SSA").Range("F"
& lread).Value) / 2 - (Worksheets("HYDRUS" & phase).Range("B" & lwrite).Value +
Worksheets("HYDRUS" & phase).Range("C" & lwrite).Value) / 2

    If medsuc > 0.01 And Worksheets("SSA").Range("F" & lread).Value < 10 Then ' the
difference should be greater than 0.03
        lwrite = lwrite + 1
    End If
    lread = lread + 1
End While
End Sub

```

```

Worksheets("HYDRUS" & phase).Range("A" & lwrite & ":D" & lwrite).Value =
Worksheets("SSA").Range("D" & lread & ":G" & lread).Value

ElseIf medsuc > 0.2 And Worksheets("SSA").Range("F" & lread).Value < 40 Then
    lwrite = lwrite + 1
    Worksheets("HYDRUS" & phase).Range("A" & lwrite & ":D" & lwrite).Value =
Worksheets("SSA").Range("D" & lread & ":G" & lread).Value

ElseIf medsuc > 0.5 Then
    lwrite = lwrite + 1
    Worksheets("HYDRUS" & phase).Range("A" & lwrite & ":D" & lwrite).Value =
Worksheets("SSA").Range("D" & lread & ":G" & lread).Value

End If

lread = lread + 1

Loop

End Sub

```

The sampler code to collect the information for the fitting of the main wetting using inverse analysis in HYDRUS-1D is presented in Box 2 (VBA language). In order to run the code, a source worksheet named “SSA” must be organized as in Figure 201 and an output worksheet named “hysteresis” as in Figure 203. The code (Box 2) fills up the columns A to P.

	A	B	C	D	E	F	G	H	I	J	K	L	M	N	O	P	Q	R	S	T	U
1	Time (h)	Precipitat	Evaporati	h crit		x	Y	type	position	weight		x	Y	type	position	weight					
2	0.01	0	0	100000		0.01	-21.8	1	1	1		0.01	-18.1	1	2	1		number of	8636		
3	1.06028	0	0.01239	100000		1.06028	-27.6	1	1	1		1.06028	-24	1	2	1		final time	2724.64		
4	2.31028	0	0.01158	100000		2.31028	-32.7	1	1	1		2.31028	-29.2	1	2	1		number of	2110		
5	3.39306	0	0.01156	100000		3.39306	-36.4	1	1	1		3.39306	-32.8	1	2	1					
6	4.57667	0	0.01161	100000		4.57667	-40	1	1	1		4.57667	-36.4	1	2	1					
7	5.72667	0	0.01174	100000		5.72667	-43.1	1	1	1		5.72667	-39.8	1	2	1		teta_r	0.16108		
8	6.89361	0	0.01157	100000		6.89361	-46.1	1	1	1		6.89361	-42.7	1	2	1		teta_s	0.6436		
9	8.02694	0	0.01191	100000		8.02694	-48.8	1	1	1		8.02694	-45.5	1	2	1		alpha	0.01109		
10	9.17722	0	0.01238	100000		9.17722	-51.3	1	1	1		9.17722	-47.9	1	2	1		n	1.7722		
11	10.2272	0	0.01192	100000		10.2272	-53.4	1	1	1		10.2272	-50.1	1	2	1		Ks	0.32486		
12	11.2608	0	0.01211	100000		11.2608	-55.4	1	1	1		11.2608	-52.1	1	2	1		l	0.03805		
13	12.3611	0	0.01227	100000		12.3611	-57.4	1	1	1		12.3611	-54.1	1	2	1		teta_m	0.6436	min	max
14	13.6611	0	0.01095	100000		13.6611	-59.2	1	1	1		13.6611	-56	1	2	1		teta_sw	0.6436	0	0.6436
15	14.9281	0	0.01104	100000		14.9281	-61.2	1	1	1		14.9281	-58	1	2	1		alpha_w	0.02217	0	10
16	16.095	0	0.01136	100000		16.095	-63	1	1	1		16.095	-59.9	1	2	1		K_sw	3.25E-01	0.001	0.32486
17	17.3783	0	0.01109	100000		17.3783	-64.4	1	1	1		17.3783	-61.5	1	2	1					
18	18.5119	0	0.01147	100000		18.5119	-65.7	1	1	1		18.5119	-62.7	1	2	1					
19	19.6119	0	0.01138	100000		19.6119	-67	1	1	1		19.6119	-64.2	1	2	1					
20	20.8956	0	0.01128	100000		20.8956	-68.5	1	1	1		20.8956	-65.6	1	2	1		initial conditions (geometry)			
21	21.8958	0	0.01251	100000		21.8958	-70	1	1	1		21.8958	-67.1	1	2	1		depth (cm)	0	6	
22	23.0172	0	0.01248	100000		23.0172	-71.7	1	1	1		23.0172	-69	1	2	1		pressure h	-23.65	-16.25	
23	24.075	0	0.01253	100000		24.075	-73	1	1	1		24.075	-70.3	1	2	1					
24	25.0903	0	0.01354	100000		25.0903	-74.7	1	1	1		25.0903	-72	1	2	1		main drying curve parameters			
25	26.1967	0	0.01398	100000		26.1967	-76.6	1	1	1		26.1967	-73.8	1	2	1		WCR	1.61E-01		
26	27.2633	0	0.01312	100000		27.2633	-77.8	1	1	1		27.2633	-75	1	2	1		WCS	6.44E-01		
27	28.1803	0	0.01365	100000		28.1803	-79.2	1	1	1		28.1803	-76.3	1	2	1		ALPHA	1.11E-02		
28	29.2136	0	0.01354	100000		29.2136	-80.7	1	1	1		29.2136	-78	1	2	1		N	1.77E+00		
29	30.1472	0	0.01367	100000		30.1472	-82.2	1	1	1		30.1472	-79.4	1	2	1		L	3.81E-02		
30	31.1472	0	0.0135	100000		31.1472	-83.6	1	1	1		31.1472	-80.8	1	2	1					
31	32.1983	0	0.01331	100000		32.1983	-85	1	1	1		32.1983	-82.3	1	2	1					
32	33.1978	0	0.01326	100000		33.1978	-86.4	1	1	1		33.1978	-83.8	1	2	1					

Figure 203 – Output worksheet ‘hysteresis’ containing the sampled boundary conditions (columns A to D), the data sets (columns F to P), data set size and time information on the top right corner, initial estimation of the input parameters right below, the initial conditions, and the fitted parameters of the main drying curve.

Box 2 – Code to sample data the boundary conditions and data sets to be used in the inverse analysis of HYDRUS-1D to obtain the main wetting parameters.

```

samplerhysteresis
Sub samplerhysteresis()

Worksheets("hysteresis").Select
    Range("A1").Value = "Time (h)"
    Range("B1").Value = "Precipitation (g/h)"
    Range("C1").Value = "Evaporation (g/h)"
    Range("D1").Value = "h crit"
    Range("F1").Value = "x"
    Range("G1").Value = "Y"
    Range("H1").Value = "type"
    Range("I1").Value = "position"
    Range("J1").Value = "weight"
    Range("L1:P1").Value = Range("F1:J1").Value

Dim lread As Integer
lread = 2
Dim lreadf As Integer
lreadf = lread + 1
Dim lwritebd As Integer ' boundary conditions: evaporation/rainfall
lwritebd = 2
Dim lwrites As Integer ' solution (for the fitting)
lwrites = 2
Dim A As Double
A = Worksheets("meta").Range("F6").Value ' cross-section area
Dim i As Integer ' to count the lines of the wetting phases

' 1st LINE (just copy)
' boundary conditions: evaporation and rainfall
Range("A" & lwritebd).Value = 0.01
Range("B" & lwritebd & ":C" & lwritebd).Value = 0
Range("D" & lwritebd).Value = 100000
' position 1 (top)
Range("F" & lwrites).Value = 0.01
Range("G" & lwrites).Value = -10 * Worksheets("SSA").Range("E" & lread).Value
Range("H" & lwrites & ":J" & lwrites).Value = 1
' position 2 (bottom)
Range("L" & lwrites & ":P" & lwrites).Value = Range("F" & lwrites & ":J" & lwrites).Value
Range("M" & lwrites).Value = -10 * Worksheets("SSA").Range("F" & lread).Value
Range("O" & lwrites).Value = 2

    lreadf = lread + 1
    lwritebd = lwritebd + 1
    lwrites = lwrites + 1

Do While Worksheets("SSA").Range("C" & lreadf).Value <> ""

    ' DRY -----
    If Worksheets("SSA").Range("A" & lreadf).Value = "0" Then
        Do While Worksheets("SSA").Range("A" & lreadf).Value = "0"
            ' weight variation
            dweight = Abs(Worksheets("SSA").Range("G" & lread).Value -
Worksheets("SSA").Range("G" & lreadf).Value)

            ' if the weight variation is greater than 0.5 and there are suction
measurements --> write
            If dweight > 0.5 And Worksheets("SSA").Range("I" & lreadf).Value <> ""
Then

```

```

' boundary conditions: evaporation and rainfall
Range("A" & lwritebd).Value = Range("A" & lwritebd - 1).Value +
Worksheets("SSA").Range("C" & lreadf).Value - Worksheets("SSA").Range("C" &
lread).Value
Range("B" & lwritebd).Value = 0
Range("C" & lwritebd).Value = dweight / (Worksheets("SSA").Range("C"
& lreadf).Value - Worksheets("SSA").Range("C" & lread).Value) / A
Range("D" & lwritebd).Value = 100000
' position 1 (top)
Range("F" & lwrites).Value = Worksheets("SSA").Range("C" &
lreadf).Value + 0.01
Range("G" & lwrites).Value = -10 * Worksheets("SSA").Range("E" &
lreadf).Value
Range("H" & lwrites & ":J" & lwrites).Value = 1
' position 2 (bottom)
Range("L" & lwrites & ":P" & lwrites).Value = Range("F" & lwrites &
":J" & lwrites).Value
Range("M" & lwrites).Value = -10 * Worksheets("SSA").Range("F" &
lreadf).Value
Range("O" & lwrites).Value = 2

lwritebd = lwritebd + 1
lwrites = lwrites + 1
lread = lreadf
lreadf = lreadf + 1

' if there are NO suction measurements
ElseIf Worksheets("SSA").Range("I" & lreadf).Value = "" Then
' if the last written suction value wasn't the last measured one -->
it writes the last values of suction
If lreadf > lread + 1 And Worksheets("SSA").Range("I" & lreadf -
1).Value <> "" Then
' boundary conditions: evaporation and rainfall
Range("A" & lwritebd).Value = Range("A" & lwritebd - 1).Value +
Worksheets("SSA").Range("C" & lreadf - 1).Value - Worksheets("SSA").Range("C" &
lread).Value
Range("B" & lwritebd).Value = 0
Range("C" & lwritebd).Value = -(Worksheets("SSA").Range("G" &
lreadf - 1).Value - Worksheets("SSA").Range("G" & lread).Value) /
(Worksheets("SSA").Range("C" & lreadf - 1).Value - Worksheets("SSA").Range("C" &
lread).Value) / A
Range("D" & lwritebd).Value = 100000
' position 1 (top)
Range("F" & lwrites).Value = Range("A" & lwritebd).Value
Range("G" & lwrites).Value = -10 * Worksheets("SSA").Range("E" &
lreadf - 1).Value
Range("H" & lwrites & ":J" & lwrites).Value = 1
' position 2 (bottom)
Range("L" & lwrites & ":P" & lwrites).Value = Range("F" & lwrites
& ":J" & lwrites).Value
Range("M" & lwrites).Value = -10 * Worksheets("SSA").Range("F" &
lreadf - 1).Value
Range("O" & lwrites).Value = 2

lwritebd = lwritebd + 1
lwrites = lwrites + 1
lread = lreadf - 1
End If

' when there arent suction measurements (it writes every 4 values)
Do While Worksheets("SSA").Range("A" & lreadf + 4).Value = 0 And
Worksheets("SSA").Range("I" & lreadf + 4).Value = ""

```

```

Range("A" & lwritebd).Value = Range("A" & lwritebd - 1).Value +
Worksheets("SSA").Range("C" & lreadf).Value - Worksheets("SSA").Range("C" &
lread).Value
Range("B" & lwritebd).Value = 0
Range("C" & lwritebd).Value = -(Worksheets("SSA").Range("G" &
lreadf).Value - Worksheets("SSA").Range("G" & lread).Value) /
(Worksheets("SSA").Range("C" & lreadf).Value - Worksheets("SSA").Range("C" &
lread).Value) / A
Range("D" & lwritebd).Value = 100000

lread = lreadf
lreadf = lreadf + 4
lwritebd = lwritebd + 1
Loop

If Worksheets("SSA").Range("A" & lreadf + 1).Value = 0 And
Worksheets("SSA").Range("I" & lreadf + 1).Value = "" Then
Do While Worksheets("SSA").Range("A" & lreadf + 1).Value = 0 And
Worksheets("SSA").Range("I" & lreadf + 1).Value = ""
lreadf = lreadf + 1
Loop
End If

Range("A" & lwritebd).Value = Range("A" & lwritebd - 1).Value +
Worksheets("SSA").Range("C" & lreadf).Value - Worksheets("SSA").Range("C" &
lread).Value
Range("B" & lwritebd).Value = 0
Range("C" & lwritebd).Value = -(Worksheets("SSA").Range("G" &
lreadf).Value - Worksheets("SSA").Range("G" & lread).Value) /
(Worksheets("SSA").Range("C" & lreadf).Value - Worksheets("SSA").Range("C" &
lread).Value) / A
Range("D" & lwritebd).Value = 100000

lread = lreadf
lreadf = lreadf + 1
lwritebd = lwritebd + 1

' if the weight variation is smaller than 0.5
Else
lreadf = lreadf + 1
End If
Loop

' WET -----
Else
' ADDED CAP (SORT OF WETTING - STEP 0)
' when it contains the data after the cap is added but NO suction measurements
If Worksheets("SSA").Range("I" & lreadf).Value = "" Then
Do While Worksheets("SSA").Range("I" & lreadf).Value = ""
' if water was added
If lreadf > lread + 1 And Worksheets("SSA").Range("G" & lreadf).Value
- Worksheets("SSA").Range("G" & lread).Value > 1 Then
' finish the previous part when water was NOT added
Range("A" & lwritebd).Value = Range("A" & lwritebd - 1).Value +
Worksheets("SSA").Range("C" & lreadf - 1).Value - Worksheets("SSA").Range("C" &
lread).Value
If (Worksheets("SSA").Range("G" & lreadf - 1).Value -
Worksheets("SSA").Range("G" & lread).Value) < 0 Then
' drying
Range("B" & lwritebd).Value = 0
Range("C" & lwritebd).Value = -(Worksheets("SSA").Range("G" &
lreadf - 1).Value - Worksheets("SSA").Range("G" & lread).Value) /

```

```

(Worksheets("SSA").Range("C" & lreadf - 1).Value - Worksheets("SSA").Range("C" &
lread).Value) / A
    Else
        ' wetting
        Range("B" & lwritebd).Value = (Worksheets("SSA").Range("G" &
lreadf - 1).Value - Worksheets("SSA").Range("G" & lread).Value) /
(Worksheets("SSA").Range("C" & lreadf - 1).Value - Worksheets("SSA").Range("C" &
lread).Value) / A
        Range("C" & lwritebd).Value = 0
    End If
    Range("D" & lwritebd).Value = 100000
    lwritebd = lwritebd + 1

    ' wetting (when water was added but no suction measurements)
    Range("A" & lwritebd).Value = Range("A" & lwritebd - 1).Value +
Worksheets("SSA").Range("C" & lreadf).Value - Worksheets("SSA").Range("C" & lreadf -
1).Value
    Range("B" & lwritebd).Value = (Worksheets("SSA").Range("G" &
lreadf).Value - Worksheets("SSA").Range("G" & lreadf - 1).Value) /
(Worksheets("SSA").Range("C" & lreadf).Value - Worksheets("SSA").Range("C" & lreadf -
1).Value) / A
    Range("C" & lwritebd).Value = 0
    Range("D" & lwritebd).Value = 100000
    lwritebd = lwritebd + 1

    lread = lreadf

    ElseIf lreadf > lread + 5 Then 'if water wasnt added but lh has already
passed
        Range("A" & lwritebd).Value = Range("A" & lwritebd - 1).Value +
Worksheets("SSA").Range("C" & lreadf).Value - Worksheets("SSA").Range("C" &
lread).Value
        If (Worksheets("SSA").Range("G" & lreadf).Value -
Worksheets("SSA").Range("G" & lread).Value) < 0 Then
            ' drying
            Range("B" & lwritebd).Value = 0
            Range("C" & lwritebd).Value = -(Worksheets("SSA").Range("G" &
lreadf).Value - Worksheets("SSA").Range("G" & lread).Value) /
(Worksheets("SSA").Range("C" & lreadf).Value - Worksheets("SSA").Range("C" &
lread).Value) / A
        Else
            ' wetting
            Range("B" & lwritebd).Value = (Worksheets("SSA").Range("G" &
lreadf).Value - Worksheets("SSA").Range("G" & lread).Value) /
(Worksheets("SSA").Range("C" & lreadf).Value - Worksheets("SSA").Range("C" &
lread).Value) / A
            Range("C" & lwritebd).Value = 0
        End If
        Range("D" & lwritebd).Value = 100000
        lwritebd = lwritebd + 1
        lread = lreadf
        lreadf = lreadf + 1

    Else
        lreadf = lreadf + 1
    End If
Loop

' finish the rest of the unknown suction part
' here lreadf already has a suction value
If lreadf > lread + 1 Then

```

```

Range("A" & lwritebd).Value = Range("A" & lwritebd - 1).Value +
Worksheets("SSA").Range("C" & lreadf).Value - Worksheets("SSA").Range("C" &
lread).Value
If (Worksheets("SSA").Range("G" & lreadf).Value -
Worksheets("SSA").Range("G" & lread).Value) < 0 Then
    ' drying
    Range("B" & lwritebd).Value = 0
    Range("C" & lwritebd).Value = -(Worksheets("SSA").Range("G" &
lreadf).Value - Worksheets("SSA").Range("G" & lread).Value) /
(Worksheets("SSA").Range("C" & lreadf).Value - Worksheets("SSA").Range("C" &
lread).Value) / A
Else
    ' wetting
    Range("B" & lwritebd).Value = (Worksheets("SSA").Range("G" &
lreadf).Value - Worksheets("SSA").Range("G" & lread).Value) /
(Worksheets("SSA").Range("C" & lreadf).Value - Worksheets("SSA").Range("C" &
lread).Value) / A
    Range("C" & lwritebd).Value = 0
End If
Range("D" & lwritebd).Value = 100000
lwritebd = lwritebd + 1
lread = lreadf
lreadf = lreadf + 1

End If

ElseIf Worksheets("SSA").Range("B" & lreadf).Value = 0 Then
    ' when suction IS known
' when step 0 -----
    ' find end of the step 0 when suction is known
    Do While Worksheets("SSA").Range("B" & lreadf + 1).Value = 0 And
Worksheets("SSA").Range("I" & lreadf + 1).Value <> ""
        lreadf = lreadf + 1
    Loop

    ' boundary conditions: evaporation/rainfall
    Range("A" & lwritebd).Value = Range("A" & lwritebd - 1).Value +
Worksheets("SSA").Range("C" & lreadf).Value - Worksheets("SSA").Range("C" &
lread).Value
    If (Worksheets("SSA").Range("G" & lreadf).Value -
Worksheets("SSA").Range("G" & lread).Value) < 0 Then
        ' drying
        Range("B" & lwritebd).Value = 0
        Range("C" & lwritebd).Value = -(Worksheets("SSA").Range("G" &
lreadf).Value - Worksheets("SSA").Range("G" & lread).Value) /
(Worksheets("SSA").Range("C" & lreadf).Value - Worksheets("SSA").Range("C" &
lread).Value) / A
    Else
        ' wetting
        Range("B" & lwritebd).Value = (Worksheets("SSA").Range("G" &
lreadf).Value - Worksheets("SSA").Range("G" & lread).Value) /
(Worksheets("SSA").Range("C" & lreadf).Value - Worksheets("SSA").Range("C" &
lread).Value) / A
        Range("C" & lwritebd).Value = 0
    End If
    Range("D" & lwritebd).Value = 100000

    ' objective function: suction
    ' first line
    ' position 1 (top)
    Range("F" & lwrites).Value = Worksheets("SSA").Range("C" &
lread).Value + 0.01

```

```

Range("G" & lwrites).Value = -10 * Worksheets("SSA").Range("E" &
lread).Value
Range("H" & lwrites & ":J" & lwrites).Value = 1
' position 2 (bottom)
Range("L" & lwrites & ":P" & lwrites).Value = Range("F" & lwrites &
":J" & lwrites).Value
Range("M" & lwrites).Value = -10 * Worksheets("SSA").Range("F" &
lread).Value
Range("O" & lwrites).Value = 2
lwrites = lwrites + 1
i = lread + 4
' middle lines
Do While i < lreadf - 4
' position 1 (top)
Range("F" & lwrites).Value = Worksheets("SSA").Range("C" &
i).Value + 0.01
Range("F" & lwrites).Value = Range("F" & lwrites - 1).Value +
Worksheets("SSA").Range("C" & i).Value - Worksheets("SSA").Range("C" & i - 4).Value
Range("G" & lwrites).Value = -10 * Worksheets("SSA").Range("E" &
i).Value
Range("H" & lwrites & ":J" & lwrites).Value = 1
' position 2 (bottom)
Range("L" & lwrites & ":P" & lwrites).Value = Range("F" & lwrites
& ":J" & lwrites).Value
Range("M" & lwrites).Value = -10 * Worksheets("SSA").Range("F" &
i).Value
Range("O" & lwrites).Value = 2

lwrites = lwrites + 1
i = i + 4
Loop
'last line
' position 1 (top)
Range("F" & lwrites).Value = Worksheets("SSA").Range("C" &
lreadf).Value + 0.01
Range("G" & lwrites).Value = -10 * Worksheets("SSA").Range("E" &
lreadf).Value
Range("H" & lwrites & ":J" & lwrites).Value = 1
' position 2 (bottom)
Range("L" & lwrites & ":P" & lwrites).Value = Range("F" & lwrites &
":J" & lwrites).Value
Range("M" & lwrites).Value = -10 * Worksheets("SSA").Range("F" &
lreadf).Value
Range("O" & lwrites).Value = 2
lwrites = lwrites + 1

lread = lreadf
lreadf = lreadf + 1
lwritebd = lwritebd + 1

Else

' WETTING STEPS -----
Do While Worksheets("SSA").Range("A" & lreadf).Value = 1 And
Worksheets("SSA").Range("B" & lreadf).Value <> 0

' look for the end of the phase
Do While (Worksheets("SSA").Range("B" & lread + 1).Value =
Worksheets("SSA").Range("B" & lreadf + 1).Value Or Worksheets("SSA").Range("B" &
lreadf + 1).Value = 0) And Worksheets("SSA").Range("I" & lreadf + 1).Value <> ""
lreadf = lreadf + 1
Loop

```



```

' BOUNDARY CONDITIONS: evaporation/rainfall
' adding water
Range("A" & lwritebd).Value = Range("A" & lwritebd - 1).Value +
Worksheets("SSA").Range("C" & lread + 1).Value - Worksheets("SSA").Range("C" &
lread).Value
If (Worksheets("SSA").Range("G" & lread + 1).Value -
Worksheets("SSA").Range("G" & lread).Value) < 0 Then
' drying
Range("B" & lwritebd).Value = 0
Range("C" & lwritebd).Value = -(Worksheets("SSA").Range("G" &
lread + 1).Value - Worksheets("SSA").Range("G" & lread).Value) /
(Worksheets("SSA").Range("C" & lread + 1).Value - Worksheets("SSA").Range("C" &
lread).Value) / A
Else
' wetting
Range("B" & lwritebd).Value = (Worksheets("SSA").Range("G" & lread
+ 1).Value - Worksheets("SSA").Range("G" & lread).Value) /
(Worksheets("SSA").Range("C" & lread + 1).Value - Worksheets("SSA").Range("C" &
lread).Value) / A
Range("C" & lwritebd).Value = 0
End If
Range("D" & lwritebd).Value = 100000
lwritebd = lwritebd + 1
' equalization

i = lread + 7
Do While i < lreadf - 6

If (Worksheets("SSA").Range("G" & i).Value -
Worksheets("SSA").Range("G" & i - 6).Value) <> 0 Then
Range("A" & lwritebd).Value = Worksheets("SSA").Range("C" &
i).Value + 0.01
If (Worksheets("SSA").Range("G" & i).Value -
Worksheets("SSA").Range("G" & i - 6).Value) < 0 Then
' drying
Range("B" & lwritebd).Value = 0
Range("C" & lwritebd).Value = -(Worksheets("SSA").Range("G" & i).Value -
Worksheets("SSA").Range("G" & i - 6).Value) /
(Worksheets("SSA").Range("C" & i).Value - Range("A" & lwritebd - 1).Value) / A
Else
' wetting
Range("B" & lwritebd).Value = (Worksheets("SSA").Range("G" & i).Value -
Worksheets("SSA").Range("G" & i - 6).Value) /
(Worksheets("SSA").Range("C" & i).Value - Range("A" & lwritebd - 1).Value) / A
Range("C" & lwritebd).Value = 0
End If
Range("D" & lwritebd).Value = 100000
lwritebd = lwritebd + 1
End If

i = i + 6

Loop

Range("A" & lwritebd).Value = Range("A" & lwritebd - 1).Value +
Worksheets("SSA").Range("C" & lreadf).Value - Worksheets("SSA").Range("C" & i -
6).Value
If (Worksheets("SSA").Range("G" & lreadf).Value -
Worksheets("SSA").Range("G" & i - 6).Value) < 0 Then
' drying
Range("B" & lwritebd).Value = 0
Range("C" & lwritebd).Value = -(Worksheets("SSA").Range("G" &
lreadf).Value - Worksheets("SSA").Range("G" & i - 6).Value) /

```

```

(Worksheets("SSA").Range("C" & lreadf).Value - Worksheets("SSA").Range("C" & i -
6).Value) / A
    Else
        ' wetting
        Range("B" & lwritebd).Value = (Worksheets("SSA").Range("G" &
lreadf).Value - Worksheets("SSA").Range("G" & i - 6).Value) /
(Worksheets("SSA").Range("C" & lreadf).Value - Worksheets("SSA").Range("C" & i -
6).Value) / A
        Range("C" & lwritebd).Value = 0
    End If
    Range("D" & lwritebd).Value = 100000
    lwritebd = lwritebd + 1

    ' SUCTION: top/bottom

    ' first line
    ' position 1 (top)
    Range("F" & lwrites).Value = Worksheets("SSA").Range("C" & lread
+ 1).Value + 0.01
    Range("G" & lwrites).Value = -10 * Worksheets("SSA").Range("E" &
lread + 1).Value
    Range("H" & lwrites & ":J" & lwrites).Value = 1
    ' position 2 (bottom)
    Range("L" & lwrites & ":P" & lwrites).Value = Range("F" & lwrites
& ":J" & lwrites).Value
    Range("M" & lwrites).Value = -10 * Worksheets("SSA").Range("F" &
lread + 1).Value
    Range("O" & lwrites).Value = 2
    lwrites = lwrites + 1
    ' middle lines
    i = lread + 5
    Do While i < lreadf - 4
        ' position 1 (top)
        Range("F" & lwrites).Value = Worksheets("SSA").Range("C" &
i).Value + 0.01
        Range("G" & lwrites).Value = -10 * Worksheets("SSA").Range("E"
& i).Value
        Range("H" & lwrites & ":J" & lwrites).Value = 1
        ' position 2 (bottom)
        Range("L" & lwrites & ":P" & lwrites).Value = Range("F" &
lwrites & ":J" & lwrites).Value
        Range("M" & lwrites).Value = -10 * Worksheets("SSA").Range("F"
& i).Value
        Range("O" & lwrites).Value = 2
        lwrites = lwrites + 1
        i = i + 4
    Loop
    ' last line
    ' position 1 (top)
    Range("F" & lwrites).Value = Worksheets("SSA").Range("C" &
lreadf).Value + 0.01
    Range("G" & lwrites).Value = -10 * Worksheets("SSA").Range("E" &
lreadf).Value
    Range("H" & lwrites & ":J" & lwrites).Value = 1
    ' position 2 (bottom)
    Range("L" & lwrites & ":P" & lwrites).Value = Range("F" & lwrites
& ":J" & lwrites).Value
    Range("M" & lwrites).Value = -10 * Worksheets("SSA").Range("F" &
lreadf).Value
    Range("O" & lwrites).Value = 2
    lwrites = lwrites + 1

    lread = lreadf

```

```

        lreadf = lreadf + 1

        Loop

    End If

End If

Loop

Range("R2").Value = "number of points of objective function"
Range("S2").Value = "=ROWS(R[0]C[-13]:R[" & lwrites - 3 & "]C[-13])*2"
Range("R3").Value = "final time"
Range("S3").Value = "=R[" & lwritebd - 4 & "]C[-18]"
Range("R4").Value = "number of variable boundary records"
Range("S4").Value = "=ROWS(R[-2]C[-18]:R[" & lwritebd - 5 & "]C[-18])"

End Sub

```

## Annex D – Saturated permeability

Table 44 – Saturated permeability of individual tests and average value per sample.

sample	soil	average	saturated permeability (m s <sup>-1</sup> )					
1.9.1	A1	9.06E-07				8.08E-07	9.14E-07	9.95E-07
1.9.2	A1	6.02E-07				6.32E-07	5.92E-07	5.88E-07
1.7.1	A2	7.05E-06	6.78E-06	6.46E-06	6.57E-06	7.68E-06	7.71E-06	7.12E-06
1.7.2	A1	2.95E-07				3.47E-07	2.73E-07	2.71E-07
1.4.1	A2	1.43E-06				1.53E-06	1.31E-06	1.31E-06
1.5.1	A2	5.95E-06				6.54E-06	5.71E-06	5.98E-06
1.5.2	A2	6.77E-07				7.48E-07	6.75E-07	6.04E-07
1.1	C2	5.26E-07		5.57E-07	5.94E-07	5.11E-07	4.82E-07	4.85E-07
1.2	C2	4.97E-07			5.43E-07	4.71E-07	4.88E-07	4.85E-07
1.3	C2	1.70E-07				1.73E-07	1.51E-07	1.86E-07
2.12.1	C1	5.93E-06	5.39E-06	5.78E-06	5.61E-06	6.28E-06	6.25E-06	6.27E-06
2.12.2	C1	2.10E-06		1.74E-06	1.80E-06	1.91E-06	2.15E-06	2.88E-06
2.13.1	C1	4.89E-06		4.55E-06	4.60E-06	5.59E-06	5.12E-06	4.61E-06
2.13.2	C1	5.33E-08			4.25E-08	4.21E-08	7.72E-08	5.15E-08
R1	A1sup	8.10E-06				8.37E-06	7.59E-06	8.33E-06
R2	A1sup	3.74E-06				3.22E-06	3.47E-06	4.54E-06
R3	A1sup	6.26E-06				5.25E-06	6.40E-06	7.13E-06

Table 45 – Saturated permeability of several samples performed by Mastantuono (personal communication).

soil	sample	$K_{sat}$ (m s <sup>-1</sup> )
A1	C8	4.25E-07
	C9	5.51E-07
	C2	1.61E-07
	C10	4.90E-07
A2	C1-F2	1.93E-07
	C1-F8	3.69E-07
	C9-F1	4.30E-06
	C9-F1A	1.43E-06
C1	C1-F8	5.94E-07
	C1-F6	8.63E-07
	C1-F1	2.32E-07
C2	C18-F1A	4.07E-09
	C18-F2A	1.01E-08

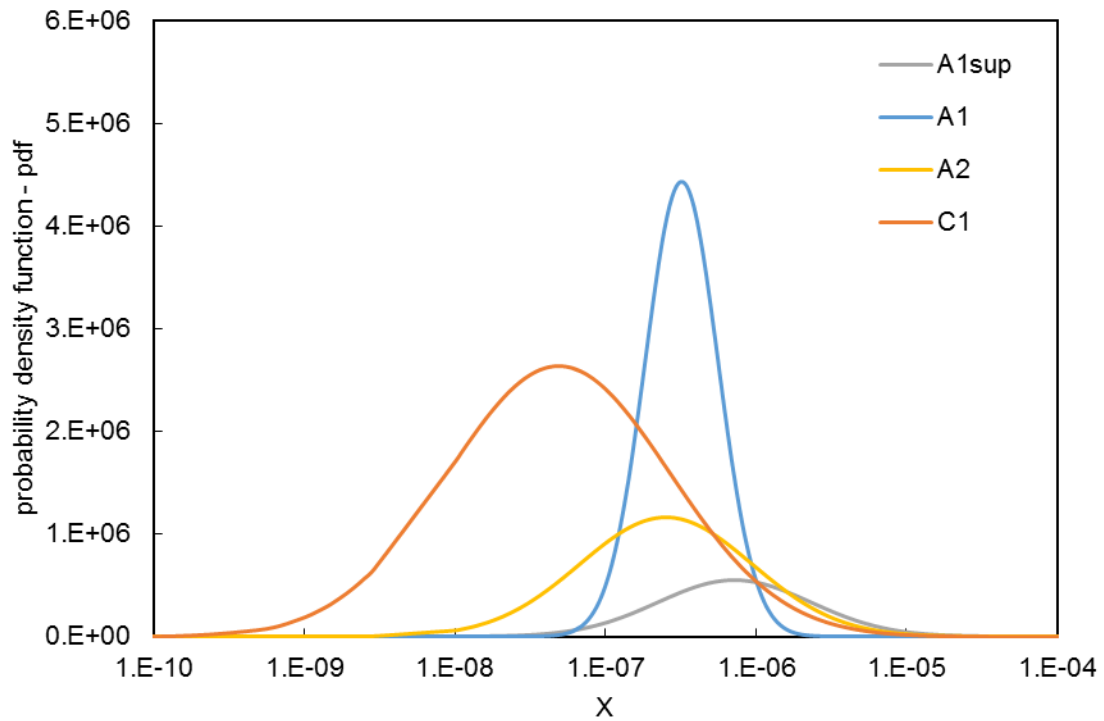


Figure 204 – Probability density function of the saturated permeability of soil A1sup, A1, A2 and C1.

## Annex E – Water content in the high suction range

*Table 46 – Measured and adopted values of volumetric water content (vwc) and suction for the objective function (inverse analysis) in the high suction range.*

soil	sample	measured		adopted	
		suction (kPa)	vwc	suction (kPa)	vwc
A1	1.11.2			600	0.164
A1	1.6.2			600	0.164
A1	1.7.2	600	0.138	600	0.138
A1	1.9.1	600	0.180	600	0.180
A1	1.9.2	600	0.185	600	0.185
A1 sup	N1			850	0.171
A1 sup	N2			850	0.171
A1 sup	R1			850	0.171
A1 sup	R2	850	0.187	850	0.187
A1 sup	R3	850	0.156	850	0.156
A2	1.1.1			600	0.136
A2	1.2.1			850	0.136
A2	1.4.1	850	0.212	850	0.136
A2	1.5.1	600	0.129	600	0.129
A2	1.5.2	850	0.136	850	0.136
A2	1.6.1			600	0.136
A2	1.7.1	600	0.161	600	0.161
C1	2.12.2	850	0.273	850	0.273
C1	2.13.1	850	0.261	850	0.261
C1	2.15.1			850	0.272
C2	1.1	850	0.282	850	0.282
C2	1.2			850	0.282
C2	1.3			850	0.282

## Annex F – Fitting of the main drying from inverse analysis

Table 47 – Fitted parameters of the main drying WRC and HPF of each sample and respective R2-index of the fitting.

soil	sample	WCR	WCS	ALPHA (kPa <sup>-1</sup> )	N	L	R2
A1	1.6.2	0.143	0.569	0.1068	1.725	0.000001	0.9997
	1.7.2	0.051	0.569	0.0533	1.515	2.398400	0.9987
	1.9.1	0.161	0.644	0.1109	1.772	0.038050	0.9991
	1.9.2	0.089	0.606	0.0874	1.424	1.451900	0.9971
	1.11.2	0.105	0.521	0.0883	1.492	1.197200	0.9982
A1 sup	R1	0.100	0.710	0.1525	1.428	2.762100	0.9830
	R2	0.143	0.635	0.1356	1.509	1.689500	0.9976
	R3	0.132	0.625	0.0142	1.626	0.957010	0.9973
	N1	0.120	0.610	0.0750	1.546	0.677140	0.9999
	N2	0.134	0.587	0.1033	1.558	0.000002	0.9995
A2	1.1.1	0.080	0.597	0.1315	1.510	-0.466950	0.9997
	1.2.1	0.104	0.580	0.1192	1.585	0.217510	0.9990
	1.4.1	0.120	0.453	0.0604	1.768	0.933960	0.9979
	1.5.1	0.082	0.549	0.0940	1.571	3.114900	0.9986
	1.6.1	0.098	0.554	0.1784	1.531	0.290140	0.9997
	1.7.1	0.115	0.594	0.1241	1.546	3.873900	0.9996
C1	2.12.2	0.261	0.660	0.0889	1.726	0.000108	0.9987
	2.13.1	0.249	0.690	0.1141	1.778	0.006155	0.9986
	2.15.1	0.262	0.700	0.1057	1.838	0.578340	0.9989
C2	1.1	0.230	0.643	0.0445	1.572	0.000344	0.9968
	1.2	0.112	0.656	0.0116	1.505	3.278400	0.9963
	1.3	0.225	0.654	0.0242	1.667	-1.511200	0.9994

Table 48 – Mean fitted parameters of the main drying WRC and HPF of each soil type.

mean	WCR	WCS	ALPHA (kPa <sup>-1</sup> )	N	L
A1	0.110	0.582	0.0893	1.586	1.01711
A1sup	0.126	0.633	0.0961	1.533	1.21715
A2	0.100	0.554	0.1179	1.585	1.32724
C1	0.257	0.683	0.1029	1.781	0.19487
C2	0.189	0.651	0.0268	1.581	0.58918

Table 49 – Standard deviation of the fitted parameters of the main drying WRC and HPF of each soil type.

std dev	WCR	WCS	ALPHA (kPa <sup>-1</sup> )	N	L
A1	0.044	0.046	0.0228	0.153	1.01520
A1sup	0.017	0.046	0.0546	0.073	1.05484
A2	0.016	0.054	0.0394	0.094	1.75283
C1	0.007	0.021	0.0128	0.056	0.33211
C2	0.067	0.007	0.0166	0.081	2.44849



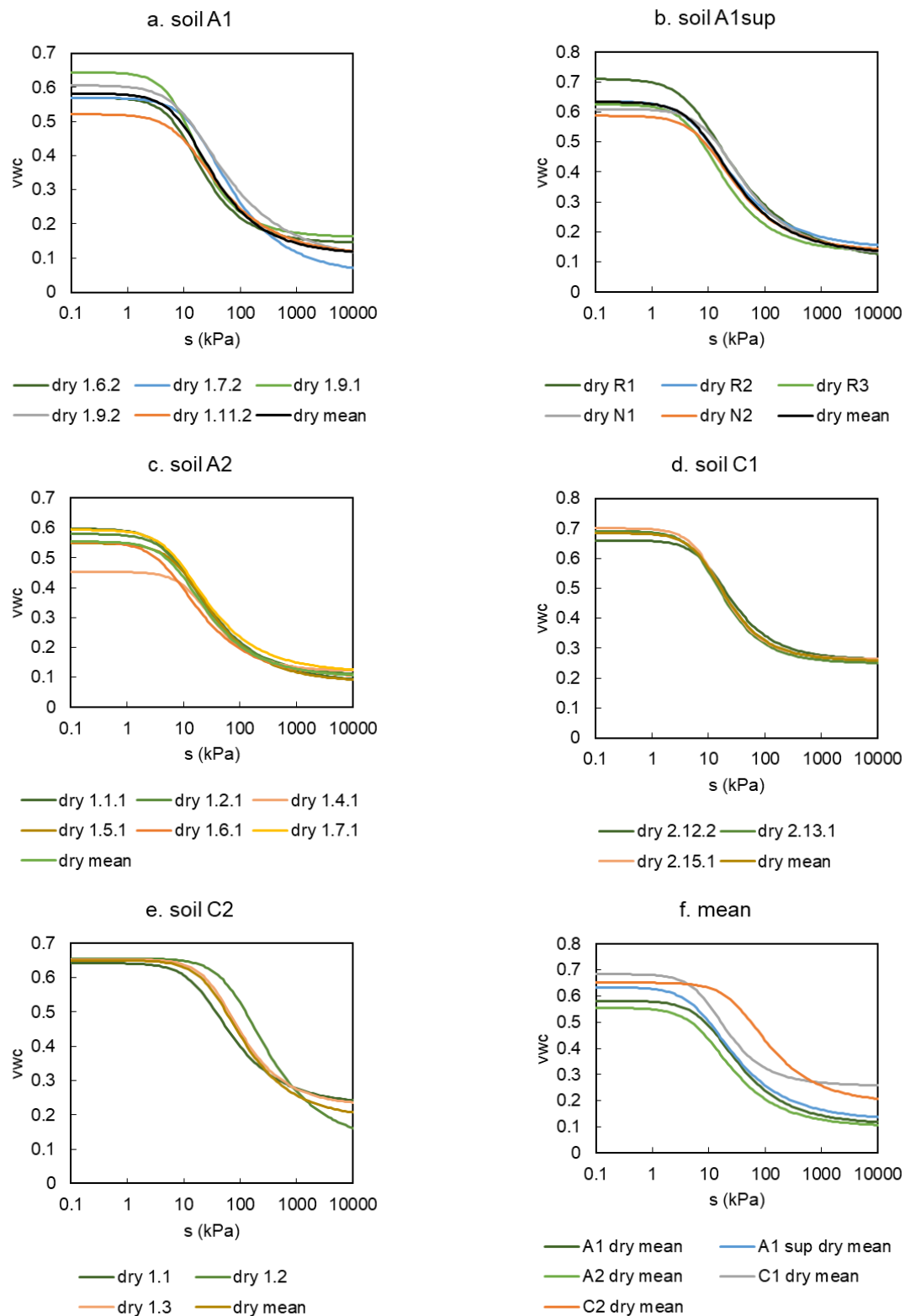


Figure 205 – Main drying WRC of each soil type (a-e) and comparison among their mean (f) obtained from inverse analysis.

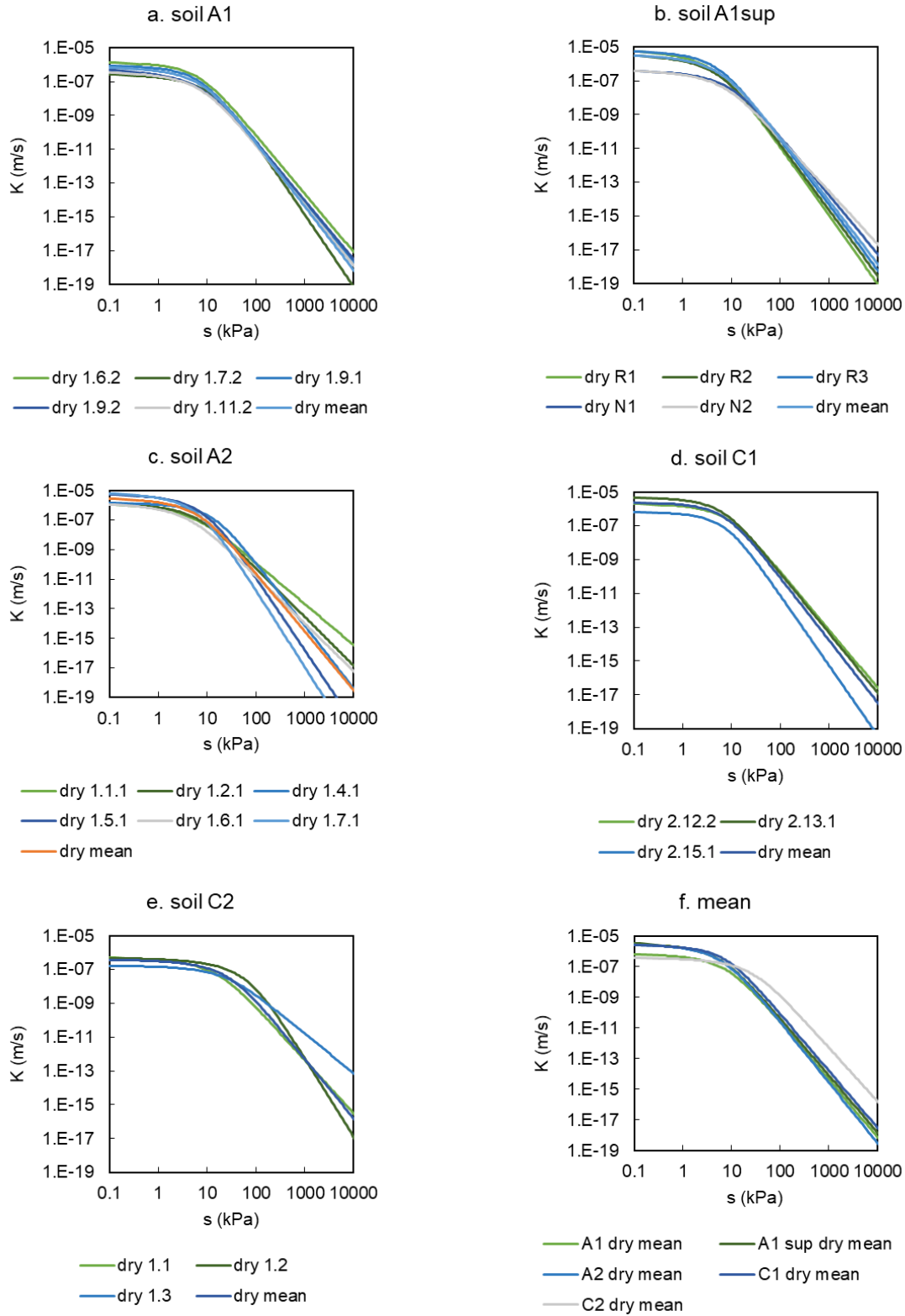


Figure 206 – Main drying HPF of each soil type (a-e) and comparison among their mean (f) obtained from inverse analysis.

## Annex G – Fitting of the main wetting with inverse analysis

Table 50 – Fitted parameters of the main wetting WRC and HPF of each sample and respective  $R^2$ -index of the fitting using data from 1 cycle, as well as the saturated hydraulic conductivity adopted in the model.

soil	sample	WCSwet	AlphaW (kPa <sup>-1</sup> )	K sat w (m s <sup>-1</sup> )	R <sup>2</sup>
A1	1.6.2				
	1.7.2	0.569	0.2114	2.93E-07	0.9875
	1.9.1	0.619	0.2926	3.37E-07	0.9959
	1.9.2	0.520	0.2011	2.02E-08	0.8513
	1.11.2				
A1 sup	R1	0.641	0.2806	4.65E-07	0.9642
	R2	0.596	0.2764	5.23E-07	0.9862
	R3	0.578	0.1812	1.06E-06	0.9908
	N1	0.610	0.2218	4.35E-07	0.9910
	N2	0.587	0.2587	4.35E-07	0.9899
A2	1.1.1				
	1.2.1	0.580	0.2706	1.43E-06	0.9855
	1.4.1	0.441	0.1477	6.06E-07	0.9849
	1.5.1	0.549	0.2195	5.94E-06	0.9635
	1.6.1				
	1.7.1	0.548	0.2146	7.10E-07	0.9909
C1	2.12.2	0.620	0.0802	1.33E-06	0.9835
	2.13.1	0.674	0.1695	1.26E-07	0.9840
	2.15.1				
C2	1.1	0.618	0.0596	1.26E-07	0.9951
	1.2				
	1.3				

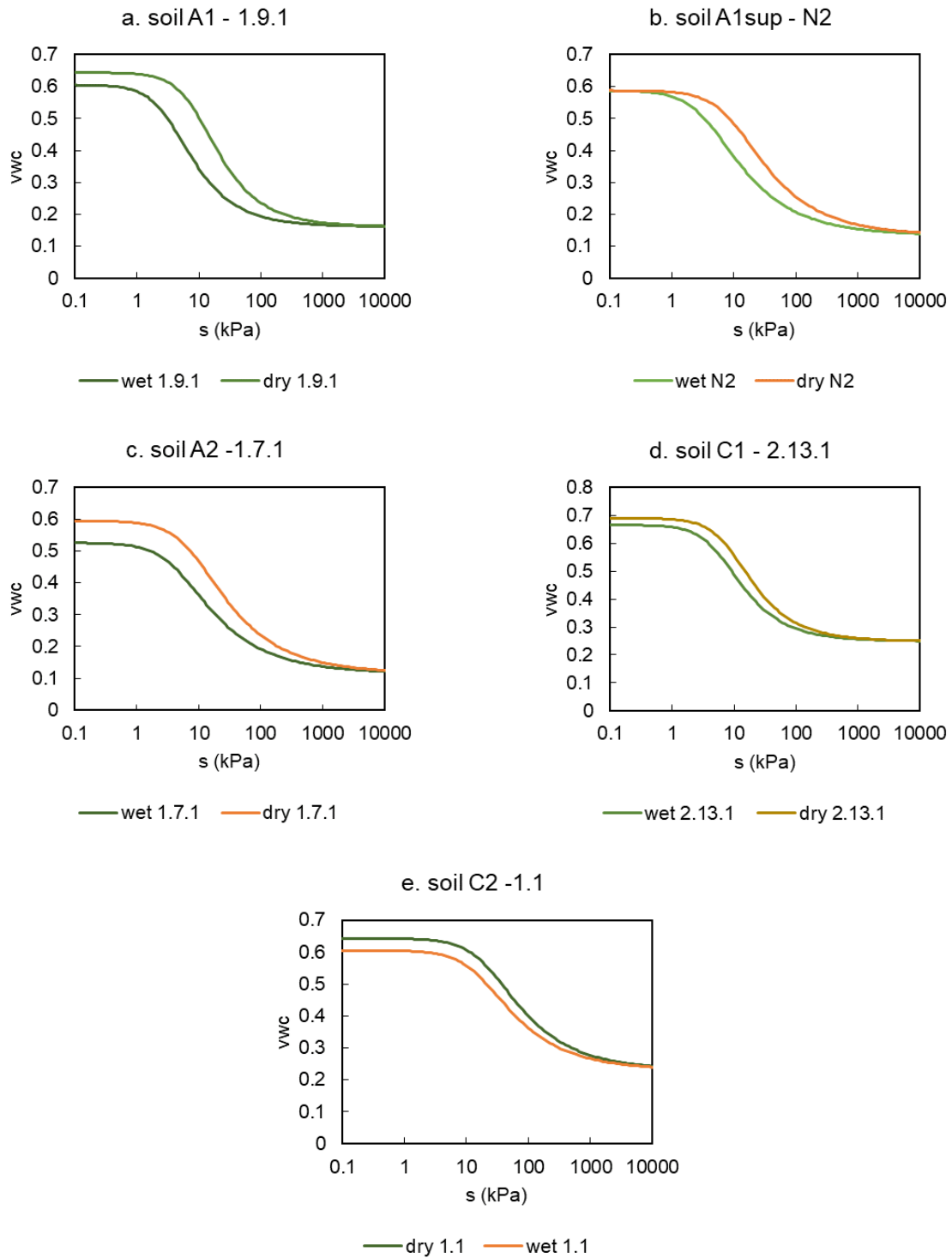


Figure 207 – Examples of main drying-wetting loops of different soil types.

*Table 51 – Mean fitted parameters of the main wetting WRC and HPF of each soil type.*

soil	WCSwet	AlphaW (kPa <sup>-1</sup> )	K sat w (m s <sup>-1</sup> )	log Ksat
A1	0.569	0.235	1.26E-07	6.900
A1 sup	0.603	0.244	5.47E-07	6.262
A2	0.529	0.213	1.38E-06	5.859
C1	0.647	0.125	4.08E-07	6.389
C2	0.618	0.060	1.26E-07	6.901

*Table 52 – Standard deviation of the fitted parameters of the main wetting WRC and HPF of each soil type.*

soil	WCSwet	AlphaW (kPa <sup>-1</sup> )	K sat w (m s <sup>-1</sup> )	log Ksat
A1	0.049	0.050	4.88E+00	0.689
A1 sup	0.025	0.042	1.46E+00	0.165
A2	0.061	0.050	2.83E+00	0.452
C1	0.039	0.063	5.30E+00	0.724
C2				

## Annex H – Sensitivity analysis examples of the main wetting fitting parameters

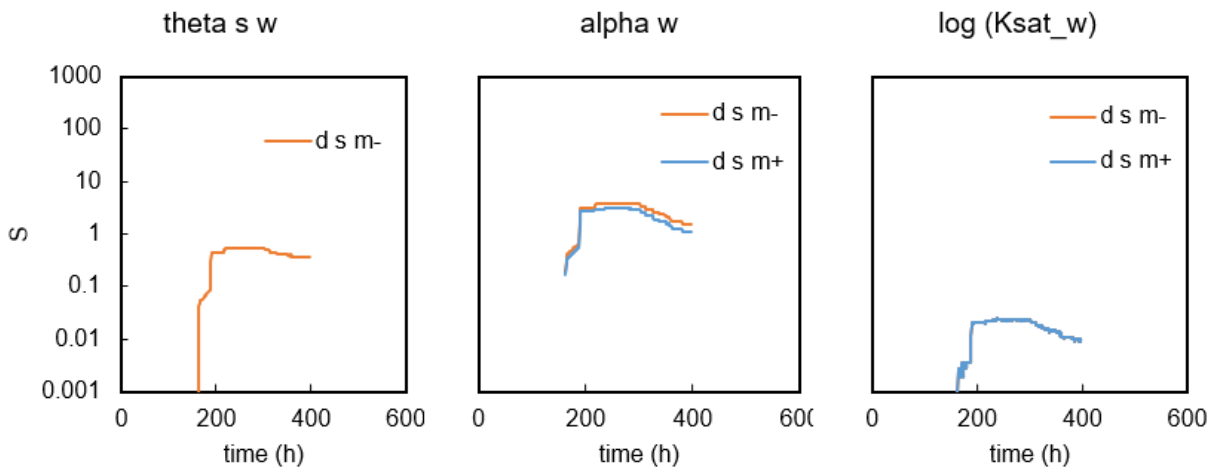


Figure 208 – Sensitivity analysis of the fitting parameters of the main wetting performed on sample N1 (soil A1sup).

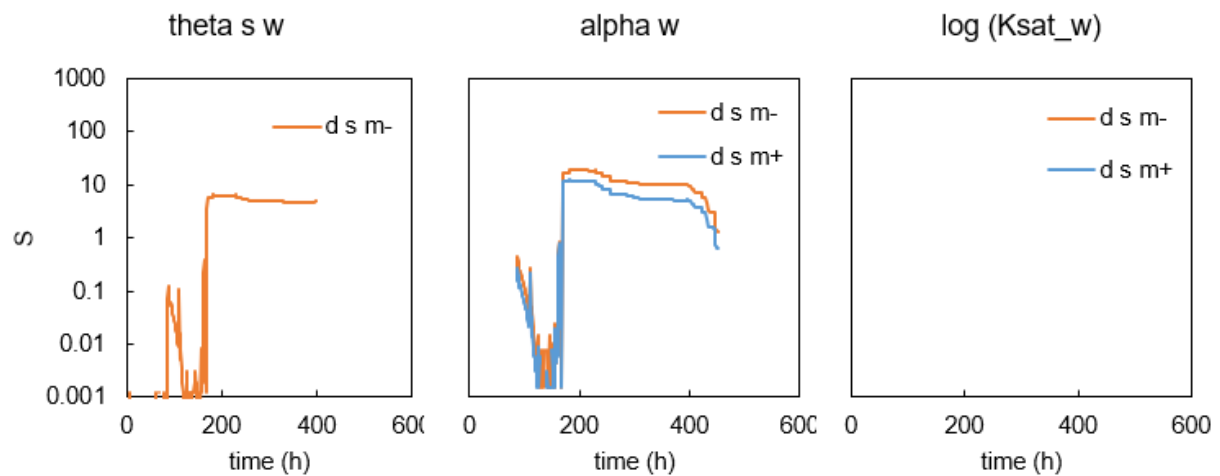


Figure 209 – Sensitivity analysis of the fitting parameters of the main wetting performed on sample 1.4.1 (soil A2).

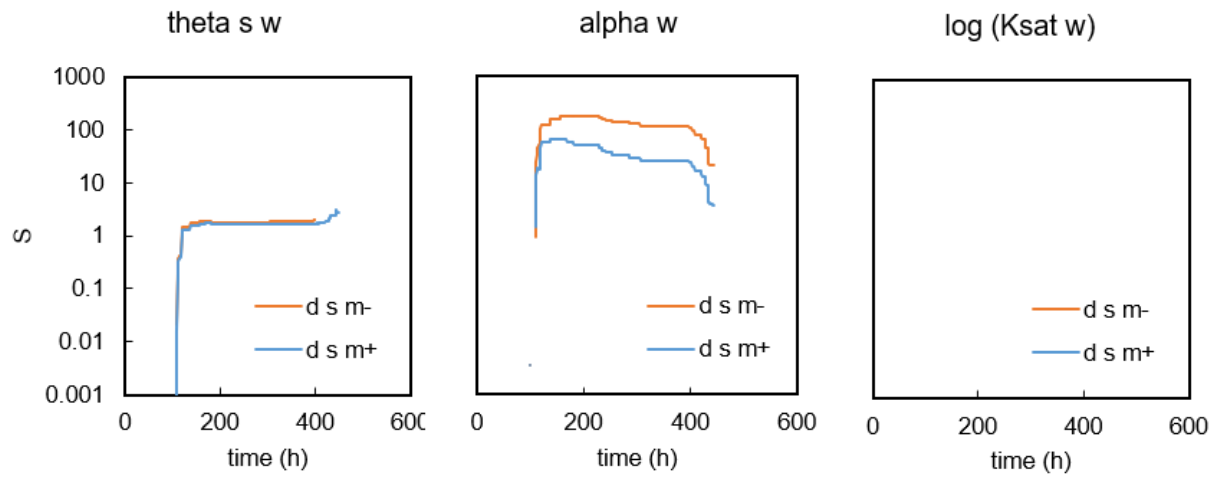


Figure 210 – Sensitivity analysis of the fitting parameters of the main wetting performed on sample 2.12.2 (soil C1).

## Annex I – Examples of simulations using fitting parameters of 1 and 2 cycles

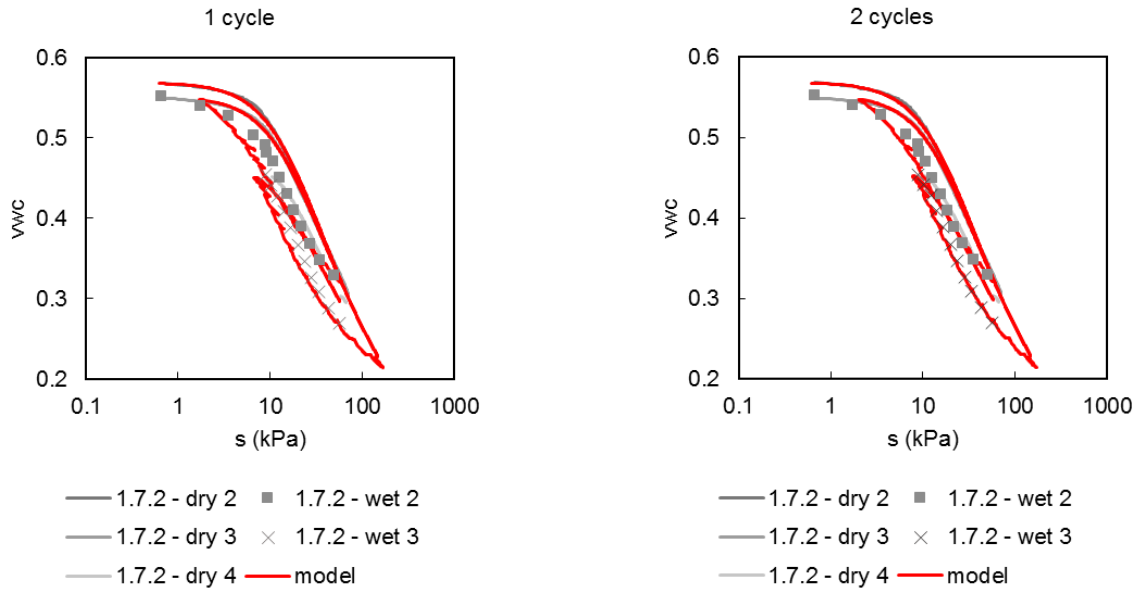


Figure 211 – Simulation of the full test using the fitting parameters from 1 cycle (left side) and 2 cycles (right side) and comparison with the experimental data of sample 1.7.2 (soil A1).

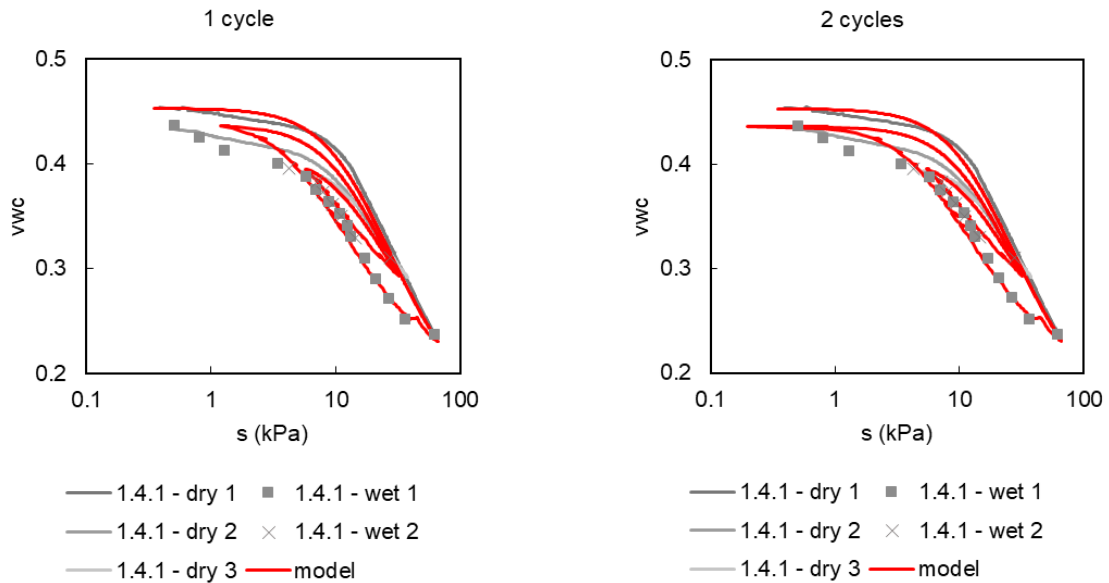


Figure 212 – Simulation of the full test using the fitting parameters from 1 cycle (left side) and 2 cycles (right side) and comparison with the experimental data of sample 1.4.1 (soil A2).



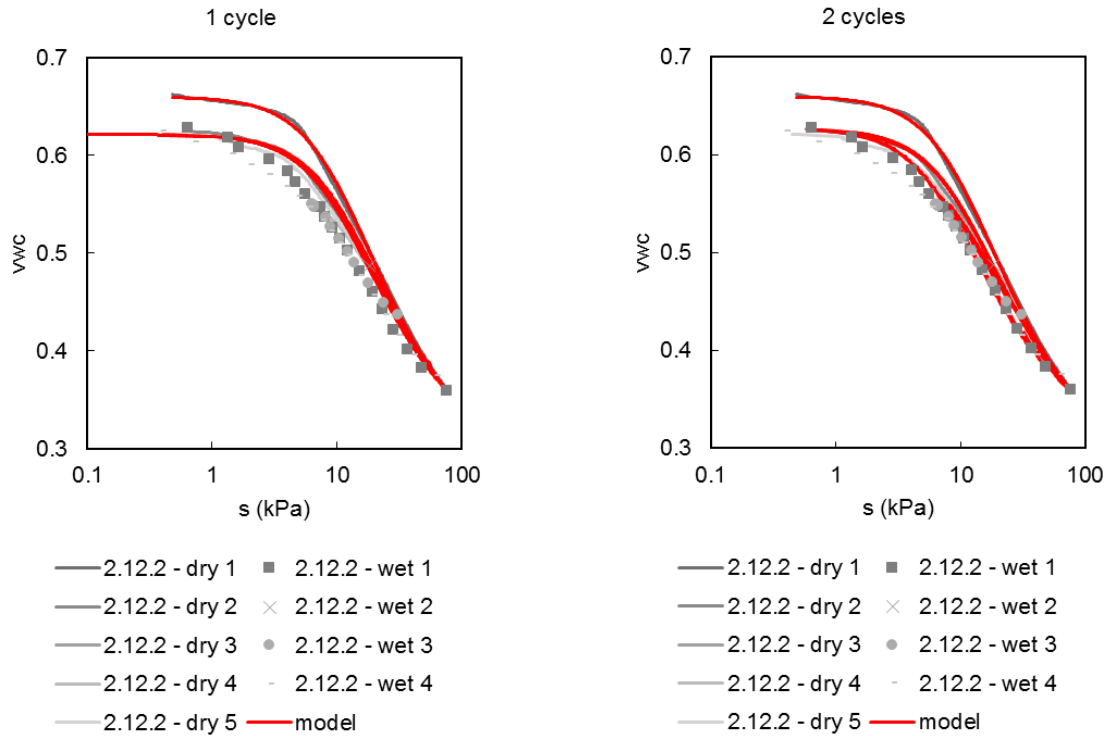


Figure 213 – Simulation of the full test using the fitting parameters from 1 cycle (left side) and 2 cycles (right side) and comparison with the experimental data of sample 2.12.2 (soil C1).

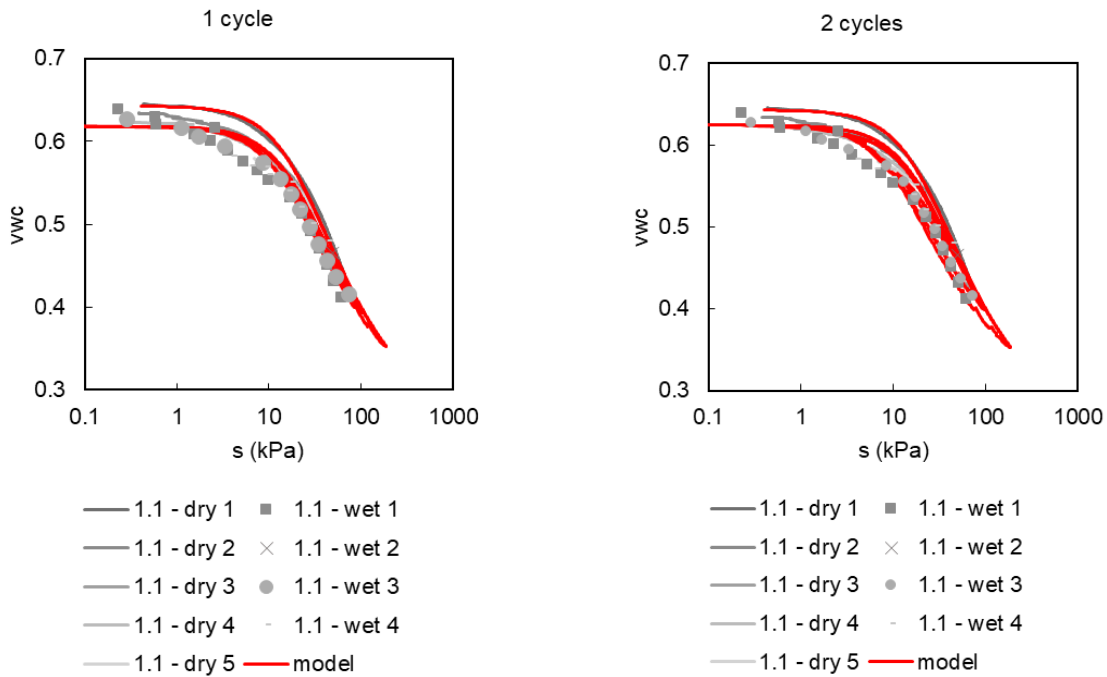


Figure 214 – Simulation of the full test using the fitting parameters from 1 cycle (left side) and 2 cycles (right side) and comparison with the experimental data of sample 1.1 (soil C2).

## Annex J – Examples of simulations used for ku-pf apparatus test replication.

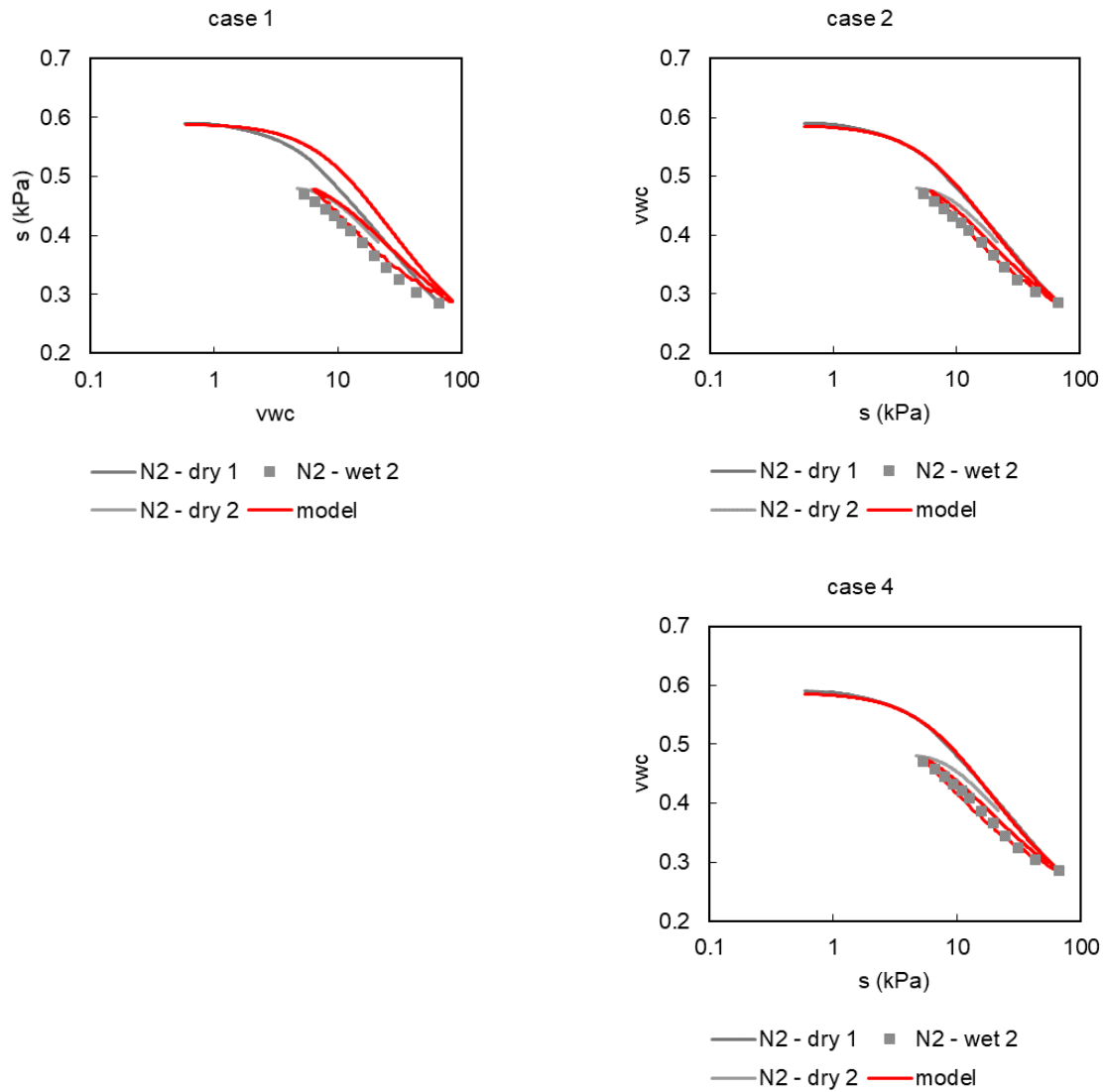


Figure 215 – Simulation of the drying and wetting cycles of sample N2 with the fitting parameters of sample N1 (soil A1sup).

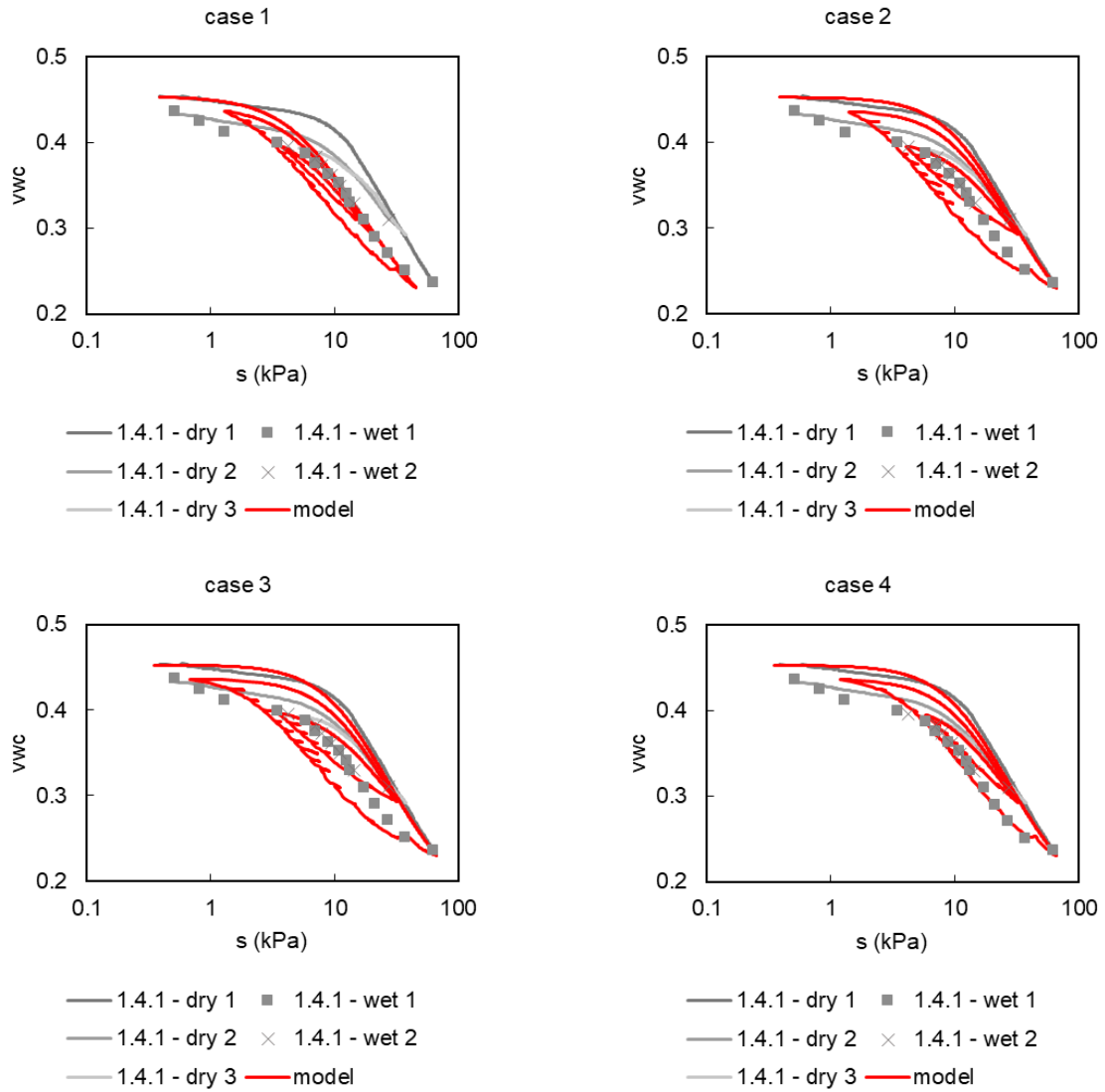


Figure 216 – Simulation of the drying and wetting cycles of sample 1.4.1 with the fitting parameters of sample 1.2.1 (soil A2).

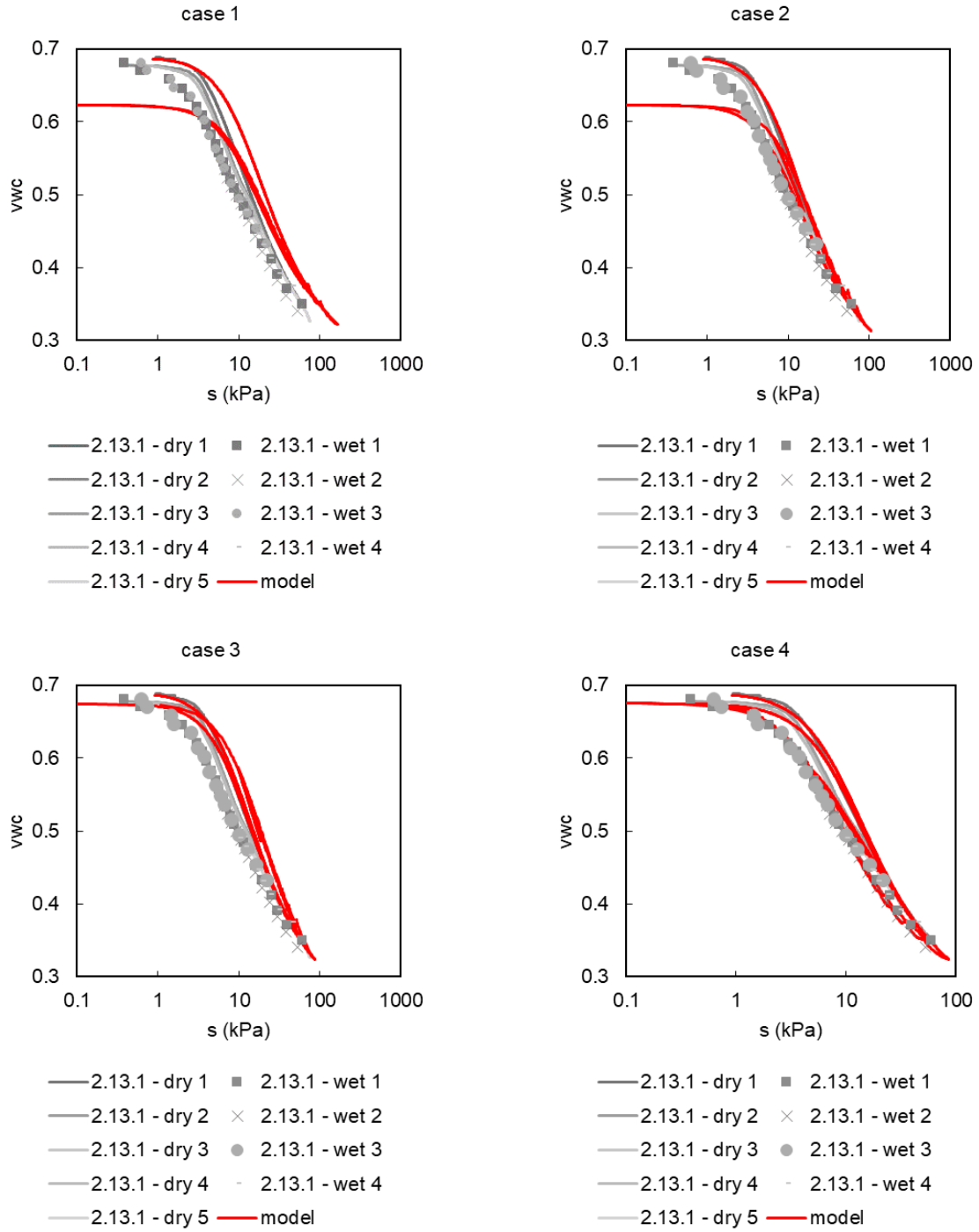


Figure 217 – Simulation of the drying and wetting cycles of sample 2.13.1 with the fitting parameters of sample 2.12.2 (soil C1).

## Annex K – Root dry biomass in the ku-pf samples

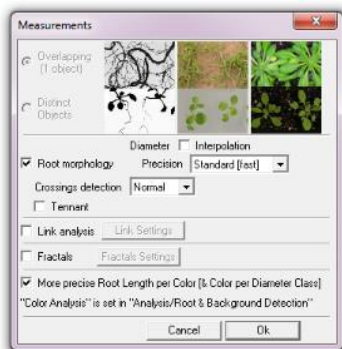
Table 53 – Roots dry biomass collected in the samples tested in the permeameter and/or the ku-pf apparatus.

soil	sample	M dry roots (g)
A1	1.11.1	0.274
A1	1.11.2	0.056
A1	1.6.2	0.065
A1	1.7.2	0.133
A1	1.9.1	1.337
A1	1.9.2	0.627
A1sup	N1	0.484
A1sup	N2	0.340
A1sup	R1	2.471
A1sup	R2	1.176
A1sup	R3	0.962
A1sup	R5	4.630
A1sup	R4	1.840
A2	1.1.1	0.072
A2	1.2.1	0.128
A2	1.4.1	0.052
A2	1.5.1	0.071
A2	1.5.2	0.049
A2	1.6.1	0.098
A2	1.7.1	0.086
C1	1.1	0.064
C1	1.2	0.951
C1	1.3	0.386
C1	2.12.2	0.360
C1	2.13.1	0.077
C1	2.15.1	0.098

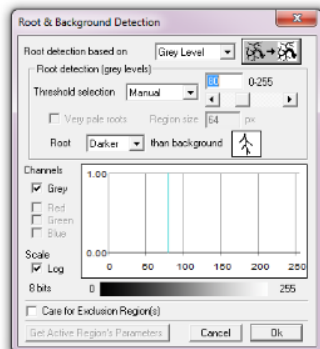
## **Annex L – WinRIZHO analysis procedure**

The steps followed in the image analysis using WinRHIZO are here listed:

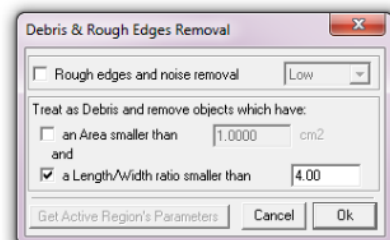
1. The settings of Figure 218(a) were activated on the measurements.
2. The grey levels were adjusted so that the root hairs, which are lighter than the roots, were ignored. The grey level threshold was set to 80 as in Figure 218(b).
3. A filter was activated as in Figure 218 (c) when necessary to avoid considering soil dragged by the roots.
4. The diameter classes were adjusted because there are roots with diameters greater than 4.5mm and creating extra classes provide useful information about the roots with mechanical contribution to the soil reinforcement. Therefore, the classes used in the analysis are presented in Figure 218(d).
5. The image to be analysed was selected from the folder and the analysis is made by clicking in the centre of the image. If the software does not allow the analysis of the full image, then portions can be selected as in Figure 218(e).
6. The software requires the information presented in Figure 218(f) in which the volume  $0\text{m}^2$  used.
7. The results are displayed as in Figure 218(g). The analysis can be repeated in case the adjustment of the grey levels and filters is required.



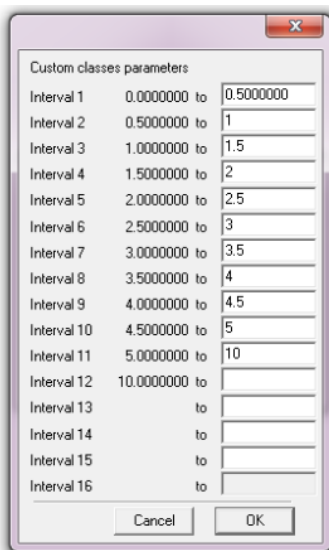
(a)



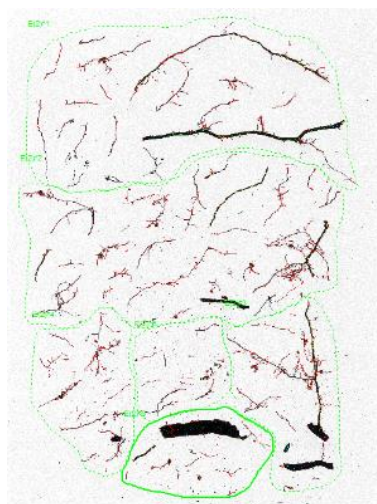
(b)



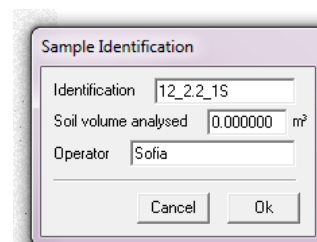
(c)



(d)



(e)



(f)



(g)

Figure 218 – Sequence of steps followed in the image analysis.

## Annex M – Fitting of the vertical root distribution model procedure

The code presented in Box 3 is used for the calibration of the vertical root distribution model. In order to run obtain the fitted parameters, a matrix with the cumulative root density indicator with depth needs to be imported. A vector with the depth of the observation points is also necessary in cm.

*Box 3 – MATLAB code to calculate the beta-value.*

```
betavalue.m
% fit beta-value
% model of Gale & Grigel (1987)

% depth=0;
% roots=0;

% import all the data
% put the depth in cm!
% a vector 'depth' with all the depths of all the verticals
% a matrix 'roots' with the correspondend cumulative root parameter

% Gale & Grigel (1987) model
fun=@(beta, x) 1-beta.^x

% to identify the limits of each verticals
% (when the depth restarts again)
i=1;
ii=i+1;
limits=[];
while ii<length(depth)
    while depth(ii)<=depth(ii+1)
        ii=ii+1;
        if ii==length(depth)
            break;
        end
    end
    limits=[limits; i ii];
    i=ii+1;
    ii=ii+2;
end

% it uses a MATLAB function to fit the parameter 'beta' of the function
% 'fun' using the least-squares method
% the fitting parameter beta goes to the vector 'fbeta'
% it plots the result somehow
fbeta=zeros(length(limits),min(size(roots)));
fr2=zeros(length(limits),min(size(roots)));

for c=1:min(size(roots))

    figure; hold on;
    for i=1:length(limits)

        % fits data
        fbeta(i,c)= lsqcurvefit(fun, 1 ,depth (limits(i,1):limits(i,2))
,roots(limits(i,1):limits(i,2),c));
        plot(roots(limits(i,1):limits(i,2),c), depth(limits(i,1):limits(i,2)),'*'
,fun(fbeta(i,c), depth(limits(i,1):limits(i,2))),depth(limits(i,1):limits(i,2)), '-
');
    end
end
```



```

        % calculates R2-index
        mdl = fitlm(roots(limits(i,1):limits(i,2),c),fun(fbeta(i,c),
depth(limits(i,1):limits(i,2)))));
        fr2(i,c) = mdl.Rsquared.Ordinary;

    end

    set(gca,'Ydir','reverse');
    legend('1C', '1Cm', '1E', '1Em', '1N', '1Nm', '1S', '1Sm', '1W', '1Wm', '2C',
'2Cm', '2E', '2Em', '2N', '2Nm', '2S', '2Sm', '2W', '2Wm');
    xlabel('cum rel trait');
    ylabel('depth (cm)');
    hold off;

end

```

## Annex N – Fitting of the spatial root distribution model procedure

The model of the spatial root distribution is fitted using the code in Box 4 that makes use of the functions presented in Box 5 and Box 6.

The distance considered as a threshold is hard coded in Box 4. This value has to be modified in the code in order to consider different tree-to-vertical distances. The data necessary to run the codes has to be presented in .txt files in the same folder of the m-files. The data for each vertical is distributed in the columns, the data of the tree-to-vertical distance and tree diameter at breast height should be presented as for the determination of the vertical root distribution, the files on the initial estimation of the parameters and limits should have a correspondence to the lines of the root distribution indicator file.

*Box 4 – MATLAB function to calculate the competition index based on Equation 60.*

```
fcompindex.m
function compind = fcompindex (alpha, vertical)

    % import data and create vectors of distance and dbh
    dist=importdata('distance.txt');
    dbh=importdata('dbh.txt');

    compind=[]; compindt=0;

    % run all the trees (27) of the vertical
    for i=1:27
        % if the distance to the point is lower than a threshold
        if dist(i, vertical)>0 && dist(i, vertical) <= 10 % d_max <---
            compindt = compindt+(dbh(i)/dist(i, vertical))^alpha;
        end
    end
    compind=[compind ; compindt];
end
```

*Box 5 – MATLAB function to calculate the estimated root density indicator based on Equation 61.*

```
frootden.m
function rootdensity = frootden (par, v)

    rootdensity=[];
    for i=1:length(v)
        rootdensity = [rootdensity ; par(2).*fcompindex(par(1),i).^par(3)];
    end
end
```

Box 6 – MATLAB script to fit the parameters of Equations 60 and 61 using the least-square method.

```
runmao.m
clear all; clc;
x=importdata('beta.txt');
parame=importdata('pari.txt');
limi=importdata('limit.txt');
results=[];

for titi=1:1:size(x,1)

    beta=x(titi,:);
    lim=limi(titi,:);
    % estimation of the fitting parameters
    par = parame(titi,:);
    lim=limi(titi,:);

    % x vector
    vertical=1:1:length(beta); vertical=vertical';

    % function
    fun = @(x,xdata)frootden(x,xdata);

    % least-square fitting ot the parameter vector 'par'
    xxx=lsqcurvefit(fun,par,vertical,beta, lim(1:3), lim(4:6));

    % R2-index
    mdl = fitlm(beta, fun(xxx, vertical));
    r2 = mdl.Rsquared.Ordinary;

    results=[ results; xxx r2];

end
```

## Annex O – Tree survey: DBH and tree-to-vertical distance

Table 54 – Diameter at breast height (DBH) and tree to profile distance.

		distance to profile											
	cell	1					2					extra	
Tree	DBH (m)	N	C	S	E	W	N	C	S	E	W	T	NT
1	0.78	10.3	11.9	13.5	13.2	10.7							15.0
2	0.57	9.9	12.3	14.5	12.1	12.8							
3	0.75	8.8	10.9	12.9	9.1	13.0	13.8						
4	0.62	15.3			14.2		13.5						
5	0.76	4.4	6.1	7.9	7.3	5.4						10.8	17.5
6	0.46	4.0	5.7	7.6	3.8	8.0	10.6	13.2		15.0	12.4	11.5	
7	0.22	5.6	4.7	5.1	2.7	7.4	6.4	8.3	10.9	10.5	7.2	8.2	
8	0.13	9.4	9.5	10.1	7.0	12.3	4.9	8.3	11.5	9.2	9.0	13.1	
9	0.45						11.9	13.8		11.7			
10	0.05	14.7	13.6	12.9		10.8						11.3	9.9
11	0.07	12.4	10.9	9.9	13.5	8.3						7.9	12.5
12	0.35	9.1	6.7	4.6	8.5	6.0	12.7	12.0	12.4	14.8	9.0	0.7	19.9
13	0.29	7.9	5.9	4.7	5.4	7.8	6.5	6.6	8.3	9.3	4.3	5.9	
14	0.20	10.3	7.9	6.0	8.4	8.8	8.9	7.5	7.9	10.3	4.5	4.5	
15	0.28			15.3			9.5	6.0	2.9	6.1	6.6	14.3	
16	0.25						10.2	8.1	6.9	5.9	10.5		
17	0.14		15.1	12.9		15.0	15.1	12.3	10.3	14.3	9.9	9.6	
18	0.83							12.8	9.8	12.0	13.5		
19	0.70						15.5			13.7			
20	0.64									17.2			
21	0.51							15.5	15.3	12.8			
22	0.13												13.7
23	0.03												9.3
24	0.09												10.9
25	0.08												8.9
26	0.80												10.9
27	0.80												12.0
min		3.99	4.7	4.6	2.7	5.44	4.85	6	2.87	5.91	4.34	0.68	8.9

Table 55 – Tree position relatively to a profile (1 – uphill, 2 – downhill).

cell	1					2					extra	
Tree	N	C	S	E	W	N	C	S	E	W	T	NT
1	1	1	1	1	1							1
2	1	1	1	1	1							
3	1	1	1	1	1			1				
4		1	1					1				
5	1	1	1	1	1						1	1
6	1	1	1	1	1	1	1	1		1	1	
7	2	2	2	1	1	1	1	1	1	1	1	
8	1	1	1	1	1	1	1	1	1	1	1	
9						1	1	1				
10	2		2	2	2						1	2
11	2	2	2	2	2						2	2
12	2	2	2	2	2	2	2	2	1	2	2	2
13	2	2	2	2	2	1	1	2	1	1	1	
14	2	2	2	2	2	2	2	2	1	2	2	
15				2		2	2	2	2	2	2	
16						2	2	2	2	2		
17	2			2	2	2	2	2	2	2	2	
18						2	2		2	2		
19							1	1				
20							1					
21						2	2		1			
22												2
23												2
24												2
25												2
26												1
27												1

Annex P – Root vertical distribution raw characterization

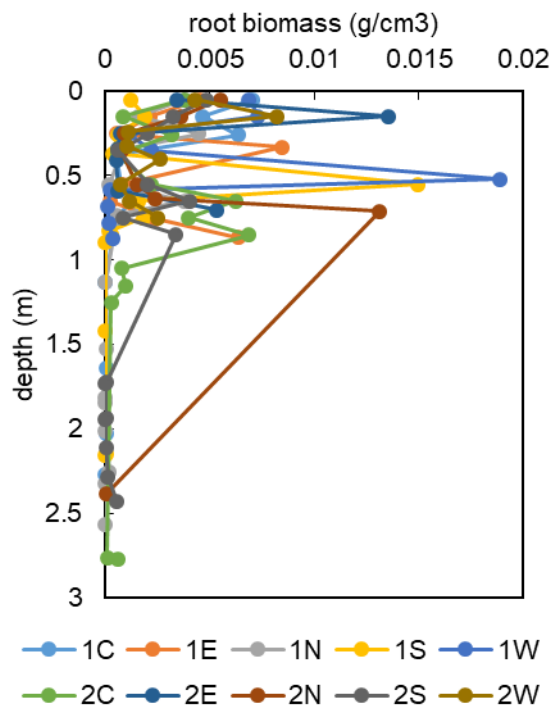


Figure 219 – Root density in terms of root dry biomass per unit volume of soil with depth.

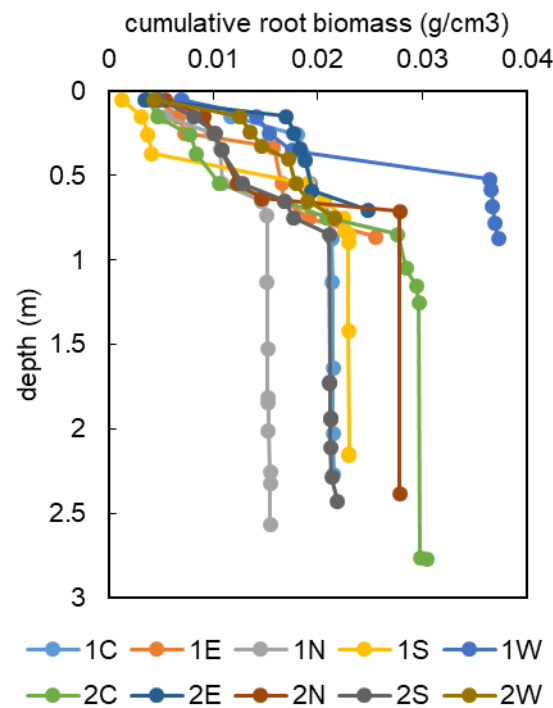


Figure 220 – Cumulative root density in terms of root dry biomass per unit volume of soil with depth.

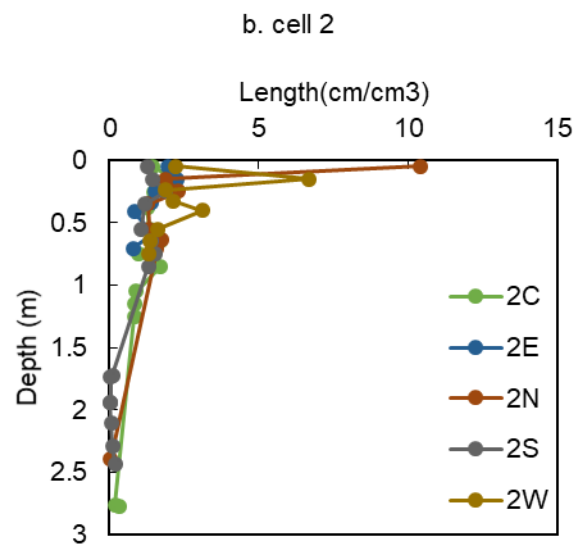
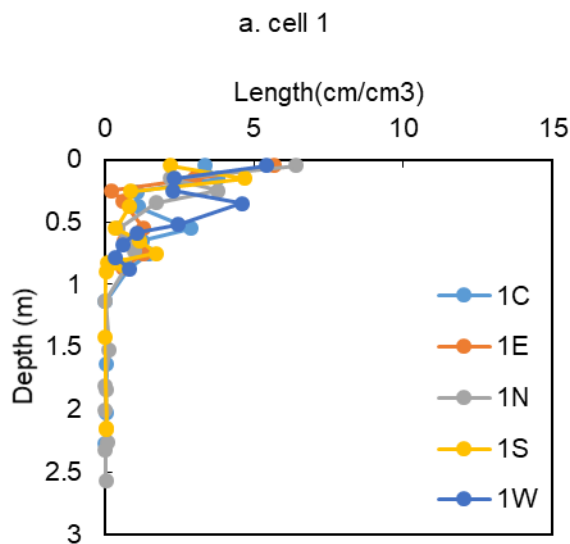


Figure 221 – Total root length per unit soil volume with depth in cell 1 (a) and cell 2 (b).

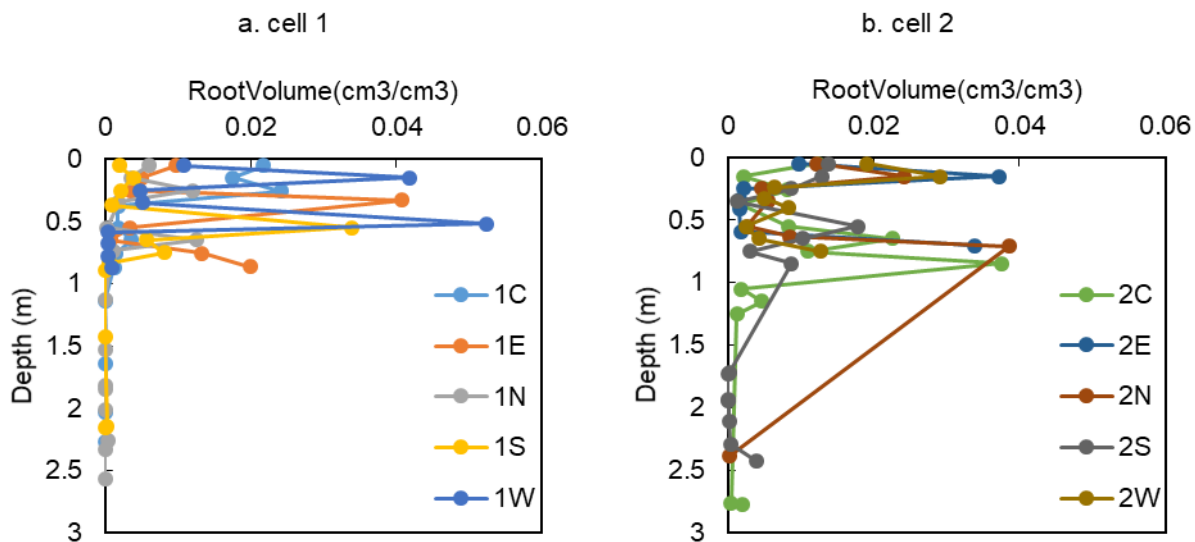


Figure 222 – Total root volume per unit soil volume with depth in cell 1 (a) and cell 2 (b).

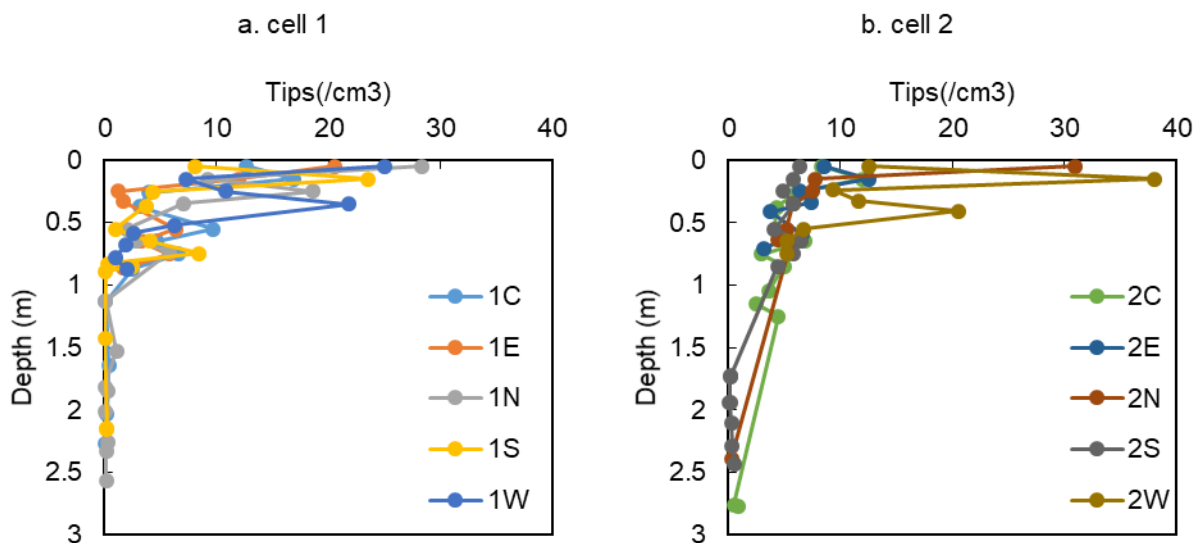


Figure 223 – Total number of root tips per unit soil volume with depth in cell 1 (a) and cell 2 (b).

## Annex Q – Vertical root distribution model fitting

Table 56 –  $\beta$ -value from the calibration of the exponential model ( $D$  stands for root diameter in mm).

2W	2S	2N	2E	2C	1W	1S	1N	1E	1C	vertical	cum				rel cum length				rel cum volume				rel cum tips																																																																																																																																																																																																																																																																																																																																																																																																																																																																																																																																																																																																																																																																																																																																																																																																																																																																																																																																																																																																																																																																																																																																																																																																																																																																																																																																													
											biomass (g cm <sup>-3</sup> )	Length (cm/cm3)	volume (cm <sup>3</sup> cm <sup>-3</sup> )	tips(cm <sup>-3</sup> )	D<0.5	0.5<D<2.0	2.0<D<4.5	D>4.5	D<0.5	0.5<D<2.0	2.0<D<4.5	D>4.5	D<0.5	0.5<D<2.0	2.0<D<4.5	D>4.5																																																																																																																																																																																																																																																																																																																																																																																																																																																																																																																																																																																																																																																																																																																																																																																																																																																																																																																																																																																																																																																																																																																																																																																																																																																																																																																																										
0.9599	0.9756	0.9828	0.9551	0.9850	0.9677	0.9780	0.9648	0.9793	0.9413																																																																																																																																																																																																																																																																																																																																																																																																																																																																																																																																																																																																																																																																																																																																																																																																																																																																																																																																																																																																																																																																																																																																																																																																																																																																																																																																																											</



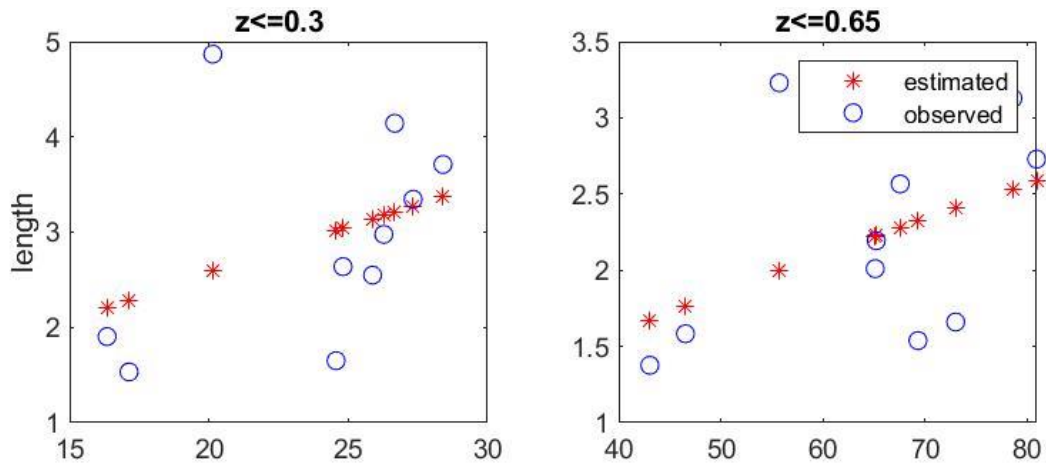
Table 57 –  $R^2$ -index relative to the fitting of the  $\beta$ -value ( $D$  stands for root diameter in mm).

	cum				rel cum length				rel cum volume				rel cum tips			
2W	2S	2N	2E	2C	1W	1S	1N	1E	1C	vertical						
0.95	0.90	0.62	0.84	0.80	0.88	0.87	0.91	0.87	0.97	biomass (g cm <sup>-3</sup> )						
0.84	0.98	0.89	0.86	0.95	0.95	0.82	0.94	0.91	0.93	Length (cm cm <sup>-3</sup> )						
0.82	0.97	0.68	0.73	0.80	0.86	0.58	0.93	0.95	0.86	volume (cm <sup>3</sup> cm <sup>-3</sup> )						
0.88	0.95	0.88	0.84	0.95	0.95	0.83	0.95	0.89	0.96	tips(cm <sup>-3</sup> )						
0.99	0.95	0.85	0.98	0.96	0.96	0.92	0.95	0.87	0.95	D<0.5						
0.97	0.92	0.89	0.98	0.89	0.95	0.91	0.98	0.91	0.97	0.5<D<2.0						
0.95	0.92	0.88	0.96	0.69	0.98	0.85	0.86	0.87	0.82	2.0<D<4.5						
0.95	0.93	0.82	0.79	0.81	0.83	0.84	0.63	0.89	0.96	D>4.5						
0.99	0.97	0.82	0.99	0.96	0.97	0.91	0.95	0.88	0.95	D<0.5						
0.98	0.93	0.90	0.95	0.89	0.94	0.92	0.98	0.87	0.97	0.5<D<2.0						
0.95	0.92	0.86	0.97	0.67	0.98	0.87	0.85	0.87	0.84	2.0<D<4.5						
0.67	0.92	0.61	0.66	0.70	0.90	0.83	0.58	0.86	0.94	D>4.5						
0.98	0.94	0.91	0.99	0.96	0.94	0.91	0.95	0.89	0.94	D<0.5						
0.97	0.94	0.88	0.98	0.94	0.95	0.94	0.98	0.93	0.96	0.5<D<2.0						
0.97	0.95	0.86	0.96	0.88	0.88	0.85	0.55	0.93	0.66	2.0<D<4.5						
0.75	0.95	0.94	0.62	0.60	0.83	0.80	0.79	0.84	0.89	D>4.5						

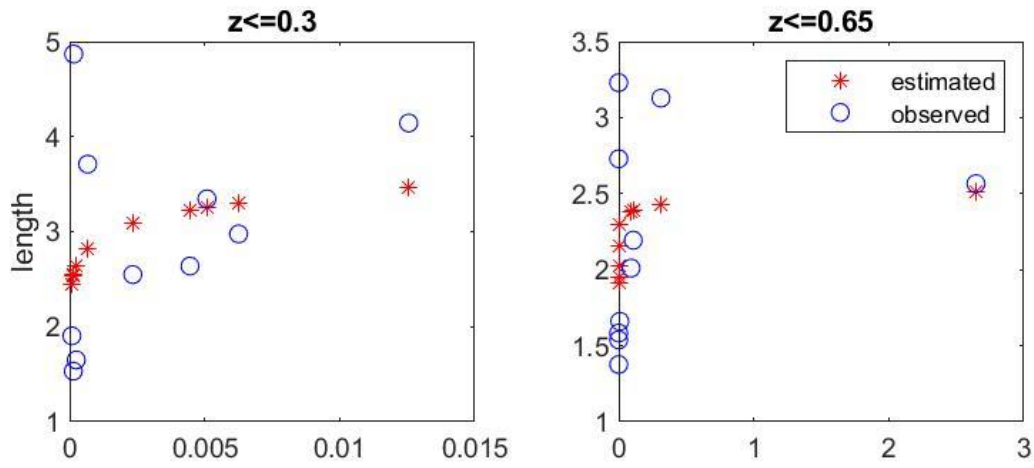
## Annex R – Root lateral distribution model fitting

Table 58 – Observed root density indicators (*D* stands for root diameter in mm).

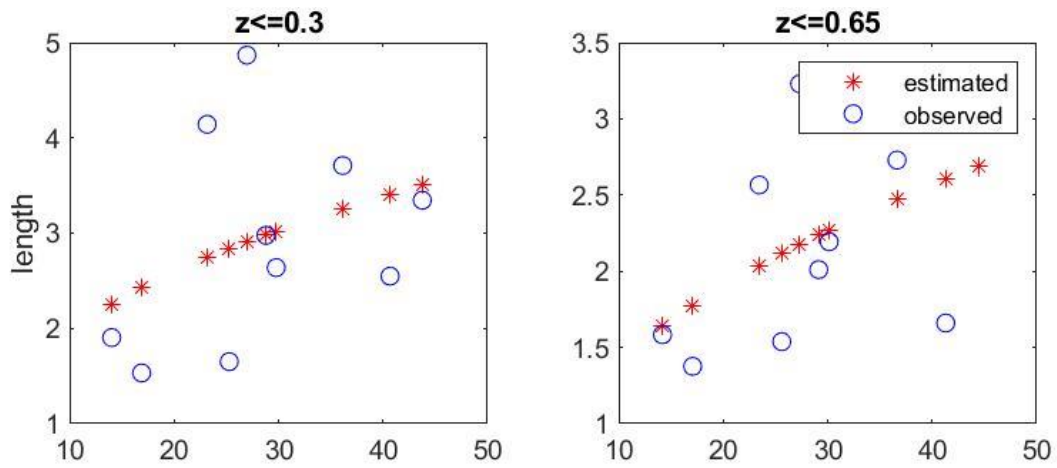
vertical	beta				tips D<0.5		length		biomass
	biomass	length	volume	tips D<0.5mm	0.15<=z<=0.3	0.45<=z<=0.65	z<=0.3	z<=0.65	0.25<=z<=0.5
1C	0.9413	0.9807	0.9778	0.9792	9.7154	7.0390	2.6381	2.1937	0.0035
1E	0.9793	0.9807	0.9823	0.9822	6.4052	4.7366	2.9763	2.0104	0.0035
1N	0.9648	0.9753	0.9737	0.9709	13.7148	2.3723	4.1430	2.5661	0.0027
1S	0.9780	0.9858	0.9892	0.9849	13.3460	2.4624	2.5484	1.6601	0.0005
1W	0.9677	0.9773	0.9801	0.9774	8.8416	3.6653	3.3452	3.1282	0.0017
2C	0.9850	0.9765	0.9822	0.9775	8.6189	5.3942	1.6505	1.5381	0.0019
2E	0.9551	0.9752	0.9836	0.9721	9.2913	6.4707	1.9034	1.5834	0.0006
2N	0.9828	0.9681	0.9835	0.9694	7.4382	4.7233	4.8687	3.2298	0.0009
2S	0.9756	0.9717	0.9760	0.9657	5.1699	5.1793	1.5323	1.3761	0.0013
2W	0.9599	0.9856	0.9834	0.9843	24.8561	5.7704	3.7103	2.7292	0.0017
T									0.0020
NT									0.0004



(a)  $d = 10$  m, all trees

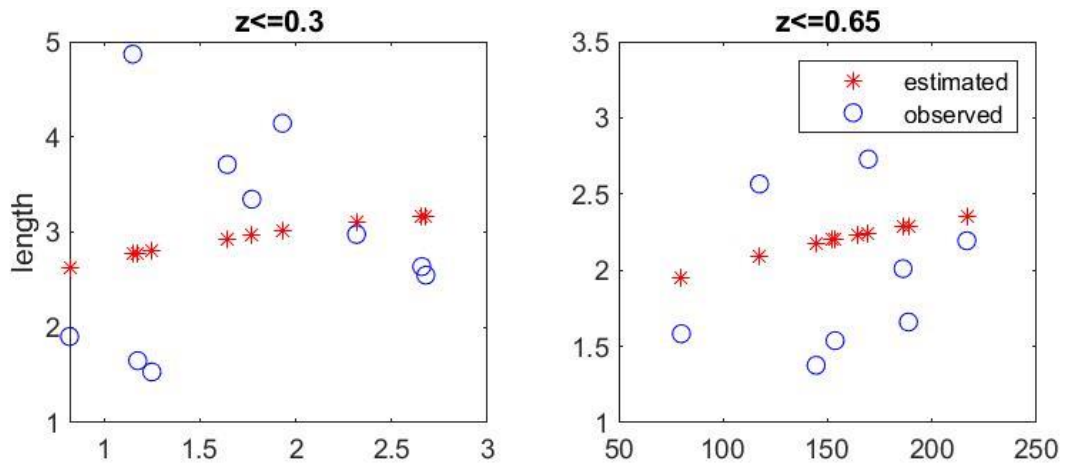


(b)  $d = 10$  m, uphill

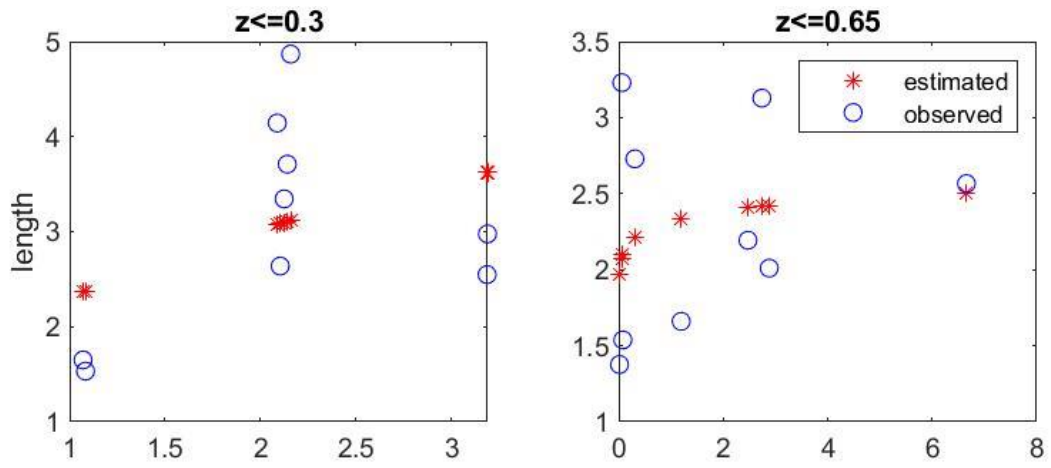


(c)  $d = 10$  m, downhill

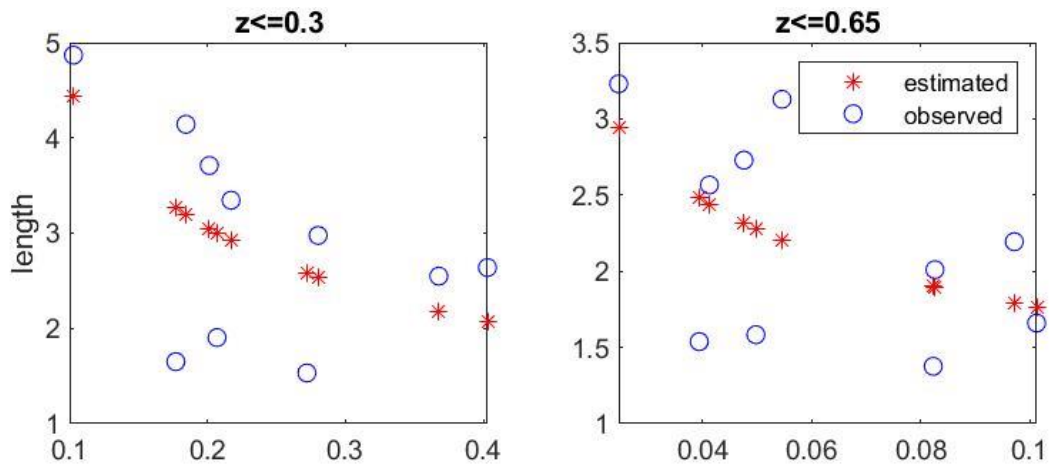
Figure 224 – Estimation of root length for verticals with different competition indexes ( $d_{\max} = 10$  m).



(a)  $d = 8$  m, all trees



(b)  $d = 8$  m, uphill



(c)  $d = 8$  m, downhill

Figure 225 – Estimation of root length for verticals with different competition indexes ( $d_{max} = 8$  m).

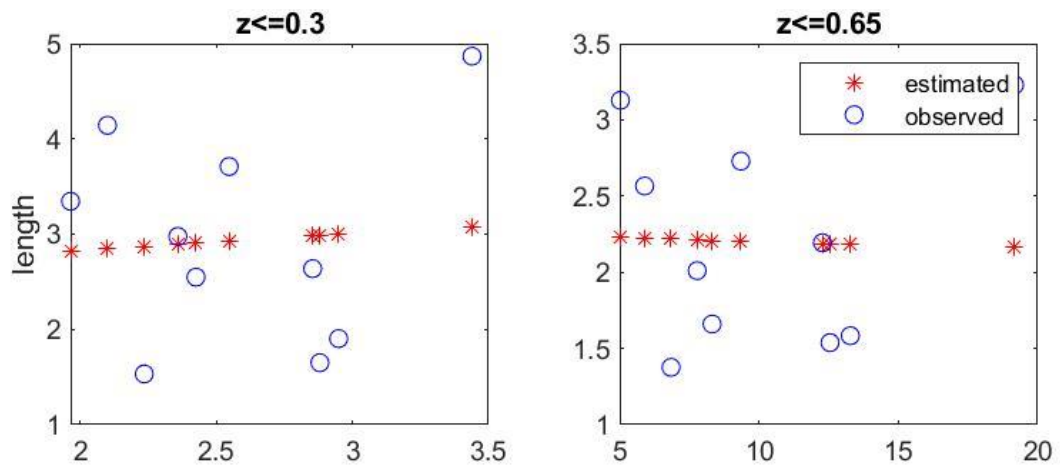
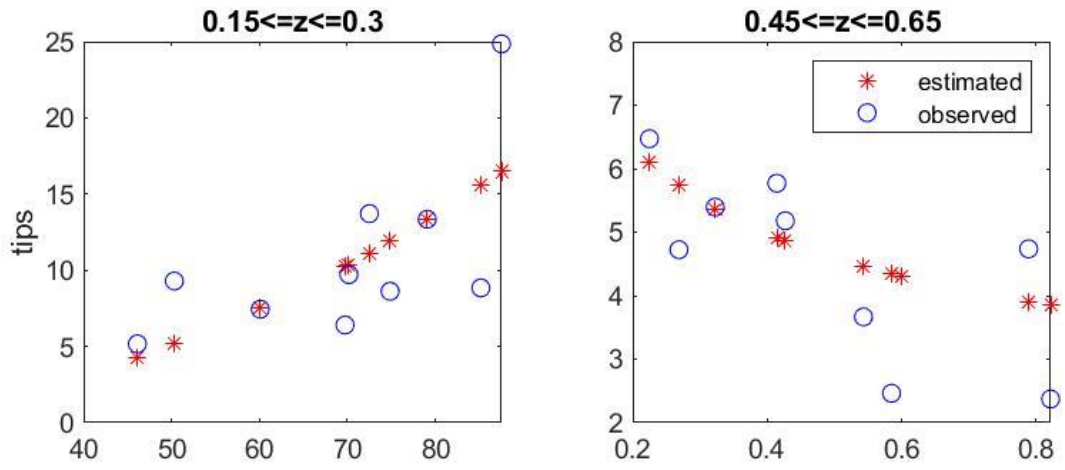
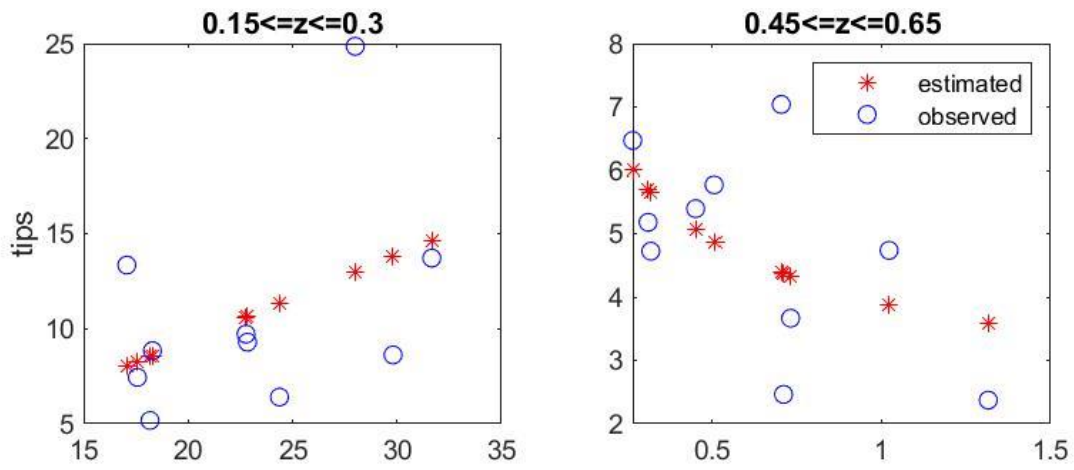


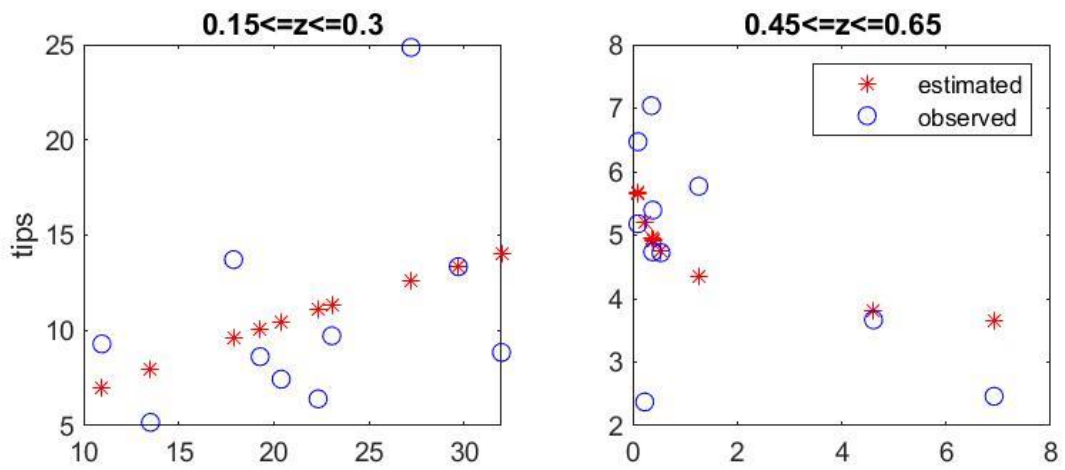
Figure 226 –Estimation of root length for verticals with different competition indexes ( $d_{min}$  ).



(a)  $d = 10$  m, all trees

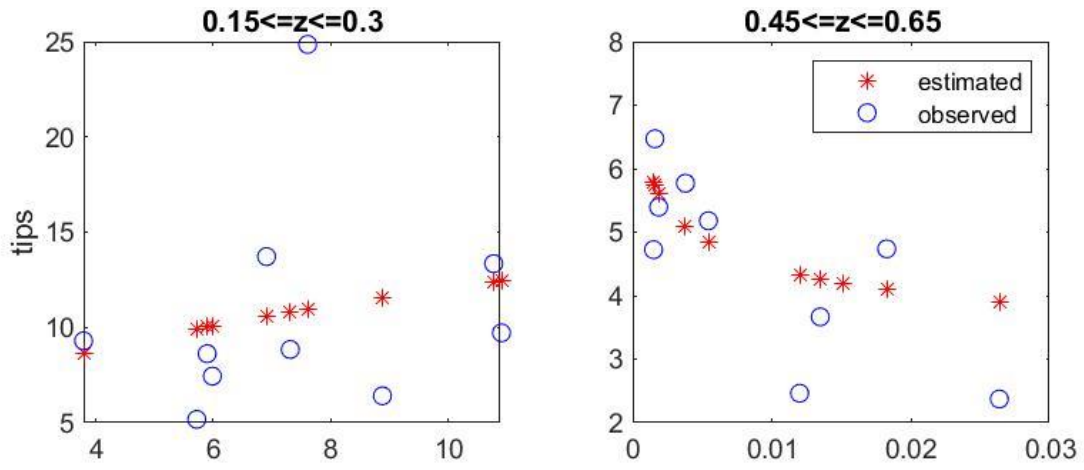


(b)  $d = 10$  m, uphill

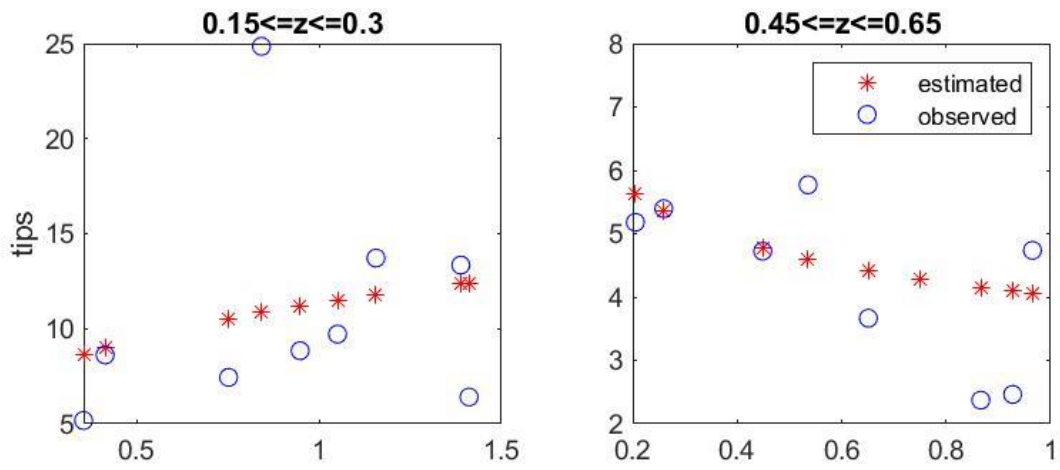


(c)  $d = 10$  m, downhill

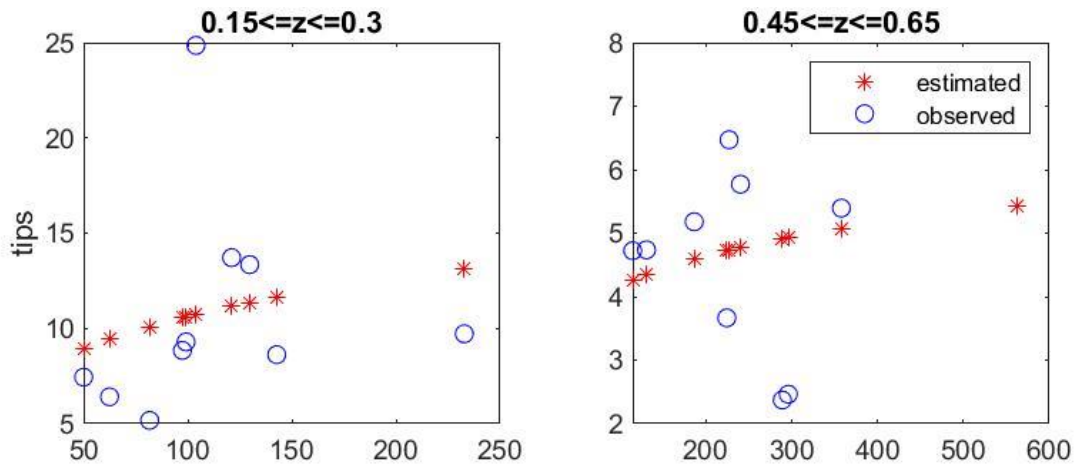
Figure 227 – Estimation of number of root tips for verticals with different competition indexes ( $d_{max} = 10$  m).



(d) d = 8 m, all trees



(e) d = 8 m, uphill



(f) d = 8 m, downhill

Figure 228 – Estimation of number of root tips for verticals with different competition indexes ( $d_{max} = 8$  m).

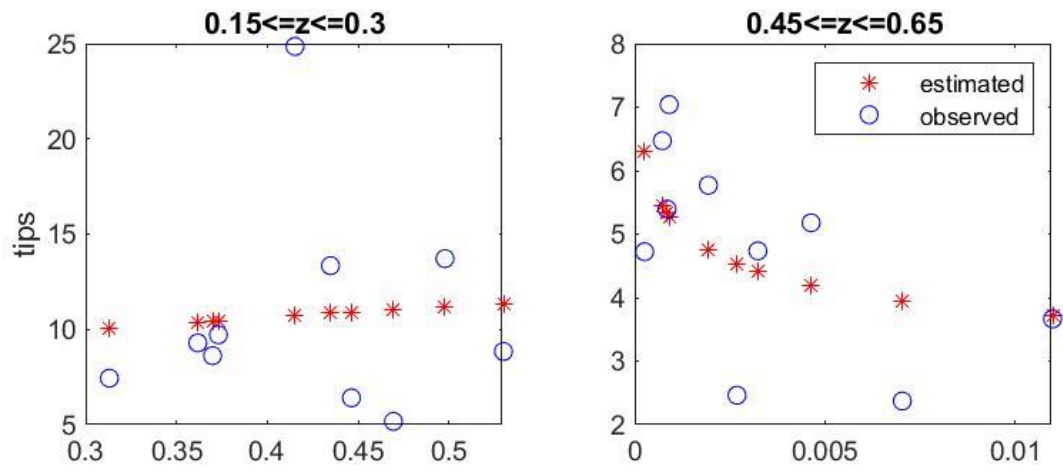


Figure 229 – Estimation of number of root tips for verticals with different competition indexes ( $d_{min}$ ).



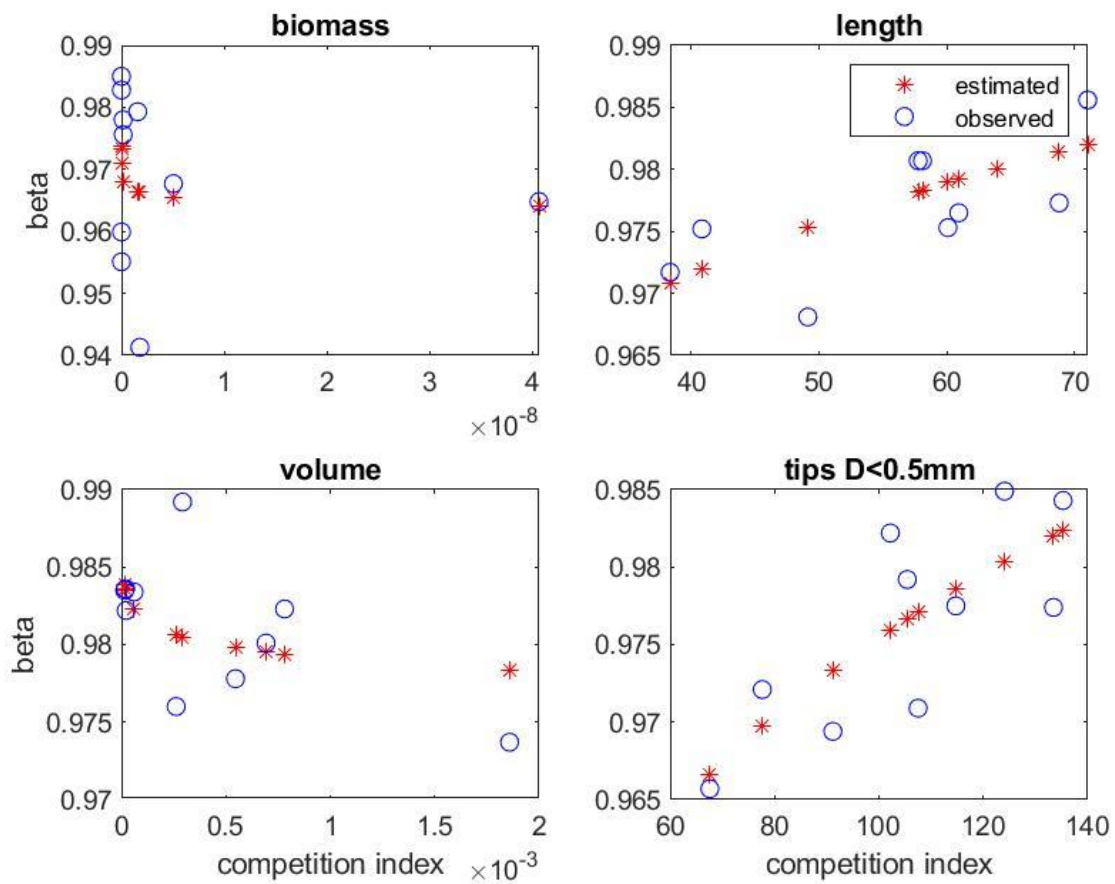


Figure 230 – Estimation of beta-values for verticals with different competition indexes ( $d = 10$  m, all trees)

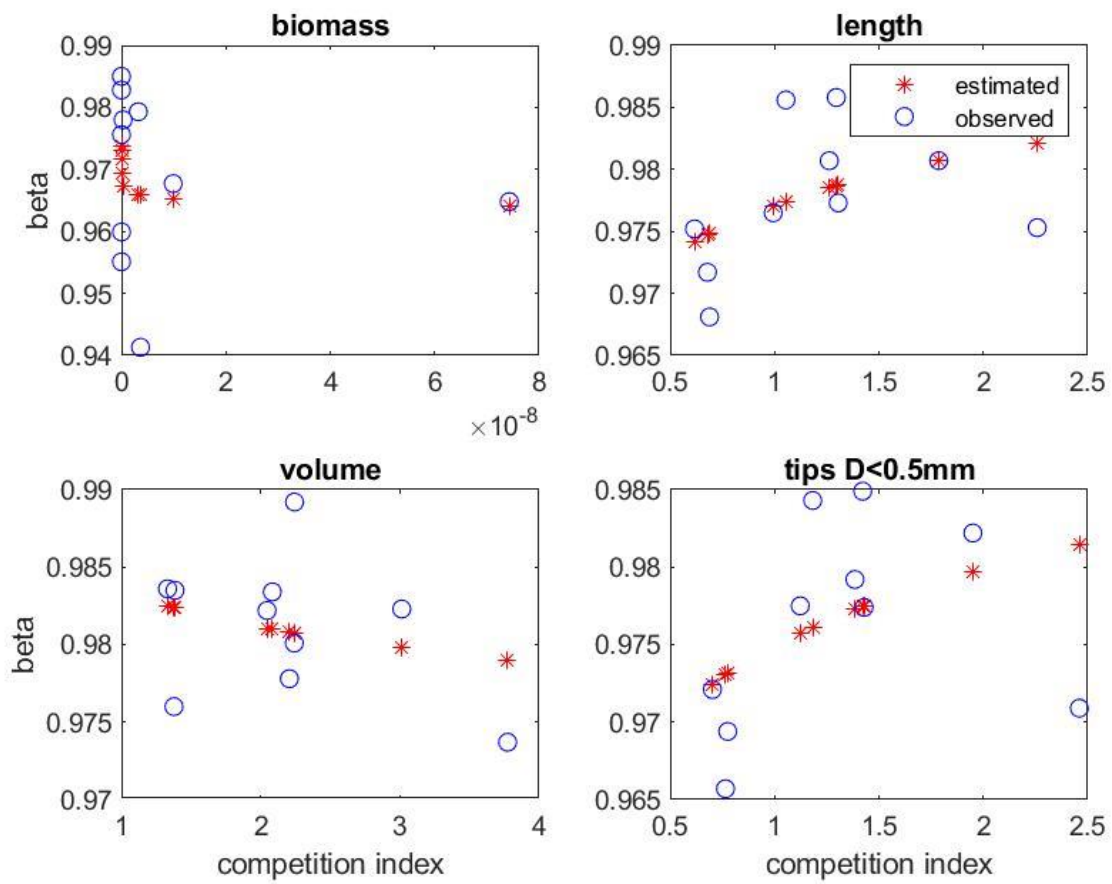


Figure 231 – Estimation of beta-values for verticals with different competition indexes ( $d = 10$  m, uphill)

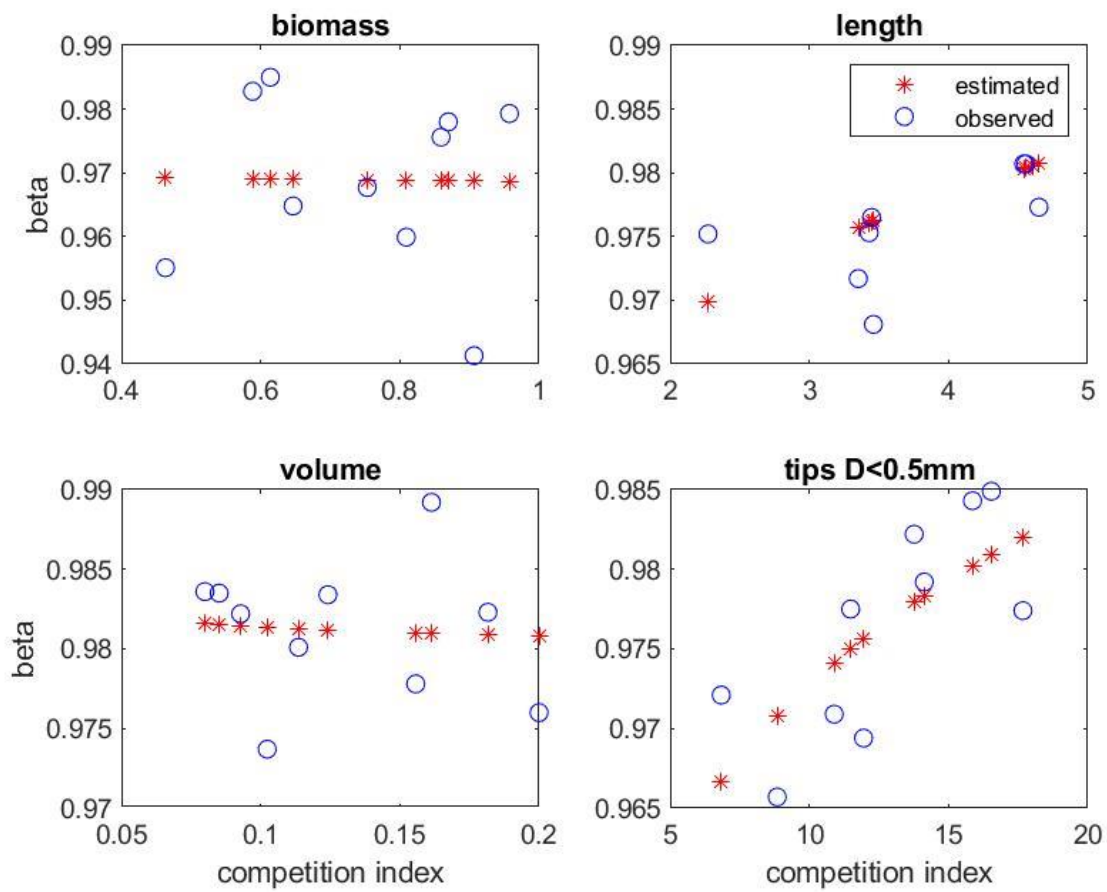


Figure 232 – Estimation of beta-values for verticals with different competition indexes ( $d = 10$  m, downhill)

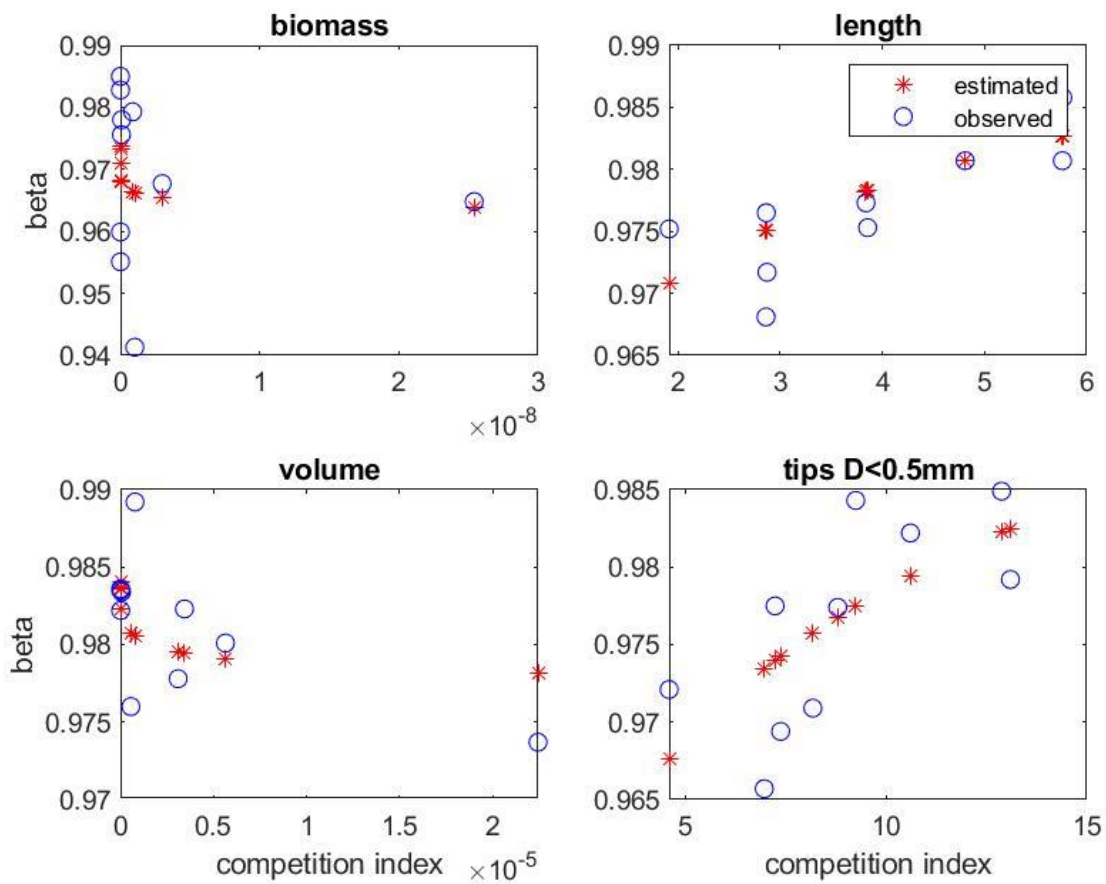


Figure 233 – Estimation of beta-values for verticals with different competition indexes ( $d = 8$  m, all trees).

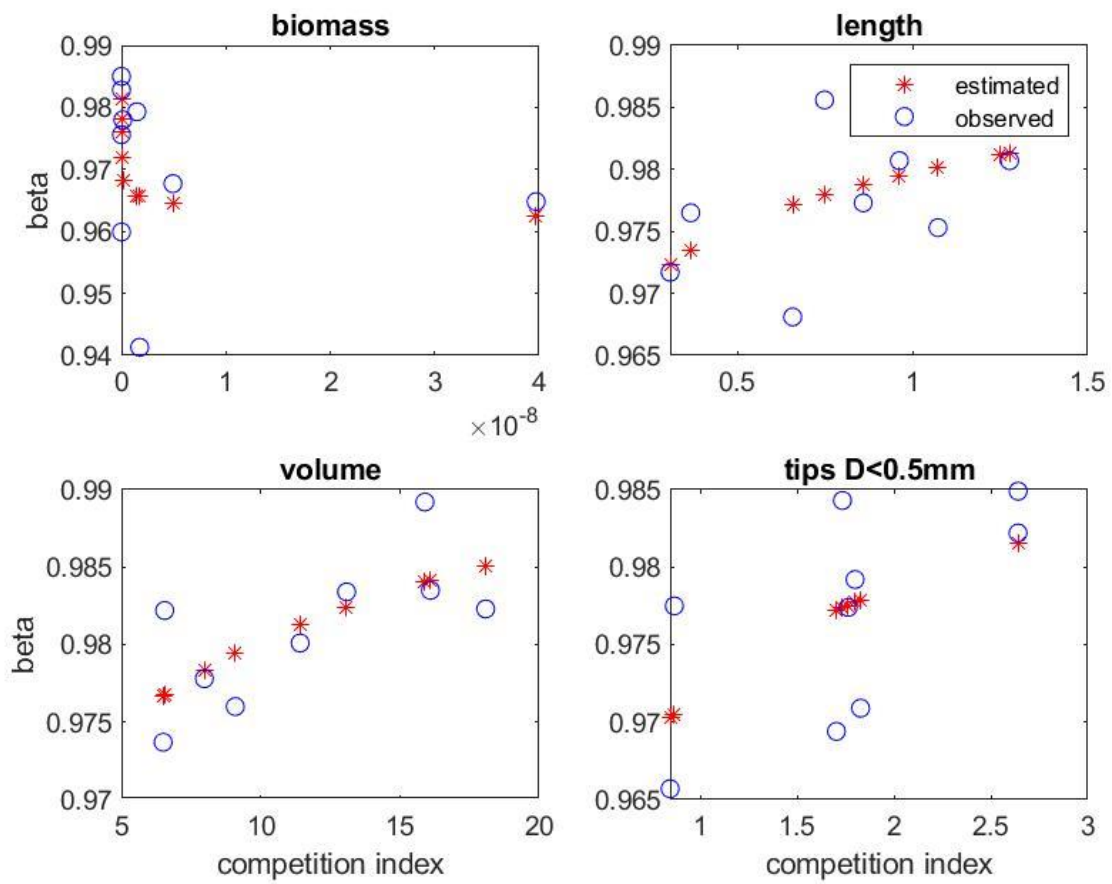


Figure 234 – Estimation of beta-values for verticals with different competition indexes ( $d = 8$  m, uphill).

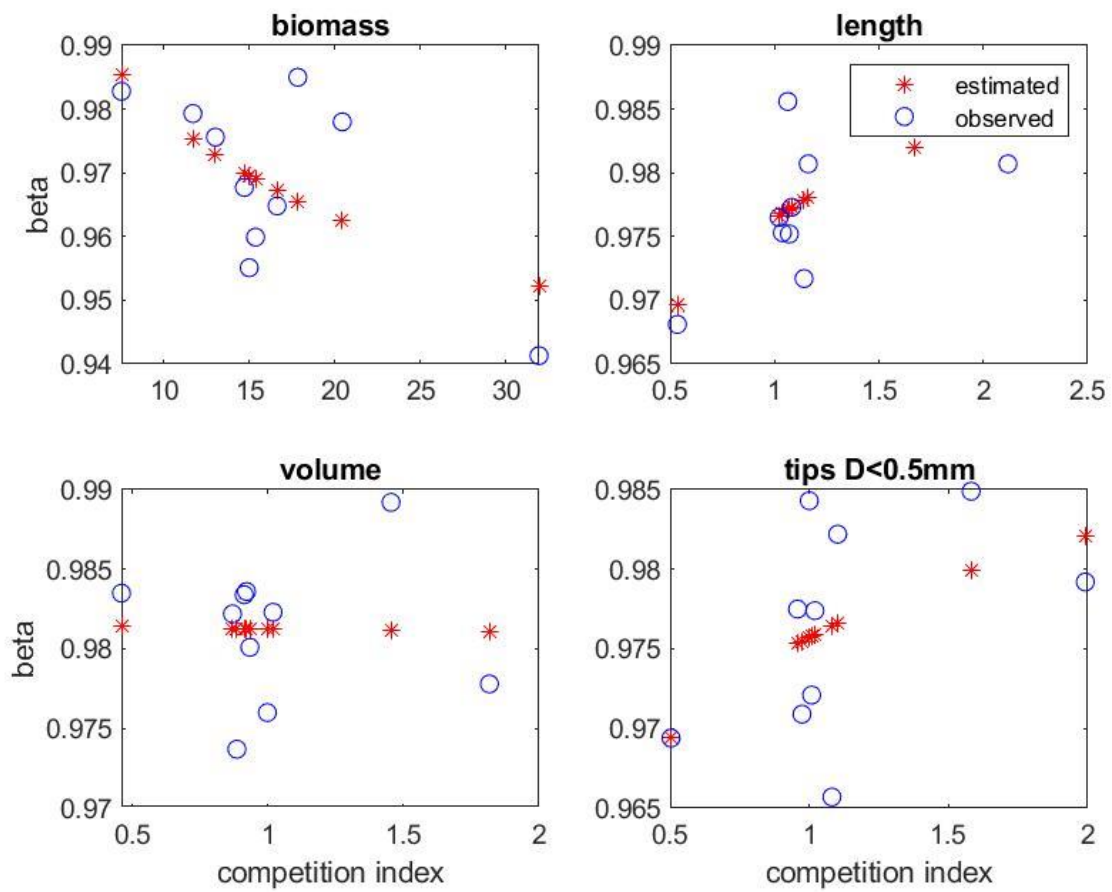


Figure 235 – Estimation of beta-values for verticals with different competition indexes ( $d = 8$  m, downhill).

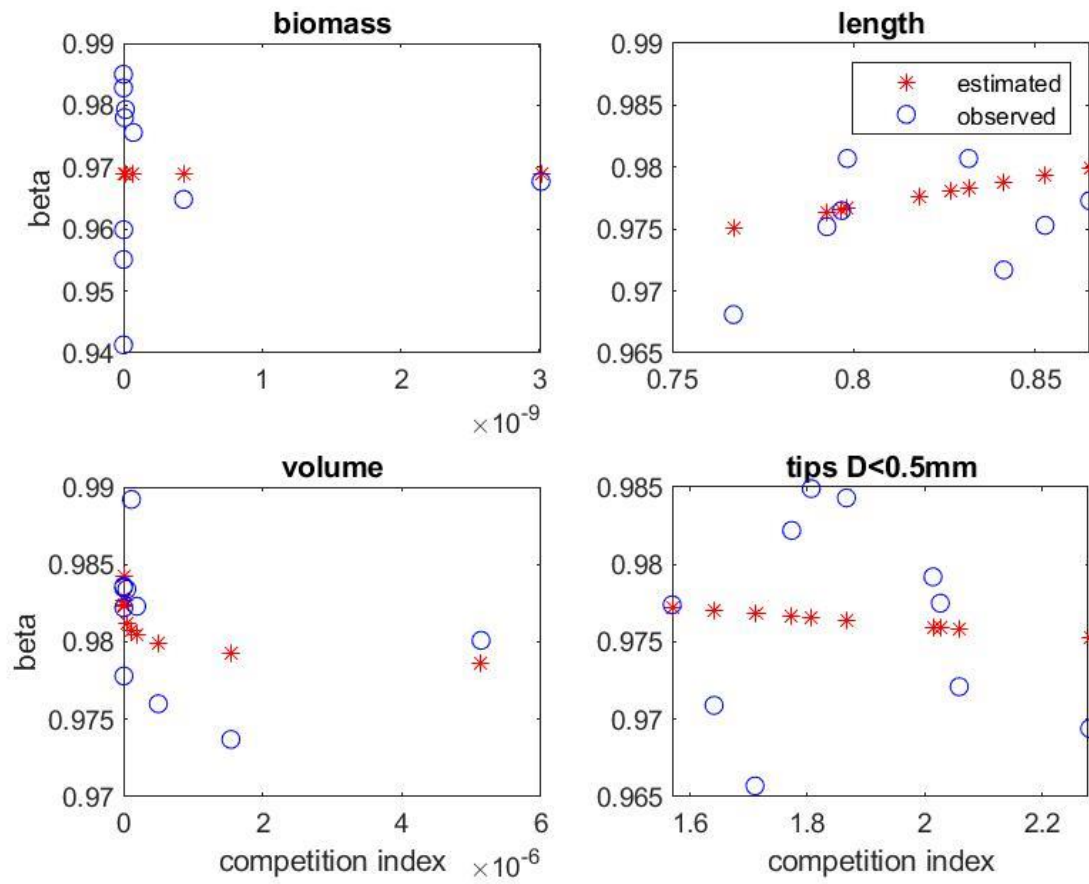


Figure 236 – Estimation of beta-values for verticals with different competition indexes ( $d = d_{min}$ ).

Table 59 – Fitting parameters of the spatial root distribution model for each root density indicator and each tree position and distance tree-to-vertical range.

d_max	Tree position	Fitting parameters	beta				tips D<0.5		length		biomass 0.25<=z<=0.5
			biomass	length	volume	tips D<0.5mm	0.15<=z<=0.3	0.45<=z<=0.65	z<=0.3	z<=0.65	
10	all	alpha	9.731	-0.653	3.747	-0.829	-0.710	0.845	-0.399	-0.689	0.371
		m	0.952	0.907	0.971	0.876	0.001	3.584	0.256	0.125	0.001
		n	-0.001	0.019	-0.001	0.023	2.103	-0.357	0.771	0.689	1.363
		R2	0.066	0.451	0.246	0.608	0.427	0.246	0.150	0.204	0.578
	uphill	alpha	9.389	0.307	0.106	0.273	-0.624	0.528	2.739	9.975	0.779
		m	0.955	0.977	0.983	0.975	0.513	3.916	4.707	3.314	0.004
		n	-0.001	0.006	-0.003	0.007	0.969	-0.322	0.070	0.016	0.504
		R2	0.070	0.214	0.070	0.200	0.177	0.288	0.116	0.112	0.481
	downhill	alpha	0.470	-0.041	1.034	-0.395	-0.546	-2.736	-0.625	-0.629	0.265
		m	0.969	0.958	0.979	0.936	1.459	14.780	0.811	0.518	0.001
		n	-0.001	0.016	-0.001	0.017	0.653	-0.104	0.387	0.434	1.454
		R2	0.000	0.388	0.012	0.530	0.154	0.231	0.150	0.256	0.335
8	all	alpha	9.998	0.014	6.159	-0.268	-0.205	2.292	0.286	-1.184	0.634
		m	0.951	0.964	0.971	0.946	5.430	2.352	2.708	0.850	0.002
		n	-0.001	0.011	-0.001	0.015	0.346	-0.138	0.160	0.189	0.681
		R2	0.068	0.443	0.254	0.457	0.046	0.226	0.032	0.031	0.309
	uphill	alpha	9.744	0.320	-0.599	0.046	0.281	0.430	-0.022	3.010	1.727
		m	0.946	0.980	0.962	0.972	11.337	4.032	2.303	3.054	0.004
		n	-0.001	0.006	0.008	0.010	0.259	-0.210	0.393	0.040	0.190
		R2	0.236	0.290	0.487	0.349	0.060	0.144	0.214	0.079	0.285
	downhill	alpha	-0.647	0.200	0.249	0.220	-1.253	-1.519	0.729	1.186	-0.106
		m	1.034	0.976	0.981	0.976	3.321	2.084	1.244	0.768	0.001
		n	-0.024	0.011	0.000	0.009	0.252	0.151	-0.559	-0.362	0.594
		R2	0.383	0.460	0.001	0.246	0.055	0.040	0.332	0.289	0.139
min		alpha	0.100	9.995	0.074	6.204	-0.230	0.323	2.298	-0.344	-0.822
		m	0.970	0.969	0.986	0.972	0.980	13.134	1.962	2.532	2.320
		n	0.010	0.000	0.041	-0.001	-0.005	0.230	-0.141	0.157	-0.024
		R2	0.000	0.000	0.070	0.153	0.008	0.006	0.292	0.004	0.001



## Annex S – Monitored volumetric water content in Mount Faito

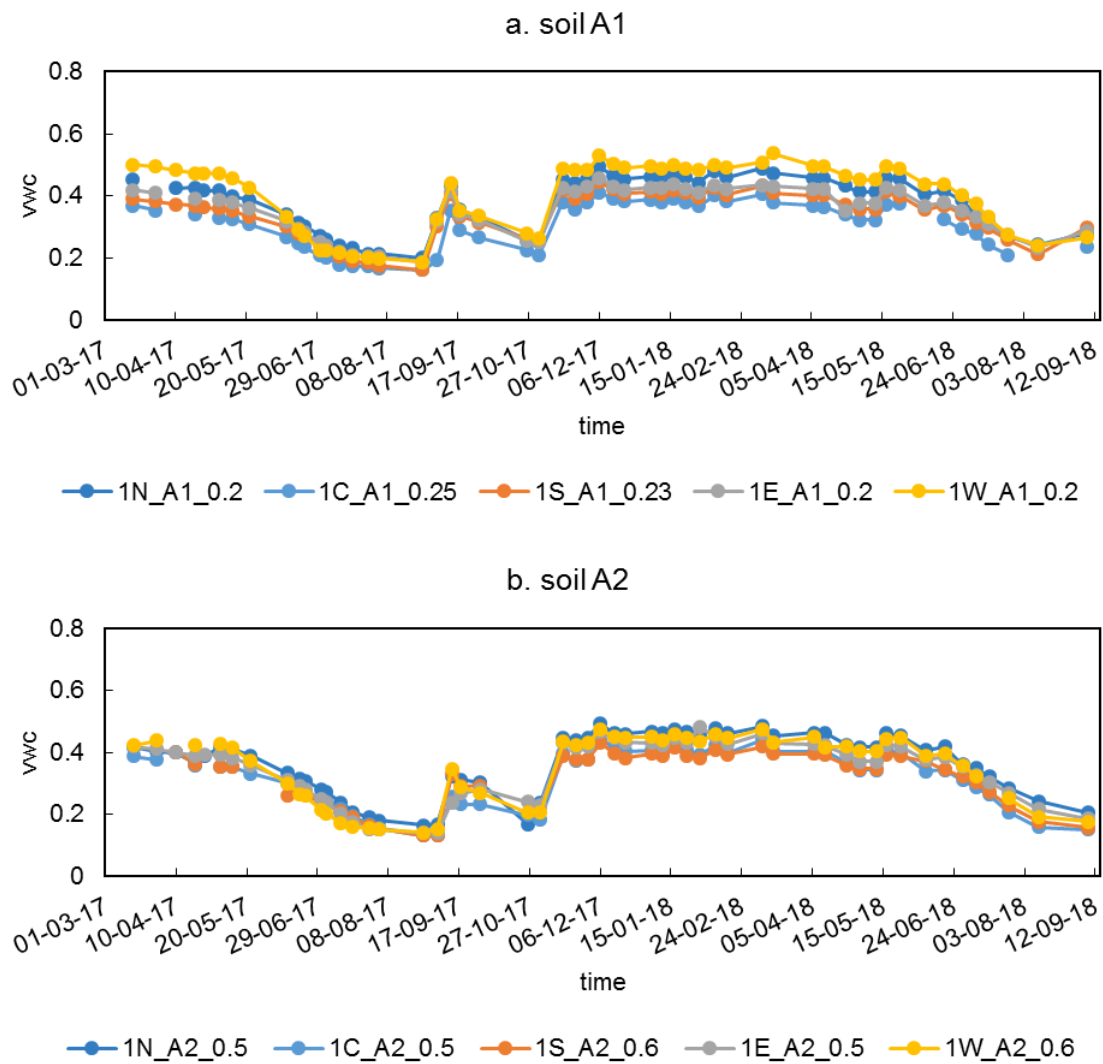


Figure 237 – Monitored volumetric water content (vwc) in cell 1 in soil A1 and A2 at Mount Faito.

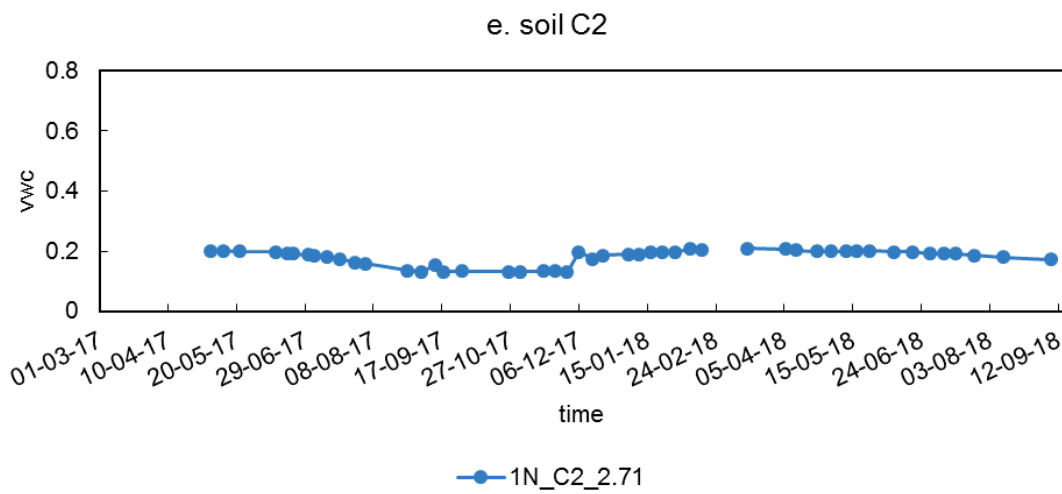
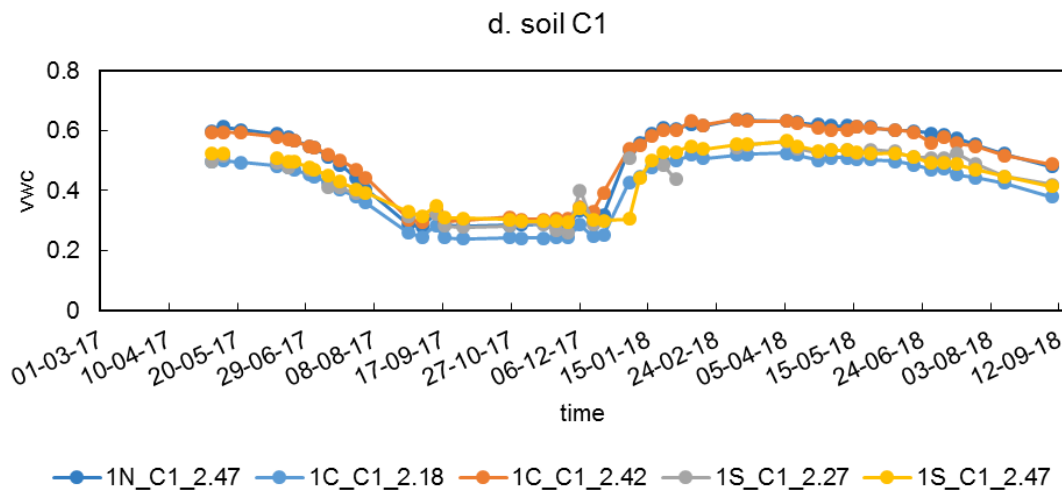
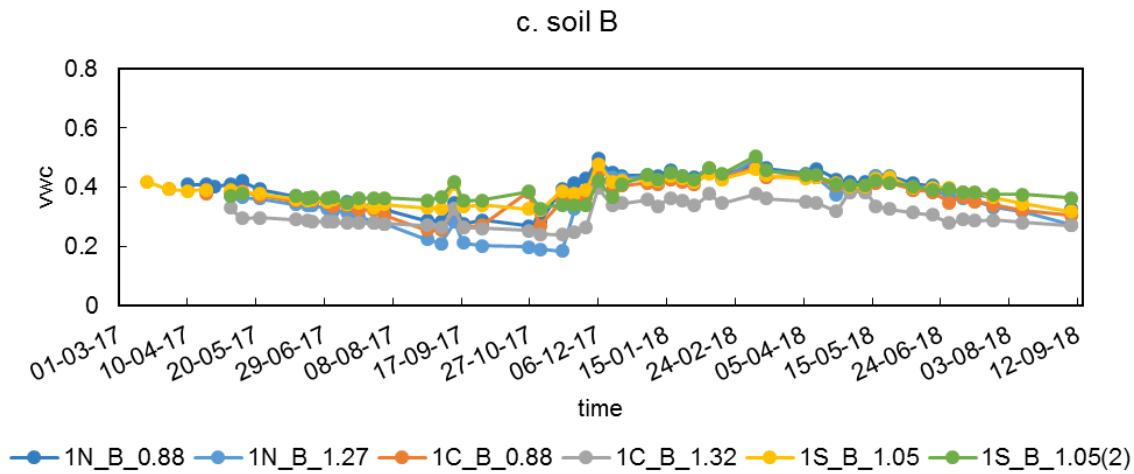


Figure 238 – Monitored volumetric water content (vwc) in cell 1 in soil B, C1 and C2 at Mount Faito.

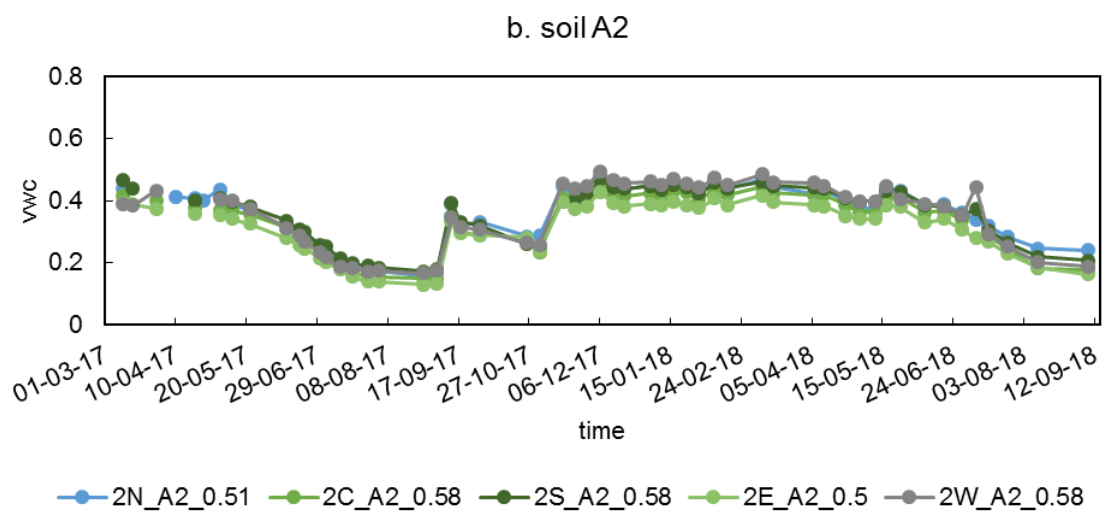
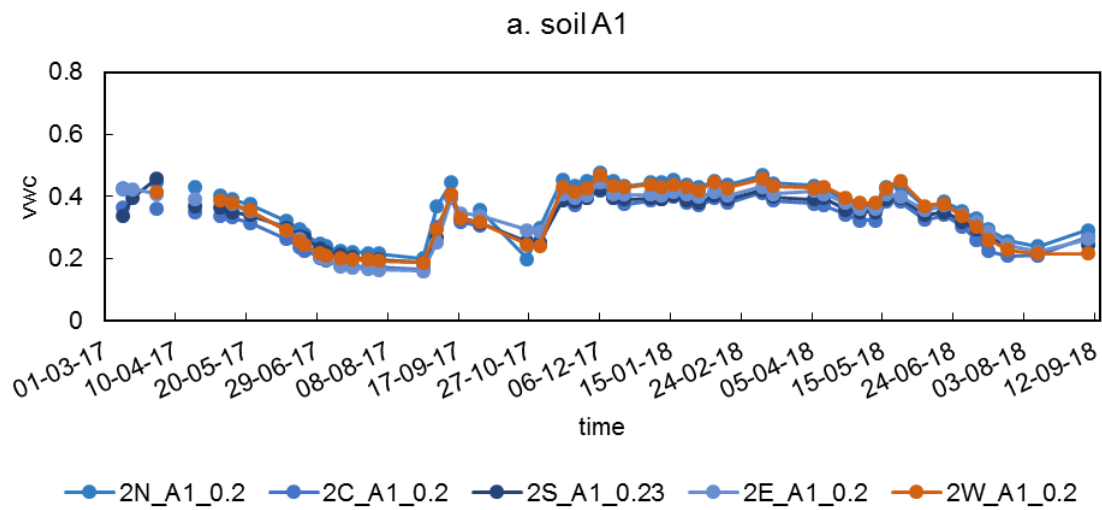


Figure 239 – Monitored volumetric water content (vwc) in cell 2 in soil A1 and A2 at Mount Faito.

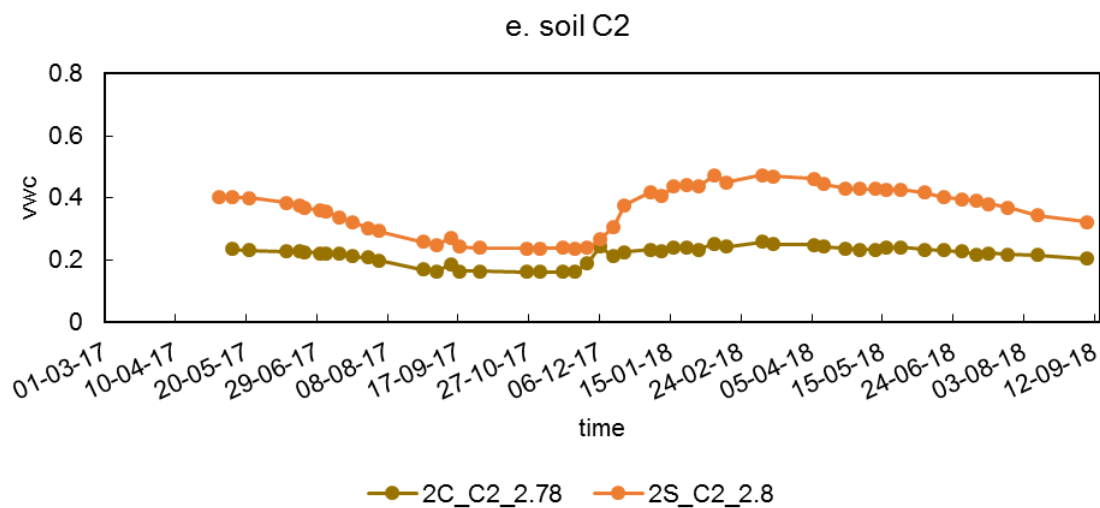
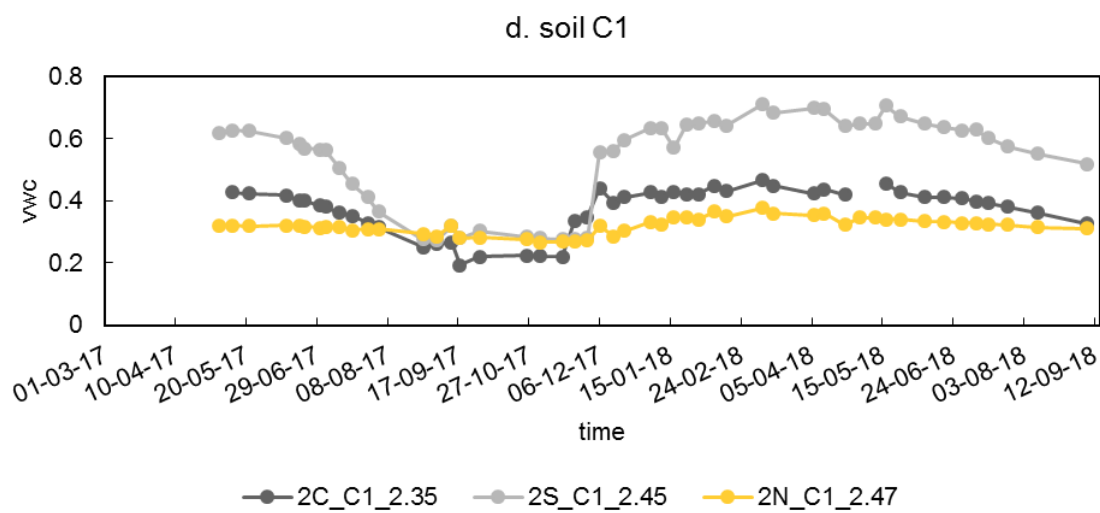
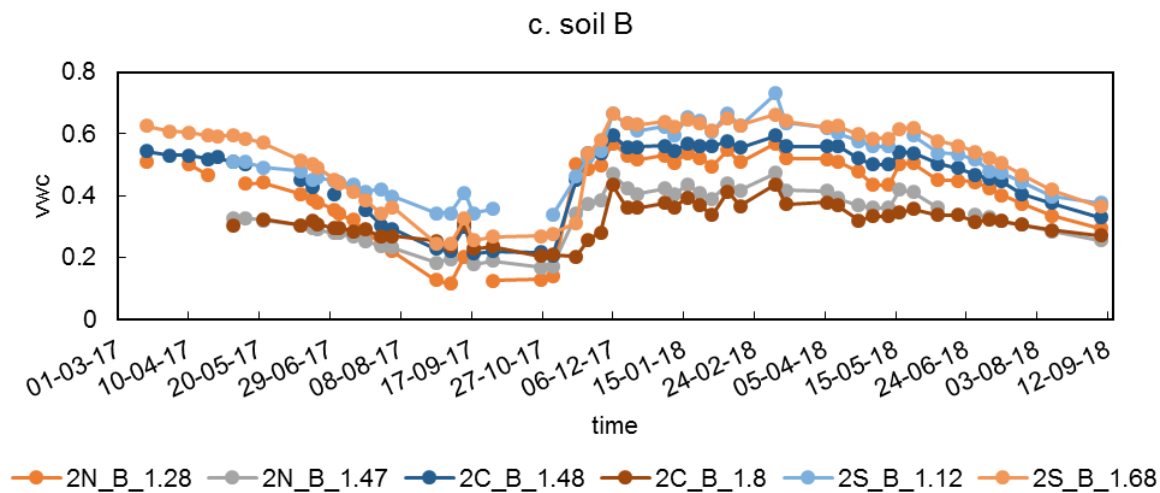


Figure 240 – Monitored volumetric water content (vwc) in cell 2 in soil B, C1 and C2 at Mount Faito.

## Annex T – Monitored suction

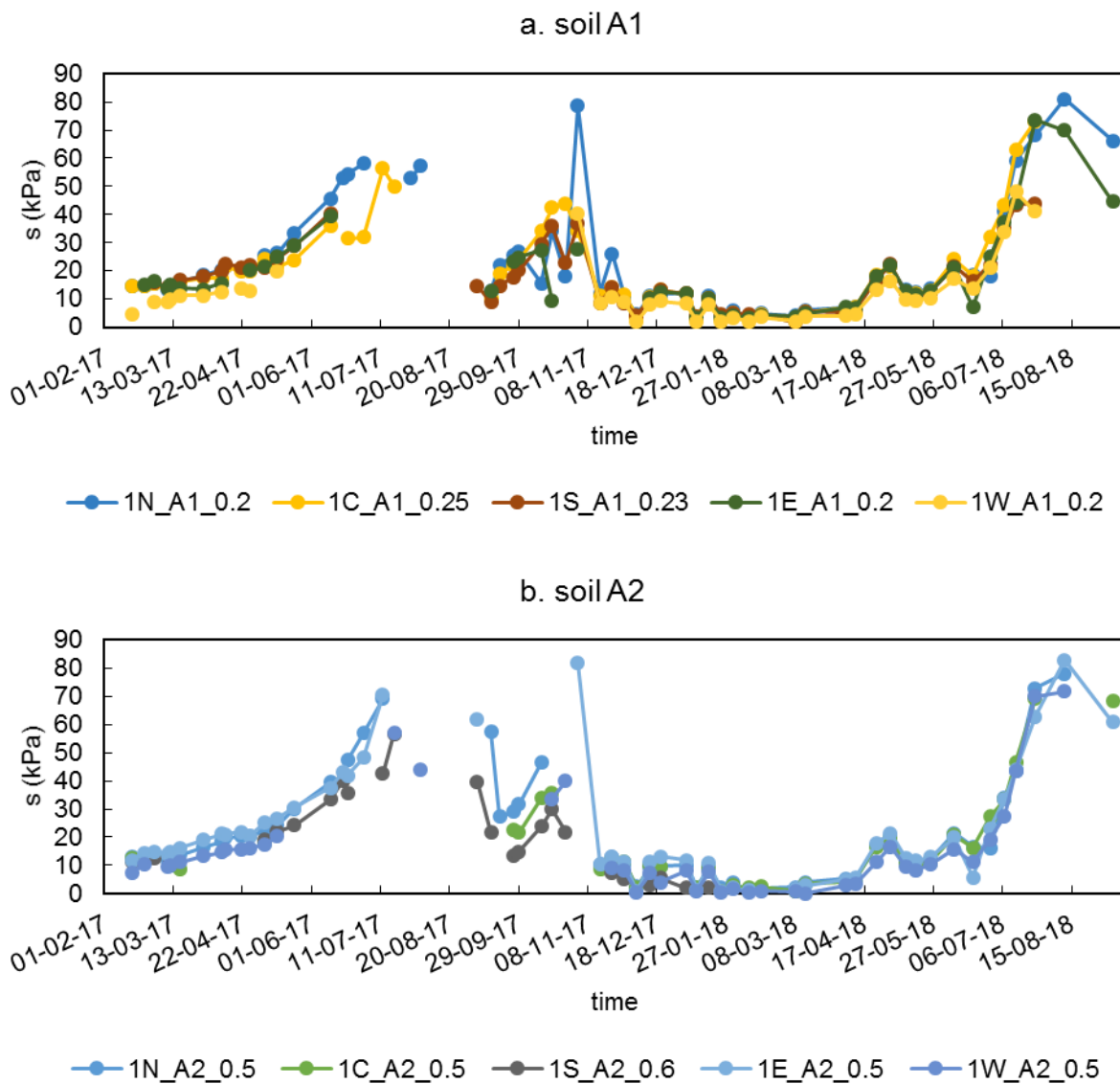


Figure 241 – Monitored suction ( $s$ ) in cell 1 in soil A1 and A2.

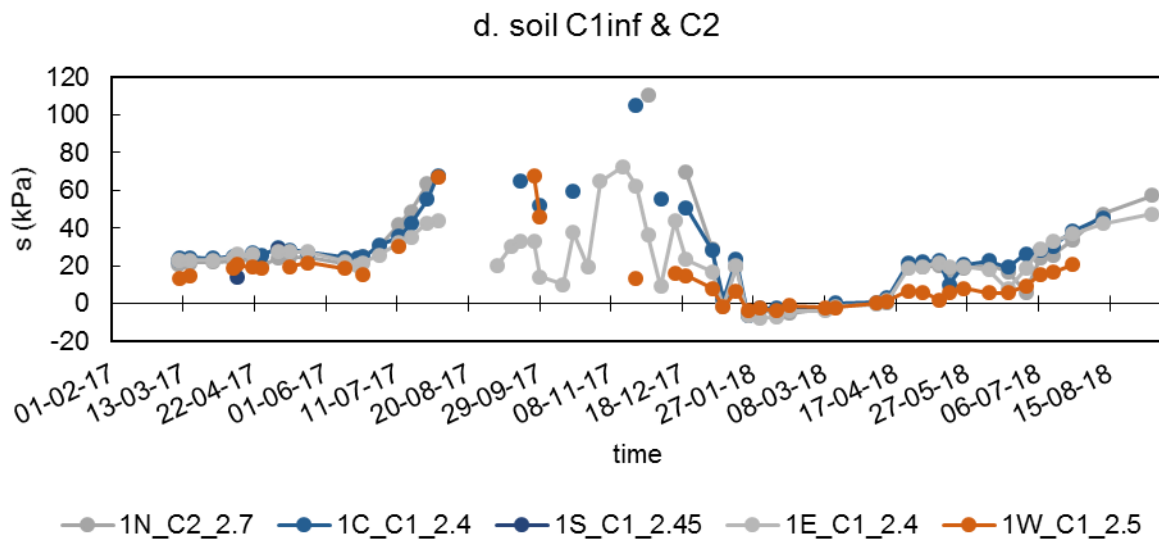
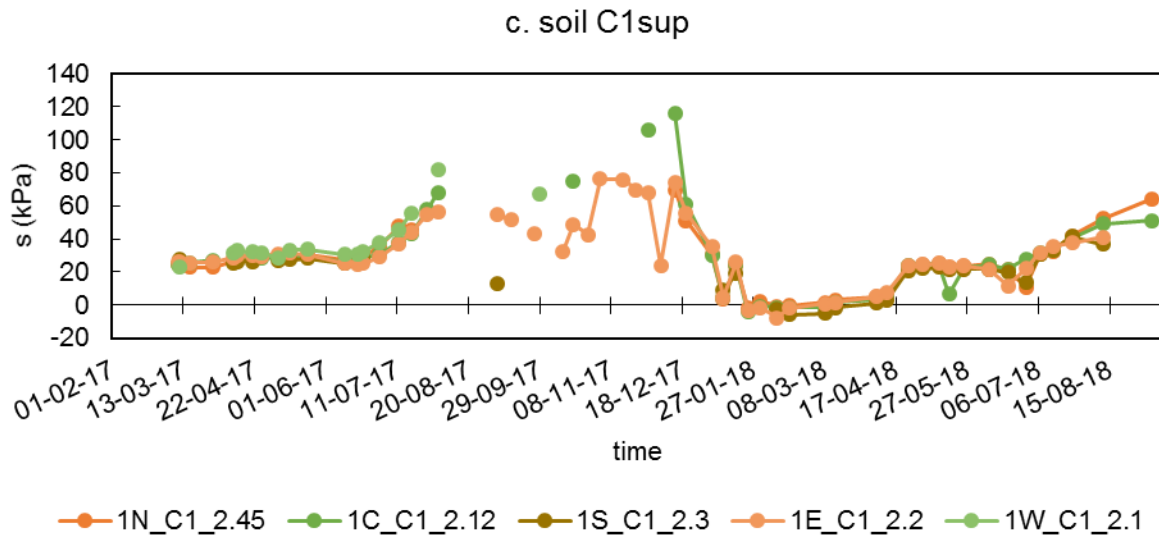


Figure 242 – Monitored suction ( $s$ ) in cell 1 in soil C1 and C2.

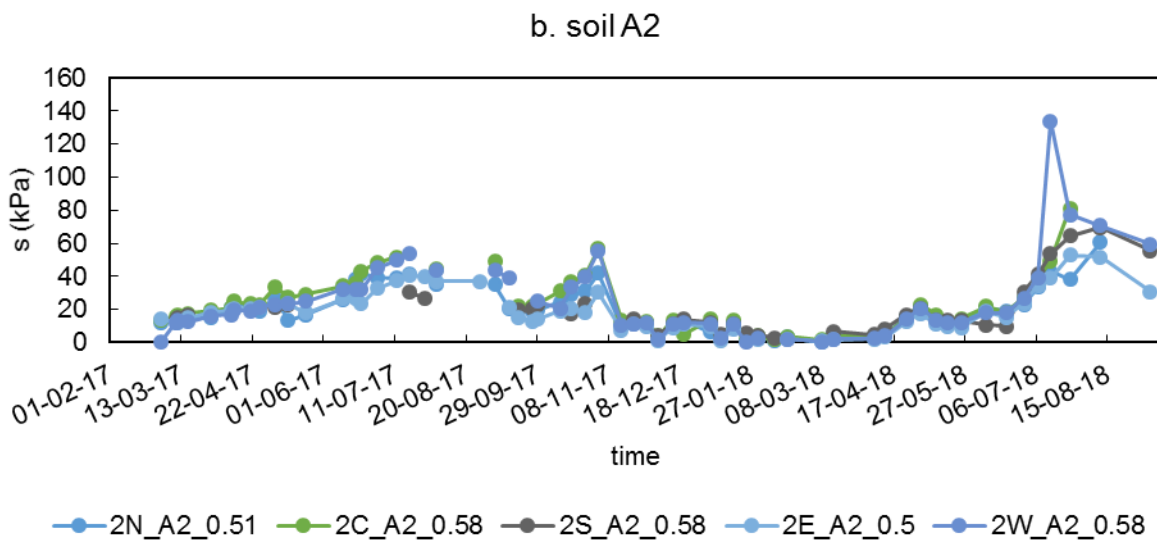
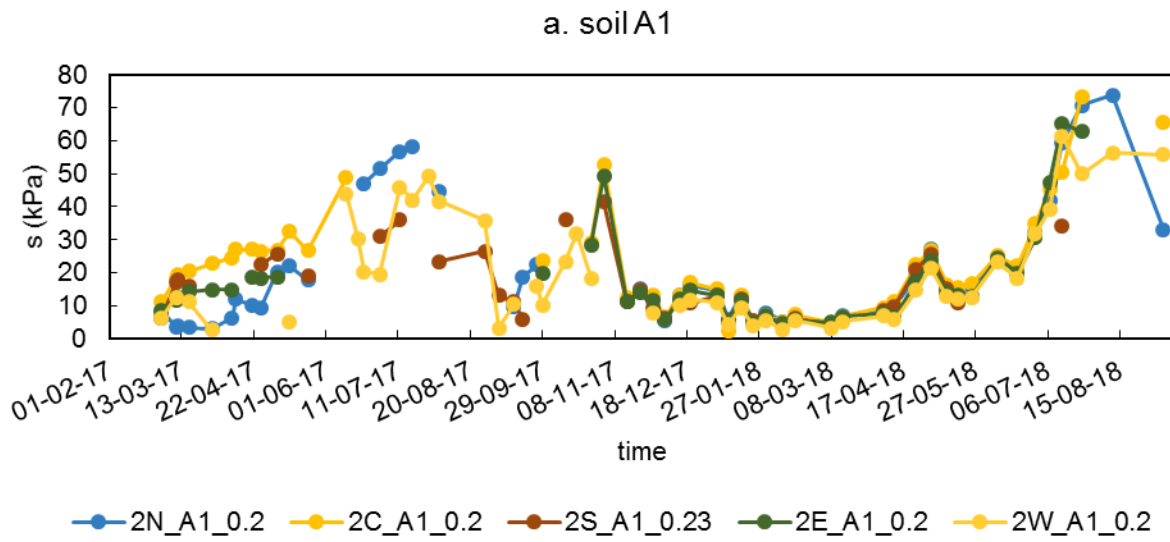


Figure 243 – Monitored suction ( $s$ ) in cell 2 in soil A1 and A2.

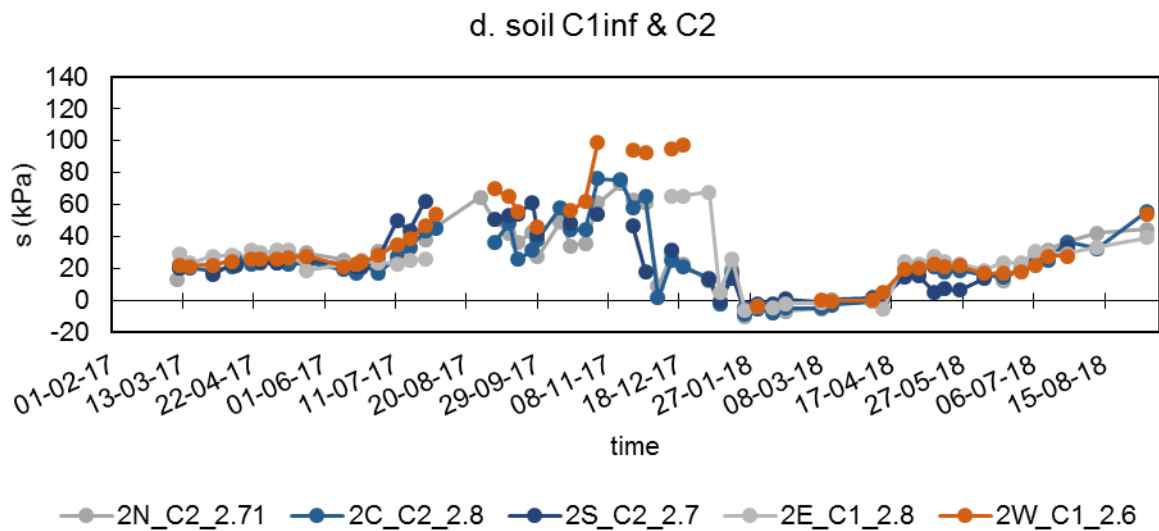
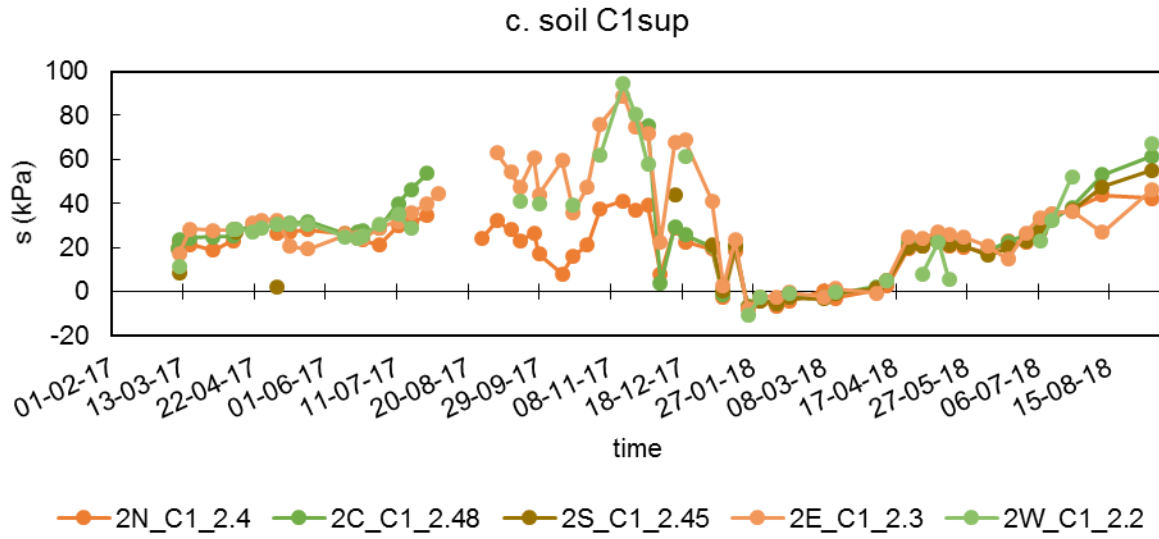


Figure 244 – Monitored suction ( $s$ ) in cell 2 in soil C1 and C2.



## Annex U – Field suction and water content in the water retention plan

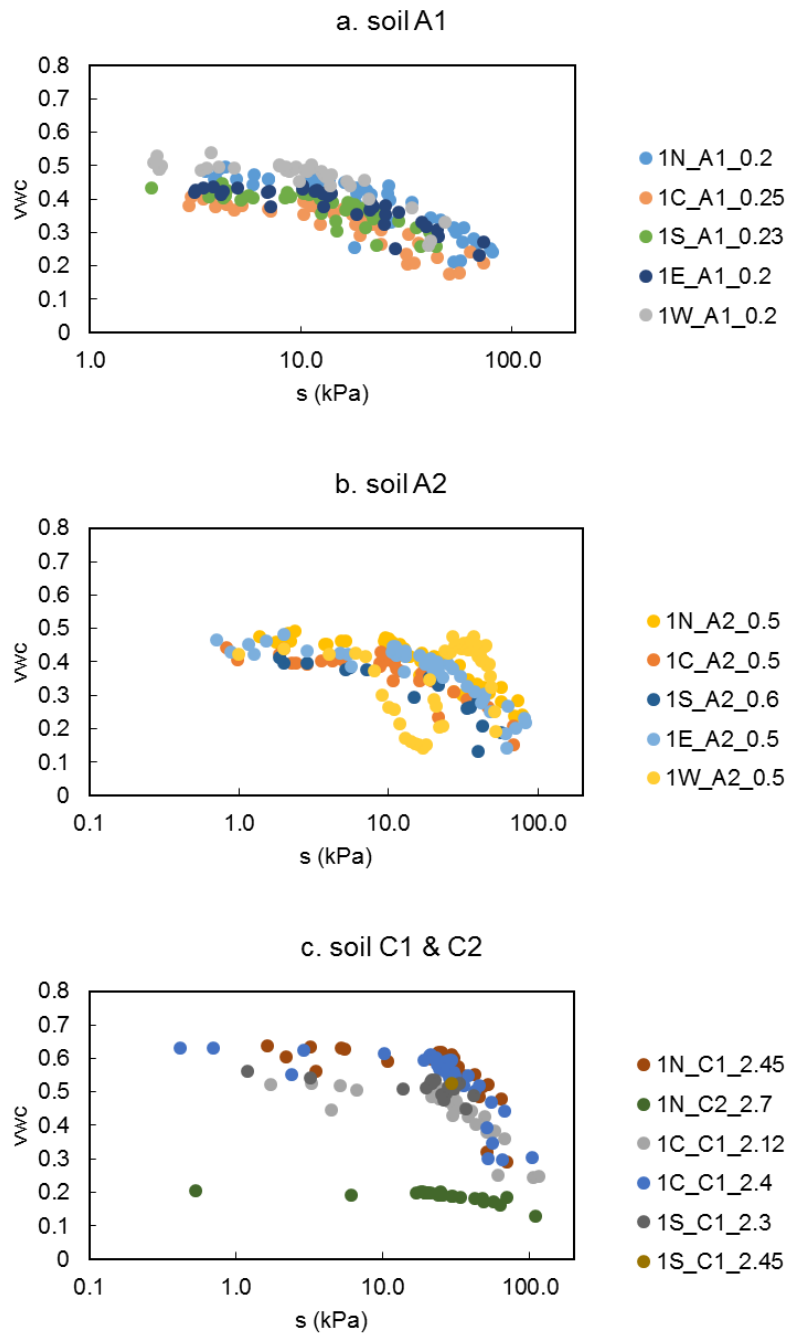


Figure 245 – Field measurements in cell 1 of volumetric water content (vwc) and suction (s).

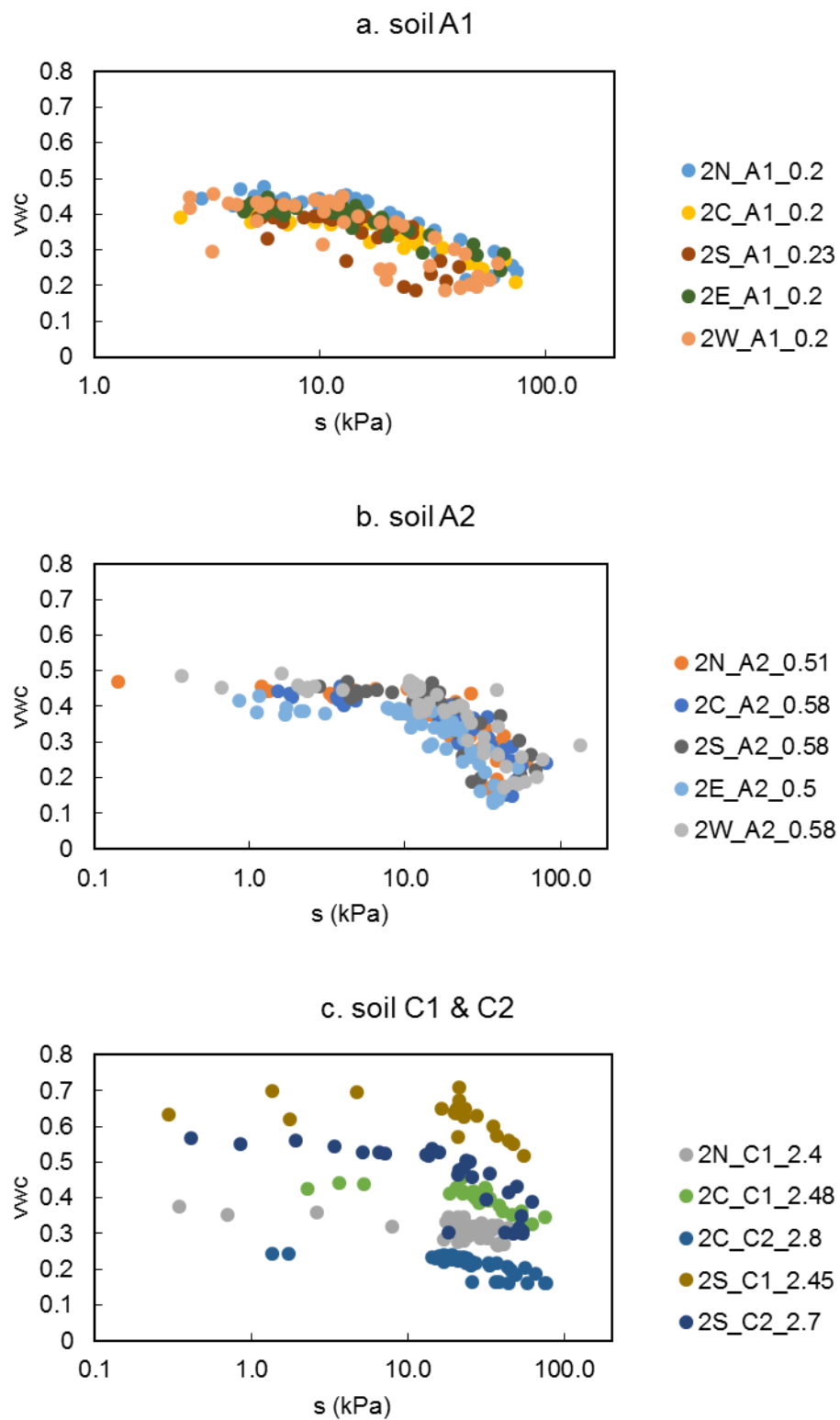


Figure 246 – Field measurements in cell 2 of volumetric water content ( $vwc$ ) and suction ( $s$ ).

## Annex V – Spatial distribution of hydraulic observations

Table 60 – Observed parameters for the fitting of the spatial distribution model.

Soil	Parameter		Verticals											
			1C	1E	1N	1S	1W	2C	2E	2N	2S	2W	T	NT
A1	vwc	max	0.411	0.457	0.495	0.445	0.538	0.421	0.447	0.477	0.456	0.468	0.424	0.457
		min	0.161	0.186	0.200	0.162	0.187	0.165	0.161	0.199	0.188	0.187	0.197	0.284
		mean (winter)	0.357	0.402	0.435	0.386	0.473	0.368	0.395	0.418	0.377	0.409	0.367	0.417
		mean (summer)	0.235	0.288	0.304	0.275	0.298	0.248	0.263	0.293	0.270	0.266	0.250	0.341
	suction	max	73.280	73.709	81.124	43.906	48.188	73.419	65.221	73.877	41.415	61.331	76.404	85.181
		min	2.930	3.124	3.544	1.952	1.997	2.417	4.615	3.000	4.660	2.644	1.842	4.513
		mean (winter)	15.434	13.335	15.942	14.765	9.249	17.603	13.535	11.519	14.226	10.286	9.228	11.617
		mean (summer)	35.720	35.289	44.797	24.949	29.141	43.271	38.645	41.618	22.641	33.589	55.888	43.953
		max variation	2.831	2.664	3.081	1.991	2.077	3.369	2.991	2.860	1.345	3.160	2.359	2.433
		min variation	-1.783	-3.011	-5.113	-2.163	-2.443	-3.092	-2.938	-1.458	-2.317	-4.070	-1.775	-2.046
A2	vwc	max	0.443	0.481	0.493	0.431	0.476	0.455	0.429	0.477	0.469	0.492	0.415	0.447
		min	0.131	0.139	0.165	0.133	0.142	0.149	0.131	0.160	0.173	0.168	0.168	0.286
		mean (winter)	0.377	0.407	0.426	0.380	0.420	0.401	0.371	0.419	0.417	0.426	0.347	0.403
		mean (summer)	0.233	0.252	0.281	0.243	0.246	0.249	0.232	0.274	0.278	0.266	0.233	0.331
	suction	max	69.069	82.816	78.186	56.624	71.833	81.311	52.992	60.694	69.697	77.413		59.884
		min	0.826	0.710	1.374	1.880	0.129	1.535	0.856	0.142	2.808	0.366	2.799	3.908
		mean (winter)	10.213	14.773	12.677	13.332	10.158	17.905	12.467	15.127	13.304	15.771	12.530	11.897
		mean (summer)	36.175	45.430	42.713	33.082	39.995	38.104	30.041	32.241	35.029	41.510		33.810
		max variation	2.040	2.036	2.670	1.997	2.384	2.913	1.693	1.707	2.090	2.315	1.229	1.577
		min variation	-1.333	-5.479	-6.014	-2.267	-1.210	-3.304	-1.733	-2.441	-1.184	-5.135	-2.437	-1.735
A1 & A2	gradient	max	5.636	2.600	4.271	1.676	1.032	2.830	7.833	9.462	0.415	2.056	1.745	6.738
		min	-1.119	-18.938	-15.778	-7.765	-10.609	-4.125	-2.786	-5.788	-6.666	-11.567	-4.667	-2.053
		mean (winter)	-0.511	-2.145	-1.055	0.104	-1.323	1.043	0.457	1.823	1.333	-2.527	2.375	1.603
		mean (summer)	-1.819	-4.289	-4.464	-5.119	-4.686	-2.998	-0.572	-1.010	-8.797	-6.516		-1.143

The values added to the gradient are summarized in Table 61. The values in Table 60 are already affected of those constants.

Table 61 – Constants added to the hydraulic observations of gradient.

mean (winter)	-0.5
mean (summer)	-3

## Annex W – Spatial distribution of hydraulic (model fitting)

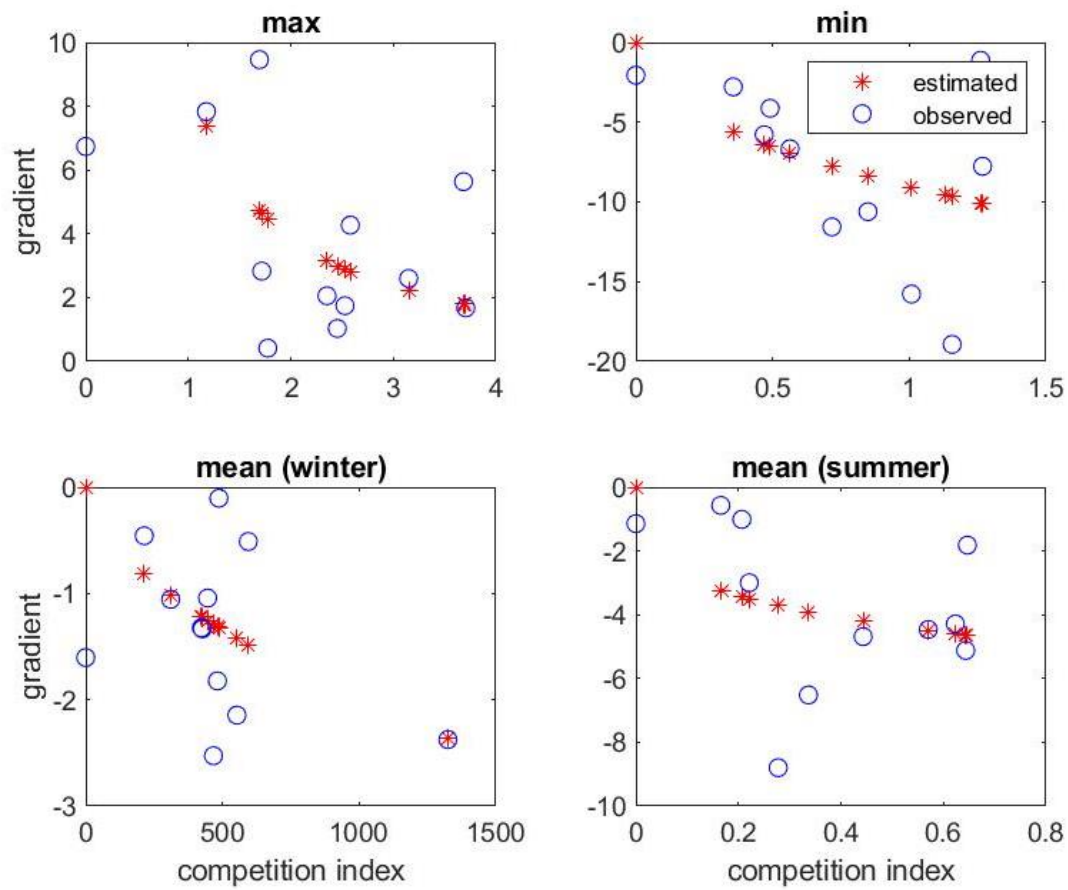


Figure 247 – Spatial distribution of the hydraulic gradient considering the effect of all the trees in a range of 8 m from the verticals.

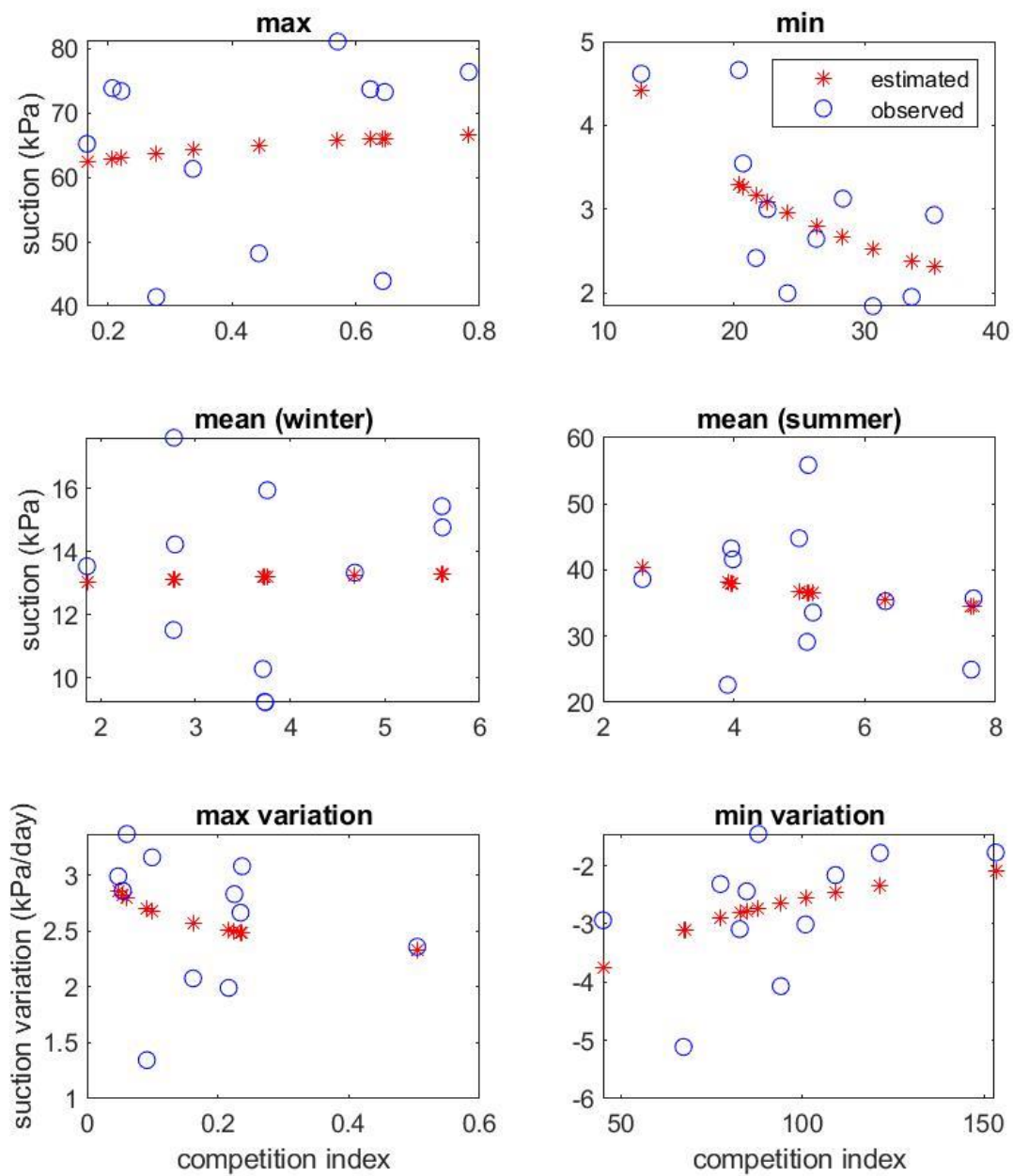


Figure 248 – Spatial distribution of suction in soil A1 considering the effect of all the trees in a range of 8 m from the verticals.

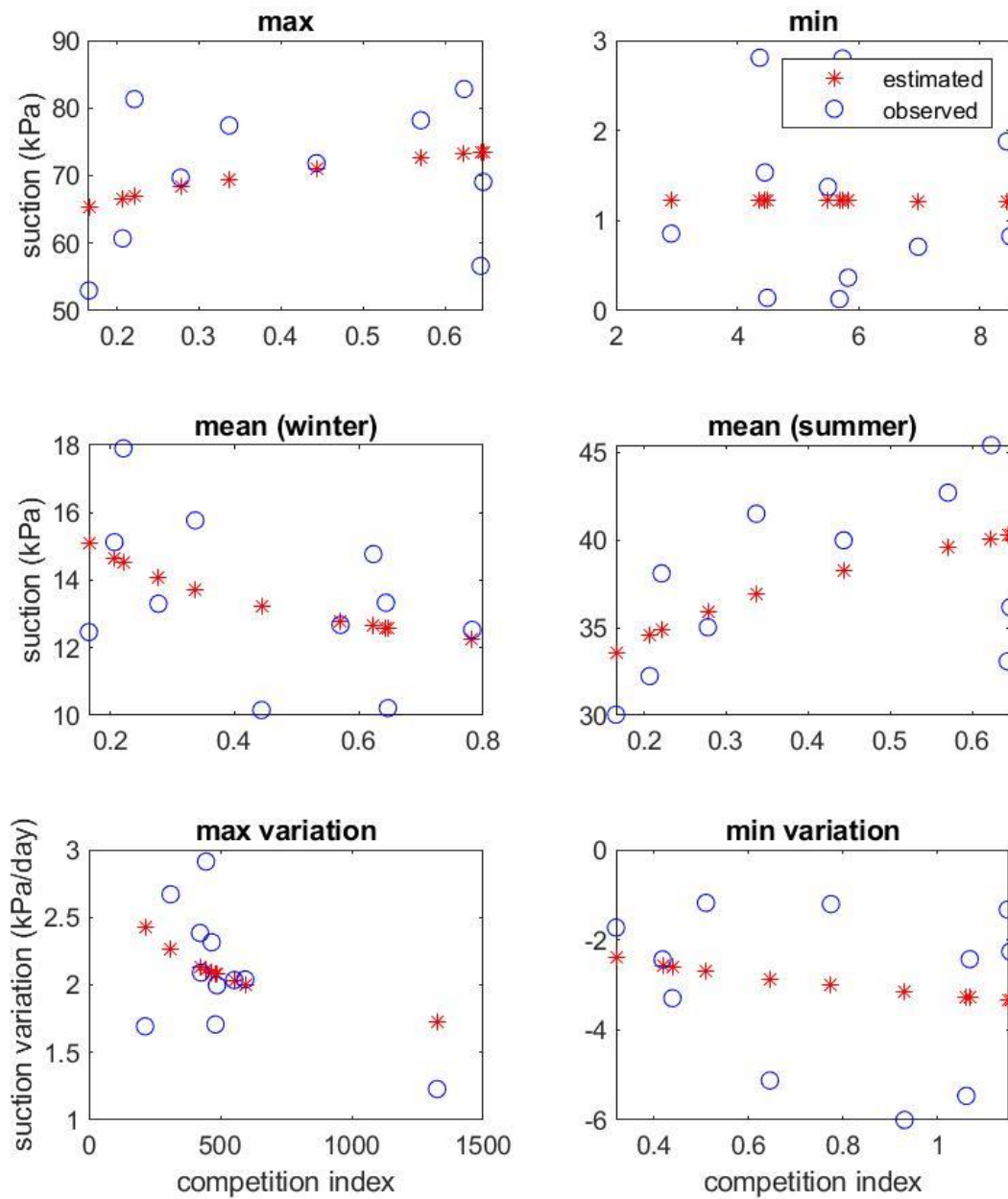


Figure 249 – Spatial distribution of suction in soil A2 considering the effect of all the trees in a range of 8 m from the verticals.

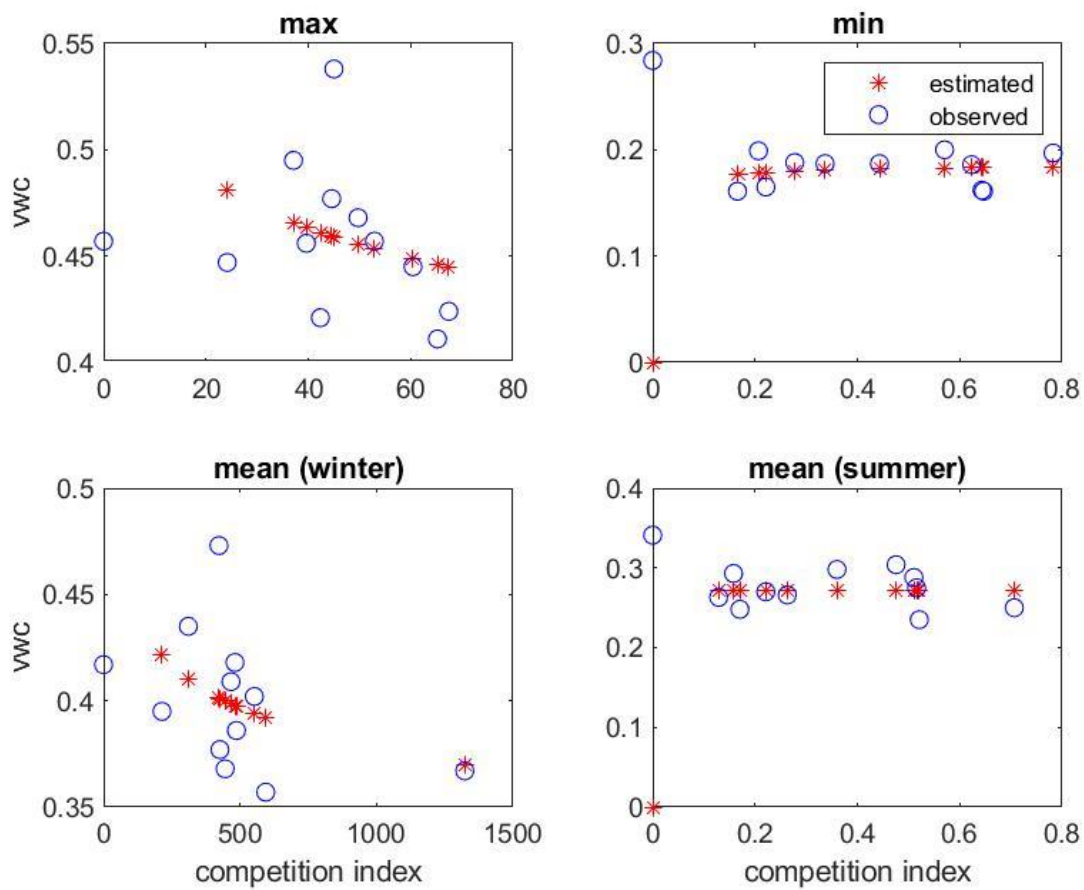


Figure 250 – Spatial distribution of the volumetric water content in soil A1 considering the effect of all the trees in a range of 8 m from the verticals.

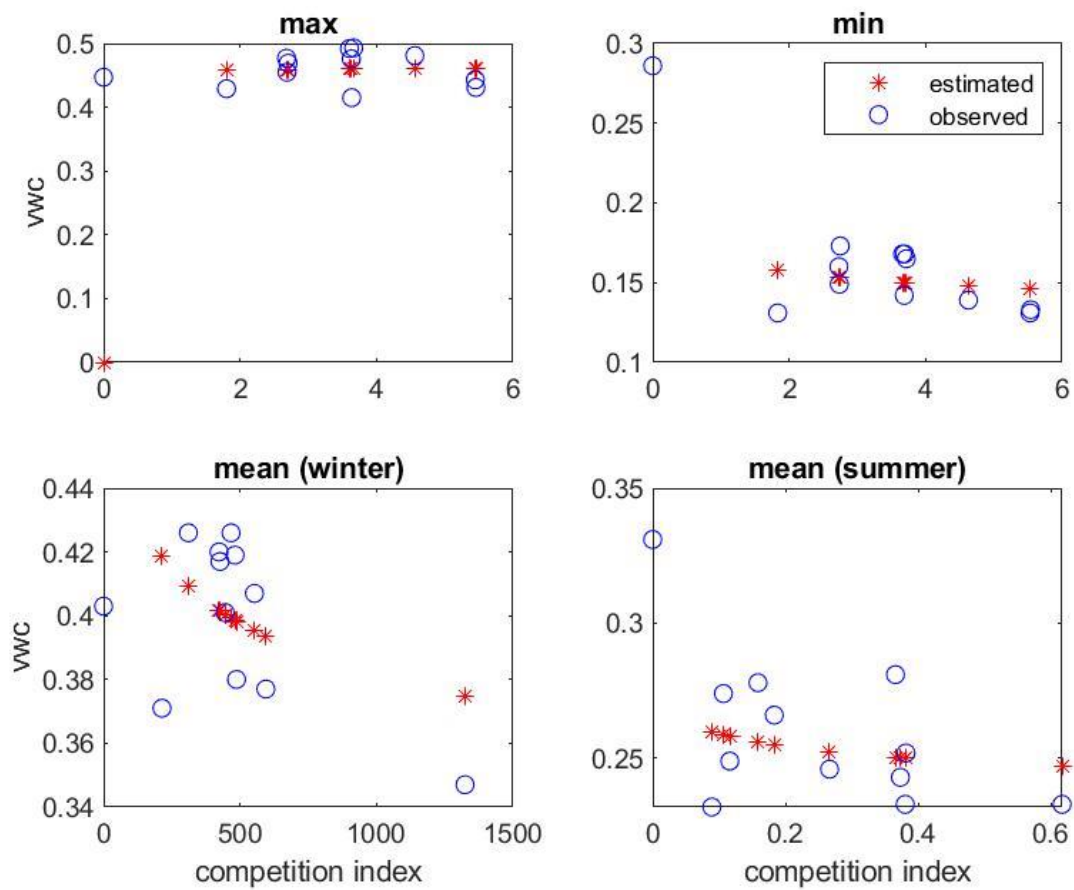


Figure 251 – Spatial distribution of the volumetric water content in soil A2 considering the effect of all the trees in a range of 8 m from the verticals.



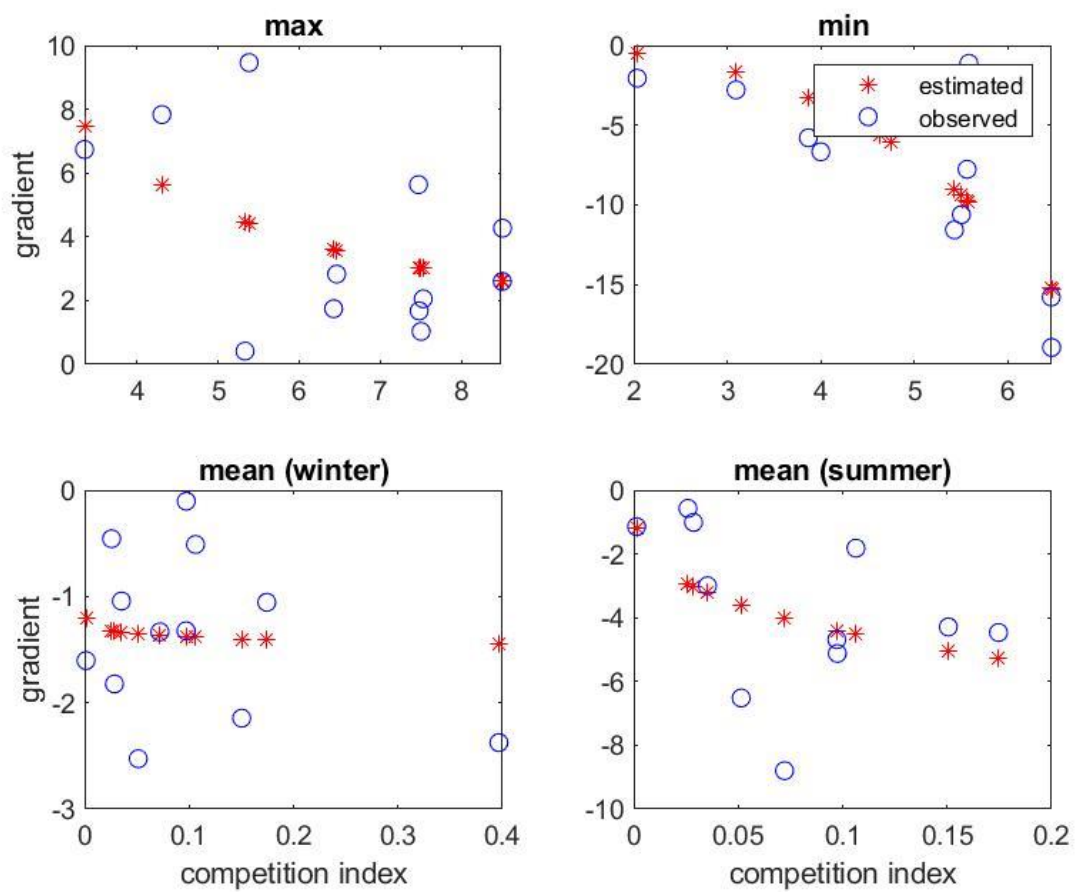


Figure 252 – Spatial distribution of the hydraulic gradient considering the effect of all the trees in a range of 10 m from the verticals.

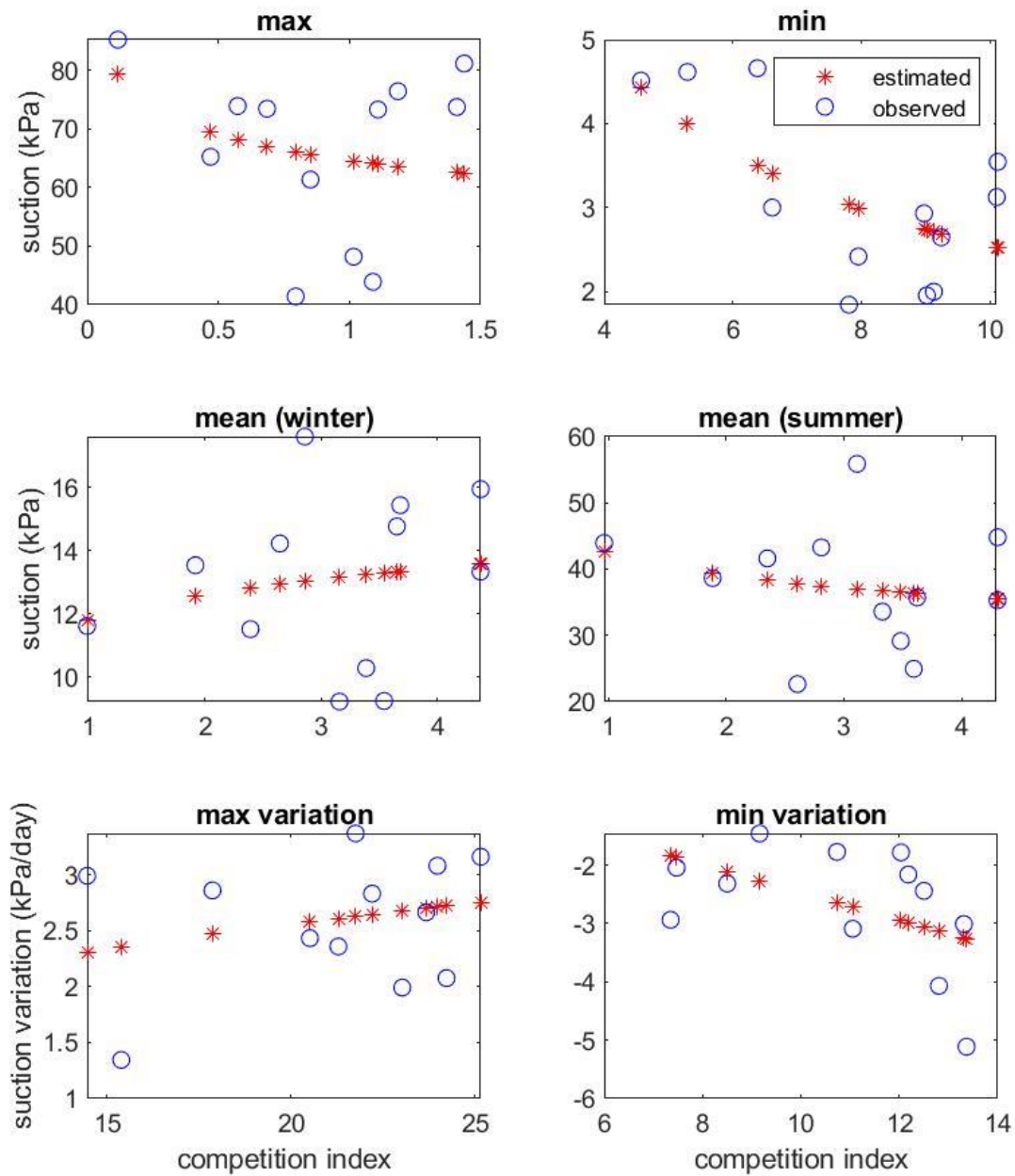


Figure 253 – Spatial distribution of suction in soil A1 considering the effect of all the trees in a range of 10 m from the verticals.

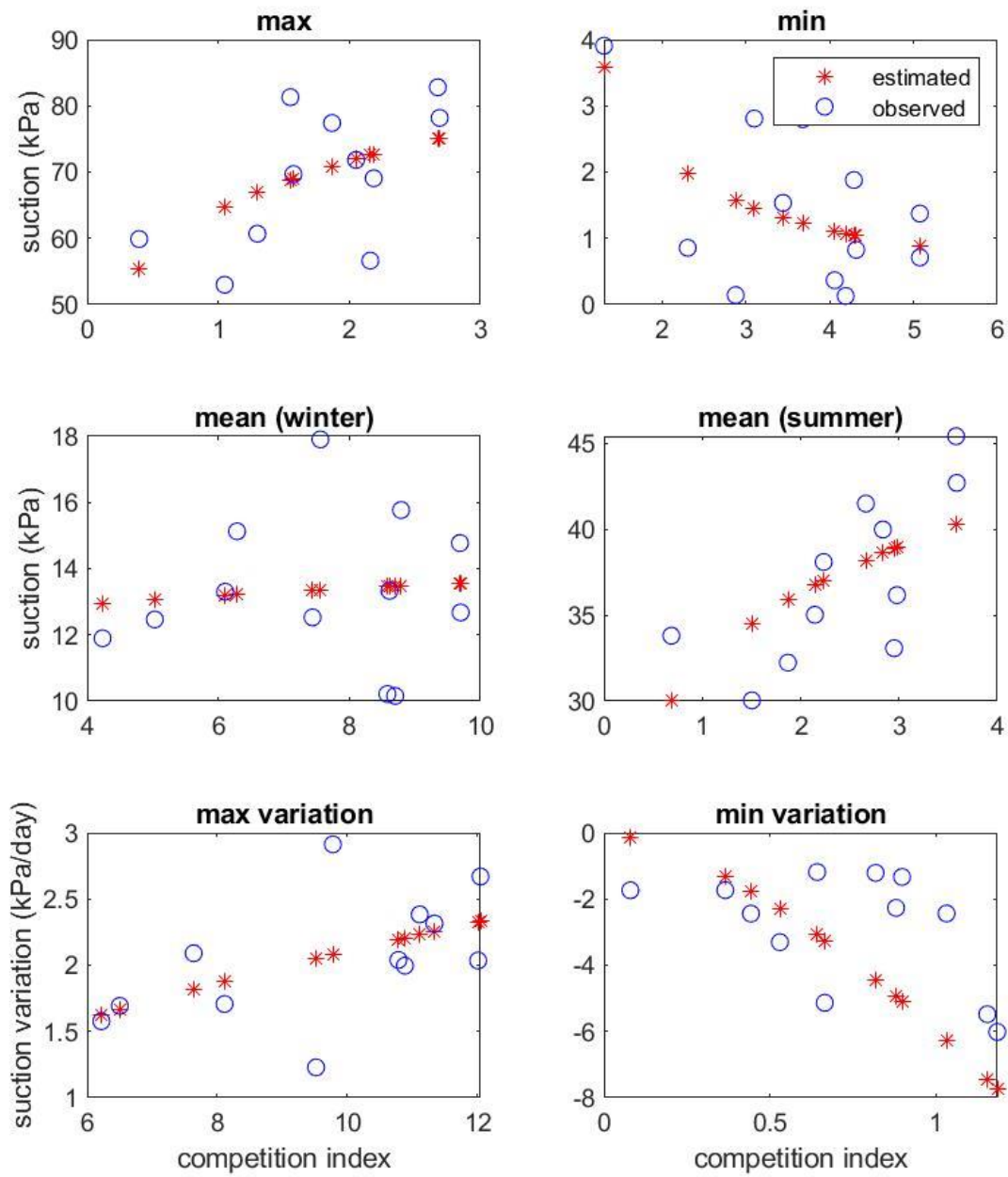


Figure 254 – Spatial distribution of suction in soil A2 considering the effect of all the trees in a range of 10 m from the verticals.

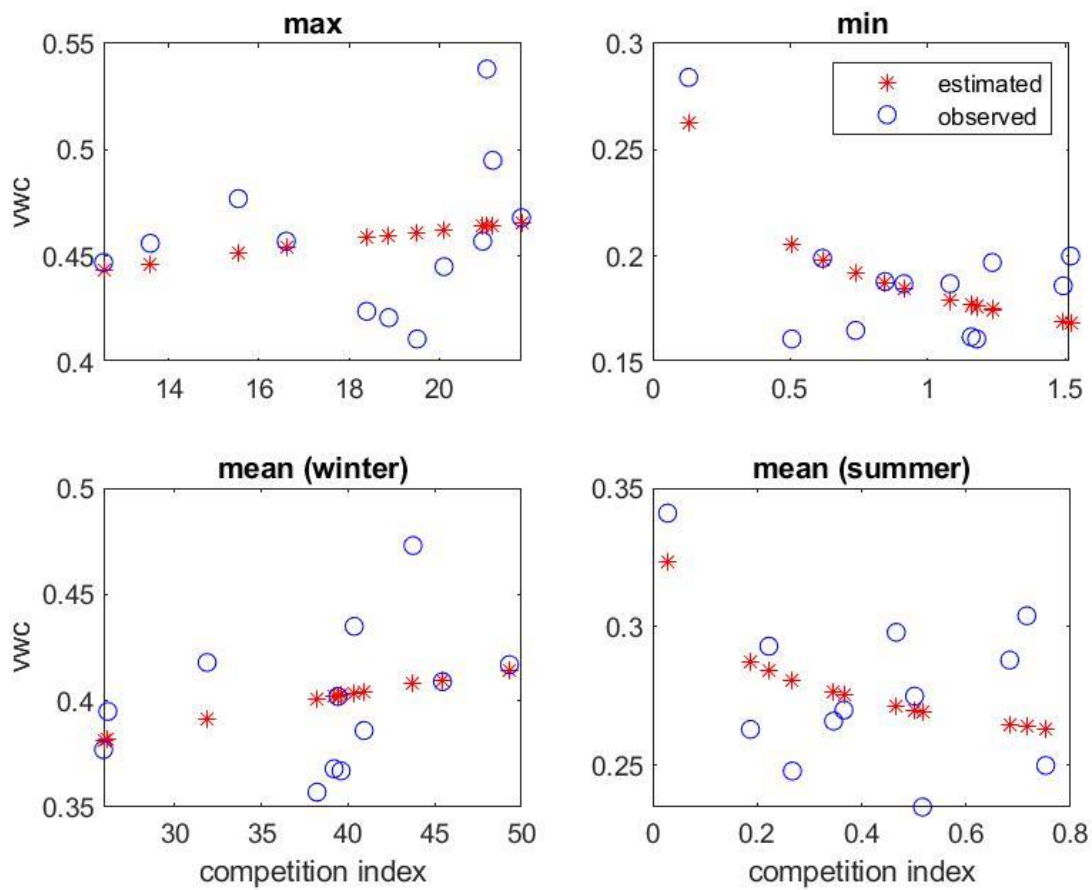


Figure 255 – Spatial distribution of the volumetric water content in soil A1 considering the effect of all the trees in a range of 10 m from the verticals.

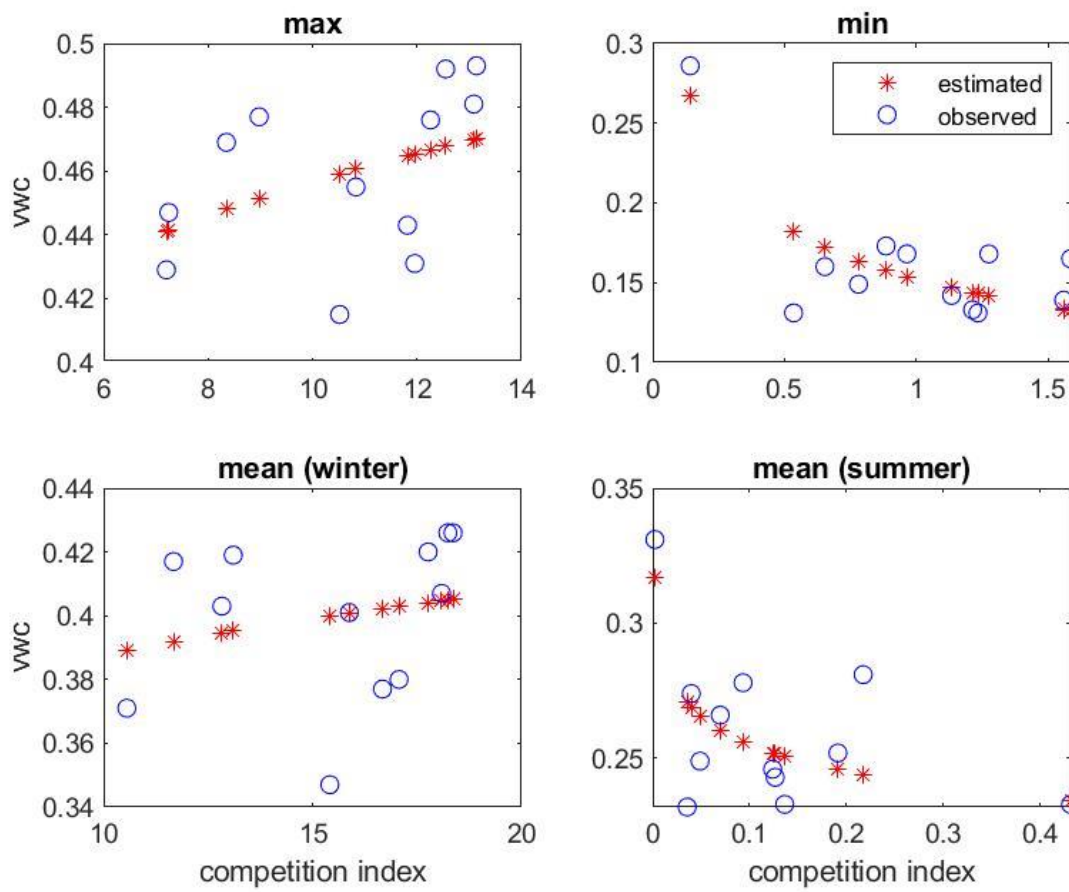


Figure 256 – Spatial distribution of the volumetric water content in soil A2 considering the effect of all the trees in a range of 10 m from the verticals.

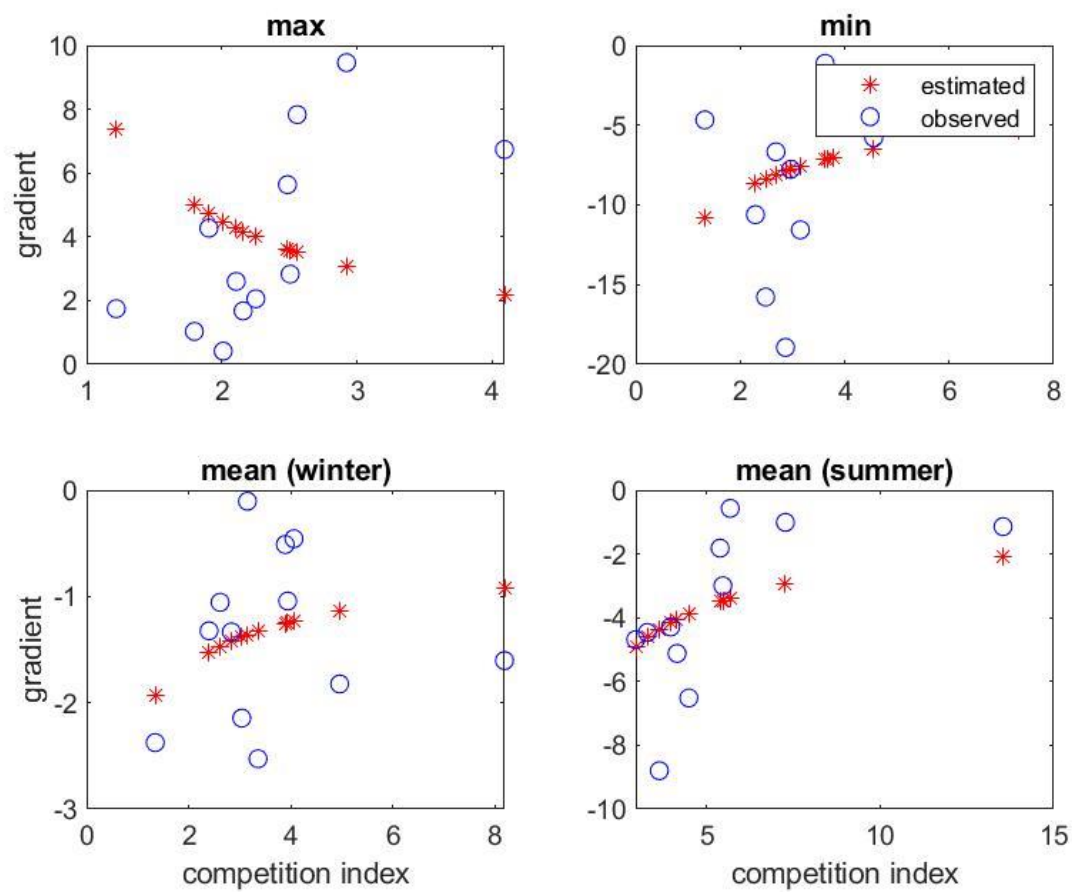


Figure 257 – Spatial distribution of the hydraulic gradient considering the effect of the closest tree from the vertical.

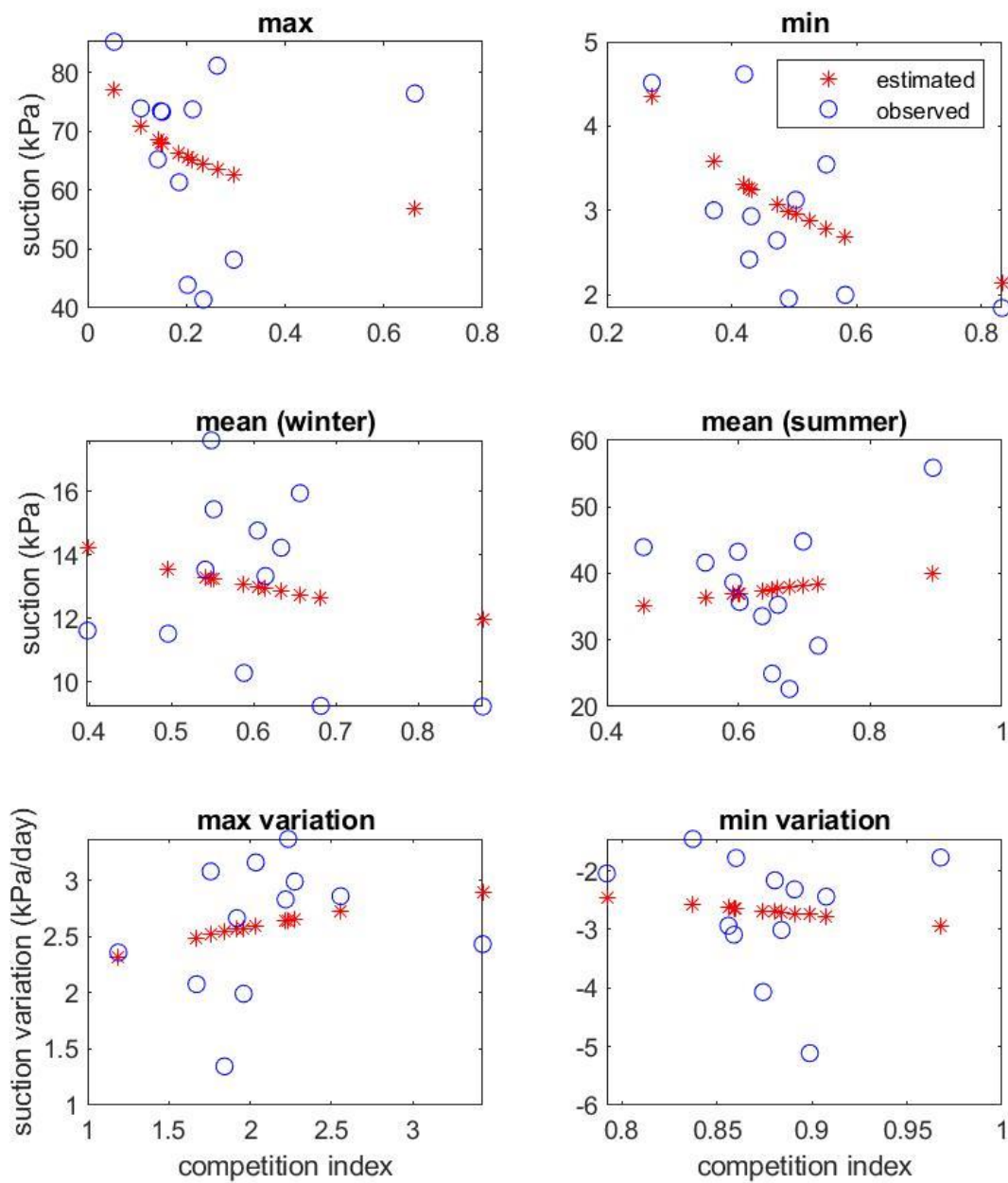


Figure 258 – Spatial distribution of suction in soil A1 considering the effect of the closest tree from the vertical.

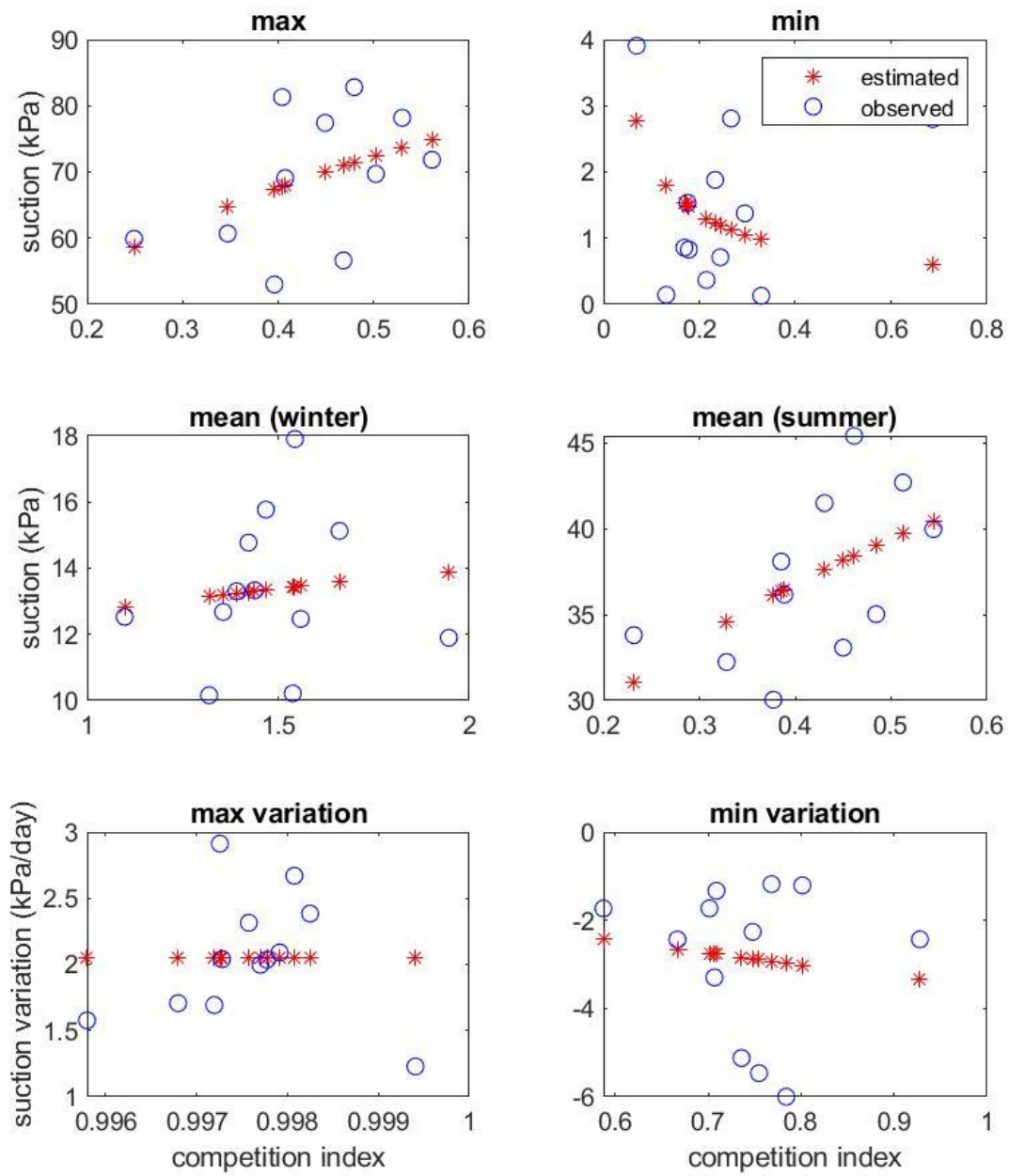


Figure 259 – Spatial distribution of suction in soil A2 considering the effect of the closest tree from the vertical.



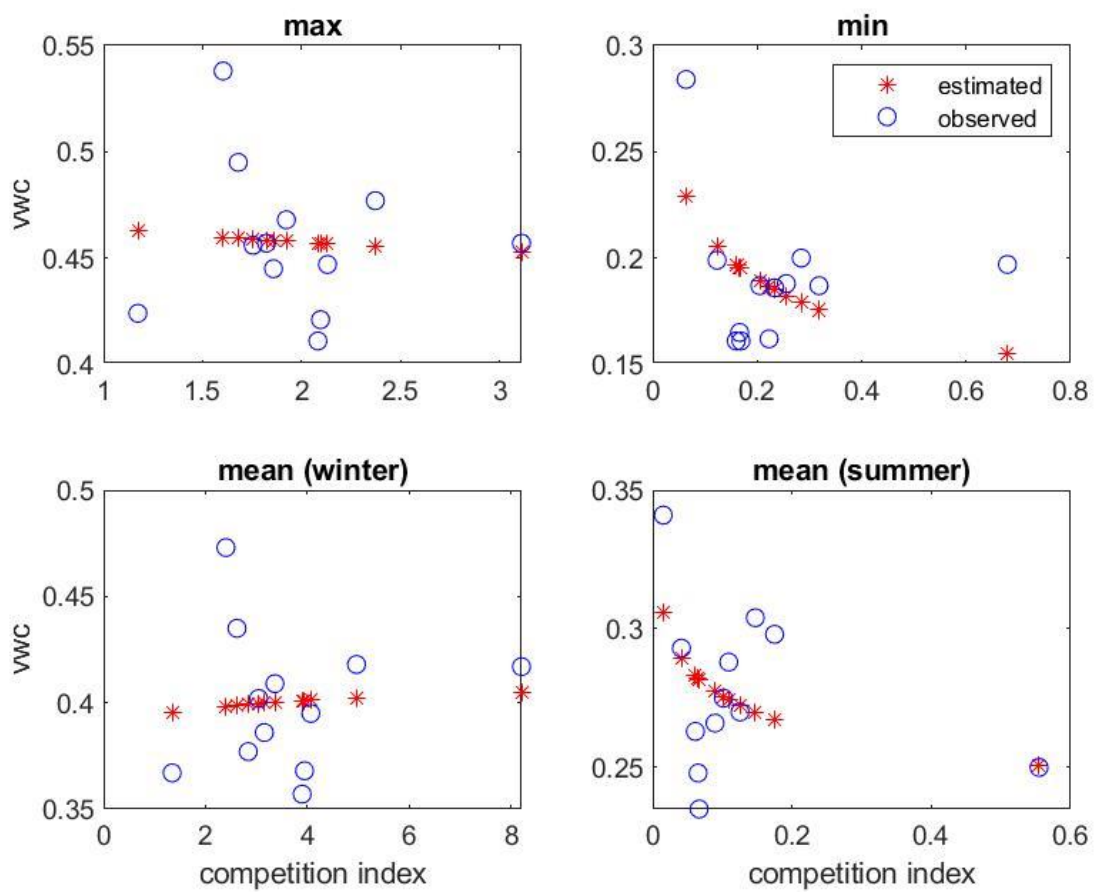


Figure 260 – Spatial distribution of the volumetric water content in soil A1 considering the effect of the closest tree from the vertical.

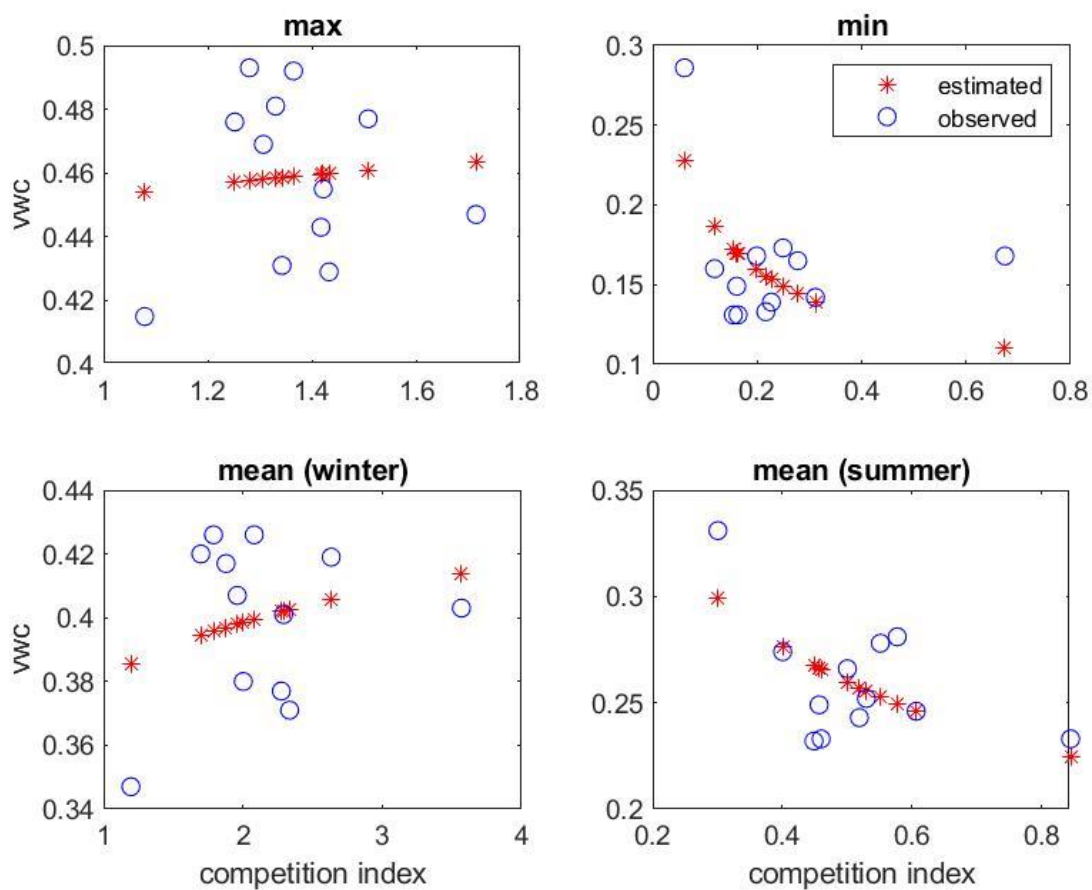


Figure 261 – Spatial distribution of the volumetric water content in soil A2 considering the effect of the closest tree from the vertical.

## Annex X – Fitting parameters of the spatial distribution model adapted to hydraulic observations

Table 62 – Fitting parameters of the spatial distribution model adapted to hydraulic observations.

Soil	Parameters		d_max = 10 m				d_max = 8 m				d_min			
			alpha	m	n	R2	alpha	m	n	R2	alpha	m	n	R2
A1	theta	max	-0.325	0.354	0.089	0.05	-0.800	0.614	-0.076	0.09	-0.241	0.465	-0.023	0.01
		min	0.604	0.182	-0.181	0.55	0.800	0.185	0.024	0.02	0.583	0.146	-0.165	0.23
		mean (winter)	-0.530	0.251	0.129	0.10	-1.500	0.617	-0.071	0.14	-0.446	0.394	0.014	0.01
		mean (summer)	0.900	0.258	-0.063	0.30	0.881	0.272	0.001	0.00	0.888	0.243	-0.055	0.20
	suction	max	0.625	64.634	-0.095	0.09	0.800	67.303	0.042	0.01	0.620	53.995	-0.122	0.10
		min	-0.080	13.103	-0.713	0.48	-0.599	23.103	-0.647	0.52	0.276	1.906	-0.635	0.27
		mean (winter)	0.212	11.829	0.093	0.03	0.024	12.880	0.019	0.00	0.195	11.644	-0.216	0.05
		mean (summer)	0.217	42.541	-0.123	0.04	-0.084	46.568	-0.147	0.04	0.167	40.776	0.189	0.01
		max variation	-0.365	0.990	0.317	0.06	1.200	2.196	-0.086	0.07	-0.261	2.238	0.208	0.06
		min variation	-0.174	-0.267	0.966	0.21	-1.000	-22.583	-0.472	0.18	0.049	-3.025	0.899	0.02
A2	theta	max	-0.168	0.358	0.106	0.17	0.033	0.458	0.003	0.00	-0.114	0.452	0.045	0.01
		min	0.587	0.152	-0.289	0.70	0.028	0.164	-0.068	0.05	0.594	0.098	-0.302	0.35
		mean (winter)	-0.276	0.328	0.073	0.05	-1.500	0.582	-0.061	0.18	-0.270	0.381	0.065	0.08
		mean (summer)	1.403	0.224	-0.057	0.52	0.999	0.244	-0.027	0.06	0.255	0.214	-0.279	0.37
	suction	max	0.388	64.138	0.160	0.32	0.800	76.214	0.085	0.09	0.295	89.138	0.301	0.22
		min	0.159	4.726	-1.038	0.35	-0.120	1.237	-0.008	0.00	0.566	0.465	-0.668	0.08
		mean (winter)	-0.066	11.930	0.056	0.01	0.800	11.876	-0.134	0.19	-0.141	12.632	0.143	0.01
		mean (summer)	0.283	32.103	0.178	0.41	0.800	42.728	0.135	0.29	0.310	48.880	0.310	0.29
		max variation	-0.139	0.595	0.549	0.28	-1.500	6.681	-0.189	0.17	0.001	2.056	0.323	0.00
		min variation	0.700	-6.000	1.500	0.27	0.588	-3.225	0.263	0.04	0.113	-3.530	0.700	0.02
A1 & A2	gradient	max	-0.021	29.000	-1.121	0.28	0.170	9.000	-1.228	0.23	-0.299	9.000	-1.001	0.37
		min	0.074	-0.056	3.000	0.64	0.554	-9.056	0.461	0.11	-0.422	-12.160	-0.410	0.09
		mean (winter)	1.500	-1.488	0.033	0.00	-1.500	-0.036	0.583	0.24	-0.446	-2.176	-0.406	0.07
		mean (summer)	1.499	-9.000	0.307	0.24	0.800	-5.190	0.260	0.06	-0.552	-9.000	-0.562	0.48

## **Annex Y – Practical steps for the operation of the unsaturated direct shear testing equipment**

### **Phase 0: Sample installation**

The installation and preparation of the cell for the following phase is here described. The soil sample should be installed in a way that good contact is guaranteed with the porous stone at the bottom.

1. Remove excess water from the chamber. The level should be maintained low but water is important to preserve some humidity in the air so that the sample does not dry.
2. Spray the porous stone with distilled water.
3. Zero all the readings [A].
4. Add the bottom ring and attach it with screws.
5. Add the metallic strips to level the gap between the bottom and upper part of the shear box.
6. Add the upper part of the box and put the screws.
7. Block the horizontal load cell.
8. Remove the screws of the upper box and then remove the metallic strips.
9. Zero the horizontal load cell [A].
10. Close the pore pressure.
11. Add the sample using an extruder.
12. Wet the upper porous stone spraying distilled water.
13. Add the upper porous stone using screws on the top to hold it.
14. Remove the screws from the upper porous stone.
15. Add the metallic sphere on which load will be applied during consolidation.
16. Close the chamber.
17. Zero only the vertical stress and the vertical lvdv [A].
18. Open air pressure valve.

### **Phase 1: Suction measurement**

The suction is measured using axis translation technique by applying an air pressure higher than the suction in the sample. The water pressure is measured and so the suction is the difference between the applied cell pressure (air) and the measured pore pressure (water).

19. Add air pressure up to 100 kPa in steps of 10 kPa [B].
20. Enter master control [C].
21. Use suggestive names for the files and phases.
22. Select control [C] and define the next inputs:
  - a. Horizontal tram – no control [-1]
  - b. Vertical tram – no control [-1]

- c. Pore water – no control [-1]
  - d. Cell control – linear [0]
    - i. Start value – 100kPa
    - ii. End value – 100kPa
    - iii. Rate – 3kPa (This parameter is set so that the pressure is adjusted if there is any disturbance of the system)
23. Select pause [P] and introduce “24,0,0” for 24 hours of measurements.
24. Select finish [F].

## Phase 2: Application of water pressure

The water pressure is applied in the sample in order to be able to maintain a constant ~~suction~~ during the consolidation and shear. The

1. Register the values of air and water pressure.
2. Select [F] and adjust the following parameters:
  - a. Interval time – 10min
  - b. Current control – 10 s
  - c. Pump – use a very high value so that the pump is not activated
3. Stop the control [D].
4. Close the tap that connects the porous stone to the pressure transducer.
5. Open the tap that connects the water pressure of the system of the pressure transducer. The pressure should decrease.
6. Apply water pressure of the same value of the previously measured one by increments of 10 kPa [B].
7. Open the tap to connect the system of the porous stone.
8. Select control [C] and define the next inputs:
  - a. Horizontal tram – no control [-1]
  - b. Vertical tram – no control [-1]
  - c. Pore water – linear [0]
    - i. Start value – assigned value of water pressure
    - ii. End value – assigned value of water pressure
    - iii. Rate – 3kPa
  - d. Cell control – linear [0]
    - i. Start value – 100kPa
    - ii. End value – 100kPa
    - iii. Rate – 3kPa
9. Select pause [P] and introduce “24,0,0” for 24 hours of measurements.

10. Select finish [F].

### Phase 3: Consolidation

In the consolidation phase, a vertical load is applied to the soil sample maintaining the water content constant. The suction value is being monitored.

1. Remove the long screw on the vertical load and replace it by a tap.
2. Stop the control [D].
3. Increase the pressure in the vertical tram in steps of 50kPa until an increase in the pressure in the pipe is felt. The pipe should be disconnected from the tram to allow the perception of the increase of pressure.
4. The pipe is connected to the vertical tram and pressure is increased in steps of 10kPa until the movement of the piston initiates.
5. Select control [C] and define the next inputs:
  - a. Horizontal tram – no control [-1]
  - b. Vertical tram – linear [0]
    - i. Start value – the initial measured value plus the value of air pressure in the cell
    - ii. End value – the consolidation stress value plus the value of air pressure in the cell
    - iii. Rate – 5 kPa
  - c. Pore water – linear [0]
    - i. Start value – assigned value of water pressure
    - ii. End value – assigned value of water pressure
    - iii. Rate – 3kPa
  - d. Cell control – linear [0]
    - i. Start value – 100kPa
    - ii. End value – 100kPa
    - iii. Rate – 3kPa
6. Select pause [P] and introduce “24,0,0” for 24 hours of measurements.
7. Select finish [F].

### Phase 4: Shear

The shear phase is performed at constant displacement rate.

1. Open the tap of the horizontal tram.
2. Stop master control [D]
3. Select control [C] and define the next inputs:

- a. Horizontal tram – linear [1]
  - i. Start value – 0 mm
  - ii. End value – 20 mm
  - iii. Rate – 0.1 mm/h
- b. Vertical tram – linear [0]
  - i. Start value – the consolidation stress value plus the value of air pressure in the cell
  - ii. End value – the consolidation stress value plus the value of air pressure in the cell
  - iii. Rate – 5 kPa
- c. Pore water – linear [0]
  - i. Start value – assigned value of water pressure
  - ii. End value – assigned value of water pressure
  - iii. Rate – 3kPa
- d. Cell control – linear [0]
  - i. Start value – 100kPa
  - ii. End value – 100kPa
  - iii. Rate – 3kPa
4. Select pause [P] and introduce “24,0,0” for 24 hours of measurements.
5. Select finish [F].

#### Phase 5: End

1. Stop master control [D].
2. Put the horizontal piston back (rewind the piston) [U].
3. Close the horizontal tram.
4. Close water pressure.
5. Decrease the pressure of the vertical tram in steps of -30 kPa [B].
6. Close the tap of the vertical tram.
7. Remove the screw of the vertical tram.
8. Add the long screw to the vertical tram to hold the vertical loading cell.
9. Decrease all the pressures [N].
10. Close the air pressure valve.
11. Disconnect the air pressure tube from the top of the chamber.
12. Open the chamber.
13. Remove the soil sample and inspect the failure surface.
14. Weight the sample and put it in the oven to determine water content.
15. Clean the porous stones and spray them with distilled water.

## Annex Z – Calculation of root cohesion

The calculation of the root cohesion using the script in

Box 10 requires the functions presented in Box 7 to

Box 9 and two text files with the depth and respective RAR of each diameter class.

*Box 7 – MATLAB function to calculate the roots tensile strength of Castanea sativa.*

```
tensilestrength.m
function [Tr] = tensilestrength(d)
    % Bischetti et al (2009)
    Tr=17.86.*d.^-0.53;

    % Genet et al. (2005)
    % Tr=31.92.*d.^-0.73;
end
```

*Box 8 – MATLAB function of W&W model.*

```
wumodel.m
function [cr] = wumodel(RAR, Tr, k, kk)

    cr=RAR.*Tr;
    cr=sum(cr)*k*kk;

end
```

*Box 9 – MATLAB function of FBM.*

```
fbm.m
function [cr] = fbm(RAR, Tr, d)

force=0.0; % force applied to all roots (MPa)
load=zeros(size(Tr)); % load taken by each root class (MPa)
resistance=Tr.*RAR; % total resistance of each root class
failed=ones(size(Tr)); % rootclasses that failed (1=no, 0=yes)
cr=zeros(1,3);
df=min(resistance(find(resistance~=0)))/10;

% empty diameter classes
failed(find(resistance==0))=0;

for i=1:3

    while sum(failed)~=0
        % distribute the force by the roots
        if i==1
            % number of root classes
            load(find(failed==1))=force/sum(failed);
            load(find(failed==0))=0;
        elseif i==2
            % mean root diameter of the class
            load(find(failed==1))=force.*d(find(failed==1))./sum(d(find(failed==1)));
            load(find(failed==0))=0;
        else

```



```

        % mean root cross-section area class
load(find(failed==1))=force.*RAR(find(failed==1))./sum(RAR(find(failed==1)));
load(find(failed==0))=0;
end

% check which roots failed
if sum(find(load>resistance))>0 % roots failed
    failed(find(load>resistance))=0;
else
    force = force + df;
end
end

% updates
cr(i)=force;
force=0;
load=zeros(size(Tr));
failed=ones(size(Tr));
failed(find(resistance==0))=0;
end
end

```

Box 10 – MATLAB script for the calculation of root cohesion using W&W model and FBM.

```

cohesion.m
clc; clear all;

% root diameter
drange=0:0.5:4.5; drange=[drange; drange+0.5]; drange(end,end)=10; % mm
dmean=(drange(1,:)+drange(2,:))/2; % mm
% root area ratio (root volume ratio in reality)
RAR=importdata('rootvolume.txt');
% exclude last diameter class
RAR(:,end)=[];
dmean(end)=[];

% depth
depth=importdata('depth.txt'); % m
i=1; x=1; limits=zeros(10,2);
while i<length(depth)
    limits(x,1)= i;
    while depth(i)<depth(i+1) && i+1<length(depth)
        i=i+1;
    end
    limits(x,2)=i;
    x=x+1;
    i=i+1;
end
limits(end, end)=length(depth);

% verticals
vert=['1C'; '1E'; '1N'; '1S'; '1W'; '2C'; '2E'; '2N'; '2S'; '2W'];

% roots tensile strength
Trmean=tensilestrength(dmean); % MPa

% constants
k=1; % angle
kk=0.56; % in Bischetti et al (2009)

% W&W model

```

```

crwu=[];
for i=1:length(RAR)
    crwu=[crwu; wumodel(RAR(i,:), Trmean, k, kk)]; % MPa
end
crwu0=[];
for i=1:length(RAR)
    crwu0=[crwu0; wumodel(RAR(i,:), Trmean, k, 1)]; % MPa
end

figure; hold on;
for i=1:length(limits)
    plot(crwu(limits(i,1):limits(i,2)),depth(limits(i,1):limits(i,2)),'*');
end
xlabel('root cohesion (MPa)');
ylabel('depth (m)');
legend('vert'); legend('Location','southeast');
set(gca,'Ydir','reverse');
hold off;

% FBM
crfbm=[];
for i=1:length(RAR)
    crfbm=[crfbm; fbm(RAR(i,:), Trmean, dmean)]; % MPa
end
kfaito=crfbm./crwu0;

for j=1:3

    figure; hold on;
    for i=1:length(limits)
        plot(crfbm(limits(i,1):limits(i,2),j),depth(limits(i,1):limits(i,2)),'*');
    end
    xlabel('root cohesion (MPa)');
    ylabel('depth (m)');
    legend('vert'); legend('Location','southeast');
    set(gca,'Ydir','reverse');
    if j==1
        title('root number');
    elseif j==2
        title('root diameter');
    else
        title('root area');
    end
    hold off;

end

% mean cohesion with depth
zrange=[0 0.2 0.4 0.6 0.8 1 1.4 1.8 2.2 2.5 2.8];
zmean=(zrange(1:end-1)+zrange(2:end))/2;
crmean=zeros(length(zmean),5);
crstdev=zeros(length(zmean),5);
crster=zeros(length(zmean),5);
temp=[];
for i=1:length(zmean) % run the range do depths
    for j=1:length(depth) % check all the points
        if depth(j)>=zrange(i) && depth(j)<=zrange(i+1)
            temp=[temp; crwu(j) crwu0(j) (crfbm(j,1:3))];
        end
    end
end

for k=1:5

```

```

        crmean(i,k)=mean(temp(:,k));
        crstdev(i,k)=std(temp(:,k));
        crstder(i,k)=crstdev(i,k)./(size(temp,1))^0.5;
    end
    temp=[];
end

figure; hold on;
for i=1:5
    plot(crmean(:,i),zmean,'*-');
    % errorbar(crmean(:,i),zmean,crstdev(:,i), 'horizontal');
end
    xlabel('root cohesion (MPa)');
    ylabel('depth (m)');
    legend('W&W', 'W&W0', 'number', 'diameter', 'area');
    legend('Location','southeast');
    set(gca,'Ydir','reverse');
    hold off;
% coefficient k''
coefk=crmean(:,3:5)./crmean(:,2);
kmin=min(coefk);

```

## Annex AA – Root cohesion calculated using different load distribution criteria in FBM

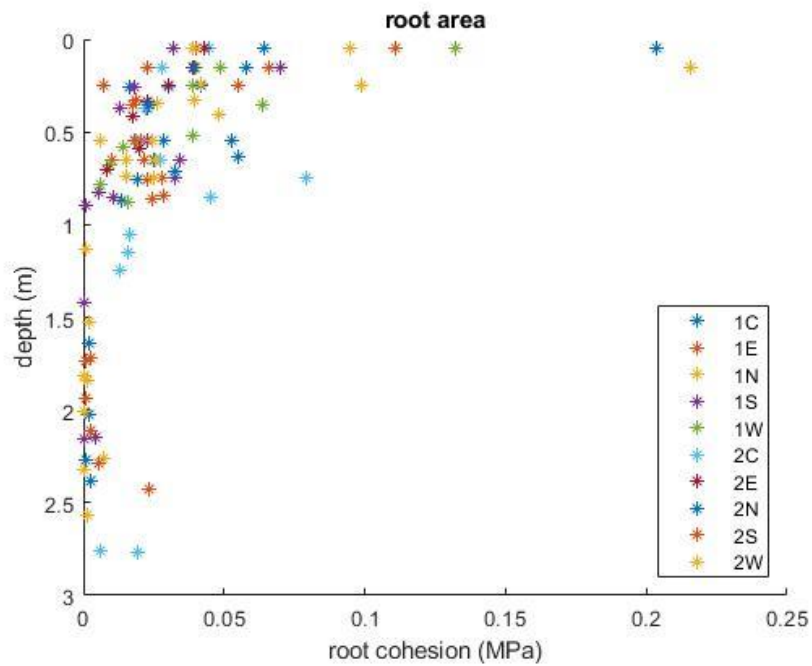


Figure 262 – Root cohesion per vertical with depth FBM (load distributed according to the root cross-section area).

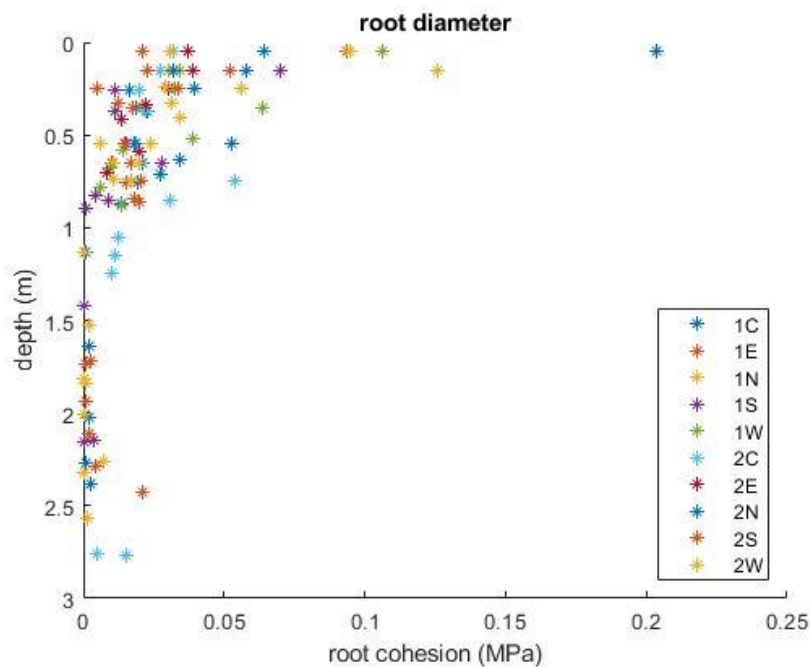


Figure 263 – Root cohesion per vertical with depth FBM (load distributed according to the root diameter).

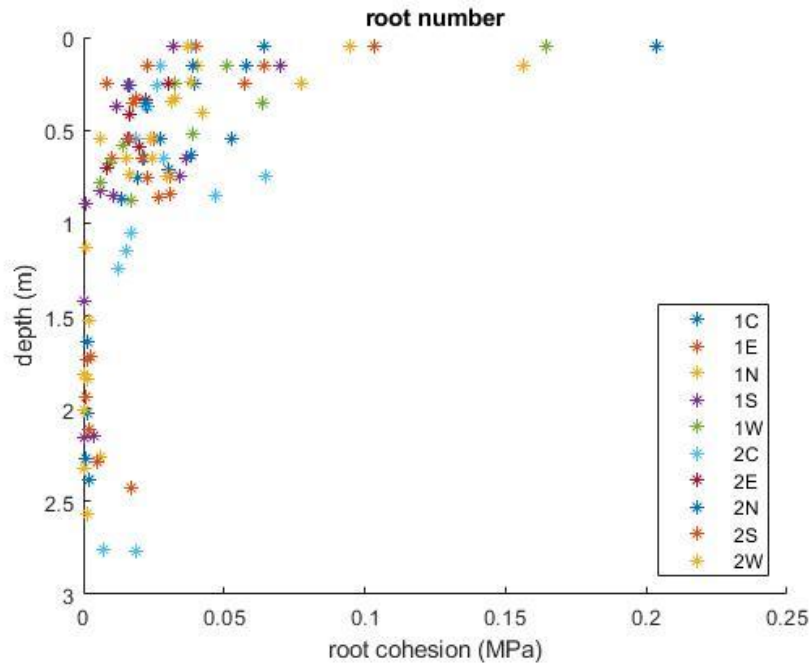


Figure 264 – Root cohesion per vertical with depth FBM (equally distributed load by all roots).

Table 63 – Mean root cohesion with depth using different models in MPa.

depth (m)	W&W	W&W0	FBM		
	k''=0.56	K''=1	number	diameter	area
0.1	0.06807	0.12155	0.06916	0.06031	0.07156
0.3	0.03240	0.05786	0.03034	0.02582	0.03240
0.5	0.02292	0.04094	0.02449	0.02198	0.02539
0.7	0.02512	0.04486	0.02460	0.01946	0.02593
0.9	0.01708	0.03050	0.01898	0.01378	0.01797
1.2	0.01018	0.01818	0.00924	0.00696	0.00927
1.6	0.00119	0.00213	0.00145	0.00147	0.00152
2.0	0.00097	0.00173	0.00120	0.00126	0.00134
2.4	0.00503	0.00898	0.00519	0.00594	0.00654
2.7	0.00744	0.01329	0.00894	0.00701	0.00879

Table 64 – Standard deviation of the root cohesion with depth using different models in MPa.

depth (m)	W&W	W&W0	FBM		
	k''=0.56	K''=1	number	diameter	area
0.1	0.04731	0.08449	0.05065	0.04549	0.05488
0.3	0.02100	0.03750	0.01779	0.01458	0.02106
0.5	0.01168	0.02085	0.01308	0.01274	0.01353
0.7	0.01469	0.02624	0.01375	0.01106	0.01722
0.9	0.01425	0.02545	0.01501	0.00947	0.01425
1.2	0.00901	0.01610	0.00796	0.00586	0.00795
1.6	0.00074	0.00131	0.00084	0.00084	0.00085
2.0	0.00086	0.00154	0.00107	0.00123	0.00127
2.4	0.00700	0.01250	0.00621	0.00765	0.00851
2.7	0.00784	0.01400	0.00886	0.00712	0.00922

Table 65 – Coefficient k'' variation with depth for each load distribution criteria of FBM.

depth (m)	number	diameter	area
0.1	0.57	0.50	0.59
0.3	0.52	0.45	0.56
0.5	0.60	0.54	0.62
0.7	0.55	0.43	0.58
0.9	0.62	0.45	0.59
1.2	0.51	0.38	0.51
1.6	0.68	0.69	0.71
2.0	0.69	0.73	0.77
2.4	0.58	0.66	0.73
2.7	0.67	0.53	0.66
min	0.51	0.38	0.51